

AD-A042 325

BOEING COMMERCIAL AIRPLANE CO SEATTLE WASH F/G 17/7
AIR TRAFFIC CONTROL EXPERIMENTATION AND EVALUATION WITH THE NAS--ETC(U)
SEP 76 A D THOMPSON, B J BURRESON, P F RIEDER DOT-TSC-707-5
D6-44050 FAA-RD-75-173-5 NL

F/G 17/7

UNCLASSIFIED

D6-44050

FAA-RD-75-173-5

NL

1 OF 4
AD
A042325



Report No. FAA-RD-75-173, V

AD A 042325

**AIR TRAFFIC CONTROL EXPERIMENTATION AND EVALUATION
WITH THE NASA ATS-6 SATELLITE**

Volume V: Multipath Channel Characterization Test

A.D. Thompson
B.J. Bureson
P.F. Rieder
P. Alexander

Boeing Commercial Airplane Company
PO Box 3707
Seattle WA 98124



**SEPTEMBER 1976
FINAL REPORT**

Document is available to the U.S. public through the
National Technical Information Service,
Springfield, Virginia 22161

Prepared for

**U.S. DEPARTMENT OF TRANSPORTATION
Federal Aviation Administration
Systems Research and Development Service
Washington DC 20591**

DISTRIBUTION STATEMENT A
Approved for public release;
Distribution Unlimited

AD No. _____
DDC FILE COPY

COPY AVAILABLE TO THE PUBLIC
PERMIT FULLY LEGIBLE PRODUCTION

DDC
RECEIVED
JUL 28 1977
F

NOTICE

This document is disseminated under the sponsorship of the Department of Transportation in the interest of information exchange. The United States Government assumes no liability for its contents or use thereof.

NOTICE

The United States Government does not endorse products or manufacturers. Trade or manufacturers' names appear herein solely because they are considered essential to the object of this report.

(18) FAA-RD-75-173, V TSC

(19) 75-173-5, + FAA-76-22-5

1. Report No. FAA RD-75-173, V	2. Government Accession No.	3. Recipient's Catalog No. (11)
4. Title and Subtitle AIR TRAFFIC CONTROL EXPERIMENTATION AND EVALUATION WITH THE NASA ATS-6 SATELLITE Volume V. Multipath Channel Characterization Test	5. Report Date September 1976	6. Performing Organization Code DOT-TSC-FAA-76-22, V
7. Author(s) A.D. Thompson, B.J. Burreson, P.F. Rieder, P. Alexander	8. Performing Organization Report No. D6-44050	10. Work Unit No. FA711/R7106
9. Performing Organization Name and Address Boeing Commercial Airplane Company* P.O. Box 3707 Seattle, WA 98124	11. Contract or Grant No. DOT-TSC-707-5	13. Type of Report and Period Covered Final Report Sep. 1973 to Dec. 1975
12. Sponsoring Agency Name and Address U.S. Department of Transportation Federal Aviation Administration Systems Research and Development Service Washington, DC 20591	14. Sponsoring Agency Code	
15. Supplementary Notes *Under contract to: U.S. Department of Transportation Transportation Systems Center Kendall Square Cambridge, MA 02142		
16. Abstract Results of aeronautical L-band multipath channel characterization tests are given. All tests were conducted between September 1974 and April 1975 as part of the U.S. DOT aeronautical technology test program. These tests were part of the international Integrated ATS-6 L-Band Experiment coordinated by the NASA/Goddard Space Flight Center. Wideband PN-coded test signals transmitted from an FAA KC-135 jet aircraft were relayed by the ATS-6 satellite for reception by the satellite aeronautical channel prober (SACP) receiver located at the NASA/Rosman ground station. Both oceanic and overland multipath data are analyzed to provide delay-Doppler characterizations of the channel. Specific analysis outputs presented include the delay-Doppler scatter function, delay spectra, Doppler spectra, frequency and time autocorrelation functions, spread parameter measures, total scattered intensity and time-domain statistics. Oceanic results are compared to expectation through the use of physical optics surface integration vector scatter model. Results are presented for a variety of aircraft/satellite geometries, signal polarizations, and terrain states. The report consists of seven volumes: I - Executive Summary; II - Demonstration of Satellite-Supported Communications and Surveillance for Oceanic Air Traffic Control; III - Summary of U.S. Aeronautical Technology Test Programs; IV - Data Reduction and Analysis Software; V - Multipath Channel Characterization Test; VI - Modem Evaluation Test; VII - Aircraft Antenna Evaluation Test.		
17. Key Words (Suggested by Author(s)) Oceanic Multipath, CONUS Multipath, Channel Characterization, Scatter Function, L-Band, SACP Satellite, Delay Spectra, Doppler, Spreads, Autocorrelation, Scatter Coefficient, Fourier Transform, Grazing Angle, Sea Slope.		18. Distribution Statement Document is available to the U.S. public through the National Technical Information Service, Springfield, Virginia 22161
19. Security Classif. (of this report) Unclassified	20. Security Classif. (of this page) Unclassified	21. No. of Pages 360
		22. Price*

*For sale by the National Technical Information Service, Springfield, Virginia 22151

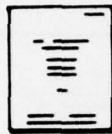
390145

15

**AIR TRAFFIC CONTROL EXPERIMENTATION AND
EVALUATION WITH THE NASA ATS-6 SATELLITE**

FINAL REPORT

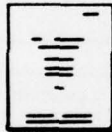
This report consists of the following volumes.



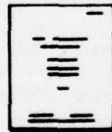
Volume I
Executive Summary



Volume II
**Demonstration of Satellite-Supported Communications
and Surveillance for Oceanic Air Traffic Control**



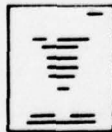
Volume III
**Summary of U.S. Aeronautical Technology
Test Program**



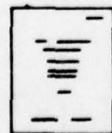
Volume IV
Data Reduction and Analysis Software



Volume V
Multipath Channel Characterization Test



Volume VI
Modem Evaluation Test



Volume VII
Aircraft Antenna Evaluation Test

PREFACE

The U.S. Department of Transportation (DOT) aeronautical test program entitled "Air Traffic Control Experimentation and Evaluation Using the NASA ATS-6 Satellite" was part of the Integrated ATS-6 L-Band Experiment. The overall ATS-6 L-band experiment was coordinated by the NASA/Goddard Space Flight Center (GSFC) and was international in scope. The following agencies were participants in the experiment:

NASA/Goddard Space Flight Center (NASA/GSFC)
 DOT/Federal Aviation Administration (DOT/FAA)
 DOT/Transportation Systems Center (DOT/TSC)
 DOT/U.S. Coast Guard (DOT/USCG)
 DOC/Maritime Administration (DOC/MarAd)
 European Space Agency (ESA)
 Canadian Ministry of Transport and Department of Communications.

Each participant performed tests in one or more of three categories: aeronautical, maritime safety, and maritime fleet operations. All tests were conducted in accordance with an overall integrated test plan coordinated by NASA/GSFC.

The U.S. DOT Aeronautical test program was under the direction and sponsorship of the Federal Aviation Administration, Systems Research and Development Service (SRDS), Satellite Branch, with the DOT/TSC conducting the technology tests and the FAA/NAFEC conducting the ATC demonstration tests. The technology tests included multipath channel characterization, modem evaluation, and aircraft antenna evaluation. Results of these tests are presented in volumes III through VII, and the results of the ATC demonstration tests are presented in volume II. The DOT/TSC test program was supported by the Boeing Commercial Airplane Company under contract DOT-TSC-707. Mr. R. G. Bland was the TSC Project Engineer and Contract Technical Monitor.

This volume describes the multipath channel characterization test. All work was performed under contract DOT-TSC-707. Sections 5.4.6, 6.5, and most of 5.5, as well as appendix C, were prepared by CNR, Inc., under subcontract to the Boeing Commercial Airplane Company.

ACCESSION for	
NTIS	White Section
DDC	Buff Section
UNANNOUNCED	<input type="checkbox"/>
JUSTIFICATION	
BY	
DISTRIBUTION/AVAILABILITY CODES	
Dist. Avail. and/or Special	

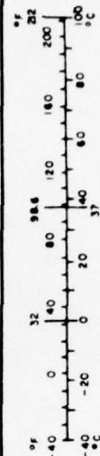
A

2

3

METRIC CONVERSION FACTORS

Approximate Conversions to Metric Measures				Approximate Conversions from Metric Measures			
Symbol	When You Know	Multiply by	To Find	Symbol	When You Know	Multiply by	To Find
LENGTH				LENGTH			
in	inches	2.5	centimeters	cm	centimeters	0.04	inches
ft	feet	30	centimeters	m	meters	0.4	meters
yd	yards	0.9	meters	km	kilometers	3.3	kilometers
mi	miles	1.6	kilometers			1.1	meters
						0.6	miles
AREA				AREA			
in ²	square inches	6.5	square centimeters	cm ²	square centimeters	0.16	square inches
ft ²	square feet	0.09	square meters	m ²	square meters	1.2	square feet
yd ²	square yards	0.8	square meters	km ²	square kilometers	0.4	square miles
mi ²	square miles	2.6	square kilometers	ha	hectares (10,000 m ²)	2.5	acres
	acres	0.4	hectares				
MASS (weight)				MASS (weight)			
oz	ounces	28	grams	g	grams	0.035	ounces
lb	pounds	0.45	kilograms	kg	kilograms	2.2	pounds
	short tons (2,000 lb)	0.9	tonnes	t	tonnes (1,000 kg)	1.1	short tons
VOLUME				VOLUME			
teaspoon	teaspoons	5	milliliters	ml	milliliters	0.03	fluid ounces
tablespoon	tablespoons	15	milliliters	l	liters	2.1	pints
fluid ounce	fluid ounces	30	milliliters	m ³	cubic meters	1.06	quarts
cup	cups	0.24	liters			0.26	gallons
pint	pints	0.47	liters			35	cubic feet
quart	quarts	0.96	liters			1.3	cubic yards
gallon	gallons	3.8	liters				
cubic foot	cubic feet	0.03	cubic meters				
cubic yard	cubic yards	0.76	cubic meters				
TEMPERATURE (exact)				TEMPERATURE (exact)			
°F	Fahrenheit temperature	5/9 (after subtracting 32)	Celsius temperature	°C	Celsius temperature	9/5 (then add 32)	Fahrenheit temperature



CONTENTS

<u>Section</u>	<u>Page</u>
1. INTRODUCTION	1-1/1-2
2. SUMMARY OF RESULTS AND CONCLUSIONS	2-1
2.1 Oceanic Multipath Test	2-1
2.2 CONUS Multipath Test	2-5
3. MULTIPATH TEST DESCRIPTION	3-1
3.1 Objectives	3-1
3.2 Multipath Test Implementation	3-1
3.2.1 Satellite/Aircraft Link Configuration	3-2
3.2.2 Satellite Aeronautical Channel Prober Test Concept	3-2
3.2.3 Terminal Instrumentation	3-5
3.2.4 KC-135 L-Band Antennas	3-8
3.2.5 Sea-State Buoy	3-11
3.3 Multipath Test Geometries and Scenarios	3-12
3.3.1 Oceanic Multipath Tests	3-12
3.3.2 CONUS Multipath Tests	3-14
3.4 Multipath Data Acquisition Summary	3-15
3.5 KC-135 Terminal RF Calibration	3-15
3.5.1 Power Monitoring and RF Insertion Loss	3-15
3.5.2 Relative RF Phase Calibration	3-18
4. MULTIPATH DATA REDUCTION AND ANALYSIS PROCEDURES	4-1
4.1 Data Processing Functional Flow	4-1
4.2 Algorithm Execution Sequence and Analytical Objectives	4-3
4.2.1 Quick-Look Real-Time Playback Data Analysis	4-3
4.2.2 Reformatted SACP Digital Tapes	4-3
4.2.3 Delay-Spectra Time History	4-3
4.2.4 Delay-Doppler Scatter Power Spectral Density: $S(\tau, \omega)$	4-6
4.2.5 Integral and Fourier Operations on $S(\tau, \omega)$	4-6
4.2.6 Channel Spread Parameters	4-7
4.2.7 Noise Determination and Removal (NDandR)	4-7
4.2.8 Antenna-Pattern-Effects Removal	4-7

CONTENTS (Continued)

<u>Section</u>	<u>Page</u>
4.2.9 Tap Amplitude and Phase Distributions	4-7
4.2.10 Tap Process Bank Cross-Correlations	4-8
4.2.11 Tap I and Q Dependency	4-8
4.2.12 Tap-Gain Autocorrelation Function: $U(\tau, \xi)$	4-8
4.2.13 System Calibration Parameter Data	4-9
4.3 Multipath Data Base	4-10
5. OCEANIC MULTIPATH TEST RESULTS	5-1
5.1 Delay-Doppler Scatter Function: $S(\tau, \omega)$	5-1
5.2 Integral and Fourier Operations on the $S(\tau, \omega)$ Function	5-18
5.2.1 Time-Frequency Autocorrelation Function: $R(\xi, \Omega)$	5-19
5.2.2 Delay Spectra: $Q(\tau)$	5-26
5.2.3 Frequency Autocorrelation Function: $R(0, \Omega)$	5-27
5.2.4 Doppler Spectra: $D(\omega)$	5-28
5.2.5 Time Autocorrelation Function: $R(\xi, 0)$	5-29
5.2.6 Total RMS Scattered Energy	5-30
5.3 Ocean Scatter Parameter Spread Values	5-35
5.3.1 Delay Spread	5-37
5.3.2 Frequency Coherence Bandwidth	5-41
5.3.3 Doppler Spread	5-43
5.3.4 Decorrelation Time	5-47
5.4 Time-Domain Statistics	5-49
5.4.1 Tap I and Q Amplitude Distributions	5-50
5.4.2 Tap Phase Distributions and Joint Amplitude Statistics	5-59
5.4.3 Tap I and Q Dependence	5-61
5.4.4 Tap Process Cross-Correlations (Copolarization)	5-63
5.4.5 Tap-Gain Autocorrelation Function	5-74
5.4.6 Cross-Polarization Joint Statistics	5-80
5.4.7 Multipath Signal Stationarity Considerations	5-84
5.5 Cross-Power Spectra for Horizontally and Vertically Polarized Returns	5-90

CONTENTS (Continued)

Section	Page
5.6 Prober Antenna Spatial Filtering Considerations	5-104
5.6.1 Mathematical Basis for Antenna Pattern Removal	5-104
5.6.2 Spatial Filtering Effects on Experimental Data	5-108
5.7 Circular Polarization Prober Results	5-123
5.8 Oceanic Multipath Test Conclusions	5-126
6. POLAR OPTICS SCATTER MODEL PREDICTIONS	6-1
Model Description	6-2
6.2 Delay-Doppler Scatter Function	6-10
6.3 Integral and Fourier Operations On $S(\tau, \omega)$	6-31
6.3.1 Joint Time-Frequency Autocorrelation Function: $R(\xi, \Omega)$	6-31
6.3.2 Delay Spectra	6-32
6.3.3 Frequency Autocorrelation Function $R(0, \Omega)$	6-36
6.3.4 Doppler Spectrum	6-36
6.3.5 Time Autocorrelation Function: $R(\xi, 0)$	6-37
6.3.6 Total RMS Scattered Energy	6-37
6.4 Spread Value Predictions	6-39
6.4.1 Delay Spread	6-40
6.4.2 Coherence Bandwidth	6-43
6.4.3 Doppler Spread	6-48
6.4.4 Decorrelation Time	6-48
6.5 Sea-State Data	6-49
6.5.1 Outline of the Model	6-50
6.5.2 Sea-State Data Reduction	6-54
6.5.3 Discussion of Experimental Results	6-63
7. CONUS MULTIPATH TEST RESULTS	7-1
7.1 Delay-Spectra Time History	7-8
7.1.1 Summary of Observations	7-8
7.1.2 Example Results	7-10

CONTENTS (Concluded)

<u>Section</u>	<u>Page</u>
7.2 CONUS Delay-Doppler Scatter Functions and Associated Parameters	7-27
7.2.1 Low Spreads.	7-28
7.2.2 Modest Spreads.	7-28
7.2.3 Asymmetrical Position Scatter.	7-28
7.2.4 Large Spreads.	7-33
7.2.5 Multimode Scatter.	7-37
7.2.6 Brewster Angle Scatter.	7-40
7.3 RMS Scatter Coefficients	7-43
7.4 Delay Spreads	7-47
7.5 Frequency Coherence Bandwidths	7-50
7.6 Doppler Spreads	7-52
7.7 Decorrelation Times	7-58
7.8 Airport Multipath Environments	7-58
7.8.1 Runway Taxi Conditions	7-61
7.8.2 Approach and Landing Maneuvers	7-61
7.9 CONUS Multipath Test Conclusions	7-69
REFERENCES	R-1
APPENDIX A—Effects of Resolution Limitations Because of Finite Filter Bandwidths and Prober Chip Rates	A-1
APPENDIX B—Effect of Gain Differential Between Quadrature Channels of Multipath SACP Receiver	B-1
APPENDIX C—Equipment Effects on Delay-Doppler Spectrum Estimates	C-1

ILLUSTRATIONS

<u>Figure</u>	<u>Page</u>
3-1 Link Configuration for DOT ATS-6 L-Band ATC Experimentation and Evaluation Tests	3-3
3-2 Satellite Aeronautical Channel Prober (SACP)	3-4

ILLUSTRATIONS (Continued)

Figure		Page
3-3	Simplified KC-135 Terminal for Multipath Test	3-6
3-4	KC-135 Antenna Locations	3-9
3-5	Polarization Switching Unit	3-10
3-6	Modem/Multipath/Antenna Evaluation—Flightpath No. 4	3-13
3-7	KC-135 Multipath Monitoring Subsystem, September 1974 to February 1975	3-17
3-8	KC-135 Multipath Monitoring Subsystem, March and April 1975	3-19
3-9	Relative Phase Measurements for KC-135 Multipath Equipment	3-20
4-1	Data Reduction and Analysis Functional Flow	4-2
4-2	Multipath Algorithm Execution Sequence; Part 1	4-4
4-3	Multipath Algorithm Execution Sequence; Part 2	4-5
5-1	Oceanic Multipath Parameters—Horizontal Polarization, 31° Grazing Angle, In-Plane Geometry	5-4
5-2	Oceanic Multipath Parameters—Horizontal Polarization, 21° Grazing Angle, In-Plane Geometry	5-5
5-3	Oceanic Multipath Parameters—Horizontal Polarization, 16° Grazing Angle, In-Plane Geometry	5-6
5-4	Oceanic Multipath Parameters—Horizontal Polarization, 10° Grazing Angle, In-Plane Geometry	5-7
5-5	Oceanic Multipath Parameters—Horizontal Polarization, 7° Grazing Angle, In-Plane Geometry	5-8
5-6	Oceanic Multipath Parameters—Vertical Polarization, 31° Grazing Angle, In-Plane Geometry	5-9
5-7	Oceanic Multipath Parameters—Vertical Polarization, 16° Grazing Angle, In-Plane Geometry	5-10
5-8	Oceanic Multipath Parameters—Vertical Polarization, 10° Grazing Angle, In-Plane Geometry	5-11
5-9	Oceanic Multipath Parameters—Horizontal Polarization, 18° Grazing Angle, 45° Heading	5-12
5-10	Oceanic Multipath Parameters—Horizontal Polarization, 12° Grazing Angle, 45° Heading	5-13
5-11	Oceanic Multipath Parameters—Horizontal Polarization, 21° Grazing Angle, Cross-Plane Geometry	5-14
5-12	Oceanic Multipath Parameters—Horizontal Polarization, 11° Grazing Angle, Cross-Plane Geometry	5-15
5-13	Mid-Angle $R(\xi, \Omega)$ Distribution—18° Grazing Angle, In-Plane Geometry	5-20
5-14	Mid-Angle $R(\xi, \Omega)$ Distribution—21° Grazing Angle, Cross-Plane Geometry	5-22

ILLUSTRATIONS (Continued)

Figure		Page
5-15	Low-Angle $R(\xi, \Omega)$ Distribution— 14° Grazing Angle, In-Plane Geometry	5-23
5-16	Low-Angle $R(\xi, \Omega)$ Distribution— 15° Grazing Angle, Cross-Plane Geometry	5-25
5-17	Oceanic RMS Total Scatter Coefficients	5-34
5-18	Spread Parameter Definitions	5-36
5-19	Oceanic Delay Spread Results—Horizontal Polarization	5-38
5-20	Oceanic Delay Spread Results—Vertical Polarization	5-39
5-21	Oceanic Coherence Bandwidth Results	5-42
5-22	Oceanic Doppler Spread Results—Horizontal Polarization, In-Plane Geometry	5-44
5-23	Oceanic Doppler Spread Results—Vertical Polarization, In-Plane Geometry	5-44
5-24	Oceanic Doppler Spread Results—Cross-Plane Geometry	5-45
5-25	Oceanic Decorrelation Time Results—In-Plane Geometry	5-48
5-26	Oceanic Decorrelation Time Results—Cross-Plane Geometry	5-48
5-27	Sample Histogram Results—Noise-Only Present	5-52
5-28	Sample Histogram Results—Low Angle, Cross-Plane Geometry	5-53
5-29	Sample Histogram Results—Low Angle, In-Plane Geometry	5-54
5-30	Sample Histogram Results—High Angle, In-Plane Geometry	5-55
5-31	I-Component Amplitude Distribution, Observed χ^2 Significance Levels	5-57
5-32	Q-Component Amplitude Distribution, Observed χ^2 Significance Levels	5-57
5-33	I and Q Amplitude Distribution, Observed χ^2 Significance Levels	5-58
5-34	Phase Distribution, Observed χ^2 Significance Levels	5-58
5-35	Joint I, Q Density, Observed χ^2 Significance Levels	5-62
5-36	I/Q Correlation Coefficients	5-64
5-37	Tap Process Cross-Correlations—Noise-Only Tap Bank Region	5-66
5-38	Tap Process Cross-Correlations—Low Angle, In-Plane Geometry	5-67
5-39	Tap Process Cross-Correlations—Low Angle, Cross-Plane Geometry	5-69
5-40	Tap Process Cross-Correlations—Mid-Angle, Cross-Plane Geometry	5-70
5-41	Tap Process Cross-Correlations—High Angle, In-Plane Geometry	5-71
5-42	$Q(\xi, \tau)$ Distribution—Low Angle, In-Plane Geometry	5-76
5-43	$Q(\xi, \tau)$ Distribution—Low Angle, Cross-Plane Geometry	5-77
5-44	$Q(\xi, \tau)$ Distribution—High Angle, In-Plane Geometry	5-78
5-45	$Q(\xi, \tau)$ Distribution—High Angle, Cross-Plane Geometry	5-79
5-46	Tap-Gain Autocorrelation Function Plots for Stationarity Investigation	5-85
5-47	Aircraft-Satellite Geometry Showing Scattering Surface Symmetry (In-Plane Flight)	5-92
5-48	Theoretical Phase Angle Versus Doppler Shift	5-101
5-49	H-V Cross Power Spectrum Phase Angle Versus Doppler Frequency Shift (10° Specular-Point Grazing Angle)	5-102

ILLUSTRATIONS (Continued)

Figure	Page
5-50 H-V Cross Power Spectrum Phase Angle Versus Doppler Frequency Shift (7.5° Specular-Point Grazing Angle)	5-103
5-51 Front Multipath Antenna Gain Pattern (Horizontal Polarization, Pointed at $\theta = 135^\circ$, $\phi = 0^\circ$)	5-110
5-52 High Angle $G_H(\tau, \omega)$ Distribution	5-111
5-53 High-Angle Antenna Gain Effects Upon the Delay-Doppler Scatter Function	5-112
5-54 High-Angle $\Delta S(\tau, \omega)$ Perturbations	5-113
5-55 High-Angle Antenna Gain Effects Upon Delay and Doppler Spectra	5-114
5-56 High-Angle Antenna Gain Effects Upon Frequency and Time Autocorrelation Functions	5-115
5-57 Front Multipath Antenna Gain Pattern (Horizontal Polarization, Pointed at $\theta = 110^\circ$, $\phi = 0^\circ$)	5-117
5-58 Low-Angle $G_H(\tau, \omega)$ Distribution	5-118
5-59 Low-Angle Antenna Gain Effects Upon the Delay-Doppler Scatter Function	5-119
5-60 Low-Angle $\Delta S(\tau, \omega)$ Perturbations	5-120
5-61 Low-Angle Antenna Gain Effects Upon Delay and Doppler Spectra	5-121
5-62 Low-Angle Antenna Gain Effects Upon Frequency and Time Autocorrelation Functions	5-122
5-63 LHC Polarization Channel Parameters—20° Grazing Angle, In-Plane Geometry . . .	5-124
5-64 RHC Polarization Channel Parameters—21° Grazing Angle, In-Plane Geometry . . .	5-125
6-1 Scatter Model Block Diagram	6-4
6-2 Scatter Model Geometry	6-6
6-3 Model-Predicted Multipath Parameters—Horizontal Polarization 31° Grazing Angle, 12° Slope, In-Plane Geometry	6-12
6-4 Model-Predicted Multipath Parameters—Horizontal Polarization, 31° Grazing Angle, 6° Slope, In-Plane Geometry	6-13
6-5 Model-Predicted Multipath Parameters—Horizontal Polarization, 31° Grazing Angle, 3° Slope, In-Plane Geometry	6-14
6-6 Model-Predicted Multipath Parameters—Horizontal Polarization, 13° Grazing Angle, 12° Slope, In-Plane Geometry	6-15
6-7 Model-Predicted Multipath Parameters—Horizontal Polarization, 13° Grazing Angle, 6° Slope, In-Plane Geometry	6-16
6-8 Model-Predicted Multipath Parameters—Horizontal Polarization, 13° Grazing Angle, 3° Slope, In-Plane Geometry	6-17
6-9 Model-Predicted Multipath Parameters—Horizontal Polarization, 31° Grazing Angle, 12° Slope, Cross-Plane Geometry	6-18

ILLUSTRATIONS (Continued)

Figure	Page
6-10 Model-Predicted Multipath Parameters—Horizontal Polarization, 31° Grazing Angle, 6° Slope, Cross-Plane Geometry	6-19
6-11 Model-Predicted Multipath Parameters—Horizontal Polarization, 31° Grazing Angle, 3° Slope, Cross-Plane Geometry	6-20
6-12 Model-Predicted Multipath Parameters—Horizontal Polarization, 13° Grazing Angle, 12° Slope, Cross-Plane Geometry	6-21
6-13 Model-Predicted Multipath Parameters—Horizontal Polarization, 13° Grazing Angle, 6° Slope, Cross-Plane Geometry	6-22
6-14 Model-Predicted Multipath Parameters—Horizontal Polarization, 13° Grazing Angle, 3° Slope, Cross-Plane Geometry	6-23
6-15 Model-Predicted Multipath Parameters—Vertical Polarization, 31° Grazing Angle, 12° Slope, In-Plane Geometry	6-24
6-16 Model-Predicted Multipath Parameters—Vertical Polarization, 31° Grazing Angle, 6° Slope, In-Plane Geometry	6-25
6-17 Model-Predicted Multipath Parameters—Vertical Polarization, 31° Grazing Angle, 3° Slope, In-Plane Geometry	6-26
6-18 Model-Predicted Multipath Parameters—Vertical Polarization, 13° Grazing Angle, 12° Slope, In-Plane Geometry	6-27
6-19 Model-Predicted Multipath Parameters—Vertical Polarization, 13° Grazing Angle, 6° Slope, In-Plane Geometry	6-28
6-20 Model-Predicted Multipath Parameters—Vertical Polarization, 13° Grazing Angle, 3° Slope, In-Plane Geometry	6-29
6-21 Model-Predicted $R(\xi, \Omega)$ Distribution, In-Plane Geometry	6-33
6-22 Model-Predicted $R(\xi, \Omega)$ Distribution, Cross-Plane Geometry	6-35
6-23 Model-Predicted Oceanic Scatter Coefficients	6-38
6-24 Model-Predicted Delay Spread—Horizontal Polarization	6-41
6-25 Model-Predicted Delay Spread—Vertical Polarization	6-41
6-26 Model-Predicted Delay Spread (Second Moment)—Vertical Polarization	6-42
6-27 Model-Predicted Delay Spread (Second Moment)—Horizontal Polarization	6-42
6-28 Model-Predicted 3-dB Coherence Bandwidth	6-44
6-29 Model-Predicted Doppler Spread—Horizontal Polarization, In-Plane Geometry	6-45
6-30 Model-Predicted Doppler Spread—Vertical Polarization, In-Plane Geometry	6-45
6-31 Model-Predicted Doppler Spread—Horizontal Polarization, Cross-Plane Geometry	6-46
6-32 Model-Predicted Decorrelation Time—Horizontal Polarization, In-Plane Geometry	6-46
6-33 Model-Predicted Decorrelation Time—Vertical Polarization, In-Plane Geometry	6-47
6-34 Model-Predicted Decorrelation Time—Horizontal Polarization, Cross-Plane Geometry	6-47

ILLUSTRATIONS (Continued)

Figure	Page
6-35 Schematic Representation of Ocean Surface Power Spectral Density	6-52
6-36 Geometric Configuration of Wave-Slope PDF From Tape SSD01	6-57
6-37 Marginal (X Direction) PDF of Wave-Slope PDF From Tape SSD01	6-58
6-38 Marginal PDF (Y Direction) of Wave-Slope PDF From Tape SSD01	6-59
6-39 Geometric Configuration of Wave-Slope PDF From Tape SSD04	6-60
6-40 Marginal PDF (X Direction) of Wave-Slope PDF From Tape SSD04	6-61
6-41 Marginal PDF (Y Direction) of Wave-Slope PDF From Tape SSD04	6-62
6-42 Acceleration Probability Density—March 25, 1975	6-64
6-43 Acceleration Probability Density—March 31, 1975 (First 800 sec)	6-65
6-44 Acceleration and Height Power Spectra, March 25, 1975	6-66
6-45 Acceleration and Height Power Spectra, March 31, 1975 (Last 800 sec)	6-67
6-46 Wave-Staff Probability Densities From Tape SSD01	6-68
6-47 Wave-Staff Probability Densities From Tape SSD04	6-69
6-48 Configuration of Wave-Staff Standard Deviations for Sea-State Data, Tape SSD01	6-70
6-49 Configuration of Wave-Staff Standard Deviation for Sea-State Data, Tape SSD04	6-71
6-50 Wave-Staff Power Spectrum Comparison	6-72
6-51 Wave-Staff and Accelerometer Height Power Spectra, March 25, 1975	6-73
6-52 Wave-Staff and Accelerometer Height Power Spectra, March 31, 1975	6-74
7-1 September 19, 1974, Flightpath Specular-Point Trajectory	7-3
7-2 October 30, 1974, Flightpath Specular-Point Trajectory	7-4
7-3 February 18, 1975, Flightpath Specular-Point Trajectory	7-5
7-4 February 19, 1975, Flightpath Specular-Point Trajectory	7-6
7-5 February 20, 1975, Flightpath Specular-Point Trajectory	7-7
7-6 Specular-Point Trajectory (September 19, 1974)—New York City, Harbor	7-11
7-7 Example of CONUS Delay-Spectra Time History	7-12
7-8 Specular-Point Overlay, Leg F-G, February 20, 1975	7-17
7-9 Delay-Spectra Time History—Leg F-G, Horizontal Polarization, February 20, 1975	7-18
7-10 Delay-Spectra Time History—Leg F-G, Vertical Polarization, February 20, 1975 (2-min Time Interval No. 4)	7-23
7-11 Delay-Spectrum Time History, Lake Michigan North Shoreline, February 19, 1975	7-24
7-12 Delay-Spectra Time History, Lake Michigan—Ice—February 19, 1975	7-25
7-13 Delay-Spectra Time History, Lake Michigan Liquid—February 19, 1975	7-26
7-14 CONUS Scatter Channel Parameters, $S(\tau, \omega)_{76}$	7-29
7-15 CONUS Scatter Channel Parameters, $R(\xi, \Omega)_{76}$	7-30
7-16 CONUS Scatter Channel Parameters, $S(\tau, \omega)_{40}$	7-31
7-17 CONUS Scatter Channel Parameters, $S(\tau, \omega)_{48}$	7-32

ILLUSTRATIONS (Concluded)

Figure		Page
7-18	CONUS Scatter Channel Parameters, $S(\tau, \omega)$	7-34
7-19	CONUS Scatter Channel Parameters, $S(\tau, \omega)$	7-35
7-20	CONUS Scatter Channel Parameters, $R(\xi, \Omega)$	7-36
7-21	CONUS Scatter Channel Parameters, $S(\tau, \omega)$	7-38
7-22	CONUS Scatter Channel Parameters, $S(\tau, \omega)$	7-39
7-23	CONUS Scatter Channel Parameters, $S(\tau, \omega)$	7-41
7-24	CONUS Scatter Channel Parameters, $S(\tau, \omega)$	7-42
7-25	CONUS RMS Scatter Coefficients—Horizontal Polarization	7-45
7-26	CONUS RMS Scatter Coefficients—Vertical Polarization	7-46
7-27	CONUS Scatter Delay Spread, 3-dB Value	7-48
7-28	CONUS Scatter Delay Spread, 10-dB Value	7-49
7-29	CONUS Scatter Coherence Bandwidth	7-51
7-30	Three-dB CONUS Scatter Doppler Spread, Fall Flights	7-53
7-31	Three-dB CONUS Scatter Doppler Spread, Winter Flights	7-54
7-32	Ten-dB CONUS Scatter Doppler Spread, Fall Flights	7-55
7-33	Ten-dB CONUS Scatter Doppler Spread, Winter Flights	7-56
7-34	CONUS Scatter Decorrelation Time, Fall Flights	7-59
7-35	CONUS Scatter Decorrelation Time, Winter Flights	7-60
7-36	Pilot's Log of Landing and Taxi at O'Hare, February 19, 1975	7-62
7-37	O'Hare Delay-Spectra Time History	7-63
7-38	O'Hare Delay Spectra (1205:17 GMT)	7-64
7-39	O'Hare Delay Spectra (1206:24 GMT)	7-65
7-40	Airport Environment Multipath Probe—Banking Maneuver	7-67
7-41	Airport Environment Multipath Probe—Landing Descent Phase	7-68
A-1	Line-of-Sight Prober Frequency Autocorrelation Magnitude	A-3
B-1	Gain Differential Effects Upon $S(\tau, \omega)$	B-2
C-1	Definition of Basic Signal-Processing Operation in Prober System	C-4
C-2	Correlation Processing of Multipath Returns	C-7
C-3	Signal-Processing Correlation Functions	C-10
C-4	Digital Filter B Frequency Response (5-MHz Clock Rate)	C-18
C-5	Digital Filter Response With Aliasing	C-19

TABLES

Table		Page
2-1	SUMMARY OF SELECTED MEASURED OCEANIC MULTIPATH PARAMETERS	2-4
2-2	SUMMARY OF MEASURED CONUS MULTIPATH PARAMETERS	2-6
3-1	SATELLITE AERONAUTICAL CHANNEL PROBER (SACP) SYSTEM FEATURES	3-7

TABLES (Concluded)

Table		Page
3-2	TYPICAL OCEANIC MULTIPATH TEST SCENARIO	3-12
3-3	MULTIPATH DATA ACQUISITION SUMMARY	3-16
3-4	MULTIPATH RELATIVE-PHASE MEASUREMENT SUMMARY FOR MARCH 1975 TEST SERIES	3-21
5-1	OCEANIC MULTIPATH PARAMETERS: FIGURE REFERENCE	5-3
5-2	TAP PROCESS CROSS-CORRELATIONS: FIGURE REFERENCE	5-65
5-3	$ Q(\xi, \tau) $ FUNCTION: FIGURE REFERENCE	5-75
5-4	ESTIMATE OF REQUIRED ENSEMBLE LENGTH	5-80
5-5	TEST CONDITIONS AND PROCESS CORRELATION COEFFICIENTS FOR PROCESSED TAPES	5-81
5-6	SIGNAL PLUS NOISE-TO-NOISE RATIOS FOR TEST TAPES EXAMINED	5-81
5-7	HORIZONTAL-VERTICAL CORRELATION COEFFICIENTS (SIGNAL-TO-NOISE COMPENSATED)	5-83
5-8	H-V CROSS-POWER SPECTRUM, MAGNITUDE, AND PHASE, IN-PLANE FLIGHT, MARCH 31, 1975	5-93
5-9	H-V CROSS-POWER SPECTRUM, MAGNITUDE, AND PHASE, IN-PLANE FLIGHT, APRIL 2, 1975	5-95
5-10	PHASE ANGLE OF CROSS-SPECTRUM VERSUS DELAY-DOPPLER COORDINATE, IN-PLANE FLIGHT, MARCH 31, 1975	5-99
5-11	PHASE ANGLE OF CROSS-SPECTRUM VERSUS DELAY-DOPPLER COORDINATE, IN-PLANE FLIGHT, APRIL 2, 1975	5-100
5-12	INFLUENCE OF ANTENNA SPATIAL FILTERING ON SPREAD PARAMETER MEASURES	5-116
5-13	CIRCULAR POLARIZATION SPREAD AND REFLECTION COEFFICIENT MEASURES	5-126
6-1	INPUT TEST PARAMETERS FOR PHYSICAL OPTICS SCATTER MODEL PREDICTIONS	6-1
6-2	MODEL-PREDICTED SCATTER PARAMETERS: FIGURE REFERENCE	6-11
6-3	MODEL-PREDICTED SPREAD PARAMETERS: FIGURE REFERENCE	6-40
6-4	TABULATION OF SEA-STATE TAPES PROCESSED AND PARAMETER VALUES DERIVED	6-55
6-5	COMPARISON OF MEASURED AND PREDICTED SLOPE PARAMETERS	6-76
7-1	SYSTEM PARAMETERS FOR SELECTED CONUS TESTS	7-2
7-2	CONUS $S(\tau, \omega)$ FUNCTION: FIGURE REFERENCE	7-33
7-3	REFERENCE PERMITTIVITY AND CONDUCTIVITY VALUES ASSUMED FOR VARIOUS TERRAINS	7-44
C-1	SACP LOW-PASS FILTERING	C-17
C-2	DIGITAL FILTER COEFFICIENTS	C-17

SYMBOLS AND ABBREVIATIONS

A/C	aircraft
A/D	analog-to-digital
A _D	direct channel antenna gain
A _I	indirect channel antenna gain
ATS-6	Application Technology Satellite 6 (NASA)
AZ _c	azimuth
bpi	bits per inch
BW	bandwidth
c	velocity of light
cw	continuous wave
CL	code length
C/N ₀	carrier-to-noise power density ratio
CONUS	Continental United States (used in general sense to mean overland as distinguished from overocean)
CP	circular polarization
CR	chip rate
C-X-L	C-band to L-band translation
dB	decibel
$\langle D ^2 \rangle$	mean square direct-path signal power
D ₁ , D ₂	code delays (chips)
DOT	Department of Transportation
DRandA	data reduction and analysis
D(ω)	Doppler spectrum
ERP	effective radiated power
f _{.5} , f _{.1}	3-dB, 10-dB Doppler spreads
f _c	carrier frequency
FMP	front multipath (antenna)
G _D	gain factor, direct channel
G _I	gain factor, indirect channel
GSFC	Goddard Space Flight Center
H	horizontal
i	$\sqrt{-1}$
ips	inches per second
$\langle I ^2 \rangle$	mean square multipath power
IF	intermediage frequency
IL	insertion loss
INS	inertial navigation system

SYMBOLS AND ABBREVIATIONS (Continued)

I/O	input/output
I.Q	in-phase, quadrature-phase
IRIG	Inter-Range Instrumentation Group
LHC	left-hand circular
L_{pol}	loss due to polarization (antenna) mismatch
LWSD	left-wing slot dipole (antenna)
L-X-C	L-band to C-band translation
mux	multiplexer
Mbps	mega bits per second
MP	multipath
NDandR	noise determination and removal
NRZ	nonreturn to zero
pdf	<i>probability distribution function</i>
psd	power spectra density
PA	power amplifier
PAT	patch (antenna)
PCM	pulse code modulation
P_D	power, direct channel
PDD	programmable data distributor
PHA	phased-array (antenna)
P_I	power, indirect channel
PM	power meter
PN	pseudo-noise
PSK	phase shift keyed
$P(\phi)$	phase probability density function
QH	quad-helix (antenna)
$Q(\tau)$	delay spectrum
RHC	right-hand circular
RWSD	right-wing slot-dipole (antenna)
RX	receiver
$R_{XY}(\xi)$	cross-correlation function
$R(0,\Omega)$	frequency autocorrelation function
$R(\xi,0)$	time autocorrelation function
$R(\xi,\Omega)$	joint time-frequency autocorrelation function
SACP	satellite aeronautical channel prober
S/I	<i>signal-to-multipath interference ratio</i>
SMP	side multipath (antenna)

SYMBOLS AND ABBREVIATIONS (Concluded)

SRDS	Systems Research and Development Service
$S(\tau, \omega)$	delay-Doppler scatter function
TFE	telemetry front end
TOP/LWSD/RWSD	top, left-wing, and right-wing slot-dipole (antenna)
TSC	Transportation Systems Center
TX	transmitter
$U(\tau, \xi)$	tap-gain autocorrelation function
V	vertical
VHF	very high frequency
V_1	aircraft in-plane velocity
V_\perp	aircraft cross-plane velocity
W/B	wing to body
WSSUS	wide-sense stationary uncorrelated scattering
XLT	cross-slot (antenna)
x_τ	complex process of tap τ in tap bank X
γ	grazing angle
Γ	channel mean square scatter coefficient
μ	mean
$\xi_{.5}, \xi_{.1}$	3-dB, 10-dB decorrelation times
ρ_{HV}	complex H-V correlation coefficient
σ_{slope}	rms surface slope
σ	standard deviation
τ, ξ	time-delay (lag) variables
$\tau_{.5}, \tau_{.1}$	3-dB, 10-dB delay spreads
ϕ_i	phase of i th tap-received signal
χ^2	chi-squared statistic
ω, Ω	frequency offset variables
$\Omega_{.5}, \Omega_{.1}$	3-dB, 10-dB coherence bandwidths.

1. INTRODUCTION

The US aeronautical technology tests were conducted by the U.S. Department of Transportation/Transportation Systems Center (DOT/TSC) as part of the Integrated L-Band Experiment (ref. 1-1). The overall objective of these tests was to provide data for the evaluation of advanced system concepts and hardware applicable to the design of future satellite-based air traffic control systems.

Three types of aeronautical technology tests were conducted by DOT/TSC:

- a. *Multipath Channel Characterization:* Pseudo-noise (PN) code modulated signals were transmitted from the KC-135 using several different antennas and various polarizations. After relay by ATS-6, the signals were received at Rosman, processed by the multipath satellite aeronautical channel prober (SACP) equipment, recorded, and later analyzed to obtain a characterization of the multipath channel.
- b. *Modem Evaluation:* Several voice, digital data, ranging, and hybrid voice/data modems were tested using signals transmitted from Rosman through ATS-6 to the aircraft. Modem demodulator outputs were recorded onboard the aircraft and analyzed to determine performance for various carrier-to-noise density (C/N_0) and signal-to-multipath interference (S/I) ratios. Modem evaluation tests are described in volume VI.
- c. *Antenna Evaluation:* A cw signal radiated by Rosman through ATS-6 was received by the various aircraft antennas under test. Data was recorded and analyzed to evaluate antenna gain and multipath rejection as a function of geometry. The antenna evaluation tests are described in volume VII.

This volume describes the multipath tests. Section 2 summarizes the results and conclusions. Section 3 describes the test implementation, and section 4 provides a summary description of the more important data analysis procedures (a detailed description is given in vol. IV). Section 5 provides experimental results for the overocean multipath tests and compares them with theoretical prediction. Section 6 describes the physical optics scatter model used to predict the overocean multipath channel characteristics. Section 7 describes results obtained for CONUS multipath tests.

2. SUMMARY OF RESULTS AND CONCLUSIONS

Mobile communication systems such as those used by aircraft are subject to multipath interference due to signal reflections from the earth's surface. The degree of system performance degradation caused by such interference depends on many factors, including (1) electromagnetic and roughness parameters of the scattering surface; (2) relative geometry of the aircraft, satellite, and scattering surface; (3) aircraft antenna pattern and signal polarization; and (4) type of message and modulation signal design. The overall test objective was to characterize the multipath sufficiently to provide the technical basis for design of both the signal structure and the hardware for aeronautical satellite communication applications.

A test signal for probing the multipath channel was formed by PSK modulation of three pseudo-noise (PN) codes on separate but frequency-coherent L-band carriers. The three PN codes had different code delays but were otherwise identical. Typically, chip rates of 5 or 10 MHz were used. The test signals were transmitted from the KC-135 using selected aircraft antennas and signal polarizations. After relay by ATS-6, the signals received at the ground station were processed by the satellite aeronautical channel prober (SACP) hardware and were recorded for off-line computer analysis. Overocean multipath data was acquired for satellite elevation angles between 3° and 32° . Overland multipath tests were conducted for various terrain types for both summer and winter conditions. Analysis of these data has concentrated primarily on determining the channel's delay-Doppler scatter function and its associated integral and Fourier parameters. In addition, for the oceanic multipath channel, a scatter model was validated, the spatial filtering effect of the prober antenna was isolated, and selected data sequences were processed to determine time-domain statistics and cross-power spectra.

2.1 OCEANIC MULTIPATH TEST

A major portion of the oceanic multipath analysis effort was directed toward verification of an appropriate scatter model that could extend the experimental results to the prediction of performance for future aeronautical satellite systems. Toward this end, a vector formulation of the widely accepted physical optics very-rough-surface scatter model has been used to correlate theory with experiment. In applying the model, the scatter cross section, coupled with complex polarization transmission coefficients, was numerically integrated over the total effective multipath surface. Model predictions were generated for a variety of surface rms slope conditions and were shown to closely emulate the measured multipath channel characteristics. These predictions and the corresponding comparisons were conducted at the level of the delay-Doppler scatter function and its associated lower order integral and Fourier parameters.

The delay-Doppler scatter function, $S(\tau, \omega)$, was found to have quite pronounced dependencies upon grazing angle, aircraft heading, and rms sea slope. Sea-slope dependencies were investigated mainly through use of model predictions. These predictions were based on an isotropic slope distribution possessing a Gaussian form. Sea-slope distributions used in model predictions were verified by sea-state buoy measurement data. With the exception of the absolute level of its power spectral density, $S(\tau, \omega)$ is only mildly dependent upon the electromagnetic polarization (horizontal, vertical, or circular) of the incident probing signal. This is particularly the case for the high-angle data, whereas at the lower grazing angles the effect of the vertical polarization reflection coefficient's spatial variation is in evidence. The sea-surface slope strongly influences the dispersion in both the delay and Doppler coordinates. More specifically, an increase in rms slope results in both increased delay dispersion and Doppler dispersion. The distribution of energy in the Doppler coordinate is also a strong function of grazing angle and aircraft heading. As the flight direction departs from the cross-plane direction, the energy distribution in the Doppler realm is no longer symmetrical with respect to the specular-point frequency. This asymmetry increases as the flight direction approaches the in-plane condition and results in the negative-frequency realm of $S(\tau, \omega)$ being significantly more spread than the positive-frequency region.¹ Elevation angle effects are primarily related to the Doppler frequency; for a decrease in elevation angle, the dispersion in the Doppler coordinate also decreases, while the asymmetry of the in-plane $S(\tau, \omega)$ function increases. Hence, $S(\tau, \omega)$ has maximum asymmetry for a combination of low-grazing-angle, high-sea-surface slope, and in-plane flight geometry.

When $S(\tau, \omega)$ is reduced to lower order parameters via integral and Fourier transform operations, its properties are generally more self-evident. Using these techniques, the channel's delay spectra, Doppler spectra, frequency autocorrelation function, and time autocorrelation function have been derived. The observed delay spectra exhibit the expected monotonic decay as a function of tap number, with the specular-point tap possessing the maximum density. The delay-spectra data showed no significant dependence upon grazing angle or flight direction. Model emulations show that the dispersion of the delay spectrum increases substantially for an increase in surface slope. The Doppler spectrum measurements exhibited a Gaussian-like distribution associated with the cross-plane flight conditions and a very asymmetrical "ramp-like" relationship for the in-plane direction. For a decrease in grazing angle, the variance of the cross-plane Gaussian Doppler spectrum decreases whereas the ramp slope of the in-plane distribution increases, with the spectrum possessing an abrupt upper frequency limit. Again, model emulation shows that an increase in sea slope results in an increase in the dispersion of the Doppler spectrum. The frequency autocorrelation function and the delay spectra are a Fourier transform pair; similarly, the time autocorrelation function and the Doppler spectra are

¹The frequency realm corresponding to scatter from the region on the "subaircraft" side of the specular point will exhibit the larger spread. For these tests, the in-plane flights were toward the satellite, and hence the negative-frequency realm shows the larger spread. For in-plane flights away from the satellite, the positive-frequency realm would have the larger spread.

another Fourier transform pair. Thus the time autocorrelation and frequency autocorrelation function dependencies upon grazing angle, flight direction, and sea slope are extensions from the above discussion (i.e., an increase in spread of a function results in a decrease in spread of its Fourier transform). These inverse relationships are clearly visible between the Fourier transform pair elements calculated from the data. It is of interest to note that, compared with the Doppler spectrum properties, the shape of the time autocorrelation function is not nearly so dependent upon aircraft heading. However it is apparent that the in-plane result is somewhat heavier tailed than the cross-plane result, as expected.

The total energy content of the scattered signal and the spread measures of the above spectra and autocorrelation functions represent the lowest echelon of channel characterization and were calculated as a function of polarization and grazing angle. Horizontal and vertical polarization total scatter coefficients were found to be within 1 or 2 dB of results predicted by the physical optics vector scatter model. The experimental scatter coefficient dependency upon sea slope was not determined explicitly because sea-slope measurements were not available for the exact times and locations of the multipath tests. The model predictions, however, indicated that the scatter coefficient magnitudes, for grazing angles above 10° , were only weakly dependent upon sea-surface slope. With the exception of the low-angle vertical polarization data, the scatter coefficients are roughly equivalent to the product of the divergence factor and Fresnel smooth-earth reflection coefficient. The low-angle vertical results are some 3 to 5 dB above this relationship; this is not unexpected and may be explained by the concept of "Brewster angle fill-in," which is discussed in more detail in section 5.2.6.

Channel spread measures were presented as a function of grazing angle. No appreciable grazing angle dependence was apparent for the delay spread data. Average delay spreads were almost constant (less than 20% change) for grazing angles ranging between 10° and 30° . The 3-dB delay spreads ranged from a low of $0.25 \mu\text{sec}$ to a high of $1.8 \mu\text{sec}$ and had a typical value of $0.8 \mu\text{sec}$; the 10-dB delay spreads ranged from 2.2 to $5.6 \mu\text{sec}$ and had an average value of $3.2 \mu\text{sec}$. Similarly, the 3-dB coherence bandwidths did not exhibit a strong grazing angle relationship and were observed to vary over a range from 70 to 380 kHz, with the higher values being associated (very weakly) with the higher grazing angles. Doppler spreads exhibited a very strong dependence upon both grazing angle and aircraft heading. For the in-plane geometry condition, very small Doppler spreads are associated with the low grazing angles; for example, at a grazing angle of 8° , typical 3- and 10-dB spread measures of 5 and 44 Hz were measured. These results are significantly lower (by a factor of 4 or more) than those obtained for the cross-plane flight vector and agree with prediction. This phenomenon does not imply a low sea-surface slope and in fact, as shown by the model predictions, the low-angle in-plane Doppler spreads may actually decrease for an increase in sea slope. At the high end of the grazing angle range, the flight direction vector had little influence on Doppler spread. For example, at 30° , the 3- and 10-dB Doppler spreads for in-plane flight were 140 and 350 Hz; the corresponding values for cross-plane flight were only about 30% larger. Measured values of selected oceanic multipath parameters are summarized in table 2-1.

TABLE 2-1. SUMMARY OF SELECTED MEASURED OCEANIC MULTIPATH PARAMETERS

Parameter	Notes	Measured range	Typical value at grazing angle specified		
			8°	15°	30°
RMS scatter coefficient (horizontal polarization)	b	-5.5 to -0.5 dB	-2.5 dB	-1.0 dB	-1.0 dB
RMS scatter coefficient (vertical polarization)	a	-15.0 to -2.5 dB	-14.0 dB	-9.0 dB	-3.5 dB
Delay spread	b				
3-dB value		0.25 to 1.8 μ sec	0.6 μ sec	0.8 μ sec	0.8 μ sec
10-dB value		2.2 to 5.6 μ sec	2.8 μ sec	3.2 μ sec	3.2 μ sec
Coherence bandwidth (3-dB value)	b	70 to 380 kHz	160 kHz	200 kHz	200 kHz
Doppler spread (in-plane geometry)	c				
3-dB value		4 to 190 Hz	5 Hz	70 Hz	140 Hz
10-dB value		13 to 350 Hz	44 Hz	180 Hz	350 Hz
Doppler spread (cross-plane geometry)	c				
3-dB value		79 to 240 Hz	79 Hz*	110 Hz	190 Hz
10-dB value		180 to 560 Hz	180 Hz*	280 Hz	470 Hz
Decorrelation time (3-dB value)	d	1.3 to 10 msec	7.5 msec	3.2 msec	2.2 msec

Notes:

*At 10° grazing angle

- a. Strong dependence on grazing angle, especially near Brewster angle
- b. No strong grazing-angle dependence
- c. Strong grazing-angle dependence
- d. Strong inverse dependence on grazing angle.

An additional dimension of the interrelationship between the oceanic surface and the complex vector nature of electromagnetic propagation was investigated by determining the degree of correlation between the simultaneous vertical and horizontal probes and by separately using right- and left-hand circular (RHC and LHC) polarization probes. With the exception of the received signal's absolute amplitude, the circular polarization data was shown to possess attributes similar to those of the linear polarization probes. With respect to the total received scattered energy during tests with circularly polarized (CP) probes, the results illustrate the phenomenon of surface-induced polarization sense reversal. This is evident since probes transmitted from the aircraft with LHC polarization are received more favorably at the right-hand circularly polarized satellite than probes transmitted with RHC polarization. The degree of correlation between the probe's horizontal and vertical polarizations was investigated by determining the amplitude of the correlation coefficient between the two signals and by examining the phase of their complex cross-power spectra. In both cases, results are in accord with vector scatter theory and indicate that the orthogonal polarization multipath processes are highly correlated, with the Fresnel reflection coefficients providing the appropriate phase relationship between the scattered vertical and horizontal probes.

Investigations were made pertaining to the complex Gaussian wide-sense stationary uncorrelated scattering (WSSUS) properties of the oceanic multipath process. After rather extensive testing, we have statistical bases for support of both the complex Gaussian statistics hypothesis and the assumption that the scatterers are uncorrelated. Also, the channel's wide-sense stationary characteristics were examined over a relatively short timespan and appeared to exhibit time-invariant statistical properties. While this test was by no means comprehensive, it is thought to be representative of expectations in that the scattering physics are influenced primarily by the surface's slope probability distribution function (pdf), which changes in a manner roughly proportional to the square root of the wind velocity. Thus, one may confidently represent the oceanic channel as a complex Gaussian WSSUS scatter process. Under these conditions the $S(\tau, \omega)$ function completely describes all statistical attributes of the channel. Since this function and the lower order measures are well duplicated by the physical optics vector scatter model, the results of this test may be easily extended and applied to detailed analyses and design of future oceanic L-band systems.

2.2 CONUS MULTIPATH TEST

One of the most obvious characteristics of the overland CONUS scatter data is its high degree of signal structure nonstationarity. This was readily confirmed through a visual observation of several delay-spectra time history segments. Similarly, the signature of the channel's delay-Doppler scatter function varies markedly with specular-point location and was used to isolate periods of very low spreading, modest spreading, biased positional scatter, large irregular Doppler spectra return, and mixed scatter process return. These data were used to delineate the salient features associated with terrain types falling under the categories of heavy vegetation cover, coastal harbors, large cities, large lakes and snow-covered plains and mountains.

The above properties of nonstationarity appear to mask out any systematic grazing angle, flight direction, or polarization dependencies that might exist for the channel's rms scatter coefficients and spread parameter measures. Table 2-2 summarizes the observed range and typical values associated with the unidimensional channel parameters.

Results from analyses of data gathered during the airport environment multipath probe were presented for test sequences entailing runway taxi, landing, and low-altitude-approach airplane maneuvers. These probes were carried out via a single crossed-slot, low-gain antenna whose polarization was left-hand circular, thus providing enhancement of the multipath signal at the expense of the direct signal. With the airplane moving on the ground, the received signal structure possessed two rather distinct attributes: (1) fairly large amplitude fluctuations of the energy received in the direct line-of-sight signal taps were observed (possibly caused by small-delay multipath components) and (2) only very low levels (at least 20 dB below the direct-path signal) of multipath power were observed for delays greater than 0.2 μ sec relative to the direct signal arrival.

TABLE 2-2. SUMMARY OF MEASURED CONUS MULTIPATH PARAMETERS

Parameter	Measured range	Typical ^a value
RMS scatter coefficient (horizontal polarization)	-18 to +2 dB	-9 dB
RMS scatter coefficient (vertical polarization)	-21 to -3 dB	-13 dB
Delay spread (3 dB)	0.1 to 1.2 μ sec	0.3 μ sec
Delay spread (10 dB)	0.2 to 3.0 μ sec	1.2 μ sec
Coherence bandwidth (3 dB)	150 kHz to 3.0 MHz	600 kHz
Doppler spread (3 dB)	20 to 140 Hz	60 Hz
Doppler spread (10 dB)	40 to 500 Hz	200 Hz
Decorrelation time (3 dB)	1 to 10 msec	4 msec

^a Grazing angle dependencies (if any) masked by nonstationarity properties.

For the approach and landing phases of the airport environment test, the data has been used to identify several fundamental characteristics of the direct and multipath signal components. As expected, airplane banking maneuvers produce substantial changes in the relative direct and multipath signal levels. This was illustrated by an example that showed the antenna's S/I parameter undergoing a change in excess of 20 dB over a time interval of about 15 sec. With respect to the influence of the aircraft's altitude decrease during the descent and landing phases, a corresponding decrease in the differential time delay and a relatively large positive differential Doppler frequency shift between the direct and multipath signals were observed. The differential delay is proportional to altitude only, whereas the differential Doppler depends on angle of approach and aircraft velocity. For the JFK approach at an altitude of approximately 0.7 km, a 34-Hz differential Doppler was measured. One further observation relates to the noted tendency for the multipath signal's delay spread to decrease with a decrease in altitude. This is in accord with theory, which predicts a delay-spectrum dispersion proportional to the altitude of the airplane.

The CONUS multipath test results provide an extensive data base relative to the overland forward-scatter multipath channel. The data base yields valuable information pertaining to scatter signatures associated with a variety of terrain features, such as electrical characteristics, macroscopic roughness (plains, mountains, etc.), and vegetation cover.

3. MULTIPATH TEST DESCRIPTION

Multipath channel characterization tests were conducted both overocean and overland (CONUS). This section describes the test objectives, implementation, and data acquisition procedures.

3.1 OBJECTIVES

For mobile communication systems operating in the vicinity of random rough surfaces, the received electromagnetic signal consists of the superposition of the transmitted direct signal plus terrain-reflected signal replicas having random amplitudes, time delays, and Doppler shifts. These multipath effects should be accounted for in the system design of an aeronautical satellite communication system. Thus the overall test objective was to characterize the multipath sufficiently to allow confident design of both the signal structure and the hardware for aeronautical satellite communication applications. Specific objectives were:

- a. Acquisition and analysis of overocean multipath data to obtain a detailed delay-Doppler characterization of the oceanic multipath channel for various satellite/aircraft geometries, signal polarizations, and sea states.
- b. Evaluation and verification of an oceanic scatter model.
- c. Acquisition and analysis of overland (CONUS) multipath data to determine the essential characteristics corresponding to a range of satellite/aircraft geometries, signal polarizations, and terrain states. Terrain types of interest included mountainous, vegetation-covered, snow-covered, barren (desert), urban (cities), lakes, and airport environments.

Validation of a laboratory multipath channel simulator using the acquired multipath data has also been identified as a DOT/TSC goal. Analysis of simulator requirements and processing of multipath data for simulator applications are planned future efforts to be conducted by DOT/TSC.

3.2 MULTIPATH TEST IMPLEMENTATION

This section describes the satellite/aircraft link, the multipath test concept, and the instrumentation at the aircraft and ground station terminals.

3.2.1 Satellite/Aircraft Link Configuration

During task I of the program, link analyses were performed to evaluate the expected performance of both the forward (Rosman/ATS-6/aircraft) and return (aircraft/ATS-6/Rosman) link configurations for multipath data acquisition. These analyses showed that (1) in either case, the achievable link performance was determined almost entirely by the aircraft/satellite L-band segment, (2) the vertical polarization case was the most critical probe in the signal-to-noise ratio sense because of the higher reflection loss at the sea surface, and (3) for the critical vertical-polarization probe, the return-link configuration (assuming a 100-W aircraft L-band transmitter) offered a signal-to-noise ratio advantage of approximately 7 dB compared with the forward-link mode. Other advantages of the return-link configuration were: (1) it resulted in a simpler and more practical aircraft installation and (2) it provided a convenient means of separating direct path signals and multipath probes using coded time delays as described in section 3.2.2. As a result, the return-link configuration was selected for implementing the multipath tests.

The basic RF link configuration used for all U.S. aeronautical technology tests is shown in figure 3-1. For multipath data acquisition, the test signals were generated onboard the KC-135 aircraft and were transmitted to the ATS-6 satellite for relay to the NASA/Rosman ground station. Forward-link transmissions received at the aircraft were used only for test coordination purposes.

The ATS-6 satellite transponder was configured for L-C, C-L frequency translation and normally operated in the coherent mode. The uplink reference carrier needed for coherent mode operation was usually transmitted from the NASA/Mojave ground station. This mode of operation referenced the frequency-conversion operation of the satellite transponder to a stable ground-based frequency standard, thus eliminating downlink frequency uncertainty and drift associated with the satellite internal master oscillator.

The ATS-6 L-band antenna was used in the fan-beam mode for all oceanic multipath tests. For CONUS tests, the pencil beam was used for several of the test legs flown.

3.2.2 Satellite Aeronautical Channel Prober Test Concept

A block diagram illustrating the satellite aeronautical channel prober (SACP) test concept is shown in figure 3-2. Three pseudo-noise (PN) sequences having different time delays but otherwise identical were generated by the SACP modulator. The values of D_1 and D_2 were selected to allow separation of the three signals by correlation techniques at the SACP receiver. These PN codes were PSK modulated onto RF carriers and were transmitted from the aircraft as the multipath channel test signals. One of these signals was transmitted directly to the satellite for relay to the ground station, where it was used as a reference signal. The other two signals served as the multipath channel probes and were usually transmitted by downward-looking antennas that had selectable pointing and

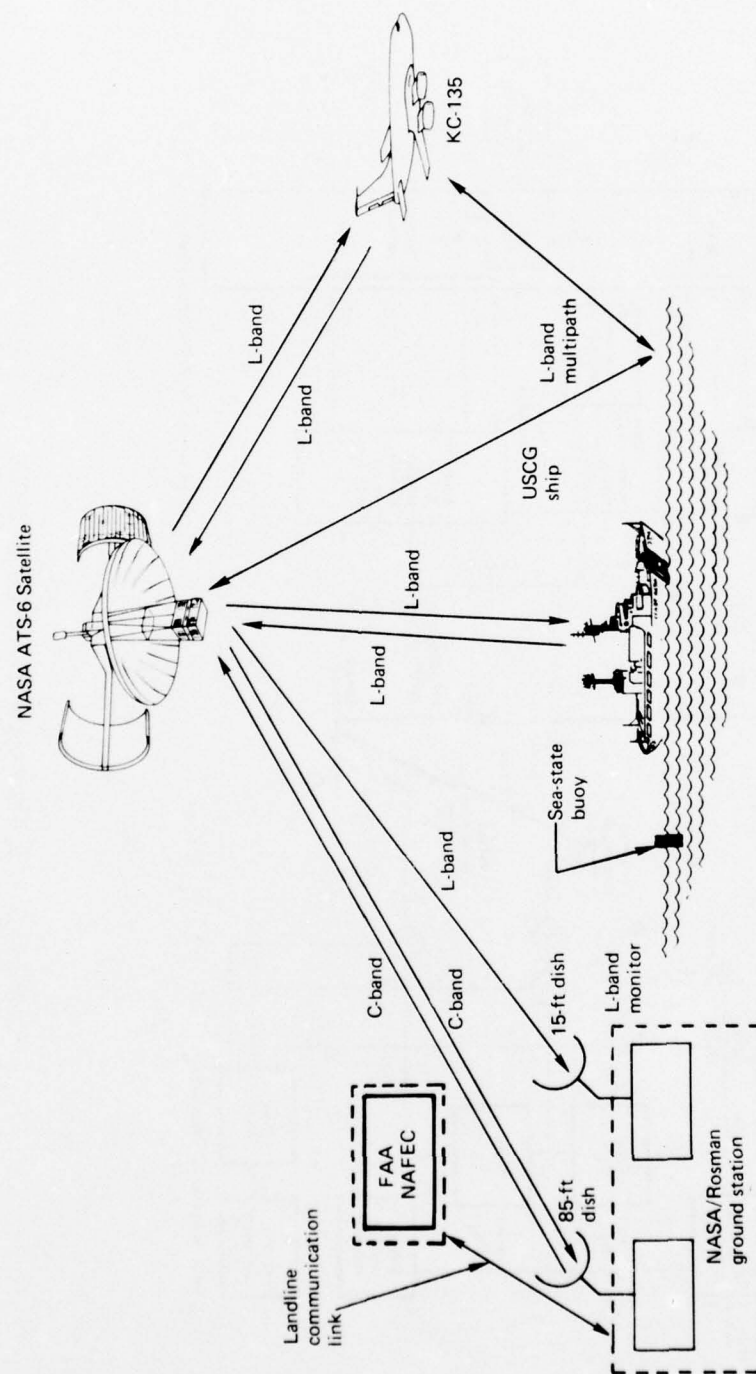


Figure 3-1. Link Configuration for DOT ATS-6 L-Band ATC Experimentation and Evaluation Tests

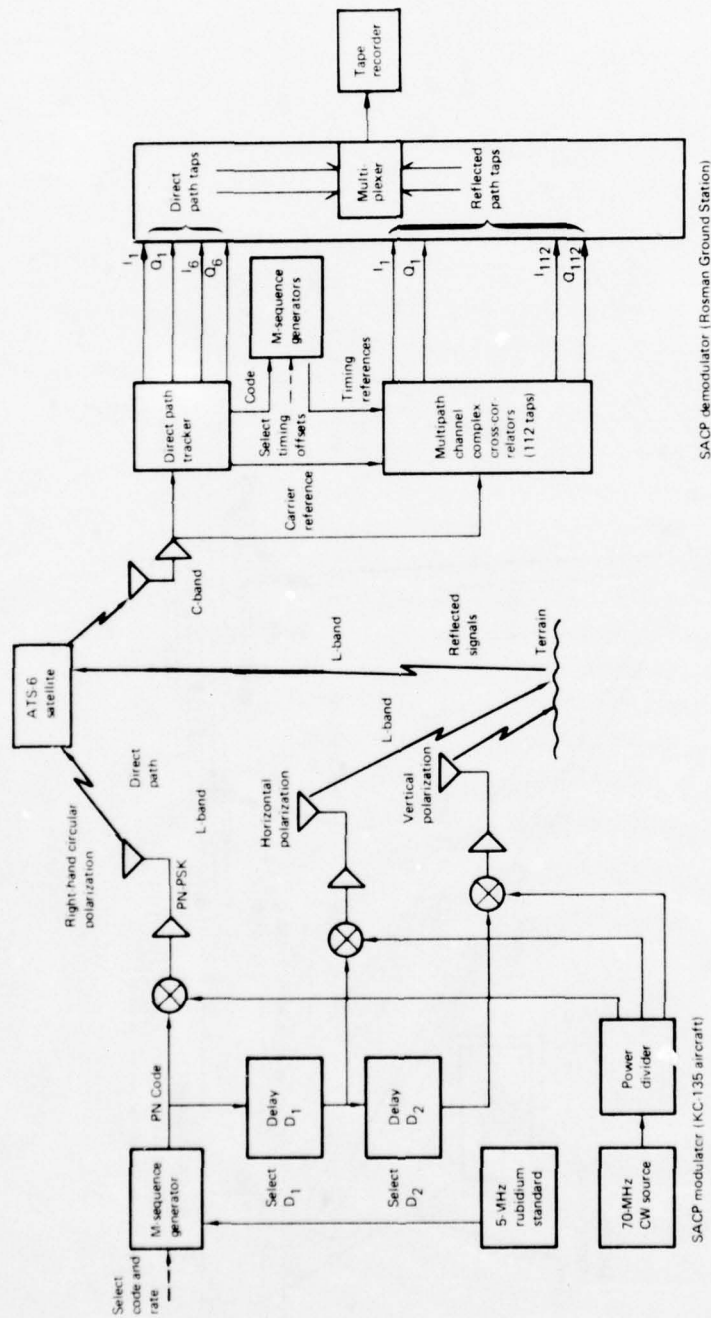


Figure 3-2. Satellite Aeronautical Channel Prober (SACP)

polarization. The three transmitted RF carriers were derived from a common frequency source and hence were coherent. Although constant RF phase differences might have been present due to path length differences in transmitters, these differences were of no consequence for most of the subsequent data analysis.¹

At the ground station, the direct path tracker of the SACP demodulator utilized coherent demodulation to track the carrier phase and PN code received over the direct path. These were used as delay and Doppler references for the 112 complex cross-correlators that processed the received reflected signals. The multipath channel measurements consisted of 112 complex cross-correlation operations between a locally generated PN sequence and the probing signal received over the link. The resultant measurement corresponded to the sampled impulse response of the channel.

The SACP probe hardware was furnished by Stein Associates, Inc.² Principal design features are given in table 3-1. A more detailed discussion is available in reference 3-1 and in appendix C of this volume.

3.2.3 Terminal Instrumentation

3.2.3.1 KC-135 Aircraft Terminal – A functional block diagram for the multipath test is shown in figure 3-3. The SACP modulator generated three PN-PSK 70-MHz IF signals that were identical except for preset time delays between the PN codes. The triple up-converter coherently translated the three signals to 1650 MHz to drive the three multipath transmitters. Each transmitter was connected to a selected L-band antenna. The reference signal (with code delay, T_0) was transmitted directly to ATS-6 via the quad-helix antenna. The other two PN-PSK signals (with code delays D_1 and D_2) drive the horizontal and vertical polarization arrays of the selected multipath antenna – usually the forward multipath antenna. Alternately, a single transmitter could be used with the LWSD/RWSD/TOP slot-dipole system, with the crossed-slot (XLT) antenna, or with the FMP antenna operating in one of its circular polarization modes. Airborne system parameters were recorded on computer-compatible 800-bpi seven-track tape (six bits plus parity) using a Kennedy 8707 recorder. Three HP 435A power meters used in conjunction with directional couplers allowed the RF power output of each channel to be monitored and recorded. Other recorded parameters included IRIG-B time code, SACP modulator code length and chip rate, selected multipath antenna and polarization mode,

¹The transmitted RF phase differences and the effects of the ATS-6 antenna are of significance for portions of the horizontal/vertical polarization cross-correlation analysis. A first-order treatment of these effects is included in the appropriate data analysis sections of this report.

²Stein Associates, Inc., "Instruction Manual for the Satellite Aeronautical Channel Prober: Volume 1, System Description and Operation," contract DOT-TSC-634, June 1974.

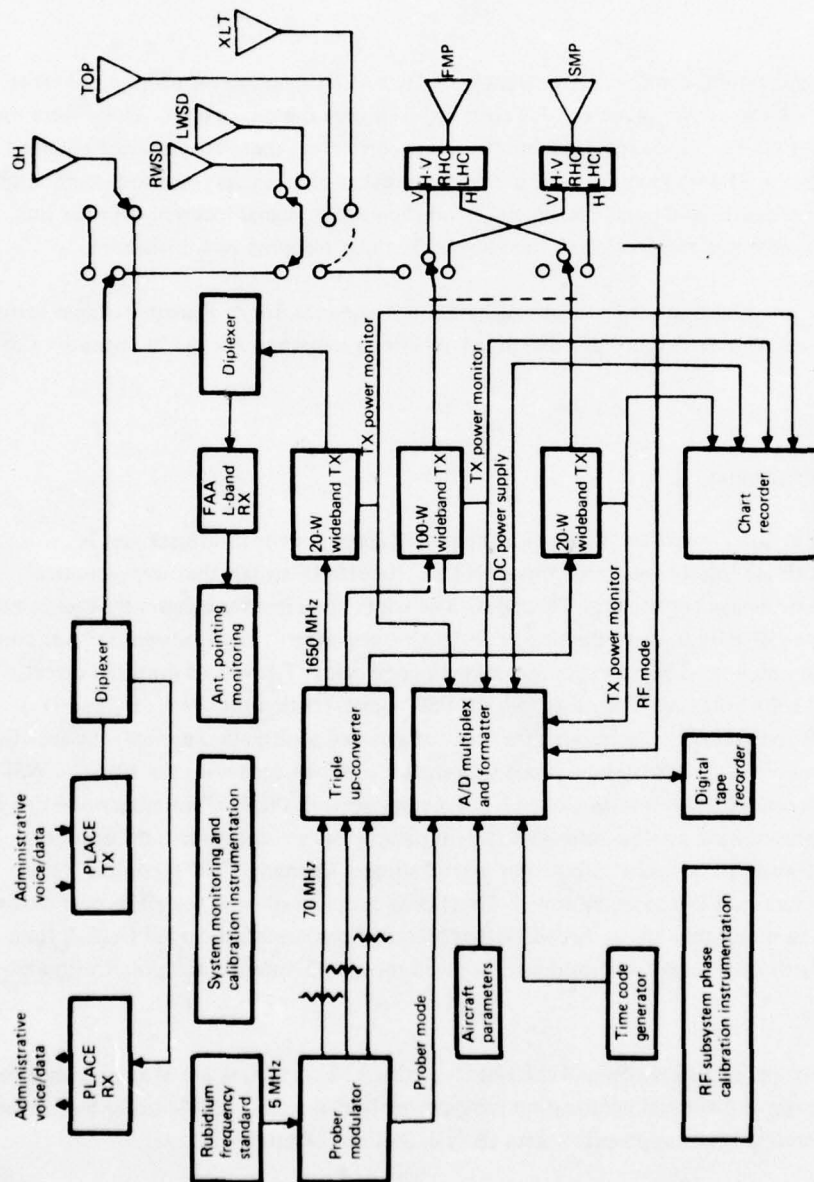


Figure 3-3. Simplified KC-135 Terminal for Multipath Test

internal power monitors of each multipath transmitter, aircraft heading, pitch, roll, altitude, and INS groundspeed. Details of the recording format are given in volume IV.

Nominal RF power outputs of 20 W were used for the direct path and horizontally polarized indirect path, while a 100-W transmitter was used for the vertically polarized indirect path or whenever an operational-type antenna was used. These levels, based on the Task I link analyses, were designed to provide adequate signal-to-noise ratio at the SACP demodulator while not exceeding a signal-to-noise ratio of -15 dB in the ATS-6 satellite 40-MHz IF bandwidth. This latter constraint was necessary to ensure that multipath test signals would be processed linearly by the ATS-6 limiting transponder. Other L-band participants such as MarAd, who used the ATS-6 L-band return link concurrently, also

**TABLE 3-1. SATELLITE AERONAUTICAL CHANNEL PROBER (SACP)
SYSTEM FEATURES**

SACP Transmission Subsystem	
Modulator	
Probing rate (selectable)	0.5, 1.0, 1.25, 2.5, 5.0, 10 Mbps
Modulation	$\pm 90^\circ$ pseudo-random PSK
PN sequence length (selectable)	1023, 511, 255
IF frequency	70 MHz
Power output (into 75 ohms)	0 dBm
SACP Receive Subsystem	
Demodulator	
IF interface frequency	70 MHz
Video PN rates (selectable)	0.5, 1.0, 1.25, 2.5, 5.0, 10.0 Mbps
Number of multipath complex demodulator taps	112
Output multipath tap low-pass filter bandwidths (1 dB) (selectable)	37.5, 75, 150, 300, and 600 Hz
Output tap dynamic range	40 dB
Number of direct path complex demodulator taps and filter characteristics	6 at 20 Hz (3 dB)
Real-Time Display	
Display method	Standard oscilloscope
Parameter displayed	Average power at each complex demodulator output
Number of outputs displayed across scope face	All complex demodulator taps (10-tap selectable zoom)
Averaging time	1/16, 1/4, 1, 4 sec
Input dynamic range	40 dB
Input bandwidth	600 Hz (3 dB)

subjected their transmissions to the same constraint (< -15 dB S/N at the satellite IF point). In addition, frequency assignments were such that co-channel and adjacent-channel interference either did not occur or was held to an acceptably low level.

3.2.3.2 Rosman Ground Station – The return-link signal was received from ATS-6 via the 85-ft antenna and C-band receiver. This signal was down-translated to the 70-MHz IF and was routed to the SACP receiver where it was demodulated, processed, and formatted along with time code for recording on wideband analog tape.

The TSC Ampex FR-1900 and the Rosman station Ampex FR-2000 tape recorders were used to direct record the multiplexed output of the SACP receiver system on seven-track, 1/2-in. analog tape. Recording speeds of 120 ips were used for both oceanic and CONUS data acquisition. For oceanic tests, 7200-ft tapes were normally used to provide uninterrupted recording for a period of 12 min. For CONUS tests, 9600-ft tapes provided uninterrupted recording for 16 min. Data tracks recorded included two multiplexed SACP receiver output data streams (recorded in duplicate for redundancy, thus occupying four tracks), IRIG-A time code, IRIG-B time code, and a bit-synchronization signal. Details of the multiplexed SACP receiver output format are given in volume IV.

3.2.4 KC-135 L-Band Antennas

The approximate locations of the L-band antennas used on the KC-135 test aircraft are shown in figure 3-4. Major features of these antennas are summarized below. Unless otherwise noted, antenna polarization is right-hand circular.

- a. *Quad-Helix (QH) Antenna:* This antenna was used for transmission of the direct signal to ATS-6 during all multipath tests requiring transmission of a separate direct path signal. The antenna has a conical beam shape approximately 19° in width at the 3-dB points. The antenna is mechanically steerable to provide coverage throughout the forward region of the upper hemisphere and provides about 15.5-dB gain toward the satellite for elevation angles above 15° .
- b. *Front Multipath (FMP) Antenna:* The FMP was the principal antenna used for transmission of the terrain-reflected signals during both overocean and CONUS multipath tests. The antenna, located within the nose radome, employs a two-element waveguide array resulting in 1-dB beamwidths of 20° in azimuth and 50° in elevation. Gain was approximately 6 dB and polarization was selectable between RHC, LHC, and dual linear (the horizontal and vertical polarization ports were simultaneously accessible on separate transmission lines). Details of the polarization switching unit are shown in figure 3-5. The antenna was mounted on a two-axis positioner, which permitted it to be mechanically steered anywhere between the horizon and 90° downward in elevation and $\pm 80^\circ$ (to either left or right) from the aircraft nose in azimuth.

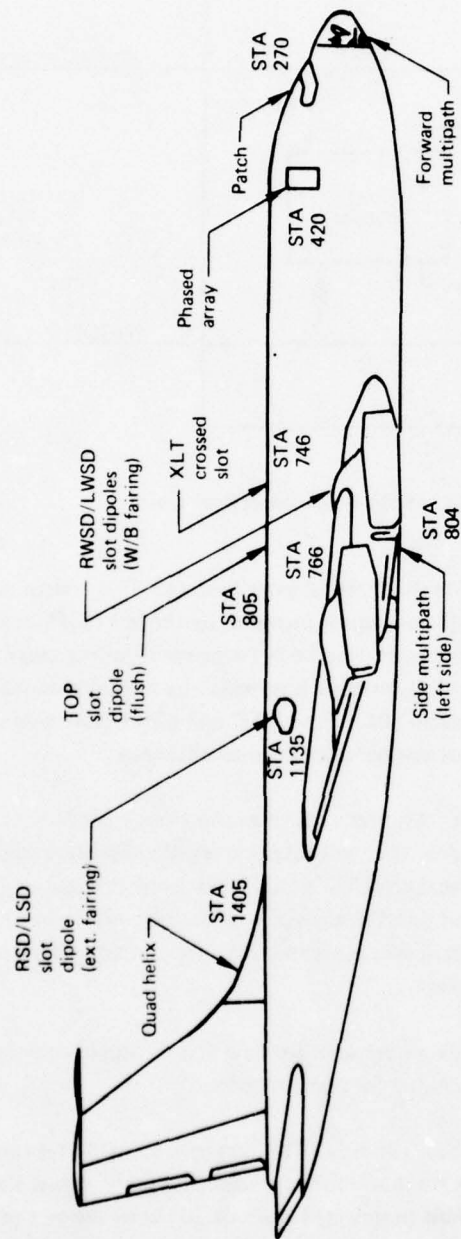


Figure 3-4. KC-135 Antenna Locations

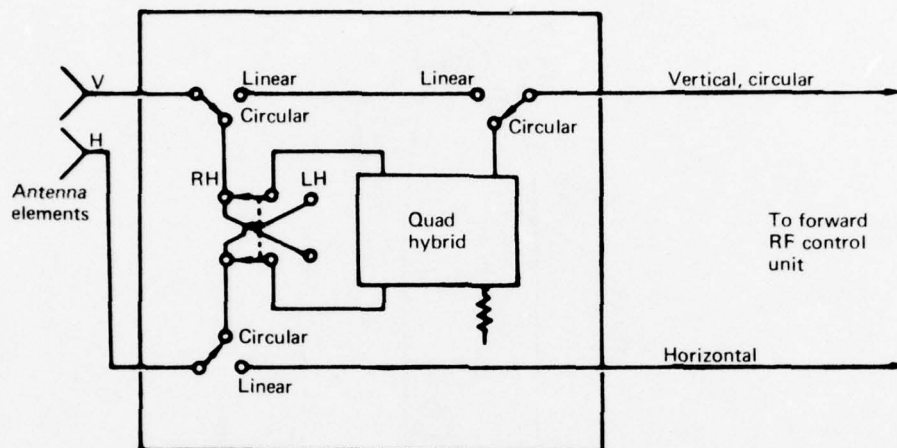


Figure 3-5. Polarization Switching Unit

- c. *Three-Antenna (LWSD/RWSD/TOP) Slot-Dipole System:* This system consists of three flush-mounted antennas. Side coverage is provided by the left (LWSD) and right (RWSD) side antennas mounted in the upper wing/body (wing-root) fairing areas at station 766. High elevation angle and fore/aft coverage is provided by a third antenna (TOP) mounted near the top centerline at station 805. The LWSD and RWSD antennas were used during overocean multipath test runs involving operational antennas.
- d. *Crossed-Slot (XLT) Antenna:* Also referred to as an orthogonal-mode cavity, this antenna was installed at station 746 near the top centerline specifically for acquisition of CONUS multipath data during the February 1975 tests. It was used primarily during approach, landing, and taxi sequences at selected airports. A limited amount of overocean multipath testing was also performed using this antenna. The antenna may be connected for either LHC or RHC polarization.

Although the following antennas were not used for data acquisition during the multipath test program, a brief description of each is included for completeness.

- a. *Side-Mounted Multipath (SMP) Antenna:* This antenna, located at station 804 and waterline 150, has a fixed beam that points approximately 15° below the horizon and 10° aft of broadside. The 3-dB beamwidth is about 20° in elevation and 45° in azimuth, and peak gain is approximately 13 dB. Polarization is selectable between dual linear, RHC, or LHC. The polarization switching network is identical to that of the forward multipath antenna. Because the forward multipath antenna beam shape was more

desirable and could be steered in both azimuth and elevation, the side multipath antenna was regarded as a backup for the forward multipath antenna and was therefore not used for multipath data acquisition.

- b. *Right/Left Slot-Dipole (RSD, LSD) Antennas:* These antennas were mounted at station 1135 approximately 35° down from the top centerline. Due to the more favorable location of the LWSD/RWSD/TOP slot dipoles, the RSD/LSD antennas were used primarily as backups and for auxiliary transmission/reception functions.
- c. *Phased-Array (PHA) Antenna:* This antenna was mounted on the right side of the aircraft at station 420, 41° down from the top centerline. With this location the main coverage was approximately broadside to the airplane. The beam was fixed in azimuth and was electronically steerable in elevation in increments of about 10° .
- d. *Patch (PAT) Antenna:* Because of its low power-handling capability, this antenna was used only for receiving. It was located near the top centerline of the fuselage at station 270 to provide forward "fill-in" coverage for the RSD/LSD antenna system.

The front multipath antenna and the LWSD/RWSD/TOP slot dipoles were furnished and installed by Boeing³ for this test program. The phased-array and patch antennas were furnished and installed specifically for the antenna evaluation tests and were not used during multipath tests. The side multipath, RSD/LSD slot-dipole, and quad-helix antennas were developed and installed by Boeing for the earlier FAA ATS-5 tests (ref. 3-2). The crossed-slot antenna was furnished by Boeing under an earlier contract (ref. 3-3) and was first used by DOT/TSC for their balloon test program.

3.2.5 Sea-State Buoy

Sea-state measurement data was acquired using a wave-following sea-state buoy furnished by the U.S. Navy USL and deployed from the USCG Cutter Gallatin. Buoy instrumentation included a magnetic compass, gimballed roll and pitch gyros, and three-axis strap-down accelerometers. The roll and pitch gyros provided angular information for determination of wave-slope distributions, while the accelerometer outputs yielded data relative to the spectra characteristics of the ocean surface. Small-scale undulations (waves of length less than approximately 1 m) were sensed by an array of 10 wave staffs. During data acquisition, the buoy was tethered to the USCG ship and information was conveyed via cable to the ship, where it was recorded on magnetic tape.

³Described in "U.S. Aeronautical L-Band Satellite Technology Test Program -- Terminal Design," Material submitted under contract DOT-TSC-707, August 1975.

3.3 MULTIPATH TEST GEOMETRIES AND SCENARIOS

Tests were conducted in accordance with a preplanned scenario specified by the test operations plan. The test operations plan specified the flightpath, test parameters, and schedule of all essential operations to be performed onboard the aircraft and at the ground station.

3.3.1 Oceanic Multipath Tests

A typical oceanic multipath flightpath is shown as the portion between waypoints F and J in figure 3-6. Tests were 1 hr in duration and consisted of four legs with three test headings: directly toward the ATS-6 subsatellite, 45° offset, and 90° offset. The reference direct path signals were always transmitted via the quad-helix antenna. Additional details are given in table 3-2.

TABLE 3-2. TYPICAL OCEANIC MULTIPATH TEST SCENARIO

Leg	Way-point	Heading relative to ATS-6, deg	Relative time, min	Direct antenna	Test antenna			
					Type	Polarization	Azimuth, deg	Elevation deg
1	FG	0	00 to 12	QH	FMP	H,V	0	-35
			12 to 18		TOP	RHC	—	—
2	GH	315	18 to 27	↓	FMP	H,V	45	-35
			27 to 32		RWSD	RHC	—	—
3	HI	0	32 to 38	↓	FMP	H,V	0	0
			38 to 42		FMP	RHC	0	-35
4	IJ	90	42 to 46	↓	FMP	LHC	0	-35
			46 to 55		LWSD	RHC	—	—
			55 to 60		FMP	H,V	270	-35

Additional test parameters:

D_1 = 127 chips, D_2 = 490 chips

CR = 5 MHz, CL = 1023 bits

τ_1 = $0.2 D_1 \mu\text{sec}$, τ_2 = $0.2 D_2 \mu\text{sec}$.

Prior to the start of a data run, the SACP modulator code length (CL), chip rate (CR), and code delays (D_1 and D_2) were set to the specified values. The two code delays were selected to allow nonambiguous identification and separation of the three probing signals (direct, H, and V) at the SACP receiver, taking into account the aircraft altitude and satellite elevation angle for a particular flight. Code chip rates were typically either 5 or 10 MHz, and the maximum code length of 1023 bits was used for all tests. The nominal aircraft altitude was 30,000 ft for all tests and nominal groundspeed was 400 kn. For the major portion of each test leg, the multipath channel probes were transmitted by the forward multipath antenna. The dual-linear polarization mode (simultaneous

Modem/Multipath/Antenna Test
 Date: November 21, 1974
 Transmission mode: TG 4

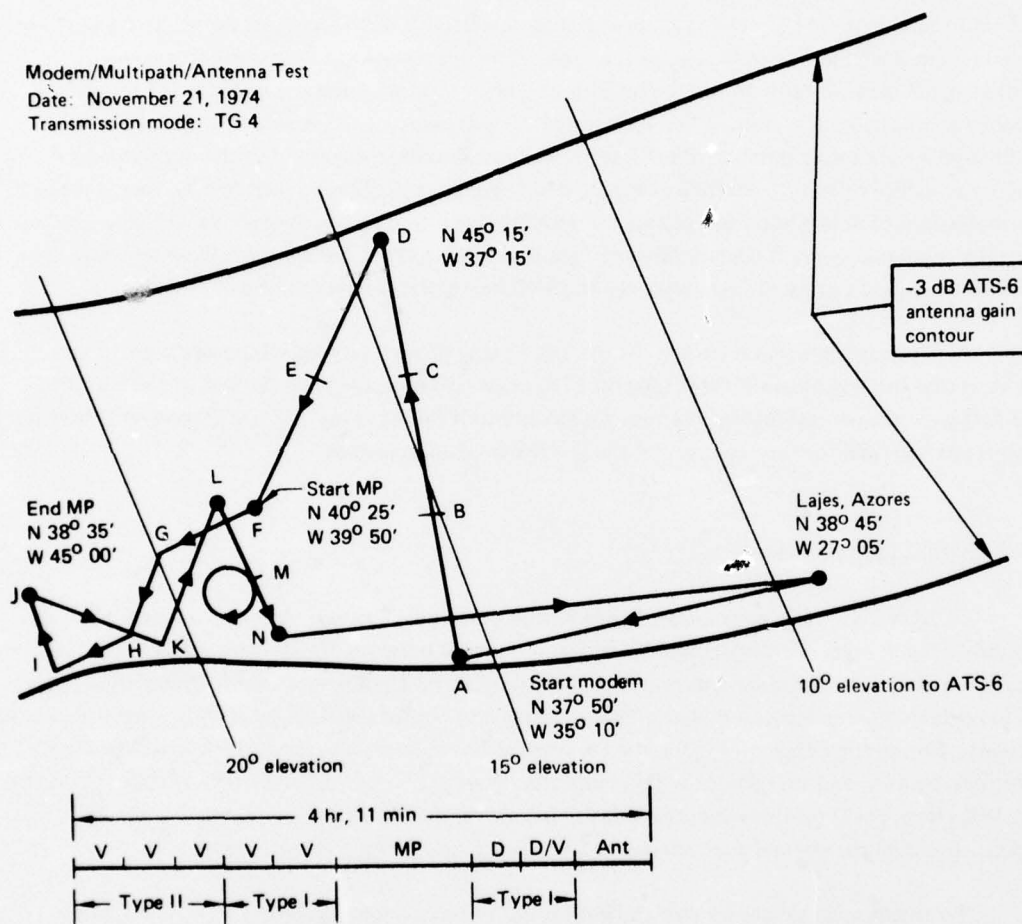


Figure 3-6. Modem/Multipath Antenna Evaluation — Flightpath No. 4

H and V probes) was most frequently used, although data was acquired for RHC and LHC antenna polarizations on a few selected flight tests. During data acquisition, the forward multipath antenna was normally pointed toward the subsatellite direction in azimuth and was depressed below the horizon to illuminate the effective scatter region in the vicinity of the specular point. For a portion of an in-plane leg (flight directly toward the subsatellite point) on each flight, the antenna was pointed at the forward horizon to provide a direct line-of-sight illumination of the satellite. Data acquired in this manner — termed “up-look mode” — was gathered to provide information relative to the satellite antenna’s polarization ellipse, as well as calibration data used in the determination of the sea-surface reflection coefficient magnitude. Usually, a portion of each test leg was devoted to the acquisition of data while transmitting the probing signal through an operational antenna. For all cases the candidate operational antenna had high multipath discrimination, with the result that the received multipath energy in each delay tap was well below the receiver’s noise density.

At Rosman, data was recorded for the last 12 min of each test leg. Recorder turn-on was timed so that the end of the 7200-ft tape (at 120 ips) would coincide with the end of the test leg. The first part of each test leg was used for reacquisition of the signal by the SACP receiver following the aircraft turn and for tape changes on the instrumentation recorder.

3.3.2 CONUS Multipath Tests

CONUS flight tests were either 4 or 4.5 hr in duration. This test time was divided into legs typically 20 min long. Test headings for the legs alternated between directly toward or 90° offset from the ATS-6 direction. En route data was usually acquired with the forward multipath antenna operating in its dual-linear polarization mode. Some testing was performed with an aircraft operational-type antenna. During the February 1975 tests, the crossed-slot antenna was used to acquire data during approach, landing, and taxi phases at three airports: Nampa (Edmonton, Alberta), O’Hare (Chicago), and JFK (New York) on three successive days. Selection of code length, code rate, T_1 and T_2 , and antenna pointing parameters were subject to the same considerations as for oceanic tests.

To enhance the power level of the multipath (reflected) signal received at Rosman, the ATS-6 L-band antenna was operated in the pencil-beam mode during many of the CONUS tests. Since the antenna’s 3-dB beamwidth is only 1.5° in the pencil-beam mode, repointing of the spacecraft antenna was usually required once or twice during a 4-hr test. This requirement was easy to satisfy and was routinely accomplished by NASA/GSFC in only a few minutes. At Rosman, data was normally recorded for the last 16 min of each 20-min test leg.

3.4 MULTIPATH DATA ACQUISITION SUMMARY

Overocean technology test flights generally involved a mix of test types. A single flight, for example, might provide oceanic multipath, antenna evaluation, and several types of modem evaluation tests. Oceanic multipath test data was acquired on 18 separate flights over a range of satellite elevation angles between 3° and 32° . Tests were spread over a 7-month period ending April 1975. Table 3-3 summarizes tests conducted.

Ocean buoys were used by DOT/TSC/USCG to acquire sea-state data on one day in January 1975 and on five days during March/April 1975. During the March/April series, three of the five days on which sea-state measurement data were acquired corresponded to days on which multipath channel characterization tests were conducted. The multipath tests and sea-state measurements were not, however, truly time coincident; typically the times of test conduct differed by several hours for the two tests in each of the above three cases. Additional sea-state buoy deployments were made for system calibration purposes during February 1975.

Sea-state data obtained from the overocean tests is presented in section 6.5. Details of the sea-state data analysis are described in volume IV, appendix B.

CONUS multipath tests were performed overland over various parts of the U.S. and Canada. These flights were devoted exclusively to the acquisition of CONUS multipath data. Dedicated ATS-6 spacecraft L-band test time was also required because of the special L-band antenna beam modes and pointing needed for coverage of the geographic areas of interest. CONUS multipath tests conducted are summarized in table 3-3.

3.5 KC-135 TERMINAL RF CALIBRATION

3.5.1 Power Monitoring and RF Insertion Loss

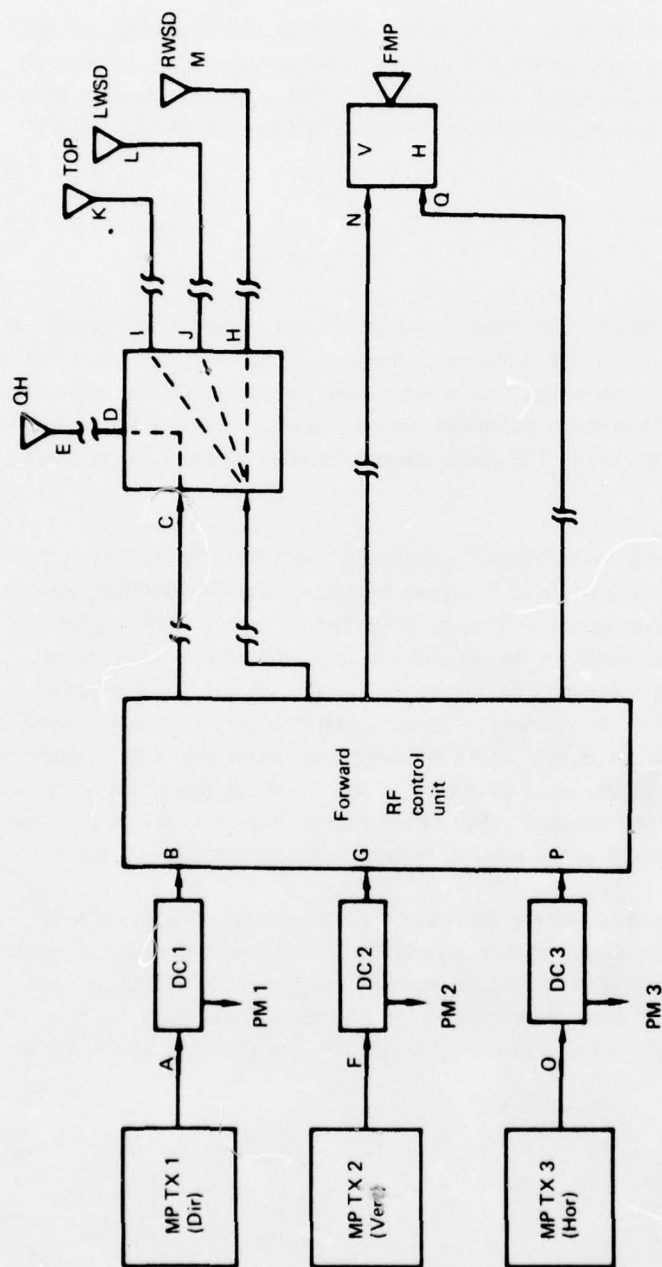
To analyze and interpret the multipath data, it was necessary to know the relative RF power levels at the inputs to the three transmitting antennas (i.e., the direct path antenna and the H and V polarization ports of the multipath antenna). RF subsystem calibration measurements were therefore made to acquire the insertion loss data needed to derive the input RF power levels at the antennas from the HP 435A power meter monitor values.

The power monitoring subsystem used for all multipath tests except the March/April 1975 series is given in figure 3-7. All insertion loss values of interest are given. These values allow the RF power meter readings to be used to calculate (1) the RF power level at any antenna input and (2) the RF power level at the output port of each transmitter.

TABLE 3-3. MULTIPATH DATA ACQUISITION SUMMARY

Date, mo-day-yr	Elevation angle, deg	Test duration, hr + min	Remarks
A. Oceanic			
9-24-74	30	1+00	Nominal
10-24-74	18 to 23	1+00	Nominal
10-28-74	8 to 12	1+00	Nominal
11-14-74	3 to 8	1+00	SACP receiver data sign bit inoperative causing all Doppler data to be of one polarity. $S(r, \omega)$ function could not be calculated. Delay spectra data unaffected.
11-15-74	8 to 13	1+00	
11-16-74	3 to 8	1+00	
11-21-74	19 to 23	1+00	
1-23-75	3 to 8	1+00	Partial data acquisition, faulty 100-W PA (30-W TWT used)
1-27-75	8 to 13	1+00	Nominal
1-28-75	19 to 23	1+20	Aircraft maneuvers due to weather avoidance
1-30-75	3 to 8	1+00	Nominal
2-27-75	30	1+20	Nominal
3-25-75	15	0+20	TOP antenna only
3-27-75	10 to 15	1+00	FMP antenna fault
3-38-75	3 to 8	1+00	FMP antenna fault
3-31-75	10 to 15	1+00	Nominal
4-02-75	7 to 11	1+00	Nominal
4-03-75	16 to 21	1+00	Nominal
		18 hr	Oceanic Test Hours
B. CONUS			
9-19-74	30 to 45	4+00	Eastern U.S., nominal
10-30-74	30 to 45	4+00	Eastern U.S., nominal
11-02-74 ^a	30 to 45	4+00	Northwest U.S., 50% of data acquired
2-18-75 ^a	16 to 27	4+30	NW Canada to Edmonton, 50% of data acquired, no useful airport landing data
2-19-75 ^a	27 to 40	4+30	Central Canada to O'Hare, nominal
2-20-75 ^a	28 to 37	4+30	N. Quebec to JFK, nominal
		25.5 hr	CONUS Test Hours

^aAcquired data with both fan and pencil beams of ATS-6.



Notes:

1. (A-B) = (F-G) = (O-P) = 0.5 dB (est)
2. (B-C) = 1.4 dB (meas); (C-D) = 0.9 dB (meas); (D-E) = 0.9 (meas) + 0.8 (est) = 1.7 dB
∴ (A-E) = 4.5 dB (20-W TX 1 to QH)
3. (G-H) = 3.3 dB (meas); (G-I) = (G-J) = 3.5 dB (est); (I-K) = (J-L) = (H-M) = 1.2 dB (est)
∴ (F-K) = 5.2 dB (VTX to TOP); (F-L) = 5.2 dB (VTX to LWSD); (F-M) = 5.0 dB (VTX to RWSD)
4. (G-N) = 1.7 dB (meas); (P-Q) = 1.9 dB (meas)
∴ (O-Q) = 2.4 dB (HTX to HFMP); (F-N) = 2.2 dB (VTX to VFMP)
5. (A-PM 1) = (O-PM 3) = 29.1 dB; (F-PM 2) = 38.8 dB for January and February 1975 series.

Figure 3-7. KC-135 Multipath Monitoring Subsystem, September 1974 to February 1975

For the March/April 1975 test series, the power meters and directional couplers associated with each of the two indirect path transmitters were relocated to a point following the forward RF control unit. Two 3-dB hybrids were also added to allow relative RF phase measurements to be made (discussed in next section). This monitoring configuration is shown in figure 3-8 and includes all insertion loss values of interest.

3.5.2 Relative RF Phase Calibration

Measurement of the relative RF phase between the horizontal and vertical probe signals as input to the antenna was desired to support the cross-correlation and cross-power analyses of horizontal and vertical tap outputs.⁴ The instrumentation used for these measurements is illustrated in figure 3-9. During the fall series, relative phase measurements were made on only one occasion due to the unavailability of required test equipment. The discussion will therefore be limited to measurements during the spring 1975 series.

With respect to figure 3-9b, relative RF phase measurements were made by exciting the SACP modulator in the cw mode. The two unmodulated cw signals were up-converted, amplified, and connected to the antennas in the normal manner. Samples of the two RF signals were coupled out for relative phase measurements using an HP 8410A network analyzer. RF cabling between the coupled points and the antennas was designed to have equal path lengths for the two channels in terms of phase. This was confirmed by measurement. Auxiliary calibrations of all couplers, hybrids, etc. were performed as needed. This system allowed RF relative phase measurements to be made by simply changing the operating mode of the SACP modulator to cw. Especially significant is the fact that no cable or connector changes were required in the RF subsystem. The two 3-dB hybrids also allowed power meter monitors to operate simultaneously without cable or connector changes.

Relative RF phase measurements made for the H and V channels during the March/April series are given in table 3-4. Some day-to-day variations, as well as time-dependent variations within a given test, are evident. These variations are attributed primarily to temperature effects in transmitters, up-converter, etc. The variations were observed to stabilize following a lengthy warmup of equipment. Warmup periods of 2 hr or more were normally used for tests acquiring relative RF phase data.

⁴For a complete characterization of equipment effects on these measures, one must also include the perturbations caused by the antennas onboard the aircraft and the ATS-6 satellite.

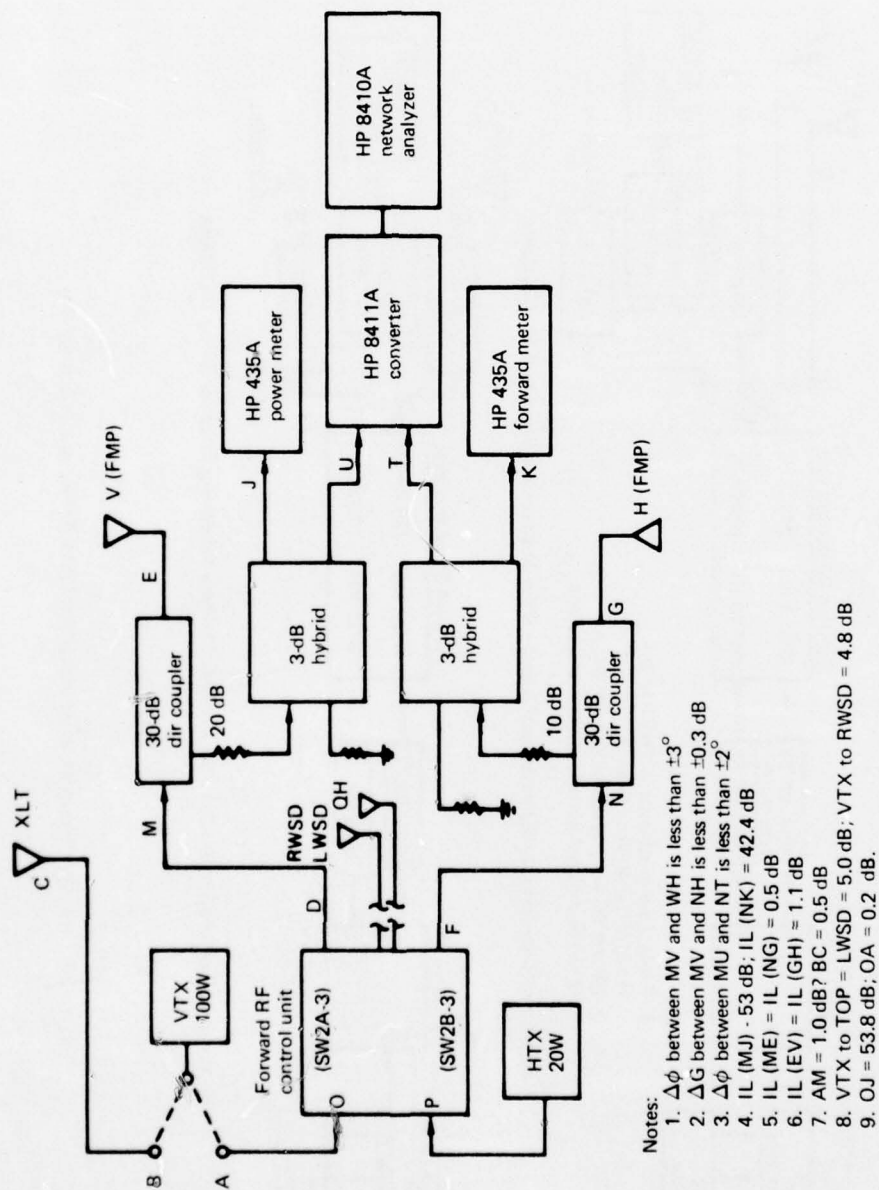


Figure 3-8. KC-135 Multipath Monitoring Subsystem, March and April 1975

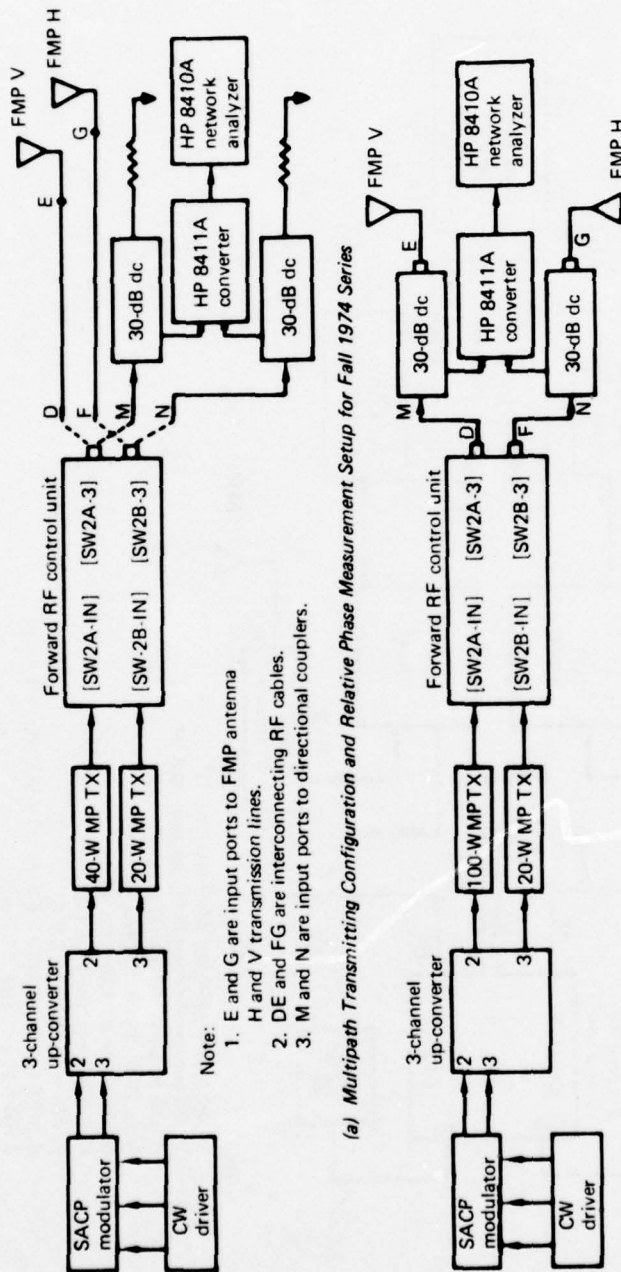


Figure 3-9. Relative Phase Measurements for KC-135 Multipath Equipment

TABLE 3-4. MULTIPATH RELATIVE-PHASE MEASUREMENT SUMMARY
FOR MARCH 1975 TEST SERIES

Date, mo-day-yr	Time, GMT	$\Delta\phi$ (V leads), deg
3-18-75	1530	98
	1700	82
	1715	80.5
	1720	79.0
	1725	83.5
	1730	83.0
3-19-75	1250	65.0
	1520	71.5
3-21-75	1505	58.0
3-24-75	0745	83.0
	1330	70.0
3-25-75	0900	71.5
	1430	59.0
3-27-75	0830	70.0
	1415	69.5
3-28-75	0817	80.1
	1404	66.2
3-31-75	0800	90.2
	1239	71.2
4-2-75	0703	97.5
	1242	71.0
4-3-75	1103	71.7

4. MULTIPATH DATA REDUCTION AND ANALYSIS PROCEDURES

This section gives a brief description of the data analysis procedures and analytical objectives of the major processing blocks. Volume IV provides a comprehensive discussion of this subject.

4.1 DATA PROCESSING FUNCTIONAL FLOW

Figure 4-1 depicts the processing steps involved in the formatting, reduction, and analysis of the recorded multipath SACP signal arrays and the aircraft-transmitter parameter tape.

Received SACP signals were direct recorded in a standard telemetry analog format (serial PCM, NRZ-L). Redundant recording was used on the analog source tape, with each of the PCM data bit streams and IRIG time-code signals recorded on two separate tracks. At the Boeing ground station facility, the data and time tracks were initially processed by telemetry front end (TFE) equipment, which for this particular application routed the played-back serial signals through its PCM subsystem to the programmable data distributor (PDD). The PDD merged time words with the data and distributed the information to one or both of the PDP 11/45 computer I/O buses. The dual PDP computer system performed three basic functions: (1) conversion of the analog-recorded data tapes into digital format computer-compatible tapes, (2) quick-look processing of the multipath data, and (3) calculation of the time-ordered delay-spectra arrays that are used to generate the time history of the multipath channel delay spectra. The normalization and three-dimensional plotting of this data were performed in the CDC 6600.

Detailed analysis of the prober data was also performed in the CDC 6600. This analysis provided a comprehensive characterization of the multipath channel for horizontal and vertical polarization, gathered over a down-looking antenna. The primary output of this routine was the delay-Doppler scatter function of the channel. Also included were the channel's total scattered intensity, delay spectrum, Doppler spectrum, frequency autocorrelation function, time autocorrelation function, spread parameter measures, and the time-domain statistics of the individual tap processes.

Sea-state buoy data was reduced and analyzed by CNR, Inc. Analog tapes were stripped and reformatted into computer-compatible digital tapes at a DOT/TSC facility. Detailed processing as described in appendix B of volume IV was performed on the DOT/TSC PDP 10 computer.

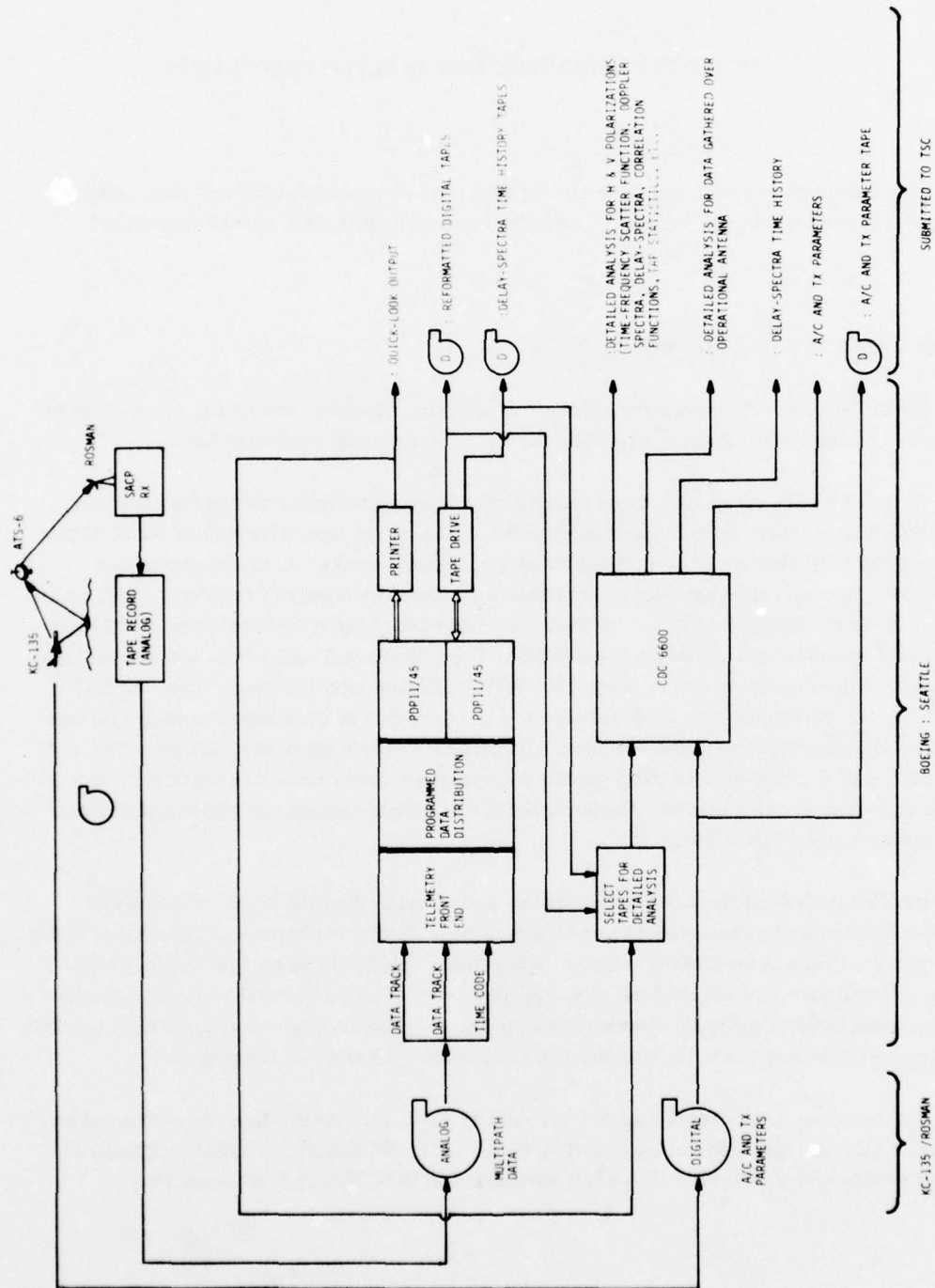


Figure 4-1. Data Reduction and Analysis Functional Flow

4.2 ALGORITHM EXECUTION SEQUENCE AND ANALYTICAL OBJECTIVES

The algorithm execution sequence for processing the multipath channel data is given in figures 4-2 and 4-3 and is described briefly as follows.

4.2.1 Quick-Look Real-Time Playback Data Analysis

The quick-look output, directly available from the PDP 11/45 system, provides both oscilloscope display plots and hard-copy numerical output. From this information, the operator may investigate receiver parameter configuration, tap frequency spread, delay power spectral density, and analog magnetic tape status descriptors. The quick-look output is used to review overall data quality and to identify candidate data intervals for detailed analysis, i.e., intervals that provide both steady-state receiver conditions and multipath scatter phenomena of particular importance.

4.2.2 Reformatted SACP Digital Tapes

Source analog tapes are processed to provide computer-compatible digital tapes that represent the complex tap voltage time-domain data of the SACP receiver. Typically, those periods of data identified by the quick-look analysis as being of particular interest (e.g., active multipath returns, large cities, land/water interfaces) were reformatted for the CONUS tests. For the oceanic tests, the bulk of the valid data was converted to digital format.

4.2.3 Delay-Spectra Time History

For all periods of valid data collection, the scatter channel's delay power spectral density (psd) is determined in a time-running nonoverlapping manner, with psd estimates being calculated over a 2-sec interval. The outputs, which occur once every 2 sec, are given in both numerical and three-dimensional plotted formats. Respectively, these data provide both a quantitative and comprehensive overview description of the channel's time-variant delay-spectra characteristics. This analysis is of particular importance for the CONUS scatter, where terrain roughness and electrical characteristics vary rapidly with distance. One use of the 3-D overview plot is to isolate time and tap bank intervals that possess data for which it is desirable to either (1) reference the numerical output to obtain quantitative delay-spectra information or (2) subject the data input string to detailed delay-Doppler psd computer processing.

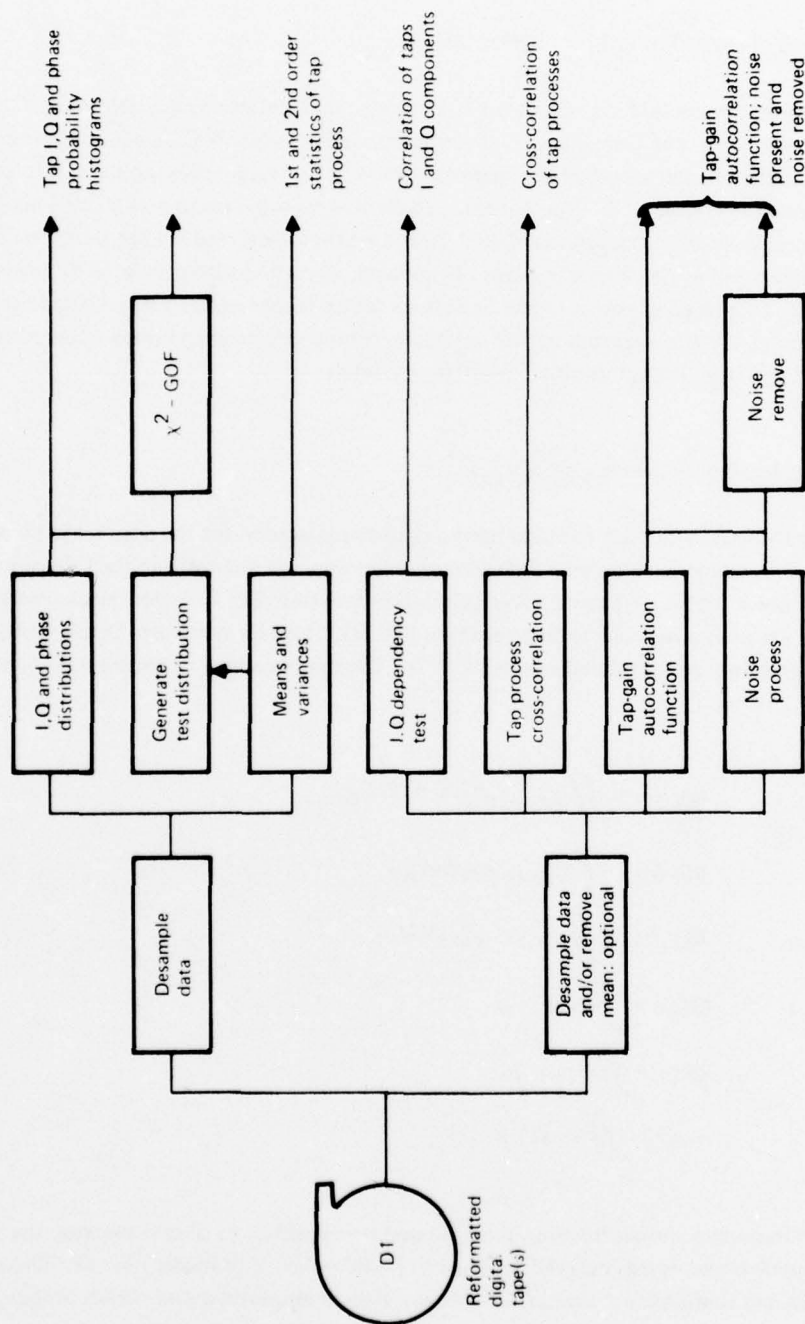


Figure 4-3. Multipath Algorithm Execution Sequence, Part 2

4.2.4 Delay-Doppler Scatter Power Spectral Density: $S(\tau, \omega)$

This function represents the distribution of diffusely scattered power arriving at the receiver with Doppler frequency ω and time delay τ . For the zero-mean complex Gaussian random-scatter process, $S(\tau, \omega)$ completely characterizes the channel statistics. For each test condition, at least one detailed $S(\tau, \omega)$ function is generated. The output is given in numerical and three-dimensional plotted form. Furthermore, since this parameter is of such fundamental importance for the interpretation, modeling, and application of the scatter channel phenomena, $S(\tau, \omega)$ is also preserved on magnetic tape. This provides a convenient and compact basis from which future analysis may be conducted without going through the time-consuming and expensive computer processing steps required to obtain the delay-Doppler psd from the reformatted SACP digital tapes.

4.2.5 Integral and Fourier Operations on $S(\tau, \omega)$

The scatter function $S(\tau, \omega)$ contains all the ingredients needed for the derivation of equivalent and lower order channel parameters. Software modules are contained within the CDC 6600 routines to derive the joint time-frequency autocorrelation function $R(\xi, \Omega)$, time autocorrelation function $R(\xi, 0)$, frequency autocorrelation function $R(0, \Omega)$, Doppler spectrum $D(\omega)$, delay spectrum $Q(\tau)$, and total rms scattered energy $\langle |I|^2 \rangle$. The mathematical expressions for these quantities are:

$$R(\xi, \Omega) = \iint S(\tau, \omega) e^{i(\Omega\tau + \xi\omega)} d\tau d\omega \quad (4-1)$$

$$R(\xi, 0) = \iint S(\tau, \omega) d\tau e^{i\xi\omega} d\omega \quad (4-2)$$

$$R(0, \Omega) = \iint S(\tau, \omega) d\omega e^{i\Omega\tau} d\tau \quad (4-3)$$

$$D(\omega) = \int S(\tau, \omega) d\tau \quad (4-4)$$

$$Q(\tau) = \int S(\tau, \omega) d\omega \quad (4-5)$$

$$\langle |I|^2 \rangle = \iint S(\tau, \omega) d\tau d\omega \quad (4-6)$$

The time-frequency autocorrelation function and its respective axial cuts measure the degree of correlation between two signals delayed in time by ξ and offset in frequency by Ω . These functions are complex and therefore are formatted in terms of their amplitudes and phases in the software output.

4.2.6 Channel Spread Parameters

From the $D(\omega)$, $Q(\tau)$, $R(\xi, 0)$, and $R(0, \Omega)$ distributions, lower echelon first-order channel parameters such as the Doppler spread, delay spread, decorrelation time, and coherence bandwidth of the scatter channel are easily estimated.

4.2.7 Noise Determination and Removal (NDandR)

The outputs of the SACP multipath correlator contain desired signal data, spurious signal terms, low-pass additive thermal noise, and receiver arithmetic noise. Under normal SACP operating conditions, the NDandR algorithm statistically eliminates these noise terms from the data on a tap-by-tap basis. The noise-free estimate of the delay-Doppler function may then be normalized for the low-pass filter attenuation and subjected to the integral, Fourier transform, and spread determination steps as previously outlined.

4.2.8 Antenna-Pattern-Effects Removal

Design criteria for the forward multipath antenna were established to provide a radiation pattern with nearly uniform coverage over the effective scatter region. However, for certain flight direction headings the fidelity of the channel measurement may be enhanced by applying the antenna-effects-removal algorithm. This routine operates on the noise-free $S(\tau, \omega)$ estimate to provide an equivalent scatter function that would be measured with a uniform gain antenna. The multipath process performs a 2-into-1 mapping operation, wherein two surface returns are mapped into one delay-Doppler point. Application of this algorithm is thus restricted to the in-plane geometry cases where the cosymmetry of the delay contours, Doppler contours, and scatter cross section (isotropic surface) is exploited.

4.2.9 Tap Amplitude and Phase Distributions

Determination of the fundamental statistical properties of the scatter process requires that the received signals' time-domain fluctuations be characterized. The probability distribution and its associated mean and variance for these fluctuations are derived for each tap's I component, Q component, and phase angle. The process composite signal, which is constructed by vectorially summing the delay tap outputs, may also be subjected to these operations. The experimental distributions are compared with theoretical expectation for the complex Gaussian channel. These correlations are implemented via the χ^2 goodness-of-fit test.

4.2.10 Tap Process Bank Cross-Correlations

The degree of coherency between any two taps in a particular tap bank or in cross-polarized banks (i.e., one horizontal, the other vertical) is measured through use of the normalized cross-correlation function; i.e.,

$$R_{XY}(\xi) = \frac{\langle X(t) Y^*(t-\xi) \rangle}{\sqrt{[\langle X(t) X^*(t) \rangle \langle Y(t) Y^*(t) \rangle]}} \quad (4-7)$$

where:

X = complex tap process in either bank

Y = complex tap process in either bank

ξ = time-lag variable.

As an option, $R_{XY}(\xi)$ may be evaluated for conditions where the means have been removed or are left included in the X and Y time arrays. In general, the results should be closely equivalent except for the case where the specular tap contains a significant "coherent" component. Similar options are available for the operations discussed in sections 4.2.11 and 4.2.12.

4.2.11 Tap I and Q Dependency

For random rough-surface scattering where the electromagnetic wave undergoes deep phase modulation at the multipath interface, we expect that the I and Q components of the received signals are statistically independent. This condition is explored by determining the zero-lag normalized correlation coefficient between a tap's orthogonal components; i.e.,

$$R_{IQ}(0) = \frac{\langle IQ \rangle}{[\langle I^2 \rangle \langle Q^2 \rangle]^{1/2}} \quad (4-8)$$

4.2.12 Tap-Gain Autocorrelation Function: $U(\tau, \xi)$

An estimate¹ of the channel's tap-gain autocorrelation function, $U(\tau, \xi)$, is derived through application of the following operation.

¹ An alternate derivation of this function may be obtained by an inverse Fourier transformation of the $S(\tau, \xi)$ function with respect to the ω variable.

$$U(\tau, \xi) = \langle X_\tau(t) X_\tau^*(t - \xi) \rangle, \quad (4-9)$$

where:

- τ = delay tap value
- X_τ = complex process of tap τ in bank X (i.e., horizontal or vertical)
- ξ = time-lag variable.

This function measures the autocorrelation function of the multipath process on a tap-by-tap basis and is available (magnitude) as a three-dimensional output plot from the software package.

Two program options exist in this algorithm: (1) cross-polarized estimate of $U(\tau, \xi)$ and (2) a first-order noise effects removal from $U(\tau, \xi)$.

The cross-polarized estimate of $U(\tau, \xi)$ is calculated by replacing the conjugated variable in equation (4-9) with the appropriate Y tap of the bank containing the orthogonal polarized return.

Assuming the independence of multipath and noise, we arrive at a noise-free estimate of the tap-gain autocorrelation function, $U_{nr}(\tau, \xi)$, as follows:

$$U_{nr}(\tau, \xi) = \langle X_\tau(t) X_\tau^*(t - \xi) \rangle = \frac{1}{N} \sum_{i=1}^N \langle X_i(t) X_i^*(t - \xi) \rangle, \quad (4-10)$$

where X_i is the complex output of a multipath-free tap (usually taken from a region of the bank preceding the specular-point return).

Typically, $\langle X_i(t) X_i^*(t - \xi) \rangle$ has significant energy only at the zero-lag value, and thus we are in essence removing an estimate of the average noise contribution to the $\xi = 0$ value of the $U(\tau, \xi)$ function.

4.2.13 System Calibration Parameter Data

Magnetically recorded data pertaining to receiver system operation (i.e., direct and multipath channel gains, etc.), transmitter power amplifier outputs, and aircraft flight parameter descriptors are computer reduced to aid in the normalization of the scatter channel power returns. These data also serve as a data collection integrity measure and are used primarily to augment the logged flight test data.

4.3 MULTIPATH DATA BASE

The data base delivered to DOT/TSC relative to the multipath channel characterization test consists of the following items:

- a. Library of analog SACP receiver source data tapes. These data were recorded at the NASA ground station on 9600- or 7200-ft reels of 1/2-in. magnetic instrumentation tape using Ampex FR-1900 and/or FR-2000 recorders. The recorded data corresponds to the unprocessed data obtained from the outputs of the SACP receiver during test conduct.
- b. Library of reformatted digital data tapes (D1). These 1600-bpi nine-track digital tapes contain the SACP receiver output data in computer-compatible digital format. The tapes are generated by the Boeing PDP-11/45 facility and have a format as described in volume IV, section 4.22.1.
- c. Library of delay-spectra time history tapes (D3). These 1600-bpi nine-track digital tapes contain the delay-spectra time history arrays computed by the dual PDP 11/45 computer system. In most cases, the files containing these data are physically located on the same tape as the corresponding reformatted digital data described as D1 (above). Tape formats are described in volume IV, section 4.22.3.
- d. Library of $S_n(\tau, \omega)$ save tapes (D2). Tape D2 contains the computed noise-present estimate of the channel's delay-Doppler scatter function. The tape format is described in volume IV, section 4.22.2.
- e. Library of airborne system parameter source tapes. These 800-bpi, seven-track, computer-compatible digital tapes are recorded onboard the KC-135 aircraft terminal using a Kennedy 8707 recorder. The tapes contain power level calibration data and other information relevant to the test parameters during test conduct. Information content and tape format are described in volume IV, section 4.23.
- f. Computer programs (card decks) and listings corresponding to the programs used for detailed analysis of the reformatted multipath data (D1) tapes. Descriptions of algorithms are given in volume IV, sections 3 and 4.
- g. Computer programs (card decks) and listings corresponding to the physical optics vector scatter model described in volume IV, section 5.
- h. Punch paper tapes providing radiation distribution plots of antenna range data for the front multipath antenna for various polarizations and pointing angles.

The following additional data base resulted from a subcontract to CNR, Inc:

- a. Reformatted 800-bpi, seven-track, multipath computer-compatible digital data tapes generated from selected Boeing PDP 11/45, 1600-bpi, nine-track D1 tapes.
- b. Transposed multipath digital data tapes identified in section 5.4.6.
- c. Sea-state buoy 800-bpi seven-track digital data tapes containing measured buoy variables stripped from the analog buoy data source tapes. (Tapes correspond to data acquired on January 29 and 30, 1975, plus March 25 through April 2, 1975.) These PCM data stripping operations used a capability existing at DOT/TSC.
- d. Backup program tape containing the programs utilized for sea-state buoy data reduction, H-V correlation and statistical analysis, and transpose and scattering function DRandA. The programs referred to are those identified in volume IV, sections 4.21 and appendix B. Programs can be run on the DOT/TSC PDP 10 in time-share or batch processing modes.

5. OCEANIC MULTIPATH TEST RESULTS

Probes of the oceanic multipath medium were conducted on 18 separate occasions covering a range of elevation angles from 3° to 32° and a variety of North Atlantic sea conditions. Results from these tests are presented to illustrate the delay-Doppler scatter function, outputs from Fourier and integral operation on the scatter function (e.g., delay spectra, autocorrelation functions, total scattered energy), the spread values of the delay spectra, Doppler spectra and autocorrelation functions, and characterization of the complex receiver's time-domain statistics. Most of the documented results pertain to the simultaneous dual-linear probe transmissions that have both vertical and horizontal polarization vectors. A limited amount of data for left- and right-hand circular polarization transmissions are also included.

Linear polarization results are compared with predictions based on surface integration of the physical optics vector scatter model (described in sec 6) as applied to a very rough surface possessing an isotropic slope distribution of the Gaussian form. When applicable, the measured channel parameters are also compared with theoretical predictions based on "steepest descent" solution to the integral formulations that develop under the closed-form approach to the channel characterization. Sea-state measurement data was acquired for one day during January and for five days during March/April 1975 by deployment of a rather sophisticated buoy sensor. Results pertaining to this surface characterization effort are presented in section 6. Since the sea-state measurements and the multipath tests were never truly coincident in either time (several hours of separation were typical) or location, a one-to-one comparison of experimental results and theory for a specific measured sea condition was not possible. A range of rms slopes and an assumed typical value were therefore used for the bulk of the correlation between experiment and theory. The measured sea-state data was used for validation of the range of sea-surface slopes encountered, as well as for validation of other assumptions relative to sea-slope distributions.

As with any remote electromagnetic sensing experiment, the spatial filtering effects of the prober antenna must be taken into consideration. These effects are evaluated in section 5.6 for selected data ensemble sets and, where possible, generalized results are applied to the pertinent section of this document. Other equipment effects and limitations on channel characterization measurements are described in appendices A, B, and C.

5.1 DELAY-DOPPLER SCATTER FUNCTION: $S(\tau, \omega)$

For oceanic scatter at L-band frequencies, there are scientific reasons based on the time-series analyses of section 5.4 to believe that the multipath channel is adequately described as a zero-mean complex Gaussian process. Since the experimental test conditions are processed in time segments on

the order of 6 sec. we may also assume in general that the effective scatter region traverses a surface area over which the significant electrical and statistical physical parameters are relatively invariant. Under these conditions the delay-Doppler scatter function, $S(\tau, \omega)$, completely characterizes the statistics of the channel (ref 5-1). $S(\tau, \omega)$ represents the power spectra density of multipath energy arriving at the receiver with delay and Doppler frequency shift. It is derived by taking the Fourier transform of the complex delay tap processes.

Several fundamental observations have been made relative to the energy distribution dependencies of $S(\tau, \omega)$ upon grazing angle,¹ flight direction, and polarization. Typically, these functional relationships are most easily discussed when the scatter function is reduced to lower echelon relationships such as the Doppler spectra, spreads, etc. Observations relative to the lower order parameters are found in section 5.2. In this section we discuss some of the more distinct properties that are visually evident in the plots of $S(\tau, \omega)$. Before discussing specific $S(\tau, \omega)$ observations, however, we comment on four features of the receiver/data reduction procedures that are visible in several of the three-dimensional plots.

The first feature relates to the SACP receiver's two's-complement arithmetic dc bias, which in the DRandA noise-removal algorithm is removed on a statistical basis and thus exhibits a residual 0-Hz component. The residual component itself varies statistically on a tap-by-tap basis; however, when integrated over the total tap bank, such as for Doppler-spectra estimation, the overall effect is observed to be completely insignificant.

The second characteristic pertains to the well-known aliasing phenomenon that occurs when a signal is undersampled. This effect is most pronounced for the high-angle in-plane flight condition where the Doppler frequency (negative) from the subaircraft side of the specular point increases rapidly with delay tap and quickly exceeds the Nyquist rate of the signal-processing algorithms. (An example that illustrates the negative Doppler energy being aliased into the positive-frequency realm is given later in fig 5-6.)

Third, we note that the specular-point return (i.e., the first multipath component to arrive at the receiver) is not usually associated with the beginning tap of the correlator bank.² This results

¹In this document the term grazing angle is used to represent the local elevation angle associated with the electromagnetic wave as incident at the specular point. It is referenced to the local horizontal tangent plane and, for synchronous satellite-to-aircraft geometry, is to very close approximation equal to the elevation angle of the direct line-of-sight ray at the airplane.

²Care must be taken *not* to identify the difference between the first tap and the specular-point tap with the differential delay between the direct and multipath returns (i.e., the *total tap bank* is in general shifted by a given delay offset from the direct path tracks).

from an intentional receiver operator procedure that was carried out to avoid contamination of the signal structure with taps near the bank origin which, on occasion, were observed to malfunction. The specular-point (or zero-delay) tap is identified by several obvious features. Specifically, it is the first tap of the bank to contain significant energy (in fact, it is generally the strongest of all taps), which in turn is dispersed over a very narrow Doppler range.

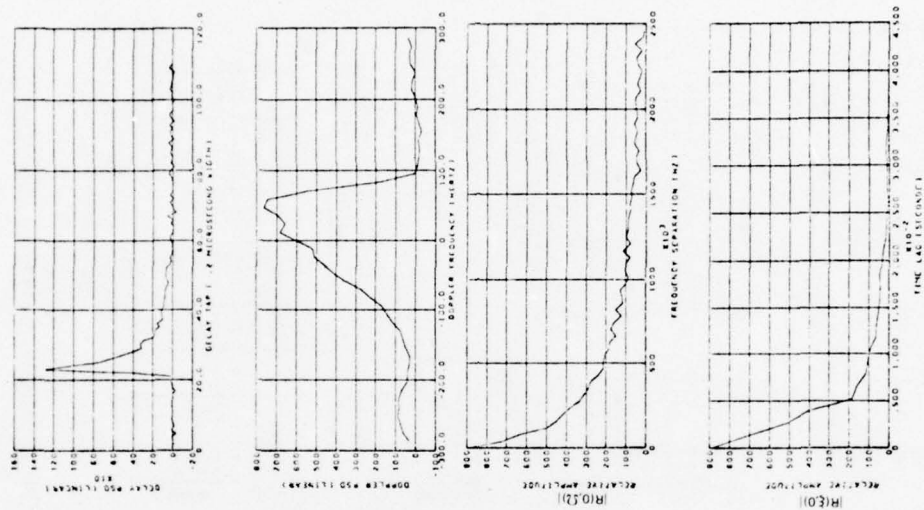
Fourth, it is well known that the outputs from a periodogram analysis such as that used for the $S(\tau, \omega)$ estimations do not converge to their mean values as the number of input points increases. To circumvent this, we use the following three devices: a data input tapering window, a spectral-average sliding window, and ensemble averaging. Different configurations of these devices are, in general, employed for each set of system parameters. However, the net effect usually provides us with a smoothed spectra estimate by including on the order of 160 independent samples in each output point of $S(\tau, \omega)$. With the exception of the ensemble-averaging procedure, these smoothing techniques tend to bias the distribution (i.e., valleys are overestimated and peaks are underestimated) while at the same time the estimate's rms uncertainty is reduced to approximately 8% of the output value. When we operate on $S(\tau, \omega)$ to obtain Doppler spectra, etc., these biases and uncertainties tend to be reduced.

Three-dimensional plots of the experimentally derived scatter function are given for a range of test parameter permutations as outlined in the cross-reference of table 5-1. In the associated figures (figs. 5-1 through 5-12), the $S(\tau, \omega)$ function is accompanied by its delay spectra, Doppler spectra, and unidimensional autocorrelation functions. Results presented emphasize horizontal polarization with in-plane geometry (i.e., KC-135 flying along a great circle route directly toward

TABLE 5-1. OCEANIC MULTIPATH PARAMETERS: FIGURE REFERENCE

Polarization	Elevation angle, deg	Flight direction	Figure
Horizontal	31	In-plane	5-1
Horizontal	21	In-plane	5-2
Horizontal	16	In-plane	5-3
Horizontal	10	In-plane	5-4
Horizontal	7	In-plane	5-5
Vertical	31	In-plane	5-6
Vertical	16	In-plane	5-7
Vertical	10	In-plane	5-8
Horizontal	18	45° heading	5-9
Horizontal	12	45° heading	5-10
Horizontal	21	Cross-plane	5-11
Horizontal	11	Cross-plane	5-12

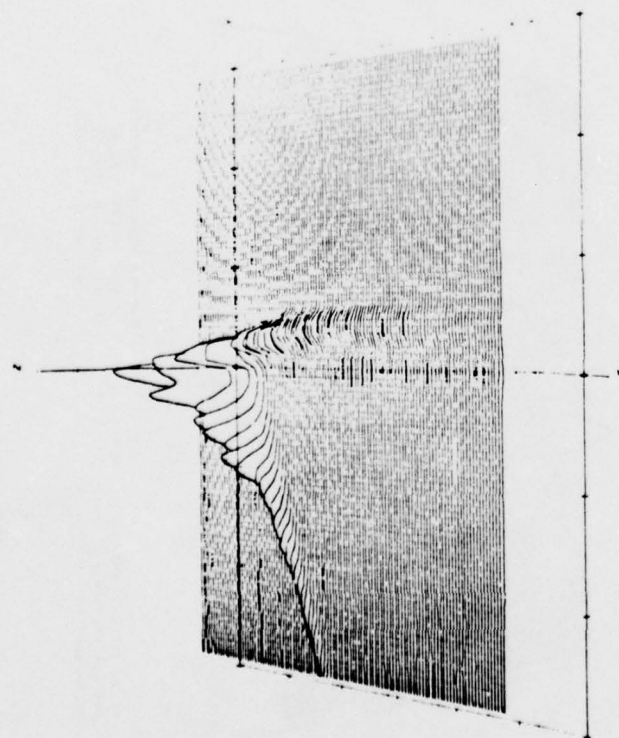
5-4



PARAMETER	MINIMUM	MAXIMUM	INCREMENT
W	0.00	120.00	20.00
Y	-300.00	300.00	100.00
Z	-5.00	30.00	5.00

Figure 5-2. Oceanic Multipath Parameters — Horizontal Polarization, 21° Grazing Angle, In-Plane Geometry

DELAY-DOPPLER SCATTER FUNCTION
 DATE 8/27/75 HORIZONTAL POLARIZATION
 TAP RESOLUTION 2 MICROSEC
 TIME INTERVAL 8/587.481 TO 8/587.618
 NOISE REMOVED



AXIS
 X DELAY TAP 1.2 MICROSEC. WIDTH 1
 Y DOPPLER FREQUENCY (HERTZ) 300.00 300.00 100.00
 Z DELAY-DOPPLER PSD (LINEAR) 5.00 20.00 5.00

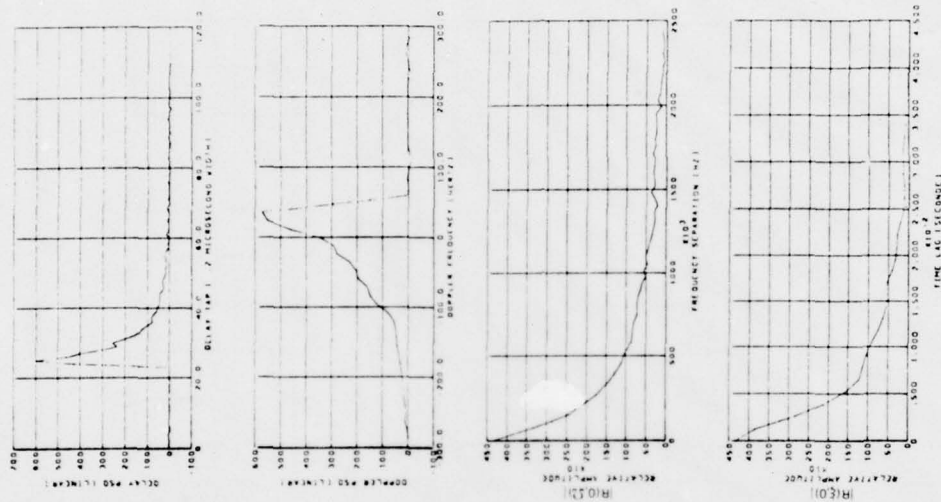


Figure 5-3. Oceanic Multipath Parameters — Horizontal Polarization, 16° Grazing Angle, In-Plane Geometry

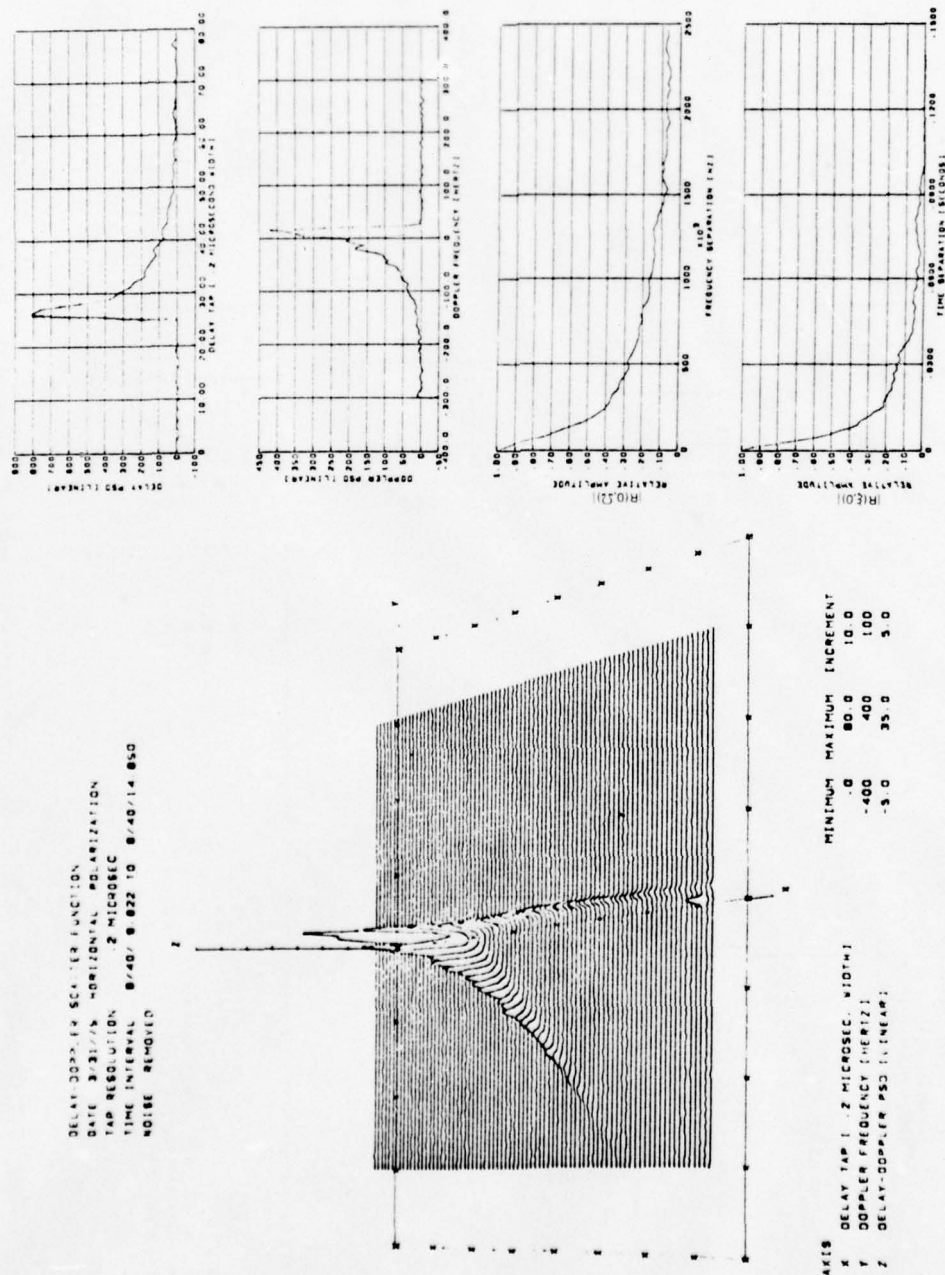


Figure 5-4. Oceanic Multipath Parameters — Horizontal Polarization, 10° Grazing Angle, In-Plane Geometry

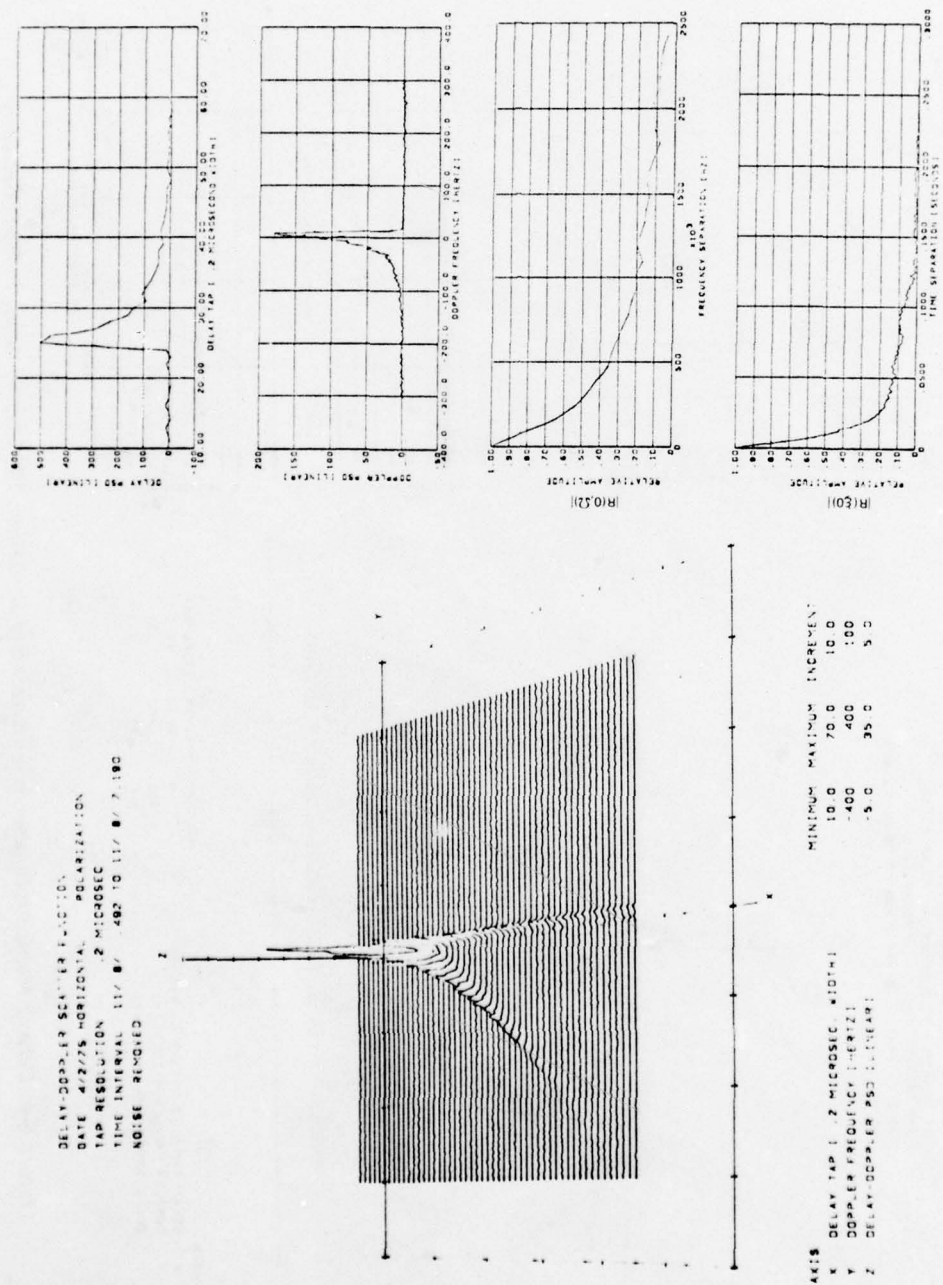
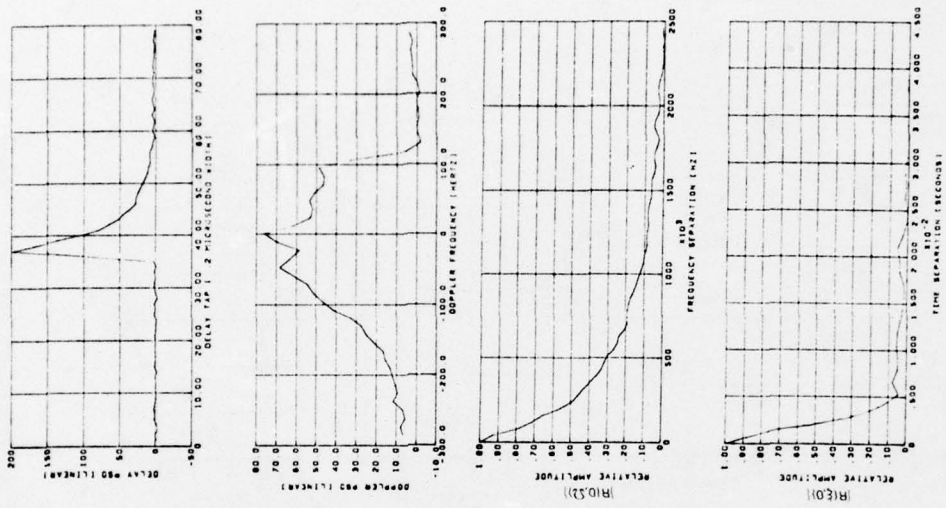
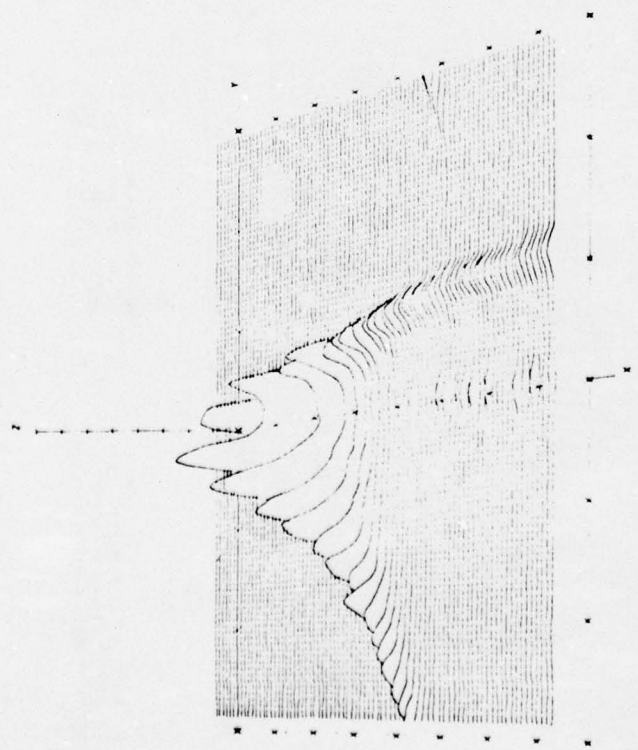


Figure 5-5. Oceanic Multipath Parameters — Horizontal Polarization, 7° Grazing Angle, In-Plane Geometry

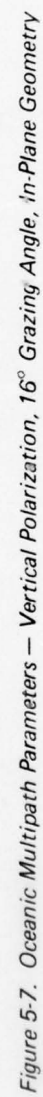


DELAY-DOPPLER SCATTER FUNCTION
 DATE 2/27/75 VERTICAL POLARIZATION
 TAP RESOLUTION 2 MICROSEC
 TIME INTERVAL 10.14/5.33/ TO 10.14/16.034
 NOISE REMOVED



AXIS	MINIMUM	MAXIMUM	INCREMENT
X DELAY TAP 1 2 MICROSEC WIDTH	0	800	100
Y DOPPLER FREQUENCY (HERTZ)	-300	300	100
Z DELAY-DOPPLER PSD (LINEAR)	-50	350	50

Figure 5-6. Oceanic Multipath Parameters — Vertical Polarization, 31° Grazing Angle, In-Plane Geometry



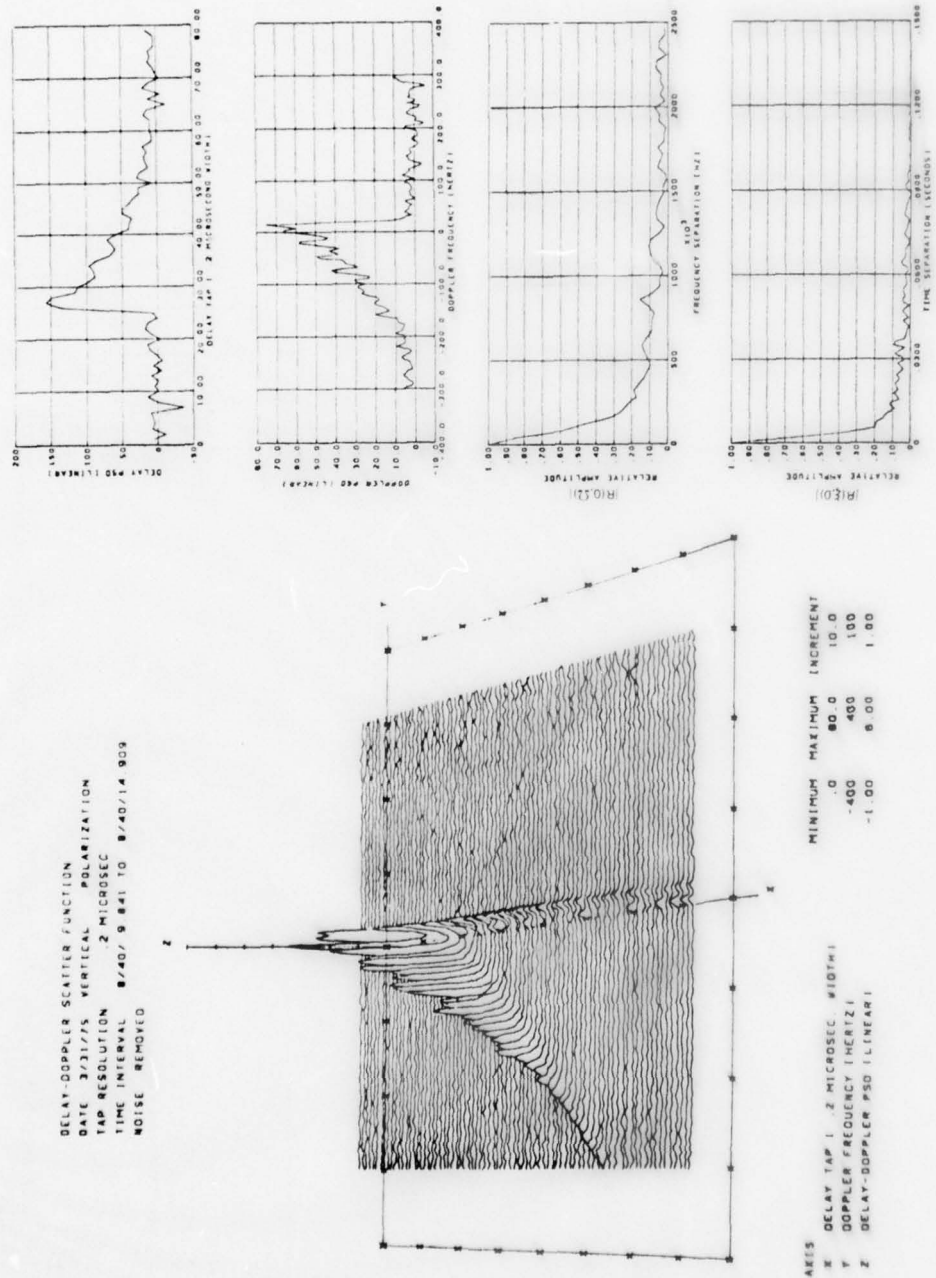
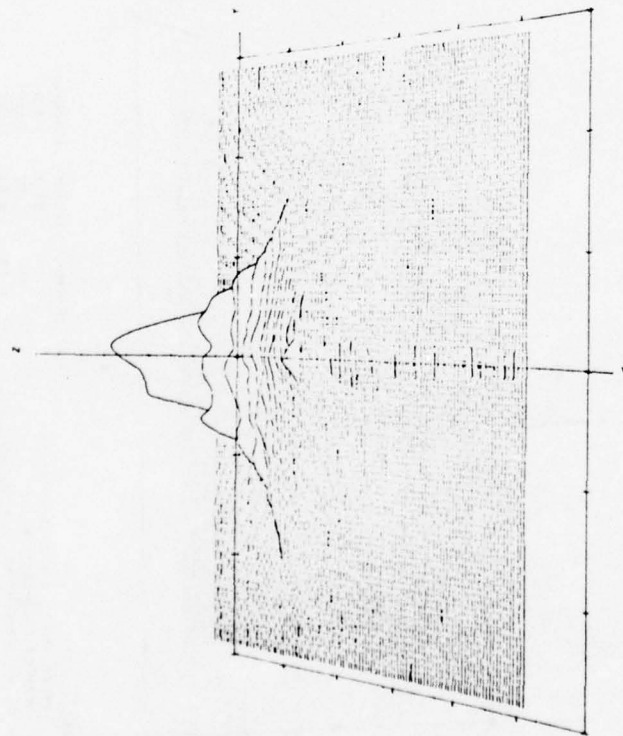


Figure 5-8. Oceanic Multipath Parameters — Vertical Polarization, 10° Grazing Angle, In-Plane Geometry

DELAY-DOPPLER SCATTER FUNCTION
 DATE 4/8/88 HORIZONTAL POLARIZATION
 TAP RESOLUTION 2 MICROSEC
 TIME INTERVAL 10/16/80 402 TO 10/16/80 410
 NOISE REMOVED



MINIMUM MAXIMUM INCREMENT
 X DELAY TAP 1 2 MICROSEC WIDTH
 Y DOPPLER FREQUENCY HERTZ
 Z DELAY-DOPPLER PWD ELIMINATE

X DELAY TAP 1 2 MICROSEC WIDTH
 Y DOPPLER FREQUENCY HERTZ
 Z DELAY-DOPPLER PWD ELIMINATE

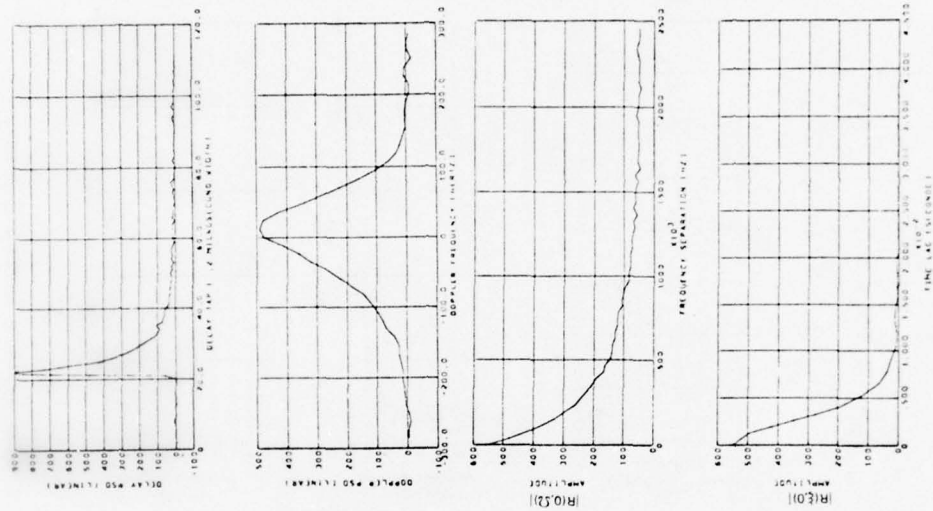


Figure 5-9. Oceanic Multipath Parameters — Horizontal Polarization, 18° Grazing Angle, 45° Heading

MINIMUM	MAXIMUM	INCREMENT
0	80 0	10 0
-300	300	100
-2 0	16 0	2 0

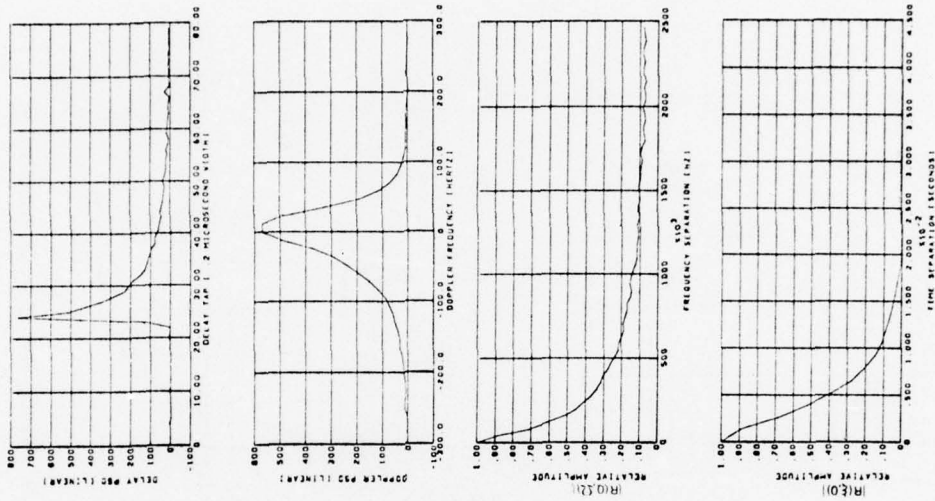
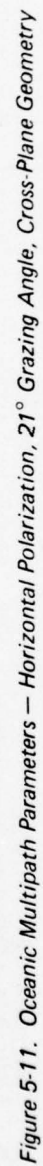


Figure 5-10. Oceanic Multipath Parameters — Horizontal Polarization, 12° Grazing Angle, 45° Heading



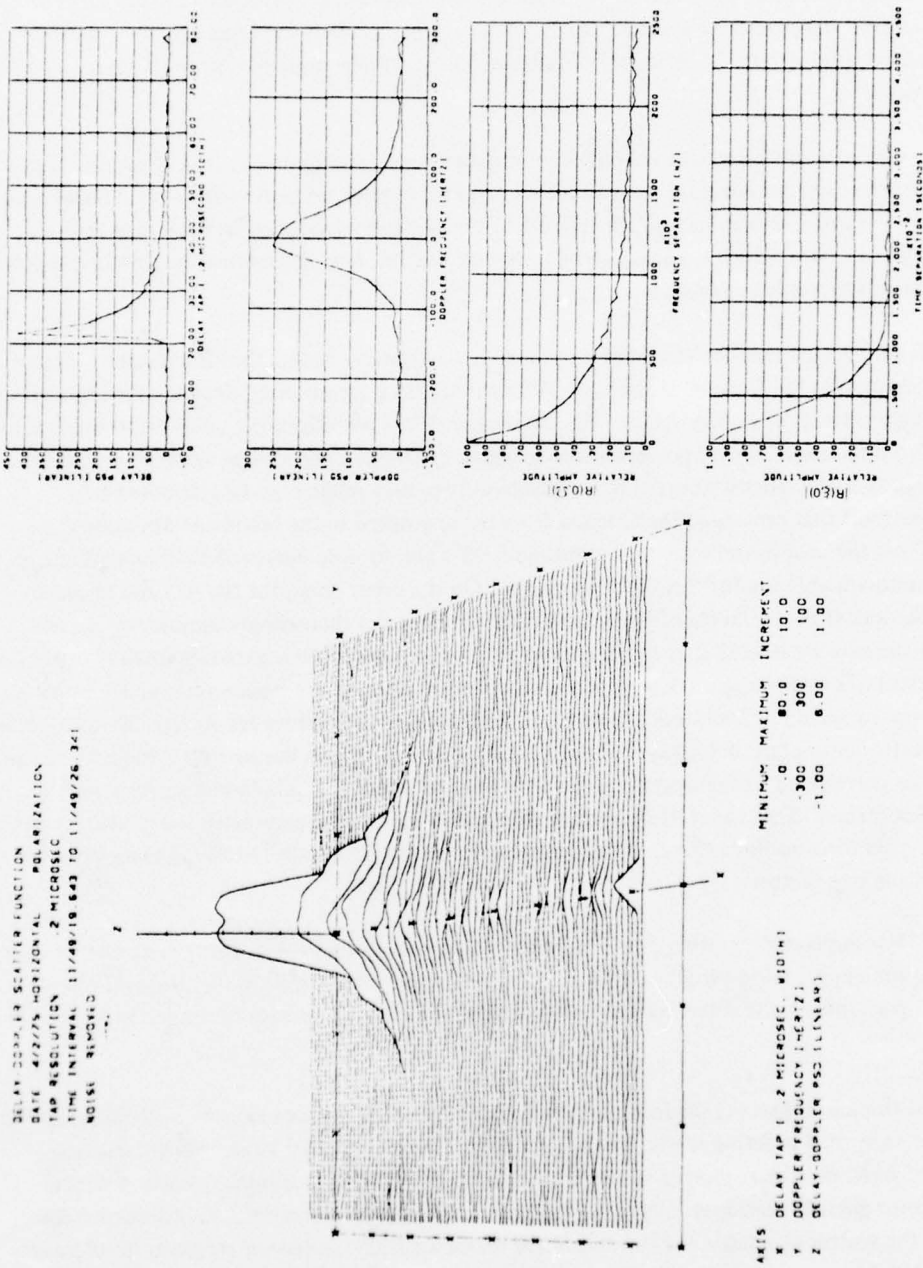


Figure 5-12. Oceanic Multipath Parameters — Horizontal Polarization, 11° Grazing Angle, Cross-Plane Geometry

ATS-6) since these conditions furnish the highest signal-to-noise fidelity and represent the preferred³ flight direction. To provide estimates of the grazing angle dependence, these data are given for a series of elevation angles ranging from 30° to 7°. A somewhat smaller, yet representative, sample selection is used to illustrate the influence of polarization and flight direction on the scatter function characteristics.

The lack of a sufficiently broad collection base of nearly simultaneous (to the electromagnetic probes) sea-surface characterization measurements makes it impossible to furnish experimental results that delineate, in a one-to-one manner, the effects of the surface's slope distribution upon $S(\tau, \omega)$. However, this influence, which is known to be rather significant, is well demonstrated in the model emulation results presented in section 6.

Referring to the figures delineated in table 5-1, we begin by noting that the scatter function's energy distribution in the Doppler variable coordinate exhibits a pronounced dependence upon the direction of the aircraft's velocity vector. For cross-plane flight directions (i.e., KC-135 flying broadside to ATS-6 direction), $S(\tau, \omega)$ possesses a high degree of Doppler coordinate symmetry; the bias toward a slightly higher energy content in the positive-frequency realm may be attributed to a physical constraint that prevented the antenna from being pointed in the broadside direction (i.e., pointed 80° off the nose as opposed to the optimum 90°) and to nose-bulkhead shielding effects on the front multipath antenna for this flight geometry. On the other hand, for the 45° and in-plane velocity direction, the asymmetry of the scatter function becomes increasingly significant. In fact, for the in-plane case we note that as the delay tap number increases, the negative-frequency dispersion of a particular tap's Doppler spectrum increases accordingly whereas the positive-frequency range is, in comparison, rather limited and has a bandwidth relatively invariant from tap to tap. We also note that for a particular in-plane delay tap (τ) the resultant Doppler spectra has two very distinct spectral "humps" that correspond to the upper and lower frequency limits over which physically possible multipath is returned. These aircraft heading dependencies are in agreement with the model-predicted results of section 6; as outlined there, we may ascribe the spectral "humps" of the in-plane data sets to the following two factors:

- a. For in-plane flight directions, the surface elements responsible for returning energy into the upper and lower Doppler limits of a particular delay tap lie along the great circle path joining the subaircraft and subsatellite points and thus may be shown to have a

³Preferred in the sense that (1) for in-plane geometry the probing antenna is more isotropic than it is for other azimuthal pointing angles and (2) symmetry conditions that exist only for in-plane direction of flight may be exploited to overcome the 2-into-1 surface mapping operation which allows antenna spatial filtering effects to be removed, as described in section 5.6. Additional discussion of the scatter geometry and the associated mathematical expressions are given in references 5-2 through 5-5.

significantly larger scatter cross section than any of the other elements that return energy into the delay tap.

- b. The second and perhaps more important factor is a consequence of the large area (maximum for each tap) that gets mapped into the extremities of a particular tap's Doppler spectrum. This occurs since the delay contour and its maximum Doppler shift contours have tangential intersection. Mathematically, this is equivalent to the Jacobian (ref 5-1) of the transformation from surface spatial coordinates to the delay-Doppler coordinates of the receiver becoming maximum.

The phenomenon described in item b above is valid for all flight test directions; however, as the direction moves increasingly away from the in-plane case, the tangential intersections between the delay contours and their extreme Doppler contours move further away from the great circle path and are accordingly associated with reduced scatter cross section (i.e., we have a tradeoff condition between area intercept and the attendant scatter cross section). For the low delay tap values associated with the 45° and cross-plane heading cases, we are able to observe that the area intercept factor outweighs the reduced scatter cross section and produces a distribution tending to be heavy tailed. The opposite conclusion appears to be true for the large delay tap values.

With respect to the grazing angle dependence of $S(\tau, \omega)$, one observes a definite decrease in Doppler dispersion for a decrease in grazing angle. A decrease in grazing angle is also accompanied by an increase in the asymmetry properties of the in-plane scatter function. This factor, in turn, is responsible for increasing the dissimilarities between the alternate flight direction $S(\tau, \omega)$ functions as the grazing angle decreases. Note that for an upper grazing angle limit of 90° the scatter function will not be influenced by the direction of the flight velocity vector.

To properly interpret the in-plane low-angle Doppler spectra characteristics (see secs. 5.2.4 and 5.3.3), it is important to note the low-grazing-angle behavior of $S(\tau, \omega)$'s positive-frequency spectra "humps." Referring to figure 5-5, for example, we observe that the scatter function's positive-frequency shoulder quickly becomes asymptotic to a relatively low-frequency Doppler value. Thus all returns with significant energy from the subsatellite side of the specular point have nearly identical Doppler shifts and produce a resultant composite signal Doppler spectrum with a very pronounced peak density.

The capability to simultaneously conduct horizontal and vertical polarization surface probes allows one to draw comparisons between the two probes under identical surface conditions. A visual analysis of the appropriate data sets of table 5-1 reveals that the vertical and horizontal $S(\tau, \omega)$ functions have, with the exception of their absolute magnitudes, distributional shapes that are quite similar. For the lower grazing angle condition (e.g., compare figs 5-4 and 5-8), we are able to discern that the relative weighting between a tap's negative and positive Doppler returns is larger for the vertical polarization data than it is for the horizontal polarization counterpart. This phenomenon,

predicted by the model results of section 6 (see figs 6-7 and 6-19), is produced by the fact that as the scatter elements move toward the subaircraft location (i.e., negative Doppler returns), their local elevation angles increase as opposed to a decrease for locations progressively closer to the subsatellite location. Since the vertical reflection coefficient (for grazing angles greater than the Brewster angle) increases with an increase in grazing angle whereas the horizontal polarization coefficient is relatively constant, this condition results in the negative Doppler return for a particular tap having a larger ratio of vertical-to-horizontal scattered energy than the positive Doppler returns. For obvious reasons we refer to this phenomenon, discussed further in section 5.2.6, as "Brewster angle fill-in."

In section 5.6 estimates of the prober antenna's spatial filtering characteristics are derived. Due to mapping ambiguities associated with forward-scatter propagation, these effects can be removed only for the in-plane geometry flight direction vectors. For the higher grazing angle conditions, the antenna's spatial filtering effects on the $S(\tau, \omega)$ function were found to be small enough to be neglected. However, at the low end of the grazing angle test conditions ($\approx 7^\circ$), the antenna characteristics are such that the negative-frequency return at the Doppler extremities (i.e., the spectral humps) is accentuated with respect to the specular-point return by as much as 20%; the positive-frequency spectral shoulder is attenuated by roughly the same percentage. This justifies the antenna-effects-removal algorithm described in section 5.6.

5.2 INTEGRAL AND FOURIER OPERATIONS ON THE $S(\tau, \omega)$ FUNCTION

To obtain an alternate representation and in some cases an easier interpretation of the multipath scatter characteristics, we subject the delay-Doppler scatter function to a variety of integral and Fourier operations that yield the following channel parameter estimates:

- Joint time-frequency autocorrelation function
- Delay spectra
- Frequency autocorrelation function
- Doppler spectra
- Time autocorrelation function
- Total rms scattered energy.

These data are related to the $S(\tau, \omega)$ function via the mathematical expression illustrated in section 4.2.

5.2.1 Time-Frequency Autocorrelation Function: $R(\xi, \Omega)$

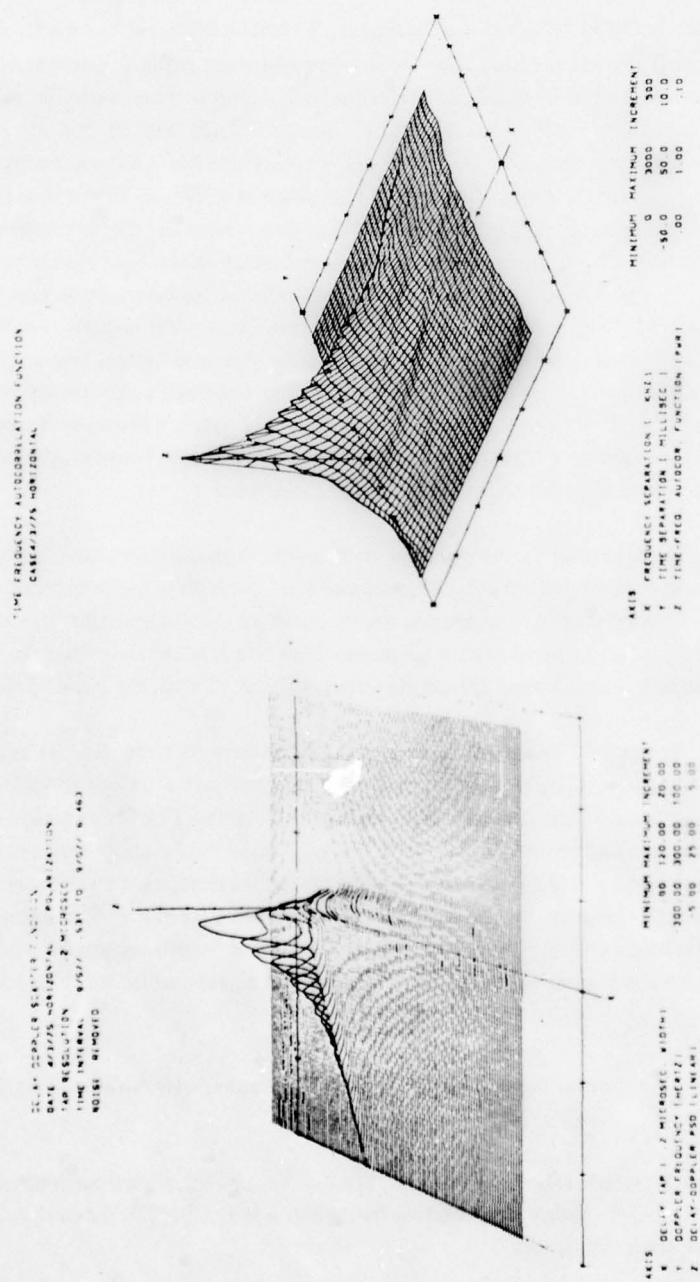
$R(\xi, \Omega)$ is a complex quantity representing the degree of correlation between two received carriers separated by Ω hertz and transmitted over the same propagation paths ξ seconds apart. As stated in section 4.2, we derive this channel parameter through a double inverse Fourier transformation operation on the experimental $S(\tau, \omega)$ function. Hence $R(\xi, \Omega)$ and $S(\tau, \omega)$ are equivalent as far as their order of measurement degree is concerned. However, from the standpoint of relating the multipath results to surface characteristics and scatterer location, the $S(\tau, \omega)$ function is in most respects preferred to the joint autocorrelation distribution. For this reason the major emphasis of the high-echelon data analysis has been directed toward characterization in terms of the delay-Doppler scatter function. The extension from this (τ, ω) domain to the (ξ, Ω) domain may be easily estimated through use of the well-known input/output Fourier transform relationships. To illustrate the interdependence between the two domains, we present data for mid- and low-grazing-angle conditions in combination with in- and cross-plane flight directions. For each combination of system parameters, both the $R(\xi, \Omega)$ and $S(\tau, \omega)$ functions are given. These data are found in figures 5-13 through 5-16. For the in-plane geometry conditions, the $R(\xi, \Omega)$ distribution is quite asymmetrical; two alternate points of view have therefore been included for these cases.

To relate the experimental results of this section to theoretical model expectation, we make reference to figures 6-21 and 6-22 of section 6.3. Because many of the system parameters of the two data sets are not in exact correspondence (e.g., grazing angle, sea slope, antenna pattern⁴), a direct correlation between experiment and theory cannot be made. However it is apparent that the major characteristics of the multipath measurement results are in general accord with the model predictions.

As indicated from figures 5-13 and 5-14, for example, we observe that the $R(\xi, \Omega)$ amplitude distribution is significantly influenced by the direction of the flight test vector. Corresponding to the symmetry properties of the $S(\tau, \omega)$ function, we note that the cross-plane $R(\xi, \Omega)$ function is quite symmetrical whereas the in-plane estimate illustrates a definite asymmetrical characteristic in the ξ variable. In particular, the in-plane $R(\xi, \Omega)$ distribution for a given nonzero frequency lag is observed to possess a definite maximum that does not coincide with the zero time lag value. Furthermore, the ξ location of this local maximum is seen to increase with an increase in frequency separation.⁵ For time lags greater than the local maximum, the $R(\xi, \Omega)$ function has a precipitous decay to a level

⁴The experimental results were derived from the noise-removed, antenna-pattern-present version of the $S(\tau, \omega)$ function.

⁵Inspection of equation (4-1), which relates $R(\xi, \Omega)$ to $S(\tau, \omega)$, reveals the following property of symmetry: $R(\xi, \Omega) = R^*(-\xi, -\Omega)$. Hence, for negative-frequency lags the $R(\xi, \Omega)$ maxima will be associated with a negative time separation.

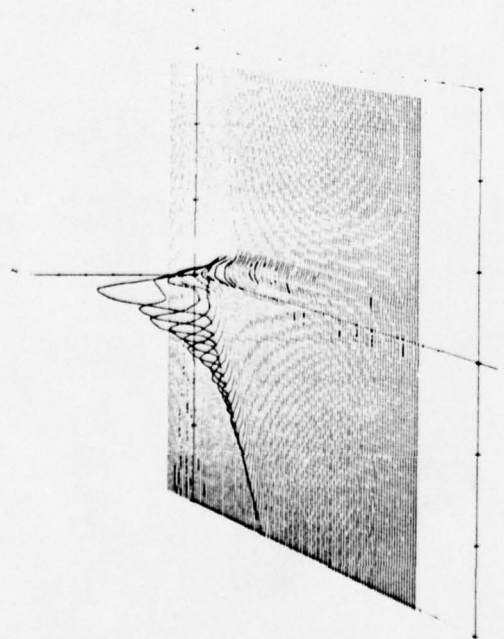


(a) Left-Side View

Figure 5-13. Mid-Angle $R(\xi, \Omega)$ Distribution — 18° Grazing Angle, In-Plane Geometry

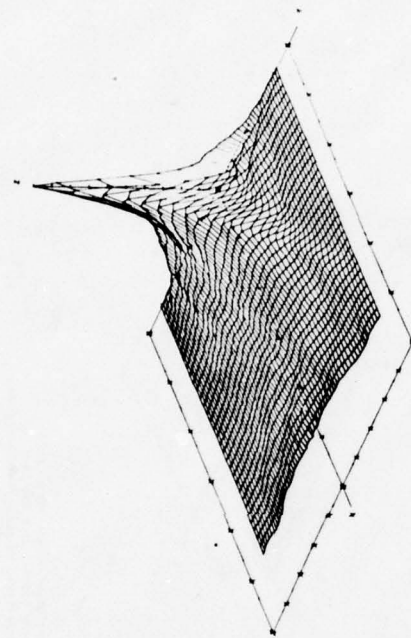
TIME-FREQUENCY AUTOCORRELATION FUNCTION
CASE 4775 HORIZONTAL

DELAY-DOPPLER SPECTROSCOPY
DATE 4/17/75 HORIZONTAL PLANE ZATION
TAP RESOLUTION 2 MICRORSEC
TIME INTERVAL 8/17/75 10 9/17/75 6 48.8
NOTES: BINGO



AXIS
X DELAY TAP 1 2 MICRORSEC WIDTH
Y DOPPLER FREQUENCY (HERTZ)
Z DELAY-DOPPLER PSD (LINEAR)

MINIMUM	MAXIMUM	INCREMENT
0.00	100.00	20.00
300.00	300.00	100.00
5.00	25.00	5.00



AXIS
X FREQUENCY SEPARATION (KHZ)
Y TIME SEPARATION (MILLISEC)
Z TIME-FREQ. AUTOCOR. FUNCTION (PWR)

MINIMUM	MAXIMUM	INCREMENT
0.00	3000.00	300.00
-10.00	50.00	10.00
0.00	1.00	0.10

(b) Right-Side View

Figure 5-13. (Concluded)

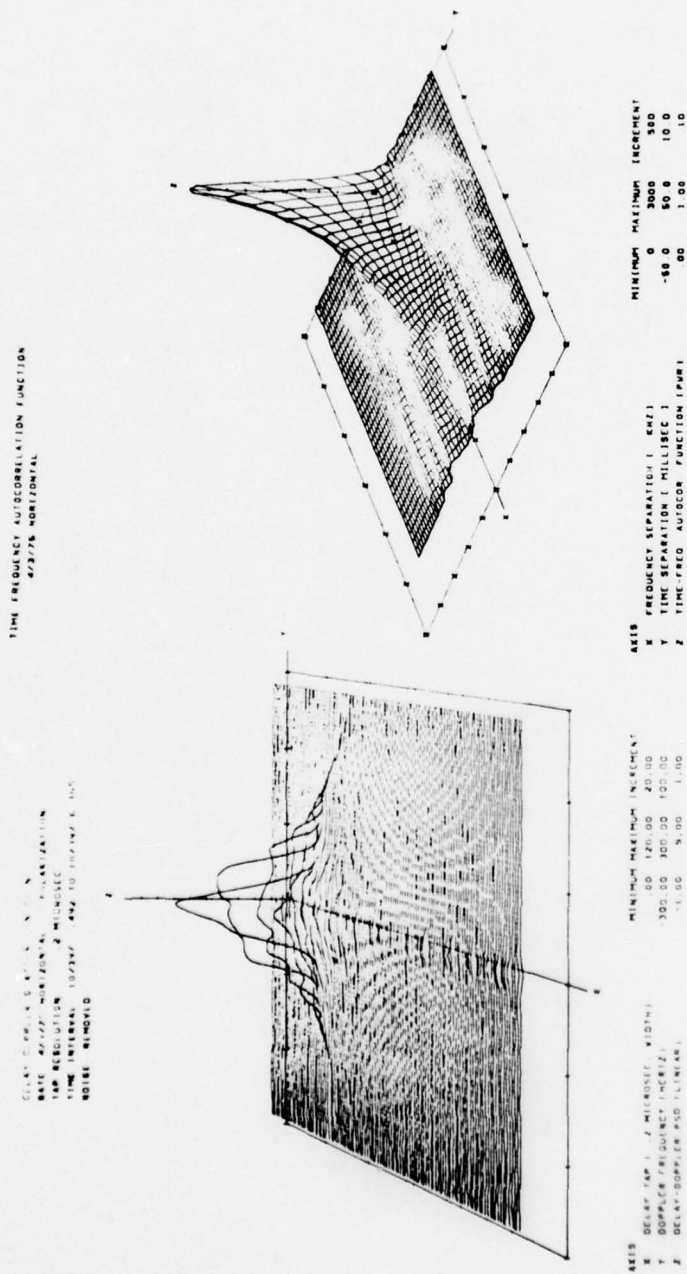
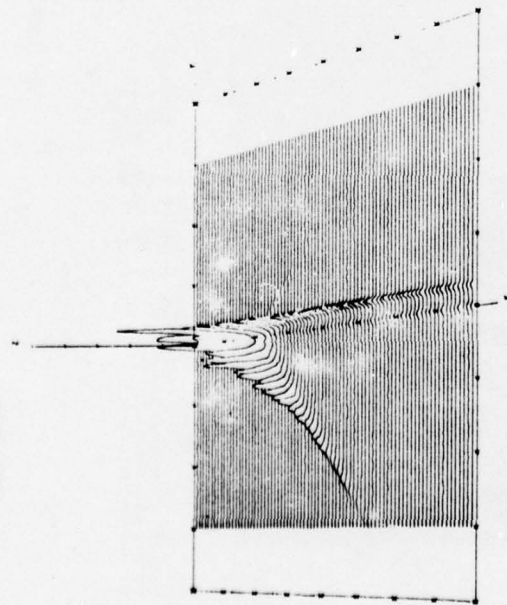


Figure 5-14. Mid-Angle $R(\xi, \Omega)$ Distribution - 21° Grazing Angle, Cross-Plane Geometry

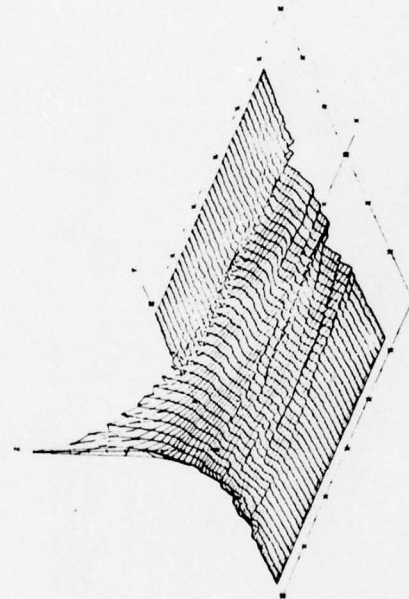
DELAY-DOPPLER SCATTER FUNCTION
 DATE 3/31/75 LMC POLARIZATION
 TAP RESOLUTION 2 MICRORSEC
 TIME INTERVAL 8/54.821 TO 8/55.819
 NOISE PRESENT

TIME-FREQUENCY AUTOCORRELATION FUNCTION
 CASE 3/31/75 LMC



AXIS
 X DELAY TAP 1.2 MICRORSEC WIDTH
 Y DOPPLER FREQUENCY (HERTZ)
 Z DELAY-DOPPLER PSD (LINEAR)

MINIMUM MAXIMUM INCREMENT
 X 0 80.0 10.0
 Y -400 400 100
 Z .0 25.0 5.0



MINIMUM MAXIMUM INCREMENT
 X 0 3000 500
 Y -150 150 50
 Z 0 1.00 1.0

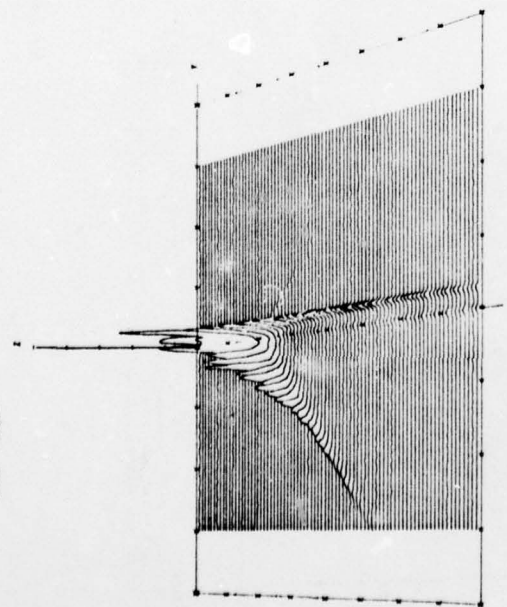
AXIS
 X FREQUENCY SEPARATION (KHZ)
 Y TIME SEPARATION (MILLISEC)
 Z TIME-FREQ AUTOCORR FUNCTION (KHZ)

(a) Left-Side View

Figure 5-15. Low-Angle $R(\xi, \Omega)$ Distribution — 14° Grazing Angle, In-Plane Geometry

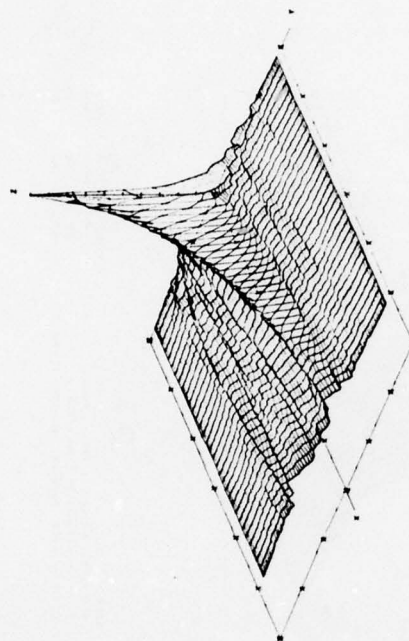
DELAY-DOPPLER SCATTER FUNCTION
 DATE 8/71/76 LMC POLARIZATION
 TAP RESOLUTION .2 MICROSEC
 TIME INTERVAL 8/ 8/64-821 10 8/ 8/58 848
 NOISE PRESENT

TIME FREQUENCY AUTOCORRELATION FUNCTION
 CASE8/31/76 LMC



AXIS DELAY TAP 1 2 MICROSEC, WIDTH 1
 Y DOPPLER FREQUENCY, HERTZ
 Z DELAY-DOPPLER PDS LINEAR

MINIMUM MAXIMUM INCREMENT
 0 800 100
 -400 400 100
 0 250 50



AXIS X FREQUENCY SEPARATION 1 HZ
 Y TIME SEPARATION 1 MILLISEC 1
 Z TIME-FREQ AUTOCOR FUNCTION (PWR)

MINIMUM MAXIMUM INCREMENT
 0 3000 500
 -150 150 50
 00 100 10

(b) Right-Side View

Figure 5.15. (Concluded)

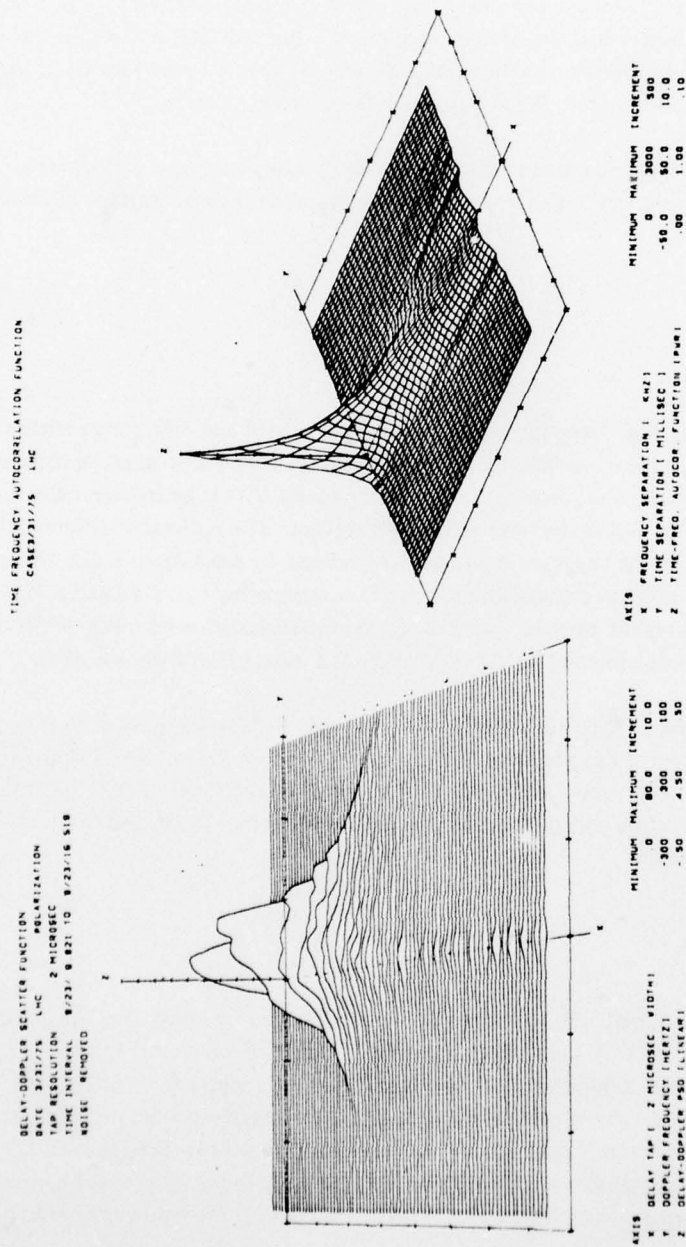


Figure 5-16. Low-Angle $R(\xi, \Omega)$ Distribution — 15° Grazing Angle, Cross-Plane Geometry

roughly equivalent to the value at its mirror image location on the negative side of the axis. Using basic Fourier transform properties, one can relate this ridgelike $R(\xi, \Omega)$ structure to the negative-frequency shoulder of the function's $S(\tau, \omega)$ counterpart. The positive $S(\tau, \omega)$ Doppler shoulder, which runs in a nearly parallel direction to the delay axis, may be shown to produce the nearly symmetrical underlying distribution in the $R(\xi, \Omega)$ function (see, for example, fig. 5-15).

Under isotropic surface and antenna illumination conditions, one expects that $S(\tau, \omega)$ will be highly symmetrical with respect to the Doppler variable for cross-plane geometry. Hence equation (4-1) predicts that

$$|R(\xi, \Omega)| \approx |R(-\xi, \Omega)|.$$

In general, the cross-plane experimental results of figures 5-14 and 5-16 substantiate this symmetry relationship, with the observed slight departures most likely due to antenna influence on the $S(\tau, \omega)$ function. This antenna perturbation (discussed in sec. 5.1) in general provides more favorable cross-plane illumination to the positive Doppler returns. The noticeable difference in the structure of $R(\xi, \Omega)$ between the experiment and model for large Ω separations is also thought to arise from the nonuniform antenna pattern illumination (i.e., comparing figs. 5-14 and 6-22, we observe that for cuts involving the extreme values of ξ , the model function has peak density at the $\Omega = 0$ value whereas the experimental distribution peaks at a value offset from the axis).

Finally, we note that an axial cut along $\xi = 0$ through $R(\xi, \Omega)$ (equivalent to the channel's frequency autocorrelation function) produces similar distributions for the in-plane and cross-plane geometry cases. This is to be expected since $R(0, \Omega)$ is related entirely to the delay spectrum, which is independent of flight direction and, as shown in the following section, is also relatively uninfluenced by the grazing angle parameter.

5.2.2 Delay Spectra: $Q(\tau)$

Estimates of the multipath delay spectra, $Q(\tau)$, are obtained by integrating the "noise-removed" delay-Doppler scatter function over the Doppler variable. Thus $Q(\tau)$ represents the power spectral density of the scattered signal component that arrives at the receiver with delay τ . In this report we select the specular-point return as the zero reference value. A comprehensive set of experimentally derived delay-spectra distributions is contained in the data sets used for the $S(\tau, \omega)$ discussion; these data may be related to system parameters through use of table 5-1. In turn, the experimental delay-spectra results may be compared with theoretical expectation through the figure cross-reference contained in table 6-1.

An obvious characteristic of the delay-spectra measurements is the very small amount of observed flight direction or grazing angle influence on the energy distribution. The flight direction independence is, of course, expected. Relative to the grazing angle effects on the delay spectra, we note that for a constant-surface slope condition the model predictions (both spectra and spreads) of section 6 similarly predict a relatively small influence.

Prober polarization influences on the reflection process are observed to produce delay spectra for vertical polarization that are much heavier tailed than their horizontal polarization counterparts. Furthermore, this effect becomes more significant as the grazing angle decreases and, as illustrated in section 5.1, is related to the phenomenon of Brewster angle fill-in.

A comparison of the experimental data with the theoretically predicted delay spectra of section 6 reveals that the above observations are fairly well duplicated by the model. In general, the model results appear to exhibit the greatest degree of similarity to the measured spectra for the assumed sea-slope condition of 6° . For example, compare the delay spectrum of figure 5-1 with that of figure 6-4 (which represents the 6° slope case) as opposed to figures 6-3 and 6-5 which pertain to the 12° and 3° slope predictions, respectively).

The effect of the prober antenna's spatial filtering characteristics is discussed in section 5.6. In general, the antenna-induced perturbation on delay-spectra measurements is relatively insignificant over the bulk of the distribution (i.e., for the low- and high-grazing-angle conditions analyzed, the antenna-induced perturbations at a spectral density 10 dB down from the specular-point tap are shown to be 3% and 7%, respectively).

5.2.3 Frequency Autocorrelation Function: $R(0, \Omega)$

The frequency autocorrelation function, $R(0, \Omega)$, represents the degree of correlation between two received signals separated by Ω hertz and traversing identical paths through the channel. In this report the direct line-of-sight signal component is *excluded* and thus $R(0, \Omega)$ is obtained in a straightforward manner by taking the inverse Fourier transform of the multipath delay spectrum. Again we refer to table 5-1 for a delineation of the sample $R(0, \Omega)$ results presented and their corresponding system parameters.

As for the delay-spectra characteristics, we observe that the magnitude of $R(0, \Omega)$ exhibits almost no dependence on aircraft heading or system grazing angle. Theoretically, aircraft heading should have no influence on the delay spectra or the frequency autocorrelation function. These results are in accord with the model predictions of section 6 under the constraint of a constant-sea-surface rms slope.

Prober polarization is observed to have by far the most significant effect on the frequency autocorrelation function, with the horizontal results being heavier tailed than their vertical polarization counterparts. The extent of this effect is seen to increase for a decrease in grazing angle. Again these results are in agreement with the model predictions of section 6 and are directly related to the observed polarization effects on the delay spectra (vertical polarization spectra are heavier tailed than the horizontal results), which in turn are related to the phenomenon of Brewster angle vertical polarization fill-in.

Prober antenna spatial filtering perturbations on the frequency autocorrelation function are rather minimal both for the high- and low-grazing-angle conditions (see sec. 5.6).

5.2.4 Doppler Spectra: $D(\omega)$

A Doppler frequency shift is induced upon the individual components of a scattered signal when a relative motion exists between the rough surface and the transmitter/receiver terminals. In general this frequency shift is expressed as the sum of two terms, one arising from the surface dynamics and the other being due to terminal motion relative to the instantaneously static surface. In our case the ATS-6 satellite is stationary and the velocity of the KC-135 jet airplane is sufficiently large to consider the oceanic surface to be frozen. Hence the Doppler shift associated with a particular surface scatter element is a function only of aircraft-oriented system parameters. As previously outlined in section 4.2, we obtain an estimate of the total scattered signals' Doppler power spectral density, $D(\omega)$, by integrating the $S(\tau, \omega)$ function over its delay variable. The Doppler coordinate variable, ω , is established relative to the frequency of the direct line-of-sight signal. For cross-plane flight directions, this reference is identical to the specular-point Doppler shift; for in-plane directions, a differential Doppler on the order of 4 Hz exists between the specular point and direct signal paths.

Sample Doppler spectra for a variety of experimental conditions cross-referenced in table 5-1 are given in figures 5-1 through 5-12.

The experimental Doppler spectra distribution may be compared with the theoretical model predictions of section 6. A visual correlation of the two data sets reveals that the model results, as evaluated under the 6° slope assumption (and for some cases the 12° slope condition), closely emulate the experimental spectra. The experimental data sets show that the channel's Doppler spectrum is very dependent upon grazing angle and flight direction system parameters. As would be expected from the corresponding $S(\tau, \omega)$ distribution, the Doppler spectrum is highly symmetrical for the cross-plane flight geometries (equipment-induced asymmetries were discussed in sec. 5.1) and resembles a zero-mean Gaussian distribution whose variance decreases with a decrease in grazing angle. These characteristics also apply fairly well to the 45° flight direction; however, there is a tendency for the negative-spectra realm to be slightly more dispersed and thus heavier tailed than the positive region.

On the other hand, for the in-plane flight direction the Doppler spectrum is highly asymmetric, with the distribution being very heavy tailed in the negative-frequency region and possessing a spectral maximum that coincides closely with a frequency upper limit in the positive Doppler realm above which the energy distribution has a precipitous fall-off. Comparing figures 5-2 through 5-5 reveals that these in-plane geometry attributes become increasingly pronounced as the grazing angle decreases. In fact, at the lower grazing angle values (e.g., fig. 5-5) we note that the Doppler spectrum has an extreme high-density peak at a very low positive Doppler value above which no energy exists and an exponential-like decay for the energies whose frequencies lie below the Doppler upper limit. As will be shown in section 5.3.3, this phenomenon results in very low Doppler spread measure for the low-angle in-plane geometry conditions.

With respect to the Doppler spectrum's in-plane geometry polarization characteristics, it may be observed that, especially for the low-grazing-angle conditions, the vertical polarization results have a significantly higher percentage of energy in the negative-frequency portion of their distributions than do the corresponding horizontal polarization data (e.g., compare figs. 5-4 and 5-8). The Brewster angle fill-in phenomenon that produces this result is also observed for the model prediction and is discussed in sections 5.1 and 6.2 of this document.

Unlike the results for the delay spectrum, the antenna pattern influence on the Doppler spectrum is shown in section 5.6 to be significant enough to merit consideration. Specifically, for the in-plane flight geometry case we expect that as the grazing angle decreases the Doppler spectrum will be subjected to an *overestimation* bias in the central portion of its negative-frequency realm. This implies that a region on the subaircraft side of the specular point receives more antenna gain than is directed toward the specular point because of the antenna beam pointing factors discussed in section 5.6. As a quantitative measure, the low-angle (7°) in-plane Doppler spectrum for a typical case is predicted to be biased by roughly +10% at its spectra mid-decile level and +30% at its lower decile level.

5.2.5 Time Autocorrelation Function: $R(\xi, 0)$

$R(\xi, 0)$, the time autocorrelation function of the multipath channel, represents the degree of correlation between two received signals that arrive at the receiver after being transmitted as cw signals with identical frequencies but offset in time by ξ seconds. We restrict our attention entirely to the multipath component of the channel and thus obtain the $R(\xi, 0)$ estimate by performing an inverse Fourier transform on the scattered signals' Doppler spectrum. Experimental results from this analysis for a variety of test conditions outlined in the cross-reference of table 5-1 are presented in figures 5-1 through 5-12. For comparison with theoretical model prediction, refer to the data sets associated with table 6-1.

From the examples, we observe that the $R(\xi, 0)$ distribution has characteristic dependencies upon aircraft heading, grazing angle, and probe polarization. While the influence of the aircraft's flight vector direction is noticeable, it is not nearly as distinct as it is for $R(\xi, 0)$'s Fourier transform, the Doppler spectrum. In general we note that the in-plane flight direction produces a time autocorrelation function that appears to be heavier tailed than its cross-plane counterpart.

As expected, the elevation dependence of $R(\xi, 0)$ is seen to produce an increase in spread for a decrease in grazing angle. Also, as would be predicted from the Doppler spectra measurements, the horizontal and vertical polarization $R(\xi, 0)$ results become increasingly dissimilar as the grazing angle decreases, with the horizontal results exhibiting a much slower decay than their vertical polarization counterparts.

In general the model emulation of section 6 duplicates the above observations to a fairly high degree. As for the other unidimensional channel distributions, the degree of correlation between the experimental and theoretical time autocorrelation functions appears to be the highest when the sea slope is chosen to be 6° or somewhat higher (for example, compare fig. 5-1 with fig. 6-4).

The effects of antenna spatial filtering on the in-plane $R(\xi, 0)$ estimates are given in section 5.6. The high-angle data is relatively uninfluenced by the antenna pattern, whereas the low-angle data exhibits effects that are consistent with the observed effects on the Doppler spectrum. In other words, the Doppler spectra overestimation produced by the antenna perturbation is translated into a time autocorrelation function effect that causes the distribution to decay too rapidly (roughly 30% at the origin).

5.2.6 Total RMS Scattered Energy

To relate the intensity of the multipath scatter process to a quantitative measure, the channel mean square scatter coefficient (Γ) has been derived for both horizontally and vertically polarized data. The term Γ , defined as the ratio of total energy scattered into the receiver relative to the energy incident upon the surface, is obtained from the following formulation:

$$\Gamma = \frac{\langle |I|^2 \rangle}{\langle |D|^2 \rangle} \Big|_{\text{dB}} + \frac{G_D}{G_I} \Big|_{\text{dB}}, \quad (5-1)$$

where:

$\langle |I|^2 \rangle$ = mean square multipath power obtained by integrating $S(\tau, \omega)$ over its delay and Doppler variables

- $\langle |D|^2 \rangle$ = mean square direct-path signal obtained by coherently summing the "direct" tap outputs to form a composite signal, which in turn is subjected to a mean square calculation
- G_D/G_I = adjustment factor to account for direct and indirect channel gain differences, etc.

In calculating G_D/G_I , the following factors (expressed in decibels) are included:

$$G_D/G_I = P_D/P_I + A_D/A_I + L_{pol} + GRX_D/GRX_I + GLPF_D/GLPF_I + L_{IS} + L_{trunc}, \quad (5-2)$$

where:

- P_D/P_I = ratio of direct power to indirect power as delivered to the inputs of the transmitting antennas (includes line losses etc.)
- A_D/A_I = ratio of direct signal antenna gain to multipath signal antenna gain. The multipath antenna gain is taken to be equivalent to the gain directed toward the specular point of the surface. This should not introduce an appreciable error due to the relatively broad-beam characteristics of the antenna and the capability for pointing it toward the effective glistening area of the surface. For the quad-helix direct antenna, a gain of 15.2 dB was used when the elevation angle of the antenna relative to the tangent plane on the skin of the aircraft was greater than 12° . For smaller angles, the aircraft skin effects influence its beam shape, and calibration measurement data obtained from up-look modes of the flight test scenarios were used to obtain the following empirical relationship: $A_D = 15.2 \text{ dB} + (\theta' - 12^\circ) (0.65 \text{ dB})$; where θ' = elevation angle of quad helix relative to its local ground plane.
- L_{pol} = a 3-dB adjustment factor to account for polarization mismatches at the satellite (i.e., ATS-6 has RHC, quad helix has RHC, and multipath antenna has linear polarization)
- GRX_D/GRX_I = ratio of receiver direct to indirect channel gain, obtained in a data analysis program module that operates on the SACP system parameters embedded on the data tape containing the receiver time-domain samples
- $GLPF_D/GLPF_I$ = the ratio of the receiver's low-pass filter gains for the direct and indirect channels. This parameter is derived from the SACP filter coefficients and includes a factor to account for the filter mode, such as "zero-stuff," when applicable (i.e., at 10-MHz chip rate and 300-Hz bandwidth, $GLPF_D/GLPF_I = 14.8 \text{ dB}$, whereas at 5-MHz chip rate and 300-Hz bandwidth (a zero-stuff mode for the indirect channel) it equals 20.8 dB)

$L_{I\Sigma}$

= an adjustment factor necessitated by the fact that the $\langle |I|^2 \rangle$ estimation technique is in essence equivalent to an incoherent power summation of the delay tap outputs. This summation does not give a true estimate of the total energy content because (1) adjacent taps one chip apart have a realm of commonality in the delay area over which their autocorrelation functions are nonzero and (2) the autocorrelation function of the probing signal's PN sequence is not uniform over a chip width but for the continuous analog case has triangular distribution with a peak equal to the sequence length and a base equal to ± 1 chip from the center. Assuming the multipath's delay spectrum is piecewise constant over a chip width, the above effects are calculated to yield $L_{I\Sigma}$ values of 1.7, 1.25, and 0 dB for probe chip rates of 2.5, 5.0, and 10.0 MHz, respectively. A coherent summation in effect provides a single tap experiment with uniform correlation over the entire tap bank range; this procedure is used to estimate $\langle |D|^2 \rangle$.

L_{trunc}

= a factor to account for the finite delay-Doppler range over which the receiver is able to capture energy. For the majority of the oceanic multipath probes, the transmitter/receiver parameters were chosen to provide a tap width of 0.2 μsec and a low-pass-filter bandwidth of 300 Hz. Thus assuming the specular-point return is placed in the mid-20's region of the correlator bank (to avoid malfunctions occasionally experienced with delay taps in the neighborhood of taps 17 to 19), we have a receiver configuration that will capture sea scatter returns whose delay (τ) and Doppler (f_d) values satisfy both of the following inequalities: $\tau \leq (110 - 25) 0.2 = 17 \mu\text{sec}$ and $f_d \leq 300 \text{ Hz}$. The incoherent sum of all energies lying outside this region is referred to as the system truncation loss component (L_{trunc}).

Using the physical optics vector scatter model (sec 6), L_{trunc} was predicted using the expression

$$L_{\text{trunc}} = -10 \log \left[\frac{\int_{\tau=0}^{17 \mu\text{sec}} \int_{f=-300 \text{ Hz}}^{+300 \text{ Hz}} S(\tau, \omega) d\tau d\omega}{\int_{\tau=0}^{\infty} \int_{f=-\infty}^{+\infty} S(\tau, \omega) d\tau d\omega} \right]$$

The value of L_{trunc} was calculated for typical system geometry configurations and for assumed sea-slope conditions. An obvious result from this analysis is that L_{trunc} increases with an increase in the

surface rms slope. With respect to the grazing angle dependency, we observed that a tradeoff occurs: the τ constraint was more significant with a decrease in grazing angle while the Doppler constraint was more significant as grazing angle increased. Aircraft heading, as expected, had no influence on the delay requirement. However, for the Doppler criteria it was observed that as the aircraft heading changed from cross-plane to in-plane orientation, the receiver, on a relative basis, captured more of the subsatellite-oriented returns and less of the subaircraft-oriented scatter.

In general, L_{trunc} was calculated to be relatively small. For example, at a grazing angle of 13° and for average and precipitous sea slopes of 6° and 12° , truncation loss values of 0.10 and 0.30 dB, respectively, were calculated for the horizontal polarization in-plane flight geometry. Since the sea slope was unknown, we have taken L_{trunc} to equal 0.2 dB for all cases.

Figure 5-17 presents the experimentally derived values of the rms scatter coefficients as a function of grazing angle. Also shown are scatter model predictions representing expected results for assumed rms sea slopes of 3° and 12° (see sec 6.3). Individual 90% confidence intervals of roughly ± 2.5 dB may be attached to each of the data points of the figure. These confidence interval measures are calculated in a manner similar to that employed in the ATS-5 data analyses (ref 5-6) and are assumed to be dependent only upon the normalization factors used to derive G_D/G_I . Hence we assume the sample space size in estimating $\langle |I|^2 \rangle / \langle |D|^2 \rangle$ is sufficiently large so that its estimation variance may be neglected.

In general, the experimental and theoretical Γ values predicted by the physical optics vector scatter model are in close accord and agree well with experimental results reported for the FAA ATS-5 oceanic multipath tests (ref 5-6, fig 13). Other analytically derived estimates (ref 5-5, table 2-9) agree well for the circular polarization modes and somewhat less well for the horizontal and vertical linear polarizations.

We note that for grazing angles greater than roughly 10° the model predicts that rms sea slope has a very small effect on the total energy content of the scattered signal. The scatter coefficient dependency upon sea slope could not be determined explicitly experimentally because sea-slope measurements with a one-to-one correspondence to the multipath measurements were not available. The experimental data for these elevation angles, however, does appear to be consistent with this observation. At the lower grazing angles the rms scatter coefficients do not appear to be totally immune from the sea-slope influence. For angles in the vicinity of the Brewster angle ($\approx 6^\circ$), the vertically polarized Γ values tend to increase with an increase in slope, whereas the opposite occurs for horizontal polarization. In the limit, as the surface slope approaches zero, the theoretical curves take on values predicted by the relationship $|DR|^2$, where D is the spherical-earth reflection coefficient and R is the smooth-earth Fresnel reflection coefficient as evaluated at the specular point. This result corresponds to the "steepest descent" closed-form integral solution to the scatter phenomenon (ref. 5-7) and, with the

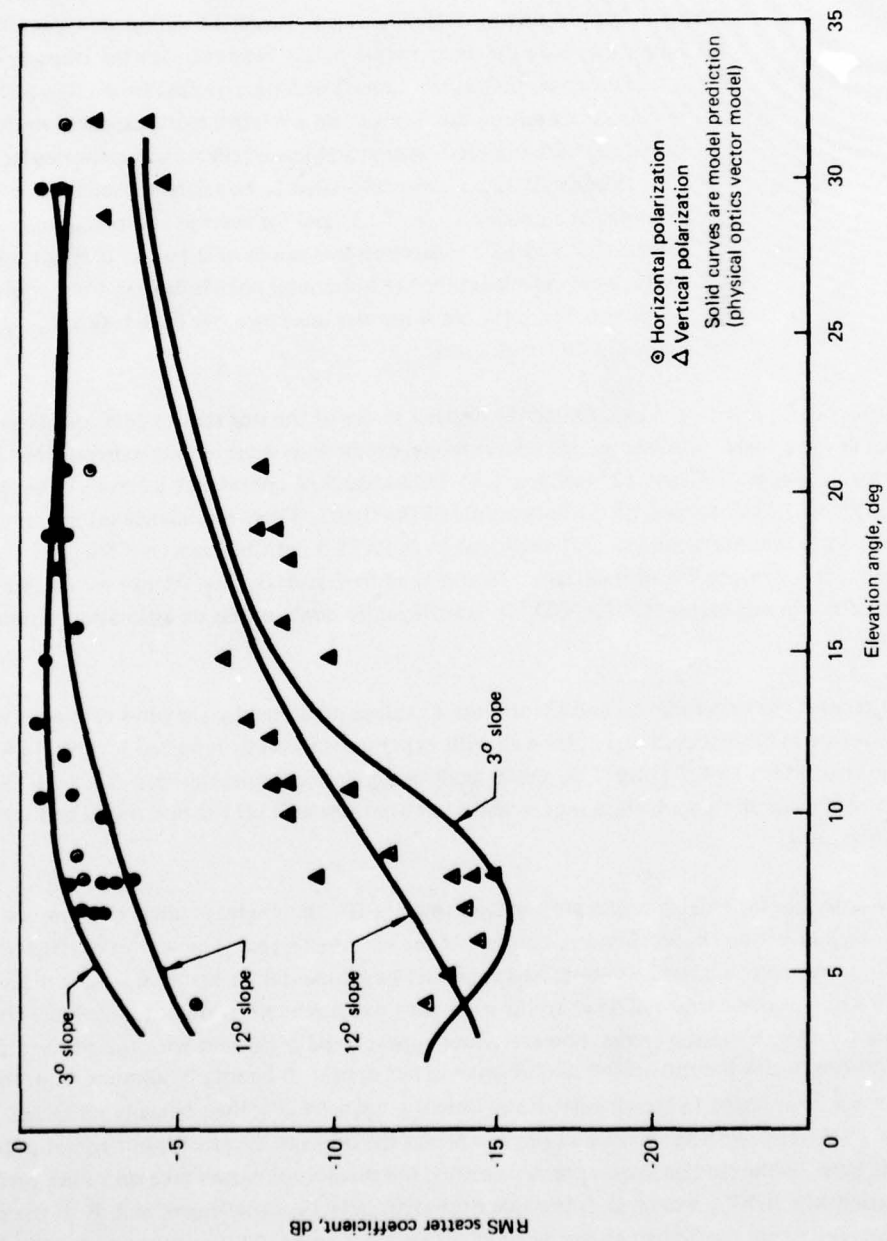


Figure 5-17. Oceanic RMS Total Scatter Coefficients

exception of the vertically polarized data in the vicinity of the pseudo-Brewster angle, yields predicted Γ relationships that agree quite well with both the theoretical and experimental results of figure 5-17. At the pseudo-Brewster angle, the expression $|DR|^2$ for vertical polarization is on the order of -20 dB, which is seen to be roughly 5 dB below the experimental data and the scatter model surface integration results.

Similar departures have also been observed for numerous VHF experiments (ref 5-8, p. 320) as well as for an ATS-5 L-band multipath experiment (ref 5-6). These departures are a direct result of the diffuse nature of the scatter surface; i.e., over the effective scatter region the reflection coefficient associated with the *tilted* surface facets responsible for favorable reflection into the receiver will differ from the reflection coefficient at the specular point. This effect is termed by us as "Brewster angle fill-in." The effect is most pronounced for the vertical polarization probes at a grazing angle equal to the Brewster angle since the reflection coefficient changes rapidly with local grazing angle and all surface scatterers will have a reflection coefficient at least as large as (if not much larger than) the specular-point value.

5.3 OCEANIC SCATTER PARAMETER SPREAD VALUES

Some of the most useful and fundamental measures of the oceanic multipath phenomena relate to the spread values associated with the scattered signal's delay spectra, Doppler spectra, time autocorrelation function, and frequency autocorrelation function. In this section, these data are given for both horizontal and vertical polarization probes as conducted during the in-plane and cross-plane flight directions. For the delay and Doppler spectra, the total two-sided 3- and 10-dB spreads are presented, whereas only the one-sided 3-dB spread is given for the autocorrelation functions.⁶ Figure 5-18 illustrates these quantities for the respective channel distributions.

In comparing the experimental spread results to theoretical expectation, primary emphasis is placed on predictions derived from the surface integration scatter model (see sec 6). Model results generated for rms total sea slopes of 3°, 6°, and 12° tend to indicate that the majority of flight test conditions were associated with the higher slope values. Hence in this section we use the average of the model predictions for the 6° and 12° sea slope as our theoretical expectation standard. Although this procedure is not rigorous, one may consider this to be representative of model results roughly

⁶For the autocorrelation functions, the 10-dB spread values occasionally exceed the resolution capabilities associated with the proper chip rate and Fourier transforms processing algorithm.

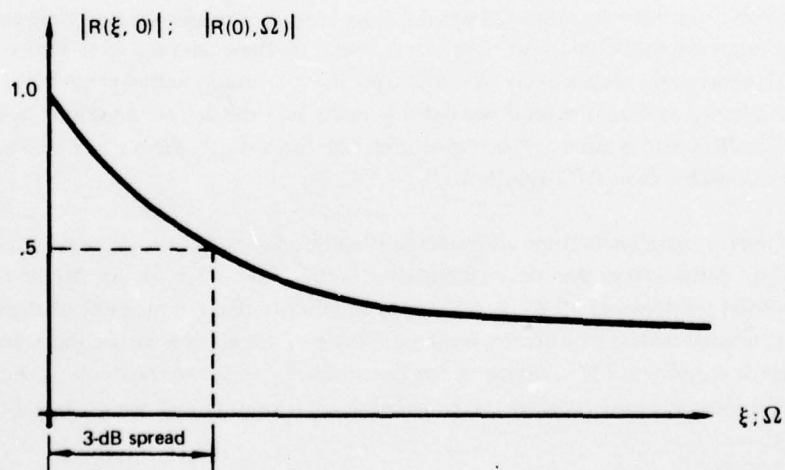
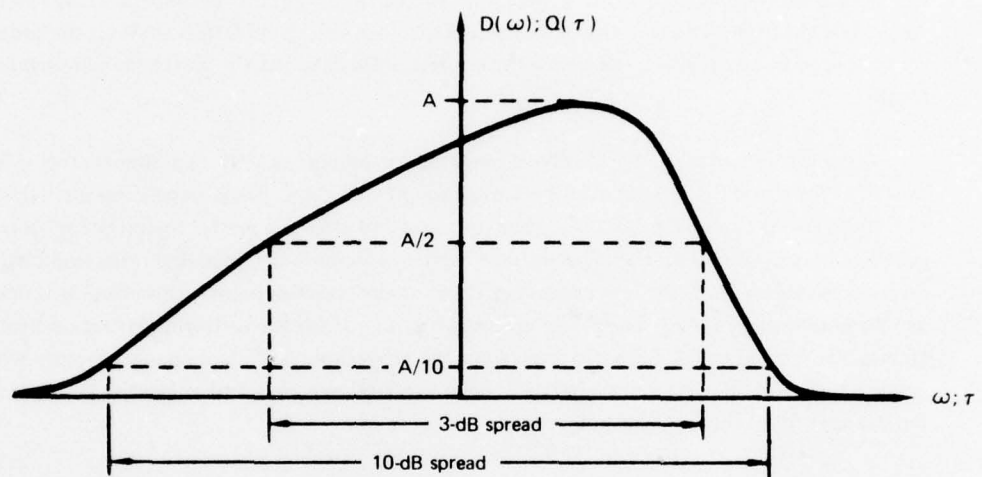


Figure 5-18. Spread Parameter Definitions

corresponding to rms sea slopes on the order of 9° .⁷ For comparison, we note that the average of all filtered (Neumann spectrum) sea slopes observed for the North Atlantic ATS-5 experiment (ref 5-6) was 6.8° , with maximum and minimum values of 12.1° and 3.4° . The concept of filtered slope is introduced to account for the finite spatial resolution capabilities of the L-band electromagnetic wavelength (i.e., the small-scale structure of the surface does not appreciably affect the forward-scatter mechanism, but may comprise a significant component of the actual surface slope).

Throughout this discussion, comparisons between measured results and predictions based on the closed form "steepest descent" integration techniques are also made.

5.3.1 Delay Spread

Delay spreads for the horizontal and vertical polarization probes are given in figures 5-19 and 5-20, respectively. The solid-line relationships in these figures correspond to the scatter model surface integration prediction as evaluated for the average of the 9° and 12° rms sea-slope conditions. A very weak increase in spread value for an increase in elevation angle is exhibited by the horizontal polarization data and by the 3-dB spread values of the vertical polarization data. For the 10-dB vertical polarization results, we observe a small increase in the spread for grazing angles in the vicinity of the pseudo-Brewster angle. Both these results are predicted by the scatter model, with the Brewster angle effect also being illustrated mildly by the vertical polarization 3-dB spreads. The increase in the spreads for the vertical polarization probe in the vicinity of 6° is related to the same phenomenon referred to previously as "Brewster angle fill-in."

For elevation angles between 10° and 31° , the horizontal polarization 3- and 10-dB spread measures are typically 0.7 and 3.0 μsec , respectively; for the vertical polarization case, these measures are slightly larger and take on typical values of 0.9 and 3.3 μsec . The dispersion associated with the experimental data may most certainly be ascribed to day-to-day changes in the surface rms slope.

An estimate of the antenna pattern's spatial filtering influence on the delay spread measures may be obtained by referring to section 5.6. Even though the spatial filtering effects were evaluated for the in-plane flight geometry coupled with a horizontal polarization mode, the delay spread (and coherence bandwidth) results should be somewhat typical for the other polarization and flight direction combinations. Thus as a generalized prediction we anticipate that at the high end of the grazing angle range (i.e., 31°) the 3- and 10-dB spread measures are underestimated by 2% and overestimated

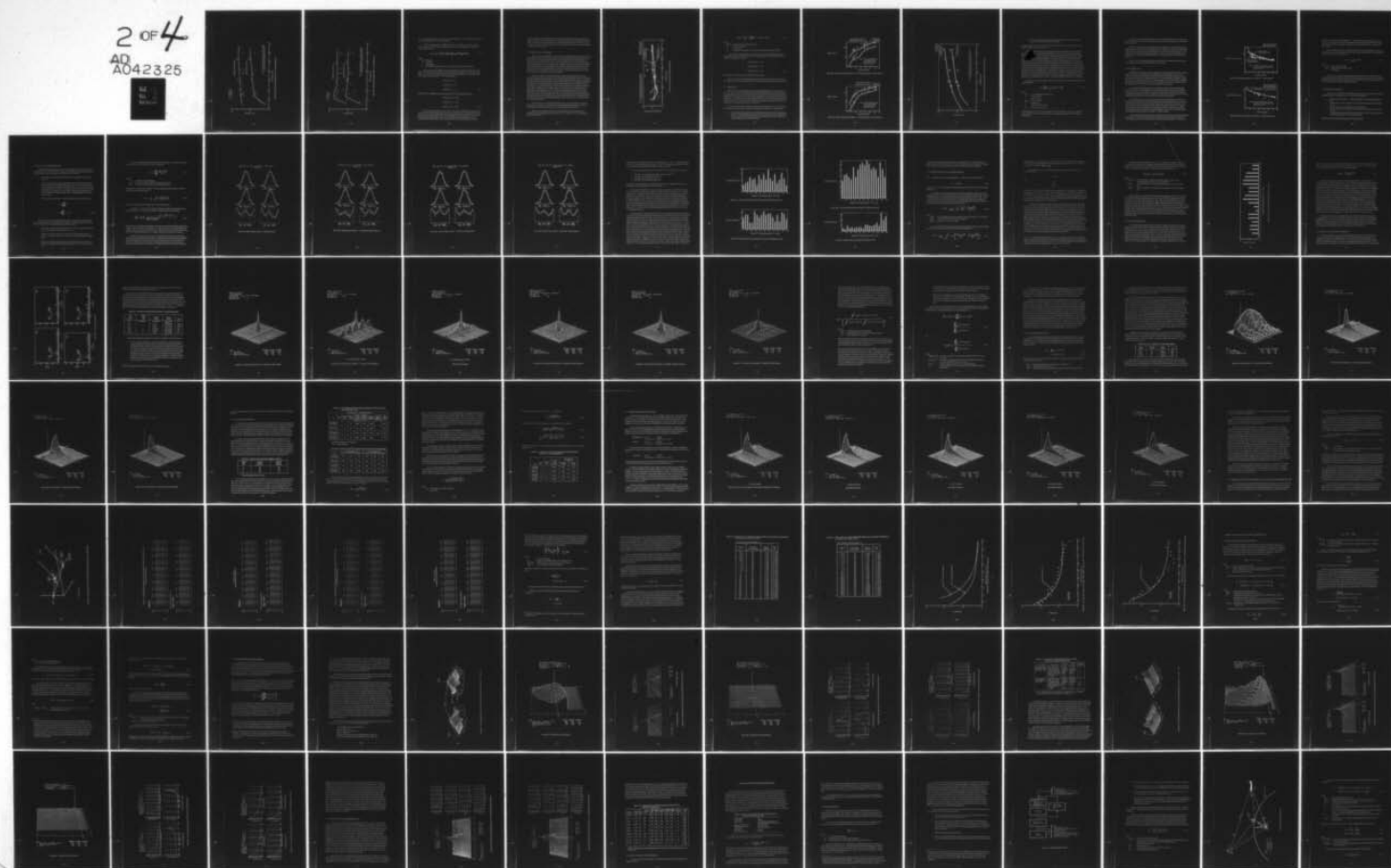
⁷Since the averaging of model-predicted results for slopes of 6° and 12° does not rigorously correspond to model predictions for slopes of 9° , the reader may, as an alternative, compare the experimental results with model predictions for specific slope values. "Model-predicted" curves for slopes of 3° , 6° , and 12° are given in section 6 for several multipath channel parameters.

AD-A042 325

BOEING COMMERCIAL AIRPLANE CO SEATTLE WASH
AIR TRAFFIC CONTROL EXPERIMENTATION AND EVALUATION WITH THE NAS--ETC(U)
SEP 76 A D THOMPSON, B J BURRESON, P F RIEDER DOT-TSC-707-5
D6-44050 FAA-RD-75-173-5 NL

UNCLASSIFIED

2 OF 4
AD
A042325



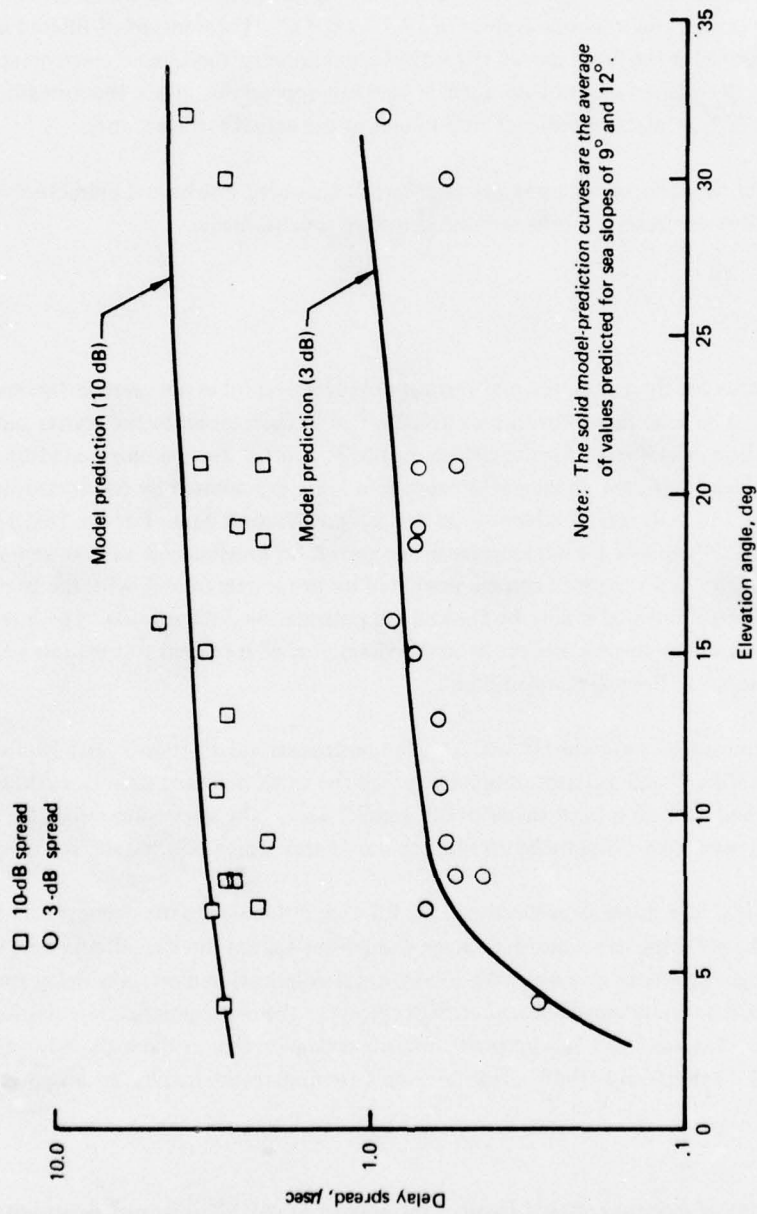


Figure 5-19. Oceanic Delay Spread Results — Horizontal Polarization

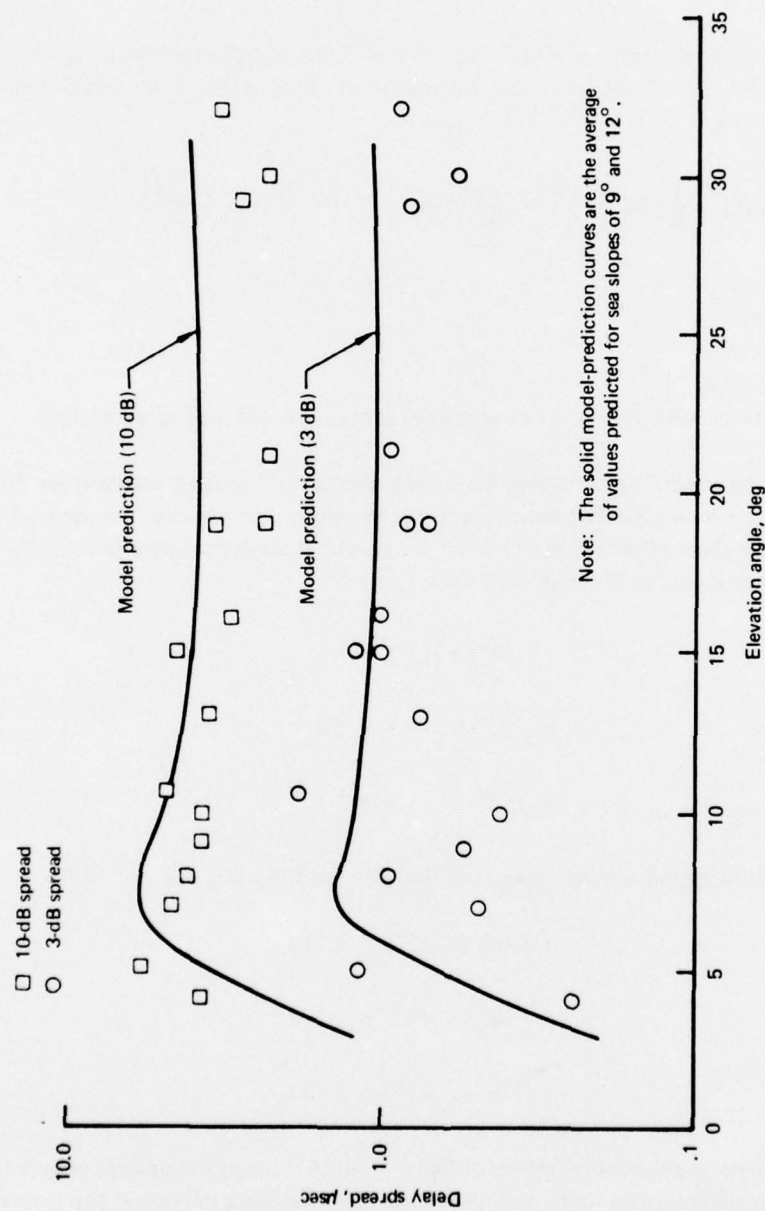


Figure 5-20. Oceanic Delay Spread Results — Vertical Polarization

by 7%, respectively. Similarly, at a grazing angle of approximately 7° the 3- and 10-dB spread measures are both overestimated by 11% and 3%, respectively.

Closed-form integral solutions of Mallinkrodt (ref 5-9) and Bello (ref 5-1) may be used to obtain "steepest descent" results for the delay-spectra spread values. Using Bello's formulation, we write the delay spectra as:

$$Q(\tau) = \frac{1}{K} \exp \left[- \left(\frac{\sin \gamma + 1/\sin \gamma}{2K} \right) \right] \cdot I_0 \left(\frac{(1/\sin \gamma) - \sin \gamma}{2K} \right) \tau, \quad (5-3)$$

where:

- $Q(\tau)$ = delay psd
- τ = delay time
- γ = grazing angle
- K = a parameter embodying the rms sea slope, aircraft altitude, and speed of light.

For the oceanic probe configuration, the aircraft altitude was roughly constant for the entire flight series. Thus, in our case K varies according to the rms slope changes only. Assuming a constant slope, we may use the above relationship to predict the grazing angle dependence of the 3-dB spread values. Relative to the spread at 5° , $\tau_{.5}(5^\circ)$, these values are:

$$\begin{aligned} \tau_{.5}(10^\circ)/\tau_{.5}(5^\circ) &= 1.5 \\ \tau_{.5}(20^\circ)/\tau_{.5}(5^\circ) &= 2.4 \\ \tau_{.5}(30^\circ)/\tau_{.5}(5^\circ) &= 3.1. \end{aligned} \quad (5-4)$$

Similarly, for the 10-dB spread angular dependence we have the following relative values:

$$\begin{aligned} \tau_{.1}(10^\circ)/\tau_{.1}(5^\circ) &= 1.238 \\ \tau_{.1}(20^\circ)/\tau_{.1}(5^\circ) &= 1.234 \\ \tau_{.1}(30^\circ)/\tau_{.1}(5^\circ) &= 1.185. \end{aligned} \quad (5-5)$$

For the horizontal polarization results of figure 5-19, the above relationships appear to follow the trend of the experimental data quite well. Since the "steepest descent" spread parameter estimates are *not* dependent upon the polarization of the electromagnetic wave, they obviously are incapable of predicting the observable difference between the horizontal and vertical polarization data sets. Compared with the physical optics vector scatter model, the steepest descent estimates in general

provide a somewhat poorer representation of the lower grazing angle vertical polarization data results shown in figure 5-20. This, of course, is to be expected since the steepest descent integration technique assumes all deterministic surface parameters take on their specular-point values, and thus it does not account for the rather extensive variation that the vertical polarization reflection coefficient experiences over the effective scatter surface.

5.3.2 Frequency Coherence Bandwidth

The term coherence bandwidth is used to describe the spread parameter measure associated with the multipath's frequency autocorrelation function. It in essence provides us with an upper frequency limit to which two simultaneously transmitted L-band carriers may be separated yet still meet a specified degree of correlation at the receiver. For this presentation we are concerned with the 3-dB coherence bandwidth (i.e., the received signals have a correlation coefficient of 0.5). We deal only with the sea-returned energy and do not include the effects of the excess time delay between the specular-point return and the direct line-of-sight signal. For direct plus multipath signal analyses, this excess differential delay is very significant and hence one cannot use the results presented herein to *directly* predict the coherence bandwidth of the composite channel.

Figure 5-21 contains as a function of elevation angle the experimentally measured 3-dB coherence bandwidth values for both horizontal and vertical polarization probes. Because the frequency autocorrelation function is derived solely from the channel's delay-spectra distribution, it is not dependent upon the airplane heading direction. Thus the results from both in- and cross-plane geometries have been combined. It is observed that the experimental results range from a low of 70 kHz to a high of 380 kHz, with a typical value of 200 kHz. The data trend does not exhibit a strong dependence upon grazing angle, although we do note a slight tendency for the results to increase with an increase in grazing angle. This dependency is in accord with the model prediction curves, which also predict a 3-dB coherence bandwidth value that, over the range of elevation angles of interest, is on the same order as the average of the experimental results. We also observe that for the lower grazing angles, the vertical polarization results are generally lower than their horizontal polarization counterparts whereas the opposite trend appears for the larger grazing angles. Again, this observation is in agreement with the model prediction results.

As shown in section 5.6, antenna spatial filtering effects on the 3-dB coherence bandwidth measurements are predicted to be rather minimal, with underestimation percentages of 4% and 7% being associated with the low and high ends of the grazing angle range, respectively.

Steepest descent integration predictions of the multipath coherence bandwidth may be obtained by using the following expression (see Staras, ref 5-7; or Bello, ref 5-1) for the frequency autocorrelation function:

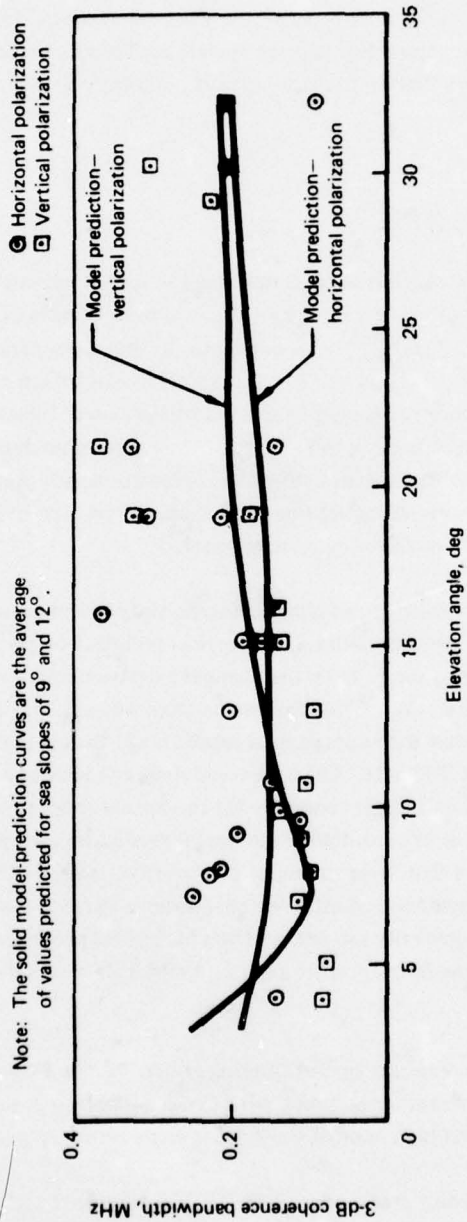


Figure 5-21. Oceanic Coherence Bandwidth Results

$$R(0, \Omega) = \left[\left(1 + i \frac{2\pi K \Omega}{\sin \gamma} \right) (1 + i 2\pi K \Omega \sin \gamma) \right]^{-1/2} \quad (5-6)$$

where:

- $R(0, \Omega)$ = complex frequency correlation function
- Ω = frequency separation
- γ = grazing angle
- K = a parameter embodying the surface slope, aircraft altitude, and speed of light.

As in the delay spread discussion, one may assume K to be constant and thereby generate the grazing angle dependence of $R(0, \Omega)$. Relative to the 5° grazing angle, the following 3-dB coherence bandwidth relationships are obtained:

$$\begin{aligned} \Omega_{.5}(10^\circ)/\Omega_{.5}(5^\circ) &= 1.95 \\ \Omega_{.5}(20^\circ)/\Omega_{.5}(5^\circ) &= 3.3 \\ \Omega_{.5}(30^\circ)/\Omega_{.5}(5^\circ) &= 4.0, \end{aligned} \quad (5-7)$$

where $\Omega_{.5}(\alpha)$ is the 3-dB coherence bandwidth at elevation angle γ .

With the exception of the slight polarization biases exhibited by the respective data sets, this relationship is observed to provide a fairly good fit to the grazing angle dependence shown by figure 5-21.

5.3.3 Doppler Spread

Results from the spread measurements on the multipath's Doppler spectra are given in figures 5-22, 5-23, and 5-24. The first two figures correspond to in-plane flight directions for horizontal and vertical polarization probes, respectively, whereas the third set presents the cross-plane spreads for both polarizations. The solid curves in each figure represent predictions derived from the surface integration scatter model. As previously discussed, the plotted model results are the average of predictions for rms sea slopes of 6° and 12° and thus represent a first-order approximation corresponding to an rms slope condition of 9° (see discussion and footnote 7, page 5-37).

For all four combinations of probe polarization and aircraft flight direction, the experimental data trends and model predictions are in fairly close agreement. In particular, it is observed that:

- a. The data trend shows a definite increase in Doppler spread for an increase in grazing angle.
- b. Both the 10- and 3-dB Doppler spread values are appreciably influenced by flight direction, with the in-plane geometry (especially for the lower grazing angle conditions) producing smaller spreads than the cross-plane condition.

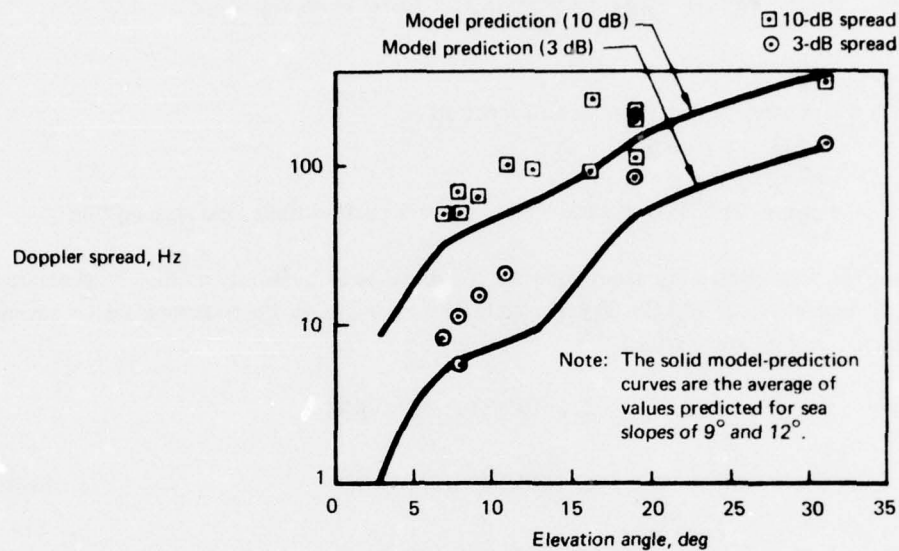


Figure 5-22. Oceanic Doppler Spread Results — Horizontal Polarization, In-Plane Geometry

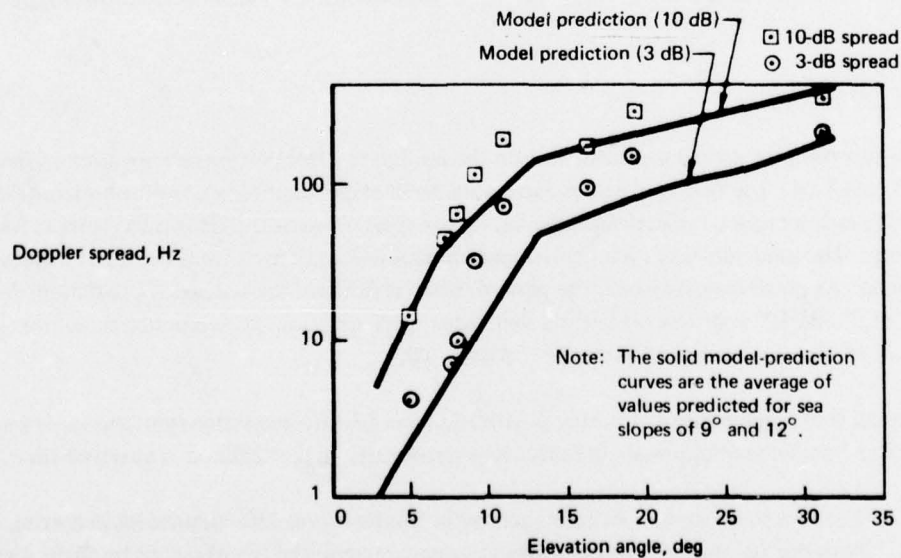


Figure 5-23. Oceanic Doppler Spread Results — Vertical Polarization, In-Plane Geometry

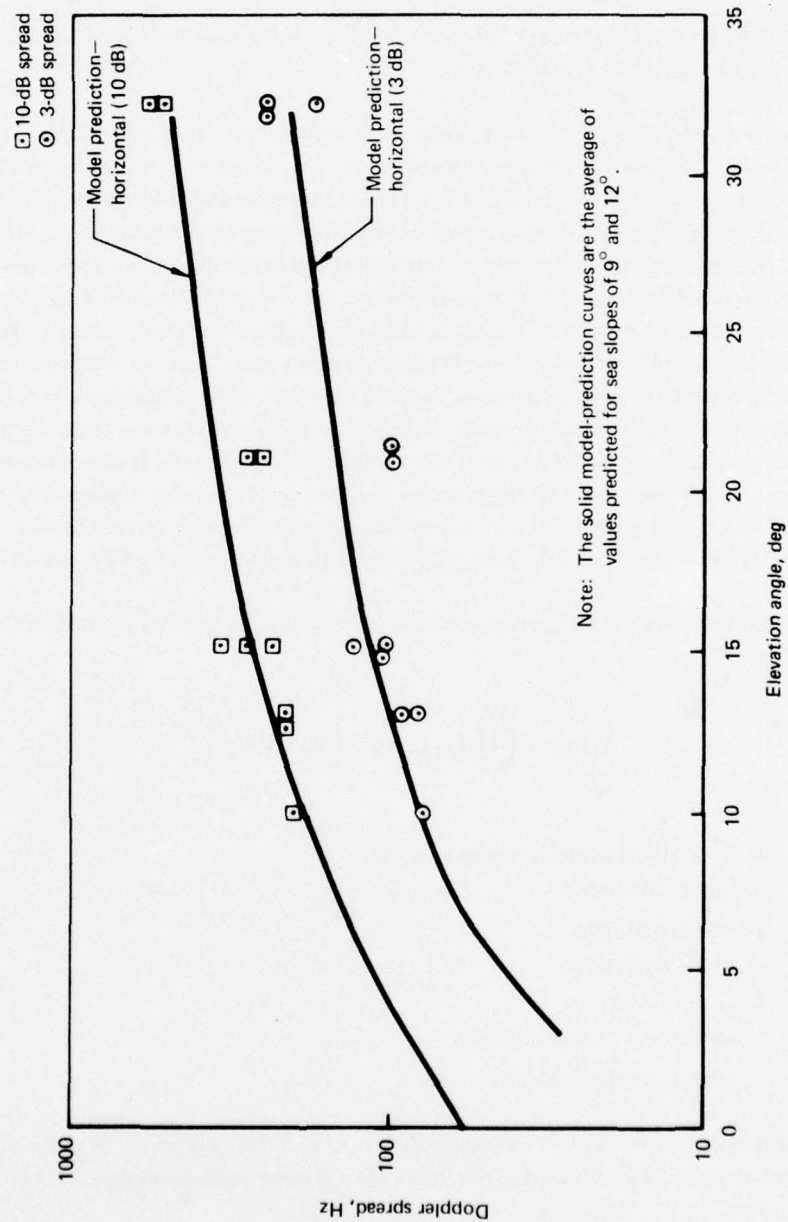


Figure 5-24. Oceanic Doppler Spread Results — Cross-Plane Geometry

- c. For the in-plane data ensembles, the spreads corresponding to vertical polarization are typically larger than their horizontal counterparts.

The physical explanation of the above observations is discussed in section 5.2.4, which relates to the multipath Doppler spectrum characteristics.

Two fairly significant factors are predicted to provide an *overestimation* bias to the in-plane low-angle Doppler spread experimental measurements. One factor relates to the antenna's spatial filtering effects which, as shown in section 5.6, result in overestimation biases on the order of 9% and 29% for the low-grazing-angle Doppler spread 3- and 10-dB measures, respectively. Antenna perturbation at the high-grazing-angle conditions are not nearly as significant, with the 3-dB measure being underestimated by 1% and the 10-dB spread measure being overestimated by 8%. The second overestimation bias factor pertains to aircraft heading meanders that would cause the flight direction vector to deviate somewhat from the true in-plane geometry condition. As discussed in section 5.2.4, the Doppler spectrum for low-grazing-angle in-plane flight direction conditions is very peaked and thus possesses a relatively small spread measure. As the flight vector moves away from the in-plane direction, the spectrum becomes increasingly more Gaussian-like and consequently is associated with a larger spread value. Assuming the aircraft flight vector is offset by 7° from the in-plane direction, the scatter model of section 6 predicts that for a 9° rms surface slope the Doppler spreads for the 10° grazing angle geometry are larger than their in-plane 3- and 10-dB counterparts by 89% and 47%, respectively.

Steepest descent channel parameter estimation techniques predict a Gaussian Doppler psd with bandwidth given by:

$$f(\gamma) \propto \left(\frac{f_c}{c}\right) \sigma_{\text{slope}} \sin \gamma \left[V_{\perp}^2 + V_I^2 \right]^{1/2}, \quad (5-8)$$

where:

- $f(\gamma)$ = 3- or 10-dB Doppler spread measure
- f_c = carrier frequency
- c = velocity of light
- σ_{slope} = rms surface slope
- γ = grazing angle
- V_{\perp} = aircraft cross-plane velocity
- V_I = aircraft in-plane velocity.

For the flight tests, $(V_{\perp}^2 + V_I^2)^{1/2}$ was generally on the order of 200 m/sec; thus for a constant sea-slope condition, the above relationship predicts a $\sin \gamma$ grazing angle dependence for both Doppler spread measures.

In general, this relationship adequately describes the cross-plane geometry spread results which, like the "steepest descent" predictions, have previously been shown to be associated with a spectrum of the Gaussian form.

Since the in-plane flight direction Doppler spectrum is highly non-Gaussian (especially for the low-grazing-angle conditions), it is not surprising that the "steepest descent" spread relationship fails to provide a close fit to the trend of the experimental data. For example, from figures 5-22 and 5-23 we observe that between the range of grazing angles from 7° to 19° the observed typical Doppler spread results increase by approximately 900%, whereas the $\sin \gamma$ relationship yields a predicted increase of only 170%.

Again, as for the delay spread predictions, we also note that the steepest descent results do not account for the observed polarization dependencies of the data sets.

5.3.4 Decorrelation Time

Decorrelation time provides us with an upper limit on the time separation for which two L-band carriers, transmitted at the same frequency, will still meet a specified degree of coherency at the receiver. It is derived from the time autocorrelation function of the multipath channel, and for this document we have selected the 3-dB spread measure (i.e., that time separation that produces a normalized correlation coefficient between the two received signals of 0.5). As in the coherence bandwidth presentation, we restrict our attention entirely to the multipath signal and do not include any effects that would arise from the presence of a direct line-of-sight received component.

Since the time autocorrelation function is derived exclusively from the multipath Doppler spectrum, one expects the decorrelation time measurements to exhibit a flight direction dependence. For this reason the results are segregated into cross- and in-plane data sets, which are presented for both polarizations in figures 5-25 and 5-26, respectively. Also contained in these figures are the spread relationships as derived from the surface integration physical optics scatter model.

The experimental results are in relatively good agreement with theoretical predictions. For both flight geometry directions, the data trend implies a decrease in decorrelation time for an increase in elevation angle. Typically, the data set averages imply decorrelation values on the order of 7 to 10 msec and 2 to 3 msec for grazing angles in the vicinity of 8° and 30° , respectively. It is apparent that the vertical polarization probes and the cross-plane flight direction produce modestly smaller decorrelation times than their respective orthogonal parameter counterparts. This tendency appears to be maximized for grazing angles in the vicinity of the Brewster angle.

Antenna spatial filtering effects upon the decorrelation time estimates for the in-plane geometry case are given in section 5.6 and indicate that for both high- and low-grazing-angle conditions the antenna influence tends to decrease the channel's true decorrelation time estimate. The decrease for

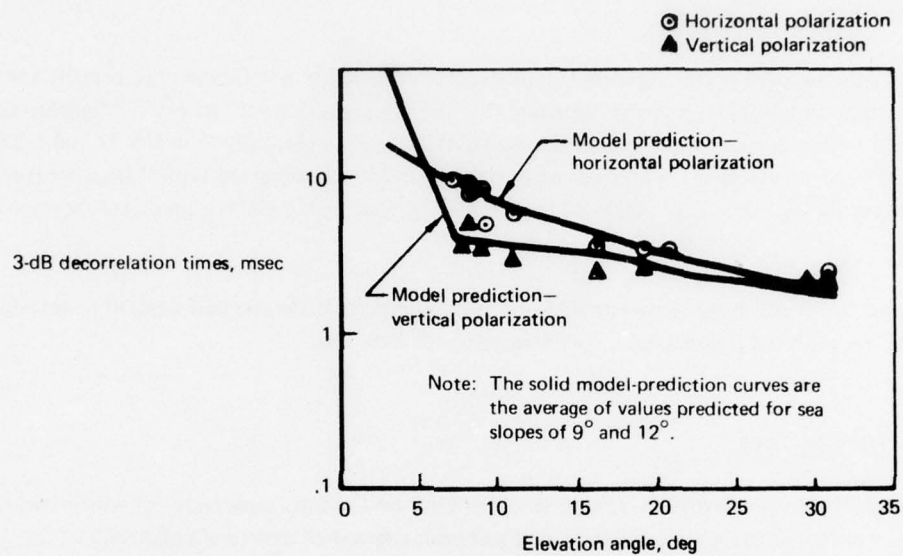


Figure 5-25. Oceanic Decorrelation Time Results — In-Plane Geometry

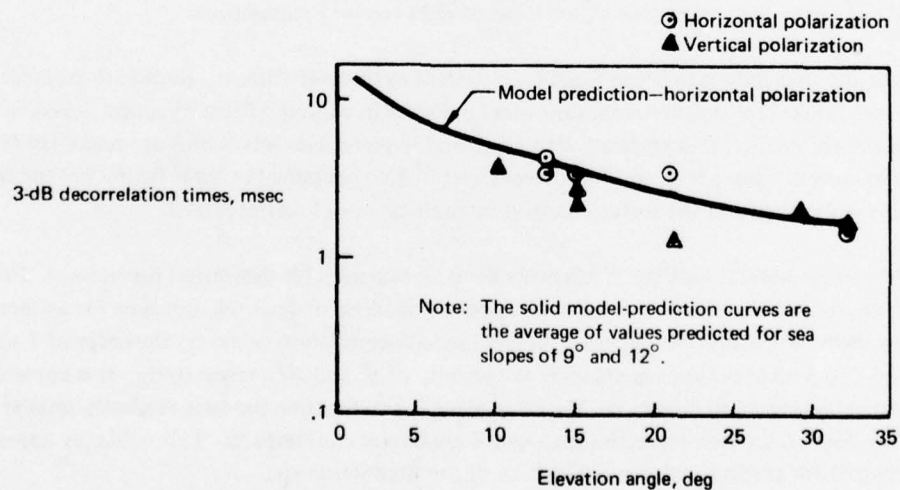


Figure 5-26. Oceanic Decorrelation Time Results — Cross-Plane Geometry

the high-grazing-angle case is rather modest ($\approx 7\%$), whereas for the low-angle condition the underestimation bias is approximately 30%. Referring again to figure 5-25, we note that the trend of the experimental data points as compared to the trend of the theoretical predictions is consistent with this contention.

Since the Doppler psd and time correlation function are Fourier transform pairs, the steepest descent solution to the time correlation function yields a Gaussian distribution with spread bandwidth inversely proportional to equation (5-8); i.e.,

$$\xi_{.5}(\gamma) = \frac{1}{\pi f_{.5}(\gamma)} \propto 1/\sin \gamma, \quad (5-9)$$

where:

- $\xi_{.5}(\gamma)$ = decorrelation time (3 dB)
- $f_{.5}(\gamma)$ = Doppler bandwidth spread (3 dB)
- γ = grazing angle.

For both the in-plane and cross-plane flight directions, the data sets are observed to exhibit a grazing angle dependence somewhat similar to the above relationship. However, as for the other spread parameter predictions, we again note the inability of the "steepest descent" to properly account for the polarization differences in the in-plane data ensembles.

5.4 TIME-DOMAIN STATISTICS

Analyses have been performed on the SACP's complex tap outputs to determine the following statistical measures of the multipath channel's time-domain representation:

- a. Histograms of the delay tap's I component amplitude, Q component amplitude, and phase
- b. Goodness-of-fit- (χ^2 test) comparisons of the above with theoretically predicted distributions
- c. Correlation of a tap's I component with its Q component
- d. Autocorrelation and cross-correlation of the individual tap processes within a common tap bank
- e. Cross-correlations and cross-power spectra estimates of the tap processes taken from the cross-polarization banks (i.e., vertical and horizontal).

Results from these measurements are given in the following sections.

5.4.1 Tap I and Q Amplitude Distributions

Amplitude probability distributions in the form of histograms are derived for the I and Q components of a given delay tap through the application of standard numerical grouping techniques. Prior to histogram sorting, three operations are performed on the input data.

- a. The data may be optionally desampled to improve the independency of the sample space array.
- b. A dither signal is added to each of the desampled data points. This is necessary since the quantizing levels of the digital SACP receiver's output are not significantly smaller than the bin widths of the histogram. The SACP receiver outputs are given as eight-bit entities ranging between -128 and +127 (receiver volts). In accord with the two's-complement arithmetic of the receiver, the dither signal is chosen from an ensemble whose values are uniformly distributed between 0 and 1. A new dither signal is used for each signal input value.
- c. The mean and standard deviation of the desampled, dithered array is determined; i.e.,

$$\mu = \frac{1}{N} \sum_{i=1}^N X_i$$
$$\sigma^2 = \frac{1}{N} \sum_{i=1}^N (x_i - \mu)^2 \quad (5-10)$$

After the sample's mean and standard deviation have been determined, the algorithm then sorts the input sample array into three histogram distributions. All three histograms are calculated for each tap component. The sorting techniques are achieved as follows:

Histogram 1: Consists of 20 bins ranging between $-\infty$ and $+\infty$, with the 18 interior bins being of equal width and spanning the range $(-3\sigma, +3\sigma)$.

Histogram 2: Similar to histogram 1 except bins are combined with their nearest neighbors if the observed frequency is less than 2% of the total elements in the sample space.

Histogram 3: Bin widths are selected so that the expected frequency (see below for discussion pertaining to expectation model) for each bin is 5%. Thus there are 20 bins total.

The three histogram distributions are then tested for normality. This is carried out via the χ^2 goodness-of-fit test. The observed χ^2 statistic is calculated as:

$$\chi^2_{\text{obs}} = \sum_{i=1}^N \frac{(EF_i - OF_i)^2}{EF_i} , \quad (5-11)$$

where:

- N = number of bins in the histogram
- EF_i = the expected number of data points falling into the i th bin
- OF_i = the observed number of data points falling into the i th bin.

Parameter EF_i is based on the assumption of a Gaussian distribution whose mean and variance are derived from the sample space array; i.e.,

$$EF_i = \frac{1}{2\pi\sigma} \int_{t_{i-1}}^{t_i} \exp\left(-\frac{(\alpha-\mu)^2}{2\sigma^2}\right) d\alpha , \quad (5-12)$$

where t_i is the upper limit of the voltage range associated with the i th bin.

Knowing the χ^2 statistic and the number of degrees of freedom ($N-3$) associated with each particular histogram, we are then able to determine the following cumulative probability:

$$P\left(\chi^2 \leq \chi^2_{\text{obs}}\right) = \frac{1}{2^{\frac{(N-3)}{2}} \Gamma\left(\frac{(N-3)}{2}\right)} \int_0^{\chi^2_{\text{obs}}} y^{\left(\frac{(N-3)}{2} - 1\right)} e^{-y/2} dy. \quad (5-13)$$

This represents the probability that a sample space selected from a Gaussian distribution with the same mean and variance as the test case will produce a χ^2 value less than that of the observed sample (i.e., if $P(\chi^2 < \chi^2_{\text{obs}})$ is consistently greater than 0.9, we would have reason to doubt the normality of the data). In the following discussions we refer to $P(\chi^2 < \chi^2_{\text{obs}})$ as the confidence level measure.

Sample histograms presented in figures 5-27 through 5-30 are representative of the results obtained from the amplitude distribution analyses. Also presented in these figures are the tap's phase distribution histograms, which will be discussed in the following section. For each distribution we present the experimental results and the theoretical expectation, which appear as the piecewise constant and the smooth curves, respectively. The amplitude distributions correspond to histogram

03/31/75 HP X-PLANE LOW ANGLE
INDIRECT TAP

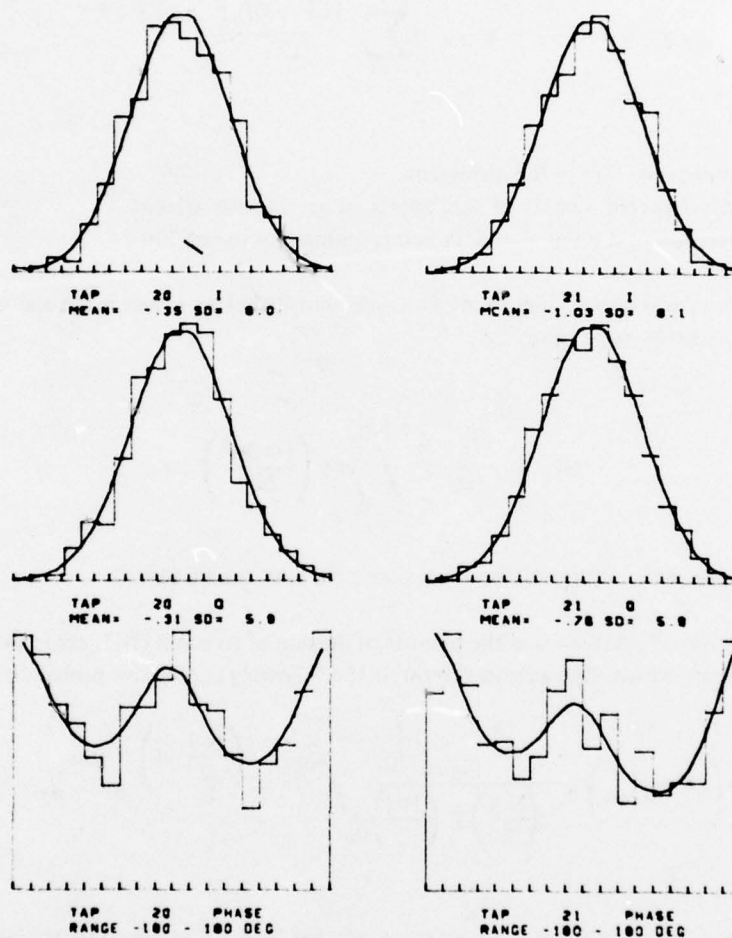


Figure 5-27. Sample Histogram Results — Noise-Only Present

03/31/75 HP X-PLANE LOW ANGLE
INDIRECT TAP

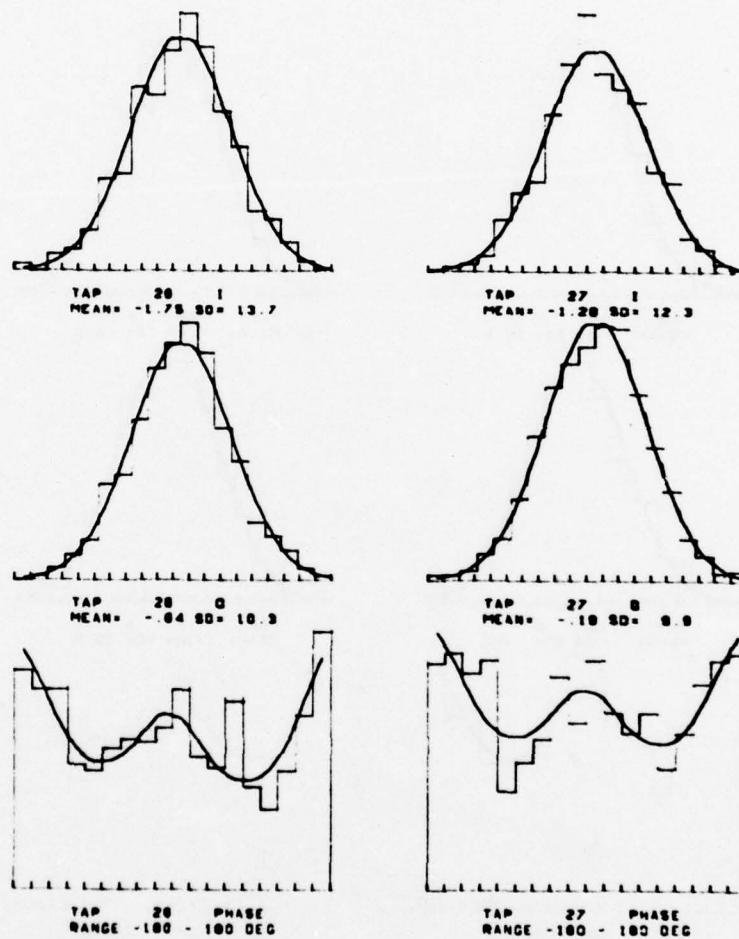


Figure 5-28. Sample Histogram Results — Low Angle, Cross-Plane Geometry

04.02.75 HP IN-PLANE LO-ANGLE
INDIRECT TAP

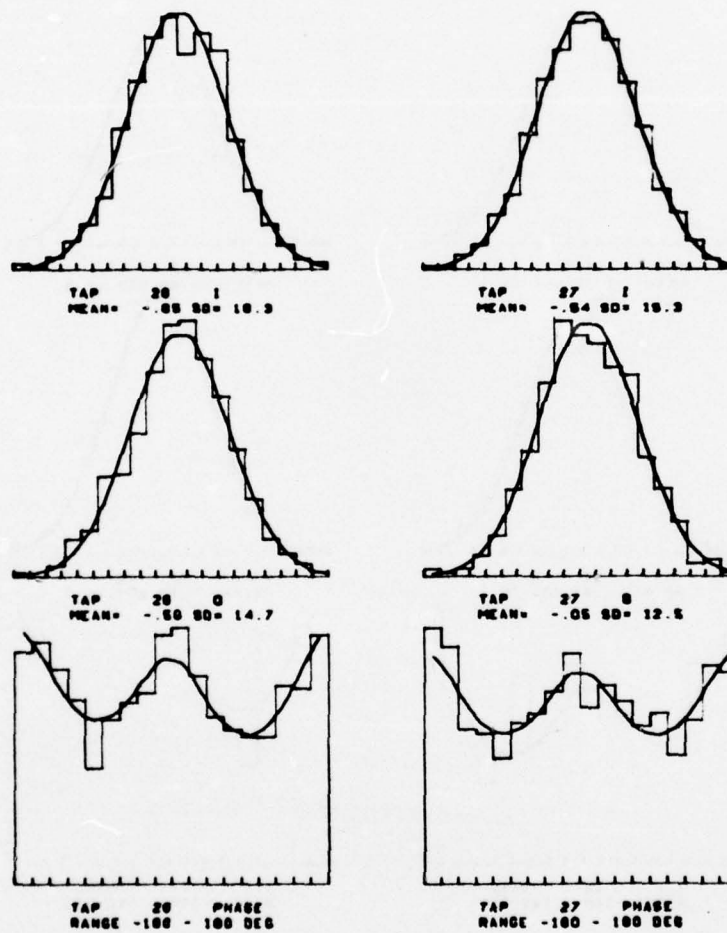


Figure 5-29. Sample Histogram Results — Low Angle, In-Plane Geometry

02.27.75 HP IN-PLANE HI-ANGLE
INDIRECT TAP

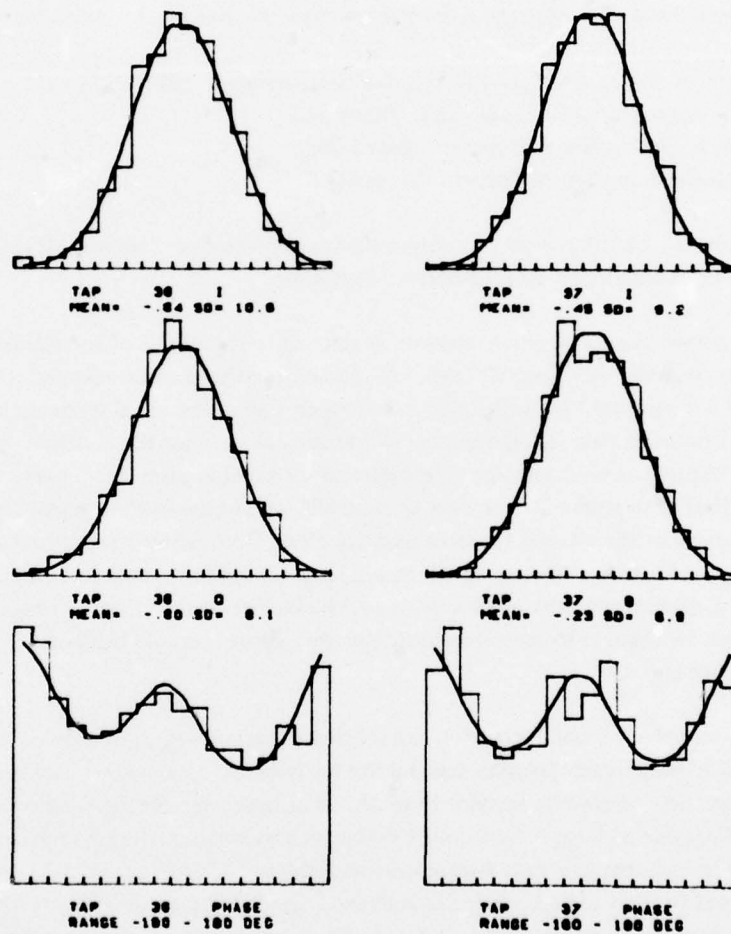


Figure 5-30. Sample Histogram Results — High Angle, In-Plane Geometry

sorting technique 1 and thereby consist of 20 bins ranging between $-\infty$ and $+\infty$, with the 18 interior bins being of equal width and spanning the range $(-3\sigma, +3\sigma)$. The sample mean and standard deviation of each distribution are presented directly below the histogram descriptor.

In selecting the sample histograms for presentation, we have chosen data that correspond to:

- a. Noise only (i.e., a tap prior to specular-point energy): figure 5-27
- b. Low angle, cross-plane multipath: figure 5-28
- c. Low angle, in-plane multipath: figure 5-29
- d. High angle, in-plane multipath: figure 5-30.

These figures show the high degree of correlation that exists between experimental results and the assumption of a Gaussian amplitude probability distribution.

Prior to presenting quantitative measures pertaining to the degree of correlation, a few observations regarding the noise-only case of figure 5-27 deserve comment. In particular: (1) the standard deviation of the *I* component is significantly greater than that of the *Q* component and (2) each component has a negative bias. These features, which also characterize the multipath-present tap processes, are related to receiver quadrature component differential gains (most likely associated with the analog-to-digital converters of the *I* and *Q* channels) and to the two's-complement arithmetic and A/D conversion of the receiver (induces negative bias). Both receiver perturbations significantly affect the phase distribution of the tap signal, as will be discussed in the following section. Additional effects of these perturbations upon other aspects of the channel characterization (e.g., $S(\tau, \omega)$) are small and (1) may be reduced by noise-removal algorithm application (dc bias) or (2) can be shown to be negligible (see app. B).

Results from the χ^2 goodness-of-fit tests indicate that the degree of correspondence between the observed and hypothesized Gaussian distribution for both tap components does not vary with polarization, flight direction, or elevation angle. In total, the observed χ^2 statistics agree very well with expectation and provide no basis for rejecting the Gaussian hypothesis. Results relating to the $P(\chi^2 < \chi_{obs}^2)$ confidence level frequency of observation are presented in figures 5-31, 5-32, and 5-33. These data were obtained from histogram sorting techniques 2 and 3 and represent results for the *I* component, *Q* component, and lumped *I* and *Q* test results, respectively. In presenting this information, we note that if the distribution hypothesis is true and as the number of observations becomes large, the $P(\chi^2 < \chi_{obs}^2)$ frequency of occurrence will be uniformly distributed over the range (0,1). On the other hand, as the actual and hypothesized distributions become increasingly dissimilar, the $P(\chi^2 < \chi_{obs}^2)$ results will exhibit a definite propensity to fall into the upper limit tail of the (0,1) region. Examination of the results given in figures 5-31 through 5-33 yields visual evidence to support the uniform distribution for the $P(\chi^2 < \chi_{obs}^2)$ frequency, which in turn implies acceptance of the Gaussian amplitude statistical hypothesis. Quantitatively we observe that the *I*, *Q*, and sum total $P(\chi^2 < \chi_{obs}^2)$ distributions have mean values of 0.53, 0.51, and 0.52, respectively, values in close accord with the expected results of 0.5. As an additional quantitative measure, we compare the observed $P(\chi^2 < \chi_{obs}^2)$ distri-

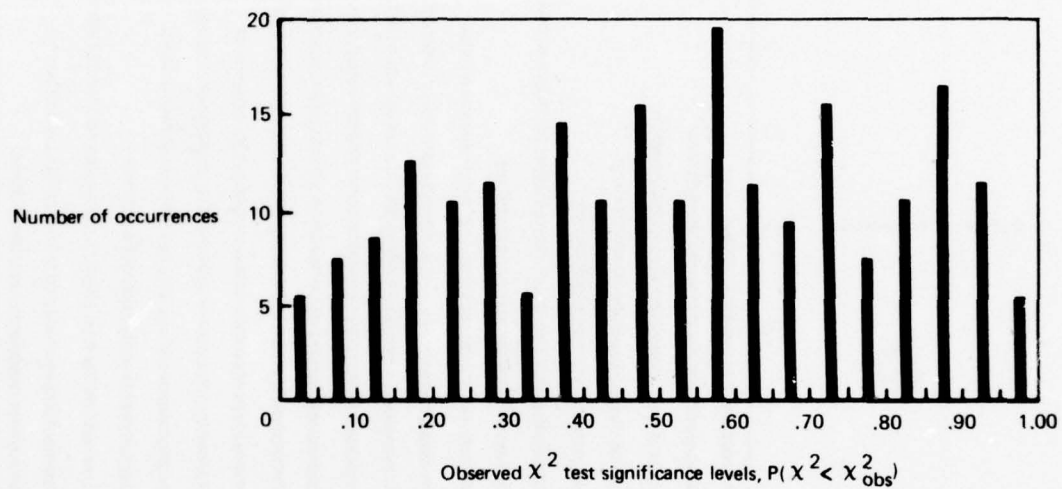


Figure 5-31. I-Component Amplitude Distribution, Observed χ^2 Significance Levels

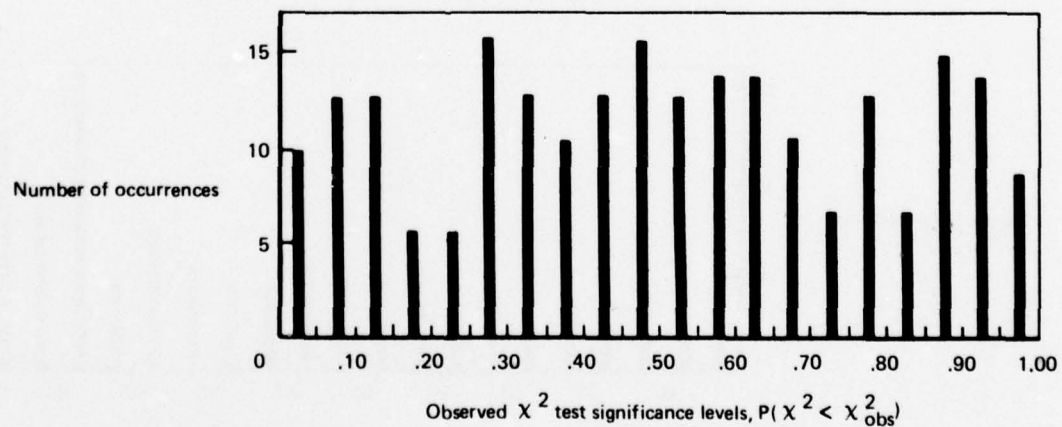


Figure 5-32. Q-Component Amplitude Distribution, Observed χ^2 Significance Levels

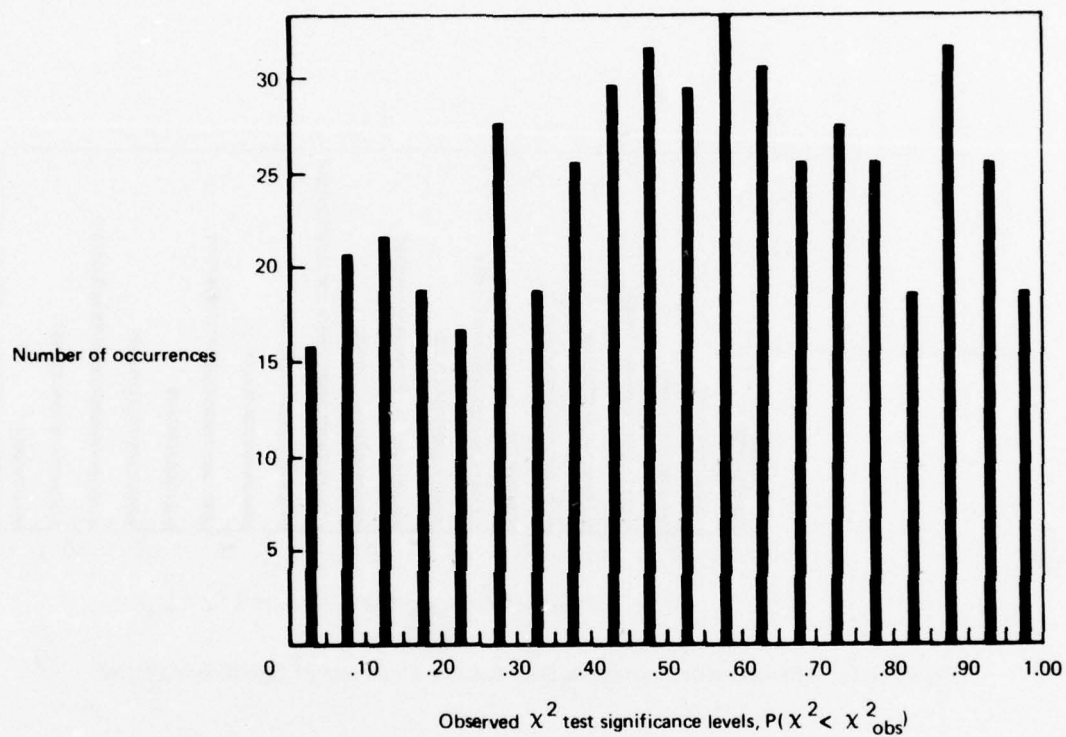


Figure 5-33. I and Q Amplitude Distribution, Observed χ^2 Significance Levels

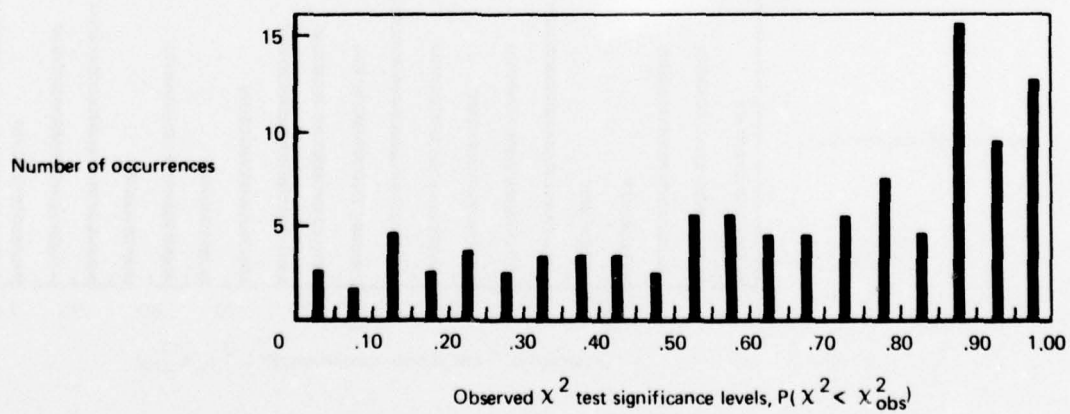


Figure 5-34. Phase Distribution, Observed χ^2 Significance Levels

butions to the expected uniform function via the χ^2 goodness-of-fit tests. These tests yield χ^2 statistics associated with confidence levels of 0.70, 0.38, and 0.69 for the I, Q, and sum total components, respectively. Hence we again have no basis for rejecting the test statistic hypothesis.

5.4.2 Tap Phase Distributions and Joint Amplitude Statistics

5.4.2.1 *Phase Distributions* – We define the phase, ϕ , of the complex tap-received signal as

$$\phi_i = \tan^{-1} Q_i/I_i, \quad (5-14)$$

where Q_i and I_i are the i th samples of a particular tap's quadrature phase and in-phase components, respectively.

The algorithm for determining the probability distribution histogram operates on the same desampled, dithered I and Q data values that are input to the amplitude statistics routine. Twenty equal-length bins are used for the histogram structure, which extends from -180° to $+180^\circ$. Via the χ^2 goodness-of-fit test as described in section 5.4.1, the observed bin densities are compared to a hypothesis resulting from the two-dimensional Gaussian distribution whose quadrature components are *independent* with nonzero means and nonidentical variances; i.e.,

$$W(I,Q) = \frac{1}{2\pi\sigma_I\sigma_Q} \exp \left(-\frac{(-\mu_I)^2}{2\sigma_I^2} - \frac{(Q-\mu_Q)^2}{2\sigma_Q^2} \right), \quad (5-15)$$

where:

- $W(I,Q)$ = joint probability density of the tap output taking on the specific I and Q values
- σ_I, σ_Q = standard deviations of the I and Q processes
- μ_I, μ_Q = means of the I and Q processes.

The phase probability density may be derived by transforming the above relationship to polar coordinates and integrating over the total extent of the radial dimension; i.e.,

$$P(\phi) = \frac{1}{2\pi\sigma_I\sigma_Q} \int_{\rho=0}^{\infty} \rho \exp \left[-\frac{(\rho \cos \phi - \mu_I)^2}{2\sigma_I^2} - \frac{(\rho \sin \phi - \mu_Q)^2}{2\sigma_Q^2} \right] d\rho. \quad (5-16)$$

Knowing $P(\phi)$, we then calculate the expected bin frequencies by integrating over the appropriate ϕ range and use steps similar to those described in the previous section to obtain the χ^2 statistic and its confidence level measure $P(\chi^2 < \chi_{\text{obs}}^2)$.

Receiver influences (i.e., differential quadrature gains and the mean level negative bias) in general are such that:

$$\sigma_I > \sigma_Q$$

and

$$\mu_I \gtrsim 0$$

$$\mu_Q \gtrsim 0.$$

Under these conditions, the $P(\phi)$ density exhibits a sinusoidal-like distribution with local maxima in the vicinities of $\phi = 0^\circ$ and $\phi = \pm 180^\circ$ and local minima near $\phi = \pm 90^\circ$. Due to the negative mean level bias for both I and Q components, we also note that the absolute maxima occur near the $\phi = \pm 180^\circ$ value whereas the $\phi = +90^\circ$ region corresponds to the absolute minimum of the function. These features are very evident in both the experimental and theoretical phase probability distributions presented in the examples of figure 5-27 through 5-30.

Tap processes corresponding to high- and low-grazing-angle conditions coupled with in-plane and cross-plane aircraft flight directions have been subjected to phase distribution tests. The results from these analyses provide no indication that the χ^2 statistic is biased one way or the other by any combination of the above system parameters. In figure 5-34 the occurrence frequency of the χ^2 test's confidence level measures, $P(\chi^2 < \chi_{\text{obs}}^2)$, is plotted. In total, over 100 distribution tests were conducted; an average confidence level measure of 0.64 is produced by these results. This average (which is considerably greater than the expected result of 0.50), coupled with the fact that the $P(\chi^2 < \chi_{\text{obs}}^2)$ observation frequencies are skewed toward the high end (i.e., hypothesis rejection) of the distribution as opposed to being uniformly distributed, gives some evidence that the assumed $P(\phi)$ distribution may be slightly inexact. Since the I and Q amplitude densities appear to be well modeled by the Gaussian distribution (see previous section), we are led to conclude that the *independence* assumption may not be totally valid. This result is in accord with the results of section 5.4.4, where we observe that the cross-correlation coefficient between the I and Q components was consistently found to be on the order of 0.05. Potential causes for the slight degree of dependency appear to be related to receiver device perturbations as discussed in section 5.4.4.

5.4.2.2 Joint Amplitude Probability Distribution — The preceding analysis relates to the phase distribution created by random variations associated with the orthogonal components of a complex tap's output. Coupled with the results of section 5.4.1, this is closely equivalent to the following discussion, which pertains to the joint amplitude statistics of a tap's I and Q outputs.

Using histogram sorting technique 3 (see sec. 5.4.1) as applied to the marginal distribution of the I,Q realm, we create the joint histogram of the complex process. Results from this grouping operation are then compared (χ^2) to a test hypothesis derived from the histograms of the individual I and Q tap amplitude analyses under the assumption of statistical independence; i.e.,

$$EF(I_m, Q_n) = [EF(I_m)][EF(Q_n)] \quad (5-17)$$

where:

- $EF(I_m, Q_n)$ = expected number of complex receiver points whose I and Q values simultaneously fall in the mth I bin and nth Q bin
- $EF(I_m)$ = measured number of I component values falling into the mth I coordinate bin
- $EF(Q_n)$ = measured number of Q component values falling into the nth Q coordinate bin

Results from the χ^2 goodness-of-fit comparison tests are presented in figure 5-35. In accord with conditions implying hypothesis acceptance, we note that the $P(\chi^2 < \chi_{obs}^2)$ results are fairly well distributed in a uniform manner and possess a mean value of 0.54. Quantitatively we observe a χ^2 significance level of 0.24 when comparing the $P(\chi^2 < \chi_{obs}^2)$ results with uniform distribution. Considering the results associated with the I,Q correlation coefficients and the phase distribution, one might expect that the joint statistics analysis would produce a more significant bias in the $P(\chi^2 < \chi_{obs}^2)$ measures toward the high end of the distribution (i.e., the I and Q components are slightly correlated, most likely due to receiver perturbations). We note that this high-side bias is visually in evidence, especially in the range 0.50 to 0.85, with the relative differences between this distribution and those for the phase $P(\chi^2 < \chi_{obs}^2)$ distribution possibly being due to insensitivities in one of the histogram grouping procedures.

5.4.3 Tap I and Q Dependence

As a first-order approximation, one may consider that a particular correlator tap centered at delay τ from the specular-point return intercepts all energy scattered into the receiver whose delays lie within the range $[\tau - \Delta/2, \tau + \Delta/2]$, where Δ is the code chip width. Translated to the surface, these returns may be shown to define an ellipsoid-like band that encircles the specular point. For nonzero values, the area included in each band is very extensive. Thus, if the surface is assumed to be random and rough in the electromagnetic sense (i.e., surface is nonperiodic and has height undulations greater than electromagnetic wavelength), we expect that the phase of one return from this area relative to any other return is uniformly distributed between 0 and 2π . This implies that a tap's in-phase (I) and quadrature-phase (Q) components are statistically independent since at any given

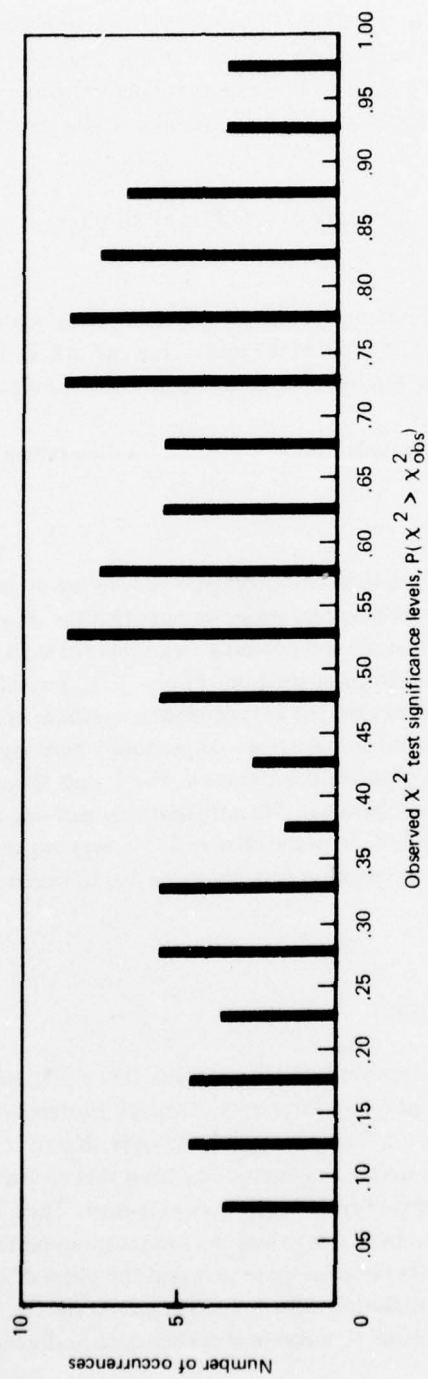


Figure 5-35. Joint I, Q Density, Observed χ^2 Significance Levels

instant of time there should be numerous returns falling into each tap. We test this hypothesis in two ways: (1) by determining the tap phase statistics histogram (see sec 5.4.2) and (2) by calculating the zero-lag correlation coefficient between the I and Q data samples; i.e.,

$$R_{I/Q}(0) = \frac{\langle IQ \rangle - \langle I \rangle \langle Q \rangle}{\sigma_I \sigma_Q} \quad (5-18)$$

Although not all flight test collection intervals have been subjected to this analysis, the resultant correlation coefficients imply that the I and Q samples are strongly independent. However, we do note that a *consistent* positive bias in the $R_{I/Q}(0)$ values is exhibited by the total data base examined. In general, values ranging between roughly -0.02 and 0.12 are returned from the $R_{I/Q}(0)$ analysis, with an average value on the order of 0.05 being obtained for the total ensemble. We illustrate this for several flight test cases presented in figure 5-36 where $R_{I/Q}(0)$ is plotted versus tap number. For each of these cases we include the results for several taps preceding the specular-point return tap, which serves as the demarcation between the "noise present only" and "multipath present" tap bank regions. It is important to note that the positive bias in the $R_{I/Q}(0)$ function is displayed by both regions of the tap bank (i.e., for noise-only region, an average $R_{I/Q}(0)$ value of 0.047 is obtained whereas for the multipath-present realm it equals 0.06). Thus we find it plausible to conclude that the consistently small but positive degree of correlation between the I and Q tap processes is due primarily to characteristics of the receiver and not to a surface phenomenon. The SACP's 70-MHz analog quadrature-phase splitter appears to be a very likely candidate for such a receiver perturbation. Typically, such devices are specified to provide outputs that may be up to $\pm 3^\circ$ away from orthogonality and have isolation ratios on the order of 30 dB at the 70-MHz frequency. Both of these factors may be shown to produce an erroneous $R_{I/Q}(0)$ bias equal to or in excess of the observed 0.06 value.

With respect to the variations of the I/Q correlation coefficients about the 0.06 mean value, the sample space size was on the order of 1000 for each case. Since the algorithm was configured to desample the data array by a 10:1 factor prior to the statistical analysis, one may consider the 1000 points to be statistically independent. Thus one expects the standard deviation of the parameter estimates due to finite-sample space size to be on the order of 0.03. The observed amount of fluctuation associated with the $R_{I/Q}(0)$ quantities is seen to be in accord with this value.

5.4.4 Tap Process Cross-Correlations (Copolarization)

Model predictions associated with aeronautical satellite oceanic channel characterization are invariably associated with the assumption that the surface scatter elements are uncorrelated. For example, one may refer to the work of Bello (ref 5-1) with respect to wide-sense stationary uncorrelated scattering (WSSUS) channel or to the surface integration model described in section 6. As a test of this hypothesis, we investigate the cross-correlation properties of the complex tap processes contained

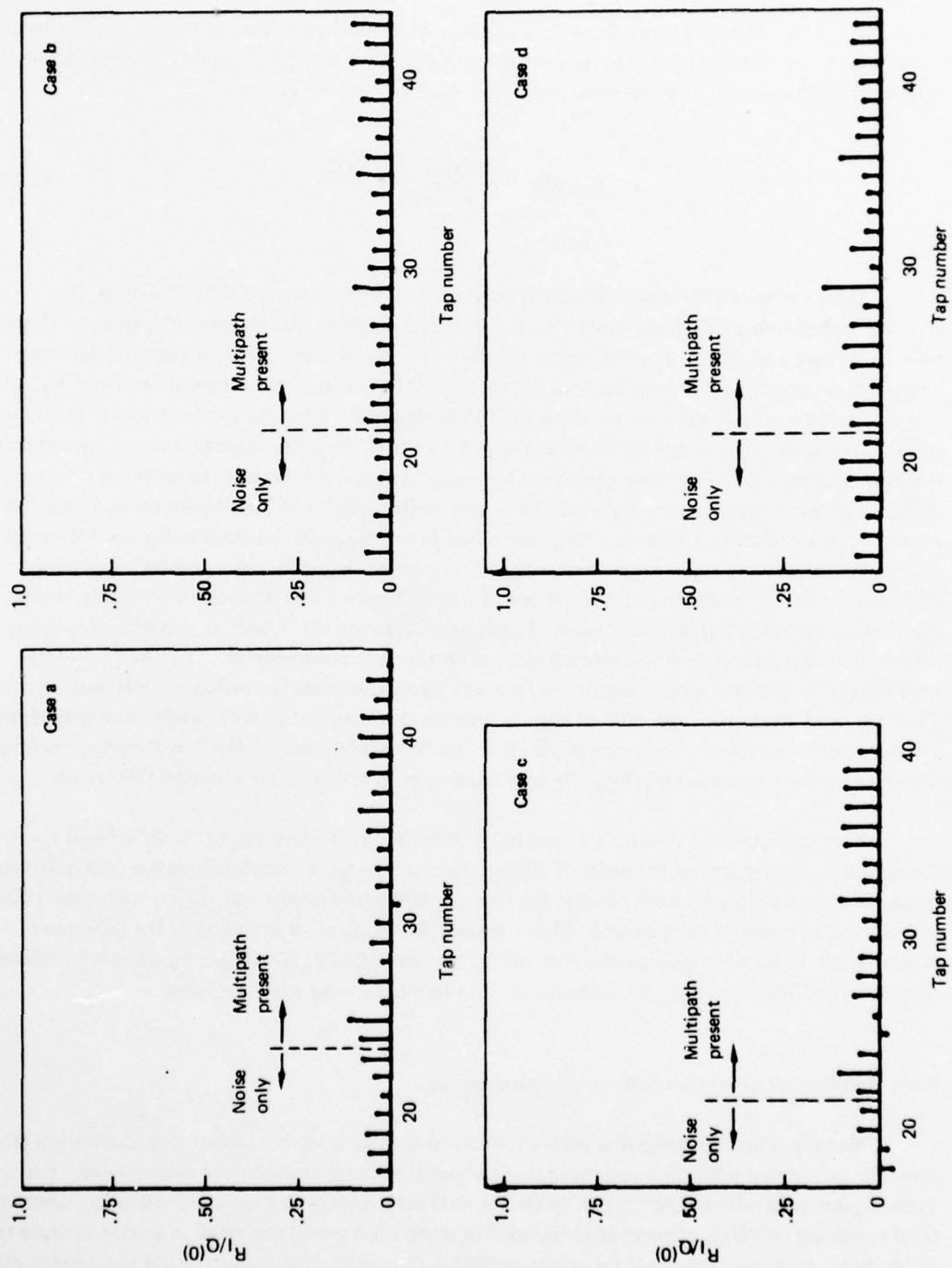


Figure 5-36. I/Q Correlation Coefficients

within a common polarization correlator bank. The cross-correlation function (mean removed) is generated in a normalized form as described in section 4.2.

Indicative of the results obtained from this analysis are the data sets presented in figures 5-37 through 5-41. These data correspond to a variety of test conditions as delineated in table 5-2; note that the first figure represents results from a noise-only region of the tap bank. The data presentation format displays a family of normalized cross-correlation functions spaced on both sides of a center curve that pertains to a particular tap's autocorrelation function (referred to as the principal tap). Each distribution offset from the center corresponds to the correlation between the principal tap and a tap separated from it by an amount equivalent to the offset of the curve (i.e., $\pm 1, 2, 3, \dots$). Approximately 13 sec of real-time data is used for each cross-correlation estimate (10,000 samples).

TABLE 5-2. TAP PROCESS CROSS-CORRELATIONS: FIGURE REFERENCE

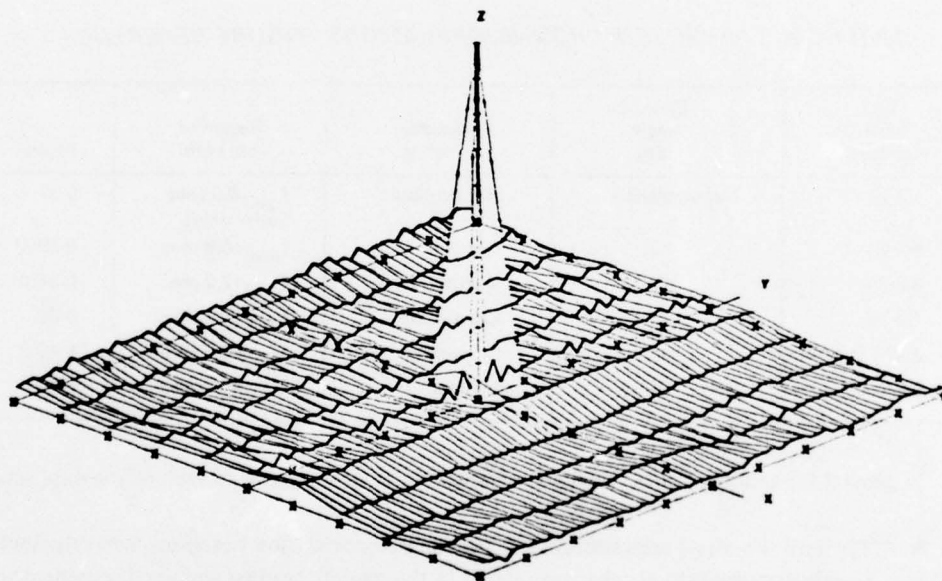
Test date, mo-day-yr	Elevation angle, deg	Airplane heading	Region of tap bank	Figure
4-2-75	Not applicable	Not applicable	$t_{\text{spec}} - 0.2 \mu\text{sec}$ (noise only)	5-37
4-2-75	7	In-plane	$t_{\text{spec}} + 0.8 \mu\text{sec}$	5-38(a)
4-2-75	7	In-plane	$t_{\text{spec}} + 2.2 \mu\text{sec}$	5-38(b)
4-2-75	11	Cross-plane	$t_{\text{spec}} + 1.0 \mu\text{sec}$	5-39
3-31-75	15	Cross-plane	$t_{\text{spec}} + 0.6 \mu\text{sec}$	5-40
2-27-75	31	In-plane	$t_{\text{spec}} + 0.8 \mu\text{sec}$	5-41

In general the following three features are observed to be common to each of the data sets.

- a. The zero tap offset relationship, i.e., the tap autocorrelation function, shows distinct signal structure patterns that are related to the aircraft heading and grazing angle; these are discussed further in section 5.4.5, which deals with the tap-gain autocorrelation function. We also note that the autocorrelation function has a sharp spike⁸ at the zero-lag value of the time separation coordinate. This is a direct result of the wideband receiver noise present in each of the taps. Between any two taps the noise process is essentially uncorrelated, and thus we do not observe the zero-lag spike for the cross-correlation distribution. As previously stated, the principal tap of figure 5-37 contains no multipath signal structure and thus gives a good representation of the noise contributions to the autocorrelation and cross-correlation results.

⁸That is, location of principal tap with respect to specular-point return (t_{spec}).

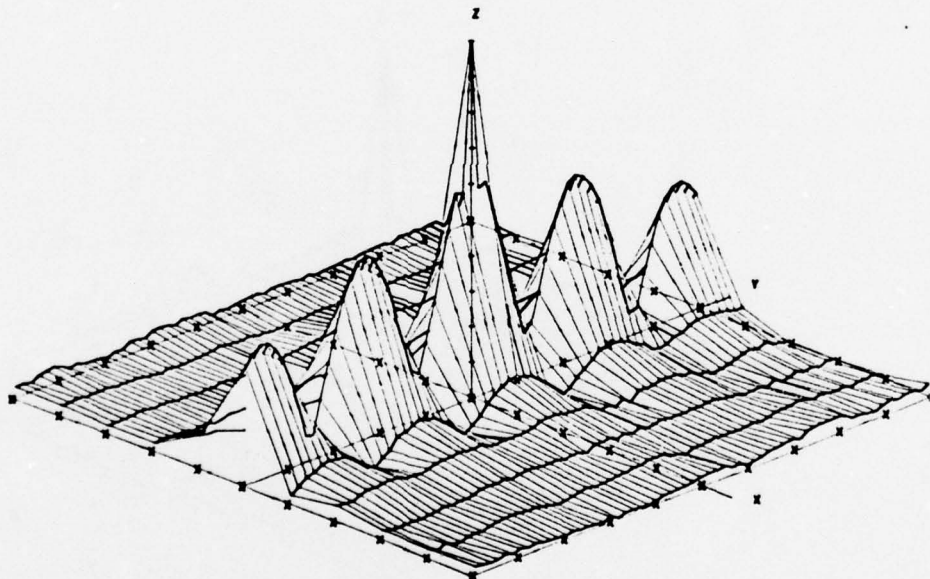
CORRELATION FUNCTION
 4-2-75 HORIZONTAL
 TIME INTERVAL 11/ 0/ .492 11/ 0/13.638
 PRINCIPLE TAP 24
 TAP RESOLUTION .20



AXIS		MINIMUM	MAXIMUM	INCREMENT
X	TAP OFFSET	-5.00	5.00	1.00
Y	TIME LAG (MSEC)	-50.0	50.0	10.0
Z	CORRELATION (MAGNITUDE)	.00	1.00	.10

Figure 5-37. Tap Process Cross-Correlations — Noise-Only Tap Bank Region

CORRELATION FUNCTION
 4-2-75 HORIZONTAL
 TIME INTERVAL 11/ 0/ .492 11/ 0/13.636
 PRINCIPLE TAP 20
 TAP RESOLUTION .20

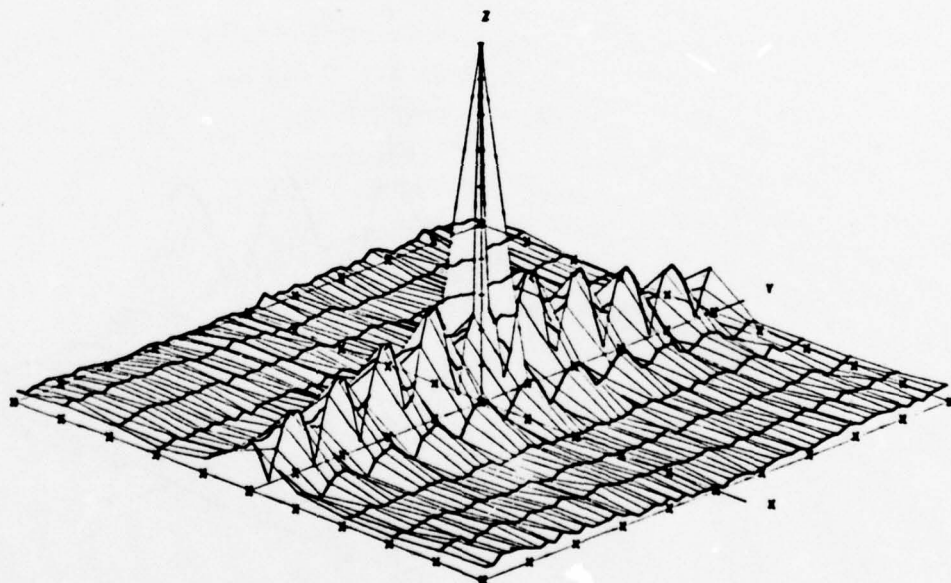


AXIS	MINIMUM	MAXIMUM	INCREMENT
X TAP OFFSET	-5.00	5.00	1.00
Y TIME LAG (MSEC)	-50.0	50.0	10.0
Z CORRELATION (MAGNITUDE)	.00	1.00	.10

(a) Tap Bank Region $t_{spec} + 0.8 \mu sec$

Figure 5-38. Tap Process Cross-Correlations — Low Angle, In-Plane Geometry

CORRELATION FUNCTION
 4-2-75 HORIZONTAL
 TIME INTERVAL 11/ 0/ .492 11/ 0/13.638
 PRINCIPLE TAP 36
 TAP RESOLUTION .20

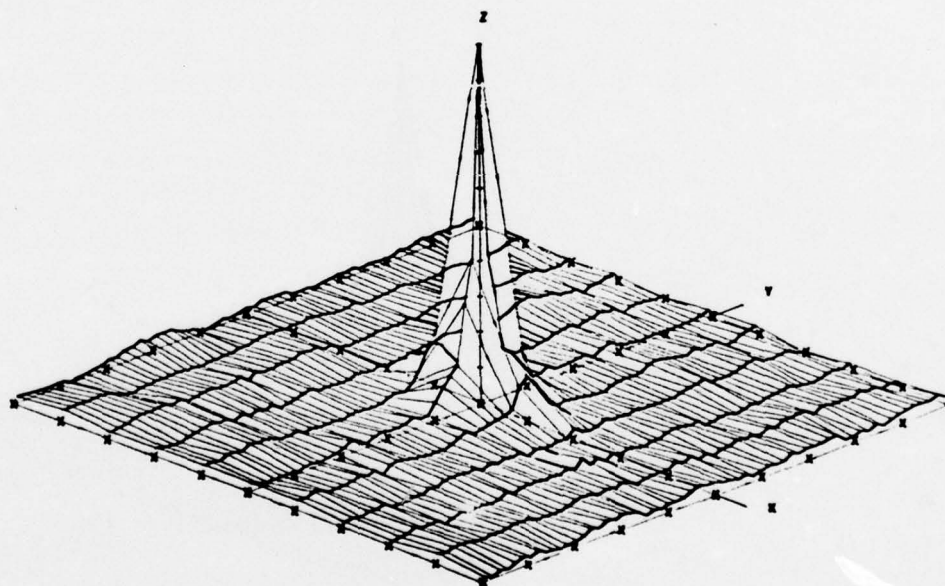


AXIS		MINIMUM	MAXIMUM	INCREMENT
X	TAP OFFSET	-5.00	5.00	1.00
Y	TIME LAG (MSEC)	-50.0	50.0	10.0
Z	CORRELATION (MAGNITUDE)	.00	1.00	.10

(b) Tap Bank Region $t_{spec} + 2.2 \mu sec$

Figure 5-38. (Concluded)

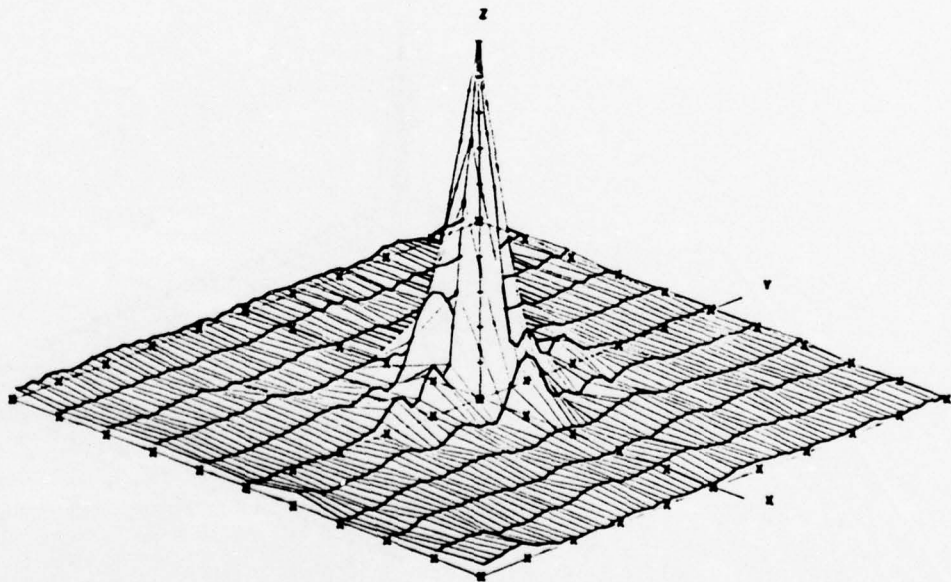
CORRELATION FUNCTION
 4-2-75 HORIZONTAL
 TIME INTERVAL 11/49/19.643 11/49/32.786
 PRINCIPLE TAP 27
 TAP RESOLUTION .20



AXIS		MINIMUM	MAXIMUM	INCREMENT
X	TAP OFFSET	-3.00	3.00	1.00
Y	TIME LAG (MSEC)	-50.0	50.0	10.0
Z	CORRELATION (MAGNITUDE)	.00	1.00	.10

Figure 5-39. Tap Process Cross-Correlations — Low Angle, Cross-Plane Geometry

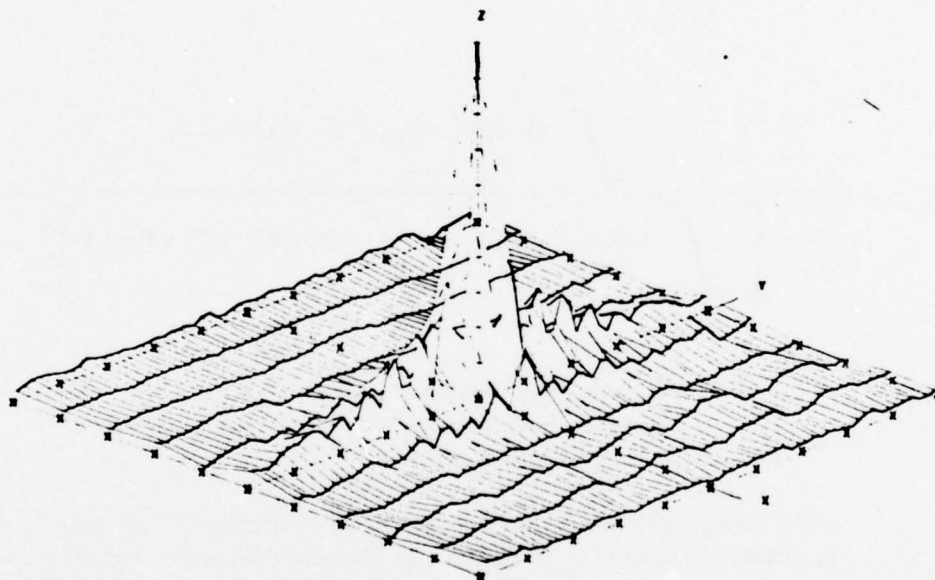
CORRELATION FUNCTION
 9-31-75 HORIZONTAL
 TIME INTERVAL 9/19/ 9.021 9/19/22.985
 PRINCIPLE TAP 23
 TAP RESOLUTION .20



AXIS		MINIMUM	MAXIMUM	INCREMENT
X	TAP OFFSET	-5.00	5.00	1.00
Y	TIME LAG (MSEC)	-50.0	50.0	10.0
Z	CORRELATION (MAGNITUDE)	.00	1.00	.10

Figure 5-40. Tap Process Cross-Correlations — Mid-Angle, Cross-Plane Geometry

CORRELATION FUNCTION
 2-27-HORIZONTAL
 TIME INTERVAL 10/13/ 493 10/13/13 836
 PRINCIPLE TAP 38
 TAP RESOLUTION .20



AXIS		MINIMUM	MAXIMUM	INCREMENT
X	TAP OFFSET	-5.00	5.00	1.00
Y	TIME LAG (MSEC)	-50.0	50.0	10.0
Z	CORRELATION (MAGNITUDE)	.00	1.00	.10

Figure 5-41. Tap Process Cross-Correlations — High Angle, In-Plane Geometry

- b. For unity tap separation, the cross-correlation distributions are fairly significant and (especially for the low-angle in-plane cases) have the appearance of being attenuated replicas of the autocorrelation process. This should *not* be interpreted to imply that the surface scatter elements that reflect energy into adjacent taps are highly correlated. It results from the fact that adjacent taps have a delay region of commonality over which their code correlation properties intercept significant energy. An estimate of the "overlap" effect on the cross-correlation properties of the time-dispersed multipath process is given in appendix C; for the purpose of this discussion we extend the analysis to account for the fact that the multipath delay spectra may exhibit appreciable variation over the duration of one or two taps. The normalized overlap contribution, $R_O(n)$, between taps n and $n-1$ is to close approximation given by:

$$R_O(n) = \frac{\int_{-\infty}^{\infty} Q(\tau) |\Psi(\tau - nT_O)| \Psi^*(\tau - nT_O + T_O) d\tau}{\left[\int_{-\infty}^{\infty} Q(\tau) |\Psi(\tau - nT_O)|^2 d\tau \int_{-\infty}^{\infty} Q(\tau) |\Psi(\tau - nT_O + T_O)|^2 d\tau \right]^{1/2}} \quad (5-19)$$

where:

- $Q(\tau)$ = multipath delay power spectral density
- $\Psi(\tau)$ = correlation property of the sampled PN probing sequence
- T_O = prober PN sequence chip width.

Under the assumption that $Q(\tau)$ is constant over the duration of two taps, $R_O(n)$ may be evaluated in a closed form. For the case where the receiver signal processing analog-to-digital sampling rate is infinite, $R_O(n)$ is equal to 0.25; when the sampling rate is twice as fast as the prober's chip rate, $R_O(n)$ decreases to 0.17.

For all data sets analyzed under this topic, the 2-to-1 sampling rate to chip rate factor was in effect; thus we may use the 0.17 value for $R_O(n)$ as our baseline. When the experimental $Q(\tau)$ distribution is included in the above relationship, one must revert to numerical integration techniques to derive an estimate of $R_O(n)$. Applying this method to the appropriate delay spectra associated with the examples of this section, we obtain results that do not generally differ from the 0.17 baseline by more than $\pm 10\%$. This relatively small variation may be attributed to the fact that the nonuniform properties of the $Q(\tau)$ distribution affect the numerator and denominator of the above $R_O(n)$ relationship by the same order of magnitude.

Comparison of the nonzero lag values for adjacent tap cross-correlations in general confirms that the expected 17% commonality factor is realized. Use of the nonzero lag values avoids the substantial noise bias effects of the zero-lag autocorrelation function.

- c. When two taps are separated by two or more chip widths, their degree of correlation is observed to be very small if not entirely negligible. Typically, the cross-correlation magnitudes for these conditions do not exceed the 0.05 value. We also note that the neighboring values of a cross-correlation estimate exhibit a high degree of correlation among themselves.

Both of the above observations under item c may be investigated through use of the following relationships (derived from Jenkins and Watts, ref. 5-10), which holds valid under the assumption that the tap outputs are uncorrelated and taken from Gaussian processes; i.e.;

$$E[|\rho_{n,m}(k)|^2] = \frac{1}{N} \sum_{r=-\infty}^{\infty} (\rho_{n,n}(r) \rho_{m,m}(r))$$

$$= \frac{\sum_{r=-\infty}^{\infty} \rho_{n,m}(r) \rho_{m,m}(r+\beta)}{\sum_{r=-\infty}^{\infty} \rho_{n,n}(r) \rho_{m,m}(r)}, \quad (5-20)$$

and

$$R_{n,m}(k,k+\beta) = \frac{\sum_{r=-\infty}^{\infty} \rho_{n,m}(r) \rho_{m,m}(r+\beta)}{\sum_{r=-\infty}^{\infty} \rho_{n,n}(r) \rho_{m,m}(r)}, \quad (5-21)$$

where:

- $E[|\rho_{nm}(k)|^2]$ = variance of $\rho_{n,m}(k)$, the cross-correlation estimate between taps n and m at lag k
- $R_{n,m}(k,k+\beta)$ = the degree of correlation between the k th and $(k+\beta)$ th lag estimates for the cross-correlation process of tap n and m
- $\rho_{n,n}(r)$ = the autocorrelation process of tap n at the r th lag output
- N = number of points in the array over which the cross-correlation estimates were derived.

For our analyses, $N = 10,000$ and the summation $\sum \rho_{nn}(r) \rho_{mm}(r)$ takes on typical values of 1 and 4 for the cases where both n and m are noise-process-only taps and where they are both occupied by multipath, respectively. Hence one expects estimation standard deviations on the order of 0.01 for the noise cross-correlations and 0.02 for the multipath cross-correlation. In general, these values appear to be well suited to the observed fluctuations of the cross-correlation estimates.

With respect to the degree of correlation between neighboring values of a particular cross-correlation estimate, we note that $R_{n,m}(k, k + \beta)$ is dependent only upon the lag separation β and is influenced solely by the nature of the n th and m th taps' autocorrelation function. Hence, even when tap n and m are uncorrelated, if either $\rho_{n,n}(r)$ or $\rho_{m,m}(r)$ falls off more slowly, then the neighboring points of the cross-correlation estimate will be highly correlated. This is dramatically illustrated in figure 5-37, where the principal tap (24) is noise-only and tap 25 is the first tap to capture multipath. Thus taps 24, 23, and 22 have autocorrelation functions that are essentially 1 at the origin and 0 elsewhere, whereas taps 25 and 26 have autocorrelation functions that change slowly. Therefore, when tap 24 is correlated with another noise-only tap, the neighboring lag outputs are not correlated to each other; on the other hand, neighboring lag outputs for the correlation of tap 24 with a multipath-present tap are observed to be highly correlated (in fact, $R_{n,m}(k, k + \beta) \approx \rho_{mm}(\beta)$; $m \geq 25$) and thus exhibit a much slower variation across the correlation function. As discussed in section 5.4.5, the tap process autocorrelation function decays more rapidly for an increase in delay; consequently we expect the neighboring lag outputs to become less correlated as the tap number increases. This result is also observed in the data structure, as may be seen by comparing figure 5-38 with figure 5-39.

5.4.5 Tap-Gain Autocorrelation Function

In the tapped delay line synthesis and interpretation of the multipath scatter phenomena it is important to have a knowledge of the channel's tap-gain autocorrelation function. This parameter is proportional to the autocorrelation of the returned signals' fluctuations in the complex tap gain at a specified delay (ref 5-1). It may be related to the channel scatter function and time-variant impulse response as follows:

$$Q(\xi, \tau) = \int S(\tau, \omega) e^{i 2\pi \omega \xi} d\omega \quad (5-22)$$

$$= \langle h(\tau, t) h^*(\tau, t + \xi) \rangle, \quad (5-23)$$

where we have assumed the surface is random wideband (i.e., no periodic component) and where the following definitions are used:

$Q(\xi, \tau)$ = tap-gain autocorrelation function for delay τ and time lag ξ

$S(\tau, \omega)$ = delay-Doppler function (sec 5.1)

$H(t, \tau)$ = complex time (t) variant channel impulse response for returns with delay equal to τ .

For this report, DRandA emphasis has been devoted to characterizing the multipath process at the delay-Doppler coordinate system of the receiver. Thus it is instructive to consider the first of the above relationships as an aid for interpreting the $Q(\xi, \tau)$ data and also to provide an extension of the results presented previously for the $S(\tau, \omega)$ function.

To begin, we note that $Q(\xi, \tau)$ is equal to the inverse Fourier transform of $S(\tau, \omega)$ on the Doppler variable. Hence, $Q(\xi, \tau)$ is influenced not only by sea slope, polarization, and elevation angle, but also by the aircraft heading. Since the tap Doppler spread increases for increasing τ and elevation angle, we expect that each tap's decorrelation time will decrease for an increase in these parameters. The aircraft heading effects upon $Q(\xi, \tau)$ may be predicted by recalling that for in-plane geometry, the $S(\tau, \omega)$ is characterized by distinct high-energy spectral humps that occur for each tap at the extremities of the range over which Doppler returns are physically possible. For taps on the order of $0.5 \mu\text{sec}$ or more removed from the specular return, very little energy falls between these humps; for the cross-plane geometry case, each tap's Doppler spectrum has an energy distribution across the permissible realm that is nearly uniform (higher slopes) or almost Gaussian (lower slopes) with very little bias toward extreme heaviness in the tails. One therefore expects that for the in-plane case the $Q(\xi, \tau)$ function will possess periodic (almost sinusoidal) behavior in the ξ variable, with an increase in frequency being associated with an increase in tap number. On the other hand, the cross-plane case should be characterized by a ξ dependence that falls off in a pseudo-Gaussian (lower slopes) or $\sin x/x$ (higher slopes) like manner, with the decay rate of the falloff increasing with tap number. Finally we note that along the $\xi = 0$ axis, the tap-gain autocorrelation function is equivalent to the channel delay spectra, and consequently $Q(0, \tau)$ should not depend on aircraft heading.

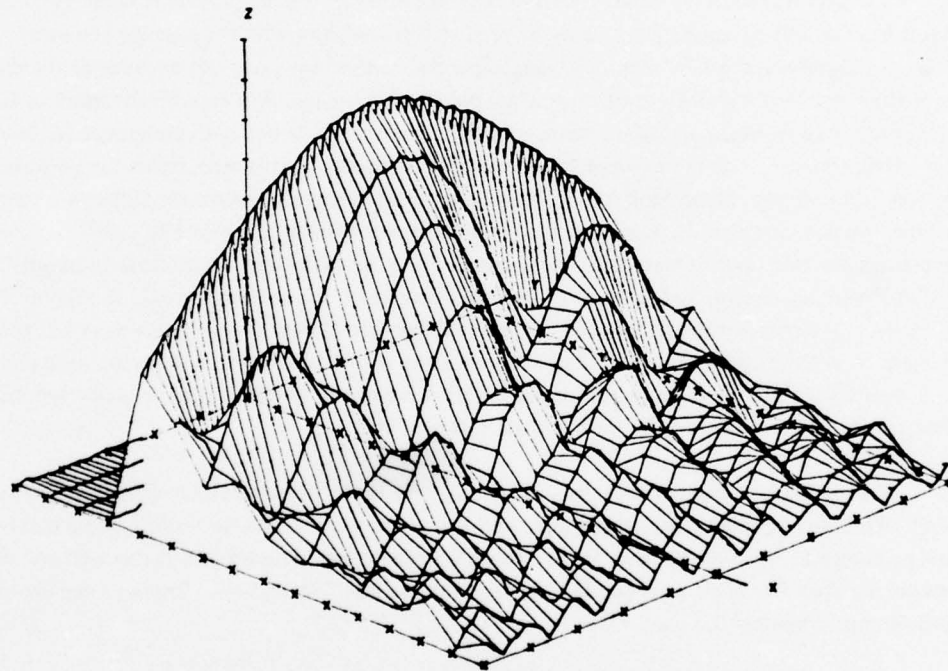
In general, these contentions are substantiated by the experimentally derived estimates of $Q(\xi, \tau)$. We illustrate this by presenting high- and low-grazing-angle data for both in-plane and cross-plane geometries (figs. 5-42 through 5-45). Table 5-3 relates figure number to test condition. For all cases polarization was horizontal and the prober chip rate was 5 MHz, which implies a tap capture width of approximately $0.2 \mu\text{sec}$.

TABLE 5-3. $|Q(\xi, \tau)|$ FUNCTION: FIGURE REFERENCE

Date, mo-day-yr	Elevation angle, deg	Flight geometry	Figure
4-2-75	7.5	In-plane	5-42
4-2-75	8.5	Cross-plane	5-43
2-27-75	30	In-plane	5-44
2-27-75	31	Cross-plane	5-45

One further observation to be drawn from the experimental data pertains to the fact that the dissimilarities between the cross-plane and in-plane geometries are not nearly as evident for the high-angle case as they are for the low-angle case. Again this result follows directly from an $S(\tau, \omega)$ function observation with regard to the Doppler variable. That is, for a decrease in grazing angle we observe that

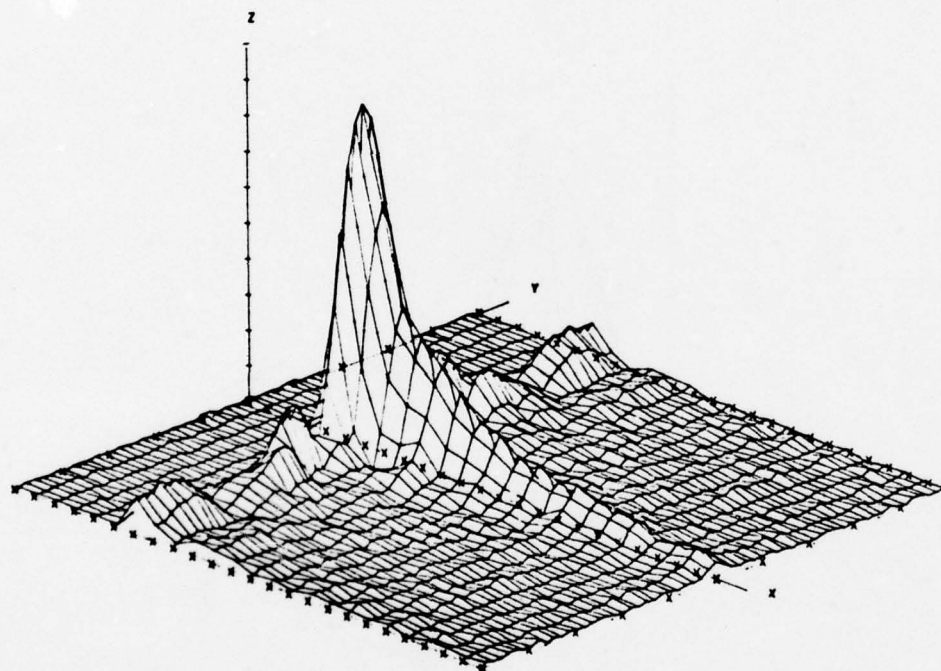
TAP AUTOCORRELATION FUNCTION
 4-2-75 HORIZONTAL
 TIME INTERVAL 11/ 9/ .492 11/ 9/ 2.217



AXIS		MINIMUM	MAXIMUM	INCREMENT
X	TAP NUMBER	21.0	38.0	1.0
Y	TIME LAG (MSEC)	-50.0	50.0	10.0
Z	TAP GAIN AUTOCORRELATION	0	450	50

Figure 5-42. $Q(\xi, \tau)$ Distribution — Low Angle, In-Plane Geometry

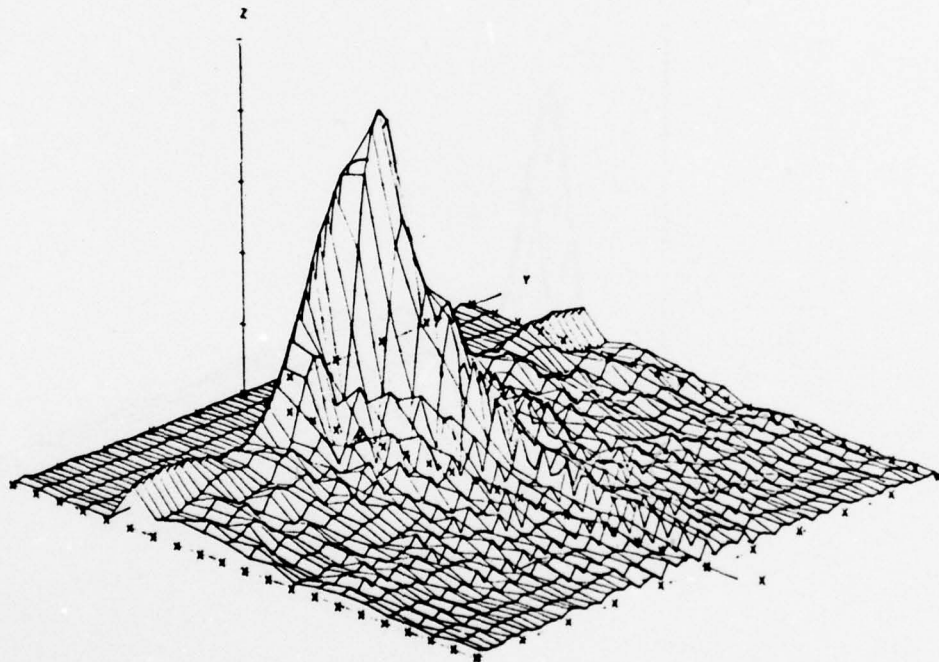
TAP AUTOCORRELATION FUNCTION
 4-2-75 HORIZONTAL
 TIME INTERVAL 11/49/19.843 11/49/21.388



AXIS		MINIMUM	MAXIMUM	INCREMENT
X	TAP NUMBER	18.0	40.0	1.0
Y	TIME LAG [MSEC]	-50.0	50.0	10.0
Z	TAP GAIN AUTOCORRELATION	0	500	50

Figure 5-43. $Q(\xi, \tau)$ Distribution — Low Angle, Cross-Plane Geometry

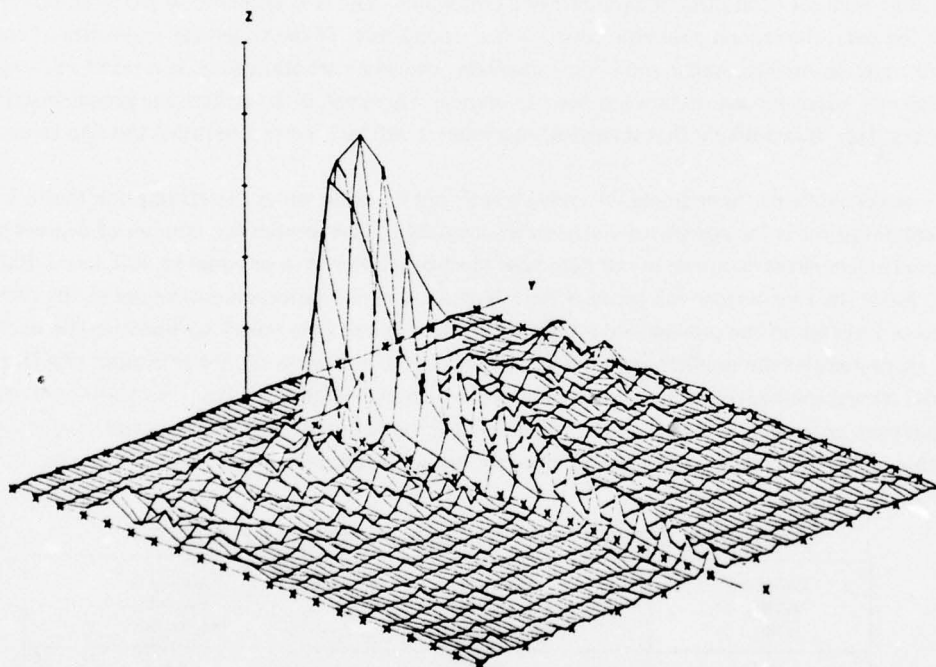
TAP AUTOCORRELATION FUNCTION
 2-27-75 HORIZONTAL
 TIME INTERVAL 10/13/ .493 10/13/ 2.218



AXIS		MINIMUM	MAXIMUM	INCREMENT
X	TAP NUMBER	30.0	50.0	1.0
Y	TIME LAG (MSEC)	-50.0	50.0	10.0
Z	TAP GAIN AUTOCORRELATION	0	150	30

Figure 5-44. $Q(\xi, \tau)$ Distribution — High Angle, In-Plane Geometry

TAP AUTOCORRELATION FUNCTION
 2-27-75 HORIZONTAL
 TIME INTERVAL 10/56/ 6.5 10/56/ 2.544



AXIS		MINIMUM	MAXIMUM	INCREMENT
X	TAP NUMBER	20.0	40.0	1.0
Y	TIME LAG (MSEC)	-50.0	50.0	10.0
Z	TAP GAIN AUTOCORRELATION	0	150	30

Figure 5-45. $Q(\xi, \tau)$ Distribution — High Angle, Cross-Plane Geometry

the channel's Doppler spectra for the alternate in-plane and cross-plane geometries become increasingly dissimilar.

5.4.6 Cross-Polarization Joint Statistics

To correctly interpret the statistical properties of the horizontal-vertical channel multipath data, some consideration must be given to stationarity and statistical significance. We approach the problem by dividing each set of multipath data into two ensembles. The first ensemble is comprised of the first half of the data; the second ensemble contains the second half. If the statistical properties of each ensemble are reasonably similar and if the underlying processes are stationary, it is safe to assume that a sufficiently large amount of data has been examined. However, if the underlying processes are not stationary, then it is unlikely that statistical equivalence will be observed between the two ensembles.

An estimate of the required ensemble length can be made under the assumption that a 5% standard deviation in the computed statistics is acceptable. This implies the number of degrees of freedom (independent samples) in our data base must be greater than or equal to 400, i.e., $1/(0.05 \times 0.05)$. Since the time-bandwidth product for a Nyquist-sampled process is equivalent to the number of degrees of freedom in the process, we can estimate the required data length by knowing the bandwidth. At 7° grazing angle (the smallest angle for which the data was processed), the minimum rms Doppler spreads (second moment) that have been observed are on the order of 30 Hz. Completing the indicated computation, an ensemble length on the order of 13 sec is required. Table 5-4 presents approximate ensemble lengths for some representative elevation angles based on typical rms Doppler spreads.

TABLE 5-4. ESTIMATE OF REQUIRED ENSEMBLE LENGTH

Elevation angle, deg	Observed rms Doppler spreads, Hz	Required ^a ensemble length, sec
7	30	13.3
10	65	6.15
11	75	5.3
32	180	2.2

^aAssumes 5% standard deviation in estimates.

Four sets of horizontal-vertical (H-V) multipath data have been processed. Pertinent test conditions, such as azimuth with respect to the satellite, elevation angle, and multipath antenna depression angle, may be found in table 5-5. This table applies to data reduction and analysis covered by this section and section 5.5, which discusses the H-V cross-covariance. Table 5-6 similarly lists the signal plus noise-to-noise ratios obtained at the tap process containing the maximum multipath energy. Values for both ensembles and the aggregate appear in this table. Under the assumption that we have achieved statistical significance and that the underlying processes are Gaussian (with constant means), then signal-to-noise ratio may be interpreted as a stationarity parameter.

TABLE 5-5. TEST CONDITIONS AND PROCESS CORRELATION COEFFICIENTS FOR PROCESSED TAPES

Linear Polarization – Front Multipath Antenna								
Tape	Azimuth, deg	Elevation angle, deg	Multipath antenna, deg	Horizontal-vertical correlation coefficient (magnitude)	Predicted envelope correlation coefficient (G.H.) ^b	Envelope correlation coefficient	Carrier ^a correlation coefficient (magnitude)	Total data processed, sec
ATO 188 (H) ATO 189 (V)	0	7	-25	0.608	0.347	0.336	—	33.52
ATO 173 (H) ATO 174 (V)	0	10	-25	0.710	0.478	0.458	—	33.52
ATO 198 (H) ATO 199 (V)	90	11	-25	0.765	0.559	0.540	0.474	33.52
ATO 124 (H) ATO 125 (V)	315	32	-45	0.845	0.690	0.691	—	3.35

^aCorrelation coefficient for H and V tap sums

^bG.H. = Gaussian hypothesis.

TABLE 5-6. SIGNAL PLUS NOISE-TO-NOISE RATIOS FOR TEST TAPES EXAMINED

Tape	Horizontal Channel, dB			Vertical Channel, dB		
	Ensemble 1	Ensemble 2	Aggregate	Ensemble 1	Ensemble 2	Aggregate
ATO 188 (H) ATO 189 (V)	8.70	8.72	8.71	3.43	3.62	3.52
ATO 173 (H) ATO 174 (V)	10.40	10.56	10.48	4.90	4.97	4.93
ATO 198 (H) ATO 199 (V)	7.18	7.42	7.30	6.44	6.47	6.46
ATO 124 (H) ATO 125 (V)	8.56	8.43	8.50	9.57	9.39	9.48

The statistical properties of the individual tap processes have been discussed in sections 5.4.1 and 5.4.4. The purpose of this section is to examine the joint statistical behavior of the horizontal and vertical tap processes and, because of the preceding results, this task is reduced to one of estimating the complex H-V correlation coefficient for the tap outputs; i.e.,

$$\rho_{HV} = \frac{\langle HV^* \rangle}{[\langle |H|^2 \rangle \langle |V|^2 \rangle]^{1/2}} \quad (5-24)$$

where $\langle \rangle$ denotes an ensemble average. The above quantity indicates the physical coupling between horizontally and vertically polarized returns for a single delay contour. In attempting to derive analytical models for the multipath scattering mechanism, this parameter plays an important role. Multipath models currently in use implicitly assume that ρ_{HV} is unity, i.e., that a surface capable of scattering vertically polarized signals will likewise scatter horizontally polarized signals, albeit with a different intensity and phase angle. These H-V tap correlation effects will also be relevant to communications diversity schemes, where a decorrelation between H and V returns would afford the opportunity to increase the receiver's immunity to fading.

Table 5-5 indicates the results obtained in processing pairs of H and V tap waveforms. Information in table 5-5 includes (1) the length in seconds of the processed data, (2) the magnitude of the horizontal-vertical channel complex correlation coefficient, (3) the horizontal-vertical channel envelope correlation coefficient, and (4) the magnitude of the horizontal-vertical channel carrier complex correlation coefficient. Note that the H-V correlation coefficients shown include both multipath and thermal noise components. Corrections must be applied to obtain correlation properties of the multipath processes alone.

If the underlying processes are complex Gaussian, a functional relationship exists between the magnitude of the complex correlation coefficient and the envelope correlation coefficient. From reference 5-11, the predicted envelope correlation coefficients are included in table 5-5. They agree favorably with the computed envelope correlation coefficient.

With the objective of establishing the reliability of parameter estimates, the signal-to-noise level at the strongest tap was evaluated. This was achieved by computing the tap signal-plus-noise power along with the noise power in a tap well removed from the signal energy peak. By assuming the average noise power to be identical for these two taps, a signal-to-noise measure can be obtained. The signal plus noise-to-noise ratios are listed and tabulated in table 5-6.

As a result of the relatively poor signal-to-noise conditions under which the tests were conducted, the correlation coefficients of table 5-5 represent process correlation coefficients and not multipath signal correlation coefficients. If we denote the instantaneous horizontal and vertical signal power by H and V, and the corresponding instantaneous noise power by N_H and N_V , then

$$\rho_p = \frac{\langle (H + N_H)(V + N_V)^* \rangle}{\sqrt{\langle |H + N_H|^2 \rangle \langle |V + N_V|^2 \rangle}}$$

where:

- ρ_p = complex process correlation coefficient
- $\langle \rangle$ = time average.

The multipath signal correlation coefficient, ρ_s , can be defined

$$\rho_s = \frac{\langle H V^* \rangle}{\sqrt{\langle |H|^2 \rangle \langle |V|^2 \rangle}} \quad (5-25)$$

Assuming that the signal and noise processes are uncorrelated, then ρ_p reduces to:

$$\rho_p = \frac{\langle H V^* \rangle}{\sqrt{\langle |H|^2 + |N_H|^2 \rangle \langle |V|^2 + |N_V|^2 \rangle}} \quad (5-26)$$

or

$$\frac{\rho_s}{\rho_p} = \sqrt{\frac{\langle |H|^2 + |N_H|^2 \rangle \langle |V|^2 + |N_V|^2 \rangle}{\langle |H|^2 \rangle^2 \langle |V|^2 \rangle^2}} \quad (5-27)$$

With the aid of table 5-6, we can estimate the ratio ρ_s/ρ_p and determine the value of ρ_s . The results appear in table 5-7.

TABLE 5-7. HORIZONTAL-VERTICAL CORRELATION COEFFICIENTS
(SIGNAL-TO-NOISE COMPENSATED)

Tape	Azimuth, deg	Elevation angle, deg	Horizontal- vertical correlation coefficient	Approximate signal- to-noise ratios, dB	
				Horizontal channel	Vertical channel
ATO 188 ATO 189	0	7	0.8763	8.08	0.97
ATO 173 ATO 174	0	10	0.9076	9.60	3.25
ATO 198 ATO 199	90	11	0.9644	6.40	5.35
ATO 124 ATO 125	315	32	0.9682	7.83	8.96

5.4.7 Multipath Signal Stationarity Considerations

Individual data analysis periods (e.g., $S(\tau, \omega)$ estimates) in general entail a data collection time interval of 5 to 13 sec. Over this time period, which for a 400-kn airplane velocity translates into a surface trajectory of up to 2600 m, it is possible that the scattering characteristics of the sea surface illuminated by the aircraft antenna could change somewhat. To detect such changes in the surface homogeneity, we may subject the outputs of the SACP receiver to signal stationarity procedures.

The concept of homogeneity refers to ensemble spatial distributions of a random process. A process is said to be wide-sense homogeneous if its mean is constant and if the correlation function between two points is a function of the vector differences between the two points. Furthermore, the process is said to be isotropic if the correlation function is not dependent upon direction; i.e.,

$$\begin{aligned} \text{Homogeneous: } & \langle \eta(r) \rangle = \text{constant} \\ & \langle \eta(r_1) \eta^*(r_2) \rangle = \text{function of } r_1 - r_2 \text{ only} \\ \text{Isotropic: } & \langle \eta(r) \rangle = \text{constant} \\ & \langle \eta(r_1) \eta^*(r_2) \rangle = \text{function of } |r_1 - r_2| \text{ only.} \end{aligned}$$

In analyzing the received signal data we are testing for stationarity. A process is stationary in the wide sense if its mean is not time dependent and its correlation function depends on time difference only; i.e.,

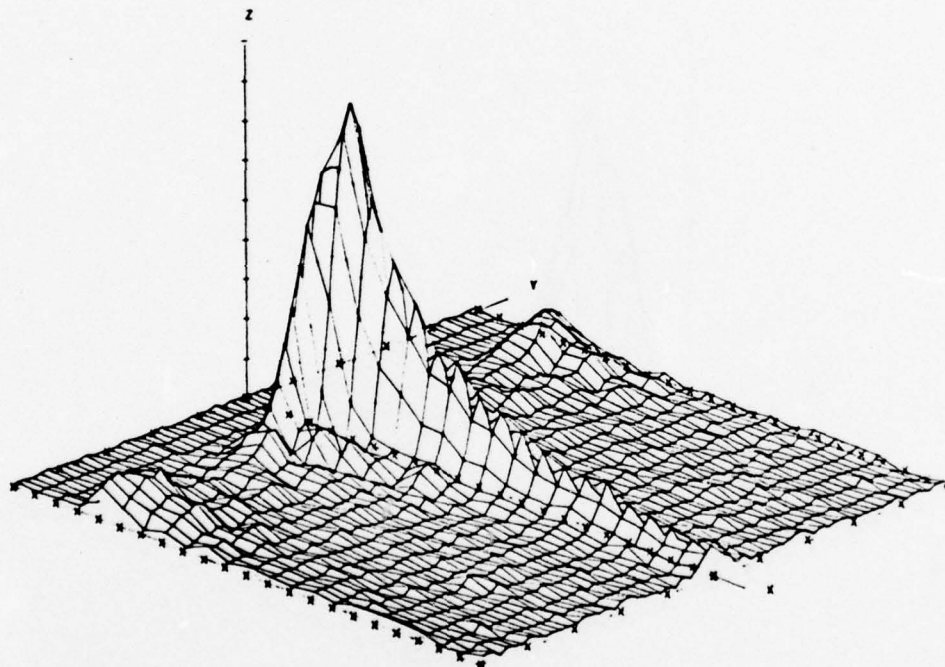
$$\begin{aligned} \text{Stationarity: } & \langle S(t) \rangle = \text{constant} \\ & \langle S(t_1) S^*(t_2) \rangle = \text{function of } t_1 - t_2 \text{ only.} \end{aligned}$$

For the multipath experiment one expects the received signal data to be stationary if the sea surface is isotropic with non-time-varying statistics over the data collection interval.

We assume the airplane velocity is large enough so that the sea surface may be considered "frozen." Thus the stationarity requirements are satisfied if the tap-gain autocorrelation function and the mean I and Q tap components of the received signal are constant. The latter requirement is fulfilled if the coherent component of the multipath signal is time invariant. For the sum total of all analyses conducted, there has been no evidence that would indicate a reflection process that is appreciably less than totally incoherent. Thus for the ensuing stationarity test example we relax the " $\langle S(t) \rangle = \text{constant}$ " investigation and concentrate on presenting results pertaining to the tap-gain autocorrelation function $Q(\xi, \tau)$.

Example stationarity test results for the cross-plane flight test leg of March 31, 1975, are given in figure 5-46. This data, gathered at an elevation angle of 15° over the horizontal polarization multipath antenna port, has a tap width duration of $0.2 \mu\text{sec}$ (i.e., 5-MHz PN chip rate). Five $Q(\xi, \tau)$ distributions are presented, with each estimate being obtained over a 1.7-sec time interval and separated

TAP AUTOCORRELATION FUNCTION
 3-31-75 HORIZONTAL
 TIME INTERVAL 9/10/ 9.021 9/10/11.546

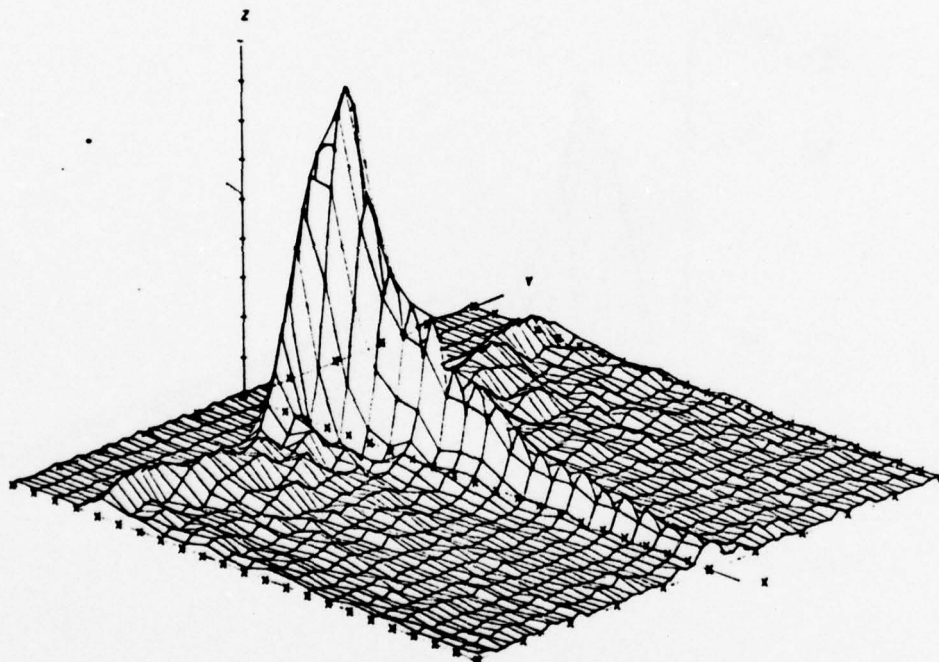


AXIS	MINIMUM	MAXIMUM	INCREMENT
X TAP NUMBER	10.0	40.0	1.0
Y TIME LAG (MSEC)	-50.0	50.0	10.0
Z TAP GAIN AUTOCORRELATION	0	450	50

(a) First Time Interval

Figure 5-46. Tap-Gain Autocorrelation Function Plots for Stationarity Investigation

TAP AUTOCORRELATION FUNCTION
 3-31-76 HORIZONTAL
 TIME INTERVAL 8/18/24.582 8/18/26.317

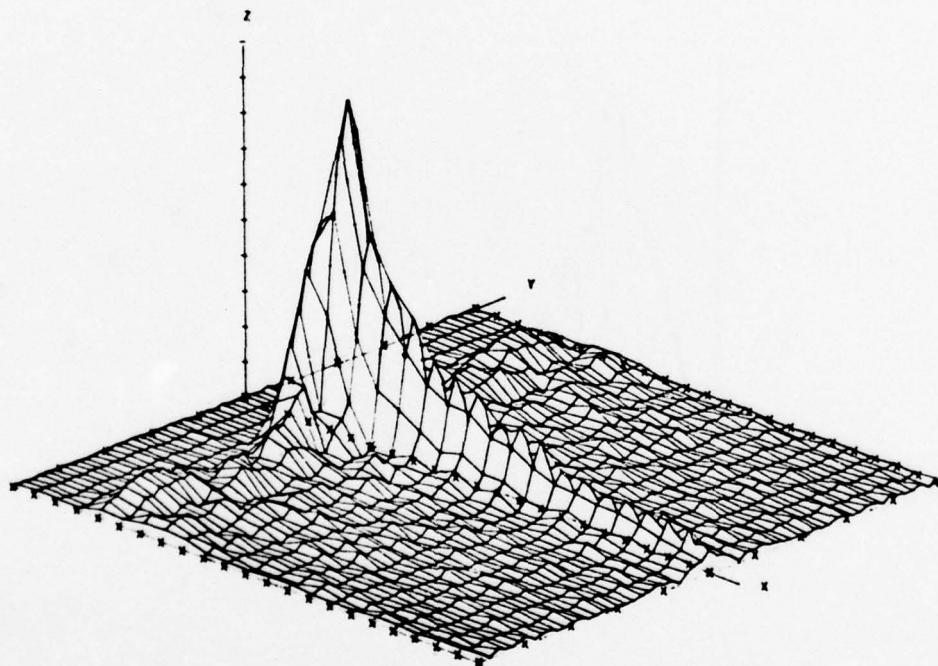


AXIS		MINIMUM	MAXIMUM	INCREMENT
X	TAP NUMBER	18.0	40.0	1.0
Y	TIME LAG (MSEC)	-50.0	50.0	10.0
Z	TAP GAIN AUTOCORRELATION	0	450	50

(b) Second Time Interval

Figure 5-46. (Continued)

TAP AUTOCORRELATION FUNCTION
 3-31-75 HORIZONTAL
 TIME INTERVAL 0/10/41.705 8/10/43.110

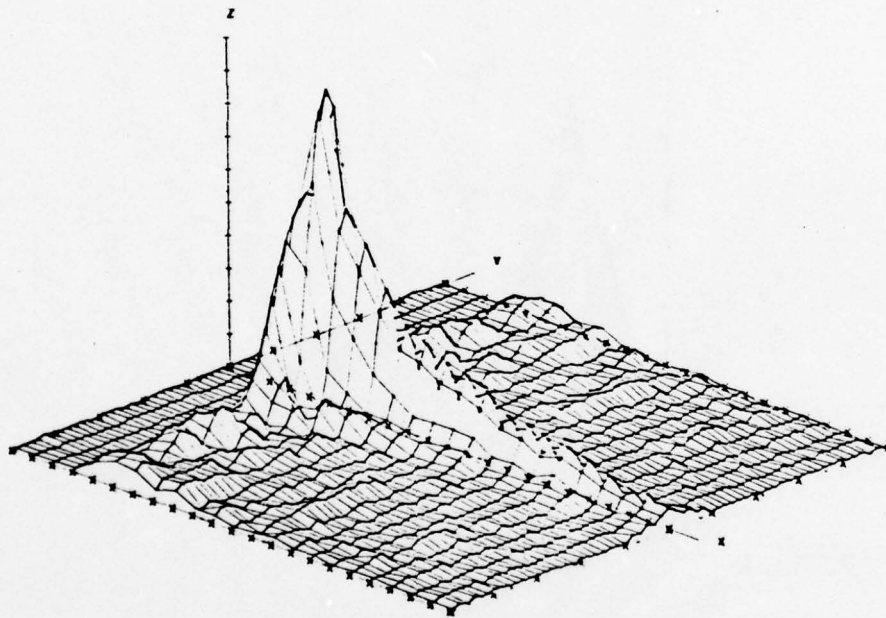


AXIS		MINIMUM	MAXIMUM	INCREMENT
X	TAP NUMBER	10.0	40.0	1.0
Y	TIME LAG (MSEC)	-50.0	50.0	10.0
Z	TAP GAIN AUTOCORRELATION	0	500	50

(c) Third Time Interval

Figure 5-46. (Continued)

TAP AUTOCORRELATION FUNCTION
 3-31-75 HORIZONTAL
 TIME INTERVAL 9/19/58.002 9/19/59.727

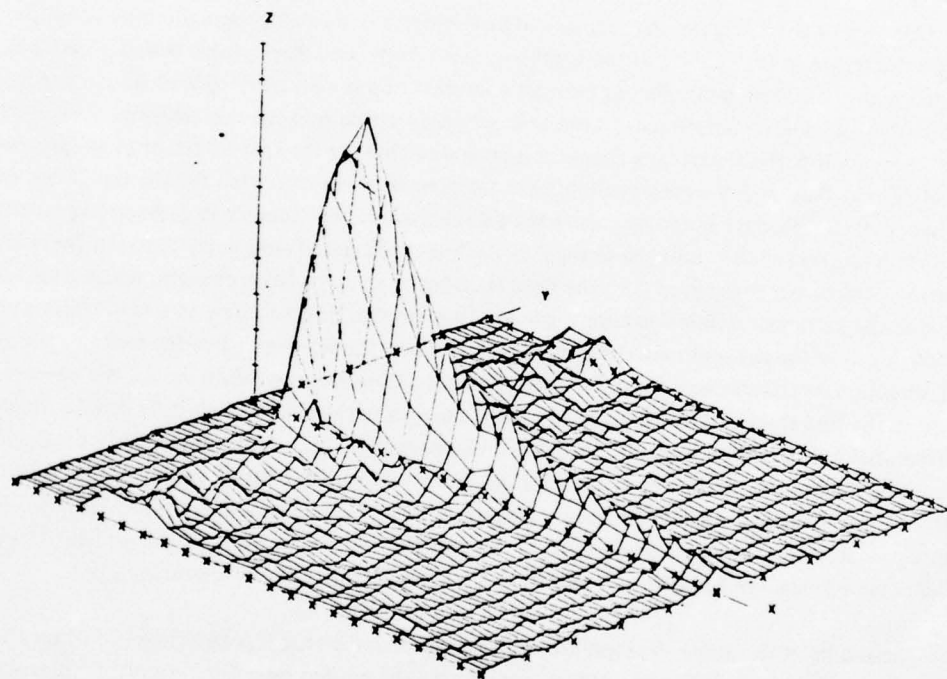


AXIS		MINIMUM	MAXIMUM	INCREMENT
X	TAP NUMBER	18.0	40.0	1.0
Y	TIME LAG (MSEC)	-50.0	50.0	10.0
Z	TAP GAIN AUTOCORRELATION	0	500	50

(d) Fourth Time Interval

Figure 5-46. (Continued)

TAP AUTOCORRELATION FUNCTION
 3-31-75 HORIZONTAL
 TIME INTERVAL 9/20/14.876 9/20/16.801



AXIS		MINIMUM	MAXIMUM	INCREMENT
X	TAP NUMBER	18.0	40.0	1.0
Y	TIME LAG [MSEC]	-50.0	50.0	10.0
Z	TAP GAIN AUTOCORRELATION	0	500	50

(e) Fifth Time Interval

Figure 5-46. (Concluded)

from its adjacent neighbor by approximately 13 sec. Thus a total time interval on the order of slightly over 1 min is represented in a sampled form.

A qualitative visual comparison of the five data sets leads one to conclude that, for the most part, the $Q(\xi, \tau)$ distributions do not exhibit any appreciable change over the time interval of record. Minor changes, of course, could be induced by changes in the surface characteristics or by the expected statistical variance associated with the finite sample time duration.

One area of the ξ, τ realm that appears to be subjected to a small systematic time variation relates to the region in the vicinity of the specular-point return (i.e., that τ value which is typically associated with the largest gain value, or perhaps a fraction of a tap on either side of it). In particular, we detect that the relative amplitudes (noticeable primarily at the zero-lag axis value) associated with the first three multipath-present taps change in such a way that for the first 40 sec or so the second multipath tap increasingly becomes predominant; the procedure reverses itself for the last 20 sec of the total time interval. We have purposely restricted this analysis to the cross-plane geometry in an attempt to avoid "sin (grazing angle)" induced changes in the bulk differential time delay between the multipath process and direct path signal (i.e., the time tracking reference). Such changes, which over a 1-min duration at the particular nominal grazing angle location are significant relative to a chip width duration, would obviously cause the multipath process to march across the tap bank. For the example being discussed, direction meanders away from the cross-plane direction could certainly induce the observed behavior in the first three multipath taps. Similarly, changes in the aircraft's altitude could influence the differential bulk delay between direct and specular-point paths (i.e., for the first 40 sec a slight aircraft heading toward the satellite or an altitude increase could produce the observed results, with the last 20 sec being associated with the opposite changes in aircraft system parameters). Alternatively the aircraft parameters may not have deviated from the specified condition, and one is then led to conclude that the observed signal phenomenon is related to the characteristics of the scatter surface.

The results of the above example are expected to be somewhat representative for other flight tests and are in accordance with expectation, considering the limited time duration of the intervals analyzed as well as the fact that rms sea slope, the most significant surface parameter, is roughly proportional to the square root of wind velocity (i.e., a 2-to-1 change in wind velocity results in a $\sqrt{2}$ change in the effective scatter characteristics).

5.5 CROSS-POWER SPECTRA FOR HORIZONTALLY AND VERTICALLY POLARIZED RETURNS

The correlation properties of the scattered H and V fields were studied in section 5.4.6, where the emphasis was on joint H and V statistics of the tap processes. Physically, a single tap process is formed from the contributions of many independent scattering surfaces lying along a constant delay contour on the ocean. The derived correlation functions therefore yield information concerning the integrated

effects along this surface. Accordingly any method of investigating scattering properties over a smaller spatial region is of interest.

One technique that provides substantial improvement in resolution is based on the method of cross-spectrum analysis. When a segment of a tap process is Fourier transformed into the frequency domain, the resulting spectral components can be identified with a specific spatial location on the appropriate delay contour. Although this mapping will not be one-to-one, advantage can be taken of the angular symmetry that prevails for in-plane flights to argue that the two spatial regions providing contributions to a particular spectral component should have identical scattering properties, i.e., the scattering angles relative to the aircraft and satellite positions will be identical for the two scattering areas. Figure 5-47 illustrates this geometrical configuration.

After spectral components for each horizontal and vertical tap process have been obtained, a cross-spectrum can be formed:

$$P_{HV}(\nu) \approx \langle H(\nu) V^*(\nu) \rangle \quad (5-28)$$

where:

- P_{HV} = the spectrum
- $H(\nu), V(\nu)$ = horizontal and vertical polarization spectra for tap k over a given data segment
- $\langle \cdot \rangle$ = time averaging over many segments of data.

The cross-spectrum $P_{HV}(\nu)$ can be normalized to yield a cross-spectrum correlation coefficient, which is then interpreted in precisely the same manner as was the correlation coefficient for the total tap processes discussed earlier in section 5.4.6, i.e., it indicates statistical dependence of the H and V scattered components over a particular spatial region. Quantitative information concerning phase relationships for the H and V scattering cross section can also be extracted directly from the cross-power spectrum.

An inherent benefit accruing from the cross-spectrum analysis is that of signal-to-noise enhancement. From the structure of the scattering functions shown in other sections and again in the cross-spectrum magnitudes to be presented, it is evident that 3-dB Doppler spreads of around 10 Hz can be anticipated at a particular multipath delay. The spectral analysis effectively provides a high resolution filtering of the tap process, resulting in a processing gain commensurate with the noise bandwidth-signal bandwidth ratio. Typically, the delay-Doppler cell signal-to-noise ratio is 20 to 30 dB at the energy peak for each tap. Less endearing is the penalty for higher resolution, which appears as a requirement for longer record lengths to achieve sufficient averaging over the signal fluctuations.

Evaluation of the tap cross-spectrum defined by equation (5-28) has been carried out for the link configurations summarized in table 5-5. Some examples of the numerical results are found in tables 5-8 and 5-9). Each pair of figures pertains to a single flight, with the (a) figure indicating behavior near the zero Doppler point and the (b) figure showing a second region further out in

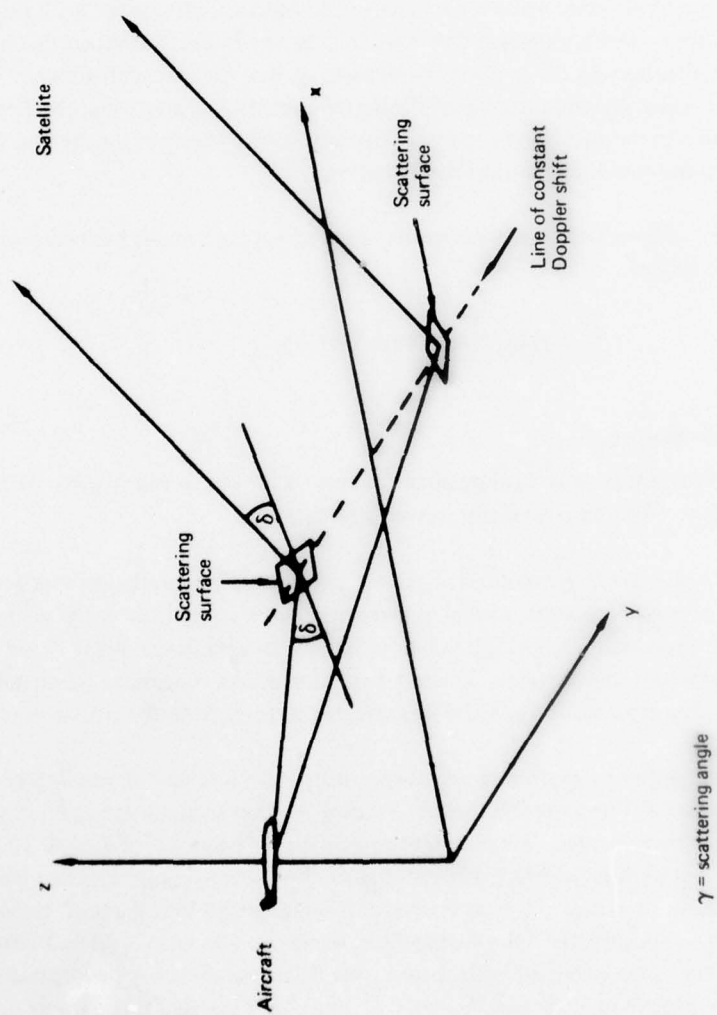


Figure 5-47. Aircraft-Satellite Geometry Showing Scattering Surface Symmetry (In-Plane Flight)

TABLE 5-8. H-V CROSS-POWER SPECTRUM, MAGNITUDE, AND PHASE, IN-PLANE FLIGHT, MARCH 31, 1975

(a) Behavior Near the Zero-Doppler Point

		Magnitude										Phase (radians)											
FREQ *		-0.595	0.000	0.595	1.191	1.787	2.383	2.979	3.574	4.170	4.765			-0.595	0.000	0.595	1.191	1.787	2.383	2.979	3.574	4.170	4.765
TAP :																							
26	1.255E+04	1.476E+04	1.756E+04	2.069E+04	2.355E+04	2.614E+04	2.744E+04	2.744E+04	2.686E+04	2.341E+04	2.114E+04	2.686E+04	2.744E+04	2.744E+04	2.686E+04	2.341E+04	2.114E+04	2.686E+04	2.744E+04	2.744E+04	2.686E+04	2.341E+04	2.114E+04
27	3.731E+03	3.459E+03	3.424E+03	3.640E+03	3.850E+03	3.967E+03	3.822E+03	3.627E+03	3.382E+03	2.983E+03	2.758E+03	3.382E+03	3.627E+03	3.822E+03	3.967E+03	3.850E+03	3.640E+03	3.459E+03	3.424E+03	3.640E+03	3.850E+03	3.967E+03	3.758E+03
28	8.424E+03	8.051E+03	7.541E+03	6.995E+03	6.800E+03	6.969E+03	6.807E+03	6.577E+03	6.300E+03	5.830E+03	5.318E+03	6.300E+03	6.577E+03	6.807E+03	6.969E+03	6.800E+03	6.995E+03	7.541E+03	7.541E+03	7.541E+03	7.541E+03	7.541E+03	7.541E+03
29	3.224E+03	2.955E+03	2.681E+03	2.358E+03	1.790E+03	1.593E+03	1.593E+03	1.593E+03	1.593E+03	1.593E+03	1.593E+03	1.593E+03	1.593E+03	1.593E+03	1.593E+03	1.593E+03	1.593E+03	1.593E+03	1.593E+03	1.593E+03	1.593E+03	1.593E+03	
30	1.155E+03	9.437E+02	9.274E+02	1.049E+03	1.026E+03	8.439E+02	7.336E+02	7.336E+02	7.336E+02	7.336E+02	7.336E+02	7.336E+02	7.336E+02	7.336E+02	7.336E+02	7.336E+02	7.336E+02	7.336E+02	7.336E+02	7.336E+02	7.336E+02	7.336E+02	
31	8.705E+02	7.330E+02	5.864E+02	4.977E+02	4.367E+02	3.656E+02	3.153E+02	3.153E+02	3.153E+02	3.153E+02	3.153E+02	3.153E+02	3.153E+02	3.153E+02	3.153E+02	3.153E+02	3.153E+02	3.153E+02	3.153E+02	3.153E+02	3.153E+02	3.153E+02	
32	3.572E+02	2.272E+02	3.722E+02	4.152E+02	3.756E+02	3.574E+02	3.653E+02	3.653E+02	3.653E+02	3.653E+02	3.653E+02	3.653E+02	3.653E+02	3.653E+02	3.653E+02	3.653E+02	3.653E+02	3.653E+02	3.653E+02	3.653E+02	3.653E+02	3.653E+02	
33	1.431E+02	2.465E+02	3.235E+02	2.959E+02	2.565E+02	2.362E+02	2.034E+02	1.958E+02	1.958E+02	1.958E+02	1.958E+02	1.958E+02	1.958E+02	1.958E+02	1.958E+02	1.958E+02	1.958E+02	1.958E+02	1.958E+02	1.958E+02	1.958E+02	1.958E+02	
34	2.136E+02	1.884E+02	1.365E+02	1.302E+02	1.456E+02	1.456E+02	1.456E+02	1.456E+02	1.456E+02	1.456E+02	1.456E+02	1.456E+02	1.456E+02	1.456E+02	1.456E+02	1.456E+02	1.456E+02	1.456E+02	1.456E+02	1.456E+02	1.456E+02	1.456E+02	
CARRIER	1.033E+05	8.959E+04	8.543E+04	9.930E+04	1.173E+05	1.307E+05	1.306E+05	1.306E+05	1.306E+05	1.306E+05	1.306E+05	1.306E+05	1.306E+05	1.306E+05	1.306E+05	1.306E+05	1.306E+05	1.306E+05	1.306E+05	1.306E+05	1.306E+05	1.306E+05	

Note: Specular point grazing angle = 10°

		Magnitude										Phase (radians)											
FREQ *		-0.595	0.000	0.595	1.191	1.787	2.383	2.979	3.574	4.170	4.765			-0.595	0.000	0.595	1.191	1.787	2.383	2.979	3.574	4.170	4.765
TAP :																							
26	-2.314E+00	-2.344E+00	-2.363E+00	-2.355E+00	-2.340E+00	-2.339E+00	-2.335E+00	-2.332E+00	-2.333E+00	-2.334E+00	-2.331E+00	-2.331E+00	-2.332E+00	-2.333E+00	-2.334E+00	-2.335E+00	-2.339E+00	-2.340E+00	-2.344E+00	-2.363E+00	-2.363E+00	-2.344E+00	-2.314E+00
27	-2.156E+00	-2.205E+00	-2.255E+00	-2.305E+00	-2.355E+00	-2.405E+00	-2.455E+00	-2.505E+00	-2.555E+00	-2.605E+00	-2.655E+00	-2.705E+00	-2.755E+00	-2.805E+00	-2.855E+00	-2.905E+00	-2.955E+00	-3.005E+00	-3.055E+00	-3.105E+00	-3.155E+00	-3.205E+00	-3.255E+00
28	-2.113E+00	-2.136E+00	-2.177E+00	-2.243E+00	-2.307E+00	-2.348E+00	-2.374E+00	-2.394E+00	-2.408E+00	-2.416E+00	-2.419E+00	-2.419E+00	-2.416E+00	-2.408E+00	-2.394E+00	-2.374E+00	-2.348E+00	-2.307E+00	-2.243E+00	-2.177E+00	-2.136E+00	-2.113E+00	-2.156E+00
29	-2.251E+00	-2.231E+00	-2.315E+00	-2.333E+00	-2.343E+00	-2.348E+00	-2.349E+00	-2.348E+00	-2.343E+00	-2.333E+00	-2.315E+00	-2.231E+00	-2.251E+00	-2.231E+00	-2.315E+00	-2.333E+00	-2.343E+00	-2.348E+00	-2.349E+00	-2.348E+00	-2.343E+00	-2.333E+00	-2.315E+00
30	-2.165E+00	-2.209E+00	-2.265E+00	-2.320E+00	-2.373E+00	-2.423E+00	-2.468E+00	-2.508E+00	-2.543E+00	-2.573E+00	-2.600E+00	-2.623E+00	-2.642E+00	-2.658E+00	-2.671E+00	-2.680E+00	-2.685E+00	-2.687E+00	-2.685E+00	-2.671E+00	-2.658E+00	-2.642E+00	-2.623E+00
31	-2.137E+00	-2.155E+00	-2.190E+00	-2.246E+00	-2.312E+00	-2.379E+00	-2.446E+00	-2.512E+00	-2.577E+00	-2.640E+00	-2.700E+00	-2.758E+00	-2.813E+00	-2.864E+00	-2.911E+00	-2.954E+00	-2.993E+00	-3.028E+00	-3.059E+00	-3.086E+00	-3.109E+00	-3.128E+00	-3.143E+00
32	-2.107E+00	-2.124E+00	-2.154E+00	-2.198E+00	-2.256E+00	-2.317E+00	-2.380E+00	-2.443E+00	-2.505E+00	-2.565E+00	-2.622E+00	-2.675E+00	-2.724E+00	-2.769E+00	-2.810E+00	-2.847E+00	-2.880E+00	-2.909E+00	-2.934E+00	-2.955E+00	-2.972E+00	-2.985E+00	-2.994E+00
33	-2.071E+00	-2.088E+00	-2.126E+00	-2.178E+00	-2.243E+00	-2.310E+00	-2.378E+00	-2.445E+00	-2.510E+00	-2.572E+00	-2.630E+00	-2.683E+00	-2.732E+00	-2.777E+00	-2.818E+00	-2.855E+00	-2.888E+00	-2.917E+00	-2.942E+00	-2.963E+00	-2.980E+00	-2.993E+00	-2.994E+00
34	-2.137E+00	-2.143E+00	-2.160E+00	-2.195E+00	-2.246E+00	-2.301E+00	-2.359E+00	-2.419E+00	-2.480E+00	-2.541E+00	-2.601E+00	-2.658E+00	-2.712E+00	-2.762E+00	-2.808E+00	-2.850E+00	-2.888E+00	-2.922E+00	-2.952E+00	-2.978E+00	-2.990E+00	-2.994E+00	-2.994E+00
CARRIER	-2.200E+00	-2.178E+00	-2.263E+00	-2.330E+00	-2.398E+00	-2.466E+00	-2.534E+00	-2.601E+00	-2.667E+00	-2.732E+00	-2.796E+00	-2.858E+00	-2.918E+00	-2.975E+00	-3.028E+00	-3.077E+00	-3.122E+00	-3.163E+00	-3.200E+00	-3.233E+00	-3.262E+00	-3.287E+00	-3.308E+00

Note: Specular-point grazing angle = 10°

TABLE 5-8 (Concluded)
(b) Behavior Removed From Zero Doppler Point

		Magnitude									
FREQ =		41.184	41.699	42.295	42.891	43.486	44.082	44.678	45.273	45.869	46.465
TAP :		----	----	----	----	----	----	----	----	----	----
26		4.975E+01	3.355E+01	2.055E+01	2.642E+01	2.394E+01	3.260E+01	2.657E+01	1.729E+01	2.445E+01	4.111E+01
27		6.140E+01	2.555E+01	1.035E+01	7.741E+00	2.579E+01	3.258E+01	7.300E+00	2.877E+01	5.718E+01	7.338E+01
28		7.468E+01	6.649E+01	4.878E+01	2.644E+01	1.609E+01	1.715E+01	2.873E+01	5.416E+01	7.402E+01	6.323E+01
29		2.404E+02	1.457E+02	1.852E+02	1.030E+02	1.055E+02	9.723E+01	7.567E+01	6.491E+01	6.271E+01	5.583E+01
30		1.303E+04	1.573E+04	1.323E+04	9.117E+03	6.057E+03	4.545E+03	3.498E+03	2.371E+03	1.539E+03	1.133E+03
31		1.557E+04	1.890E+04	2.322E+04	2.560E+04	2.788E+04	2.570E+04	3.034E+04	3.441E+04	2.543E+04	2.233E+04
32		3.815E+03	4.154E+03	4.384E+03	4.522E+03	5.033E+03	7.424E+03	9.012E+03	1.021E+04	1.155E+04	1.287E+04
33		9.302E+02	1.121E+03	1.290E+03	1.365E+03	1.495E+03	1.634E+03	1.777E+03	2.069E+03	2.387E+03	2.526E+03
34		4.422E+02	5.075E+02	5.863E+02	6.493E+02	6.831E+02	6.537E+02	6.144E+02	5.840E+02	5.503E+02	5.634E+02
CARRIER		6.002E+04	6.245E+04	6.334E+04	6.338E+04	6.405E+04	6.574E+04	6.258E+04	5.803E+04	5.509E+04	5.990E+04

		Phase (radians)									
FREQ =		41.184	41.699	42.295	42.891	43.486	44.082	44.678	45.273	45.869	46.465
TAP :		----	----	----	----	----	----	----	----	----	----
26		-1.960E+00	-1.814E+00	-2.239E-01	6.463E-01	1.955E+00	2.871E+00	-2.759E+00	-2.697E+00	2.038E+00	1.563E+00
27		-2.007E+00	-1.974E+00	-2.453E+00	2.307E+00	1.995E+00	1.913E+00	2.169E+00	-1.972E+00	-2.133E+00	-2.188E+00
28		-2.715E+00	-2.453E+00	-2.228E+00	-2.318E+00	-2.543E+00	-2.140E+00	-1.696E+00	-1.565E+00	-1.403E+00	-1.443E+00
29		-2.563E+00	-2.575E+00	-2.258E+00	-2.354E+00	-2.440E+00	-2.417E+00	-2.238E+00	-2.103E+00	-2.075E+00	-2.093E+00
30		-2.604E+00	-2.688E+00	-2.575E+00	-2.582E+00	-2.556E+00	-2.575E+00	-2.579E+00	-2.581E+00	-2.640E+00	-2.595E+00
31		-2.555E+00	-2.514E+00	-2.511E+00	-2.525E+00	-2.556E+00	-2.574E+00	-2.573E+00	-2.576E+00	-2.575E+00	-2.573E+00
32		-2.618E+00	-2.635E+00	-2.650E+00	-2.666E+00	-2.667E+00	-2.640E+00	-2.591E+00	-2.543E+00	-2.535E+00	-2.533E+00
33		-2.589E+00	-2.615E+00	-2.633E+00	-2.650E+00	-2.652E+00	-2.638E+00	-2.640E+00	-2.724E+00	-2.685E+00	-2.615E+00
34		-2.544E+00	-2.555E+00	-2.609E+00	-2.633E+00	-2.694E+00	-2.748E+00	-2.799E+00	-2.884E+00	-2.953E+00	-2.953E+00
CARRIER		-2.698E+00	-2.567E+00	-2.548E+00	-2.535E+00	-2.517E+00	-2.501E+00	-2.497E+00	-2.515E+00	-2.563E+00	-2.614E+00

Note: Specular-point grazing angle = 10°

TABLE 5.9. H-V CROSS POWER SPECTRUM, MAGNITUDE, AND PHASE, IN-PLANE FLIGHT, APRIL 2, 1975

(a) Behavior Near the Zero Doppler Point

Magnitude											
FREQ *	-0.596	0.000	0.596	1.191	1.787	2.383	2.979	3.574	4.170	4.766	
TAP :											
25	1.543E+04	2.023E+04	2.565E+04	2.694E+04	2.565E+04	2.623E+04	2.602E+04	2.555E+04	2.402E+04	2.250E+04	
26	1.543E+04	2.023E+04	2.565E+04	2.694E+04	2.565E+04	2.623E+04	2.602E+04	2.555E+04	2.402E+04	2.250E+04	
27	1.543E+04	2.023E+04	2.565E+04	2.694E+04	2.565E+04	2.623E+04	2.602E+04	2.555E+04	2.402E+04	2.250E+04	
28	1.543E+04	2.023E+04	2.565E+04	2.694E+04	2.565E+04	2.623E+04	2.602E+04	2.555E+04	2.402E+04	2.250E+04	
29	1.543E+04	2.023E+04	2.565E+04	2.694E+04	2.565E+04	2.623E+04	2.602E+04	2.555E+04	2.402E+04	2.250E+04	
30	1.543E+04	2.023E+04	2.565E+04	2.694E+04	2.565E+04	2.623E+04	2.602E+04	2.555E+04	2.402E+04	2.250E+04	
31	1.543E+04	2.023E+04	2.565E+04	2.694E+04	2.565E+04	2.623E+04	2.602E+04	2.555E+04	2.402E+04	2.250E+04	
32	1.543E+04	2.023E+04	2.565E+04	2.694E+04	2.565E+04	2.623E+04	2.602E+04	2.555E+04	2.402E+04	2.250E+04	
33	1.543E+04	2.023E+04	2.565E+04	2.694E+04	2.565E+04	2.623E+04	2.602E+04	2.555E+04	2.402E+04	2.250E+04	
CARRIER	0.515E+04	0.551E+04	0.615E+04	0.742E+04	7.641E+04	7.195E+04	6.900E+04	6.734E+04	6.622E+04	6.377E+04	

Note: Specular-point grazing angle = 7.5°

Phase (radians)											
FREQ =	-0.596	0.000	0.596	1.191	1.787	2.383	2.979	3.574	4.170	4.766	
TAP :											
25	-1.294E+00	-1.294E+00	-1.294E+00	-2.005E+00	-2.005E+00	-2.005E+00	-2.005E+00	-2.005E+00	-2.005E+00	-2.005E+00	
26	-1.294E+00	-1.294E+00	-1.294E+00	-2.005E+00	-2.005E+00	-2.005E+00	-2.005E+00	-2.005E+00	-2.005E+00	-2.005E+00	
27	-1.294E+00	-1.294E+00	-1.294E+00	-2.005E+00	-2.005E+00	-2.005E+00	-2.005E+00	-2.005E+00	-2.005E+00	-2.005E+00	
28	-1.294E+00	-1.294E+00	-1.294E+00	-2.005E+00	-2.005E+00	-2.005E+00	-2.005E+00	-2.005E+00	-2.005E+00	-2.005E+00	
29	-1.294E+00	-1.294E+00	-1.294E+00	-2.005E+00	-2.005E+00	-2.005E+00	-2.005E+00	-2.005E+00	-2.005E+00	-2.005E+00	
30	-1.294E+00	-1.294E+00	-1.294E+00	-2.005E+00	-2.005E+00	-2.005E+00	-2.005E+00	-2.005E+00	-2.005E+00	-2.005E+00	
31	-1.294E+00	-1.294E+00	-1.294E+00	-2.005E+00	-2.005E+00	-2.005E+00	-2.005E+00	-2.005E+00	-2.005E+00	-2.005E+00	
32	-1.294E+00	-1.294E+00	-1.294E+00	-2.005E+00	-2.005E+00	-2.005E+00	-2.005E+00	-2.005E+00	-2.005E+00	-2.005E+00	
33	-1.294E+00	-1.294E+00	-1.294E+00	-2.005E+00	-2.005E+00	-2.005E+00	-2.005E+00	-2.005E+00	-2.005E+00	-2.005E+00	
APF IEP	-1.294E+00	-1.294E+00	-1.294E+00	-2.005E+00	-2.005E+00	-2.005E+00	-2.005E+00	-2.005E+00	-2.005E+00	-2.005E+00	

TABLE 5-9. (Concluded)
(b) Behavior Removed From Zero-Doppler Point

		Magnitude									
FREQ =	41.104	41.699	42.295	42.891	43.486	44.082	44.678	45.273	45.869	46.465	
TAP :											
25	7.430E+01	3.694E+01	3.202E+01	6.942E+01	8.210E+01	6.843E+01	7.525E+01	9.311E+01	7.312E+01	4.397E+01	
26	1.335E+01	1.160E+01	2.029E+01	2.623E+01	2.277E+01	1.426E+01	8.498E+00	4.260E+00	1.145E+01	2.100E+01	
27	3.500E+01	2.433E+01	2.460E+01	5.061E+01	6.463E+01	3.343E+01	9.796E+00	2.448E+01	6.548E+01	8.071E+01	
28	1.561E+01	2.503E+01	4.007E+01	3.465E+01	1.802E+01	2.691E+01	3.910E+01	4.186E+01	5.553E+01	5.610E+01	
29	1.548E+03	1.275E+03	7.692E+02	4.419E+02	2.889E+02	1.882E+02	1.115E+02	8.217E+01	8.616E+01	9.153E+01	
30	8.483E+03	8.928E+03	9.351E+03	9.132E+03	8.531E+03	7.954E+03	7.400E+03	6.589E+03	5.563E+03	4.447E+03	
31	1.583E+03	2.143E+03	2.476E+03	2.830E+03	3.060E+03	3.553E+03	4.263E+03	4.875E+03	5.221E+03	5.788E+03	
32	3.667E+02	4.782E+02	5.774E+02	6.889E+02	7.465E+02	7.939E+02	8.671E+02	9.133E+02	8.893E+02	9.175E+02	
33	1.800E+02	1.961E+02	1.925E+02	1.835E+02	1.517E+02	1.908E+02	2.386E+02	3.003E+02	3.783E+02	4.043E+02	
CARRIER	1.833E+04	1.884E+04	1.896E+04	2.009E+04	1.975E+04	1.805E+04	1.663E+04	1.545E+04	1.392E+04	1.320E+04	

		Phase (radians)									
FREQ =	41.104	41.699	42.295	42.891	43.486	44.082	44.678	45.273	45.869	46.465	
TAP :											
25	-2.820E-01	-6.444E-01	-2.251E+00	-3.973E+00	-3.040E+00	-2.598E+00	-2.841E+00	-1.817E+00	-1.753E+00	-1.442E+00	
26	-2.235E+00	-1.827E+00	-1.301E+00	-1.480E+00	-2.094E+00	-2.406E+00	-9.243E-01	-8.820E-01	-2.939E+00	-2.765E+00	
27	-2.938E+00	3.080E+00	-2.327E+00	-2.668E+00	-2.642E+00	-2.412E+00	-7.356E-01	1.597E+00	2.323E+00	2.490E+00	
28	-1.996E+00	3.145E-02	-1.122E-01	-8.891E-01	-1.797E+00	2.506E+00	2.466E+00	2.953E+00	-3.130E+00	-3.021E+00	
29	-2.375E+00	-2.892E+00	-2.940E+00	-2.962E+00	-2.372E+00	-2.518E+00	-1.983E+00	-2.030E+00	-2.526E+00	-2.532E+00	
30	-2.761E+00	-2.794E+00	-2.795E+00	-2.778E+00	-2.784E+00	-2.819E+00	-2.852E+00	-2.862E+00	-2.845E+00	-2.835E+00	
31	-2.703E+00	-2.705E+00	-2.722E+00	-2.698E+00	-2.633E+00	-2.605E+00	-2.655E+00	-2.682E+00	-2.722E+00	-2.743E+00	
32	-2.950E+00	-2.838E+00	-2.602E+00	-2.492E+00	-2.481E+00	-2.564E+00	-2.620E+00	-2.622E+00	-2.682E+00	-2.561E+00	
33	-2.445E+00	-2.656E+00	-2.755E+00	-2.709E+00	-2.765E+00	-2.949E+00	-2.919E+00	-2.691E+00	-2.537E+00	-2.556E+00	
CARRIER	-2.335E+00	-2.756E+00	-2.664E+00	-2.654E+00	-2.700E+00	-2.763E+00	-2.810E+00	-2.781E+00	-2.676E+00	-2.615E+00	

Note: Specular-point grazing angle = 7.5°

frequency. Magnitude and phase characteristics are also shown. Careful examination of the magnitude array discloses a marked ridge effect. Comparison of these values with values removed from the ridge illustrates the dramatic signal-to-noise improvement alluded to above. In this regard, it would appear that additive thermal noise does not constitute a serious problem as far as estimation performance is concerned. Neglecting errors attributable to the noise, it can be shown⁹ that the normalized rms error in estimates of P_{HV} ; i.e., fractional error, can be expressed as:

$$\epsilon = \left(\frac{E\{|\hat{P}_{HV} - P_{HV}|^2\}}{|P_{HV}|^2} \right)^{1/2} = \frac{1}{|\rho_{HV}| \sqrt{N}} \quad (5-29)$$

where:

- E = statistical expectation
- N = number of independent samples used in equation (5-28)
- \hat{P}_{HV}, P_{HV} = estimated and true cross-spectrum values at frequency ν
- ρ_{HV} = the corresponding correlation coefficient.

The number of segments N used in the data reduction was 35 or less. Consequently, the fractional error will be

$$\begin{aligned} \epsilon &= \frac{1}{\sqrt{N} |\rho_{HV}(\nu)|} \\ &\approx 0.16 \text{ for } \rho_{HV} \approx 1.0. \end{aligned} \quad (5-30)$$

Percentage variations of this order are apparent in the data tabulated in tables 5-8 and 5-9.

Similarly, the rms error in estimating the cross-spectrum phase component can be expressed as:⁹

$$\begin{aligned} \phi_{\text{rms}} &\approx \frac{1}{\sqrt{2N}} \\ &\approx 0.1 \text{ radian} \\ &\approx 6^\circ. \end{aligned}$$

⁹P. Alexander, "Performance of the H-V Correlation Coefficient Estimator," CNR Internal Memo, November 1975.

Variation in phase estimates of this scale can readily be seen from the delay-Doppler arrays in tables 5-8 and 5-9. The estimate fluctuations become even more extreme away from the main energy ridge, as can be verified from the figures. It is further noted that for in-plane flight direction, the spectra ridges in the delay-Doppler realm correspond to scattered energy arriving from surface elements spaced along the great circle axis joining the subaircraft and subsatellite locations. Hence, the scattering processes associated with these returns are *not* subjected to the phenomenon of depolarization. This fact greatly simplifies the correlation of measurement with theoretical expectation (e.g., the relative amplitude difference between the H and V prober at the transmitter may be ignored).

Geometrical relationships and Fresnel smooth-earth reflection coefficients are employed to predict the theoretical H and V probe phase differences that exist for scattered energy from the great circle surface axis. Each location along this path has a *unique* Doppler shift, which allows the predicted phase angle to be correlated to the measured value via the frequency coordinate of the cross-power spectrum estimate.

Experimental values (ridge) of the cross-power spectra phase measure for two flight tests are itemized in tables 5-10 and 5-11. Both data ensembles pertain to the in-plane geometry flight vector direction and, as indicated in the tabulation, present phase angle versus the delay-Doppler receiver coordinate. Corresponding to the 10° and 7.5° specular-point grazing angles of these tests, we present theoretical relative phase angle estimates versus Doppler frequency shift in figure 5-48. The plotted phase, ϕ_e , is derived from

$$\phi_e = \angle R_H - \angle R_V \quad (5-31)$$

where R_H and R_V are the classical Fresnel sea water reflection coefficients for horizontal and vertical polarization, respectively.

Combining the data from tables 5-10 and 5-11 and figure 5-48 provides a means for comparing experiment with theory. These relationships are given in figures 5-49 and 5-50 for the 10° and 7.5° grazing angle cases, respectively. To account for phase biases associated with the ATS-6 satellite antenna and the initial condition of the prober as the biases leave the transmitter, the ϕ_e estimates have been shifted by a constant value. For the 10° and 7.5° grazing angle conditions, this adjustment factor amounts to 0.3 and 0.18 radian, respectively. For both data sets we observe a high degree of correspondence between experiment and theory; areas where departures are in evidence can be related to airplane and ATS-6 antenna polarization vector nonuniformities over the surface "glistening zone."

TABLE 5-10. PHASE ANGLE OF CROSS-SPECTRUM VERSUS DELAY-DOPPLER COORDINATE, IN-PLANE FLIGHT, MARCH 31, 1975

Note: Specular-point grazing angle = 10°

Frequency, Hz	Tap number (0.2- μ sec steps)	Relative magnitude	Phase, rad
+ 13.7	34	1.04	-1.84
+ 13.1	32	1.47	-1.97
+ 12.5	32	1.47	-1.92
+ 11.3	31	1.62	-2.05
+ 10.1	30	2.19	-1.99
+ 9.5	29	2.16	-2.00
+ 8.3	29	2.48	-2.00
+ 7.1	28	2.98	-2.13
+ 5.9	28	2.88	-2.13
+ 4.2	27	4.38	-2.27
+ 2.4	27	3.16	-2.26
+ 0	27	3.44	-2.20
- 5	27	2.65	-2.21
- 10	27	3.57	-2.32
- 15	27	4.59	-2.41
- 20	28	3.66	-2.46
- 25	28	3.10	-2.48
- 30	29	3.65	-2.48
- 35	30	2.59	-2.49
- 40	30	2.03	-2.60
- 45	31	2.44	-2.57
- 50	32	2.62	-2.59
- 55	32	1.78	-2.63
- 60	33	1.48	-2.65
- 65	34	2.08	-2.69
- 70	34	1.35	-2.80

TABLE 5-11. PHASE ANGLE OF CROSS-SPECTRUM VERSUS DELAY-DOPPLER COORDINATE,
IN-PLANE FLIGHT, APRIL 2, 1975

Note: Specular-point grazing angle = 7.5°

Frequency, Hz	Tap number (0.2- μ sec steps)	Relative magnitude	Phase, rad
+ 10.1	33	0.818	- 1.61
+ 9.5	31	1.09	- 1.56
+ 8.3	30	2.12	- 1.58
+ 7.1	28	3.18	- 1.68
+ 5.9	27	3.14	- 1.77
+ 4.2	26	4.54	- 1.85
+ 2.4	26	5.87	- 1.78
+ 0	26	2.59	- 1.89
- 2.4	25	2.62	- 2.06
- 4.2	25	2.40	- 2.13
- 6.5	25	1.56	- 2.06
- 10.1	26	2.66	- 2.15
- 12.5	26	3.02	- 2.30
- 15.4	26	1.80	- 2.33
- 20.0	27	1.96	- 2.47
- 25.0	28	1.02	- 2.42
- 30.0	28	1.19	- 2.59
- 35.0	29	1.00	- 2.72
- 40.0	30	0.847	- 2.72
- 45.0	30	0.659	- 2.86
- 50.0	31	0.865	- 2.85
- 55.0	32	0.55	- 2.78
- 60.0	32	0.418	- 2.78
- 70.0	33	0.106	- 2.65

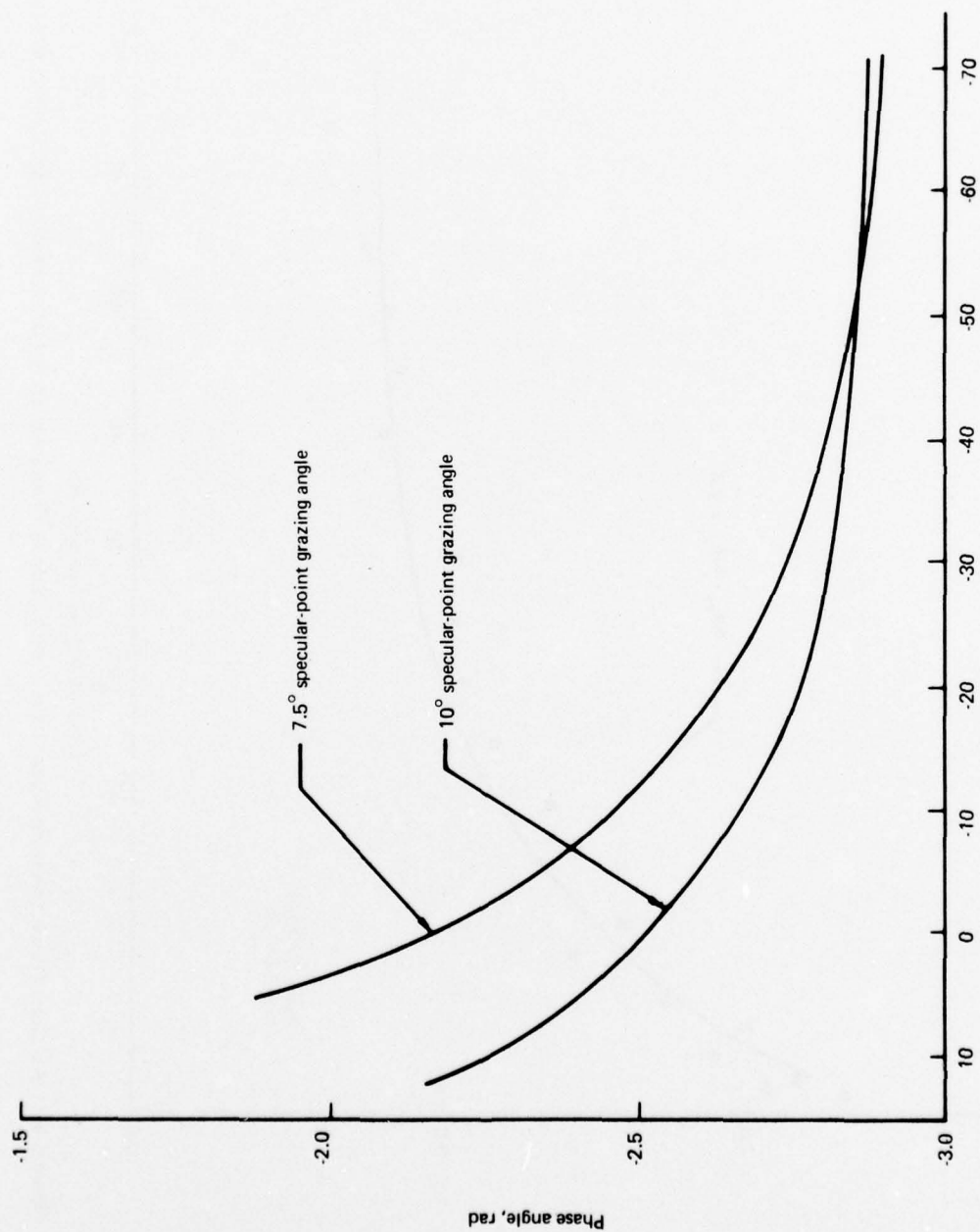


Figure 5-48. Theoretical Phase Angle Versus Doppler Shift

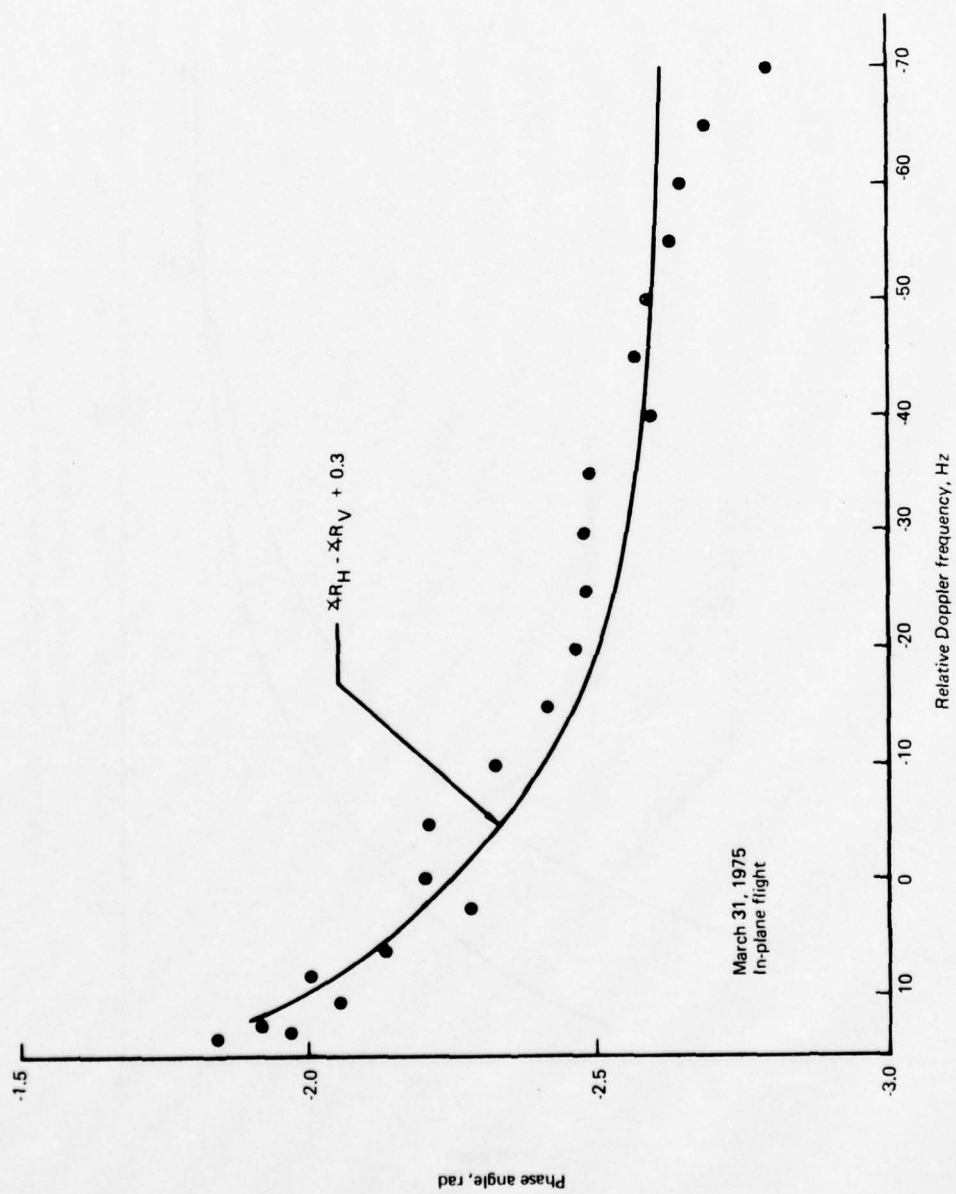


Figure 5-49. H-V Cross Power Spectrum Phase Angle Versus Doppler Frequency Shift (10° Specular-Point Grazing Angle)

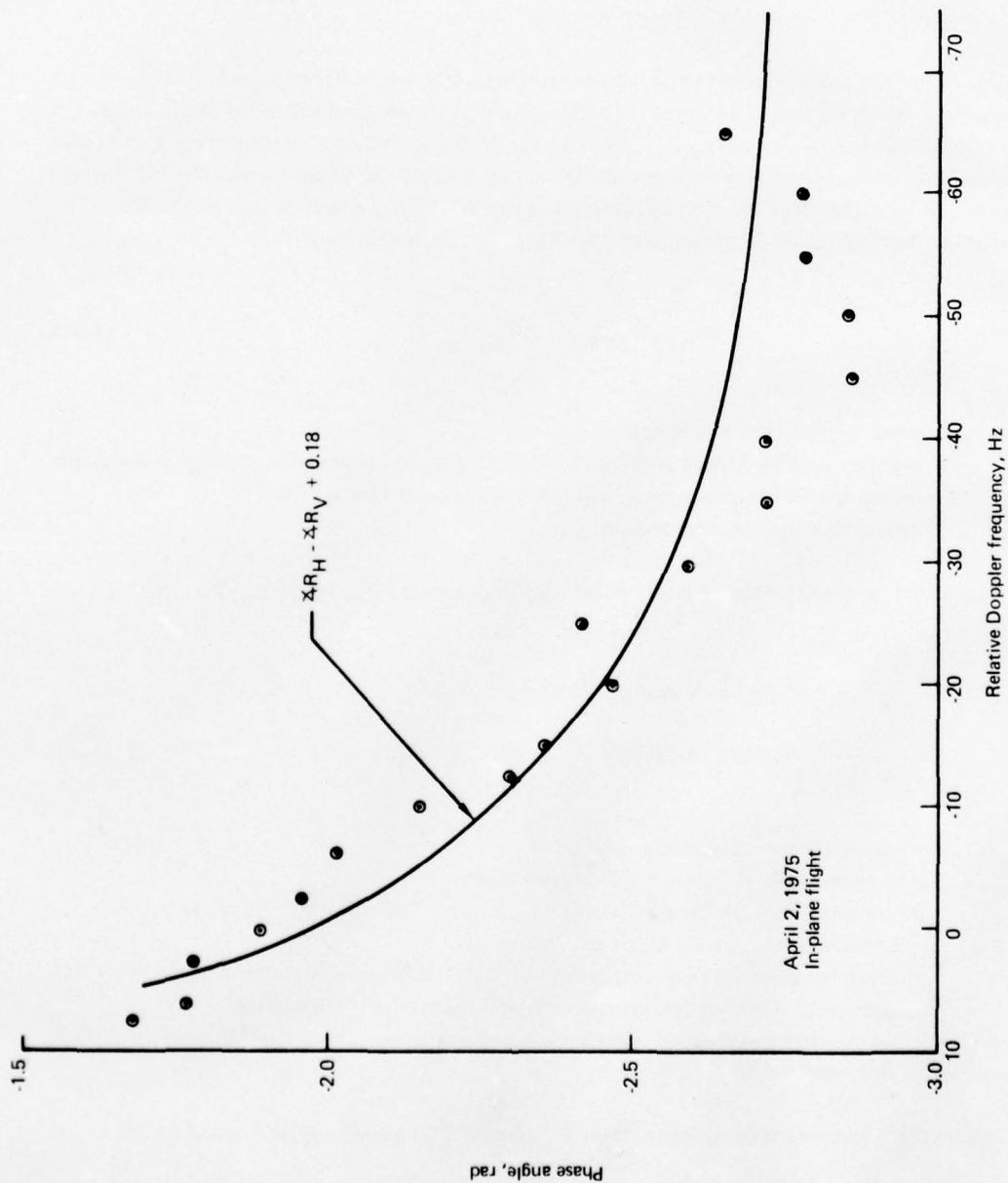


Figure 5-50. H-V Cross Power Spectrum Phase Angle Versus Doppler Frequency Shift (7.5° Specular-Point Grazing Angle)

5.6 PROBER ANTENNA SPATIAL FILTERING CONSIDERATIONS

5.6.1 Mathematical Basis for Antenna Pattern Removal

To remove the prober aircraft antenna pattern effects from the channel measurements, it is first necessary to make some assumptions with regard to the mechanism by which the electromagnetic waves are scattered from the sea surface. In line with the most widely accepted theoretical treatments and the good agreement between experiment and theory as presented in section 6, we base our analysis upon the vector formulation of the physical optics very-rough-surface scatter model. Under this assumption the received power from an increment of surface area is expressed as

$$dP_{rcvd} \propto (T_{cf} \cdot T_{cf}^*) \sigma_{xs}, \quad (5-32)$$

where:

- dP_{rcvd} = power received per incremental area
- T_{cf} = complex coefficient that accounts for coupling losses between the incident polarization vector, the tilted surface facet, and the receiver polarization vector
- σ_{xs} = surface area scatter cross section.

The aircraft antenna influence is embodied only in parameter T_{cf} , which may be represented as:

$$T_{cf} \propto R_{||}(a) \left[(A \cos \delta_i + B \sin \delta_i) (C \cos \delta_s + D \sin \delta_s) \right] \\ - R_{\perp}(a) \left[(B \cos \delta_i - A \sin \delta_i) (-D \cos \delta_s + C \sin \delta_s) \right], \quad (5-33)$$

where:

- $R_{||}(a)$ = parallel Fresnel reflection coefficient
- $R_{\perp}(a)$ = perpendicular Fresnel reflection coefficient
- a = angle between the incident wave and the normal to a properly tilted (to produce reflection into receiver) surface facet
- δ_i = angle between the theta component of the incident wave and the incident "parallel" unit vector (i.e., vertical polarization with respect to tilted surface)
- A, B, C, D = transmitter and receiver complex antenna polarization vector coefficients as described below.

Polarization vectors for the transmit (\bar{P}_T) and receive (\bar{P}_R) antenna system are given by:

$$\bar{P}_T = A \hat{i}_{TT} + B \hat{i}_{PT}, \quad (5-34)$$

$$\bar{P}_R = C \hat{i}_{TR} + D \hat{i}_{PR} \quad (5-35)$$

where:

$\hat{i}_{TT}, \hat{i}_{PT}$ = unit vectors in the theta and phi directions, respectively, with respect to coordinates centered on transmitter
 $\hat{i}_{TR}, \hat{i}_{PR}$ = unit vectors in the theta and phi directions, respectively, with respect to coordinates centered on receiver.

In our case transmissions originate from the KC-135 and are received at the ATS-6 satellite. The satellite antenna is assumed to be right-hand circular (RHC) with 0-dB ellipticity; thus:

$$C = \sqrt{G_s}/2$$

$$D = j\sqrt{G_s}/2, \quad (5-36)$$

where G_s is the gain magnitude of satellite antenna.

Parameters A and B for the aircraft antenna pattern are derived from scale-model antenna range measurements. The antenna-effects-removal algorithm is applied to the specific case where the probe is operating in the simultaneous horizontal/vertical polarization mode. These probe polarization descriptions are nominal because for aircraft antenna systems one usually expects the presence of cross-polarization terms. Thus for the nominal horizontal polarization probe, B represents the principal polarization term and A is a measure of the cross-polarization term (vice versa for nominal vertical polarization). From the antenna range radiation distribution plots it is observed that, for the various probe antenna pointing directions, the ratio of principal-to-cross polarization terms is typically on the order of 20 dB over the effective "glistening" area of the surface. Hence, to good approximation we consider only the principal terms of the polarization vectors and write T_{cf} for the horizontally polarized probe as:

$$T_{cf} = \sqrt{\frac{G_H G_S}{2}} \left[R_{||}(a) \sin \delta_i (\cos \delta_s + j \sin \delta_s) - R_{\perp}(a) \cos \delta_i (\sin \delta_s - j \cos \delta_s) \right], \quad (5-37)$$

and, for the vertical polarized probe:

$$T_{cf} = \frac{G_V G_S}{2} \left[R_{||}(a) \cos \delta_i (\cos \delta_s + j \sin \delta_s) + R_{\perp}(a) \sin \delta_i (\sin \delta_s - j \cos \delta_s) \right], \quad (5-38)$$

where:

G_H = gain of horizontally polarized probe

G_V = gain of vertically polarized probe .

Parameters G_H and G_V do not have constant gain over the scattering surface. To remove this spatial filtering effect, we operate in the delay-Doppler coordinate system of the receiver. The scatter function, $S(\tau, \omega)$, is related to dP_{rcvd} through the following formulation (ref 5-1).

$$S(\tau, \omega) = J_1(\tau, \omega) dP_{\text{rcvd},1} + J_2(\tau, \omega) dP_{\text{rcvd},2} , \quad (5-39)$$

where $J(\tau, \omega)$ is the Jacobian of the transformation from surface coordinates to (τ, ω) receiver coordinates.

In the above equation, subscripts 1 and 2 denote the fact that the scattering operation is a 2-into-1 mapping process (that is, two surface points are mapped into one delay-Doppler location). In general, even for isotropic antennas, $dP_{\text{rcvd},1}$ does not equal $dP_{\text{rcvd},2}$; thus without making some assumptions with regard to the σ_{XS} distribution, it becomes impossible to properly adjust $S(\tau, \omega)$ for the antenna filtering effects. To circumvent this ambiguity, we restrict our attention entirely to the data gathered during the in-plane legs of the test scenario. The symmetry properties of the delay contours, Doppler contours, and dP_{rcvd} function¹⁰ are thereby exploited and we may write $S(\tau, \omega)$ as:

$$S(\tau, \omega) = J_1(\tau, \omega) dP'_{\text{rcvd},1} (G_1 + G_2) , \quad (5-40)$$

where:

$dP'_{\text{rcvd},1} = dP'_{\text{rcvd},2}$ = the received energy from incremental areas 1 or 2, given that the antenna illumination is isotropic.

¹⁰Examination of the first equation (5-32) in this section reveals that for in-plane flight, dP_{rcvd} will be cross-plane symmetrical (apart from antenna asymmetry affects) if (1) the sea-surface slope distribution is isotropic, a valid assumption per data from Cox and Munk (ref 5-12), and (2) the polarization planes of the transmit and receive antennas are linear and lie either in or perpendicular to the plane containing the KC-135, specular point, and ATS-6 satellite. The latter restriction is necessary to assure that $T_{\text{cf},1} = T_{\text{cf},2}$. In our case this condition is *not* met since the satellite antenna polarization is circular. However, it can be shown that for grazing angles greater than a few degrees, the induced error is relatively small when compared with other factors such as the antenna gain characterization.

Now under the same geometry and surface assumption we may express $S(\tau, \omega)$ for the isotropic antenna gain case as:

$$\begin{aligned} S_I(\tau, \omega) &= J_1(\tau, \omega) dP'_{\text{rcvd},1} + J_2(\tau, \omega) dP'_{\text{rcvd},2} \\ &= 2J_1(\tau, \omega) dP'_{\text{rcvd},1} \end{aligned} \quad (5-41)$$

Thus for in-plane flight the scatter function, $S_I(\tau, \omega)$, corresponding to an ideal isotropic antenna is related to the version of $S(\tau, \omega)$ corresponding to the experimental nonisotropic antenna by the simple expression

$$S_I(\tau, \omega) = \frac{S(\tau, \omega)}{G(\tau, \omega)}, \quad (5-42)$$

where $G(\tau, \omega)$ is equal to $(G_1 + G_2)/2$.

In the steepest descent integration analysis of forward scatter multipath (mathematically appropriate under the constraint that the grazing angle is much greater than the surface rms slope), one usually assumes that the antenna coverage is adequately described by its specular-point gain. For this reason we have chosen to relate our antenna-corrected version of the scatter function to the gain directed toward the specular point; i.e.,

$$\begin{aligned} S_{AC}(\tau, \omega) &= S_I(\tau, \omega) G(0,0) \\ &= \frac{S(\tau, \omega)}{G(\tau, \omega)} G(0,0), \end{aligned} \quad (5-43)$$

where:

$S_{AC}(\tau, \omega)$ = scatter function corrected for isotropicity imperfections of the forward multipath antenna, with gain referenced to $G(0,0)$

$G(0,0)$ = specular-point antenna gain (i.e., $\tau = \omega = 0$).

In addition we also calculate a difference function, $\Delta S(\tau, \omega)$, between the corrected and uncorrected versions of the scattering function; i.e.,

$$\Delta S(\tau, \omega) = S(\tau, \omega) - S_{AC}(\tau, \omega). \quad (5-44)$$

This function is available as a three-dimensional plot and provides a compact description of the prober's spatial filtering characteristics as translated to the delay-Doppler coordinates of the receiver.

5.6.2 Spatial Filtering Effects on Experimental Data

Design goals for the front multipath probe antenna were established to provide a nearly uniform illumination over the surface area responsible for most of the returned multipath energy. Only if this goal is adequately met will $S(\tau, \omega)$ be a satisfactory approximation to the channel's relative delay-Doppler energy distribution. The antenna was designed to achieve 1-dB beamwidths of 20° in azimuth and 50° in elevation,¹¹ while meeting other design requirements pertaining to beam steerability, polarization nodes, gain, etc. Scale-model antenna range data indicated that these beamwidths were closely approximated by the antenna as installed on the aircraft.¹²

5.6.2.1 Effect of Antenna Spatial Filtering on RMS Scatter Coefficients – The rms scatter coefficients previously reported in section 5.2.6 (fig. 5-17) utilized the uncorrected version of $S(\tau, \omega)$. The gain of the multipath antenna was taken to be the gain toward the specular point, $G(0,0)$. This factor was embodied in the factor A_D/A_I of the G_D/G_I term of equation (5-2). To assess the magnitude of error introduced in the calculated rms scatter coefficients, a quantity ΔE was determined for a range of grazing angles. The quantity ΔE is defined as:

$$\Delta E = 10 \log \left[\frac{\iint S_{AC}(\tau, \omega) d\tau d\omega}{\iint S(\tau, \omega) d\tau d\omega} \right]$$

The value of ΔE can be either positive or negative because the peak of the multipath antenna beam was (by intention) usually not pointed exactly toward the specular point in elevation. Hence, the specular-point gain, $G(0,0)$, does not necessarily equal the peak gain of the antenna. Typically, ΔE was found to be approximately equal to -0.2 dB for the higher elevation angles and $+0.3$ dB at the lower elevation angles. From equations (5-1) and (5-43) it can be readily seen that ΔE corresponds directly to the error in the rms scatter coefficient magnitude, $|I|$, of figure 5-17. Error magnitudes are therefore estimated as typically less than 0.3 dB at the grazing angle extremes (5° and 30°).

¹¹This antenna beamwidth design goal was originally based, in part, on DeRosa's (ref 5-5, table 2-1; and ref 5-13) estimates of multipath power loss. Extrapolating from these calculations, the multipath power loss for the stated beamwidths relative to a uniform gain antenna was predicted to be substantially less than 1.0 dB for the range of grazing angles (and sea states) of interest.

¹²Antenna design details are described in "U.S. Aeronautical L-band Satellite Technology Test Program – Terminal Design," material submitted under contract DOT-TSC-707, August 1975. Scale-model antenna range radiation distribution plots have been submitted in the form of punched paper tapes.

5.6.2.2 *Effect of Antenna Spatial Filtering on Spread Values* — At the higher grazing angles, spread values calculated using the uncorrected $S(\tau, \omega)$ function typically differed by less than 8% from those calculated using $S_{AC}(\tau, \omega)$. One may therefore consider $S(\tau, \omega)$ to be a reasonable approximation to the channel's relative delay-Doppler energy distribution at the higher elevation angles. At the lower grazing angles, the effect of the multipath antenna nonisotropy on certain spread values is more pronounced; e.g., for a grazing angle of 7° , the 10-dB Doppler spread using $S(\tau, \omega)$ is roughly 30% in error, as compared with the value calculated when using $S_{AC}(\tau, \omega)$.

In the following discussion the probe antenna's spatial filtering effects for a typical high-angle (February 27, 1975) and low-angle (April 2, 1975) set of experimental results are illustrated. For both cases, the antenna was operating in its horizontal polarization mode.

Prior to presenting the detailed results, we summarize the spatial filtering effects in table 5-12, which represents the antenna influence upon the spread measures of the delay spectra, Doppler spectra, coherence bandwidth, and decorrelation time. Spread measure definitions identical to those used in section 5.3 are used, and attention is directed to the last column of table 5-12, where the relative difference between antenna-corrected and noncorrected results are delineated. As indicated, antenna influence upon the high-angle data is rather modest, with a maximum perturbation of about 8% being calculated. For the low-angle data we also observe fairly small error perturbations (typically less than 10%) except for the 10-dB Doppler spread and decorrelation time, which are on the order of 30%. It is of interest to note that contrary to what one might expect, the 10-dB spread values for the delay and Doppler parameters are actually *increased* by the antenna pattern spatial filtering effects. This results from the fact that the multipath probing antenna was always pointed so that its beam peak location occurred on the subaircraft side of the specular point (i.e., for the 7° grazing angle test, the beam peak was directed at a -25° elevation angle). This provides optimum glistering region coverage and introduces a positive bias in the midtail region of the Doppler and delay distribution. These effects are visually evident in the detailed data presentation that follows. One other interesting observation relates to the dependence between the 10-dB Doppler spread and the 3-dB decorrelation time, and similarly between the 10-dB delay spread and the coherence bandwidth. That is, we note that the respective error percentages are roughly equal in magnitude and opposite in sign (an expected result based on Fourier transform characteristics).

Detailed results pertaining to the high-angle antenna spatial filtering characteristics are provided in figures 5-51 through 5-56. The data in these figures pertain to:

- Front multipath antenna pattern: figure 5-51
- $G_H(\tau, \omega)$: figure 5-52
- $S(\tau, \omega)$ and $S_{AC}(\tau, \omega)$: figure 5-53
- $\Delta S(\tau, \omega)$: figure 5-54
- Corrected and uncorrected delay and Doppler spectra: figure 5-55
- Corrected and uncorrected autocorrelation functions: figure 5-56.

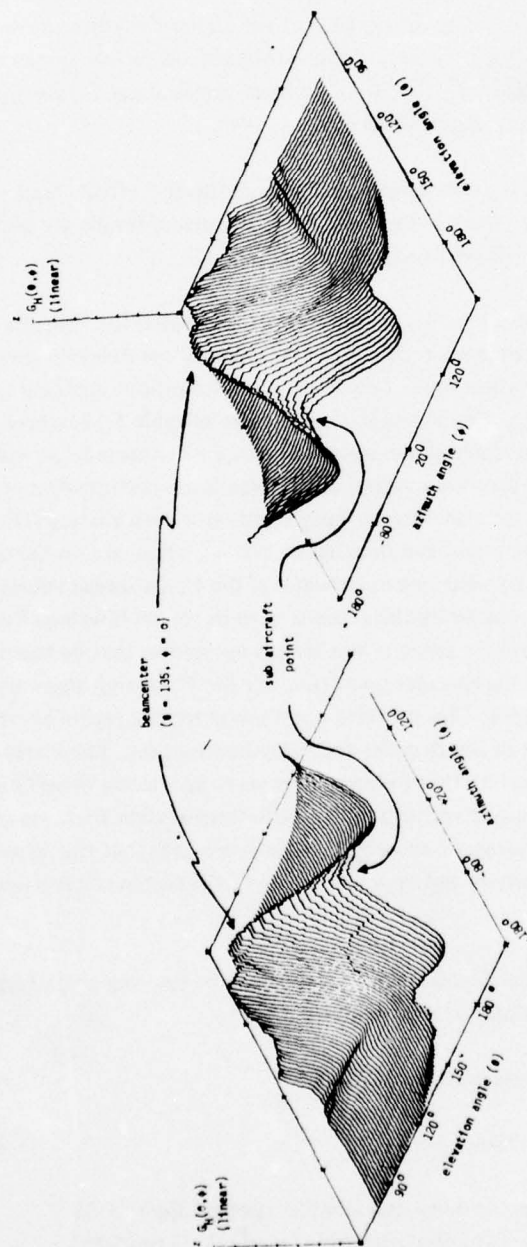
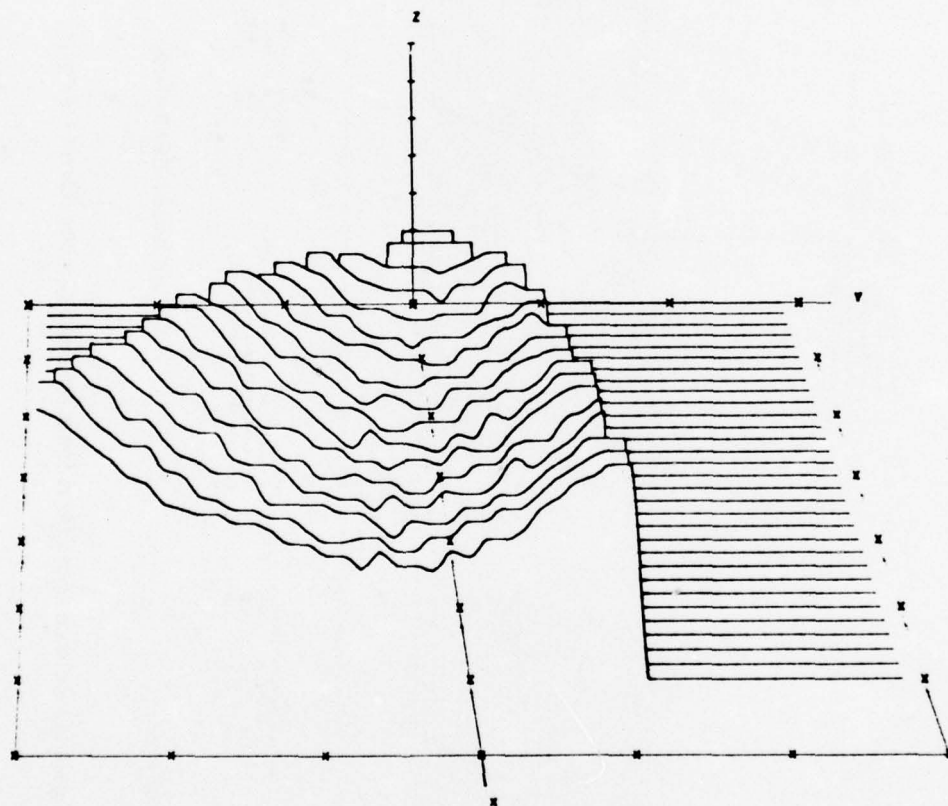


Figure 5-51. Front Multipath Antenna Gain Pattern (Horizontal Polarization, Pointed at $\theta = 135^\circ$, $\phi = 0^\circ$)

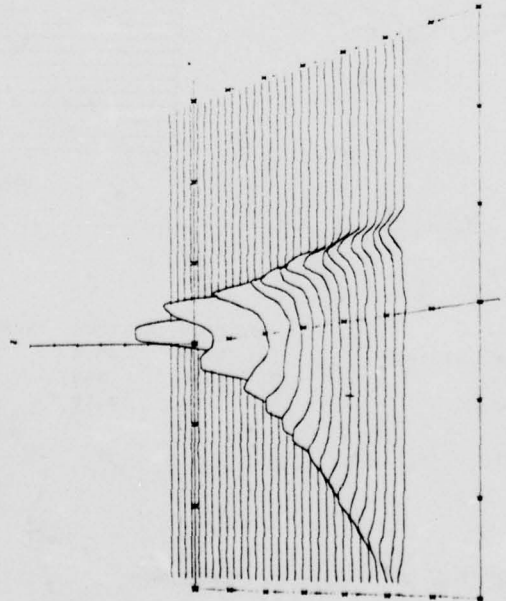
DELAY-DOPPLER SCATTER FUNCTION
 DATE 2/27/75 HORIZONTAL POLARIZATION
 TAP RESOLUTION .2 MICROSEC
 TIME INTERVAL 10/13/ .493 TO 10/13/ 7.190
 ANTENNA GAIN



AXIS		MINIMUM	MAXIMUM	INCREMENT
X	DELAY TAP (.2 MICROSEC. WIDTH)	20.0	55.0	5.0
Y	DOPPLER FREQUENCY (HERTZ)	-300	300	100
Z	DELAY-DOPPLER PSD (LINEAR) $G_H(\tau, \omega)$.00	3.50	.50

Figure 5-52. High Angle $G_H(\tau, \omega)$ Distribution

DELAY-DOPPLER SCATTER FUNCTION
 DATE 2/27/76 HORIZONTAL POLARIZATION
 TAP RESOLUTION 2 MICROSEC
 TIME INTERVAL 10/13/ 483 TO 10/13/ 7 180
 NOISE REMOVED

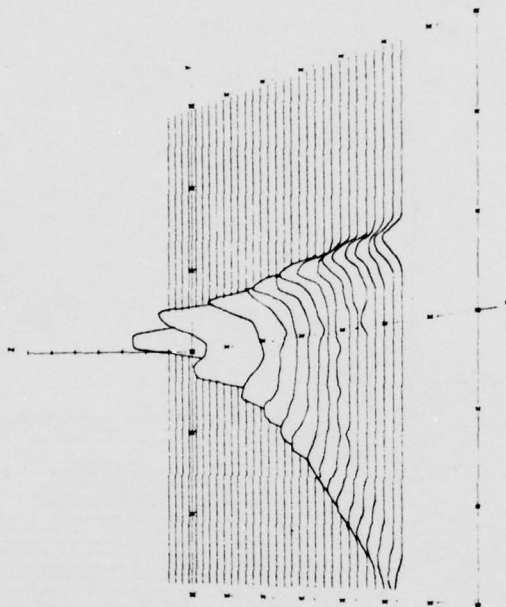


AXES
 X DELAY TAP 1 2 MICROSEC WIDTH 1
 Y DOPPLER FREQUENCY HERTZ 1
 Z DELAY-DOPPLER PSD (LINEAR)

MINIMUM MAXIMUM INCREMENT
 20.0 50.0 5.0
 300 300 100
 .50 3.00 50

(a) No Antenna Correction

DELAY-DOPPLER SCATTER FUNCTION
 DATE 2/27/76 HORIZONTAL POLARIZATION
 TAP RESOLUTION 2 MICROSEC
 TIME INTERVAL 10/13/ 483 TO 10/13/ 7 180
 ANTENNA GAIN CORRECTED



AXES
 X DELAY TAP 1 2 MICROSEC WIDTH 1
 Y DOPPLER FREQUENCY HERTZ 1
 Z DELAY-DOPPLER PSD (LINEAR)

MINIMUM MAXIMUM INCREMENT
 20.0 50.0 5.0
 -300 300 180
 .50 3.00 50

(b) Antenna Gain Corrected

Figure 5-53. High-Angle Antenna Gain Effects Upon the Delay-Doppler Scatter Function

DELAY-DOPPLER SCATTER FUNCTION
 DATE 2/27/75 HORIZONTAL POLARIZATION
 TAP RESOLUTION .2 MICROSEC
 TIME INTERVAL 10/13/ 493 TO 10/13/ 7.190

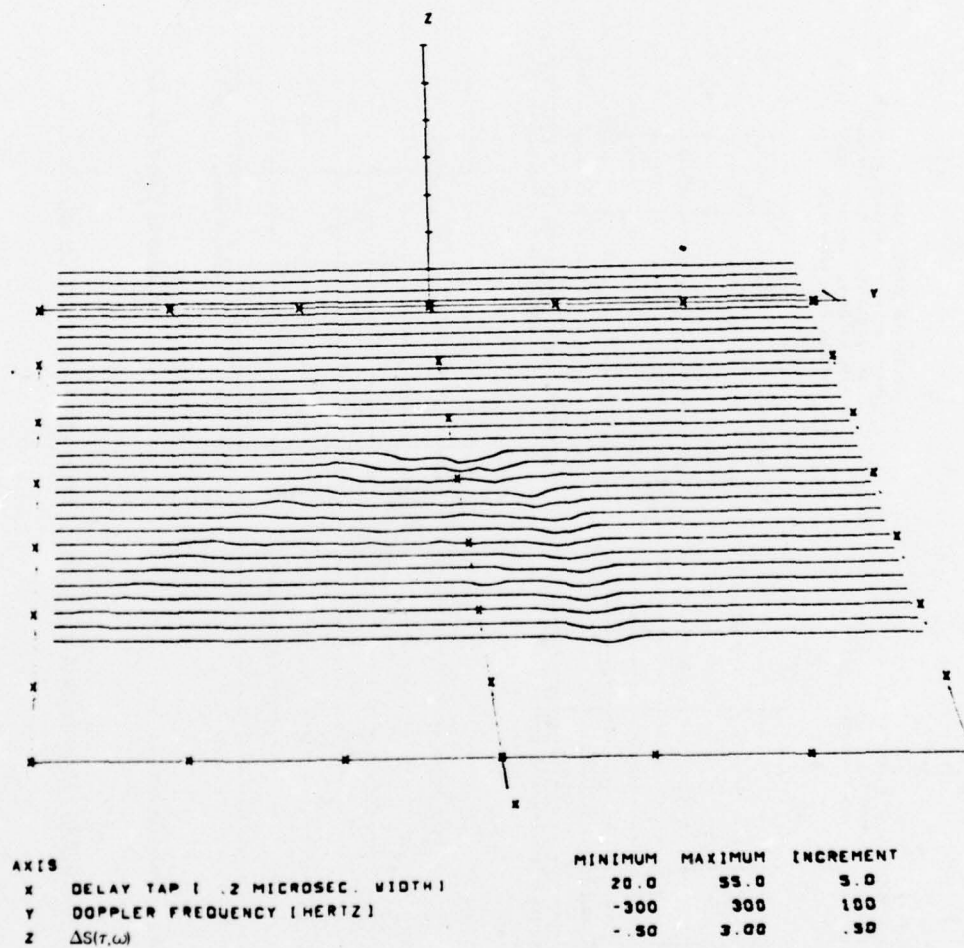
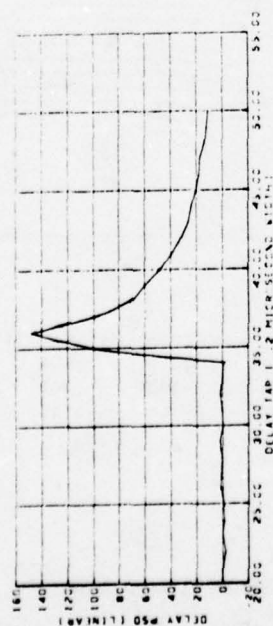
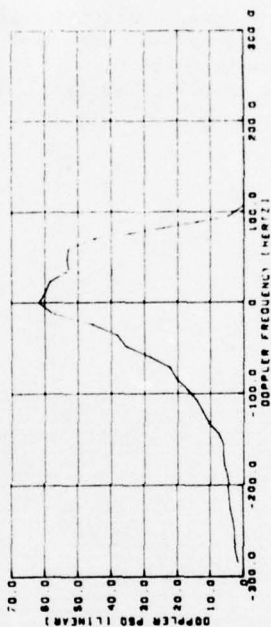
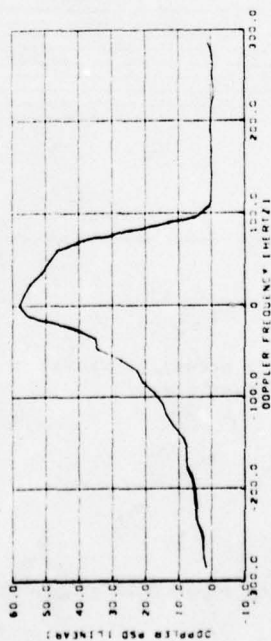
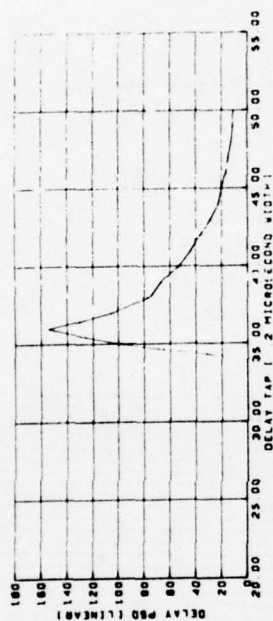


Figure 5-54. High-Angle $\Delta S(\tau, \omega)$ Perturbations

DELAY AND DOPPLER SPECTRA
 DATE 2/27/75 HORIZONTAL POLARIZATION
 TAP RESOLUTION 2 MICROSEC
 TIME INTERVAL 10/13/ 481 TO 10/13/ 7 190
 NOISE REMOVED



DELAY AND DOPPLER SPECTRA
 DATE 2/27/75 HORIZONTAL POLARIZATION
 TAP RESOLUTION 2 MICROSEC
 TIME INTERVAL 10/13/ 481 TO 10/13/ 7 180
 ANTENNA GAIN CORRECTED

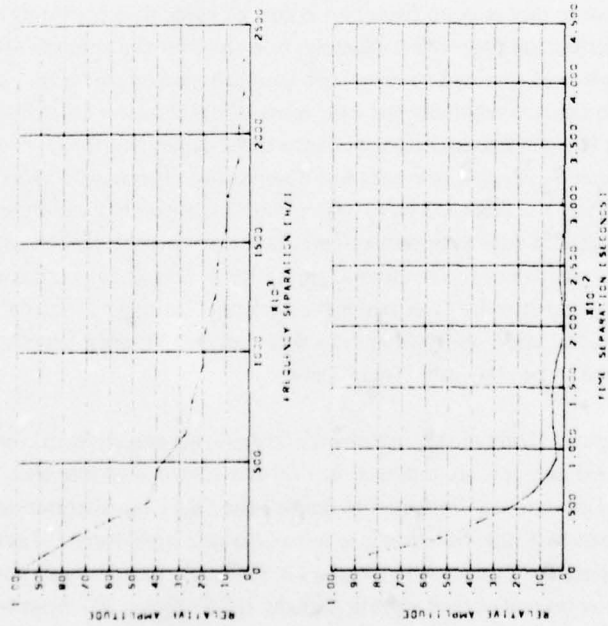


(a) No Antenna Correction

(b) Antenna Gain Corrected

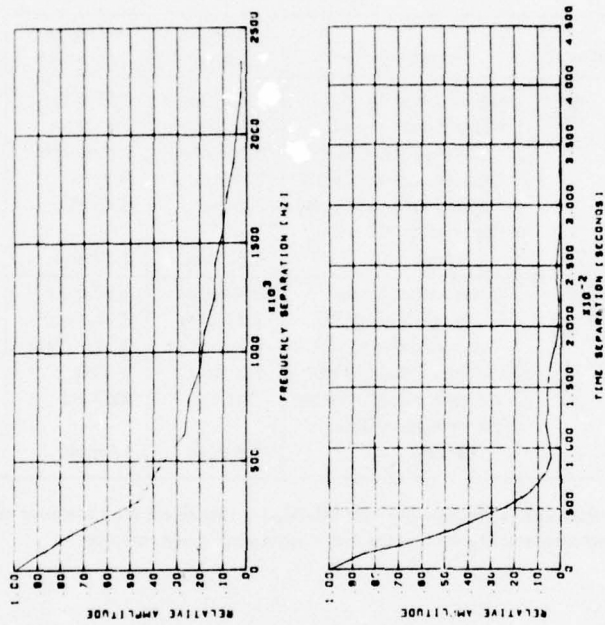
Figure 5-55. High-Angle Antenna Gain Effects Upon Delay and Doppler Spectra

AUTOCORRELATION FUNCTIONS
 DATE 2/27/75 HORIZONTAL POLARIZATION
 TAP RESOLUTION .2 MICROSEC
 TIME INTERVAL 10/13/ 403 TO 10/13/ 7 190
 NOISE REMOVED



(a) No Antenna Correction

AUTOCORRELATION FUNCTIONS
 DATE 2/27/75 HORIZONTAL POLARIZATION
 TAP RESOLUTION .2 MICROSEC
 TIME INTERVAL 10/13/ 403 TO 10/13/ 7 190
 ANTENNA GAIN CORRECTED



(b) Antenna Gain Corrected

Figure 5-56. High-Angle Antenna Gain Effects Upon Frequency and Time Autocorrelation Functions

TABLE 5-12. INFLUENCE OF ANTENNA SPATIAL FILTERING
ON SPREAD PARAMETER MEASURES

Test condition	Spread measure	Antenna included	Antenna corrected	Error percentage ^a
High grazing angle (February 27, 1975, grazing angle = 30°)	Delay spread (3 dB)	0.60 μ sec	0.61 μ sec	-2
	Delay spread (10 dB)	2.67 μ sec	2.5 μ sec	7
	Coherence BW (3 dB)	0.265 MHz	0.286 MHz	-7
	Doppler spread (3 dB)	134 Hz	135 Hz	-1
	Doppler spread (10 dB)	289 Hz	268 Hz	8
	Decorrelation time (3 dB)	2.8 msec	3.1 msec	-7
Low grazing angle (April 2, 1975, grazing angle = 7°)	Delay spread (3 dB)	0.63 μ sec	0.56 μ sec	11
	Delay spread (10 dB)	2.28 μ sec	2.22 μ sec	3
	Coherence BW (3 dB)	0.259 MHz	0.270 MHz	-4
	Doppler spread (3 dB)	8.8 Hz	8.1 Hz	+9
	Doppler spread (10 dB)	55.1 Hz	42.7 Hz	29
	Decorrelation time (3 dB)	9.8 msec	14 msec	-30

^aThe error percentage is the quantity $100 (M_I/M_R) - 100$ where M_I = measure with antenna influence included and M_R = measure with antenna influence removed.

The antenna pattern plot is given from two points of view, thus providing a clear indication of the salient radiation distribution properties. Namely, one observes the antenna's relatively broad beamwidth in the elevation plane as opposed to its narrow azimuth plane beamwidth. These characteristics yield a $G_H(\tau, \omega)$ function that is relatively flat over most of the effective scatter region (i.e., the scatterers located along the $\phi = 0$ axis are mapped into the shoulders of the $G(\tau, \omega)$ distribution). In comparing the $S(\tau, \omega)$ and $S_{AC}(\tau, \omega)$, one does not observe any pronounced visual dissimilarity; this observation is confirmed by the $\Delta S(\tau, \omega)$ plot, which for comparison has the same x,y,z scale factors as the $S(\tau, \omega)$ plots. In accord with previous statements concerning the proper antenna pointing angle, we note that $\Delta S(\tau, \omega)$ is positive in the negative Doppler realm (i.e., subaircraft direct from specular point) and negative in the positive Doppler realm (i.e., subsatellite side of specular point). The effects of the small $\Delta S(\tau, \omega)$ perturbation on the channel's delay spectra, Doppler spectra, and autocorrelation functions are in turn seen to be relatively insignificant.

The spatial filtering effects of the antenna for low-grazing-angle conditions are given in figures 5-57 through 5-62. These data sets are arranged in a format identical to that used for the high-angle case. Again, two points of view are illustrated to display the $G_H(\tau, \omega)$ distribution as given in figure 5-57. Like its high-angle counterpart, this function is seen to possess a high degree of symmetry in the ϕ coordinate. However, note that, on a relative basis, the low-angle pattern has a somewhat larger variation in the gain distribution as measured over elevation angles subtending $\pm 20^\circ$ from boresight (along the $\phi = 0$ axis). This variation, coupled with the 7° specular-point grazing angle geometry, produces a

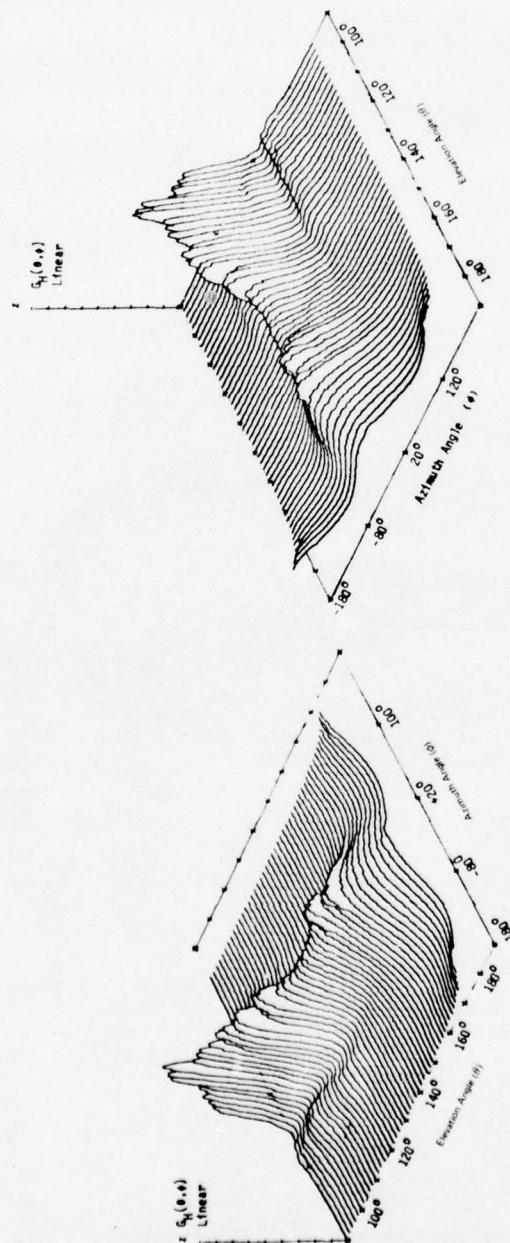


Figure 5-57. Front Multipath Antenna Gain Pattern (Horizontal Polarization, Pointed at $\theta = 110^\circ$, $\phi = 0^\circ$)

DELAY-DOPPLER SCATTER FUNCTION
 DATE 4/2/75 HORIZONTAL POLARIZATION
 TAP RESOLUTION .2 MICROSEC
 TIME INTERVAL 11/ 8/ .482 TO 11/ 8/ 7.190
 ANTENNA GAIN

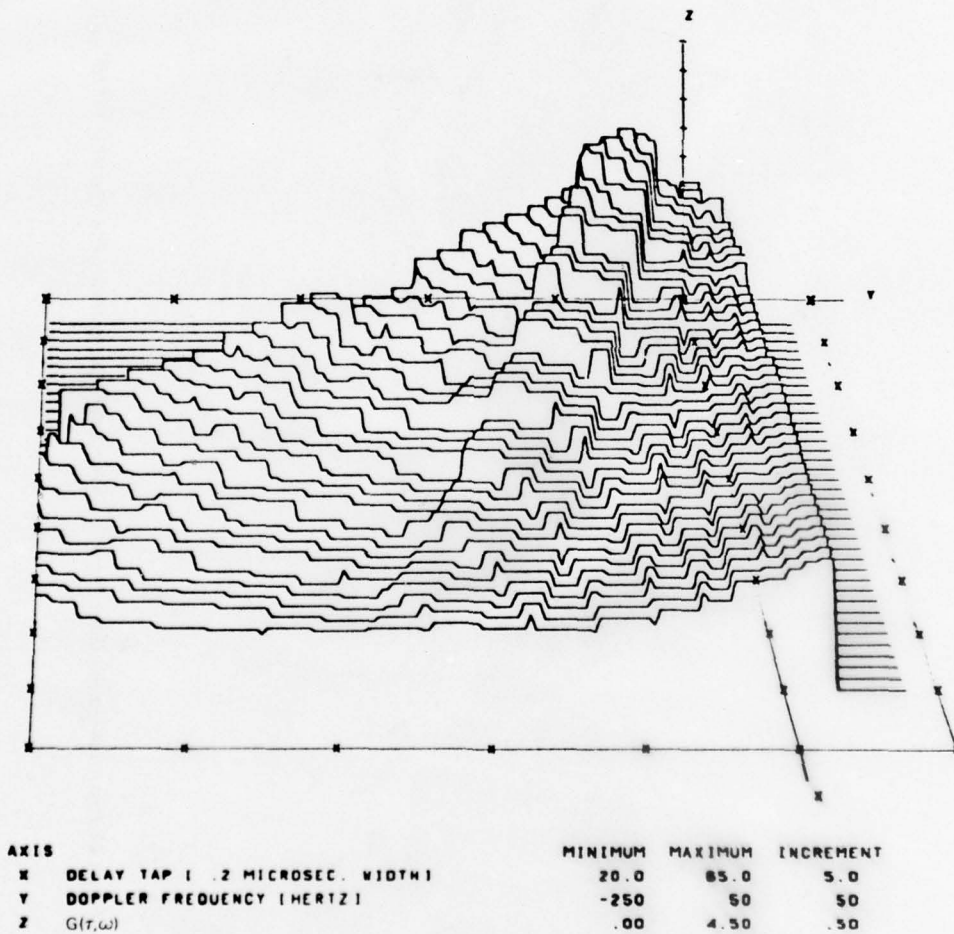
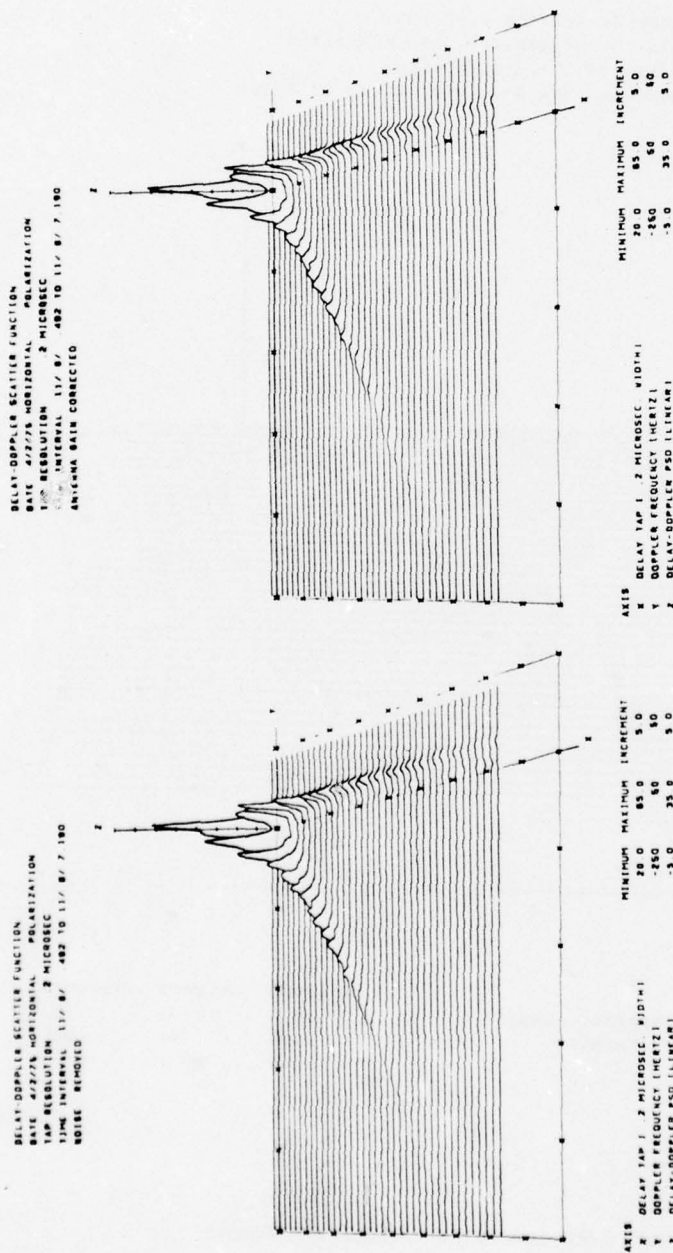


Figure 5-58. Low-Angle $G_H(\tau, \omega)$ Distribution



(a) No Antenna Correction

(b) Antenna Gain Corrected

Figure 5-59. Low-Angle Antenna Gain Effects Upon the Delay-Doppler Scatter Function

DELAY-DOPPLER SCATTER FUNCTION
 DATE 4/2/75 HORIZONTAL POLARIZATION
 TAP RESOLUTION .2 MICROSEC
 TIME INTERVAL 11/ 8/ .492 TO 11/ 8/ 7.180

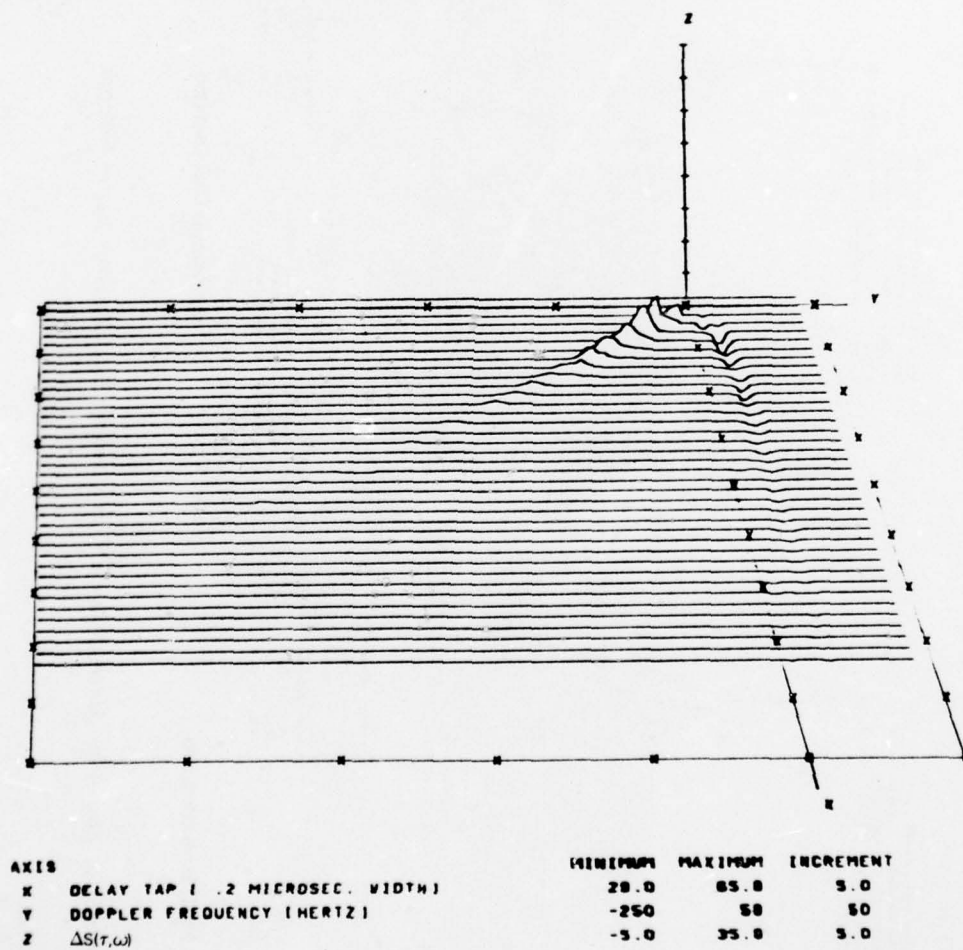
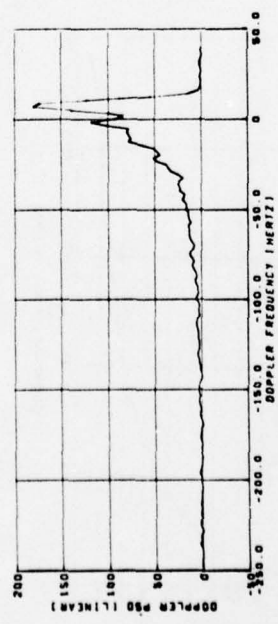
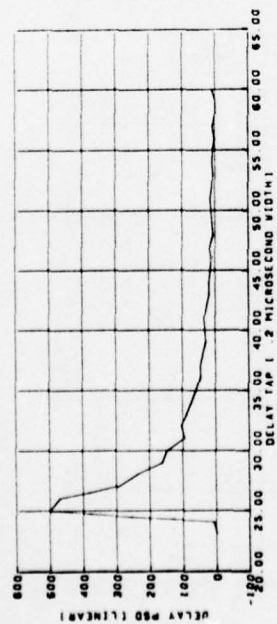


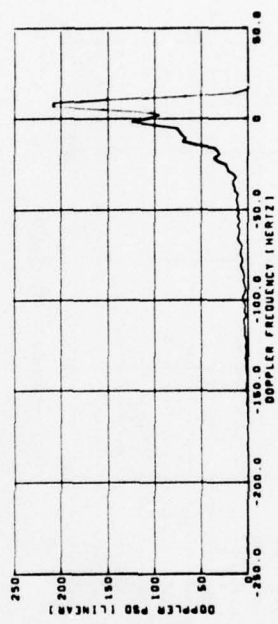
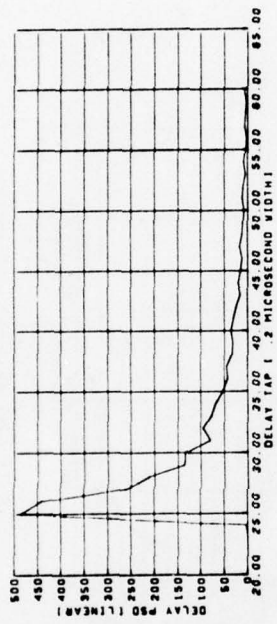
Figure 5-60. Low-Angle $\Delta S(\tau, \omega)$ Perturbations

DELAY AND DOPPLER SPECTRA
 DATE 4/2/75 HORIZONTAL POLARIZATION
 TAP RESOLUTION .2 MICROSEC
 TIME INTERVAL 11/ 8/ .492 TO 11/ 8/ 7.190
 NOISE REMOVED



(a) No Antenna Correction

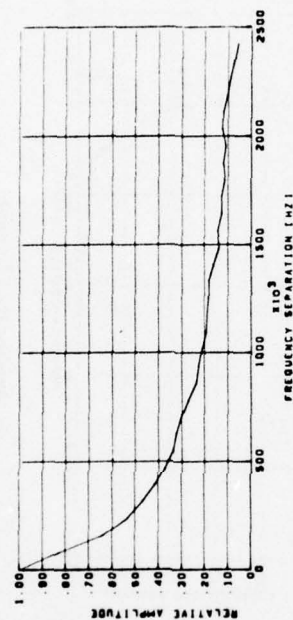
DELAY AND DOPPLER SPECTRA
 DATE 4/2/75 HORIZONTAL POLARIZATION
 TAP RESOLUTION .2 MICROSEC
 TIME INTERVAL 11/ 8/ .492 TO 11/ 8/ 7.190
 ANTENNA GAIN CORRECTED



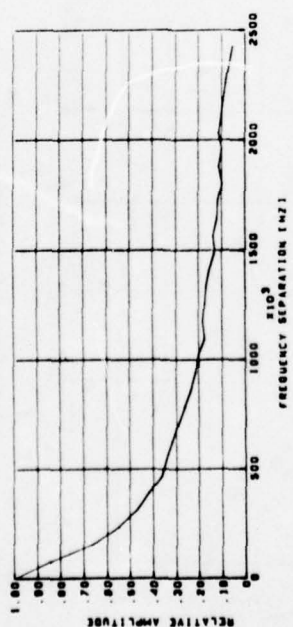
(b) Antenna Gain Corrected

Figure 5-61. Low-Angle Antenna Gain Effects Upon Delay and Doppler Spectra

AUTOCORRELATION FUNCTIONS
 DATE 4/2/75 HORIZONTAL POLARIZATION
 TAP RESOLUTION .2 MICROSEC
 TIME INTERVAL 11/ 8/ .482 TO 11/ 8/ 7.100
 ANTENNA GAIN CORRECTED



AUTOCORRELATION FUNCTIONS
 DATE 4/2/75 HORIZONTAL POLARIZATION
 TAP RESOLUTION .2 MICROSEC
 TIME INTERVAL 11/ 8/ .482 TO 11/ 8/ 7.100
 NOISE REMOVED



(a) No Antenna Correction

(b) Antenna Gain Corrected

Figure 5-62. Low-Angle Antenna Gain Effects Upon Frequency and Time Autocorrelation Functions

$G_H(\tau, \omega)$ function as illustrated in figure 5-58. The most obvious characteristic of the $G_H(\tau, \omega)$ distribution pertains to the relative difference between the negative-frequency gains as compared to the positive-frequency values for a given delay tap. This difference is a direct result of the antenna boresight gain being pointed toward the subaircraft side of the specular point, and it produces a discernible difference in the $S(\tau, \omega)$ and $S_{AC}(\tau, \omega)$ distributions presented in figure 5-59. We further note from the $\Delta S(\tau, \omega)$ plot of figure 5-60 that, relative to the specular-point return, the antenna pattern's spatial distribution enhances the negative shoulder of the scatter function whereas the positive shoulder is attenuated. For the in-plane flight geometry coupled with low-grazing-angle conditions, this will appreciably affect the Doppler spectra shape and its corresponding Fourier transform, as illustrated in figures 5-61 and 5-62, respectively. The reason for this pronounced filtering effect on the Doppler spectra relates to the fact that the position Doppler frequency shoulder of the $S(\tau, \omega)$ function is to a large extent mapped into a single peak density point of the Doppler spectra, whereas the negative shoulder is dispersed in the Doppler coordinate (i.e., the antenna filtering tends to decrease the peakedness of the spectra while at the same time increasing the density of the distribution's tail). This tends to yield Doppler spreads somewhat larger than we would observe had the prober antenna been perfectly uniform.

5.7 CIRCULAR POLARIZATION PROBER RESULTS

In the design of operational aeronautical satellite systems, effects of the oceanic multipath interface on circularly polarized waves are of particular importance. Accordingly, several right- and left-hand circular polarization probes of the oceanic surface were conducted during the latter part of the flight test series. From the standpoint of the physical optics vector scatter formulation, one does not need to perform model alterations to include the effects of any given receive or transmit polarization vector. In general, model predictions for the LHC and RHC prober configurations yield spectral distributions and autocorrelation functions very similar to the corresponding parameters associated with the linear polarization emulations. Similarly, the predicted values of the circular and linear polarization spread parameters are in close accord. As expected, the one area in which the LHC and RHC polarization influence is of significance relates to the total rms scattered energy content of the signal. Since the satellite antenna has RHC polarization, the polarization sense-reversal properties of the surface cause the scattered energy corresponding to probes transmitted with LHC polarization to be received with less loss than the scattered energy for probes transmitted with RHC polarization. This effect is due to the polarization dependence of the phase change at the reflecting surface. The observed phenomenon is predicted for all grazing angles greater than the pseudo-Brewster angle and should become more significant as the grazing angle decreases.

Typical $S(\tau, \omega)$ and associated integral and Fourier transform data sets are given in figures 5-63 and 5-64 for probes conducted with LHC and RHC polarization, respectively. These data were gathered for the in-plane flight direction condition at a grazing angle of approximately 20° and may be compared with figure 5-2 of section 5.1 to obtain a visual estimate of the degree of correlation between respective

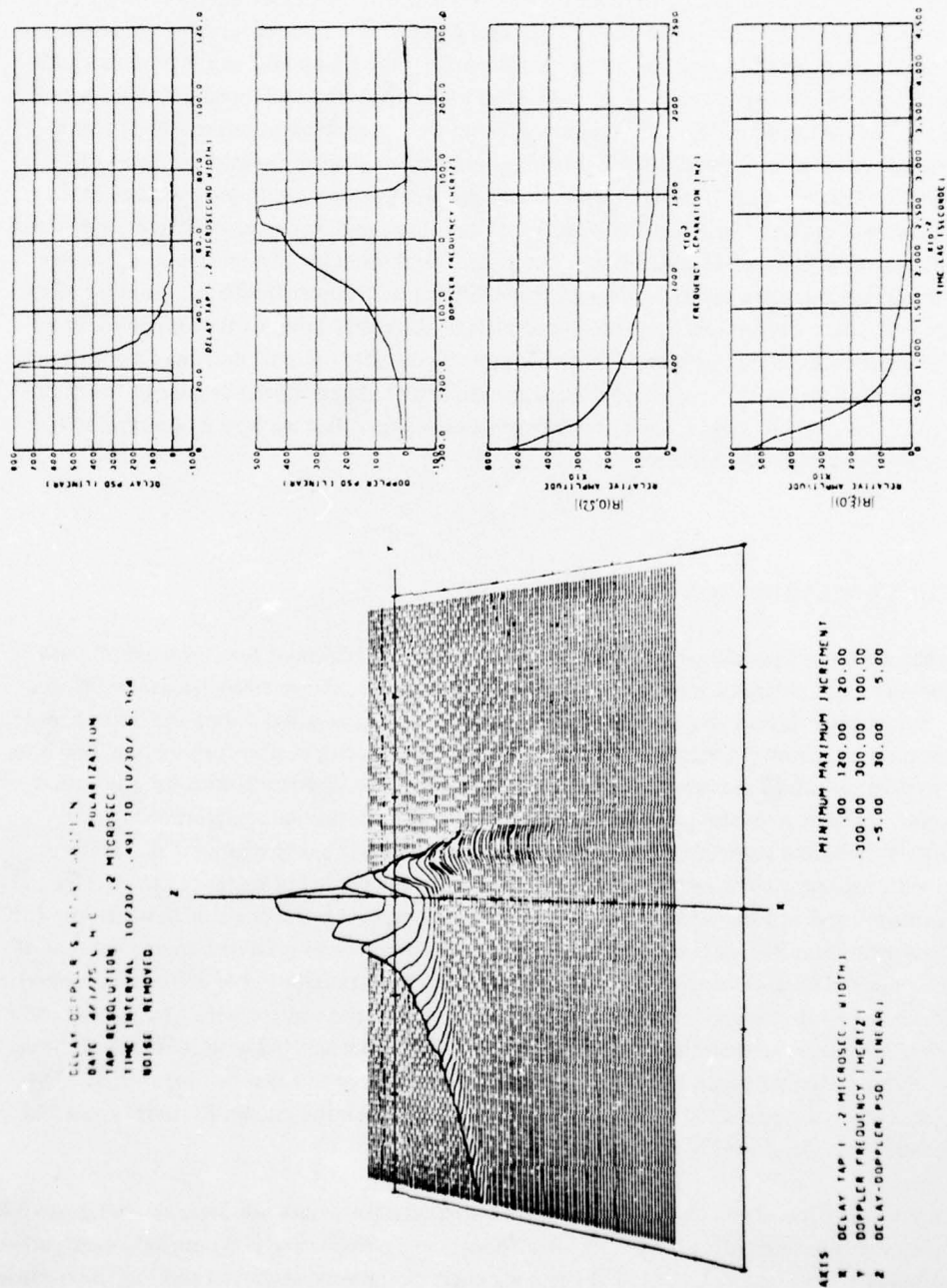
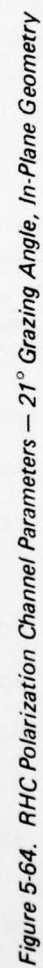


Figure 5-63. LHC Polarization Channel Parameters — 20° Grazing Angle, In-Plane Geometry



parameters for the circular and linear polarization cases. A summary of spread parameter measures and total rms signal energy content obtained for a number of circular polarization probes is given in table 5-13. With the exception of the scatter coefficients, these data are in accord with the linear polarization spread results given in section 5.3. The measured scatter coefficients may be compared with model-predicted results that appear within the parentheses on table 5-13. In general, the experimental and theoretical coefficients are relatively close. However, the RHC coefficients are typically somewhat less than the predicted values whereas the opposite applies for the LHC results. This observation could suggest that the ATS-6 antenna's polarization may not be perfectly circular.

TABLE 5-13. CIRCULAR POLARIZATION SPREAD AND REFLECTION COEFFICIENT MEASURES

Date, mo-day-yr	Polarization	Elev, deg	A/C heading, deg	Delay spread		Coherence BW, 3 dB, kHz	Doppler spread		Decorr time, 3 dB, msec	Scatter coeff, ^a dB
				3 dB, μ sec	10 dB, μ sec		3 dB, Hz	10 dB, Hz		
2-27-75	LHC	32	0	0.93	2.74	234	185	383	2.6	-3.71 (-2.2)
2-27-75	RHC	32	90	0.88	3.26	207	178	440	1.8	-14.6 (-16.8)
4-3-75	LHC	21	90	0.58	2.69	203	143	313	2.5	-3.3 (-3.0)
4-3-75	RHC	21	90	0.72	2.60	203	113	257	2.6	-13.1 (-13.2)
4-3-75	LHC	19	0	0.77	3.02	234	131	222	3.9	-7.7 (-3.2)
4-3-75	RHC	19	0	0.54	2.15	351	119	174	5.2	-11.3 (-12.7)
3-31-75	LHC	15	90	0.76	3.37	168	113	260	3.1	-6.2 (-4.1)
3-31-75	RHC	15	90	0.57	2.57	196	92	211	3.7	-12.4 (-11.6)
3-31-75	LHC	14	0	0.65	2.82	210	43	148	4.4	-6.5 (-4.5)
3-31-75	RHC	14	0	0.59	2.30	237	37	111	6.7	-11.5 (-11.6)

^aQuantity in parenthesis is value predicted by the physical optics vector model. Model predictions shown are for a sea slope of 9° .

5.8 OCEANIC MULTIPATH TEST CONCLUSIONS

A summary of results and conclusions for the oceanic multipath channel characterization test is given in section 2.1.

6. PHYSICAL OPTICS SCATTER MODEL PREDICTIONS

One of the major objectives of this experiment was to substantiate a scatter model that will accurately predict multipath channel characteristics pertinent to future operational oceanic aeronautical satellite systems. For this report, experimental results were correlated with theoretical predictions based on a surface integration of the classical physical optics vector formulation scatter model. Comments on comparisons between model prediction and experimental results were made in section 5, where experimental test results were presented. In this section, we deal primarily with a presentation of the model results. A brief description of the model and its computer implementation are given in section 6.1. Sections 6.2 through 6.4 contain the channel parameter predictions provided by the model for a variety of system configurations and assumed surface characteristics. Test parameters input to the model were selected to closely emulate the experimental conditions and correspond to the range of values shown in table 6-1.

TABLE 6-1. INPUT TEST PARAMETERS FOR PHYSICAL OPTICS SCATTER MODEL PREDICTIONS

Aircraft altitude	10 km
Aircraft speed	200 m/sec
Aircraft heading	a) Toward satellite; great circle path b) Broadside to satellite; great circle path
Aircraft antenna polarization	Horizontal, vertical
ATS-6 antenna polarization	Right-hand circular
Grazing angles	3°, 7°, 13°, 19°, 25°, 31°
Surface type	Sea water
Surface rms slope (total)	3°, 6°, 12°

Using the Cox and Munk (ref 5-12) empirical relationship, we may relate the actual rms surface slope to wind velocity (V_w) 42 ft above the surface:

$$V_w = \frac{[\tan(\text{slope})]^2 - 0.003}{0.00264}, \text{ knots.}$$

Thus 3° and 12° actual surface rms slopes correspond to average wind velocities of near-zero and 18 kn, respectively. The January series, which was conducted in the vicinity of the Azores, coincided with some rather severe storms in that area. Since a good percentage of the useful oceanic multipath data was collected during this series, one might expect the data presented in the previous sections to be more correlated with the 12° or 6° slope predictions than with the 3° slope prediction.

It is of importance to note that for L-band forward scatter, the multipath interface will appear as a smoothed (i.e., filtered) version of the actual surface. This smoothing effect reduces the contribution to the surface characteristics of the small-scale surface structure and thereby yields an "effective

rms sea slope" value smaller than the actual rms surface slope. As shown in ref (5-6), the physical optics model predicts that for a given wavelength, the extent of the filtering increases as the grazing angle decreases. Thus V_w represents a lower bound (especially for grazing angles less than roughly 15°) on the wind velocities required to produce an rms slope corresponding to the "effective rms sea slope" value.

For one flight test (March 31, 1975), a sea-state data measurement buoy was deployed to gather quantitative data on the surface's slope probability distribution. Results of this measurement are found in section 6.5.

6.1 MODEL DESCRIPTION

The choice of an appropriate model for the analysis of electromagnetic surface scatter is determined almost exclusively by the roughness characteristics of the reflecting medium. Surfaces are usually classified as slightly rough, very rough, or composite, depending on the magnitude of the height irregularities (ref 5-8). In general, different scatter theories are used in each of these situations (ref 6-1).

For the case of L-band aeronautical satellite oceanic scatter, the surface will almost always appear to be very rough; this implies that the following is approximately satisfied (ref 6-2):

$$\frac{2\pi\sigma_H}{\lambda} \cos \theta_i > 1.0 ,$$

where:

- λ = electromagnetic wavelength
- σ_H = standard deviation of surface height irregularities
- θ_i = incident angle of ray upon the surface as measured from the normal.

Analysis of scattering from very rough surfaces is usually developed through the physical optics tangent-plane method (ref 6-1). Commonly called the Kirchhoff approximation, this model is based on the assumption of a locally plane surface over the distance of many wavelengths. This constraint is considered to be satisfied if the radius of curvature of the surface undulations (ρ_c) is much greater than λ ; i.e., $\lambda \ll 4\rho_c \cos \theta_i$.¹

¹In addition to this inequality, the physical optics model is also restricted to conditions where surface shadowing and multiple reflections are negligible. Thus, predictions for rear-grazing incidence in combination with large rms surface slopes should not be considered to be strictly valid. An example of such a condition is the 3° grazing angle case combined with the 12° rms slope condition of table 6-1.

For this analysis we employ the vector formulation (ref 6-3) of the physical optics model and thus are able to properly account for the electromagnetic polarization dependencies of each particular scattering facet on the surface. Because of the model's complexity, it is not possible to arrive at adequate channel parameter solutions in a closed form. This is circumvented through use of a computerized technique that subdivides the spherical scatter surface into incrementally small areas and then determines the scatter cross section (including polarization transformation factors), Doppler shift, and time delay associated with each area. The complex vector representation of the scattered signal is coupled to the receiver antenna characteristics, thereby providing an estimation of the received power from the particular surface patch. This allows the channel's delay-Doppler scatter function, $S(\tau, \omega)$, to be constructed.² From $S(\tau, \omega)$, steps identical to those described in section 4 are employed to determine the channel's time-frequency autocorrelation function, delay spectrum, Doppler spectrum, time autocorrelation function, frequency autocorrelation function, total energy content, and spread values of the unidimensional distributions.

A block diagram illustrating the computer model's input/output and basic processing functions is given in figure 6-1. Inputs to the program include:

- a. System geometry parameters (aircraft altitude, speed, velocity vector direction, grazing angle at specular point, and transmitted frequency)
- b. Complex polarization vectors of airplane and satellite antenna (satellite's polarization characteristics are assumed to be isotropic over the scatter surface; aircraft antenna radiation distribution characteristics may be accounted for mathematically or by including an azimuthal-elevation angle look-up table to derive complex horizontal and vertical polarization coefficients)
- c. RMS surface slope and electrical parameters
- d. Surface area resolution parameter (determines the size of the incremental surface area used in the surface integration routine and thus ultimately affects the fidelity of the predictions).

²Closed-form evaluations of $S(\tau, \omega)$ have been constructed by Mallinkrodt (ref 5-9) and Bello (ref 5-1). Evaluations of $S(\tau, \omega)$ using surface integration techniques have been performed by DeRosa (ref 6-4 and 5-4) and Schneider (ref 5-3). Mallinkrodt, Bello, and the earlier of the two DeRosa works cited used a scalar formulation, while the later DeRosa work and Schneider used a vector scatter formulation.

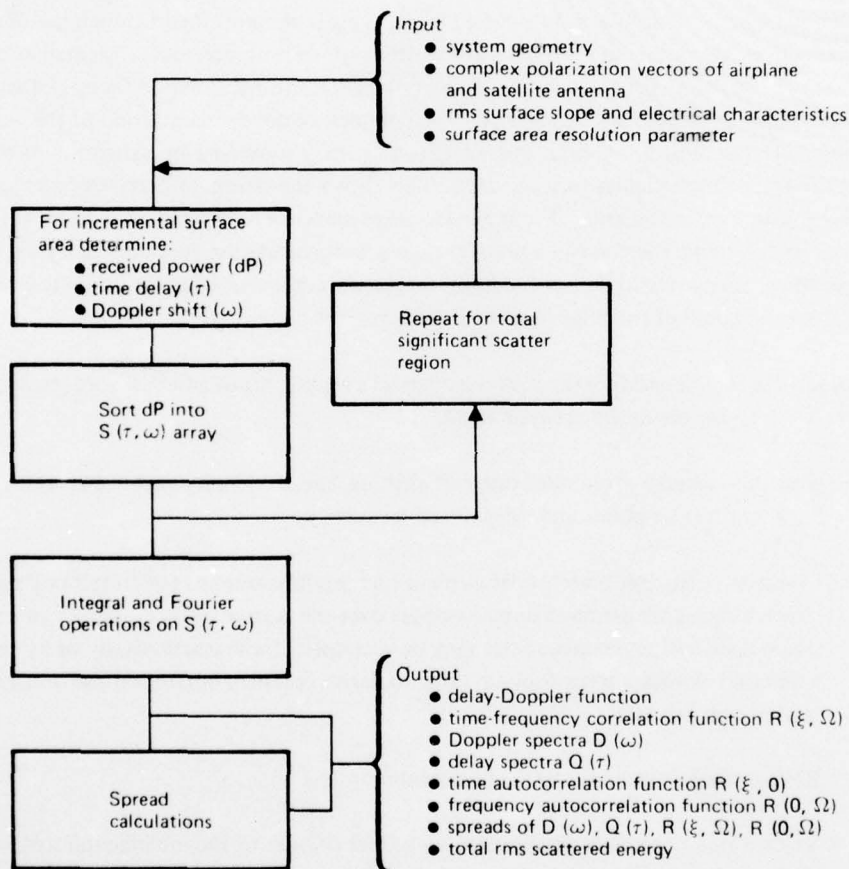


Figure 6-1. Scatter Model Block Diagram

The basic processing function of the computer code may be broken down into three categories.

- a. For each incremental surface area (dS) considered in the integration, calculate the received scattered power (dP), the time delay (τ), and Doppler shift (ω) associated with the return.
- b. Sort the power returned from each incremental area into a two-dimensional array (τ, ω) to yield an estimate of the channel's scatter function $S(\tau, \omega)$.
- c. Perform Fourier and integral operations on $S(\tau, \omega)$ to derive the channel's time-frequency autocorrelation function, time autocorrelation function, frequency autocorrelation function, Doppler spectrum, delay spectrum, total rms scattered energy, and spread values of the unidimensional parameters.

Category c utilizes algorithmic operations identical to those described in section 4. The second category (b) is a relatively straightforward two-dimensional bin-sorting algorithm and needs no further explanation.

Category a represents the surface scatter boundary interface component of the model and, to a large extent, is based on the work of Peake (ref. 6-5). Drawing from this source we briefly present, with the aid of figure 6-2, the underlying mathematics associated with the derivation of dP , τ , and ω . For ease of interpretation, parameter dP is calculated relative to the power received over the direct path link whereas ω and τ are evaluated relative to the direct path Doppler and the specular-point delay values, respectively. The normalized received power from incremental area dS is thus expressed as:

$$dP = \frac{r_d^2 (T_{cf} \cdot T_{cf}^*) \sigma_{xs} dS}{4\pi r_1^2 r_2^2 |\bar{G}_p \cdot \bar{G}_s|^2}, \quad (6-1)$$

where:

- r_1, r_2, r_d = distances as illustrated in figure 6-2.
- T_{cf} = complex coefficient that accounts for coupling between incident polarization vector, tilted dielectric surface element, and receiver polarization vector
- σ_{xs} = surface scatter cross section
- dS = elemental surface area
- \bar{G}_p = airplane complex polarization vector for direct-link path
- \bar{G}_s = satellite complex polarization vector.

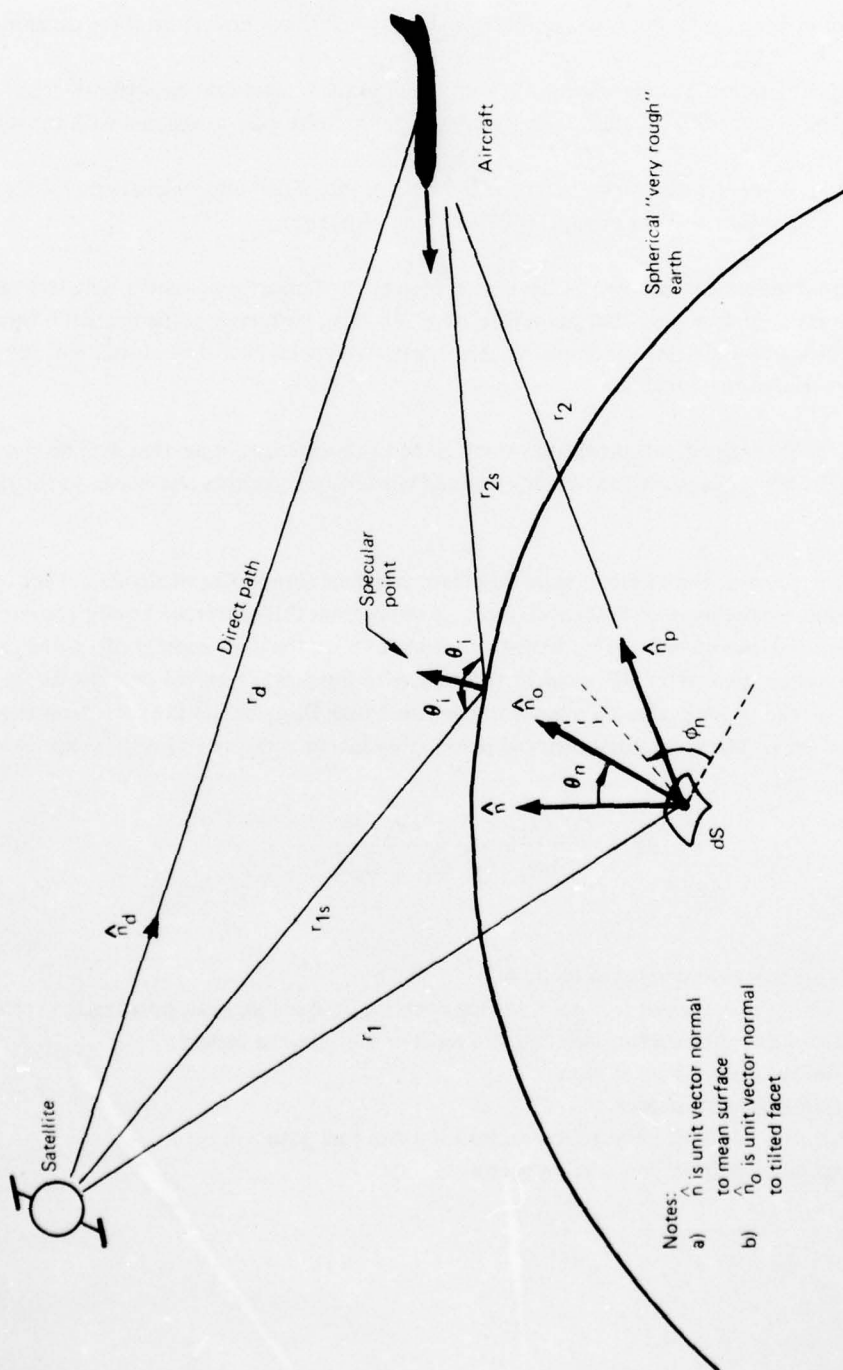


Figure 6-2. Scatter Model Geometry

The complex transmission coefficient embodies the aircraft antenna spatial filtering and is calculated as:

$$T_{cf} = (DI) \left[R_{||}(a) (A \cos \delta_i + B \sin \delta_i) (C \cos \delta_s + D \sin \delta_s) - R_{\perp}(a) (B \cos \delta_i - A \sin \delta_i) (C \sin \delta_s - D \cos \delta_s) \right], \quad (6-2)$$

where:

- DI = spherical-earth divergence factor
- $R_{||}(a)$ = parallel Fresnel reflection coefficient = $(\epsilon^2 \cos a - E)/(\epsilon^2 \cos a + E)$
- $R_{\perp}(a)$ = perpendicular Fresnel reflection coefficient = $(\cos a - E)/(\cos a + E)$
- ϵ = complex index of refraction of the surface
- $E = (\epsilon^2 - \sin^2 a)^{1/2}$
- a = angle between incident wave and normal of properly tilted (to produce reflection into receiver) surface facet
- δ_i = angle between "theta" component of incident wave and the incident "parallel" unit vector (i.e., vertical polarization with respect to tilted surface)
- δ_s = angle between "theta" component of scattered wave and the reflected "parallel" unit vector
- A,B,C,D = transmitter and receiver complex antenna polarization vector coefficients as described below.

Polarization vectors for the transmit (\bar{P}_T) and receive (\bar{P}_R) antenna system are given by:

$$\bar{P}_T = A \hat{L}_{TT} + B \hat{L}_{PT} \quad (6-3)$$

$$\bar{P}_R = C \hat{L}_{TR} + D \hat{L}_{PR}, \quad (6-4)$$

where:

- $\hat{L}_{TT}, \hat{L}_{PT}$ = unit vectors in the theta and phi directions, respectively, with respect to coordinates centered on transmitter
- $\hat{L}_{TR}, \hat{L}_{PR}$ = unit vectors in the theta and phi directions, respectively, with respect to coordinates centered on receiver.

The physical optics very-rough-surface scatter cross section is obtained from:

$$\sigma_{xs} = \frac{\pi}{\cos \theta_n} p_{ss}(\theta_n, \phi_n), \quad (6-5)$$

AD-A042 325

BOEING COMMERCIAL AIRPLANE CO SEATTLE WASH

F/G 17/7

AIR TRAFFIC CONTROL EXPERIMENTATION AND EVALUATION WITH THE NAS--ETC(U)

SEP 76 A D THOMPSON, B J BURRESON, P F RIEDER DOT-TSC-707-5

UNCLASSIFIED

D6-44050

FAA-RD-75-173-5

NL

3 OF 4
AD
A042325



where:

θ_n, ϕ_n = angles as illustrated in figure 6-2

$p_{ss}(\theta_n, \phi_n)$ = surface slope probability density function; i.e., the probability that the surface normal lies within the solid angle $d\Omega_n = \sin \theta_n d\theta_n d\phi_n$ is given by the quantity $p_{ss}(\theta_n, \phi_n) d\Omega_n$.

For this particular analysis, the slope pdf was assumed to be isotropic with the following Gaussian-like form:

$$p_{ss}(\theta_n, \phi_n) = \frac{\cos \theta_n}{\pi \eta^2} \exp \left[\frac{-\tan^2 \theta_n}{\eta^2 (1 + 2\eta^2)} \right], \quad (6-6)$$

where $\eta^2 = \langle \tan^2 \theta_n \rangle$ = mean square surface slope.

According to Peake (ref 6-5), this representation is quite similar to the standard Cox and Munk (ref 5-12) distribution and, for surfaces of moderate slope, very nearly satisfies the normalization conditions:

$$\begin{aligned} \iint p_{ss}(\theta_n, \phi_n) d\Omega_n &= 1 \\ \iint p_{ss}(\theta_n, \phi_n) \tan^2 \theta_n d\Omega_n &= \eta^2, \end{aligned} \quad (6-7)$$

It is further noted that for the slope conditions considered in this report, the $p_{ss}(\theta_n, \phi_n)$ distribution closely resembles a Gaussian density for a two-dimensional isotropic surface. That is, for $\eta^2 \ll 1$ the exponential factor of the slope distribution decays rapidly and is significant only for small θ_n ; hence $\cos \theta_n$ is well approximated by unity. Furthermore, in the denominator of the exponent, the factor $(1 + 2\eta^2) \approx 1$,³ and thus

$$p_{ss}(\theta_n, \phi_n) \approx \frac{1}{\pi \eta^2} \exp \left[\frac{-\tan^2 \theta_n}{\eta^2} \right]. \quad (6-8)$$

The above relationship, under the constraint that $\cos \theta_n = 1$, exactly satisfies the pdf normalization condition and is identical in form to that of equation (3.25) of reference 5-6, which was derived for an isotropic interface whose joint second-order surface height and correlation properties are Gaussian; i.e.,

$$p(\tan \beta, \phi_n) = \frac{1}{\pi \tan^2 \beta_0} \exp \left[\frac{\tan^2 \beta}{\tan^2 \beta_0} \right] \quad (6-9)$$

where:

$p(\tan \beta, \phi_n)$ = the polar coordinate equivalent of the slope distribution described in section 6.5.3, page 6-75 (i.e., $\eta^2 = \sigma^2_{\text{slope}}$, $t_x = s_x$, $t_y = s_y$)

³For the 12°, 6°, and 3° rms slopes, the approximation $(1 + 2\eta^2) \approx 1$ decreases the denominator of the exponent by approximately 9%, 2%, and less than 1%, respectively.

- β = angle made by the bisector of the incident and scattered rays with the local normal to the mean surface (i.e., β describes the requisite geometry for favorable scatter)
 $\tan^2 \beta_0$ = total mean square surface slope = η^2
 $\tan^2 \beta$ = $t_x^2 + t_y^2 = \tan^2 \theta_n$
 t_x, t_y = slopes of the surface normal in the x and y directions, respectively.

The joint probability densities $p(t_x, t_y)$, $p(\tan \beta, \phi_n)$ and $p_{ss}(\theta_n, \phi_n)$ are related through the expressions

$$p_{ss}(\theta_n, \phi_n) d\Omega_n = p(t_x, t_y) dt_x dt_y = p(\tan \beta, \phi_n) \tan \beta d\tan \beta d\phi_n.$$

It can readily be shown that $\tan \beta$ is Rayleigh distributed. Using equation (6-7) in the form

$$\int p_{ss}(\theta_n, \phi_n) d\Omega_n = \iint p(\tan \beta, \phi_n) \tan \beta d\tan \beta d\phi_n = 1,$$

and substituting for $p(\tan \beta, \phi_n)$ from equation (6-9), one obtains (after performing the integration over the ϕ_n variable),

$$\int \frac{2 \tan \beta}{\tan^2 \beta_0} \exp \left[\frac{-\tan^2 \beta}{\tan^2 \beta_0} \right] d\tan \beta = 1.$$

The integrand in this expression is the marginal pdf for $\tan \beta$ and is readily recognizable as the Rayleigh pdf, with variable $\tan \beta$ and parameter $\tan^2 \beta_0$.

The correspondence between $p_{ss}(\theta_n, \phi_n)$ and $p(\tan \theta_n, \phi_n)$ may be obtained through the following relationships for an isotropic surface (see Hagfors, ref 6-6):

$$\begin{aligned}
 p_{ss}(\theta_n, \phi_n) &= \frac{1}{2\pi} p_{ss}(\theta_n) \\
 p_{ss}(\theta_n) &= \frac{2\pi}{\cos^3 \theta_n} p(\tan \theta_n, \phi_n)
 \end{aligned} \tag{6-10}$$

Thus,

$$p_{ss}(\theta_n, \phi_n) = \frac{1}{\cos^3 \theta_n} p(\tan \theta_n, \phi_n) \tag{6-11}$$

Equation (6-11) may be used to give an alternate expression for the scatter cross section; i.e.,

$$\sigma'_{xs} = \pi \sec \theta_n p(\theta_n, \phi_n) = \pi \sec^4 \theta_n p(\tan \theta_n, \phi_n),$$

which when substituted into the previously presented relationship for dP equation (6-1) yields:

$$dP = \frac{1}{4\pi} \left(\frac{r_d}{r_1 r_2} \right)^2 \frac{|T_{cf}|^2}{|\bar{G}_p \cdot \bar{G}_s|^2} \frac{\sec^4 \theta_r}{\tan^2 \beta_o} \exp \left[\frac{-\tan^2 \theta_n}{\tan^2 \beta_o} \right] dS. \quad (6-12)$$

This expression is easily identified as the normalized $(|\bar{G}_p \cdot \bar{G}_s|^2)$ vector $(T_{cf} \Rightarrow \Gamma)$, equivalent to the formulation given by Staras (eq 2 of ref 5-7).

The delay and Doppler variables associated with a given incremental area are determined from:

$$\omega = \frac{2f_o \pi}{c} \left(-\bar{n}_p \cdot \bar{v} + \bar{n}_d \cdot \bar{v} \right) \quad (6-13)$$

$$\tau = \frac{1}{c} (r_1 + r_2 - r_{1s} - r_{2s}) \quad (6-14)$$

where f_o is the transmitted frequency, c is the velocity of light, and the other parameters are as illustrated in figure 6-2.

6.2 DELAY-DOPPLER SCATTER FUNCTION

Section 6.1 outlined that the multipath's delay-Doppler scatter function serves as the basic system function from which the other model predictions are derived. Consequently, this function has been generated for all parameter combinations delineated in section 6. As a representative subset of the total ensemble, we present $S(\tau, \omega)$ distributions corresponding to horizontal and vertical polarization probes for high (31°) and low (13°) grazing angles, coupled with 12° , 6° , and 3° rms sea-slope conditions. The horizontal data is given for both in-plane and cross-plane flight directions whereas only the in-plane data is presented for the vertical polarization probes. In the following section, the integral and Fourier operations on the model-predicted $S(\tau, \omega)$ function are discussed. Examples used for that discussion are derived from the $S(\tau, \omega)$ distributions of this section. For the purpose of continuity, the data sets are therefore left in integrated form (i.e., in each figure we present $S(\tau, \omega)$, $Q(\tau)$, $D(\omega)$, $R(0, \Omega)$, and $R(\xi, 0)$ for a particular set of system and surface conditions). Table 6-2 provides a cross-reference between figure number, sea-surface slope, grazing angle, and aircraft heading.

The $S(\tau, \omega)$ scatter functions associated with figures 6-3 through 6-20 provide detailed insight regarding the grazing angle, polarization, flight direction, and sea-surface slope dependencies of the

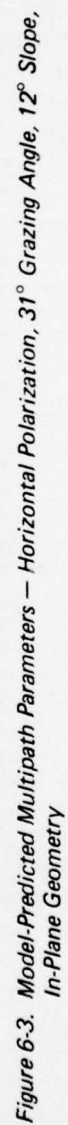
oceanic forward-scatter L-band phenomenon.⁴ One readily observes that the Doppler frequency distribution of the returned energy is strongly influenced by aircraft heading (i.e., compare figs 6-3 and 6-9). The dissimilarities between the in-plane and cross-plane $S(\tau, \omega)$ functions are seen to increase as the rms slope increases and as the grazing angle decreases. For the cross-plane case, individual delay taps possess Doppler spectra that are symmetrical with respect to the specular-point return frequency of 0 Hz. On the other hand, the Doppler spectra associated with the individual taps for the in-plane geometry (with flight toward the satellite) are highly asymmetrical, with the negative-frequency return being significantly more dispersed than the positive-frequency scatter.

TABLE 6-2. MODEL-PREDICTED SCATTER PARAMETERS: FIGURE REFERENCE

Polarization	Sea slope, deg	Grazing angle, deg	A/C heading	Figure
Horizontal	12	31	In-plane	6-3
Horizontal	6	31	In-plane	6-4
Horizontal	3	31	In-plane	6-5
Horizontal	12	13	In-plane	6-6
Horizontal	6	13	In-plane	6-7
Horizontal	3	13	In-plane	6-8
Horizontal	12	31	Cross-plane	6-9
Horizontal	6	31	Cross-plane	6-10
Horizontal	3	31	Cross-plane	6-11
Horizontal	12	13	Cross-plane	6-12
Horizontal	6	13	Cross-plane	6-13
Horizontal	3	13	Cross-plane	6-14
Vertical	12	31	In-plane	6-15
Vertical	6	31	In-plane	6-16
Vertical	3	31	In-plane	6-17
Vertical	12	13	In-plane	6-18
Vertical	6	13	In-plane	6-19
Vertical	3	13	In-plane	6-20

For all elevation angles and sea-slope conditions associated with the in-plane flight geometry, we note that $S(\tau, \omega)$ is characterized by two distinct sets of spectral "humps." For a given delay tap, these humps correspond to the upper and lower Doppler spectra limits over which physically possible multipath scatter will be returned; the negative-frequency portion is due to scatterers being located on

⁴It should be noted that $S(\tau, \omega)$ is theoretically a "smooth function" of τ and ω . The "choppy" appearance of certain $S(\tau, \omega)$ function plots results from the choice of cell-size quantitation used in the model-production computer programs.



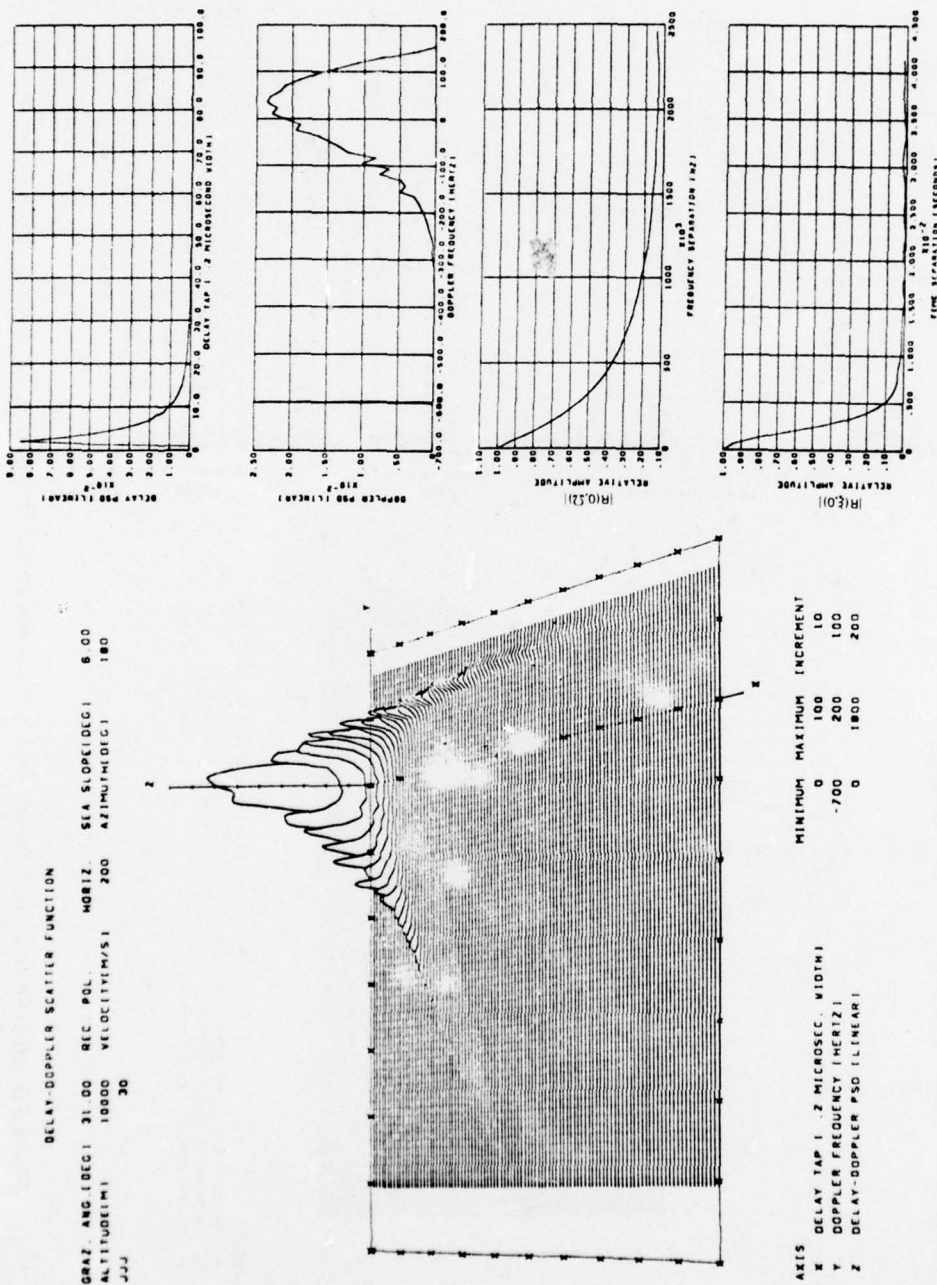
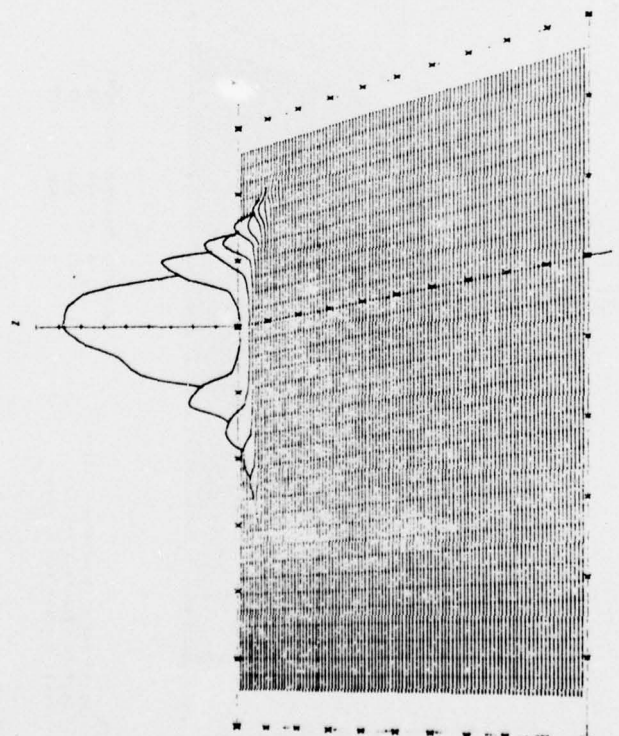


Figure 6-4. Model-Predicted Multipath Parameters — Horizontal Polarization, 31° Grazing Angle, 6° Slope, In-Plane Geometry

DELAY-DOPPLER SCATTER FUNCTION

GRAZ. ANG. (DEG) 31.00 HORIZ. SEA SLOPE (DEG) 3.00
 ALTITUDE (M) 10000 VELOCITY (M/S) 200 AZIMUTH (DEG) 180
 JJJ 30



AXIS
 X DELAY TAP 1 Z MICROSEC. WIDTH 1
 Y DOPPLER FREQUENCY (HERTZ) 100
 Z DELAY-DOPPLER PSC (LINEAR) 500

MINIMUM MAXIMUM INCREMENT
 0 100 10
 -300 150 50
 0 4500 500

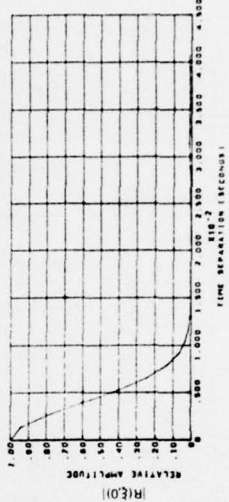
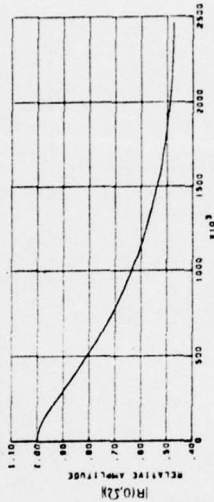
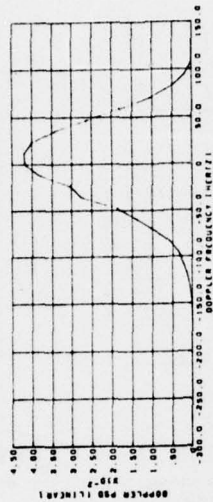
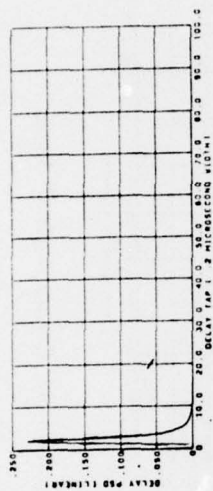
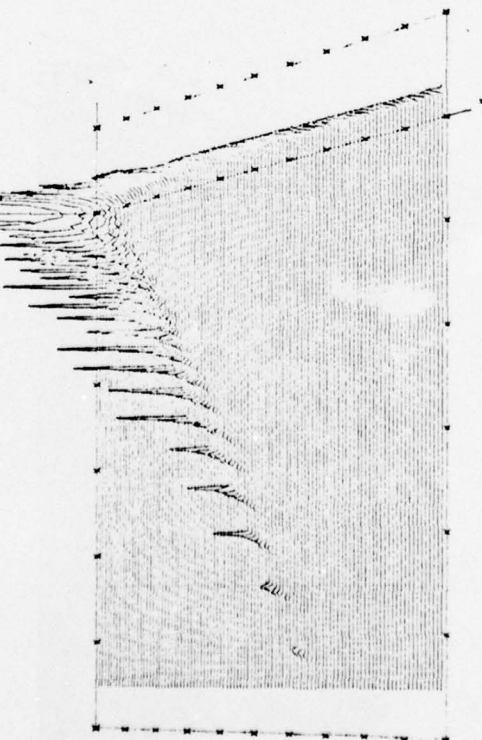


Figure 6-5. Model-Predicted Multipath Parameters — Horizontal Polarization, 31° Grazing Angle, 3° Slope, In-Plane Geometry

DELAY DOPPLER SCATTER DATA

GRAZ ANGLE DEG 13.00 REC POL. HGT/STA SLOPE DEG 12.00
 ALTITUDE MI 10000 VELOCITY M/S 200 AZIMUTH DEG 180
 90

Note: $S(\tau, \omega)$ is theoretically a smooth function of τ and ω . "Choppy" appearance is due to choice of cell-size quantization used in the model computer programs.



AXES
 X DELAY TAP 1/2 MICROSEC. WIDTH
 Y DOPPLER FREQUENCY HERTZ
 Z DELAY DOPPLER PSE. TIME AREA

MINIMUM MAXIMUM INCREMENT
 0 100 10
 600 100 100
 0 450 50

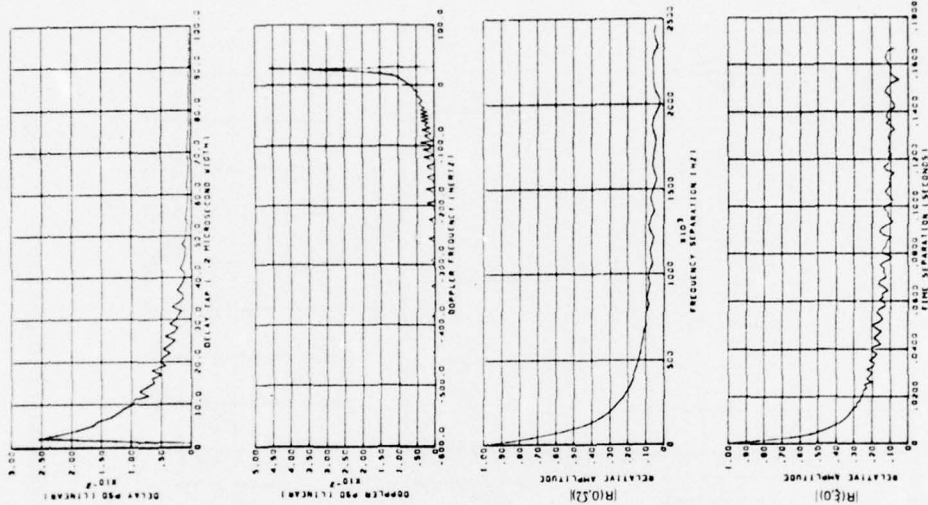


Figure 6-6. Model-Predicted Multipath Parameters — Horizontal Polarization, 13° Grazing Angle, 12° Slope, In-Plane Geometry

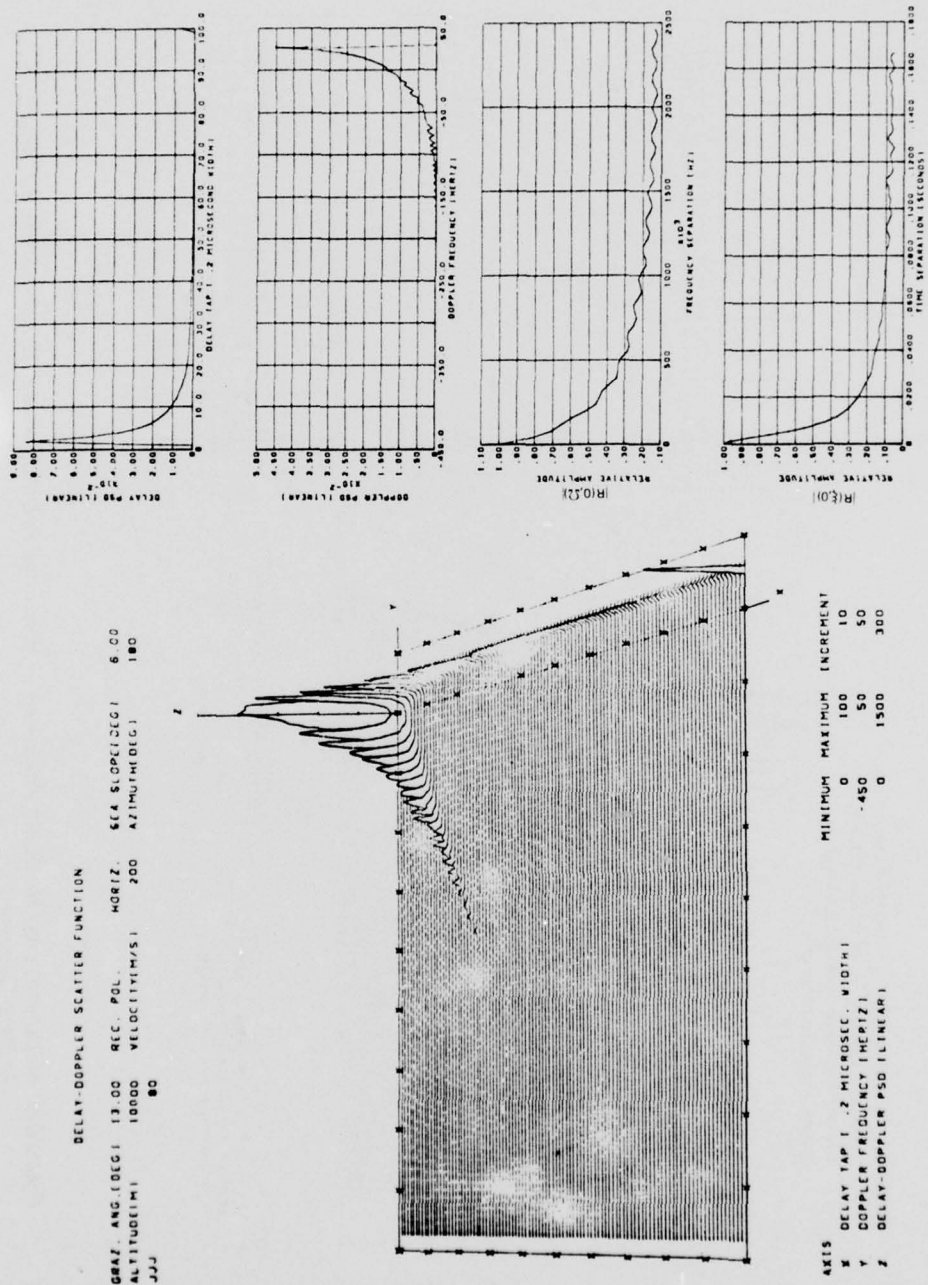
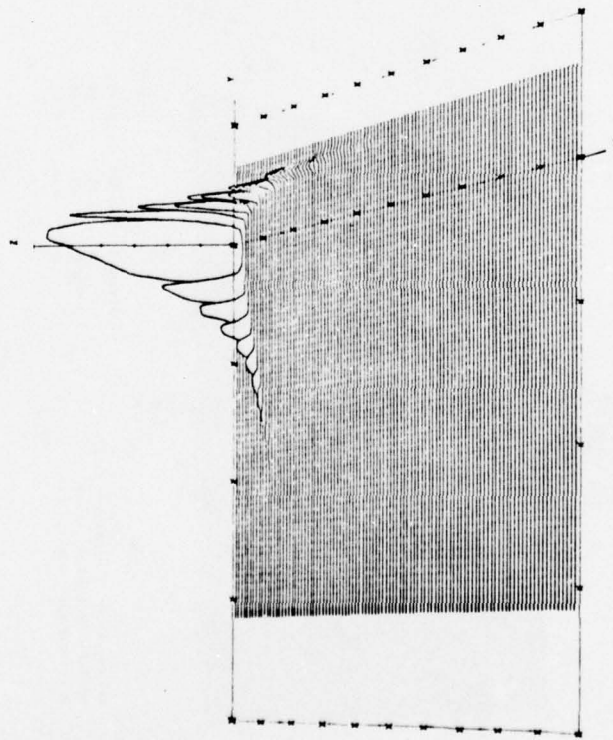


Figure 6-7. Model-Predicted Multipath Parameters — Horizontal Polarization, 13° Grazing Angle, 6° Slope, In-Plane Geometry

DELAY-DOPPLER SCATTER FUNCTION

GRAZ ANG (DEG) 13.00 REC POL HORIZ SEA SLOPE (DEG) 3.00
 ALTITUDE (M) 1000 VELOCITY (M/S) 200 AZIMUTH (DEG) 180
 JJJ 80



AXIS
 X DELAY TAP 1 2 MICROSEC. WIDTH
 Y DOPPLER FREQUENCY (HERTZ)
 Z DELAY-DOPPLER PSD (LINEAR)

MINIMUM MAXIMUM INCREMENT

0 100 10

-200 50 50

0 3000 500

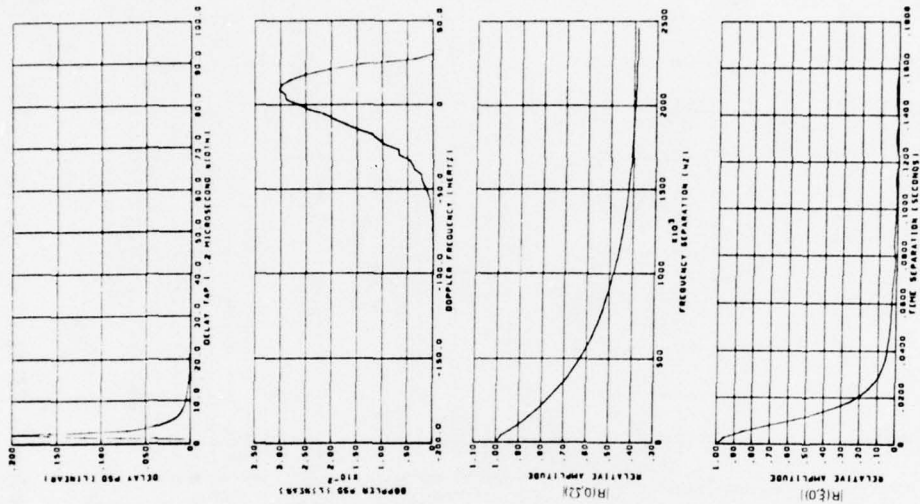


Figure 6-8. Model-Predicted Multipath Parameters — Horizontal Polarization, 13° Grazing Angle, 3° Slope, In-Plane Geometry

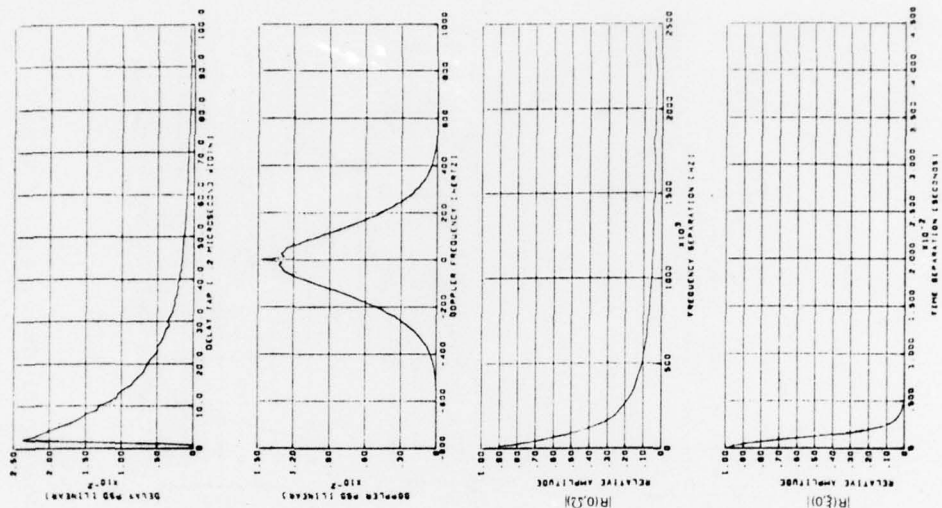
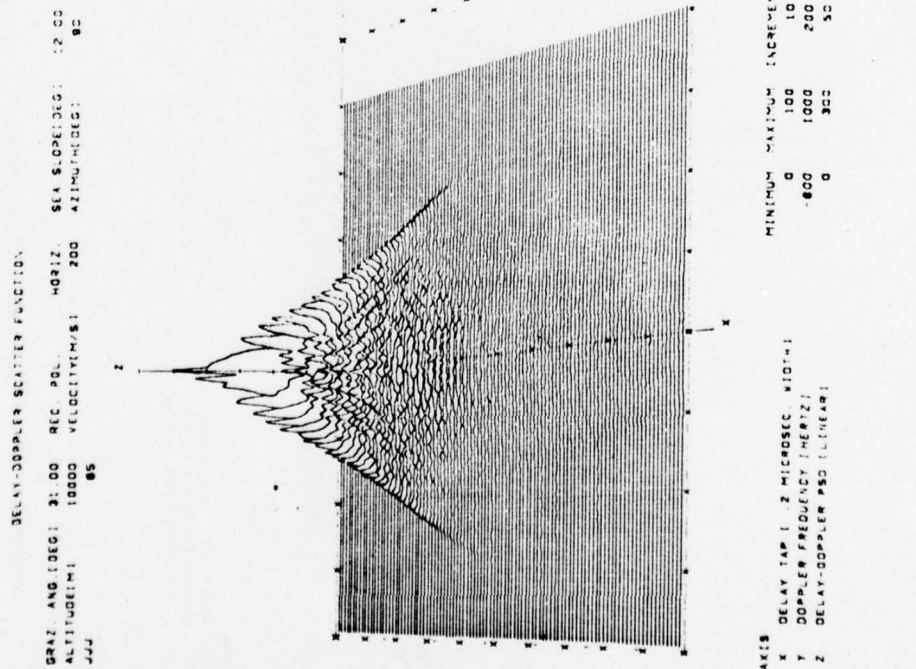


Figure 6-9. Model-Predicted Multipath Parameters — Horizontal Polarization, 31° Grazing Angle, 12° Slope, Cross-Plane Geometry

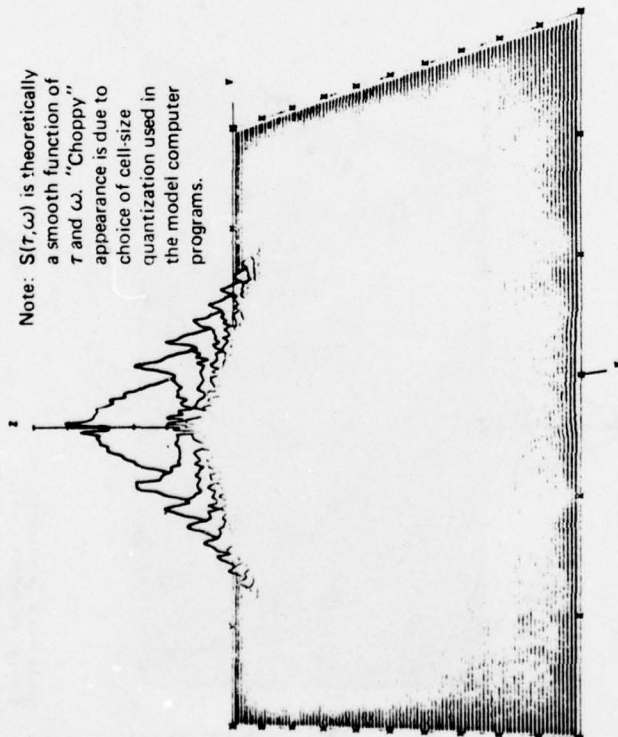


Figure 6-11. Model-Predicted Multipath Parameters — Horizontal Polarization, 31° Grazing Angle, 3° Slope, Cross-Plane Geometry

DELAY-DOPPLER SCATTER FUNCTION

GRAZ. ANG (DEG) 13.00 REC. POL. HORIZ. GRAZ. SLOPE (DEG) 12.00
 ALTITUDE (M) 18000 VELOCITY (M/S) 200 AZIMUTH (DEG) 90
 JJJ 100

Note: $S(\tau, \omega)$ is theoretically a smooth function of τ and ω . "Choppy" appearance is due to choice of cell-size quantization used in the model computer programs.



AXIS
 X DELAY TAP 1 2 MICROSEC. WIDTH
 Y DOPPLER FREQUENCY (HERTZ)
 Z DELAY-DOPPLER PSD (LINEAR)

MINIMUM	MAXIMUM	INCREMENT
0	100	10
-300	300	100
0	120	20

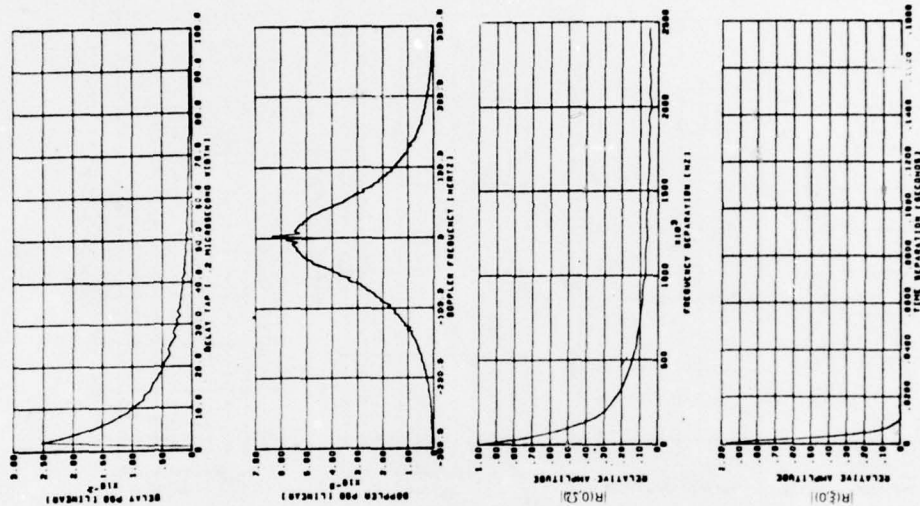
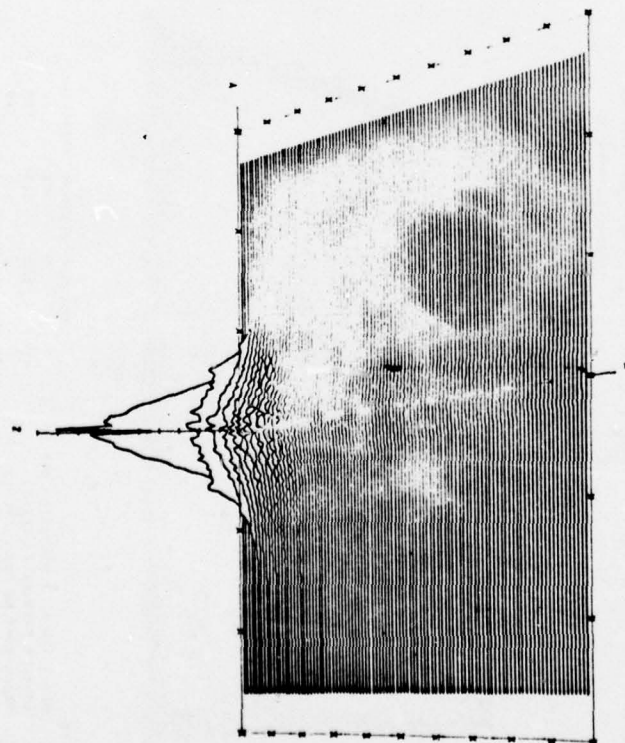


Figure 6-12. Model-Predicted Multipath Parameters — Horizontal Polarization, 13° Grazing Angle, 12° Slope, Cross-Plane Geometry

DELAY-DOPPLER SCATTER FUNCTION

GRAZ. ANG.(DEG) 13.00 REC. PBL. SEA SLOPE(DEG) 0.00
 ALTITUDE(M) 10000 VELOCITY(M/S) 200 AZIMUTH(DEG) 90
 JJJ 120



AXIS DELAY TAP 1 .2 MICROSEC. WIDTH
 X DOPPLER FREQUENCY (HERTZ)
 Y DELAY-DOPPLER PSD (LINEAR)
 Z DELAY-DOPPLER PSD (LINEAR)

MINIMUM MAXIMUM INCREMENT
 0 100 10
 -300 300 100
 0 500 50

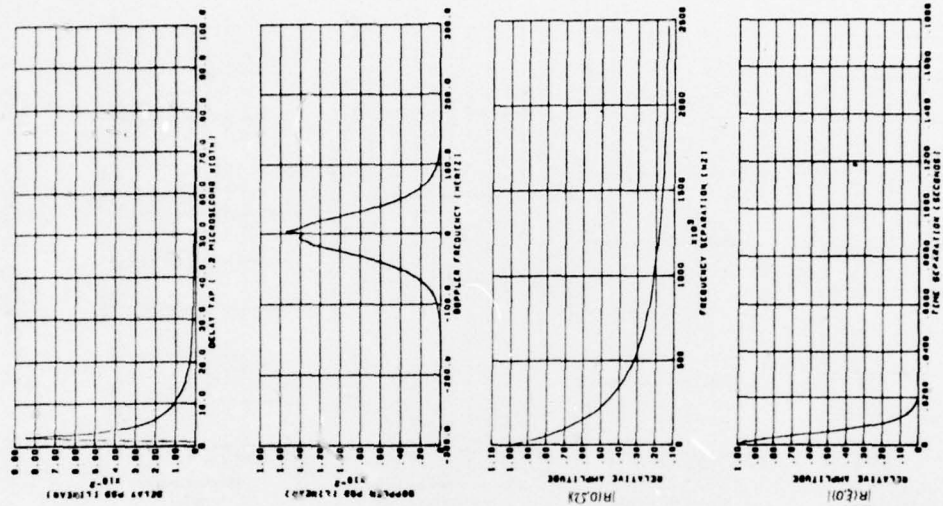


Figure 6-13. Model-Predicted Multipath Parameters — Horizontal Polarization, 13° Grazing Angle, 6° Slope, Cross-Plane Geometry

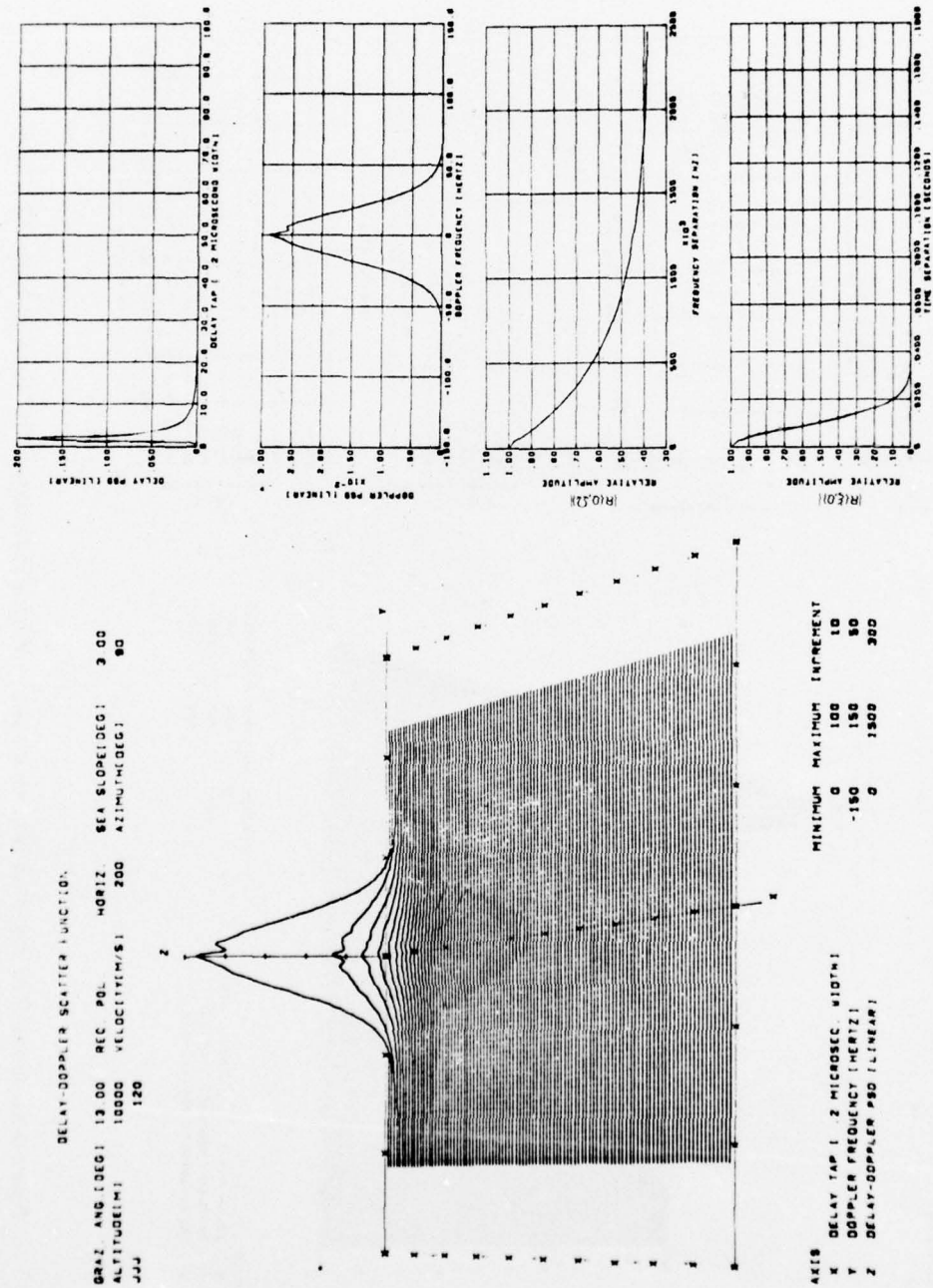
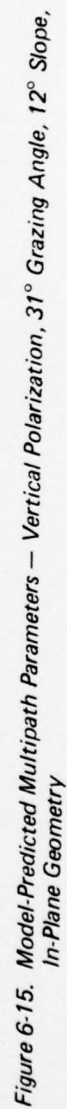
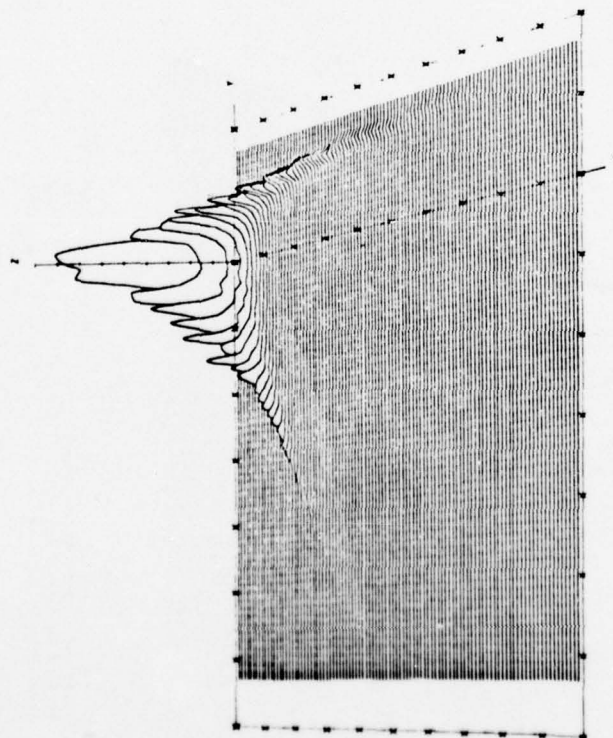


Figure 6-14. Model-Predicted Multipath Parameters — Horizontal Polarization, 13° Grazing Angle, 3° Slope, Cross-Plane Geometry



DELAY-DOPPLER SCATTER FUNCTION

GRAZ ANG (DEG) 31.00 REC POL VERT SEA SLOPE (DEG) 6.00
 ALTITUDE (M) 10000 VELOCITY (M/S) 200 AZIMUTH (DEG) 180
 JJJ 30



AXIS
 X DELAY TAP 1 2 MICROSEC WIDTH
 Y DOPPLER FREQUENCY (HERTZ)
 Z DELAY-DOPPLER PSD (LINEAR)

MINIMUM	MAXIMUM	INCREMENT
0	100	10
-700	200	100
0	900	100

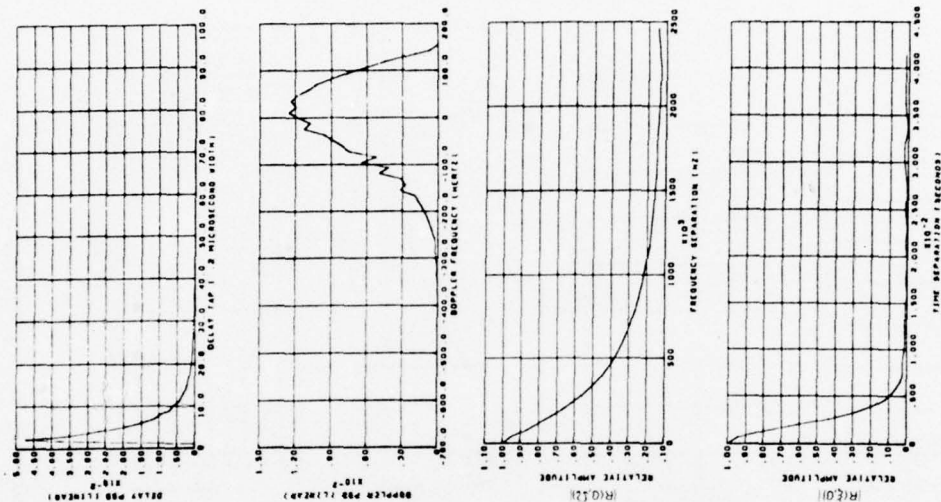


Figure 6-16. Model-Predicted Multipath Parameters — Vertical Polarization, 31° Grazing Angle, 6° Slope, In-Plane Geometry

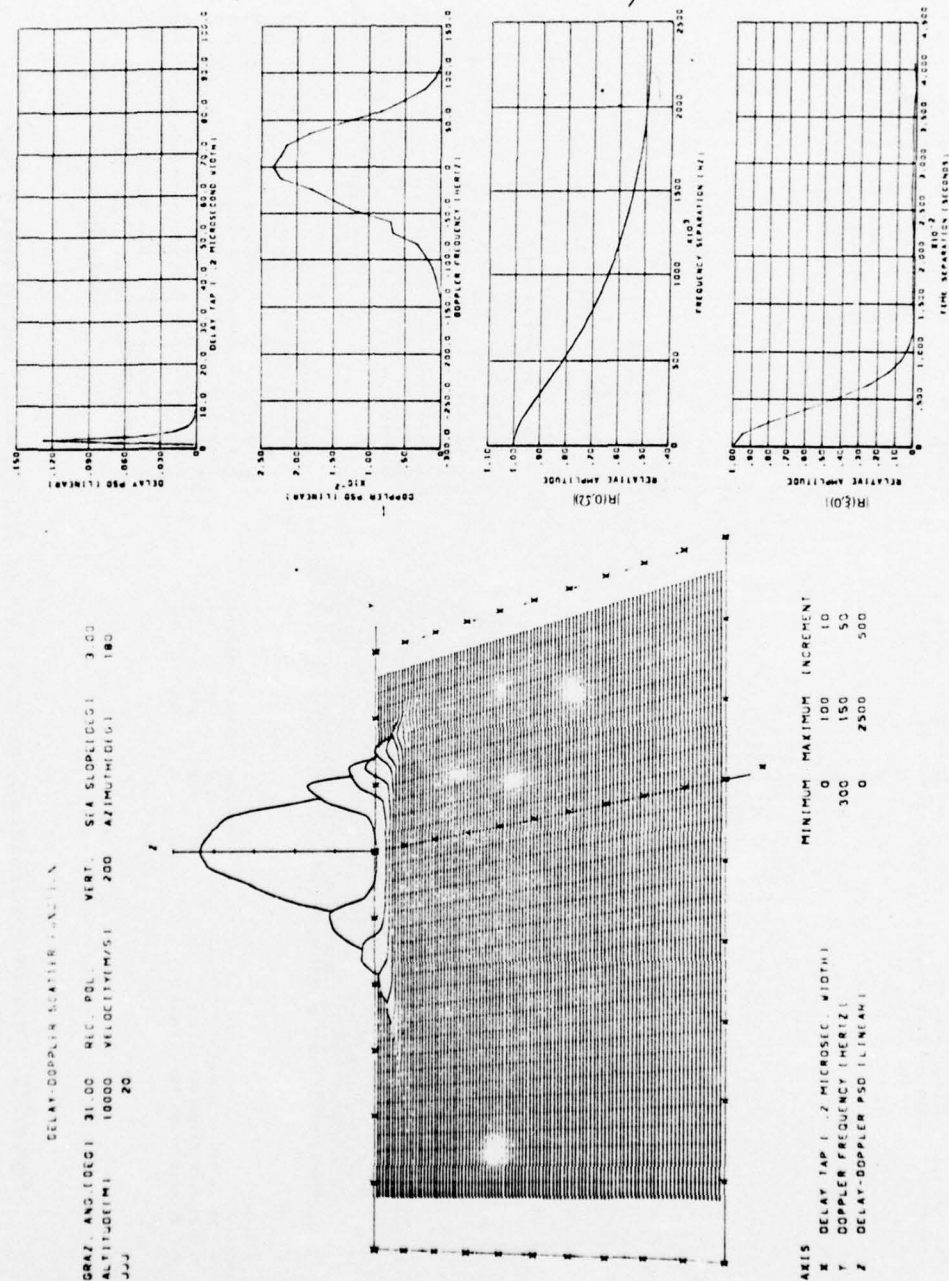
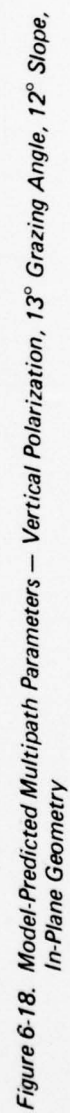


Figure 6-17. Model-Predicted Multipath Parameters — Vertical Polarization, 31° Grazing Angle, 3° Slope, In-Plane Geometry



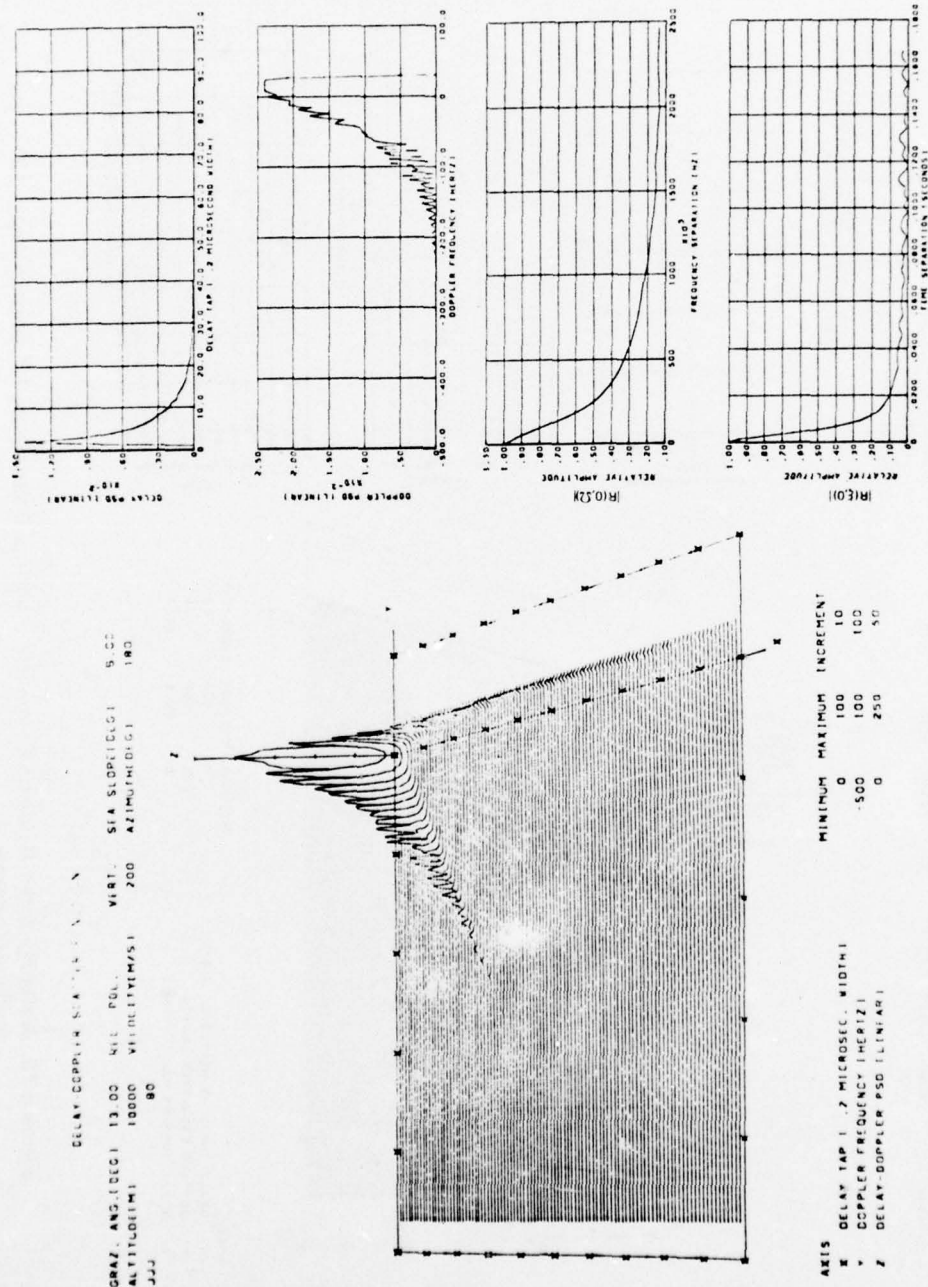


Figure 6-19. Model-Predicted Multipath Parameters — Vertical Polarization, 13° Grazing Angle, 6° Slope, In-Plane Geometry

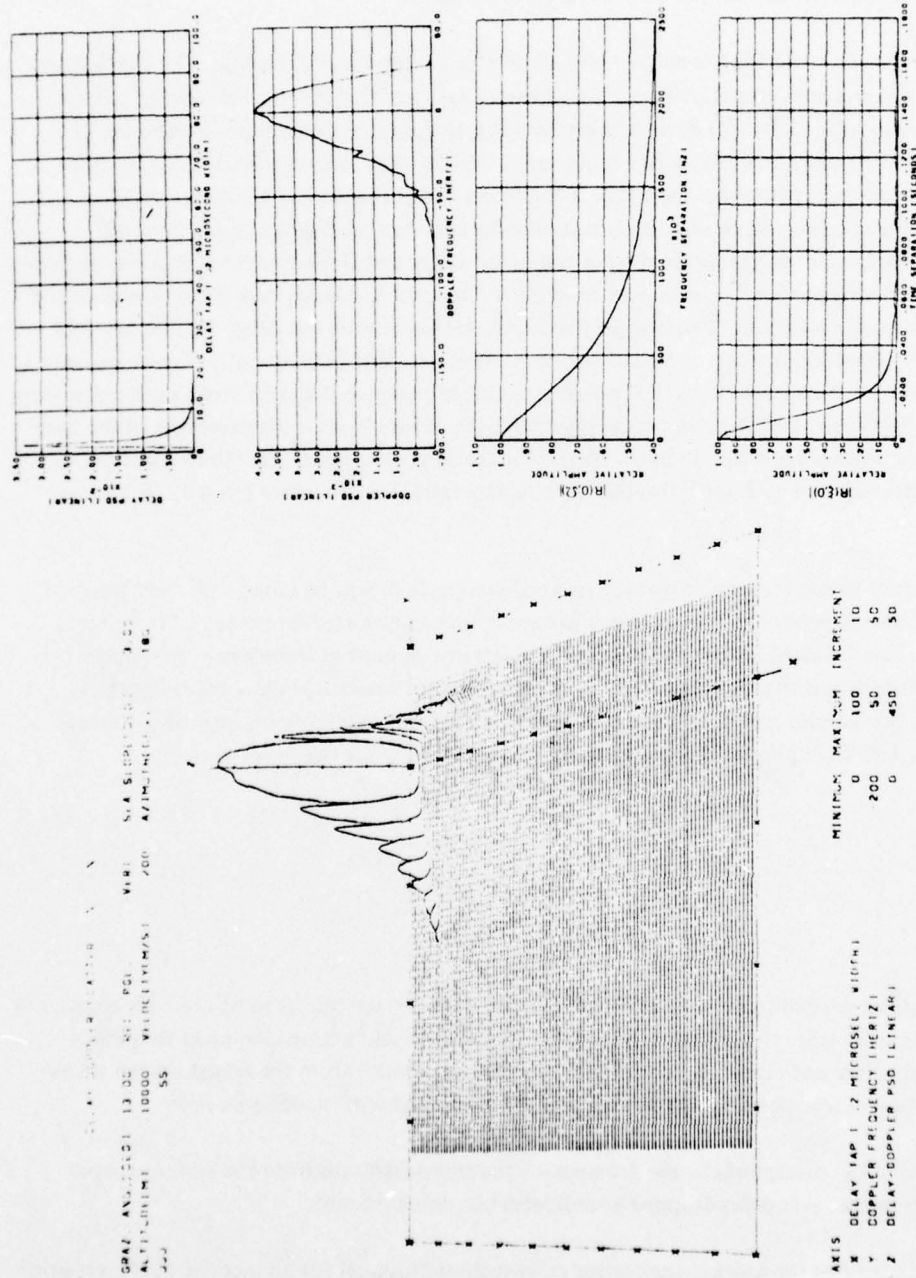


Figure 6-20. Model-Predicted Multipath Parameters — Vertical Polarization, 13° Grazing Angle, 3° Slope, In-Plane Geometry

the subaircraft side of the specular point whereas the positive-frequency component arises from scatters located toward the subsatellite side of the specular point.⁵

There are two reasons for the existence of these high-energy spectral humps. The first relates to the fact that for in-plane geometry the surface elements responsible for returning energy into the upper and lower Doppler limits of a particular tap lie along the great circle path joining the subaircraft and subsatellite points and thus have a much larger scatter cross section than any of the other elements that return energy into the delay tap. The second and perhaps more significant cause is a consequence of the relatively large area size (maximum for each tap) that gets mapped into the extremities of a particular tap's Doppler spectra due to the delay and Doppler contours in the surface having a tangential intersection.⁶ This occurs regardless of aircraft heading; however for any geometry other than in-plane, the locations of the tangential intersections between the delay contour and the extremities of the Doppler contours move off the great circle path and consequently do not possess as large a scatter cross section as other scatterers that are located closer to the great circle path and return energy into the delay tap. For the cross-plane geometry, the off-great-circle displacement of the tangential intersection areas is significantly large; thus as the sea slope decreases⁷ the relative amount of energy in the extremities of each tap's Doppler spectra decreases (e.g., compare figs 6-12, 6-13, and 6-14).

With respect to the Doppler frequency spectral humps, it should be noted that their position in the $S(\tau, \omega)$ realm depends only upon system geometry and transmitted frequency of the electromagnetic wave. The sea-surface rms slope controls the relative amount of energy in each spectral bin. An increase in slope is accompanied by a flow of energy from the low-delay tap numbers to the higher delays and from the interior region of a tap's Doppler spectrum to the exterior limits for the cross-plane geometry, with the opposite Doppler redistribution occurring for the in-plane case.

⁵These observations pertain to in-plane flights directly toward the satellite as in this test program. For in-plane flights away from the satellite, the roles of the positive and negative Doppler frequency realms discussed here and elsewhere would be reversed, since scatter from the region on the subaircraft side of the specular point would, in that case, be associated with positive Doppler.

⁶Mathematically, this corresponds to the Jacobian of the transformation from the surface spatial coordinates to the receiver delay-Doppler coordinates becoming infinite.

⁷The lower the sea slope the quicker the scatter cross section drops off for an increase in the off-great-circle location of a surface element.

For large-delay tap numbers, the behavior of the in-plane geometry spectral humps is of significant interest. In particular we note that for an increase in delay, the frequencies associated with the negative Doppler extremity increase whereas the positive maxima remain at a Doppler frequency that is essentially invariant. These features are readily explained in terms of the rate of change that the angle between vectors \bar{v} and \bar{n}_p of figure 6-2 undergoes for a change in scatter location along the great circle line joining the subaircraft and subsatellite points (i.e., the Doppler shift associated with reflection from a surface element is proportional to the cosine of the angle between velocity vector and reflected ray, which angle changes much more slowly in the subsatellite direction than in the subaircraft direction).

Finally it may be observed that under identical surface and geometrical conditions, the $S(\tau, \omega)$ functions for the horizontal and vertical polarization are in close accord. However, as was mentioned in section 5.1, we are able to discern that the relative weightings between the negative and positive Doppler returns are larger for the vertical polarization data than for their horizontal counterparts. This results from the fact that as the scatterers move toward the subaircraft location, their local elevation angles increase as opposed to a decrease for locations toward the subsatellite point. Hence for the grazing angles associated with the examples of this section, the negative-frequency returns (subaircraft direction) have a larger vertical-to-horizontal polarization reflection coefficient ratio than the positive-frequency returns. For specular-point grazing angles in the vicinity of the Brewster angle, this observation will of course no longer hold true.

6.3 INTEGRAL AND FOURIER OPERATIONS ON $S(\tau, \omega)$

Model predictions relating to the multipath channel's joint time-frequency autocorrelation function, delay spectra, frequency autocorrelation function, Doppler spectra, time autocorrelation function, and total rms scattered energy are derived through integral and Fourier operations on the model-generated $S(\tau, \omega)$ function (see sec 4.2 for the mathematical relationships). Results pertaining to these predictions are given in this section.

6.3.1 Joint Time-Frequency Autocorrelation Function: $R(\xi, \Omega)$

$R(\xi, \Omega)$ is related to $S(\tau, \omega)$ through a double inverse Fourier transform operation on the τ and ω variables; thus one domain influences the other via the well-known properties associated with the Fourier transform (e.g., an increase in spread of the τ variable results in a decrease in the Ω spread, etc.). Hence the overall grazing angle and slope dependencies of $R(\xi, \Omega)$ may be predicted from the previous discussion in section 6.2.

Correspondingly, we expect that $R(\xi, \Omega)$ is strongly dependent upon aircraft heading. To illustrate this dependence, $R(\xi, \Omega)$ distributions are given in figures 6-21 and 6-22 for the in-plane and cross-plane flight directions, respectively. Accompanying each $|R(\xi, \Omega)|$ example is the $S(\tau, \omega)$ function from which it was derived. These data were generated for a horizontal polarization probe at a grazing angle of 19° with an rms sea slope of 6° . For the in-plane geometry case, the $R(\xi, \Omega)$ function is given from two alternate points of view.

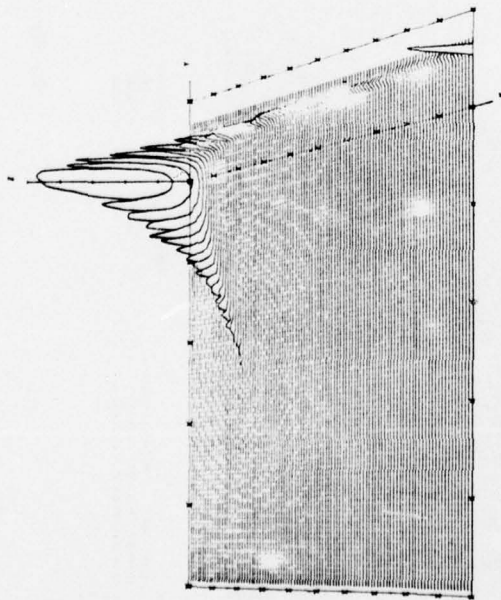
Perhaps one of the most obvious features of these two figures relates to the symmetry properties of the $R(\xi, \Omega)$ distribution with regard to the time-lag variable ξ , a direct result of the Doppler (ω) coordinate symmetry properties of the $S(\tau, \omega)$ counterparts. For both $R(\xi, \Omega)$ examples we see that, as expected, the function has peak value for the simultaneous zero time (ξ) and frequency (Ω) lags. In general $R(\xi, \Omega)$ decreases for an increase in either the ξ or Ω variables. This decrease is fairly monotonic for the cross-plane geometry yet we note a distinct oscillatory structure in the variable of the in-plane data example. Furthermore, for a given Ω , the oscillatory characteristic results in a local maximum that does not (except for $\Omega = 0$) coincide with the $\xi = 0$ axis. Rather, we observe that the ξ value corresponding to the local $R(\xi, \Omega)$ maximum is positive and systematically increases for an increase in Ω . For ξ values greater than the local maximum, the $R(\xi, \Omega)$ function has a precipitous dropoff to a level closely equivalent to its mirror-image value on the negative side of the axis. It may be shown that the local maximum shoulder associated with the in-plane $R(\xi, \Omega)$ distribution is a direct result of the negative Doppler (i.e., returns arriving from the subaircraft side of the specular point) shoulder of the $S(\tau, \omega)$ function. The positive Doppler shoulder, which in comparison with the negative shoulder quickly becomes asymptotic to the delay axis, gives rise to the symmetrical component contained in the $R(\xi, \Omega)$ in-plane distribution.

6.3.2 Delay Spectra

This parameter is obtained by integrating the model-generated $S(\tau, \omega)$ function over its Doppler variable. Delay spectra dependence upon the polarization, grazing angle, flight direction, and sea-slope parameters can be estimated by referring to the figures listed in table 6-2. Significant observations are listed below.

- a. The delay spectrum does not depend on the velocity vector of the airplane. The minute differences visible between the in-plane and cross-plane spectra (e.g., figs 6-3 and 6-9) result from differences in the surface integration parameters chosen for the two cases. The parameter JJJ contained in the computer printout heading of each figure is an indication of this.
- b. Sea-surface slope has a much greater influence on the delay spectrum than does the grazing angle parameter; the higher the sea slope, the heavier tailed the distribution becomes. In section 6-4, delay spread parameters are shown to have only a weak dependence upon

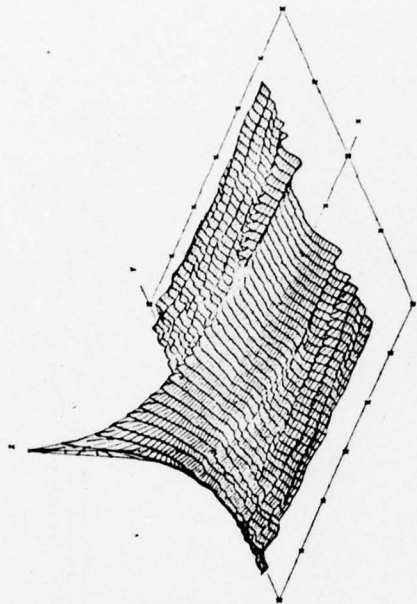
DELAY-DOPPLER SCATTER FUNCTION
 GRAZ. ANG (DEG) 18.00 REC. POL. HORIZ SEA SLOPE (DEG) 8.00
 ALTITUDE (M) 10000 VELOCITY (M/S) 200 AZIMUTH (DEG) 180
 JJJ



AXIS
 X DELAY TAP 1.2 MICROSEC. WIDTH (M)
 Y DOPPLER FREQUENCY INHERZ
 Z DELAY-DOPPLER PSD ILINARI

MINIMUM MAXIMUM INCREMENT
 X 0 100 10
 Y -500 100 100
 Z 0 1500 300

TIME-FREQUENCY AUTOCORRELATION FUNCTION
 GRAZ. ANG (DEG) 18.00 REC. POL. HORIZ SEA SLOPE (DEG) 8.00
 ALTITUDE (M) 10000 VELOCITY (M/S) 200 AZIMUTH (DEG) 180
 JJJ



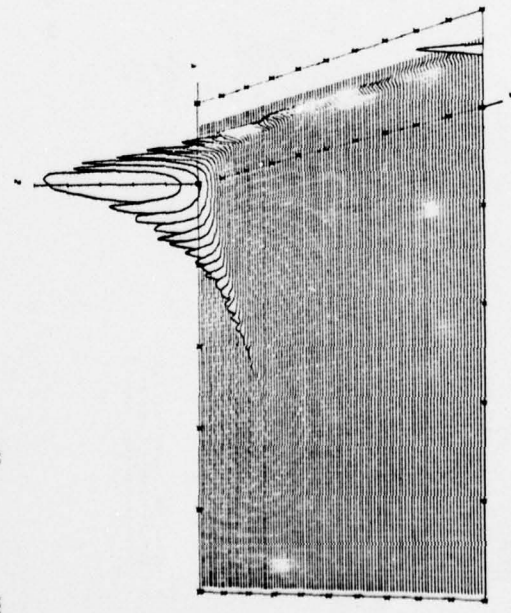
AXIS
 X FREQUENCY SEPARATION (KHZ)
 Y TIME SEPARATION (MILLISEC)
 Z TIME-FREQ AUTOCOR. FUNCTION (PWS)

MINIMUM MAXIMUM INCREMENT
 X 0 3000 300
 Y -100 100 50
 Z .00 1.00 1.0

(a) Left-Side View

Figure 6-21. Model-Predicted $R(\xi, \Omega)$ Distribution, In-Plane Geometry

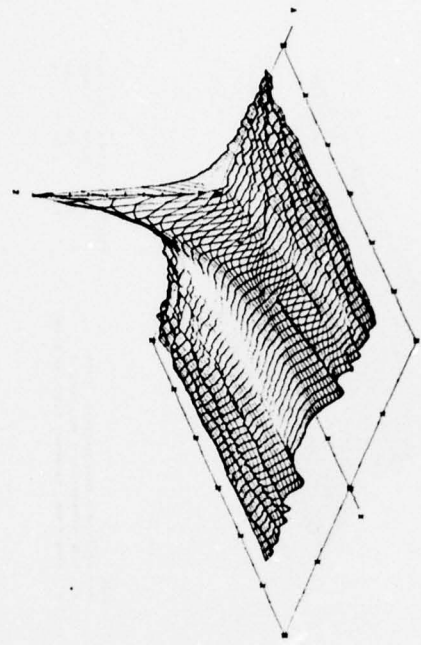
DELAY-DOPPLER SCATTER FUNCTION
 GRAZ. ANG. (DEG) 18.00 REC. POL. HORIZ. SEA SLOPE (DEG) 6.00
 ALTITUDE (M) 10000 VELOCITY (M/S) 200 AZIMUTH (DEG) 180
 JJJ 50



AXIS
 X DELAY TAP 1.2 MICROSEC. WIDTH
 Y DOPPLER FREQUENCY (HERTZ)
 Z DELAY-DOPPLER PSD (LINEAR)

MINIMUM MAXIMUM INCREMENT
 X 0 100 10
 Y -500 100 100
 Z 0 1500 300

TIME FREQUENCY AUTO CORRELATION FUNCTION
 GRAZ. ANG. (DEG) 18.00 REC. POL. HORIZ. SEA SLOPE (DEG) 6.00
 ALTITUDE (M) 10000 VELOCITY (M/S) 200 AZIMUTH (DEG) 180
 JJJ 50



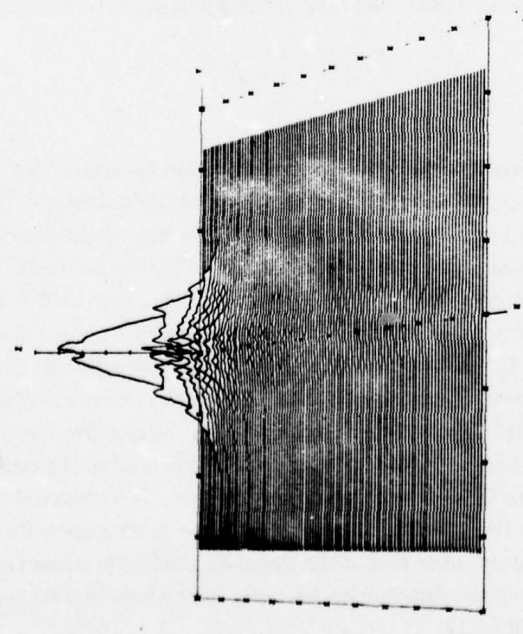
AXIS
 X FREQUENCY SEPARATION (KHZ)
 Y TIME SEPARATION (MILLISEC)
 Z TIME-FREQ AUTO CORRELATION FUNCTION (PWR)

MINIMUM MAXIMUM INCREMENT
 X 0 3000 500
 Y -100 100 50
 Z 0 1 00 10

(b) Right-Side View

Figure 6-21. (Concluded)

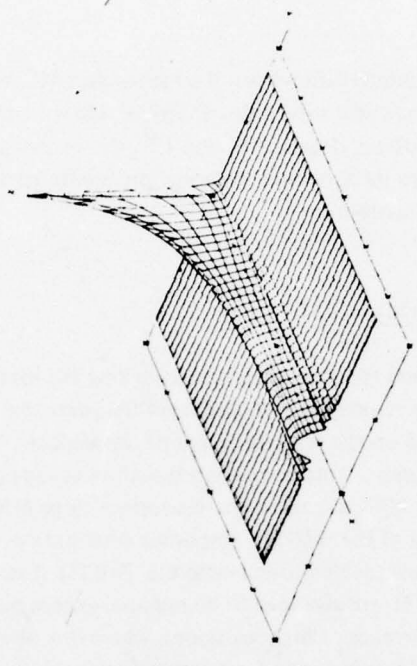
DELAY-DOPPLER SCATTER FUNCTION
 GRAZE ANG (DEG) 19.00 REC. PUL. HORIZ. SEA SLOPE (DEG) 9.00
 ALTITUDE (M) 18000 VELOCITY (M/S) 200 AZIMUTH (DEG) 90
 JJJ 76



AXIS
 X DELAY TAP 1 2 MICROSEC. #107M
 Y DOPPLER FREQUENCY (HERTZ)
 Z DELAY-DOPPLER PSD (LINEAR)

MINIMUM MAXIMUM INCREMENT
 0 100 10
 -400 400 100
 0 700 100

TIME FREQUENCY AUTOCORRELATION FUNCTION
 GRAZE ANG (DEG) 19.00 REC. PUL. HORIZ. SEA SLOPE (DEG) 9.00
 ALTITUDE (M) 18000 VELOCITY (M/S) 200 AZIMUTH (DEG) 90
 JJJ 76



AXIS
 X FREQUENCY SEPARATION (KHZ)
 Y TIME SEPARATION (MILLISEC)
 Z TIME-FREQ. AUTOCOR. FUNCTION (PARE)

MINIMUM MAXIMUM INCREMENT
 0 2000 500
 -100 100 50
 00 1.00 .10

Figure 6-22. Model-Predicted $R(\xi, \Omega)$ Distribution, Cross-Plane Geometry

grazing angles and almost no dependence for angles above 15° in conjunction with low-to-moderate sea slopes.

- c. Apart from the relative magnitude differences, the high-angle (31°) vertical and horizontal polarization delay spectra have very similar distributions. On the other hand, the low-angle data (13°), coupled with sea slopes of 6° and 12° , shows a vertical polarization spectrum which, compared to its horizontal polarization counterpart, is visibly more dense in the interior region of its distribution.

6.3.3 Frequency Autocorrelation Function: $R(0, \Omega)$

Since the frequency autocorrelation function is derived by taking the inverse Fourier transform of the delay spectrum, many of its attributes may be deduced from the preceding discussion. First, we observe that $R(0, \Omega)$ does not depend on the velocity vector of the airplane. Also, since the delay spectrum is everywhere positive, the frequency autocorrelation function, as expected, has maximum amplitude for the 0-Hz separation value. With respect to the sea-surface slope effects, it is noted that a decrease in slope results in a broadening of the $R(0, \Omega)$ amplitude distribution. In contrast, the grazing angle dependence produces no appreciable difference in the $R(0, \Omega)$ distributions for the cases illustrated. Polarization effects on $R(0, \Omega)$ are also seen to be minimal except perhaps for the low-grazing-angle cases coupled with the occurrence of high sea slopes, where it is observed that the horizontal polarization distributions are heavier tailed than their vertical polarization counterparts.

6.3.4 Doppler Spectrum

Compared with the other multipath channel unidimensional measures considered, the Doppler spectrum shows, by far, the greatest dependency upon grazing angle and flight direction system parameters. It is also influenced significantly by the sea-surface rms slope and has a slight dependence upon the polarization of the incident electromagnetic wave. Referring to the figures delineated in table 6-2 we observe that for cross-plane flight geometries the Doppler spectrum has a distribution that closely resembles zero mean Gaussian, with variance increasing in a linear fashion with an increase in rms sea slope. These characteristics, especially for the larger sea slopes, are distinctly different from those associated with the in-plane flight geometry. In general, the Doppler spectra of the in-plane flight cases are highly asymmetric, with the distribution being heavy tailed in the negative-frequency realm and possessing a spectral maximum that coincides with a frequency upper limit in the positive realm. Above this maximum the energy density falls off in a precipitous manner. It is observed that these attributes become more pronounced as the sea slope increases and as the grazing angle decreases (i.e., compare figs 6-3, -5, -6, and -8). In fact, we note that as the opposite conditions occur (low slopes coupled with high grazing angle), the in-plane distribution becomes increasingly similar to its cross-plane counterpart (compare figs 6-5 and 6-11).

The dependence of the in-plane Doppler spectra upon the sea-slope parameter is of particular interest. For an increase in slope we observe⁸ that energy near the 0-Hz center of the function is dispersed toward the extremities of the distribution, with the manner of redistribution being markedly different for the negative and positive halves of the spectrum. The positive realm is seen to become increasingly peaked, with the peak shifting toward the high-frequency cutoff of the spectrum; the spectra density in the negative-frequency region becomes more and more dispersed with the falloff resembling an exponential decay. As discussed in section 6.2, the behavior of the in-plane Doppler spectra's peak distribution and sharp high-frequency cutoff is a direct result of the asymptotic behavior of the positive-frequency shoulder of the $S(\tau, \omega)$ function.

With respect to the polarization characteristics of the Doppler spectrum, we note that for high grazing angles and low slopes the vertical and horizontal polarization data are in close agreement. For the low-grazing-angle and high-slope conditions, the vertically polarized spectrum is seen to have a much higher percentage of energy in the negative portion of the distribution than does the corresponding horizontal data. The phenomenon that produces this observation was discussed previously in section 6.2.

6.3.5 Time Autocorrelation Function: $R(\xi, 0)$

Even though the channel's time autocorrelation function is related to the Doppler spectrum by way of the Fourier transform, we observe that its distribution has the same general shape for both choices of aircraft heading. However, for the large sea slopes the in-plane $(R\xi, 0)$ function decays considerably slower than the cross-plane distribution. This feature is a result of the very peaked maximum that the high-slope in-plane Doppler distributions possess. In general a systematic increase in the dispersion of $R(\xi, 0)$ is associated with a decrease in the sea-surface slope and a decrease in the grazing angle. Also, as one would expect from the Doppler spectra observations, the horizontal and vertical polarization $R(\xi, 0)$ results are fairly similar except for the low-angle high-slope condition, where the horizontal polarization function exhibits a much slower decay than its vertical polarization counterpart.

6.3.6 Total RMS Scattered Energy

Model predictions of the sea surface's total scattered energy as received over the satellite-to-airplane link are presented in figure 6-23. This data has been normalized relative to the energy received over the direct line-of-sight path, which for geostationary satellite altitudes is closely equivalent to a

⁸Note that the Doppler shift associated with reflection off a surface element is proportional to the cosine of the angle between the incident and reflected rays.

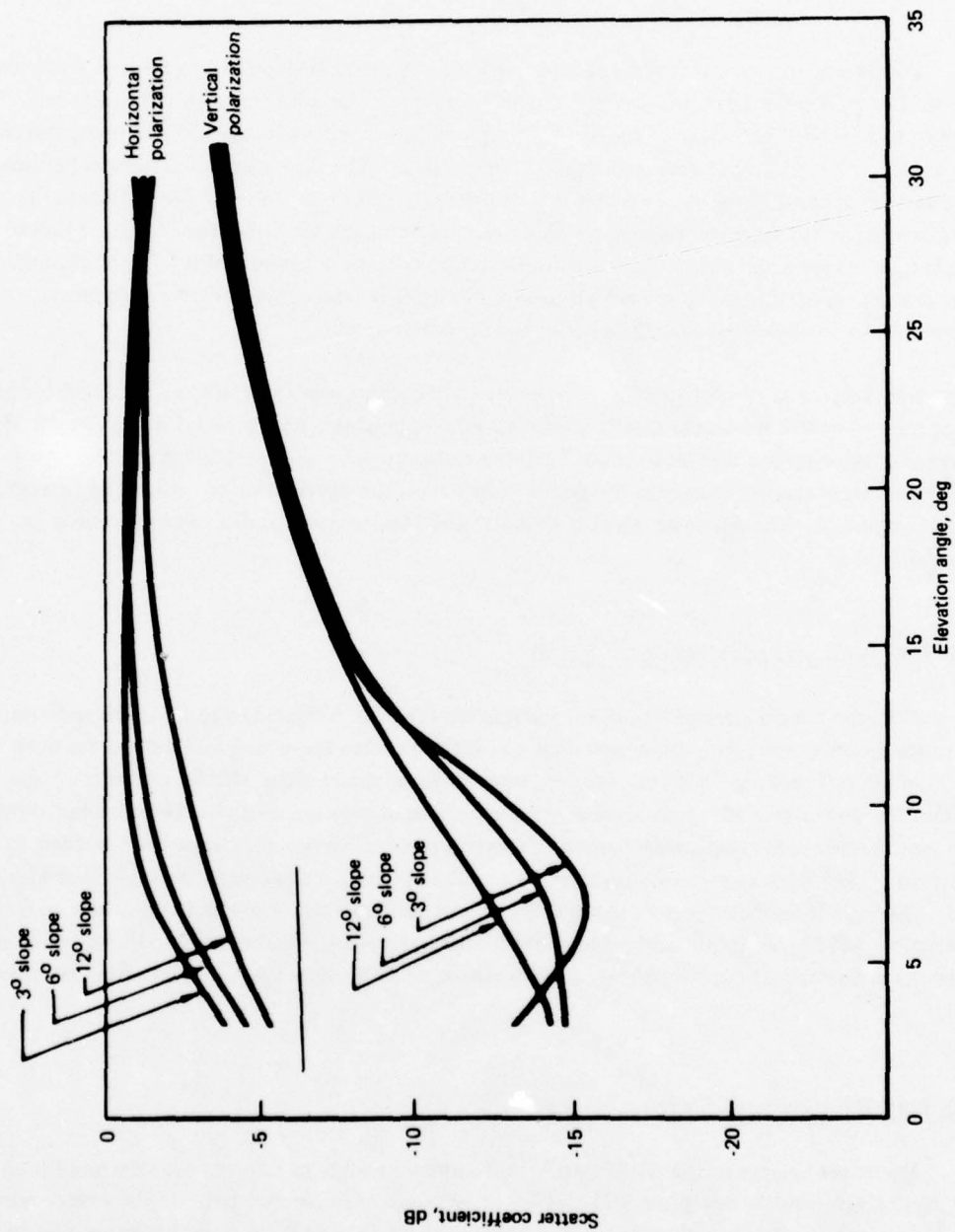


Figure 6-23. Model-Predicted Oceanic Scatter Coefficients

normalization with respect to the energy incident upon the surface. Important features pertaining to the scatter coefficients are listed below.

- a. Sea slope has a very minor effect on the higher grazing angle ($\geq 10^\circ$) data.
- b. For the low-grazing-angle results, we note that the vertical polarization coefficients tend to increase with an increase in sea slope whereas the opposite dependence holds true for the horizontal polarization results. This behavior results from a combination of (1) an increased "active" scatter area for the larger surface slopes, coupled with (2) an effective depolarization of the incident electromagnetic wave, which increases as the scatterer moves further from the specular point. For example, with respect to the individual "tilted" flat surfaces that favorably reflect energy into the receiver, the vertical polarization probe will in fact have a polarization vector that contains a horizontal component and is reflected with less loss than the vertical component. Other reasons include (3) the fact that at the lower grazing angles in the vicinity of the Brewster angle ($\sim 7^\circ$) the vertical and horizontal reflection coefficients are substantially different from their higher angle counterparts, and (4) the "Brewster angle fill-in" effect, which has been discussed previously in section 5.6.2.
- c. The lower the sea slope the closer the scatter coefficient approaches the classical Fresnel smooth flat-earth reflection coefficient result as modified by the spherical-earth divergence factor.

6.4 SPREAD VALUE PREDICTIONS

Model-predicted spread values for the multipath channel's delay spectra, frequency autocorrelation function, Doppler spectra, and time autocorrelation function are presented in this section. Definitions pertaining to the spread parameter measures given in section 5.3 apply to the model predictions. In addition, we present the delay spectra's second moment relative to the specular-point return. This measure is calculated as:

$$\sigma_{Q(\tau)} = \left\{ \frac{\sum_{\tau} (\tau - \tau_{SP})^2 Q(\tau)}{\sum_{\tau} Q(\tau)} \right\}^{1/2} \quad (6-15)$$

where:

- $\sigma_{Q(\tau)}$ = delay spectra's second moment with respect to specular delay
- τ_{SP} = specular tap
- $Q(\tau)$ = mean square energy at output of delay tap.

Spread value results are presented graphically as a function of grazing angle (3° to 31°) for sea slopes of 3° , 6° , and 12° in figures 6-24 through 6-34. Refer to table 6-3 to obtain the correspondence between figure number, spread measure, probe polarization, and aircraft heading. Observations pertaining to the spread measure characteristics are summarized below.

TABLE 6-3. MODEL-PREDICTED SPREAD PARAMETERS: FIGURE REFERENCE

Parameter	Spread measure	Polarization	Heading	Figure
Delay	3 dB 10 dB	Horizontal	a	6-24
Delay	3 dB 10 dB	Vertical	a	6-25
Delay	$\sigma_{Q(\tau)}$	Horizontal	a	6-26
Delay	$\sigma_{Q(\tau)}$	Vertical	a	6-27
Coherence bandwidth	3 dB	Horizontal and Vertical	a	6-28
Doppler	3 dB 10 dB	Horizontal	In-plane	6-29
Doppler	3 dB 10 dB	Vertical	In-plane	6-30
Doppler	3 dB 10 dB	Horizontal	Cross-plane	6-31
Decorrelation time	3 dB	Horizontal	In-plane	6-32
Decorrelation time	3 dB	Vertical	In-plane	6-33
Decorrelation time	3 dB	Horizontal	Cross-plane	6-34

^aDelay spectra not a function of heading.

6.4.1 Delay Spread

Delay spread results are presented in figures 6-24 through 6-27.

- a. Aircraft heading has no effect on parameters associated with the delay spectrum.
- b. For horizontal polarization and low-to-modest sea slopes (i.e., up to 6°), the 3- and 10-dB delay spreads are relatively uninfluenced by the grazing angle parameter. The vertical

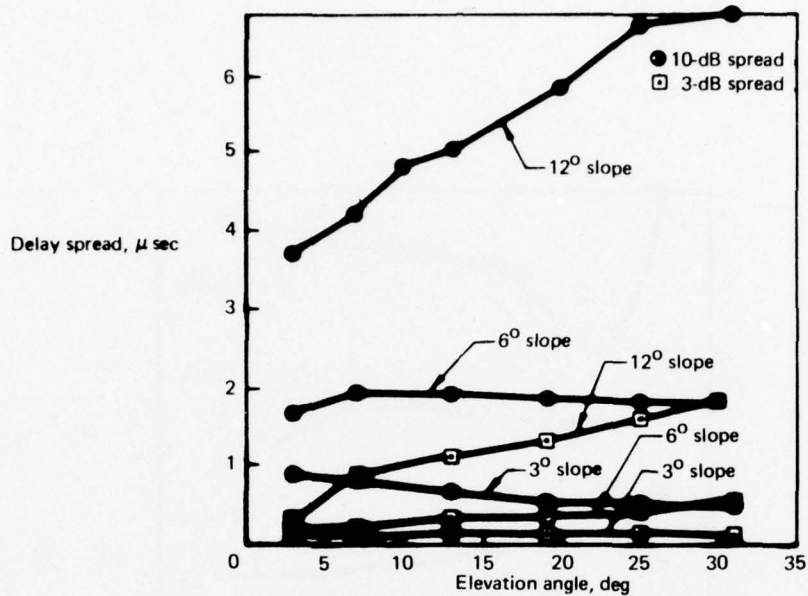


Figure 6-24. Model-Predicted Delay Spread — Horizontal Polarization

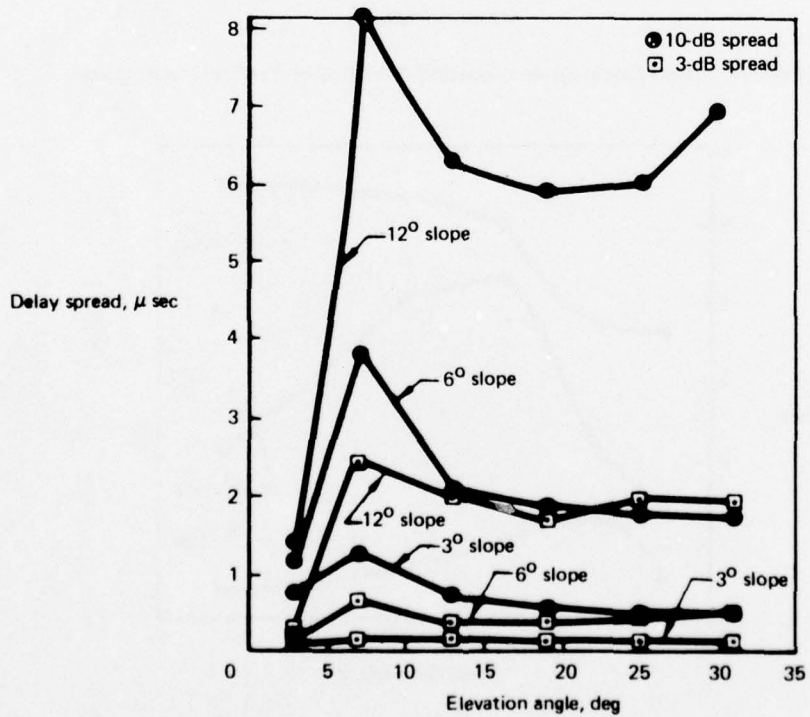


Figure 6-25. Model-Predicted Delay Spread — Vertical Polarization

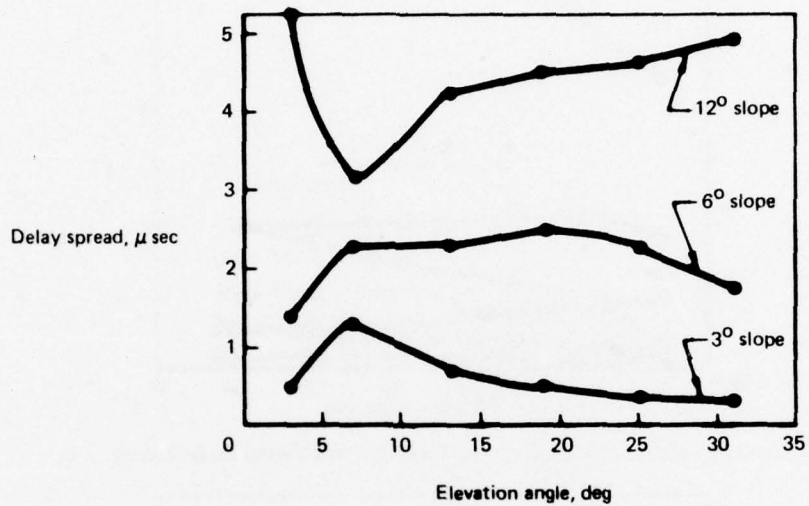


Figure 6-26. Model-Predicted Delay Spread (Second Moment) — Vertical Polarization

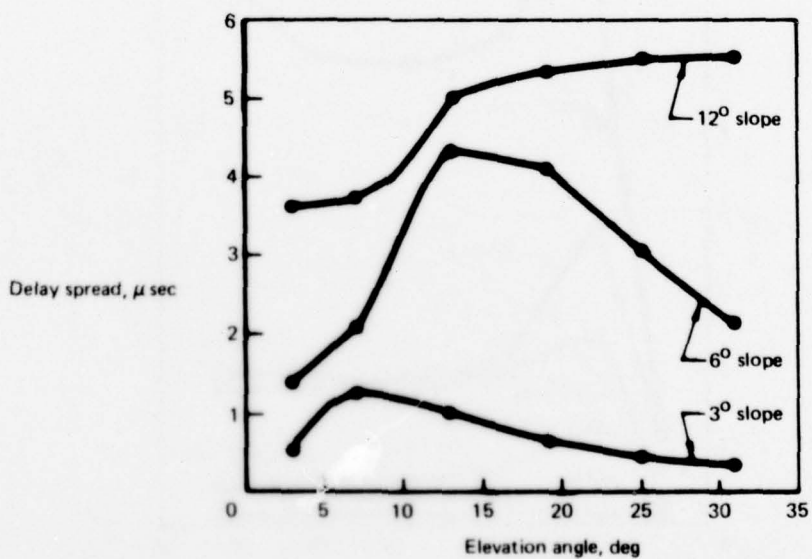


Figure 6-27. Model-Predicted Delay Spread (Second Moment) — Horizontal Polarization

polarization data for these slopes is characterized by a local maximum in the vicinity of the Brewster angle; otherwise it also has a relatively flat grazing angle dependence.

- c. For the larger slopes, the delay spreads tend to increase with grazing angle; the dependency is relatively strong for grazing angles below approximately 15° and quite weak thereafter.
- d. The similarity between the vertical and horizontal spreads is seen to increase with an increase in grazing angle and a decrease in sea slope; for the lower grazing angle and higher slopes, the vertical polarization data in general has the larger 3- and 10-dB spread value.
- e. The $\sigma_{Q(\tau)}$ spread values have the same order of magnitude as the 10-dB spreads; however, as opposed to the above observation, we note that the horizontally polarized second-moment spread is generally larger than its vertical polarization counterpart.
- f. All spread measures (3-dB, 10-dB, and $\sigma_{Q(\tau)}$) are observed to increase with an increase in rms surface slope; the functional form of the increase, however, does not appear to be systematic.

6.4.2 Coherence Bandwidth

Figure 6-28 illustrates model results for the coherence bandwidth.

- a. For the higher sea slopes, model results indicate that the 3-dB coherence bandwidth has a very weak dependence upon grazing angle, whereas the 3° sea slope yields 3-dB coherence bandwidth that increases rather sharply for an increase in grazing angle. This result is somewhat in opposition to that obtained for the delay spread parameter.
- b. In general, the horizontal and vertical polarization data are in fairly close accord.
- c. Coherence bandwidth decreases with an increase in sea slope.
- d. For the 12° sea-slope case, a 3-dB coherence bandwidth of roughly 85 kHz appears to be typical for grazing angles lying between 3° and 31° ; the 6° slope data yields 3-dB coherence bandwidths ranging from roughly 200 to 275 kHz, with the higher values being associated with the larger grazing angles.

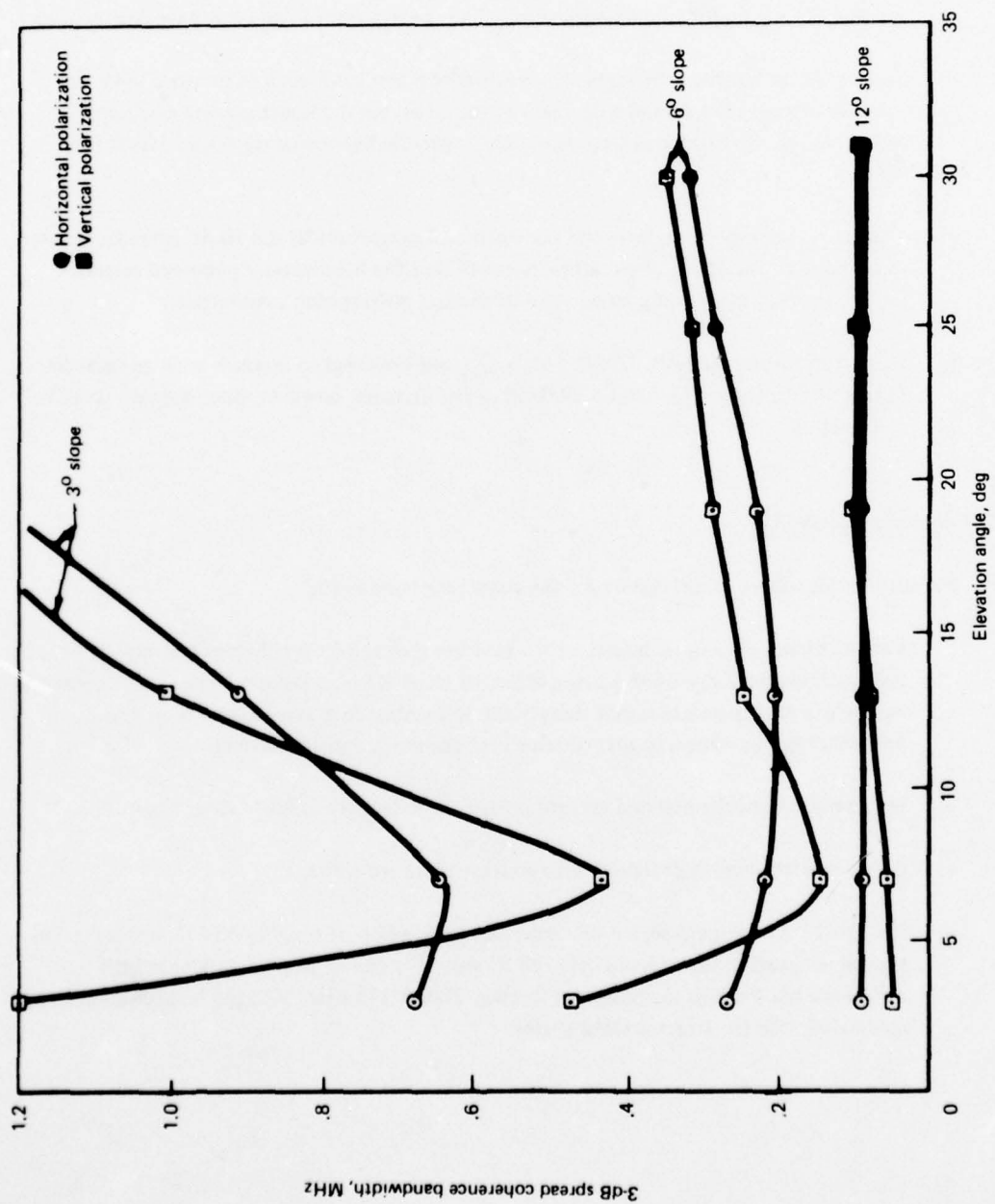


Figure 6-28. Model-Predicted 3-dB Coherence Bandwidth

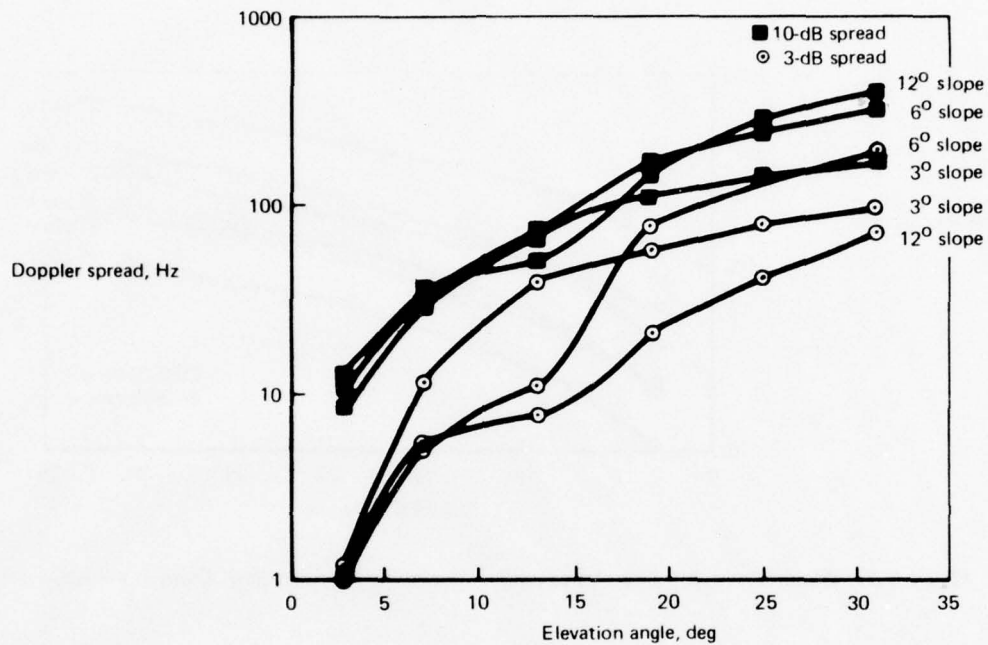


Figure 6-29. Model-Predicted Doppler Spread — Horizontal Polarization, In-Plane Geometry

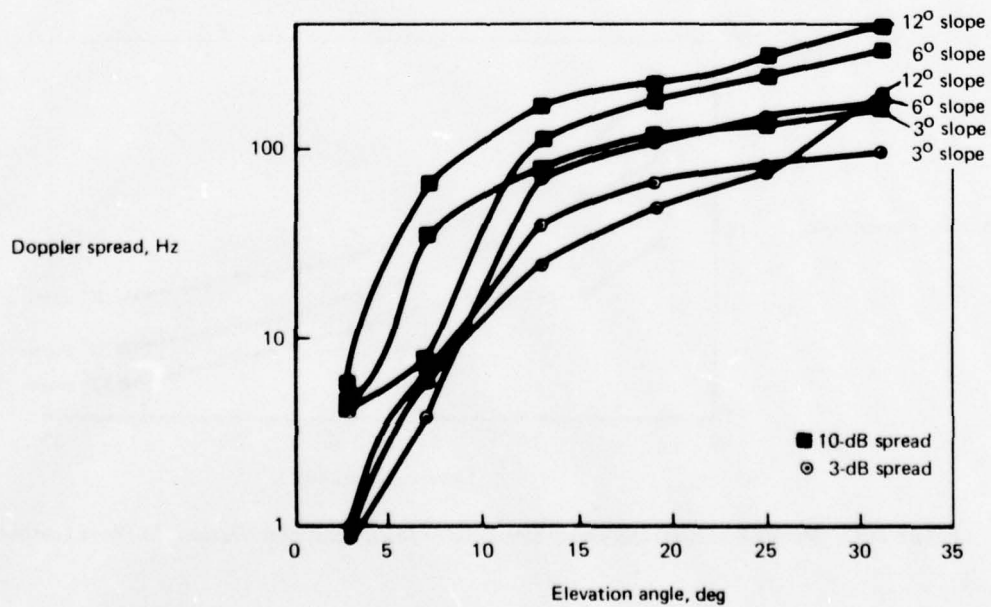


Figure 6-30. Model-Predicted Doppler Spread — Vertical Polarization, In-Plane Geometry

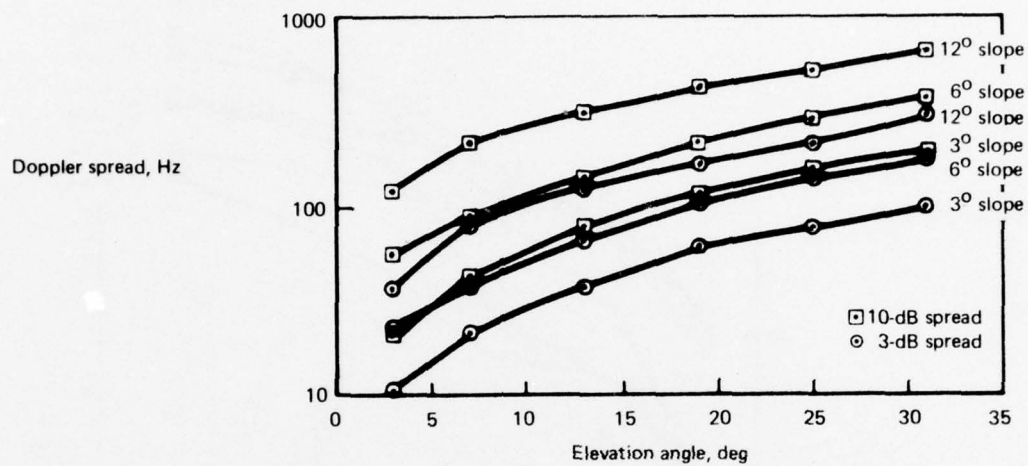


Figure 6-31. Model-Predicted Doppler Spread — Horizontal Polarization, Cross-Plane Geometry

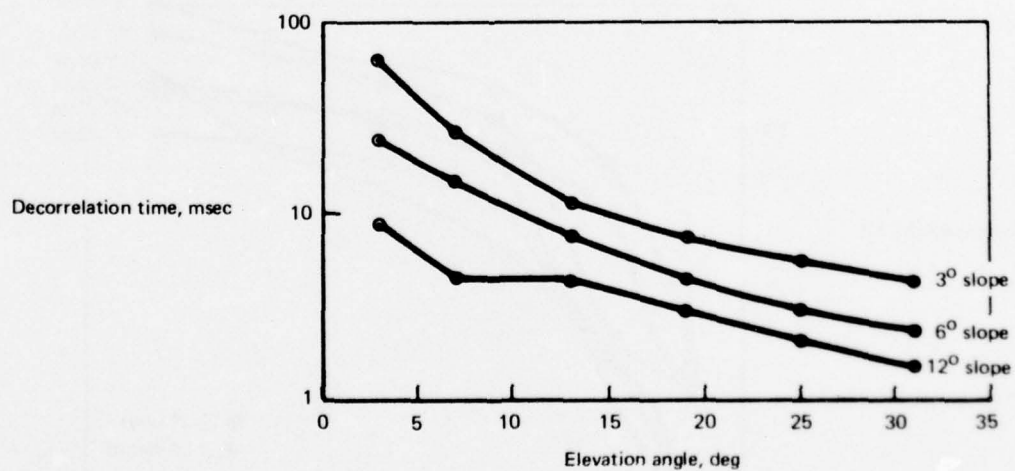


Figure 6-32. Model-Predicted Decorrelation Time — Horizontal Polarization, In-Plane Geometry

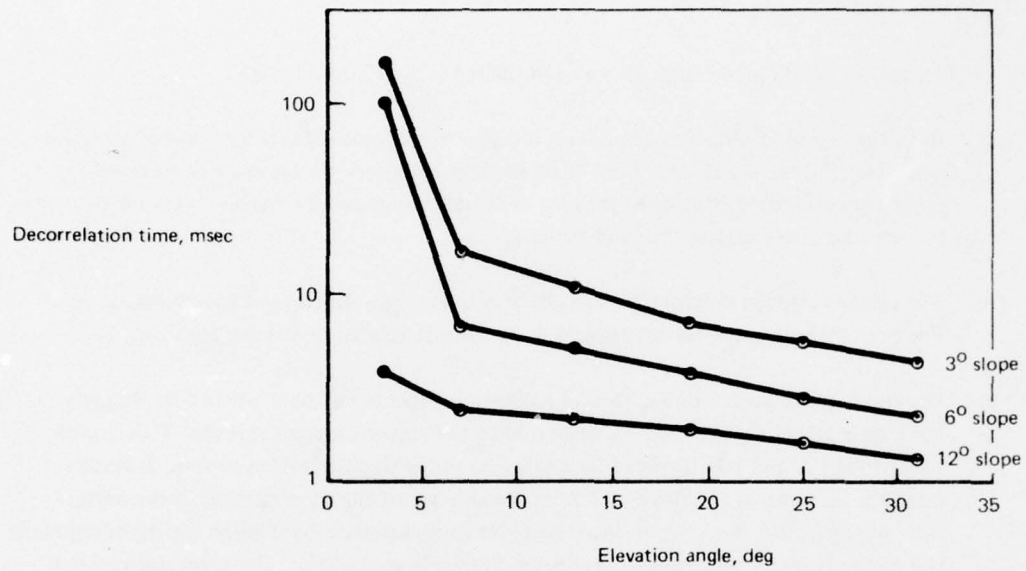


Figure 6-33. Model-Predicted Decorrelation Time — Vertical Polarization, In-Plane Geometry

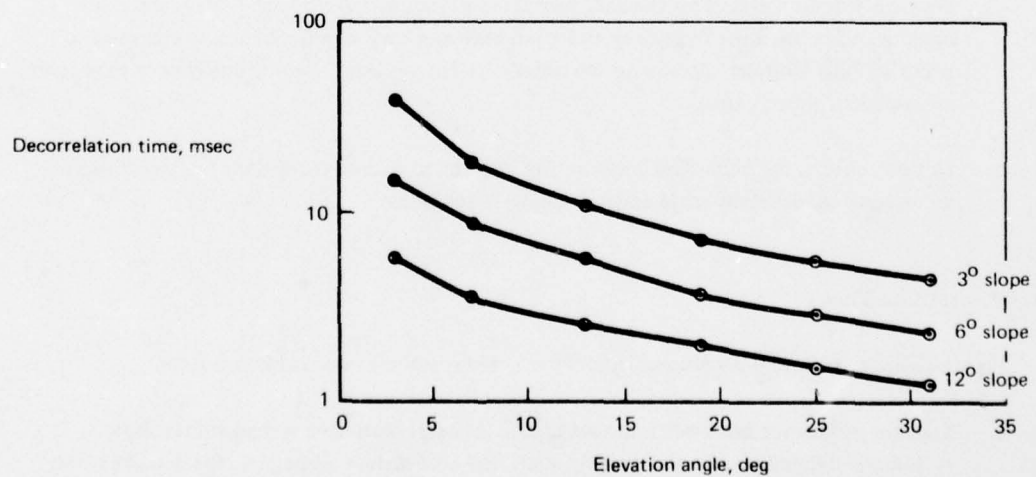


Figure 6-34. Model-Predicted Decorrelation Time — Horizontal Polarization, Cross-Plane Geometry

6.4.3 Doppler Spread

Doppler spread model predictions are given in figures 6-29, 6-30, and 6-31.

- a. Both the 3- and 10-dB spread measures increase monotonically as a function of elevation angle for all three sea slopes. For the cross-plane geometry this increase is, to close approximation, proportional to the sine of the elevation angle, whereas a very nonsystematic behavior characterizes the in-plane data.
- b. The spreads associated with the cross-plane data increase with an increase in sea slope. For both measures, the spread appears to be linearly related to the surface slope.
- c. For the in-plane geometry we observe a rather unexpected slope dependency. Namely, the largest slopes do not always correspond to the largest Doppler spreads. This occurs for both the 3- and 10-dB spread measures and for both polarization modes. It results from the fact that as the slope increases, the amount of energy contained in the asymptotic region of the $S(\tau, \omega)$'s positive shoulder increases, thereby causing the high-frequency end of the Doppler spectrum to become increasingly peaked (i.e., the asymptotic region is mapped into a single Doppler location). On the other hand, the increase in slope will cause an increase in dispersion associated with the other regions of the spectrum. Thus for the in-plane flight direction 3- and 10-dB Doppler spread measures we have a tradeoff between two factors that have an opposite slope dependence spread effect. These effects are visibly demonstrated by the data presented in figures 6-6 through 6-8. For the low grazing angles, the high-frequency end peak becomes very significant and is observed to result in 3-dB Doppler spreads on the order of 1 Hz (about 10 to 40 times lower than their cross-plane counterparts).
- d. Doppler spread dissimilarities between the in-plane and cross-plane data sets decrease for an increase in elevation angle and a decrease in sea slope.

6.4.4 Decorrelation Time

Figures 6-32, 6-33, and 6-34 present model-predicted results for decorrelation time.

- a. Like the coherence bandwidth measures, the decorrelation time spread values show systematic dependencies upon grazing angle and rms surface slope, i.e., the decorrelation times monotonically decrease for an increase in either the slope or grazing angle.
- b. The grazing angle dependence appears to follow a \sin^{-1} (grazing angle) relationship, especially for the cross-plane flight geometry cases.

- c. For most of the grazing angles, decorrelation time decreases approximately linearly with an increase in sea slope.
- d. Aircraft heading mildly influences decorrelation time, with the in-plane data having slightly larger decorrelation times than the cross-plane data (particularly for the large sea-slope conditions).
- e. In general the vertical and horizontal polarization results are in close agreement; however, we do note that for the 6° and 12° slope cases the vertical polarization data tends to have a slightly lower decorrelation time than the horizontal equivalent (with the exception of the 3° grazing angle condition coupled with the 6° surface slope).
- f. Decorrelation time difference between the in-plane and cross-plane cases tends to decrease for an increase in grazing angle and a decrease in sea slope.

6.5 SEA-STATE DATA

In the propagation of signals between satellite and aircraft, unwanted multipath energy is scattered from the ocean surface. To fully understand this scattering mechanism, a basic knowledge of the interaction between the surface characteristics and the electromagnetic signal must be obtained. In this section, a description is given of sea-state measurements and their analysis. This measurement program was carried out in conjunction with the aeronautical tests to provide a source of fundamental data that could be correlated with the measured link scattering properties.

The basic instrumentation was comprised of three-axis accelerometers, roll and pitch gyros, and a magnetic compass, all mounted on a wave-following buoy. Damping was provided so that the buoy responded to wave motion in the same way that an equivalent volume of water would. The roll and pitch gyros provide data concerning wave-slope distributions, while the accelerometer outputs may be processed to yield spectral attributes of the ocean surface. Because of its size, the buoy responds only to wave lengths greater than a meter or so. To allow measurement of the properties of smaller waves, the buoy was fitted with an array of 10 wave staffs to sense small-scale undulations directly.

Analysis of data collected from these sensors provides information on the ocean properties relevant to the scattering of electromagnetic waves. In addition to the validation of postulated models, valuable insight is gained to provide a basis for either extending the models to be more accurate or simplifying them to the point where elementary descriptors, such as windspeed, may be used to estimate scattering properties.

6.5.1 Outline of the Model

Leading into a discussion of the coupling between sea-state observables and multipath scattering, a brief description of oceanic wave motion is given.

6.5.1.1 Tutorial Discussion of Wave Motion – The ocean surface can be described and classified in a variety of ways. The most complete description of current surface scatter models for the ocean consists of the joint probability density function of wave slopes along two orthogonal axes $p_{11}(z_x, z_y)$, the probability density function of wave height $p_0(z)$, and the power spectral density of the small-scale surface heights $S_{00}(k_x, k_y)$ ⁹. Other important parameters, some of which can be derived from the above functions, are the rms wave height, the rms wave slope (omnidirectionality assumed), and the windspeed and wind direction.

The above functions and parameters derive from a mathematical model for the mean surface, to which reference is also required for the breakdown and interpretation of sea-state data. Most generally, the wave surface is represented as a three-dimensional function, $\eta(x, y, t)$, which is taken to be a random process in space and time. The process can be advantageously viewed as an infinite sum of propagating sinusoidal waves with random coefficients. The sinusoidal dependence of each term has the form:

$$\cos(\omega t - \vec{k} \cdot \vec{r} + \epsilon), \quad (6-16)$$

where:

- ω = angular frequency (radians per second)
- \vec{k} = vector wave number (radians per meter), with components k_x and k_y in the x and y directions, respectively
- \vec{r} = surface position vector with components x and y
- ϵ = an arbitrary phase angle.

The dot product in equation (6-16) is given by

$$\vec{k} \cdot \vec{r} = k_x x + k_y y. \quad (6-17)$$

⁹A complete discussion of these functions and their relationships to multipath effects is given in (ref. 5-5).

One of the most important means of classifying ocean waves derives from the nature of the oscillating behavior content in equation (6-17). The descriptive parameters are the temporal angular frequency ω and the spatial angular frequency $|\vec{k}|$ in the direction of \vec{r} . An illustration of this type of classification is provided in figure 6-35. The wavelength referred to in figure 6-35 is (ref 6-7) that obtained by writing the magnitude of \vec{k} in the form

$$|\vec{k}| = \frac{2\pi}{\ell} \quad (6-18)$$

In this expression, ℓ is the exact analog of wavelength in electromagnetic theory. The terminology "infragravity waves", "long period waves", etc. used in figure 6-35 refers to the mechanism whereby the wave is generated and sustained or, in an obvious way, refers to the scale length ℓ .

For gravity waves, the aforementioned constraint between temporal and spatial frequency is provided by the dispersion relation

$$\omega^2 = |\vec{k}| g, \quad (6-19)$$

where g is the constant acceleration due to gravity (9.8 m/sec^2). In terms of the wavelength ℓ and the temporal period T , this relation can be written in the form

$$\ell = \frac{g}{2\pi} T^2. \quad (6-20)$$

For the interpretation of experimental data, these two relations provide insights into the relation between the temporal and spatial behavior of the ocean surface.

6.5.1.2 Relationship of Sea-State Data to Multipath Scattering — As discussed in reference 5-5 and by DeRosa in reference 5-4, the scattering cross section for the ocean surface can be represented in terms of the joint probability density function of the wave slopes along two orthogonal axes $p_{11}(z_x, z_y)$. Once the cross section is known, the delay-Doppler scatter function, $S(\tau, \omega)$, can be determined along with all of the lower echelon parameters such as rms multipath spread, Doppler spread, coherence bandwidths of the channel, etc. Thus, all the important parameters required to characterize the multipath channel are derivable from the joint pdf $p_{11}(z_x, z_y)$. There is a sound physical interpretation of this function's role in the scattering process; the multitude of wave surfaces provide opportunities, in any spatial region, for the correct alignment of a surface at the mirror angle between the aircraft and the satellite. Scattering regions more widely separated from the specular path require steeper wave slopes to achieve the correct facet alignment, and the fact that this is less likely to occur for regions widely

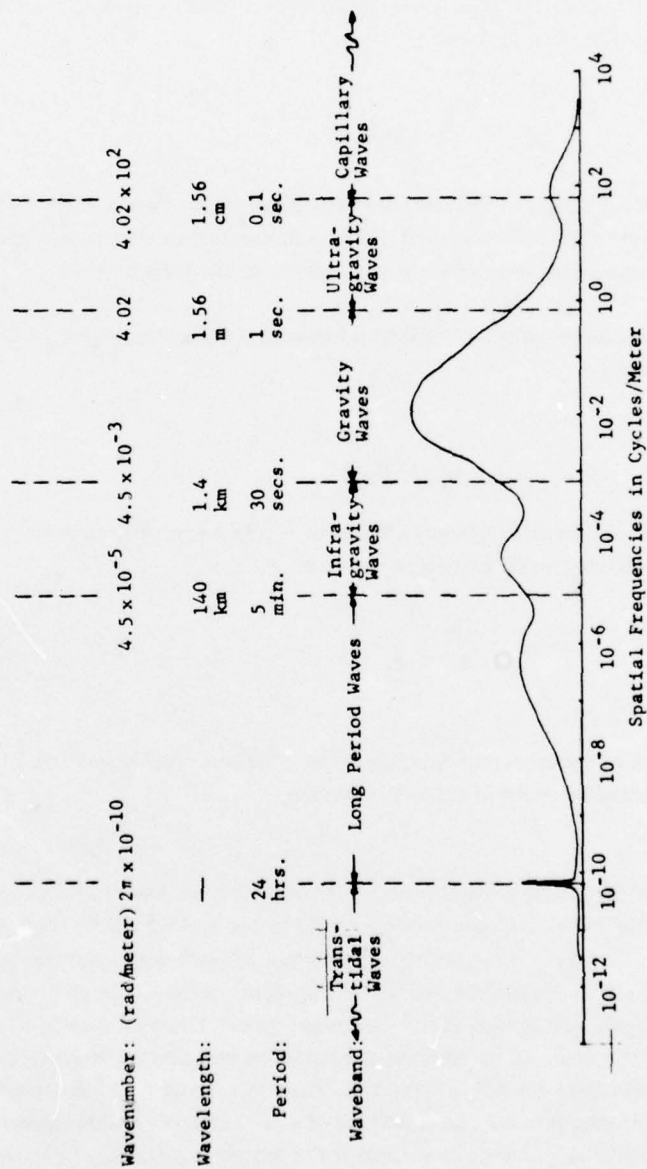


Figure 6-35. Schematic Representation of Ocean Surface Power Spectral Density

separated from the specular path than for paths near specular can be described in a quantitative way with the use of a waveslope pdf.

In addition to their representation in terms of $p_{11}(z_x, z_y)$, the channel parameters and subsidiary functions (delay and Doppler power spectral densities) can be represented directly in terms of σ_{slope} , the rms fluctuations of the surface slope. This kind of representation is achieved via the assumption of a specific form (e.g., joint Gaussian) for the slope density and the method of "steepest descent," which provides a satisfactory solution for most aeronautical satellite applications. As examples we point out the explicit relation between 3-dB Doppler spread presented in this report and Bello's representation of the delay power spectral density as a function of σ_{slope} and geometric parameters (ref 5-1).

It should be pointed out that the availability of experimental joint pdf's for wave slope allows a direct comparison of model calculations using measured pdf's and model calculations using a joint Gaussian pdf parameterized appropriately with the measured value of σ_{slope} .

The prediction of multipath effects in operational systems would be greatly facilitated if one could make predictions based solely on standard oceanic observables such as wind velocity and/or wave height. Usefulness of such an approach currently hinges on the validity of relationships such as those presented in reference 6-8 (p. 16) which have been called from other references (refs. 5-12 and 6-9). From reference 6-9 we have a functional relationship between the rms wave height, σ_h , and the windspeed, V , given by

$$\sigma_h = 0.00455 V^2, \quad (6-21)$$

with σ_h given in ft and V in knots. From reference 5-12 we have the relation between rms wave slope, σ_{slope} , and windspeed V :

$$\sigma_{\text{slope}} = 0.1 (a + b V)^{1/2}, \quad (6-22)$$

where a and b are constants that depend on whether the slope is in the upwind direction, the crosswind direction, or is omnidirectional. Specifically, the coefficients are

Upwind:	$a = 0, b = 0.163$
Crosswind:	$a = 0.3, b = 0.099$
Total:	$a = 0.3, b = 0.264$

Again, V is in knots¹⁰ and the slope parameter σ is dimensionless.

Combining the two relations above, one obtains a velocity-independent relation between the rms wave height and rms slope:

$$\sigma_h = 0.00455 \left(\frac{100\sigma_{\text{slope}}^2 - a}{b} \right)^2 \quad (6-23)$$

The objectives of the sea-state data reduction effort are seen then primarily in terms of the derivation of experimental slope distributions and wave-number spectra, along with the correlation of slope data with observed windspeed and sea conditions.

6.5.2 Sea-State Data Reduction

The sea-state measurement periods generally covered periods of 40 min of buoy deployment. Altogether, seven different data segments are available, some corresponding to days on which the aircraft was flown in the multipath tests. However, on these occasions there was a time differential between the two sets of measurements of approximately 5 hr, so it would be unwise to expect very close predictions of actual scattering conditions from the sea-state data.

Table 6-4 lists the data segments processed and includes all relevant parameters. For these measurement days, the data reduction included:

- a. Wave-slope pdf's from roll, pitch, and compass variables
- b. Wave-height and acceleration spectra from accelerometer variables
- c. Small-scale wave-height spectra from the wave staffs
- d. Statistical analysis of wave-height acceleration.

Details of this processing are given below. Further discussion of the wave instrumentation is contained in appendix B of volume IV.

¹⁰In deriving the empirical relationship of equation (6-22), Cox and Munk used data acquired for a range of wind velocities up to 18 kn. Data presented later in table 6-5 applies this relationship for measured wind velocities slightly in excess of this value.

TABLE 6-4. TABULATION OF SEA-STATE TAPES PROCESSED AND PARAMETER VALUES DERIVED

Date (1975)	Tape number	Segment length, min	Wind velocity, kn	Sea state	Slope parameter			Standard deviation				
					σ_x	σ_y	ρ	A_z	A_x	A_y	Wave staff 1	Wave staff 5
Jan. 29	SSD06	32	26	1 ft	—	—	—	0.18	0.035	0.036	0.100	0.100
Jan. 30	SSD07	32	5	1 ft	0.127	0.167	-0.86	0.20	0.033	0.032	0.103	0.105
Mar. 25	SSD01	16	10	2-ft swell	0.019	0.021					0.074	0.079
Mar. 27	SSD02	24	20	2 ft	0.080	0.066	0.162	0.29	0.043	0.035	0.161	0.164
Mar. 28	SSD03	16	16	2-ft swell	0.082	0.069	0.118	0.25	0.045	0.045	0.161	0.147
Mar. 31	SSD04	32	20	2 ft	0.065	0.051					0.084	0.149
Apr. 1	SSD05	24	19	2 ft	0.037	0.035	-0.045	0.20	0.05	0.06	0.089	0.129

6.5.2.1 *Slope Probability Density Functions and RMS Values* — Sea-state data measurements of roll and pitch from the tapes listed in table 6-4 were used to generate plots, printouts, and data file copies of the joint wave-slope probability density functions. As derived in section B.1.6 of appendix B, volume IV, removal of bias was effected before the transformation of the raw roll and pitch data to slopes. Also, as described in detail in the above appendix, the reference coordinate system is rotated so that the positive x-axis points in the direction of the satellite.

The slope distribution parameters derived from tapes SSD01 to SSD07 are summarized in table 6-4.

The joint probability density function for wave slopes taken from sea-state data tape SSD01 is illustrated in figure 6-36. The distribution in this figure is quantized to 10 levels and is meant only to illustrate the geometric configuration of the distribution. The elongation in the y-direction is misleading; due to the nature of the printout, there is a 3:2 stretching of the y-axis relative to the x-axis. The figure, however, does provide a rough indication of the distribution and shows no over-riding irregularities or asymmetries.

The correlation coefficients, along with the mean values (biases) for the wave slopes and the individual standard deviations, are listed in the figure. The rms wave slopes σ_{sx} and σ_{sy} in the x- and y-direction have the numerical values:

$$\sigma_{sx} = 0.01909 \text{ and } \sigma_{sy} = 0.02182.$$

As regards the standard deviations, one can note that a slope value of 0.02 corresponds to an angle $\theta = 1.15^\circ$

The marginal slope densities $p_1(x)$ and $p_1(y)$ plotted in figures 6-37 and 6-38 provide a more accurate quantitative picture of the wave statistics. These pdf's, of course, are calculated according to

$$p_1(x) \approx \int_{-\infty}^{\infty} p_{11}(x,y) dy ,$$

with a similar relation existing for $p_1(y)$.

The Gaussian-like behavior of these functions is evident and there is little difference between them.

The data from tape SSD04 gives rise to the geometric configuration of figure 6-39. One can see immediately the greater spreading due to the rougher seas.

The marginal slope densities for this tape (plotted in figs 6-40 and 6-41) also indicate greater spreading (notice the difference in horizontal scale). For this tape, the rms slope values σ_{sx} and σ_{sy} in the x- and y-directions have the numerical values

$$\sigma_{sx} = 0.06546 \text{ and } \sigma_{sy} = 0.05128.$$

Table 6-4 contains a complete summary of all data segments processed, including the rms slope values. Note that an "omnidirectional" rms slope measure, σ_{slope} , can be derived from

$$\begin{aligned} \sigma_{\text{slope}} &= \sqrt{\sigma_{sx}^2 + \sigma_{sy}^2} \\ &\approx \sqrt{2} \sigma_{sx} \quad \text{when } \sigma_{sx} \approx \sigma_{sy}. \end{aligned}$$

The parameter σ_{slope} represents rms variation of the slope normal vector projected onto a horizontal plane without regard to direction.

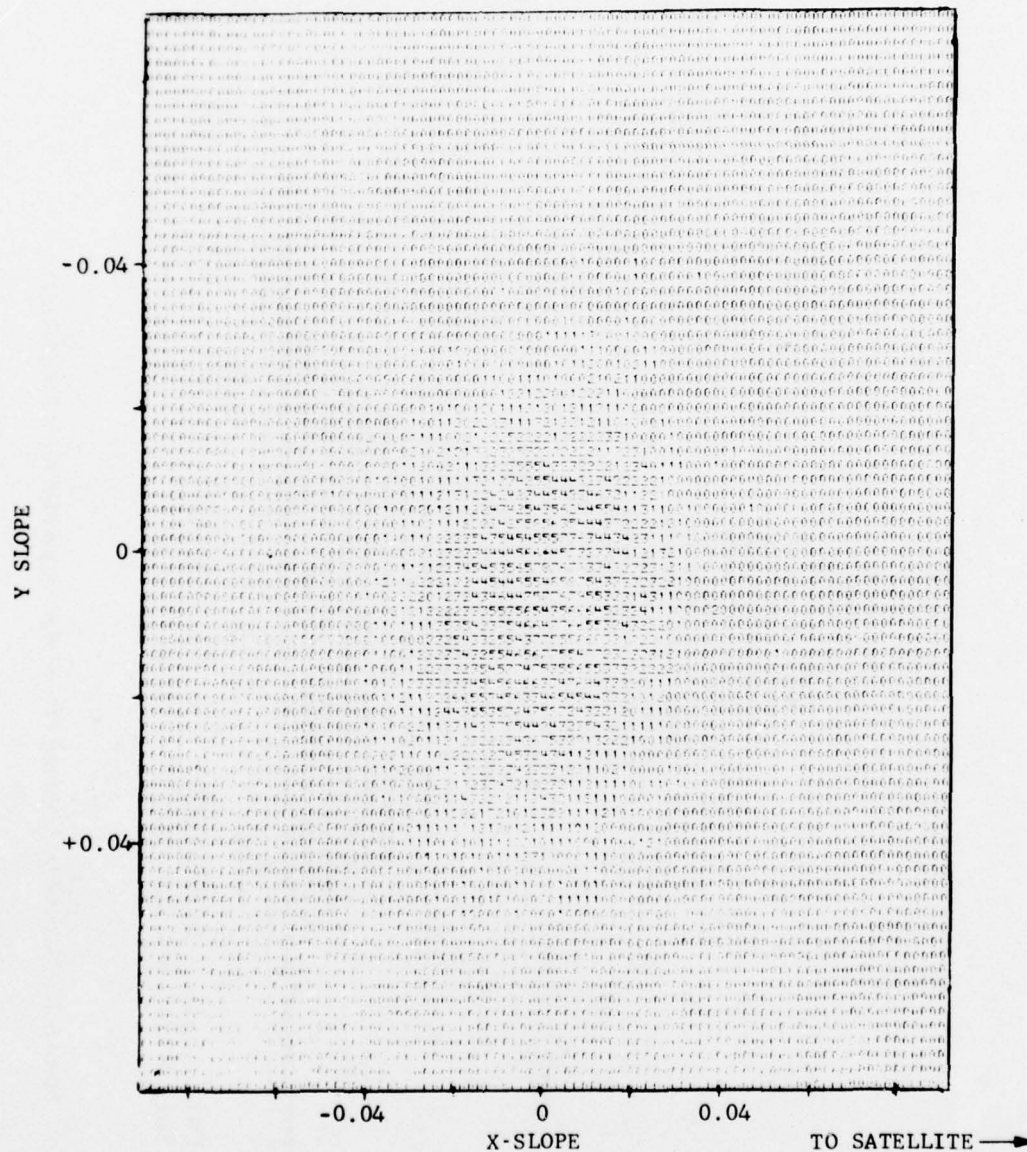


Figure 6-36. Geometric Configuration of Wave-Slope PDF From Tape SSD01

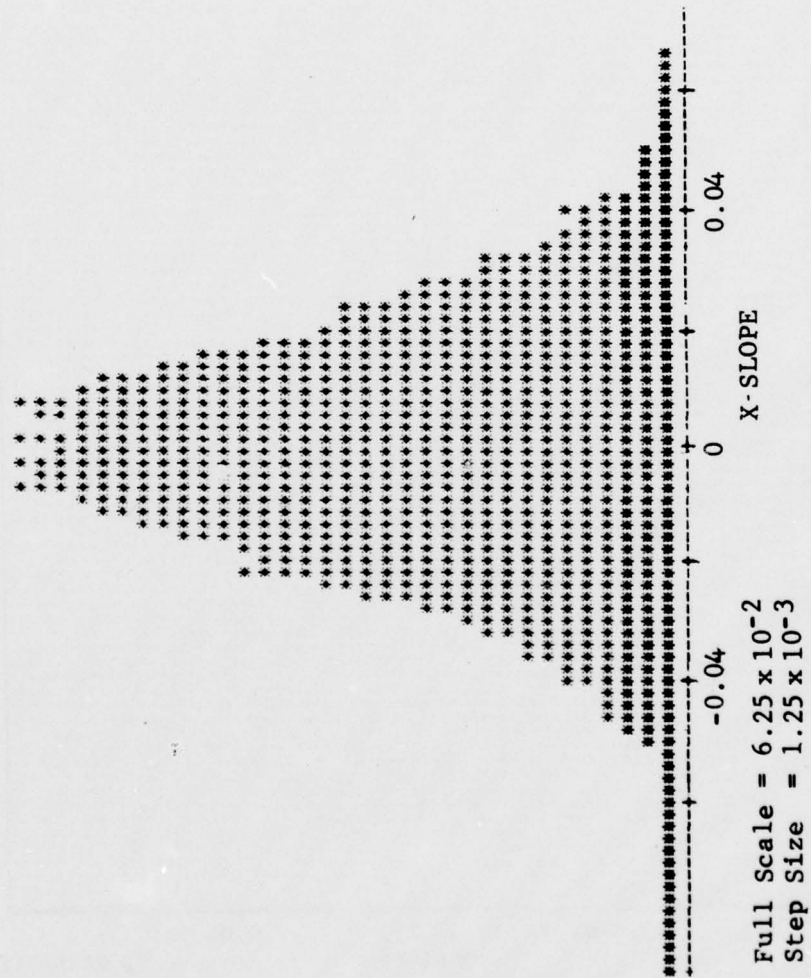


Figure 6-37. Marginal (X Direction) PDF of Wave-Slope PDF From Tape SSD01

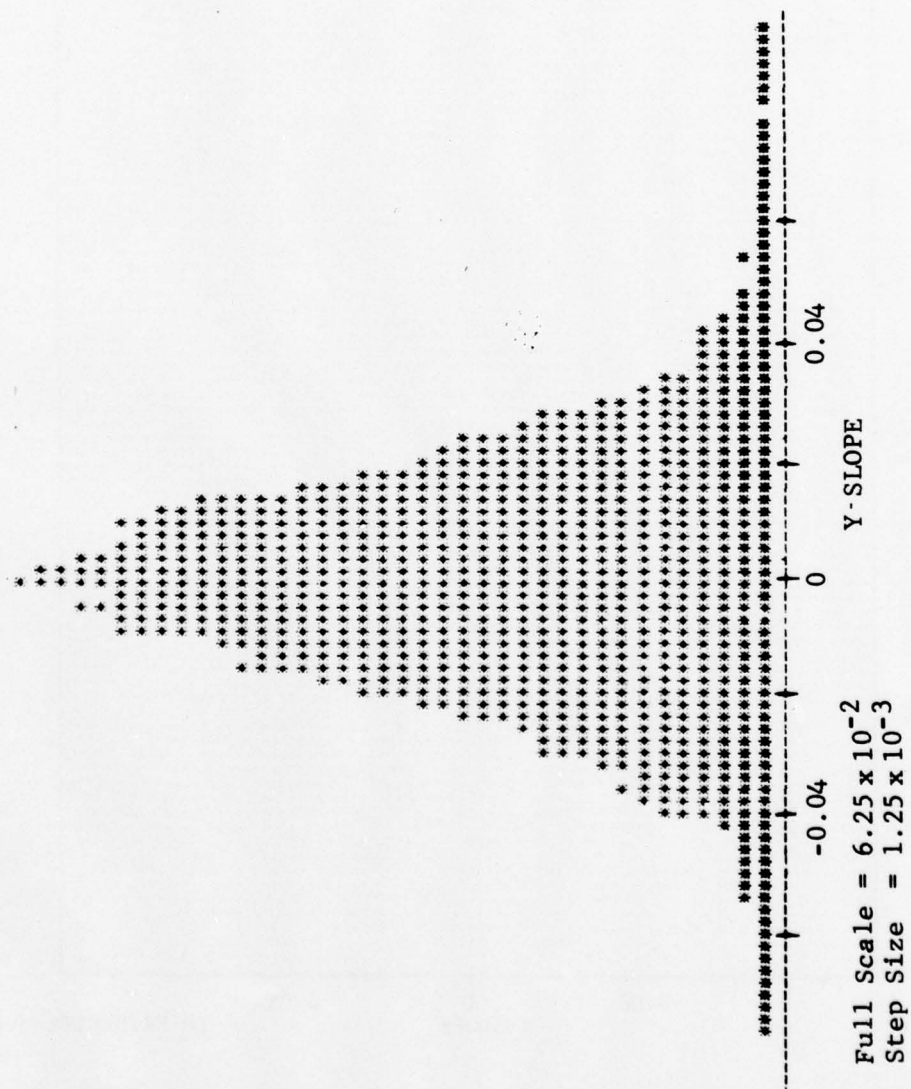


Figure 6-38. Marginal PDF (Y Direction) of Wave-Slope PDF From Tape SSD01

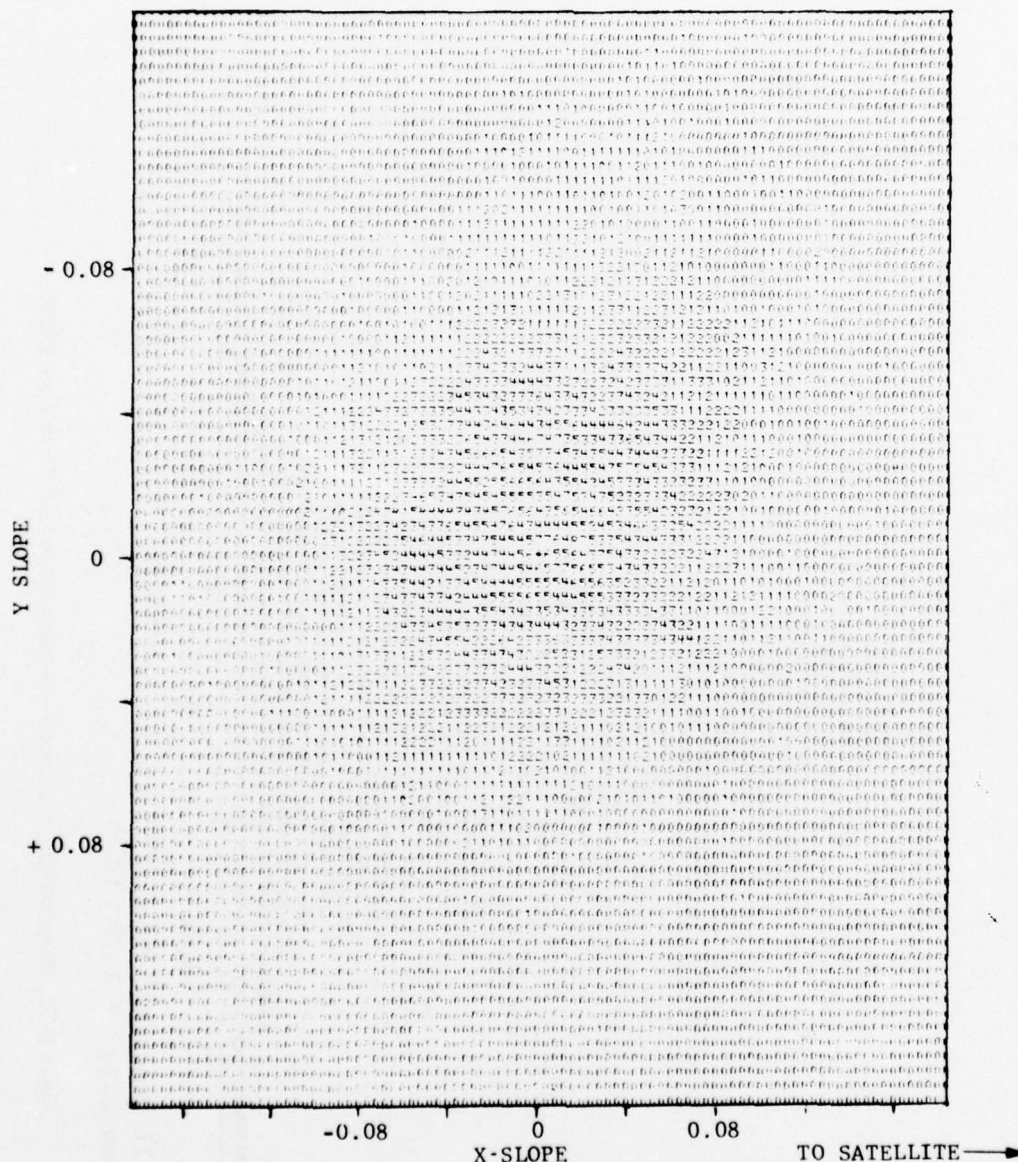


Figure 6-39. Geometric Configuration of Wave-Slope PDF From Tape SSD01

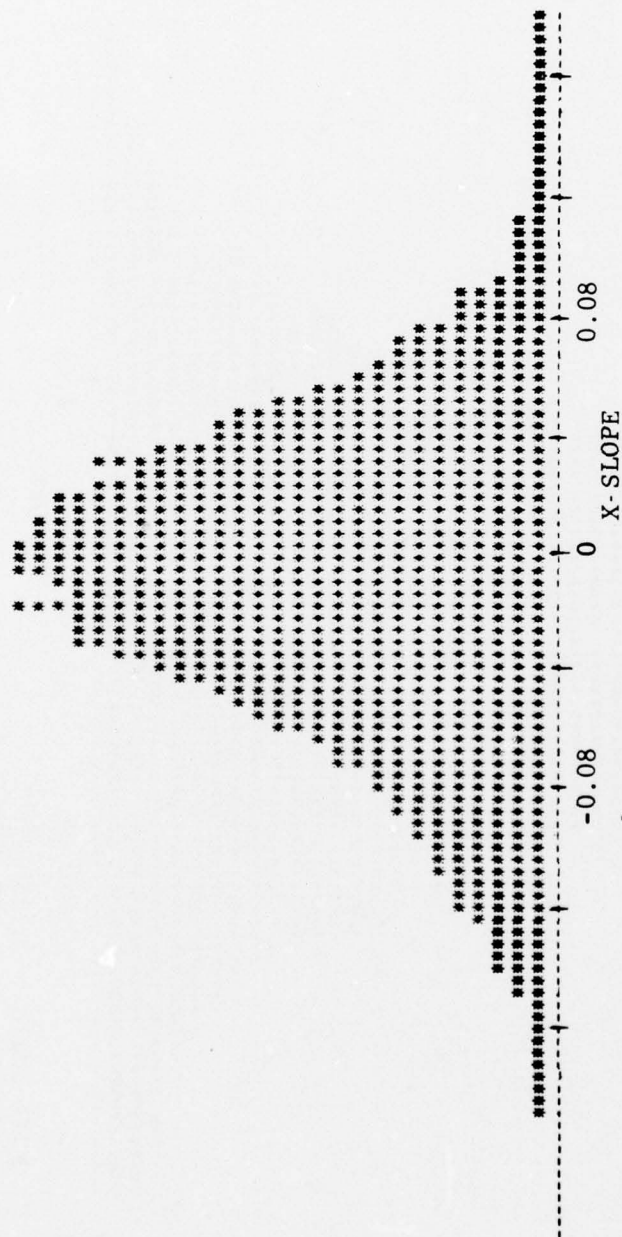


Figure 6-40. Marginal PDF (X Direction) of Wave-Slope PDF From Tape SSD04

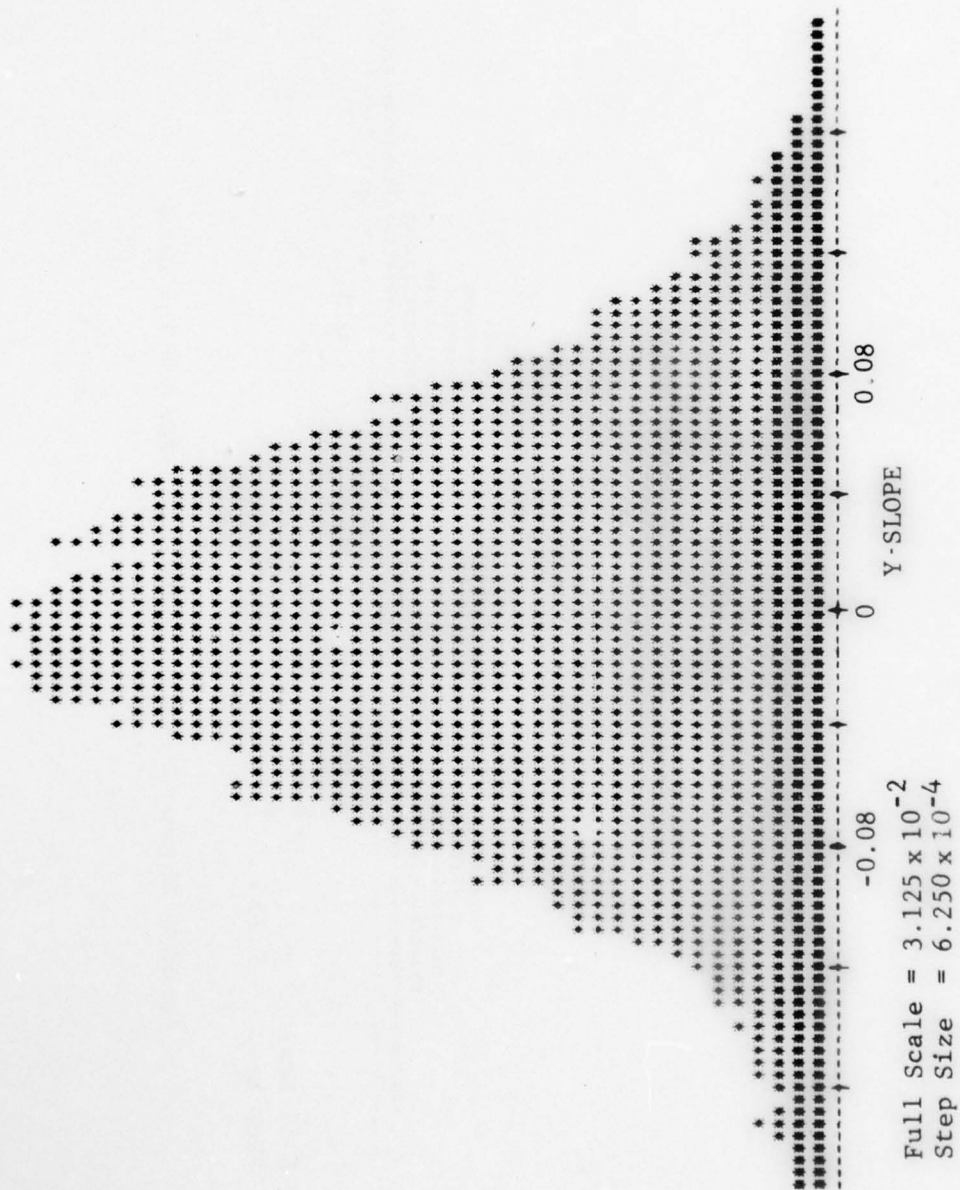


Figure 6-41. Marginal PDF (Y Direction) of Wave-Slope PDF From Tape SSD04

6.5.2.2 *Reduction of Buoy Acceleration Data* — The vertical acceleration of the buoy can be used to derive the spectrum of both acceleration and wave-height variations. As discussed in section 6.5.1, the ocean surface can be thought of in terms of a superposition of propagating sinusoidal waves, each with a velocity determined by the dispersion relationship (eq. 6-19). This relationship between wavelength and frequency of height fluctuations observed at a point in space allows the acceleration spectrum to be interpreted in terms of a distribution of wavelengths.

Statistical analysis of acceleration yields plots such as those of figure 6-42 (March 25, 1975) and figure 6-43 (March 31, 1975). Typical power spectra for acceleration and height are shown in figures 6-44 and 6-45. The height spectra were obtained by weighting the acceleration spectral estimates with $1/f^4$. Note that some difficulty can be expected in attempting to extract the mean square wave height by integrating these spectral estimates. To do so successfully would require the acceleration spectra to roll off toward the origin at low frequencies as f^4 or better. Recourse to a time-domain approach involving a double integration of the data does nothing to obviate this difficulty.

6.5.2.3 *Wave-Staff Data* — Typical probability density functions generated the wave-staff height records for tapes SSD01 and SSD04, which are illustrated in figures 6-46 and 6-47, respectively. The most obvious and significant feature contained in the figures is the increased standard deviation of the data on the second tape. This is in agreement with the relative loading of the joint wave-slope pdf's depicted earlier and, similarly, reflects a rougher sea condition for the second tape.

The dependence of each staff's rms height on staff location within the wave-staff geometry is illustrated in figures 6-48 and 6-49. In figure 6-48 (tape SSD01), the standard deviation ranges from 8.419 cm at wave-staff 1 to 18.08 cm at wave-staff 7. Clearly, the wide range of data on the second tape implies that wave-staff data taken during rough seas may have very limited value.

Spectral analysis of the various wave staffs produces characteristics such as those shown in figure 6-50. When combined with the accelerometer data, as shown in figures 6-51 and 6-52 for two particular days, the wave-staff spectra provide an extension to the high-frequency portion of the curve.

6.5.3 Discussion of Experimental Results

The sea-state data analysis has given additional weight to the wave-slope and wave-height models used previously in aeronautical channel models. The experimentally derived slope pdf's are shown to have the general form of a two-dimension Gaussian distribution with very nearly circular symmetry, i.e., $\sigma_x \approx \sigma_y$ and $\rho \approx 0$. This allows the slope distribution used in multipath models to be approximated with a simple single parameter form; i.e.,

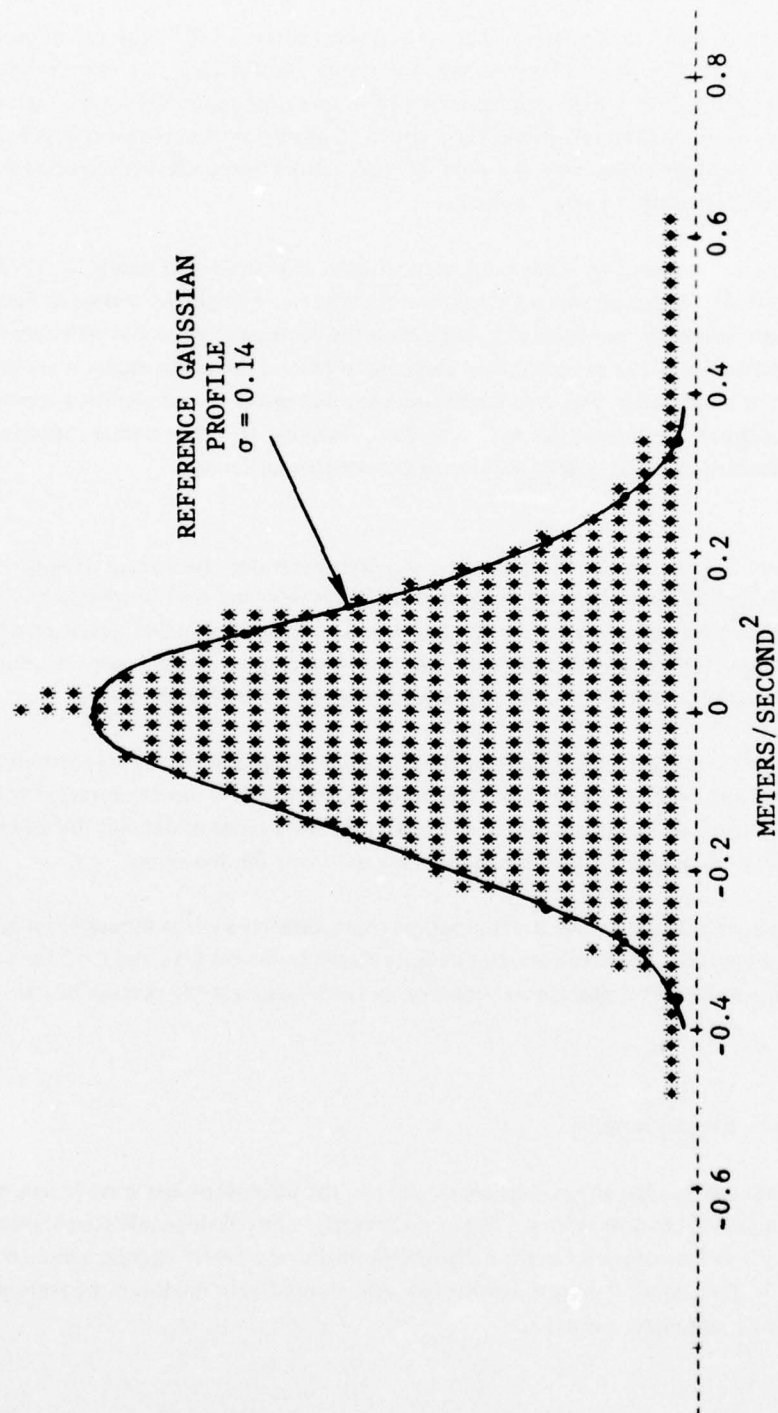


Figure 6-42. Acceleration Probability Density — March 25, 1975

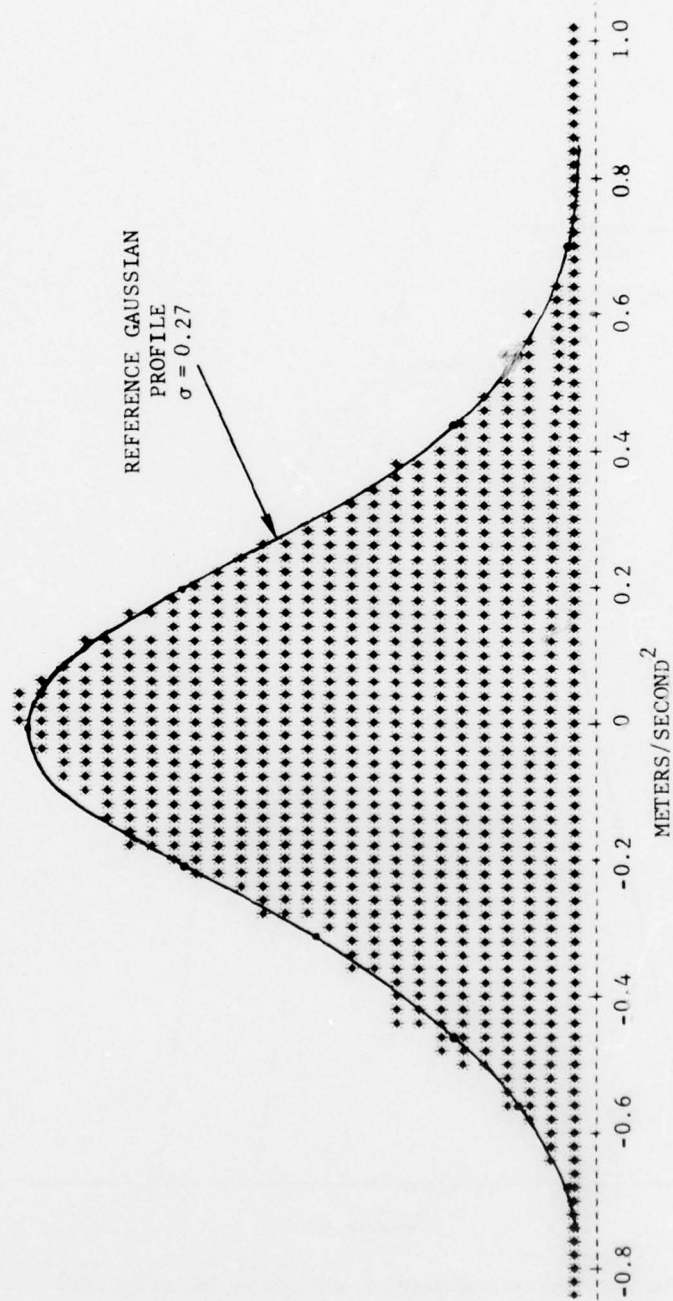


Figure 6-43 Acceleration Probability Density — March 31, 1975 (First 800 sec)

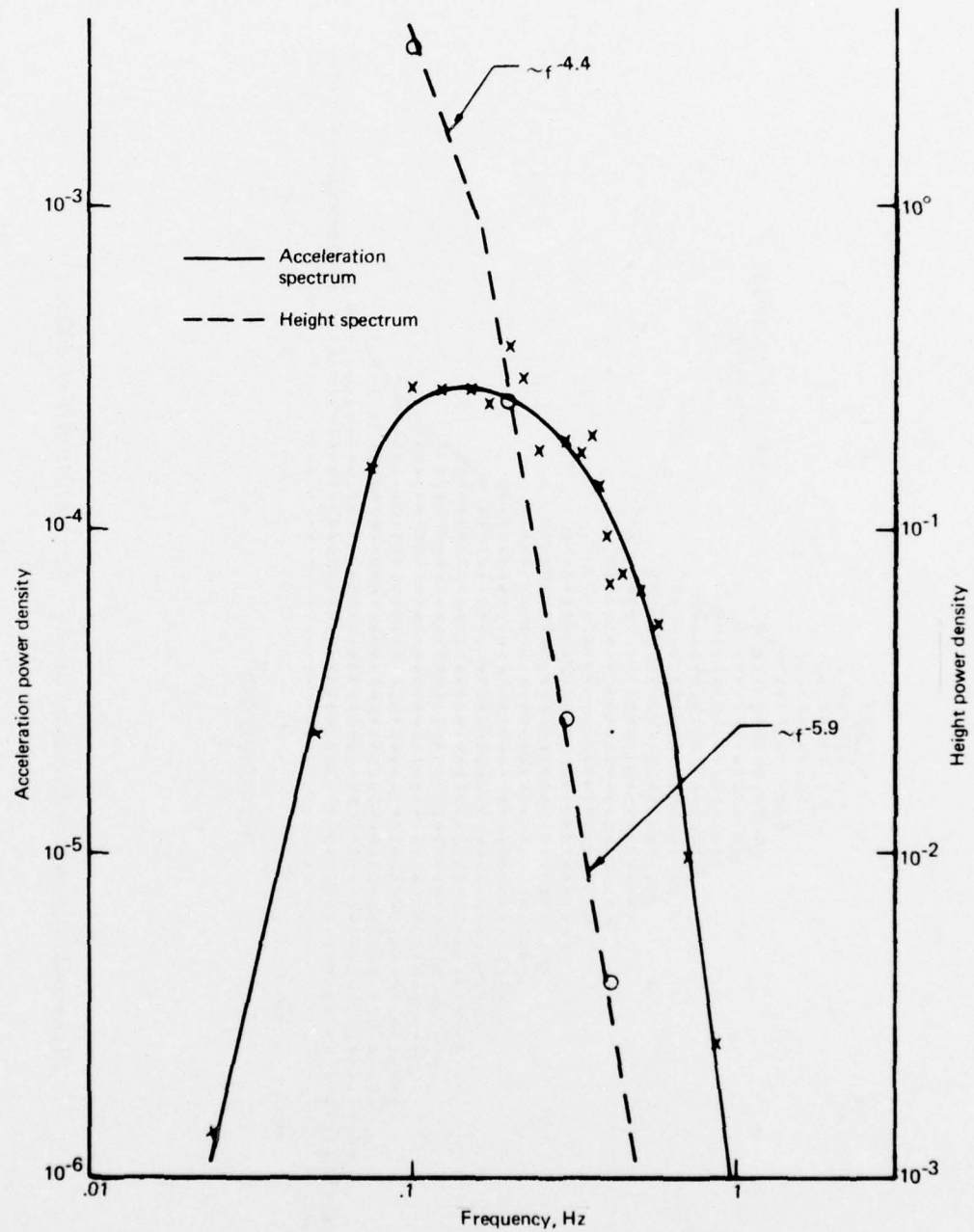


Figure 6-44. Acceleration and Height Power Spectra, March 25, 1975

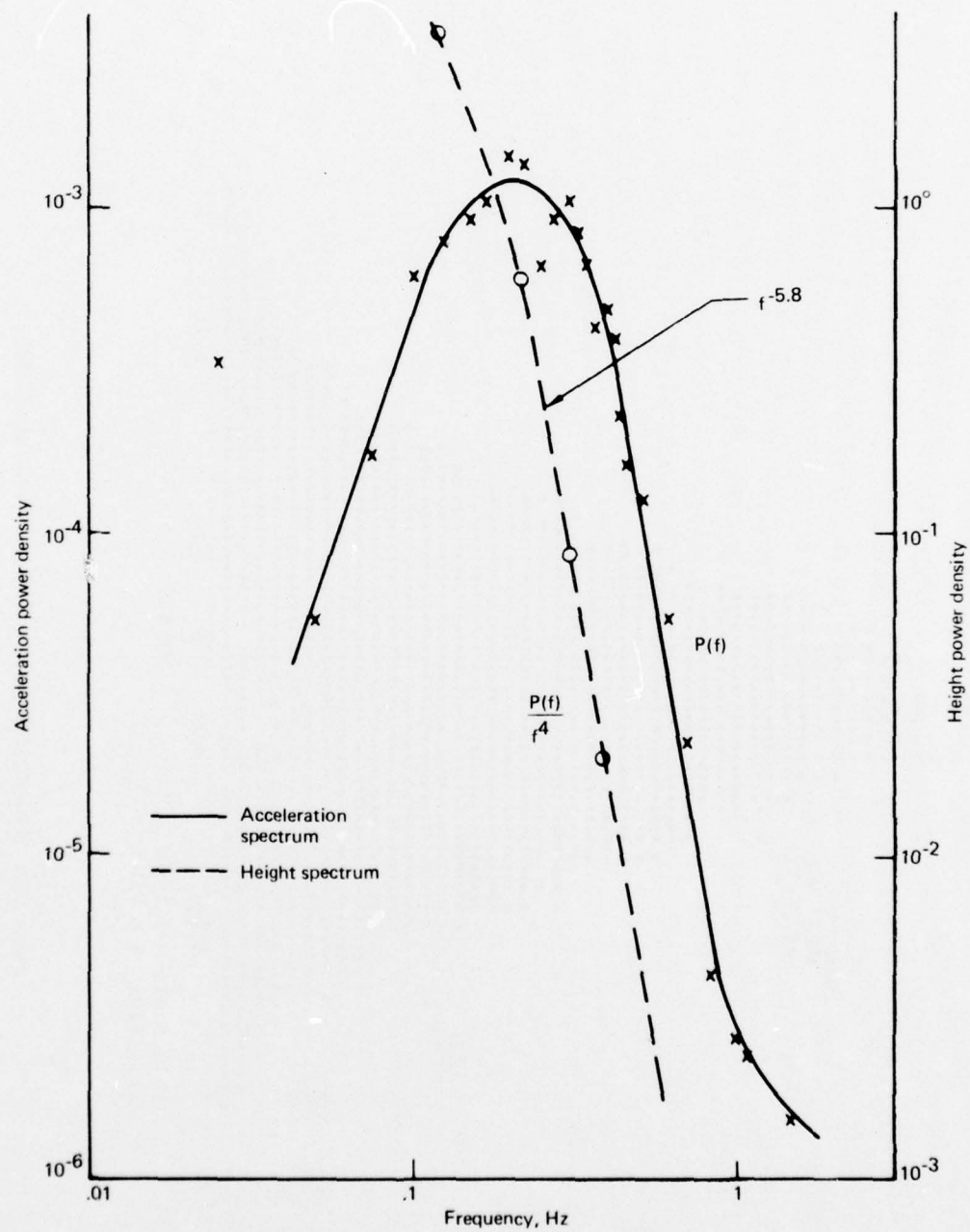


Figure 6-45. Acceleration and Height Power Spectra, March 31, 1975 (Last 800 sec)

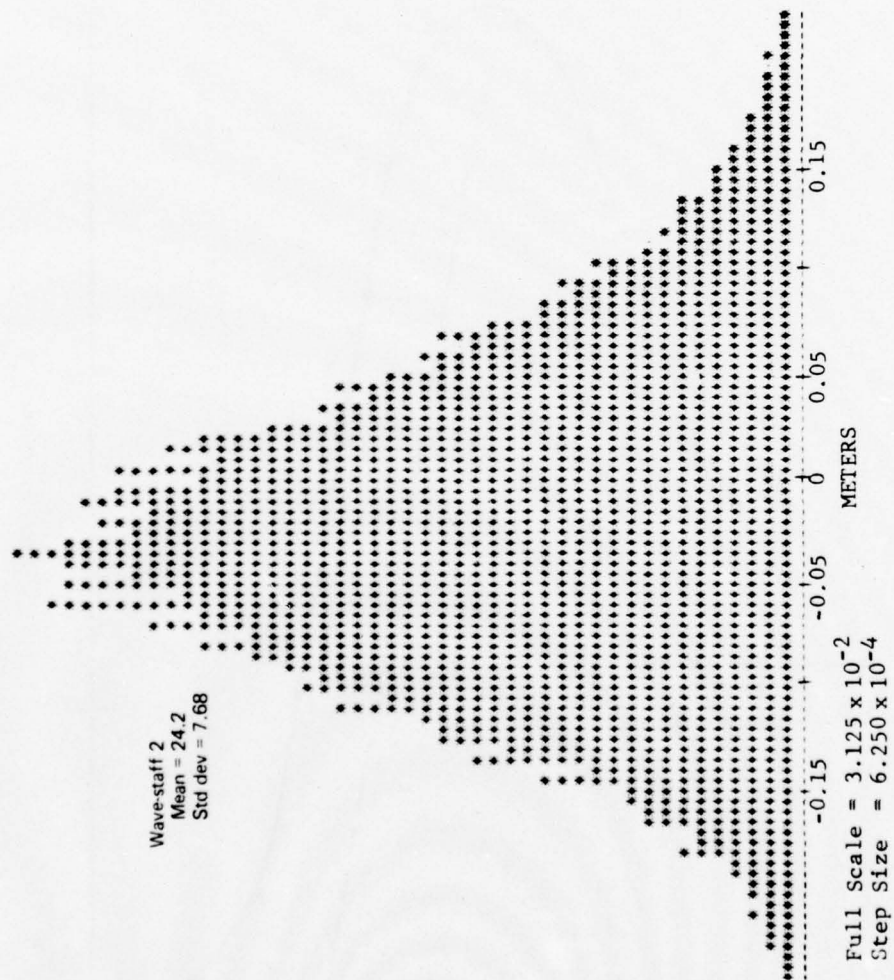


Figure 6-46. Wave-Staff Probability Densities From Tape SSD01

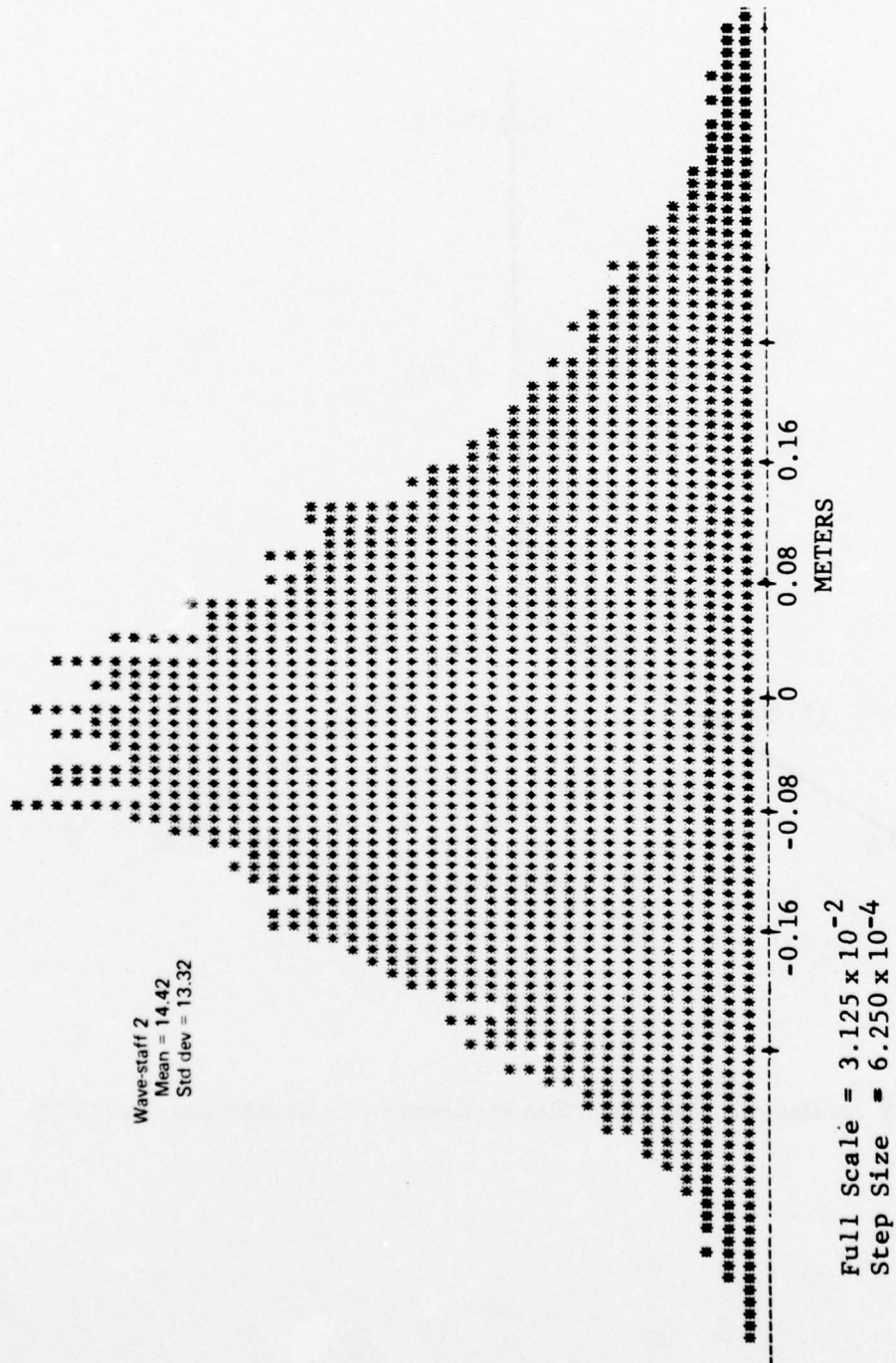


Figure 6-47. Wave-Staff Probability Densities From Tape SSD04

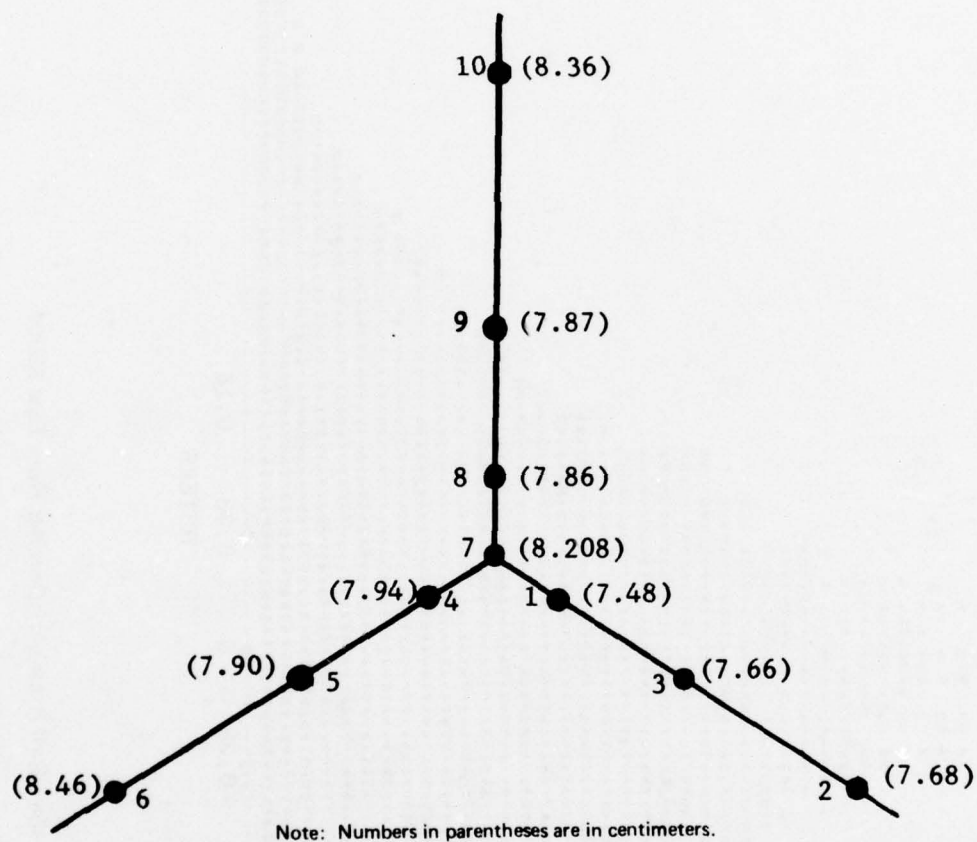
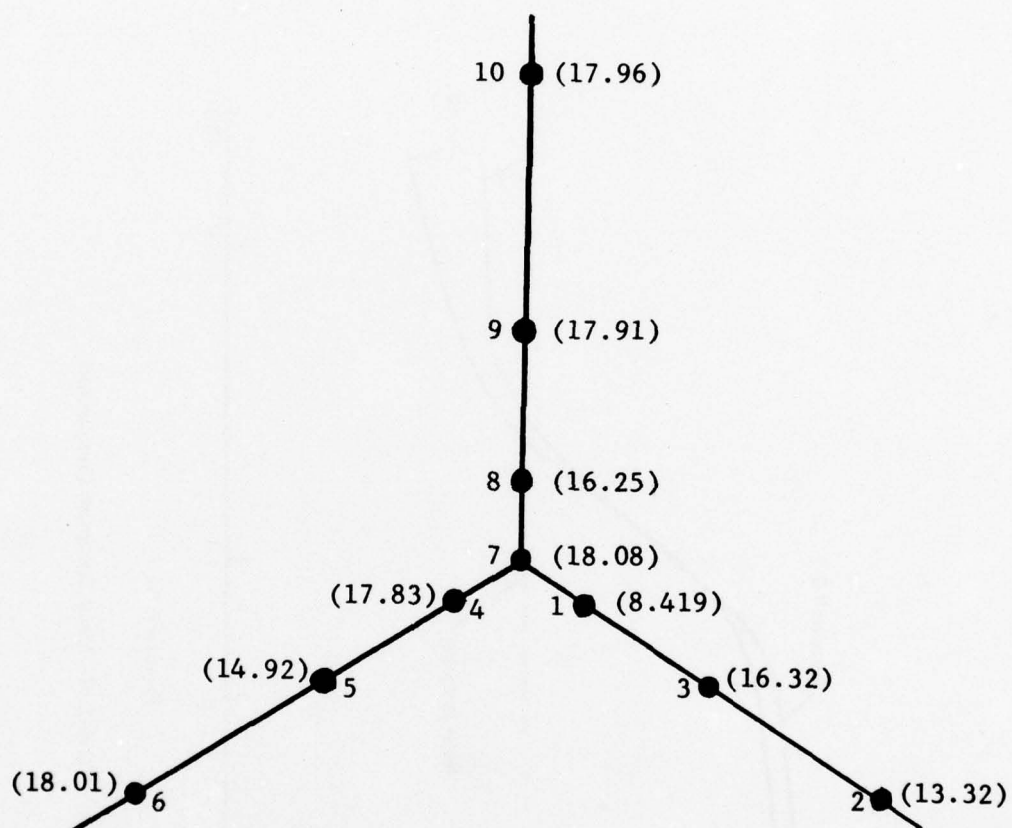


Figure 6-48. Configuration of Wave-Staff Standard Deviations for Sea-State Data, Tape SSD01



Note: Numbers in parentheses are in centimeters.

Figure 6-49. Configuration of Wave-Staff Standard Deviation for Sea-State Data, Tape SSD04

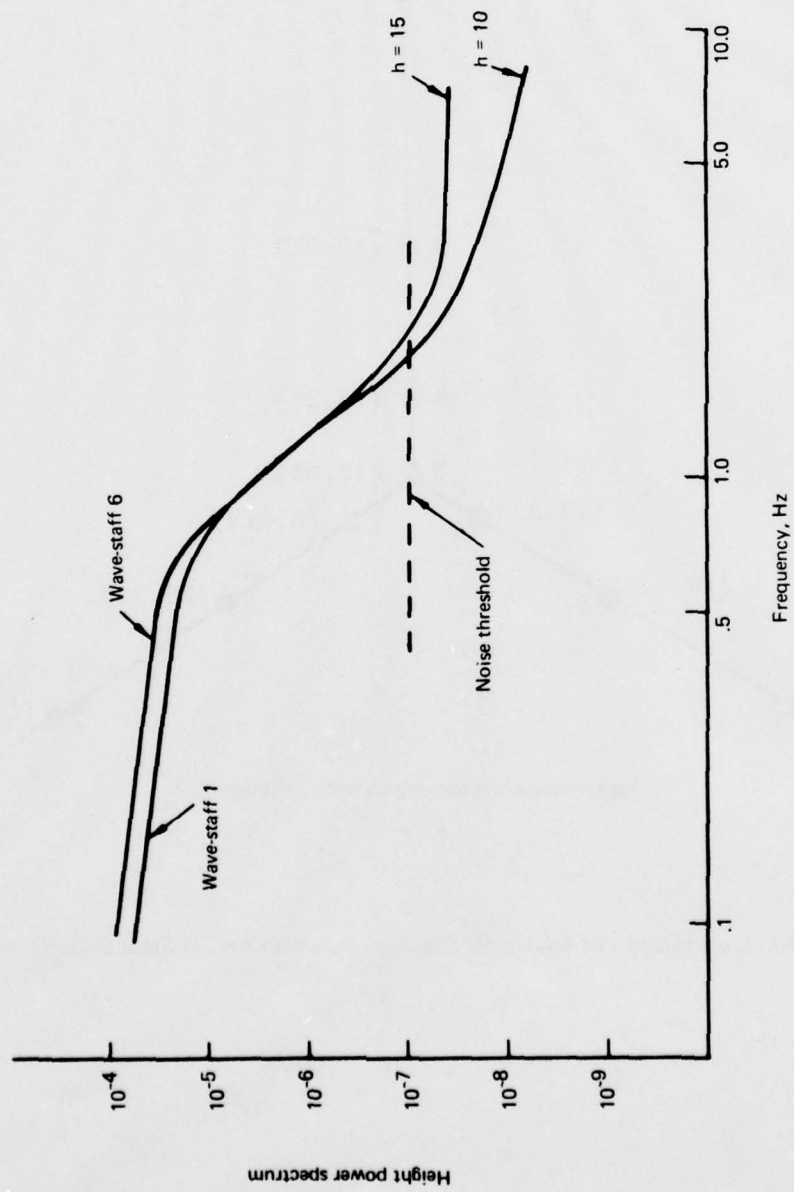


Figure 6-50. Wave-Staff Power Spectrum Comparison

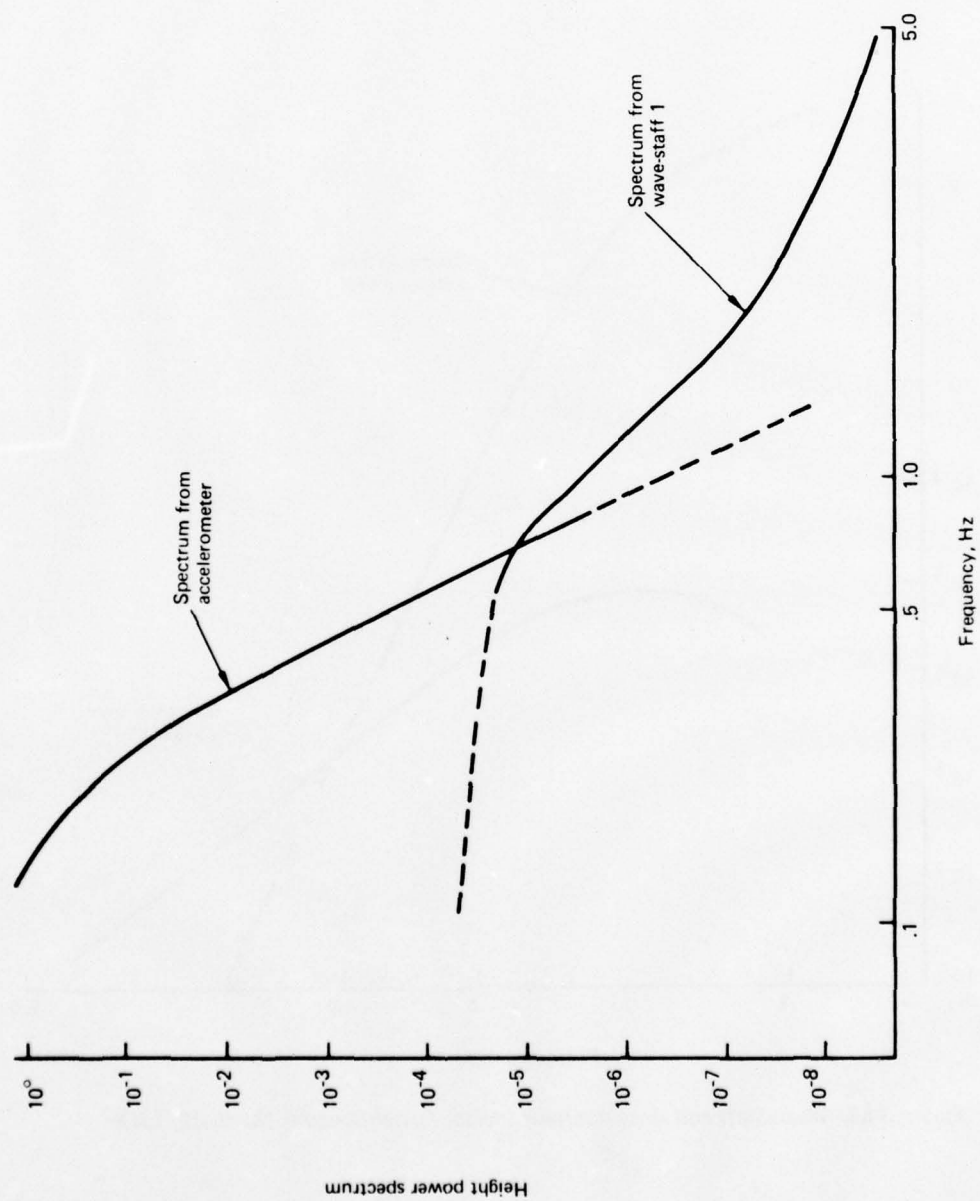


Figure 6-51. Wave-Staff and Accelerometer Height Power Spectra, March 25, 1975

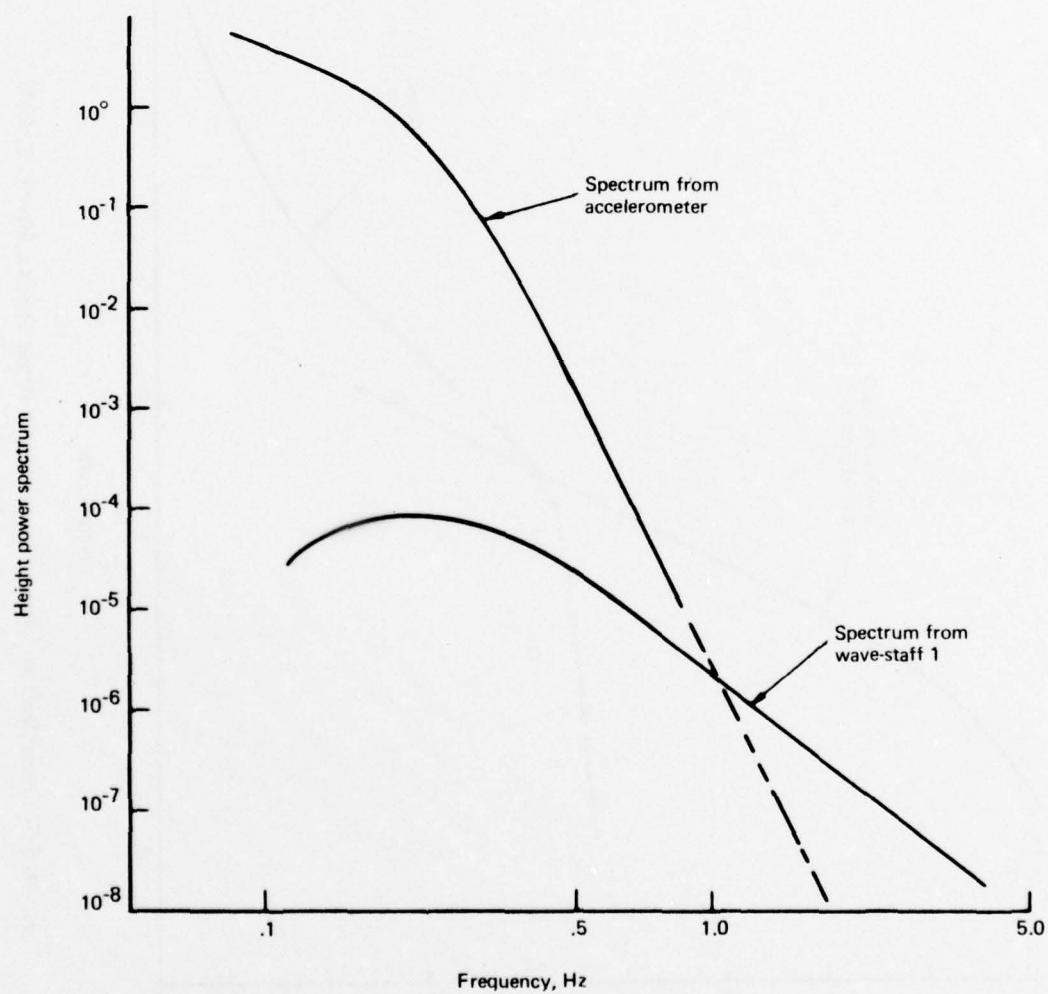


Figure 6-52. Wave-Staff and Accelerometer Height Power Spectra, March 31, 1975

$$p(s_x, s_y) = \left[\frac{1}{\sqrt{2\pi} \sigma_s} \right]^2 \exp \left\{ - \left(s_x^2 + s_y^2 \right) / 2 \sigma_s^2 \right\},$$

with $\sigma_{\text{slope}} = \sqrt{2} \sigma_s$.

Wave-height spectra obtained from the buoy accelerometer and wave staffs conform with previous theoretical and experimental estimates. Note that slope distributions are obtained by sensing tilting motion of the buoy and, therefore, include only the effects of waves with frequencies on the order of 1 Hz or less. In effect, the buoy acts as a 1-Hz filter on the roll, pitch, and acceleration processes.

The acceleration spectrum can be related to the roll and pitch (or, equivalently, slope) spectra. It can be shown for a superposition of gravity waves that

$$S_x(f) + S_y(f) = \frac{1}{g^2} S_a(f),$$

where:

- S_x = spectrum for x-slope
- S_y = spectrum for y-slope
- S_a = spectrum for vertical acceleration
- g = gravitational constant.

Thus, the slope spectrum can be expected to have the same kind of high-frequency rolloff as that exhibited by the acceleration. From an integration of the acceleration spectrum over frequency up to a maximum of f_0 , one can determine the slope parameter σ_{slope} , which applies to waves having wavelength less than

$$L_0 = \frac{g}{2\pi f_0^2}$$

From the two spectra presented, it would appear that the main contribution to the derived values of wave-slope standard deviation comes from waves of frequency less than 0.5 Hz; i.e., 6.2 m wavelength.

It was suggested in section 6.5.1.2 that sea-state parameters should be available from observations of quantities such as windspeed and rms wave height. Table 6-5 indicates the values of σ_{slope} predicted from windspeed using equation (6-22). These results were obtained using the data from table 6-4; in table 6-5 the values of σ_{slope} resulting from slope measurements are shown for comparison purposes. Agreement is not particularly good, possibly because of the several hours difference

between wind and slope measurements. Also indicated in table 6-5 are the values of rms height σ_h predicted from wind velocity using equation (6-21).

TABLE 6-5. COMPARISON OF MEASURED AND PREDICTED SLOPE PARAMETERS

Date (1975)	Wind velocity, kn	Predicted		Measured		
		σ_h , ft	σ_{slope}	σ_x	σ_y	σ_{slope}
Jan. 30	5	0.11	0.13	0.127	0.167	0.20
Mar. 25	10	0.45	0.17	0.019	0.021	0.03
Mar. 27	20	1.82	0.23	0.08	0.066	0.10
Mar. 28	16	1.16	0.21	0.082	0.069	0.11
Mar. 31	20	1.82	0.23	0.065	0.051	0.08
Apr. 1	19	1.64	0.23	0.037	0.035	0.05

7. CONUS MULTIPATH TEST RESULTS

An extensive data base of CONUS forward-scatter multipath has been obtained. This collection covers a range of grazing angles from 22° to 48° and a variety of terrain electrical characteristics (lakes to dry snow), surface roughness (flat plains to mountainous), and vegetation coverage (heavily forested to barren). In addition, several hours of data pertaining to multipath reflections during the approach, taxi, and takeoff phases at large airport environments was obtained.

Due to the nonisotropic nature of the overland scatter surface, the analysis and modeling of the CONUS multipath channel is not nearly as straightforward as it is for the oceanic case and almost necessitates that each return signal structure be treated as a separate entity. Such a treatment is beyond the scope of this document; nevertheless, we do attempt to provide representative results that illustrate some of the fundamental scatter signatures associated with the data. For example, multipath returns from the following terrain features receive specific attention in the remaining sections of this document:

- Vegetation-covered terrain
- Snow-covered terrain
- Lakes (frozen and liquid)
- Coastal harbor/large city areas
- Airport landing environments.

The data base for the CONUS multipath channel characterization was obtained from the September 19 and October 30, 1974, flights over the eastern United States; the February 18 and 19, 1975, flights over central Canada; and the February 20, 1975, flight over eastern Canada and the U.S. Due to experimental difficulties, the West Coast mountain terrain flight of November 2, 1974, produced little valid data and therefore is not included in this report. A small section of that data has been published in an earlier interim report.

Pertinent system parameters for each of the flight tests are listed in table 7-1.

In an attempt to correlate gross terrain features with the results given in this section, each flight test's specular-point trajectory is shown superimposed upon global navigation and planning charts. These trajectories were derived through use of the KC-135's INS latitude and longitude outputs and have been time tagged to provide cross-reference between the geographic area and certain data sets of this report. The specular-point overlays are given in figures 7-1 through 7-5 and are related to the test dates as follows:

September 19, 1974	Figure 7-1
October 30, 1974	Figure 7-2
February 18, 1975	Figure 7-3
February 19, 1975	Figure 7-4
February 20, 1975	Figure 7-5.

In general, the February flights provide us with snow-covered and winter lake (both frozen and liquid) terrain features, whereas the September and October series gathered data from heavily vegetation-covered terrain (both flat and mountainous) and coastal harbor/large city environments (e.g., New York). Typically, the flight legs running in the north-south direction correspond to in-plane flight velocity vectors and the east-west directions represent cross-plane velocity legs.

TABLE 7-1. SYSTEM PARAMETERS FOR SELECTED CONUS TESTS

Parameter	Measure
Aircraft groundspeed	Approx 190 m/sec
Aircraft barometric altitude	Approx 31,000 ft
Elevation angle	30° to 40°; Sep. 19, 1974
	40° to 48°; Oct. 30, 1974
	22° to 27°; Feb. 18, 1975
	27° to 39°; Feb. 19, 1975
	28° to 37°; Feb. 20, 1975
Probing rate	10-MHz for Sep. 19 and Oct. 30, 1974, and the airport environment probes
	5 MHz for <i>en route</i> portions, Feb. 18, 19, 20, 1975

Also included in the specular-point trajectories are delimiters that indicate the local terrain area from which a delay-Doppler scatter function, $S(\tau, \omega)$, and the associated integral, Fourier, and spread parameters were obtained. For example, refer to figure 7-1 which presents the September 19, 1974, flight test specular-point overlay, and note a descriptor $S(\tau, \omega)_{18}$ tagged to the last leg of the test (1249 to 1300). The subscript 18 is in a similar fashion appended to all parameters that we derive from $S(\tau, \omega)_{18}$. Hence, the subscripts appearing in the spread parameter and other results presented later in this document may be related back to the appropriate specular-point location from which they were produced.

In presenting the results of the CONUS multipath probes, we begin with a fairly general description of the channel and proceed toward more specific parameters by reducing the order, or degrees of freedom, of the signal structure. Hence, section 7.1 is devoted to the time-variant nature of the multipath channel characteristics and serves to illustrate the nonisotropic properties of over-land surface scattering. This is accomplished through use of the delay-spectra time history data reduction output. Section 7.2 presents the channel's $S(\tau, \omega)$ function, which for a very short "snapshot" time segment yields a characterization in terms of the delay and Doppler variables associated

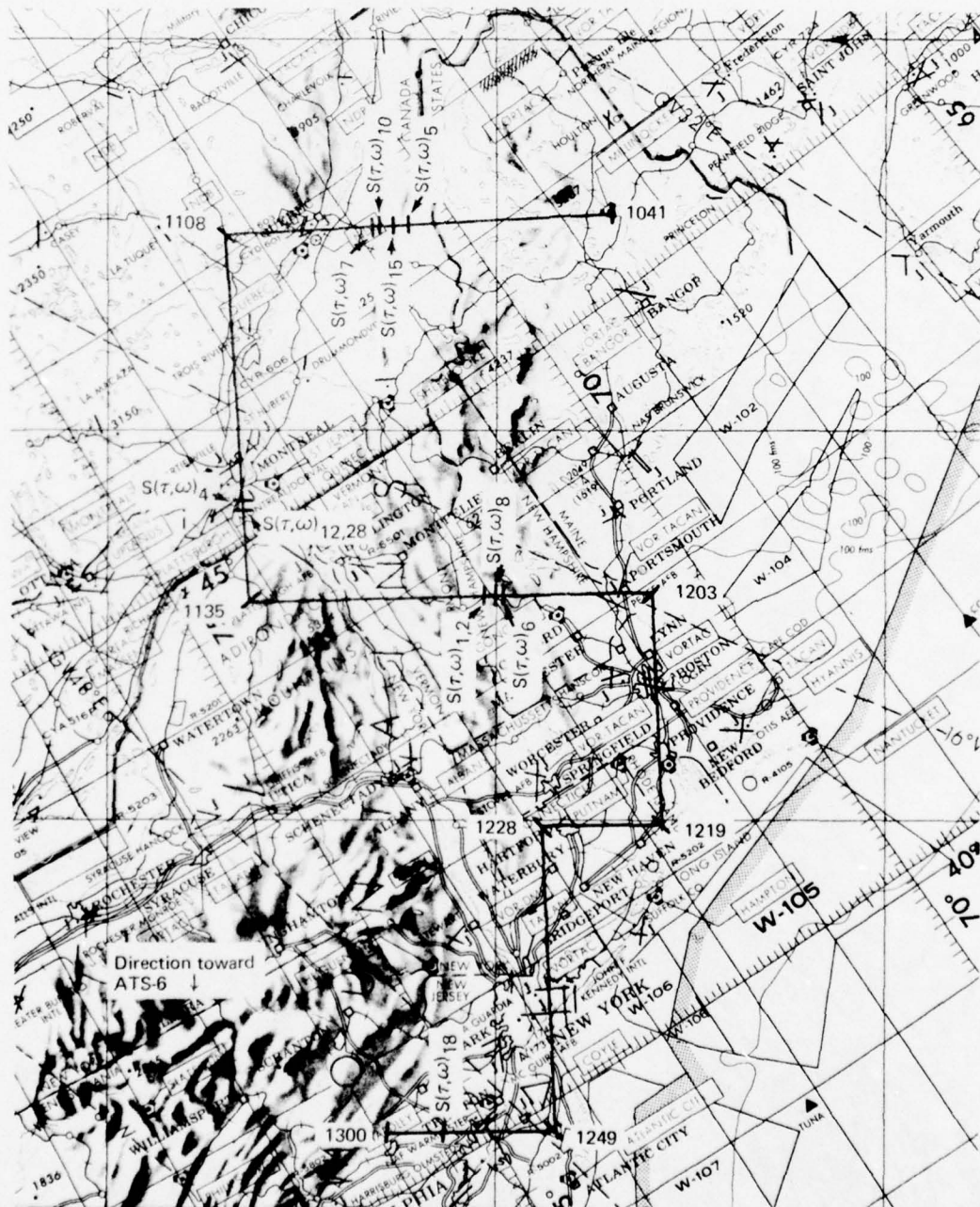


Figure 7-1. September 19, 1974, Flightpath Specular-Point Trajectory

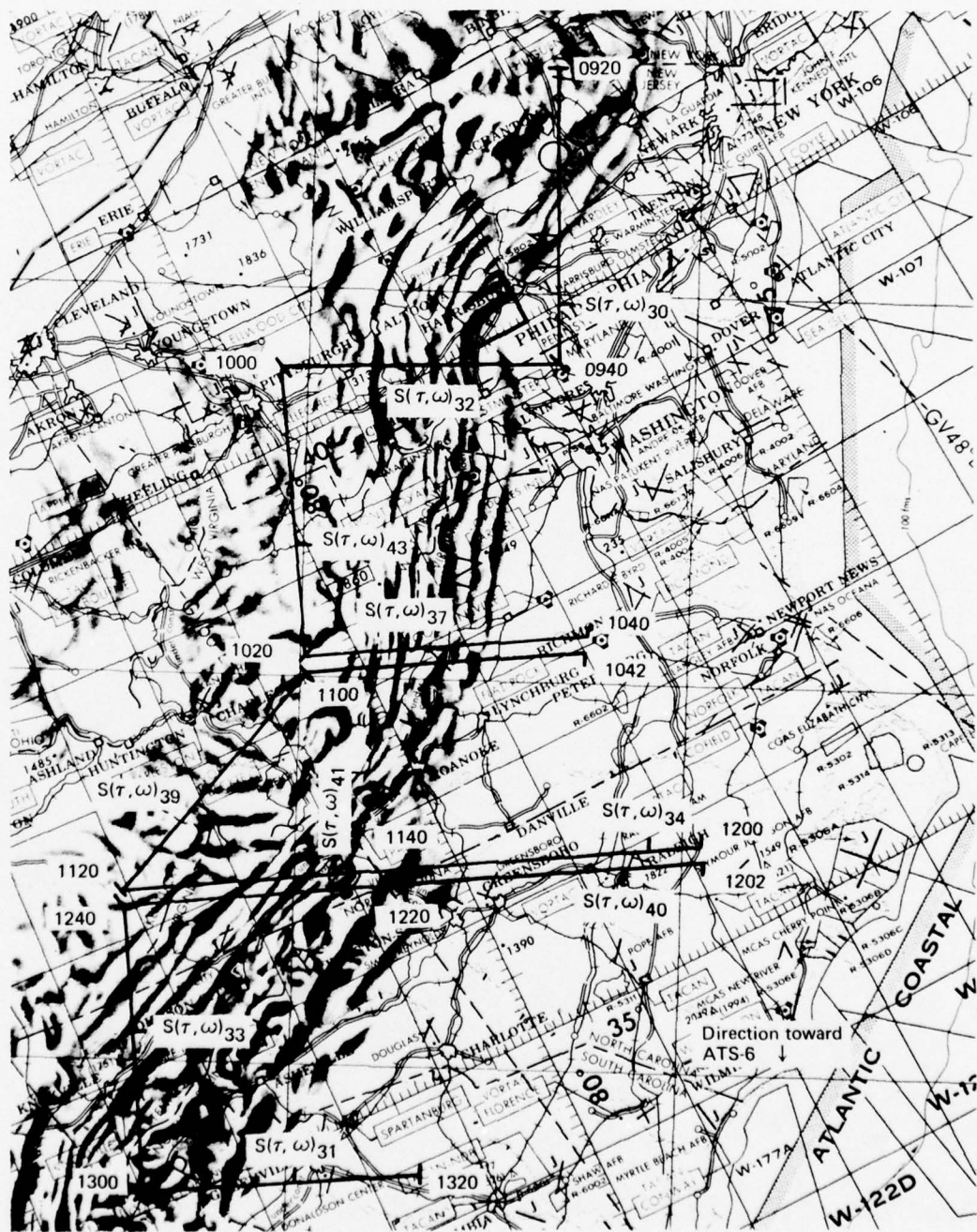


Figure 7-2. October 30, 1974, Flightpath Specular-Point Trajectory

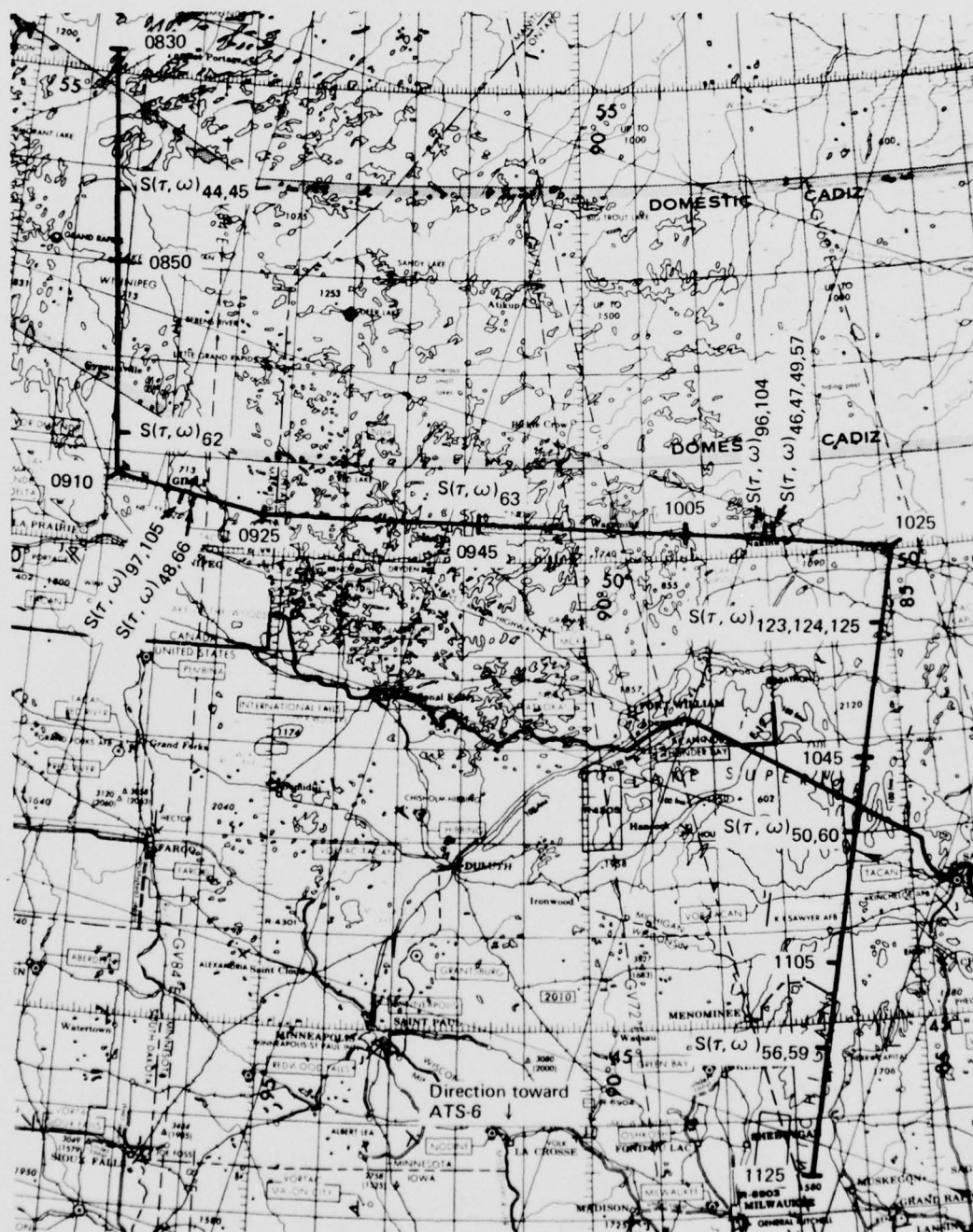


Figure 7-4. February 19, 1975, Flightpath Specular-Point Trajectory

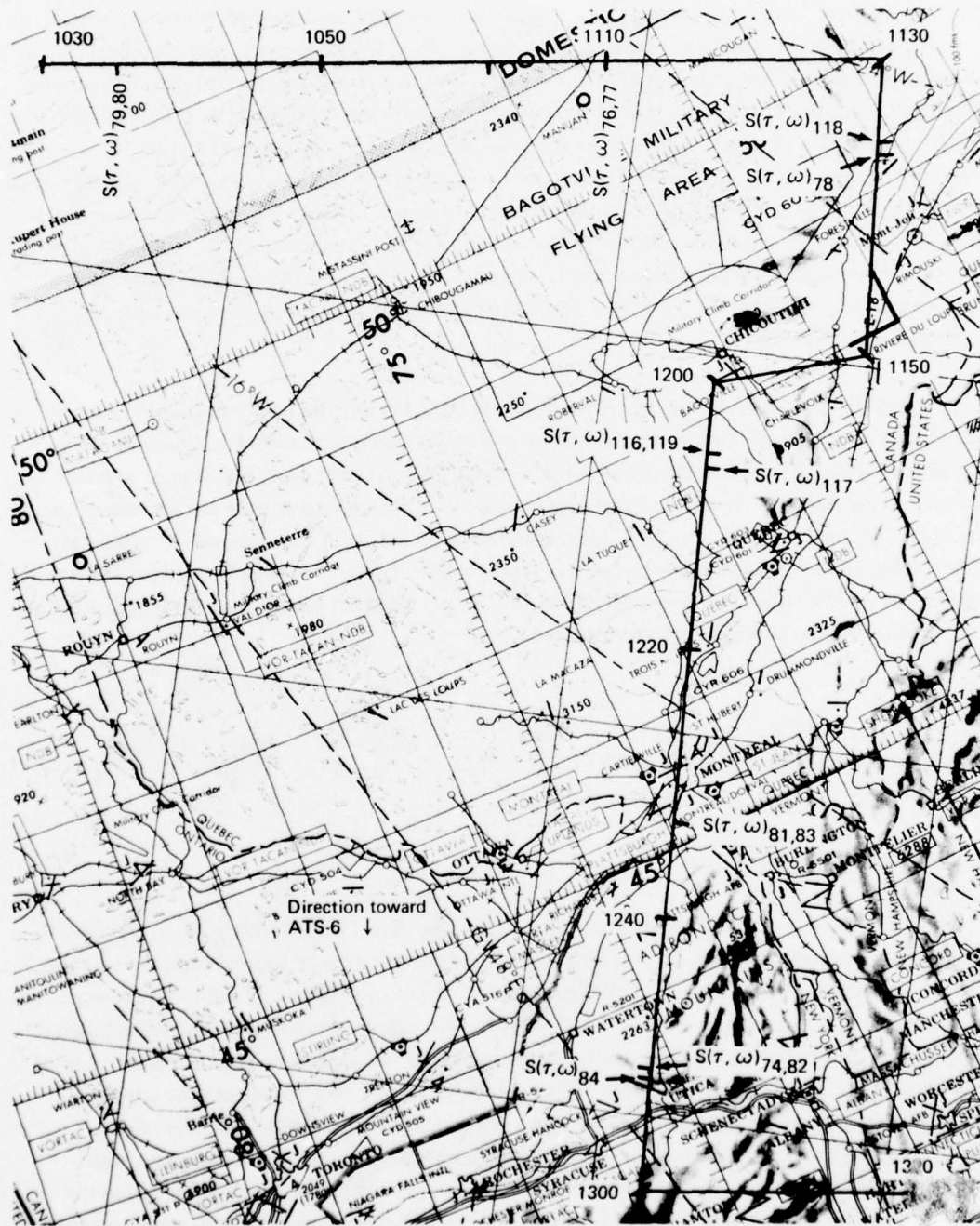


Figure 7-5. February 20, 1975, Flightpath Specular-Point Trajectory

with the multipath signal. In turn, $S(\tau, \omega)$ is reduced to lower, or equivalent, echelon parameters through integral and Fourier operations on the delay and Doppler coordinates. These procedures yield an estimation of the channel's joint and separate time and frequency autocorrelation functions, delay spectrum, Doppler spectrum, and total rms scatter coefficient. With the exception of the scatter coefficients, examples pertaining to the above parameters are also given in section 7.2. Although the rms scatter coefficient measure and the spread parameter measures of the unidimensional channel spectra and autocorrelation functions are at the low end of the degree of signal characterization, they provide us with some of the most useful and applicable properties of the multipath phenomena. These results are given in sections 7.3 through 7.7. The airport landing, taxi, and takeoff multipath environment results are treated separately from the en route CONUS results and are presented in section 7.8.

With the exception of the airport environment tests, the CONUS data was gathered over the simultaneous vertical and horizontal polarization probes. For all intervals of valid data collection (totaling roughly 12 hr of test time), the channel's delay-spectra time history has been determined for each of the polarization states. These outputs were used not only to provide an overview of the channel's time-variant characteristics but also to aid in the selection of time intervals to which the detailed $S(\tau, \omega)$ spectral analysis was applied. When possible, at least one time interval per flight test leg (14 min of data collection) was subjected to the $S(\tau, \omega)$ analysis; usually an interval producing a very active or strong multipath return was chosen.

7.1 DELAY-SPECTRA TIME HISTORY

7.1.1 Summary of Observations

The channel's delay-spectra time history, $Q(t, \tau)$, provides a partial illustration of the time-variant nature of the CONUS multipath probes. In addition, $Q(t, \tau)$ may be used to obtain an overview of the magnitude and delay-spectra characteristics associated with generalized terrain characteristics over which the specular-point traverses. For this reason each interval of valid data collection has been subjected to delay-spectra time history analysis. In total this represents approximately 12 hr of experiment time, providing an extensive data base from which one may (1) select time intervals of interest that warrant further data analysis (e.g., $S(\tau, \omega)$) and (2) delineate the more obvious scatter signatures associated with a variety of CONUS terrain conditions. The remainder of this discussion relates to item 2. Although somewhat of an overgeneralization, we have segregated the terrain types into the following categories: vegetation-covered, snow-covered plains, snow-covered

mountains, large-size lakes, coastal harbors, large industrial cities, and residential areas. The salient $Q(t,\tau)$ features of each category are discussed below.

Vegetation-Covered: Signal amplitude return was very low, most likely due to foliage absorption of the electromagnetic wave. The observable signal structure was relatively time invariant, except for intervals when the specular point traversed a small area of high reflectivity (e.g. lake, river, road, rock outcropping). By comparison these intervals produced high-energy unitap signals that appear as spikes superimposed upon the low-level, modestly spread background return.

Snow-Covered Plains: Snow-covered plains produced relatively intense low-spread returns, with a modest amount of signal stationarity. The defoliated deciduous trees in the "glistening region" usually effectively attenuated, or broadly dispersed, the signal.

Snow-Covered Mountains: Returns were fairly strong, with spreads occasionally somewhat equivalent to the higher grazing angle oceanic data. Possibly due to the large-scale size of the scattering elements, the delay spectra exhibited a high degree of granularity and non-stationarity.

Large Lakes (Liquid): In their liquid state, large lakes produced $Q(t,\tau)$ arrays with attributes similar to the oceanic test probes. Namely, the signal strength was very large (roughly equivalent to the Fresnel reflection coefficient magnitude) and the surfaces produced a broadly dispersed return. These characteristics were essentially invariant over the duration of the probes; however it is believed that wind and fetch conditions significantly influence the spread properties of the signal.

Large Lakes (Frozen): A frozen lake presents either an ice- or snow-covered surface. The snow-covered large lakes had signatures similar to those of the flat snow-covered terrain. In general, partially frozen lakes (e.g., frozen along the shoreline) produced larger spreads than lakes totally frozen and covered by snow. This is thought to relate to a "rafting and ridging" phenomenon that accompanies the freezing, thawing, and wind-generated wave pressures acting upon the ice/water interface of partially frozen lakes.

Coastal Harbors: For the relatively small amount of coastal harbor data gathered, the $Q(t,\tau)$ function revealed characteristics similar to those of the oceanic and large-lake probes. As previously stated, this implies a high-energy, broadly dispersed signal that is fairly stable except for the shoreline areas.

Industrial Areas: Delay-spectra signatures from industrial and business areas typically exhibited very little spreading, with the bulk of the returned energy being contained within 0.1 or 0.2 μ sec of the specular-point return. A probable explanation for this is that industrial buildings are box shaped, in general with flat roofs and sides perpendicular to the level ground. Such conditions allow little energy to be returned from regions other than near the vicinity of the specular-point area.

Residential Areas: The residential areas produced multipath signatures distinctly different from those of the industrial areas. Typically, the residential returns did not have an overwhelming amount of energy in the specular-point tap and gave the appearance of being either highly attenuated or broadly dispersed. These characteristics are somewhat similar to those of the vegetation-covered terrain probes, although much of the residential area traversed (i.e., Brooklyn, New York City) did not have a substantial vegetation cover. The difference between the industrial and residential area multipath signatures might be related to roof structures, with the residential buildings generally being more peaked and thus producing a more broadly dispersed return.

7.1.2 Example Results

The following paragraphs present $Q(t,\tau)$ examples that illustrate signal structure characteristics of scatter from several of the categories delineated in section 7.1.1.

7.1.2.1 Coastal Harbors/Large-City Areas/Vegetation-Covered Terrain – This example, taken from a leg of the September 19, 1974, multipath test (see fig 7-1), presents $Q(t,\tau)$ characteristics associated with multipath return from coastal harbors, large-city areas, and vegetation-covered terrain. A detailed specular-point trajectory for this particular segment is presented in figure 7-6, with the corresponding $Q(t,\tau)$ function illustrated in figure 7-7(a) through (d). It is noted that the example delay-spectra time history corresponds to traversal of Long Island Sound, Long Island, Lower New York Bay, and a segment of northeastern New Jersey.

The boundaries of these individual terrain characteristics are quite explicit; thus ground and delay-spectra features are easily compared and enable us to isolate return from:

Coastal harbors	1238:22 to 1239:23
	1242:15 to 1244:00
Large-city areas	1239:23 to 1242:15
Vegetation-covered terrain	1244:00 to 1245:56.

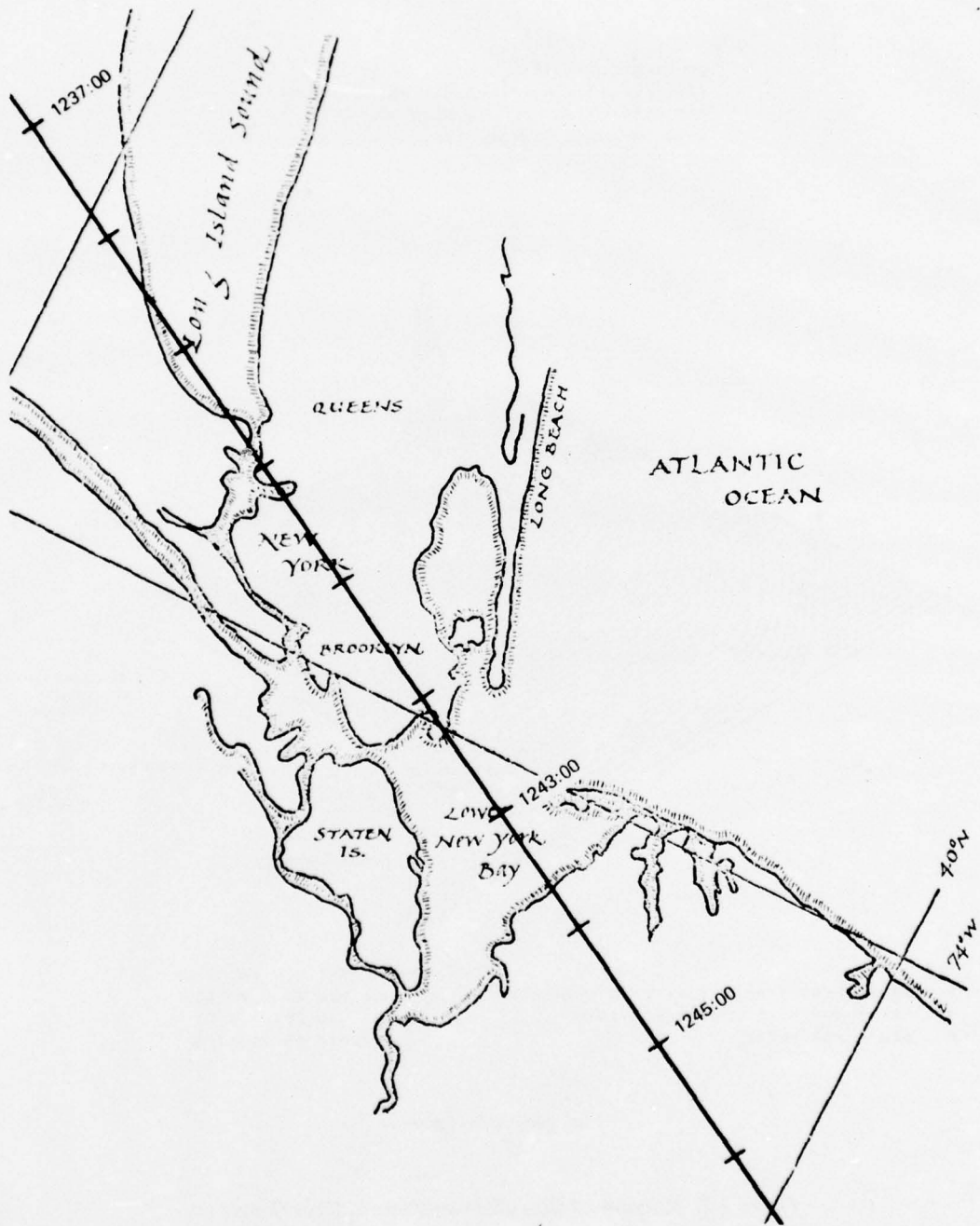
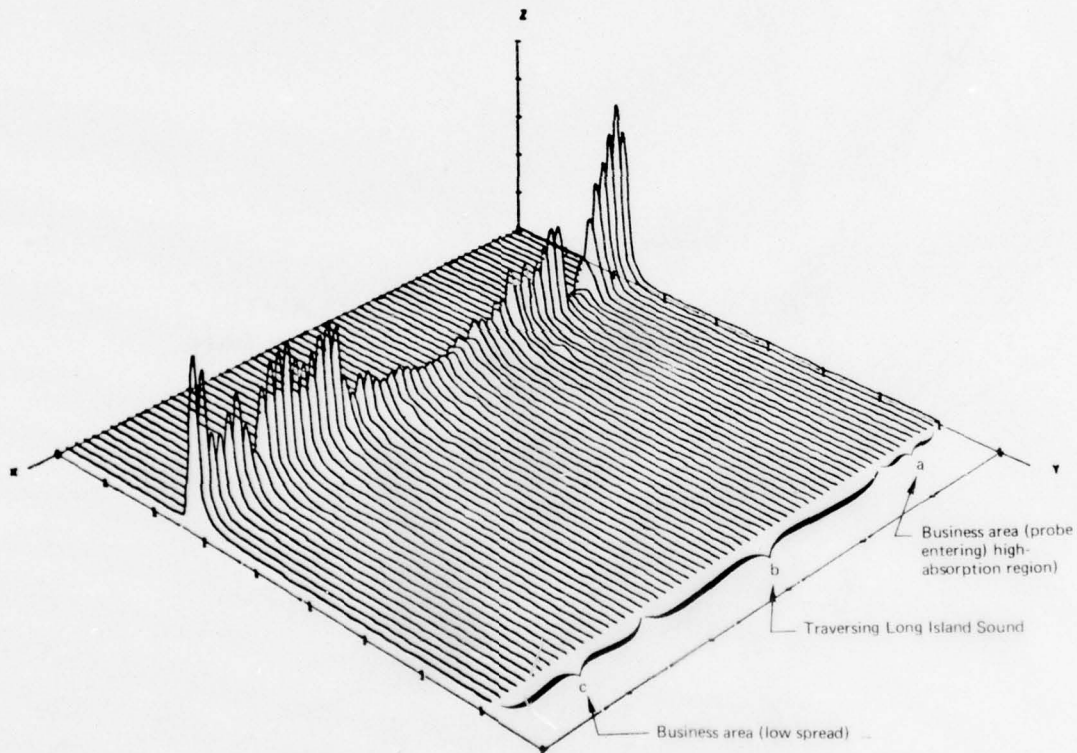


Figure 7-6. Specular-Point Trajectory (September 19, 1974) — New York City, Harbor

DELAY SPECTRA TIME HISTORY
 DATE 8/19/74 HORIZONTAL POLARIZATION
 TAP RESOLUTION .1 MICROSEC
 TIME INTERVAL 12/30/ .061 TO 12/30/59.090

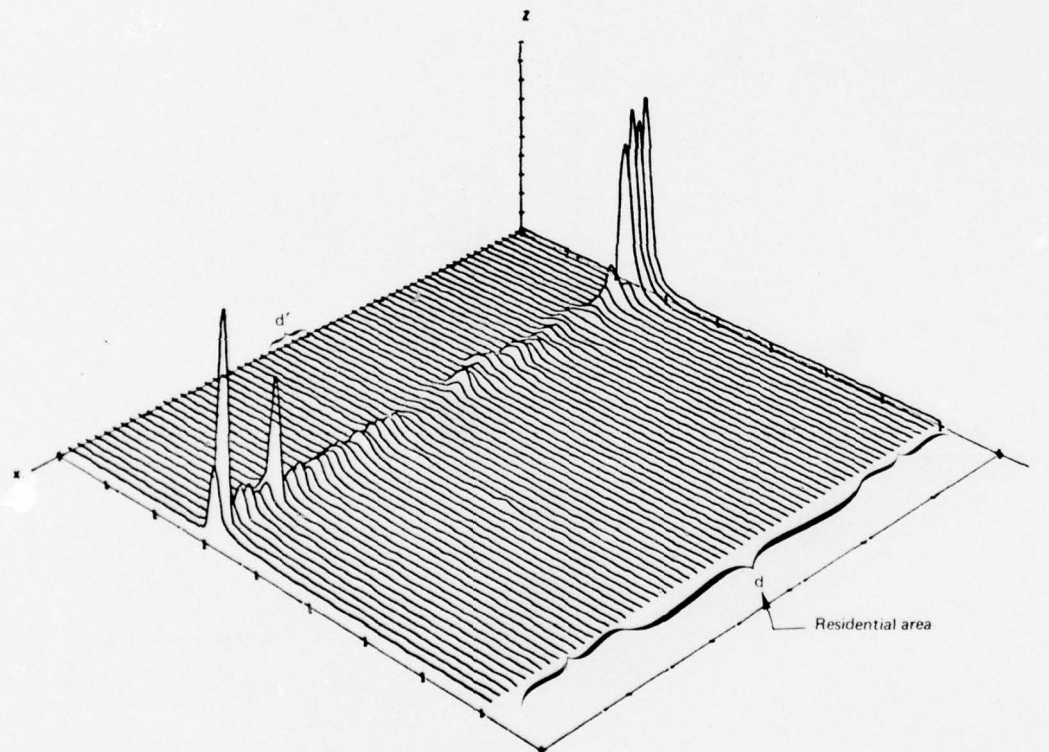


AXIS		MINIMUM	MAXIMUM	INCREMENT
X	EXPERIMENT TIME RELATIVE TO T-START (SEC)	.00	120.00	20.00
Y	DELAY TAP (.1 MICROSEC. WIDTH)	30.00	75.00	5.00
Z	DELAY PSD (LINEAR)	.0015000	3000.00	3000.00

(a) Long Island Sound

Figure 7-7. Example of CONUS Delay-Spectra Time History

DELAY SPECTRA TIME HISTORY
 DATE 9/19/74 HORIZONTAL POLARIZATION
 TAP RESOLUTION .1 MICROSEC
 TIME INTERVAL 12/39/59.095 TO 12/41/58.135

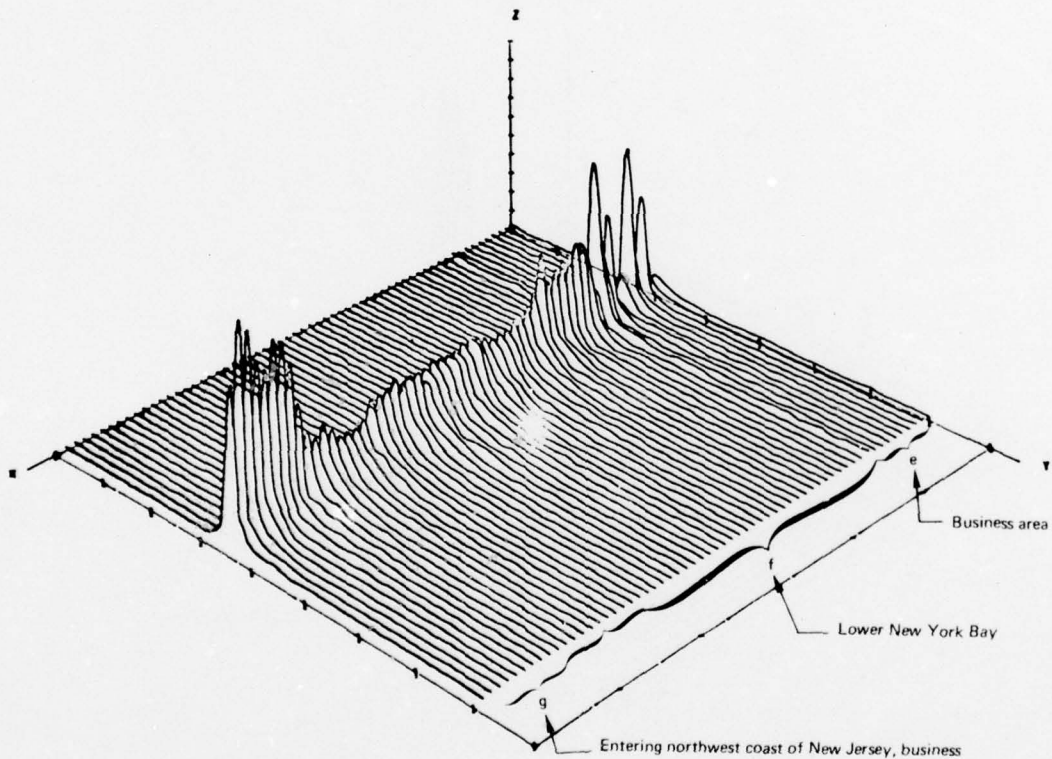


AXIS		MINIMUM	MAXIMUM	INCREMENT
X	EXPERIMENT TIME RELATIVE TO T-START(SEC)	.00	120.00	20.00
Y	DELAY TAP (.1 MICROSEC. WIDTH)	30.00	75.00	5.00
Z	DELAY PSD (LINEAR)	.0010000.00	1000.00	

(b) Long Island

Figure 7-7. (Continued)

DELAY SPECTRA TIME HISTORY
 DATE 9/18/74 HORIZONTAL POLARIZATION
 TAP RESOLUTION .1 MICROSEC
 TIME INTERVAL 12/41/58.140 TO 12/43/57.175

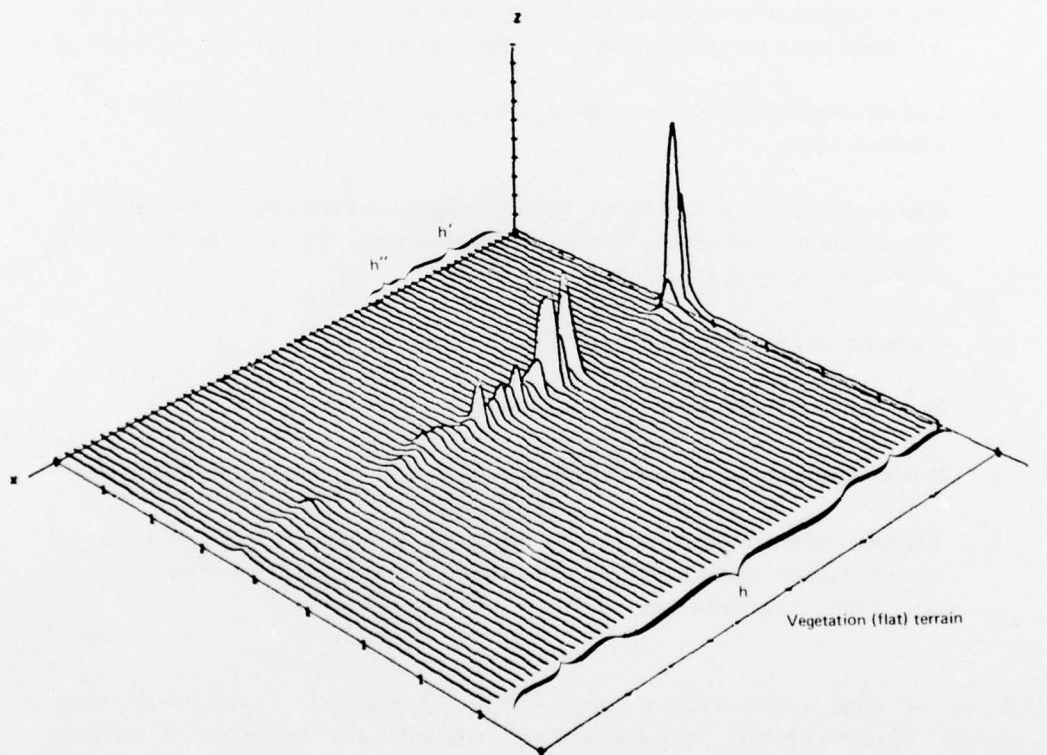


AXES		MINIMUM	MAXIMUM	INCREMENT
X	EXPERIMENT TIME RELATIVE TO T-START (SEC)	.00	120.00	20.00
Y	DELAY TAP (.1 MICROSEC WIDTH)	30.00	75.00	5.00
Z	DELAY PSD (LINEAR)	.0010000	.00	1000.00

(c) Lower New York Bay

Figure 7-7. (Continued)

DELAY SPECTRA TIME HISTORY
 DATE 9/19/74 HORIZONTAL POLARIZATION
 TAP RESOLUTION .1 MICROSEC
 TIME INTERVAL 12/43/57.193 TO 12/45/56.213



AXIS		MINIMUM	MAXIMUM	INCREMENT
X	EXPERIMENT TIME RELATIVE TO T-START(SEC)	.00	120.00	20.00
Y	DELAY TAP (.1 MICROSEC. WIDTH)	30.00	75.00	5.00
Z	DELAY PSD (LINEAR)	.0010000	.00	1000.00

(d) Northwest New Jersey

Figure 7-7. (Concluded)

Figure 7-7 has been time-segmented by brackets a through h; the segmented times are briefly discussed below.

- a. Characteristic $Q(t, \tau)$ signatures of probe moving from business areas to high-scatter areas (i.e., vegetation or rural areas).
- b. Probe entering, traversing, and leaving Long Island Sound. Note the increase in delay spread and signal stationarity as the probe-illuminating area is predominantly over water.
- c. Low spreading (almost unitap), characteristic of flat-top building reflections (i.e., industrial areas).
- d. High scatter or absorption area; low-level delay amplitudes relatively unchanged from that seen for building scatter. Typical of residential areas. Note the high absorption at d' ; possibly traversing a park area.
- e. Characteristics similar to item c; probably more business in area.
- f. Same characteristics as item c; crossing Lower New York Bay.
- g. Presents characteristics similar to items e and c; therefore appears to be business area.
- h. Vegetation-covered terrain; high absorption during interval h' of figure 7-7(d) is typical of dense foliage. High-amplitude fluctuations of h'' are related to the presence of small lakes, rivers, or flat open areas.

7.1.2.2 Snow-Covered Semimountainous Terrain — As noted in section 7.1.1, snow-covered terrain may produce $Q(t, \tau)$ features with a high degree of signal nonstationarity, especially if the terrain is forested (deciduous or nondeciduous) or mountainous. A semimountainous leg associated with the flight test conducted on February 20, 1975, is presented as an example of this terrain type. Pertinent system parameters are:

Flight direction:	In-plane (toward ATS-6)
Airplane speed:	Approximately 190 m/sec
Airplane altitude:	Approximately 9.5 km (31,000 ft)
Elevation angle:	Approximately 30°

Using a log of the KC-135's INS latitude and longitude outputs, the specular-point trajectory for this leg has been superimposed upon a terrain profile map as shown in figure 7-8. The channel delay-spectra time history for horizontally polarized signals is illustrated in figure 7-9(a) through (d).

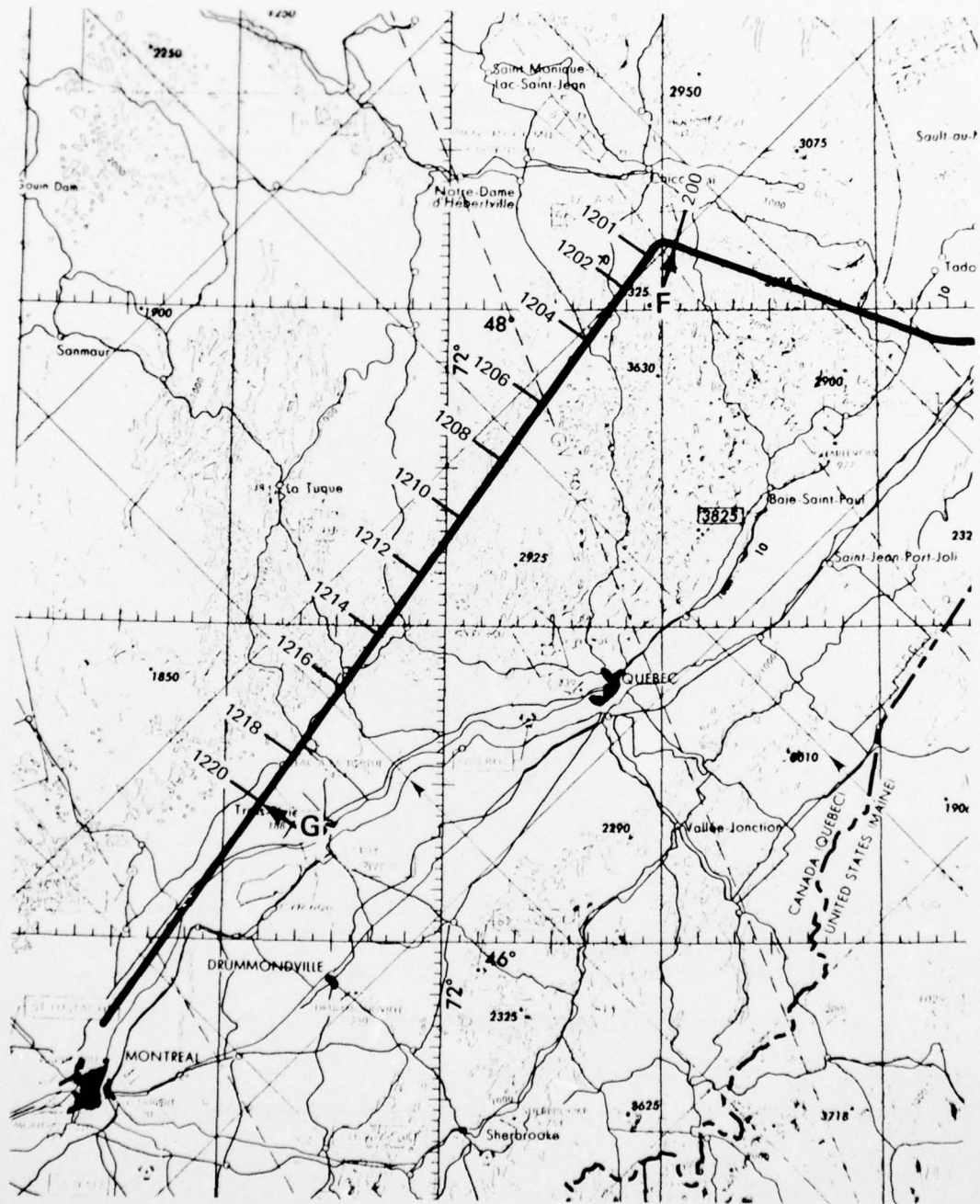
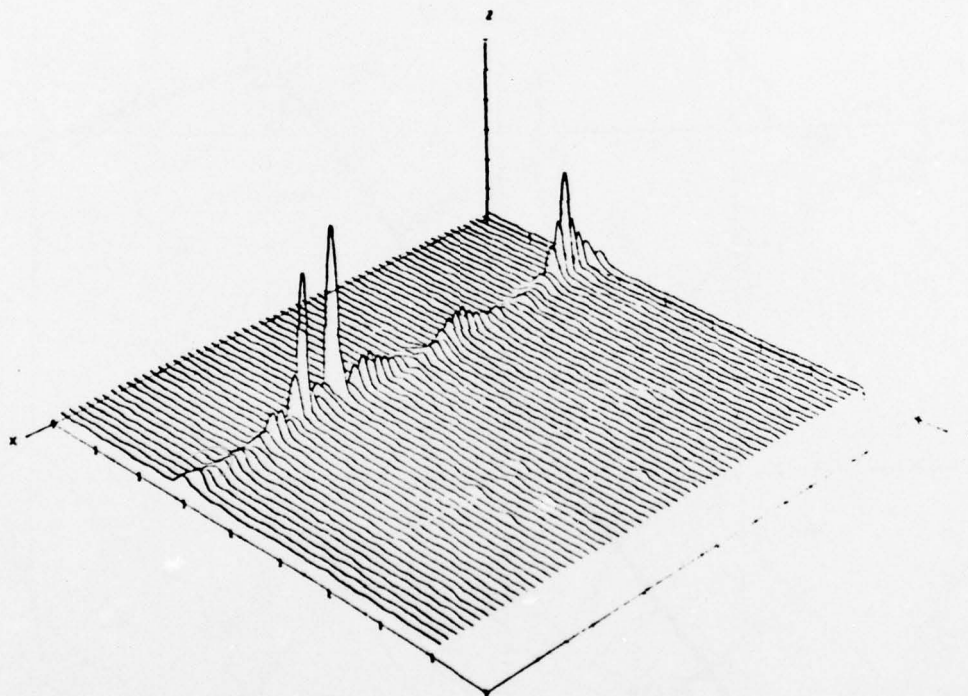


Figure 7-8. Specular-Point Overlay, Leg F-G, February 20, 1975

DELAY SPECTRA TIME HISTORY
 DATE 2/20/75 HORIZONTAL POLARIZATION
 TAP RESOLUTION .2 MICROSEC
 TIME INTERVAL 12/ 5/34.007 TO 12/ 7/34.208

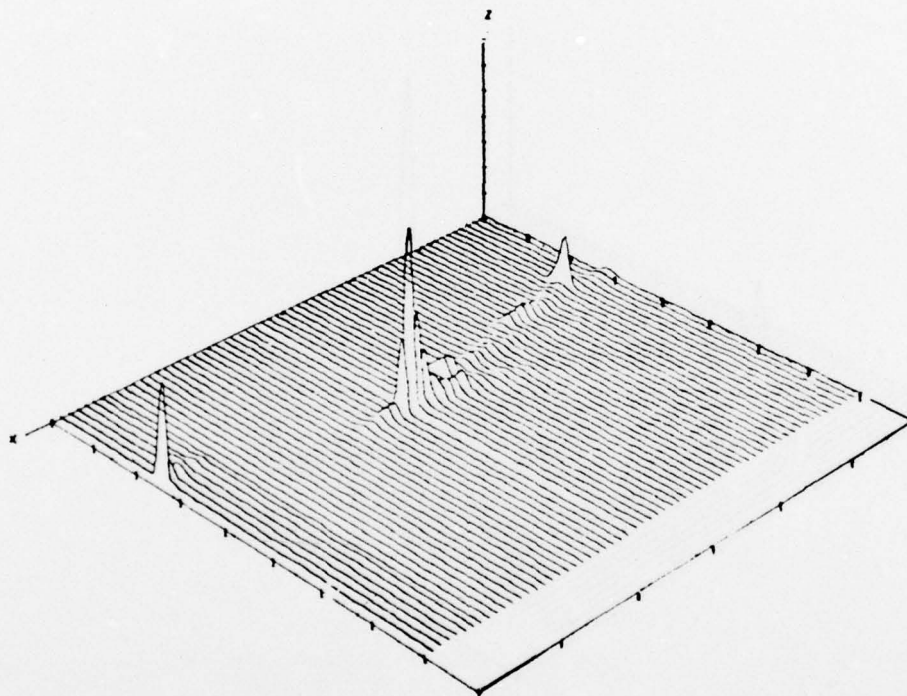


AXIS	MINIMUM	MAXIMUM	INCREMENT
X EXPERIMENT TIME RELATIVE TO T-START(SEC)	.00	120.00	20.00
Y DELAY TAP (.2 MICROSEC. WIDTH)	20.00	65.00	5.00
Z DELAY PSD (LINEAR)	.00	3000.00	500.00

(a) 2-min Time Interval No. 1

Figure 7-9. Delay-Spectra Time History — Leg F-G, Horizontal Polarization, February 20, 1975

DELAY SPECTRA TIME HISTORY
 DATE 2/20/75 HORIZONTAL POLARIZATION
 TAP RESOLUTION .2 MICROSEC
 TIME INTERVAL 12/ 7/34.215 TO 12/ 9/34.415

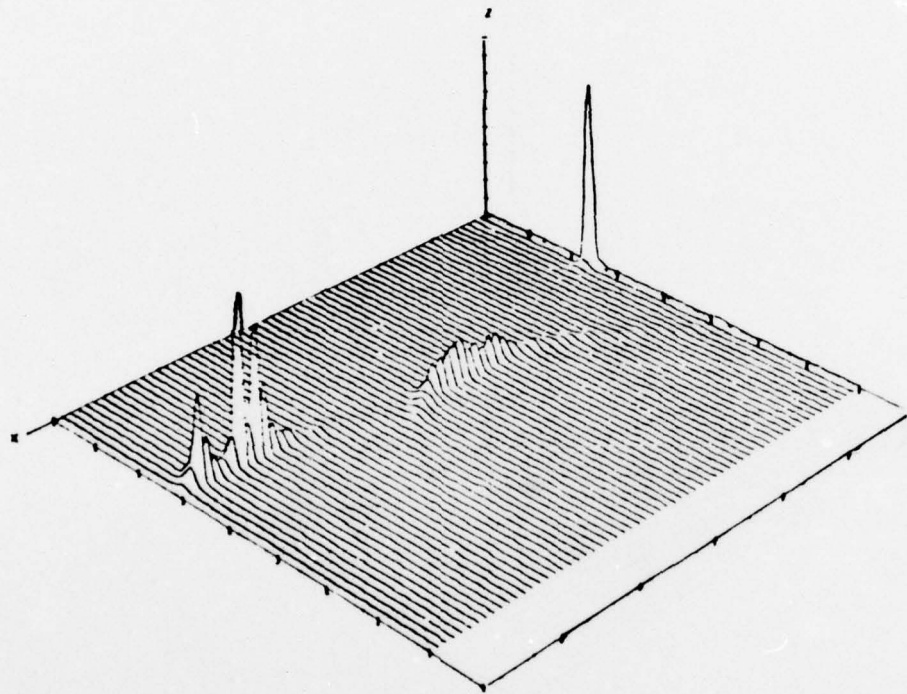


AXIS		MINIMUM	MAXIMUM	INCREMENT
X	EXPERIMENT TIME RELATIVE TO T-START(SEC)	.00	120.00	20.00
Y	DELAY TAP (.2 MICROSEC. WIDTH)	20.00	65.00	5.00
Z	DELAY PSD (LINEAR)	.00	7000.00	1000.00

(b) 2-min Time Interval No. 2

Figure 7-9. (Continued)

DELAY SPECTRA TIME HISTORY
 DATE 2/20/75 HORIZONTAL POLARIZATION
 TAP RESOLUTION .2 MICROSEC
 TIME INTERVAL 12/ 9/34.422 TO 12/11/34.622

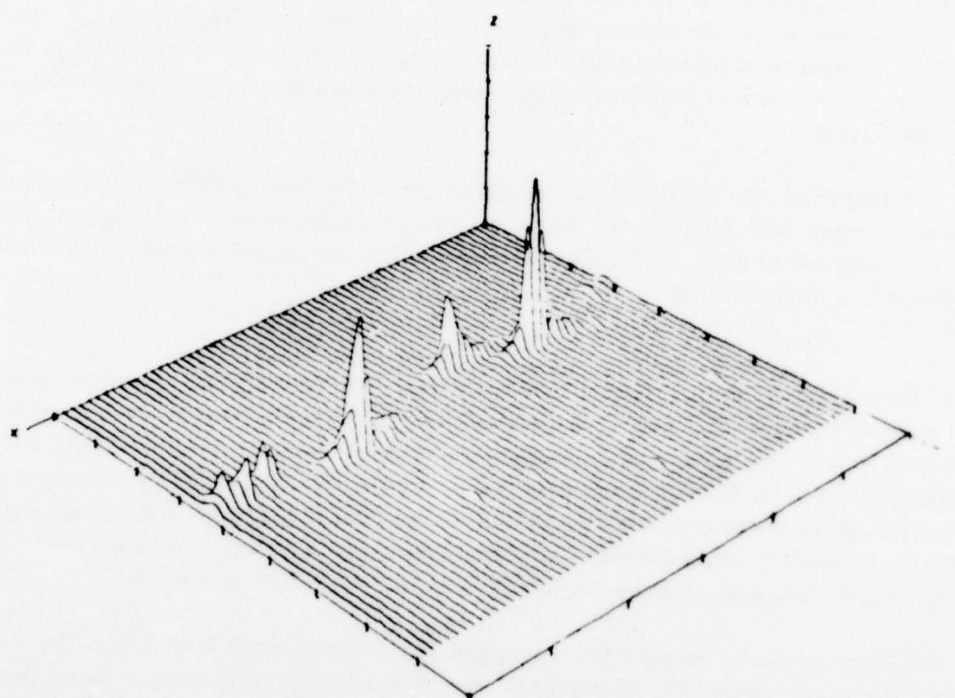


AXES		MINIMUM	MAXIMUM	INCREMENT
X	EXPERIMENT TIME RELATIVE TO T-START(SEC)	.00	120.00	20.00
Y	DELAY TAP (.2 MICROSEC. WIDTH)	20.00	85.00	5.00
Z	DELAY PSD (LINEAR)	.00	5000.00	500.00

(c) 2-min Time Interval No. 3

Figure 7-9. (Continued)

DELAY SPECTRA TIME HISTORY
 DATE 2/20/75 HORIZONTAL POLARIZATION
 TAP RESOLUTION .2 MICROSEC
 TIME INTERVAL 12/11/34.629 TO 12/13/34.829



AXIS		MINIMUM	MAXIMUM	INCREMENT
X	EXPERIMENT TIME RELATIVE TO 1-START(SEC)	.00	120.00	20.00
Y	DELAY TAP (.2 MICROSEC. WIDTH)	20.00	65.00	5.00
Z	DELAY PSD (LINEAR)	.00	2500.00	500.00

(d) 2-min Time Interval No. 4

Figure 7-9. (Concluded)

To enhance the output resolution, the mean square energy outputs corresponding to only a 40-tap region in the vicinity of the most active return have been plotted (rather than all 112 taps).

A cursory analysis of the data reveals the presence of a variety of spectra signatures ranging from high-energy, single-tap to relatively low-energy, multitap occupancy. We also observe the occurrence of what appears to be a multimode reflection process (e.g., 1208:30). No definitive correlations of these phenomena with terrain features have been attempted although it appears that whenever the specular point traverses a body of fresh water (probably frozen for the February series) such as a river, the return has a characteristic high-energy unitap reflection component in its delay-spectra time history.

For comparison, the vertical polarization counterpart of the above data for a 2-min segment is presented in figure 7-10. Note that the vertical and horizontal probes occur simultaneously. Comparing the horizontal data of figure 7-9(d) with vertical data reveals that the two sets vary in concert with each other to a relatively high degree.

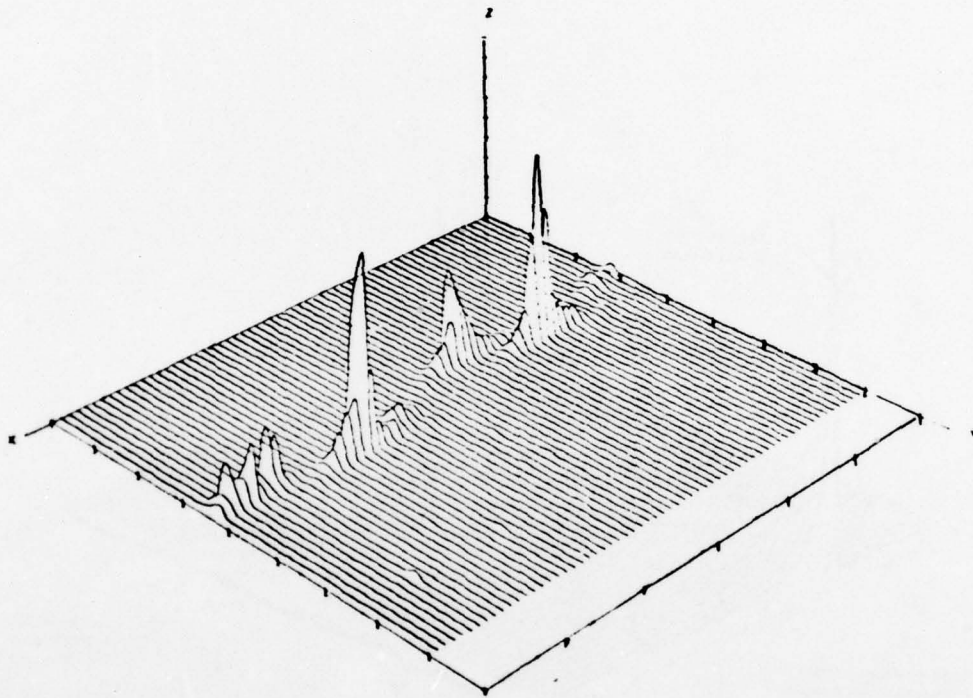
7.1.2.3 Large Lakes – Due to fresh water's relatively high reflection coefficient magnitude, lake scatter probably represents one of the most significant CONUS multipath interferences. As stated earlier, small bodies of water surrounded by vegetation-covered or mountainous terrain contribute to the nonstationarity of the CONUS signal structure and appear as high-level unitap returns superimposed upon broadly spread, low-level spectra from the surrounding terrain. In general, as the lake dimensions increase, the background scatter diminishes and the multipath signature eventually becomes unimodal when the area of the lake encompasses the "glistening region" of the multipath process.

A portion of the February 19, 1975, multipath test was flown in the north-south direction over the Great Lakes (see fig 7-4). Sample results are presented for the horizontally polarized probe's traversal of Lake Michigan. Information¹ obtained from the Great Lakes Environmental Research Laboratory indicates that the northern 20 miles of this lake was frozen, whereas the interior lake region was in the liquid state.

The example $Q(t,\tau)$ probe data are given in figures 7-11, 7-12, and 7-13. Figures 7-11 and 7-12 are time-sequential $Q(t,\tau)$ plots corresponding to the probe's lake entry and first 12-mile traversal (i.e., ice covered). The third figure represents return from the midlake region (i.e., liquid state).

¹ A report being published by the Great Lakes Environmental Research Laboratory will contain this and other information.

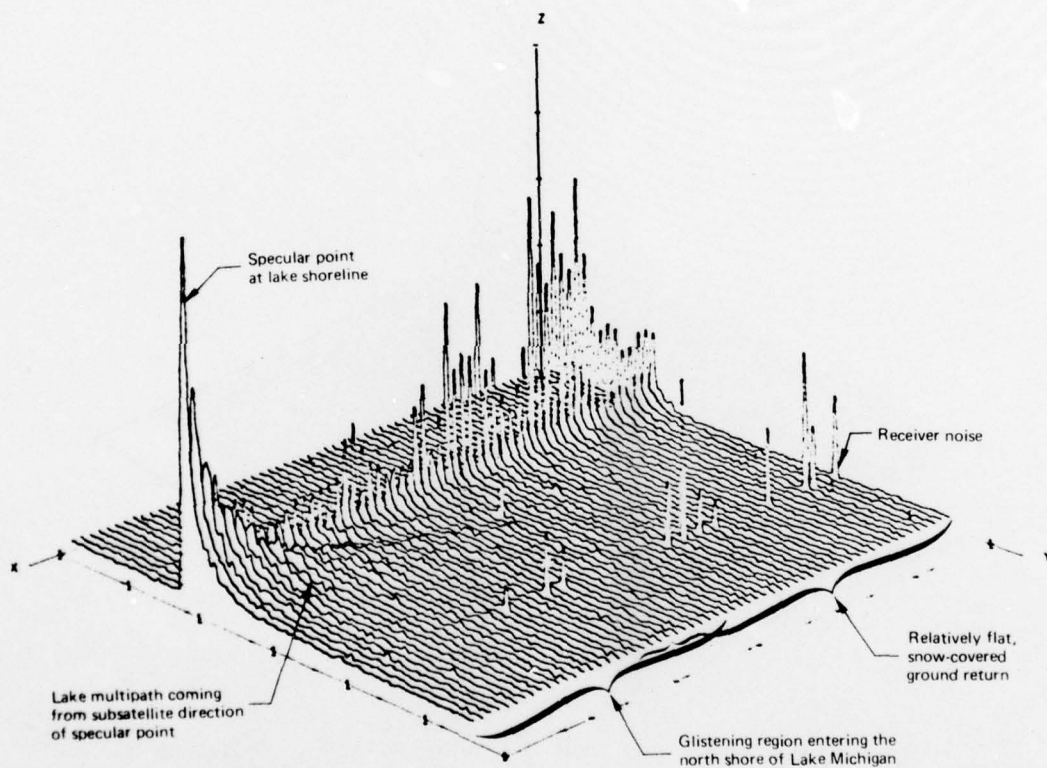
DELAY SPECTRA TIME HISTORY
 DATE 2/20/75 VERTICAL POLARIZATION
 TAP RESOLUTION .2 MICROSEC
 TIME INTERVAL 12/11/34.629 TO 12/13/34.629



AXIS		MINIMUM	MAXIMUM	INCREMENT
X	EXPERIMENT TIME RELATIVE TO Y-START (SEC)	.00	120.00	20.00
Y	DELAY TAP (.2 MICROSEC. WIDTH)	20.00	85.00	5.00
Z	DELAY PSD (LINEAR)	.00	4500.00	500.00

Figure 7-10. Delay-Spectra Time History — Leg F-G, Vertical Polarization, February 20, 1975
 (2-min Time Interval No. 4)

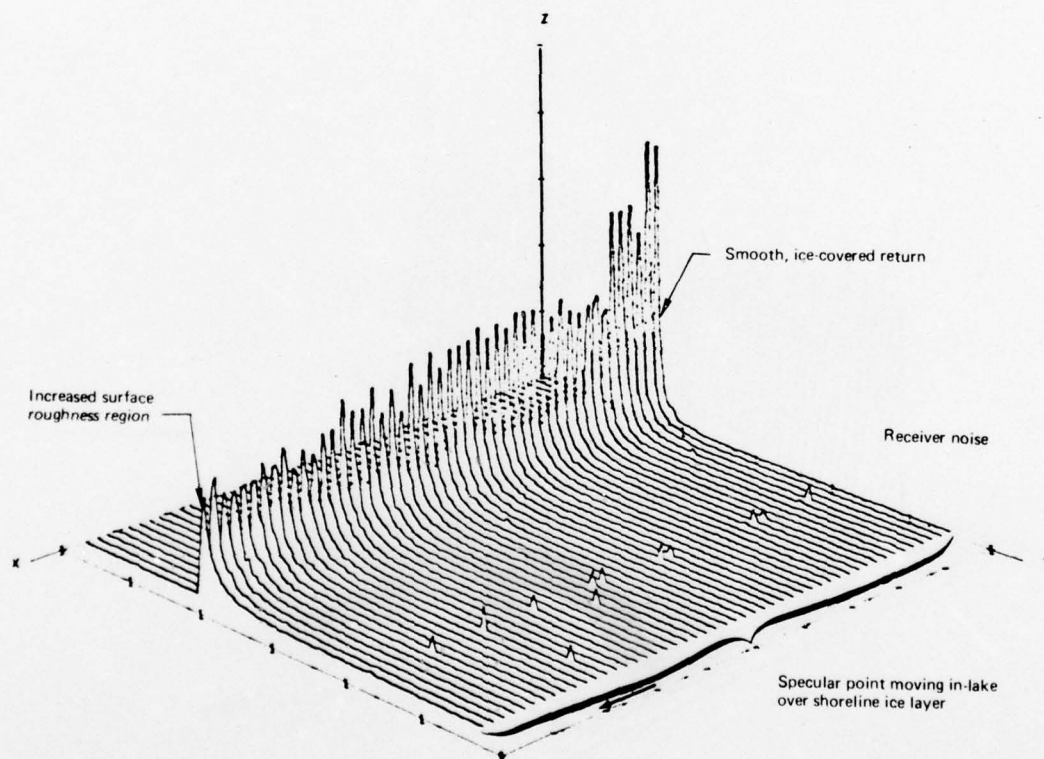
DELAY SPECTRA TIME HISTORY
 DATE 2/19/75 HORIZONTAL POLARIZATION
 TAP RESOLUTION .2 MICROSEC
 TIME INTERVAL 11/ 1/ .208 TO 11/ 3/ .408



AXIS		MINIMUM	MAXIMUM	INCREMENT
X	EXPERIMENT TIME RELATIVE TO T-START (SEC)	0	120	20
Y	DELAY TAP (.2 MICROSEC. WIDTH)	0	120	20
Z	DELAY PSD (LINEAR)	0	250	50

Figure 7-11. Delay-Spectrum Time History, Lake Michigan North Shoreline, February 19, 1975

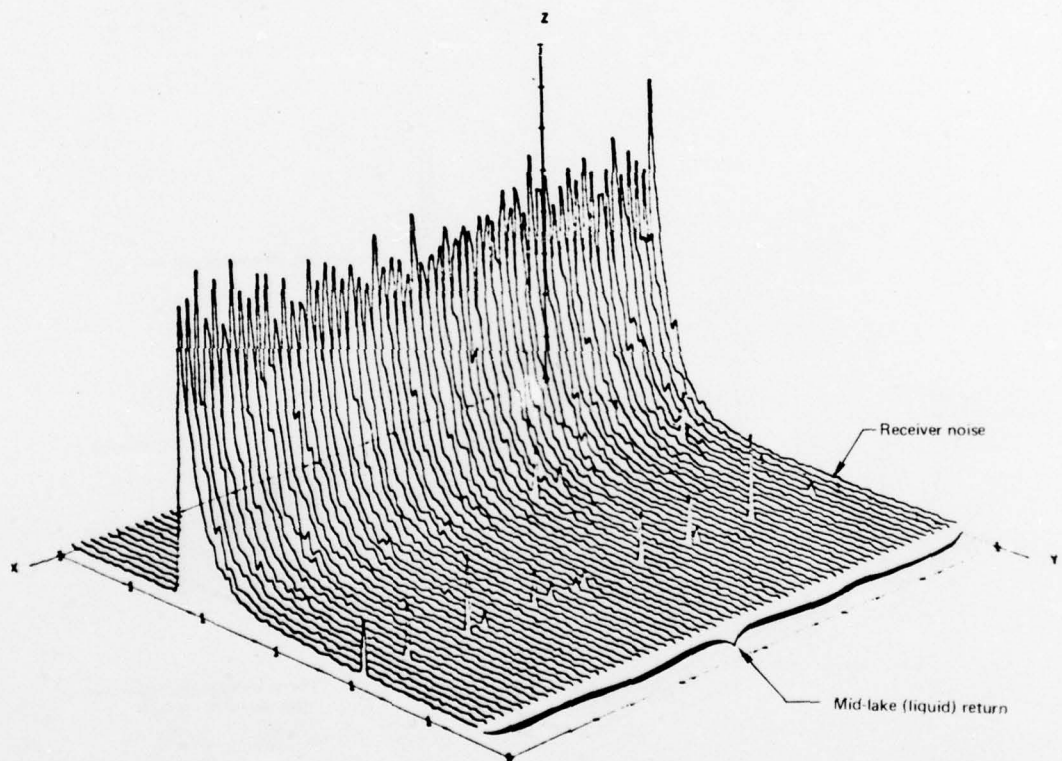
DELAY SPECTRA TIME HISTORY
 DATE 2/19/75 HORIZONTAL POLARIZATION
 TAP RESOLUTION .2 MICROSEC
 TIME INTERVAL 11/ 3/ .415 TO 11/ 4/30.578



AXIS		MINIMUM	MAXIMUM	INCREMENT
X	EXPERIMENT TIME RELATIVE TO Y-START[SEC]	0	100	10
Y	DELAY TAP [.2 MICROSEC. WIDTH]	0	120	20
Z	DELAY PSD [LINEAR]	0	1500	300

Figure 7-12. Delay-Spectra Time History, Lake Michigan — Ice— February 19, 1975

DELAY SPECTRA TIME HISTORY
 DATE 2/19/75 HORIZONTAL POLARIZATION
 TAP RESOLUTION .2 MICROSEC
 TIME INTERVAL 11/12/25.200 TO 11/14/25.400



AXIS		MINIMUM	MAXIMUM	INCREMENT
X	EXPERIMENT TIME RELATIVE TO T-START[SEC]	0	120	20
Y	DELAY TAP [.2 MICROSEC. WIDTH]	0	120	20
Z	DELAY PSD [LINEAR]	0	400	30

Figure 7-13. Delay-Spectra Time History, Lake Michigan — Liquid— February 19, 1975

Descriptions delineating pertinent terrain and signal structure characteristics have been included with the $Q(t,\tau)$ plots. These characteristics are discussed below.

- a. Prior to the specular point entering the lake (fig 7-11), we observe a signature characteristic of fairly flat, snow-covered terrain. Also, as the specular point approaches the shoreline, the tails of the delay spectrum become enhanced by the arrival of far-forward scatter from the lake surface. The enhancement moves inward toward the origin of the delay spectrum the closer the probe gets to the lake boundary.
- b. Figure 7-12 covers the first 12 min of lake traversal and illustrates a delay spectrum that progressively increases in spread. This is attributed to an increase in deformities (rafting and ridging) associated with the interior regions of the lake ice.
- c. The interior segment of the lake's $Q(t,\tau)$ distribution (fig 7-13) is highly stationary, with a relatively large dispersion. These attributes are similar to the high-angle oceanic multipath signatures (further discussion relating to Fourier operations on the midlake return is given in the next section).

7.2 CONUS DELAY-DOPPLER SCATTER FUNCTIONS AND ASSOCIATED PARAMETERS

The preceding section provided a sample overview of the CONUS channel delay-spectra signatures. As one would expect, when a high degree of nonstationarity in the channel delay spectra is observed, there exists a corresponding degree of delay-Doppler scatter function, $S(\tau,\omega)$, nonstationarity. In this section several samples are presented to illustrate the variety of CONUS scatter functions observed.

$S(\tau,\omega)$ represents the power spectral density of received multipath energy having delay τ and Doppler frequency shift ω . Typically, we derive $S(\tau,\omega)$ over a 7-sec time interval. In many cases the surface characteristics being probed will change appreciably over this time interval; thus it should not be assumed that $S(\tau,\omega)$ represents a complete statistical description of the channel.

Each CONUS delay-Doppler scatter function has been assigned a subscript number cross-referencing it to the specular-point trajectories shown in figures 7-1 through 7-5.

In the following sample presentation, each $S(\tau,\omega)$ distribution is accompanied by its delay spectrum, frequency autocorrelation function, Doppler spectrum, and time autocorrelation function. For several of the examples, the channel's joint time-frequency autocorrelation function is also presented. For clarity, this distribution is plotted from two alternate points of view. Relationships between the above channel measures and the $S(\tau,\omega)$ function are given in section 4.

AD-A042 325

BOEING COMMERCIAL AIRPLANE CO SEATTLE WASH

F/G 17/7

AIR TRAFFIC CONTROL EXPERIMENTATION AND EVALUATION WITH THE NAS--ETC(U)

SEP 76 A D THOMPSON, B J BURRESON, P F RIEDER DOT-TSC-707-5

UNCLASSIFIED

D6-44050

FAA-RD-75-173-5

NL

4 OF 4
AD
A042325



END
DATE
FILMED
8-77
DDC

As one might expect, the CONUS scatter medium provides an ensemble of unique $S(\tau, \omega)$ functions. Although it may represent somewhat of an oversimplification, we have categorized the signatures according to the following list:

- Low spreads
- Modest spreads
- Asymmetrical Doppler spread
- Large spreads
- Multimode returns
- Brewster angle scatter.

Samples for each of these categories are furnished in figures 7-14 through 7-24. These data are related to the above scatter signatures and terrain profile characteristics through use of table 7-2; a brief discussion pertaining to each category is given below.

7.2.1 Low Spreads (figs. 7-14 and 7-15)

When the scatter medium is relatively flat over the entire surface responsible for returning energy under normal to precipitous slope conditions, the received signal structure will be unimodal with very low spreads in both the delay and Doppler coordinates. Such conditions were observed to occur primarily over large frozen lakes and sections of the central plains of Canada. The example presented corresponds to scatter from a frozen lake and possesses delay and Doppler spectra that decay very quickly. Conversely, the joint autocorrelation function and its axial cuts were observed to fall off slowly.

7.2.2 Modest Spreads (fig. 7-16)

A high percentage of the CONUS returns from the east coast flight trajectories yield signatures that fall into this category. The example of figure 7-16 pertains to a cross-plane flight track over farmland. Delay and Doppler two-sided 3-dB spread values of 0.3 μ sec and 70 Hz are associated with this signature. These spread values (see sections 7.4 and 7.6) are fairly typical for the majority of the CONUS test results but are much smaller than typical spreads observed for oceanic scatter. The observed CONUS spreads appear to be representative of expectation based on an rms slope of roughly 3° .

7.2.3 Asymmetrical Position Scatter (fig. 7-17)

In general, inhomogeneities in the electrical and slope statistics of a reflecting surface will result in a scatter intensity that does not exhibit a highly asymmetrical distribution about the specular-

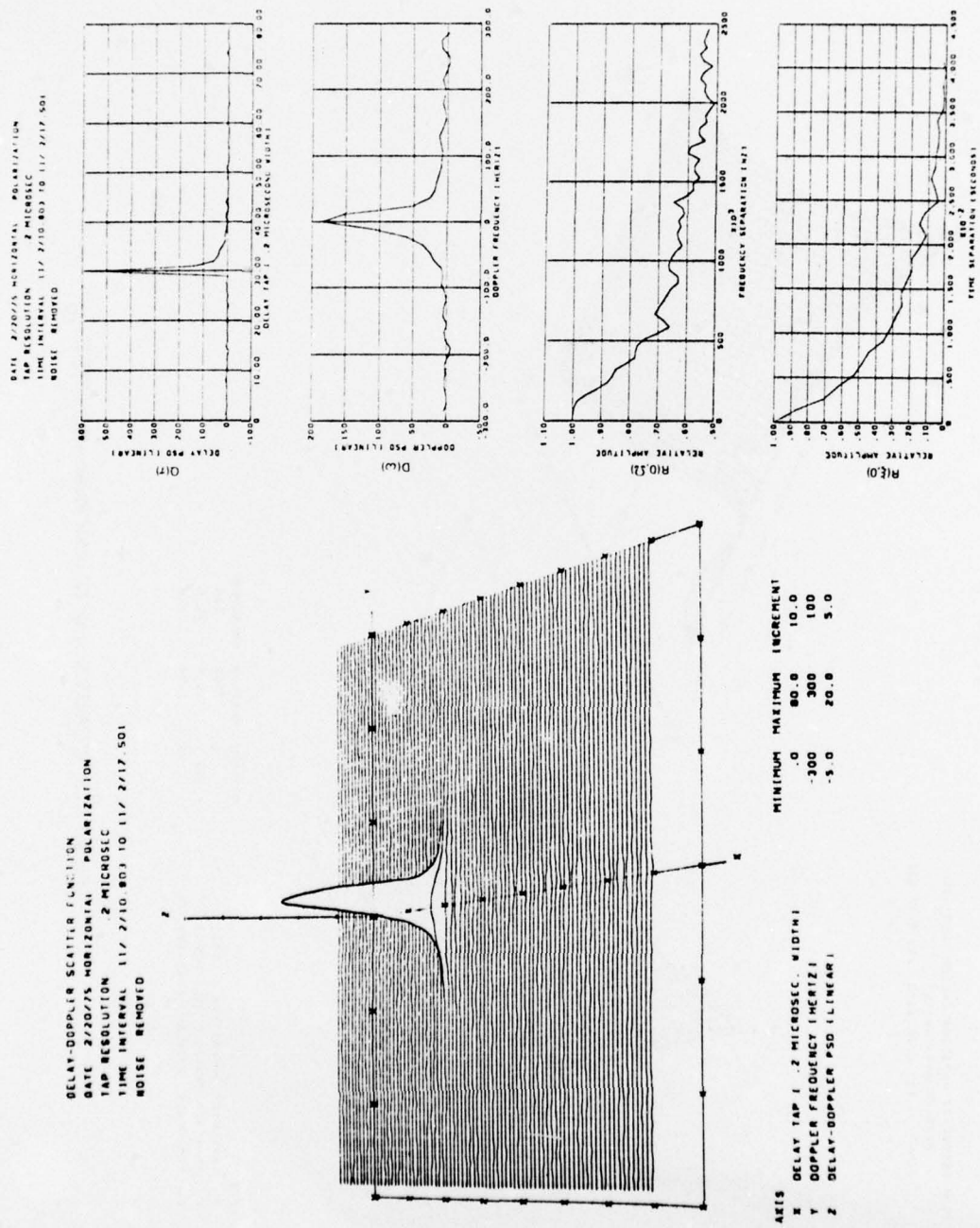
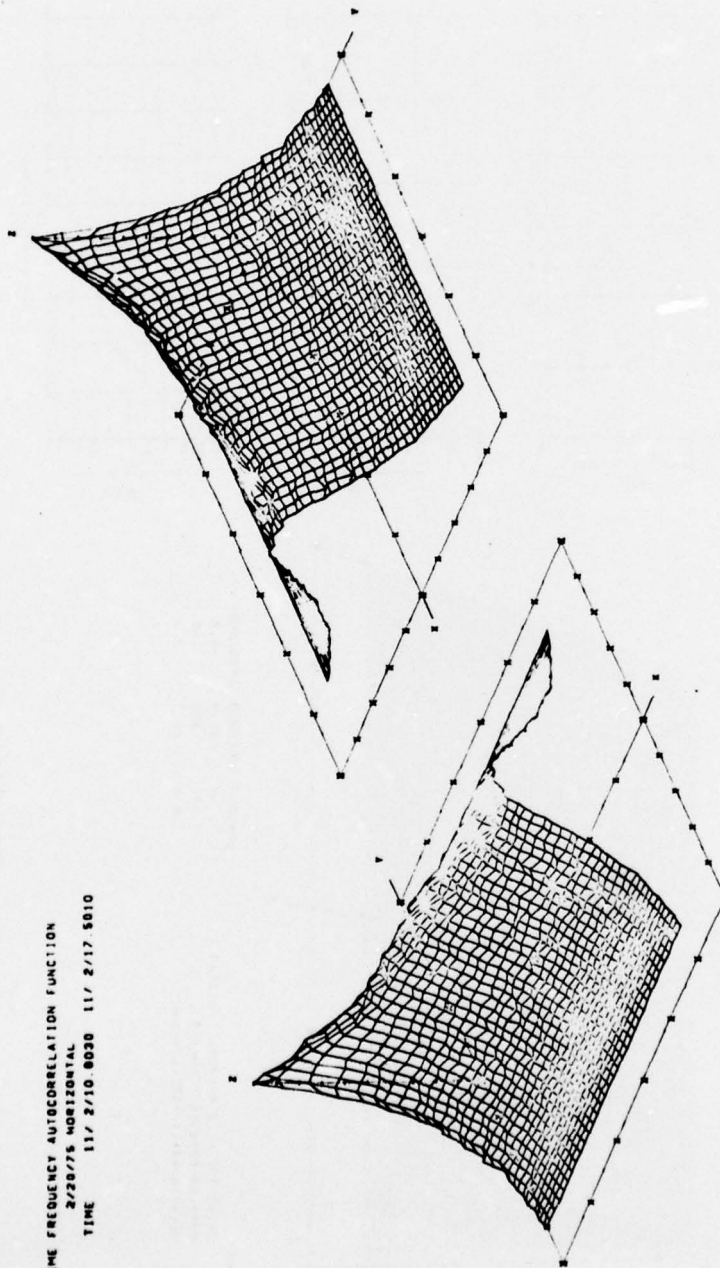


Figure 7-14. CONUS Scatter Channel Parameters, $S(\tau, \omega)/76$

TIME FREQUENCY AUTOCORRELATION FUNCTION
 2/20/75 HORIZONTAL
 TIME 11/ 2/10 8030 11/ 2/17 5010



AXIS	MINIMUM	MAXIMUM	INCREMENT
X FREQUENCY SEPARATION (KHZ)	0	3000	300
Y TIME SEPARATION (MILLISEC)	-50.0	50.0	10.0
Z TIME-FREQ. AUTOCOR. FUNCTION (PWR)	.00	1.00	.10

Figure 7-15. CONUS Scatter Channel Parameters, $R(\xi, \Omega)$ 76

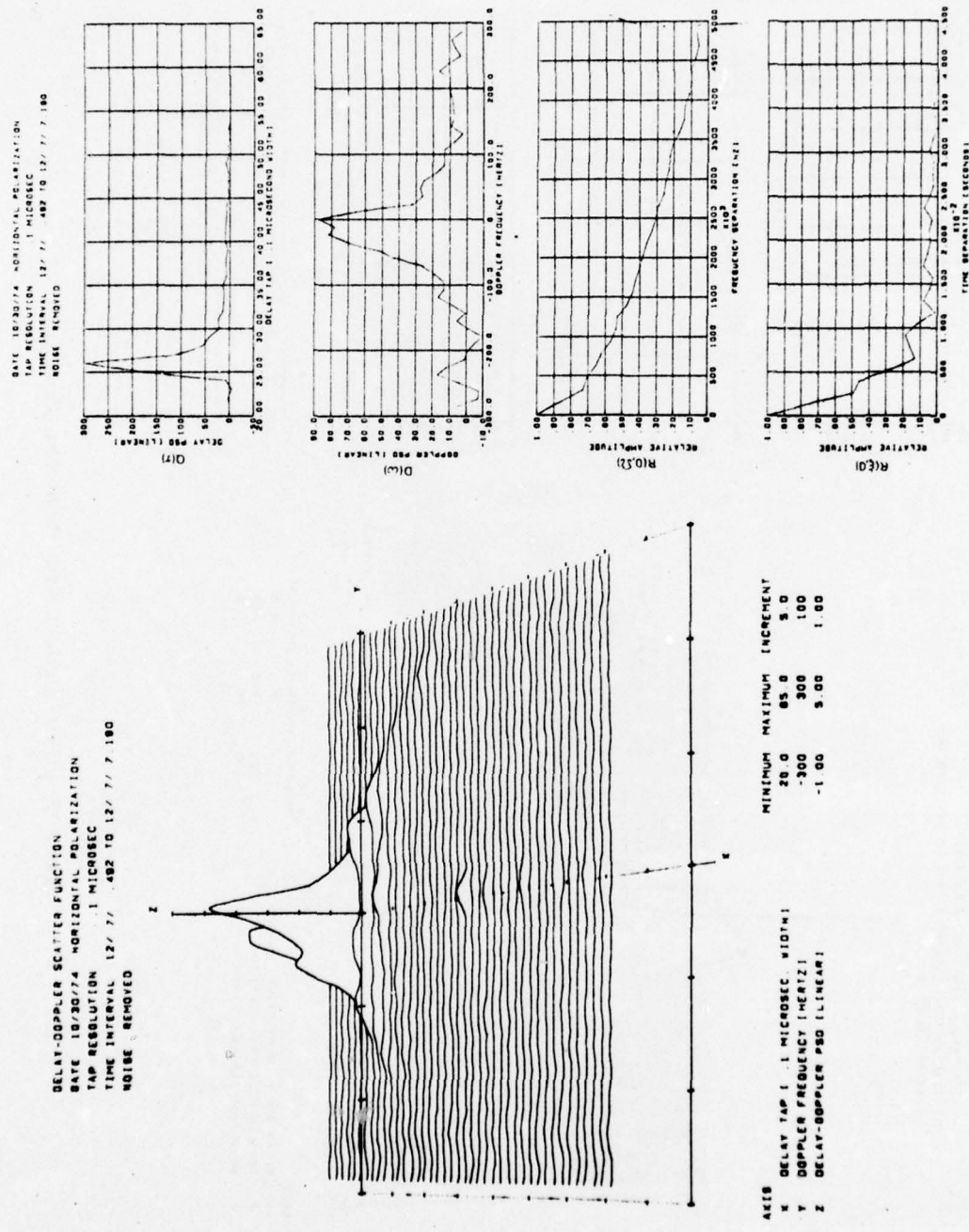


Figure 7-16. CONUS Scatter Channel Parameters, $S(\tau, \omega)/40$

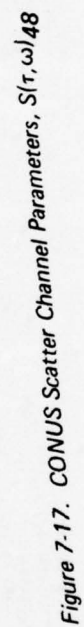


TABLE 7-2. CONUS $S(\tau, \omega)$ FUNCTION: FIGURE REFERENCE

Category	Figure	Function	Remarks	Test date, mo-day-yr	Cross-reference to specular-point overlay
Low spreads	7-14	$S(\tau, \omega)_{76}$	Probe traversing a lake, probably frozen	2/20/75	Fig. 7-5
	7-15	$R(\xi, \Omega)_{76}$	Time-frequency autocorrelation function of $S(\tau, \omega)_{76}$	2/20/75	Fig. 7-5
Modest spreads	7-16	$S(\tau, \omega)_{40}$	Cross-plane flight, gently rolling land	10/30/74	Fig. 7-2
Asymmetrical scatter	7-17	$S(\tau, \omega)_{48}$	Probe traversing lakeshore line	2/19/75	Fig. 7-4
Large spreads	7-18	$S(\tau, \omega)_{56}$	Probe traversing Lake Michigan	2/19/75	Fig. 7-4
	7-19	$S(\tau, \omega)_{74}$	Winter mountainous overland probe	2/20/75	Fig. 7-5
	7-20	$R(\xi, \Omega)_{74}$	Time-frequency autocorrelation function of $S(\tau, \omega)_{74}$	2/20/75	Fig. 7-5
Multimode scatter	7-21	$S(\tau, \omega)_{43}$	Lake return superimposed upon foliage-covered mountain return	10/30/75	Fig. 7-2
	7-22	$S(\tau, \omega)_{61}$	Multimodal return producing double-peaked Doppler spectra	2/18/75	Fig. 7-3
Brewster angle scatter	7-23	$S(\tau, \omega)_{44}$	Traversing Lake Winnipeg, horizontal polarization	2/19/75	Fig. 7-4
	7-24	$S(\tau, \omega)_{45}$	Traversing Lake Winnipeg, vertical polarization	2/19/75	Fig. 7-4

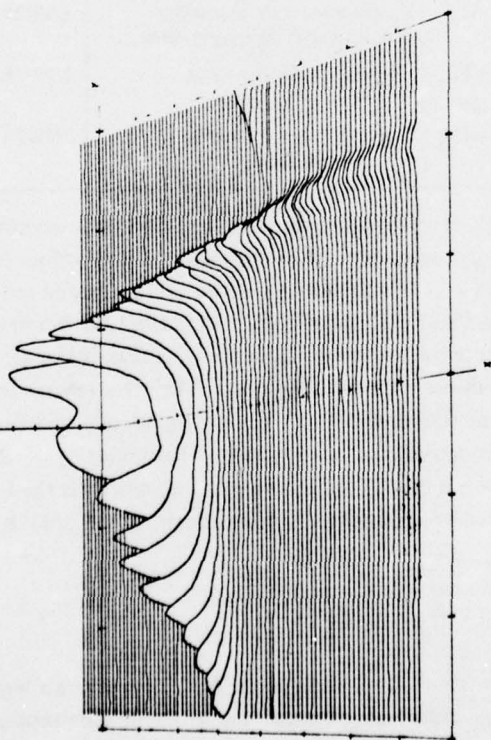
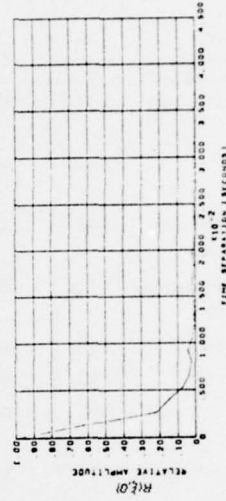
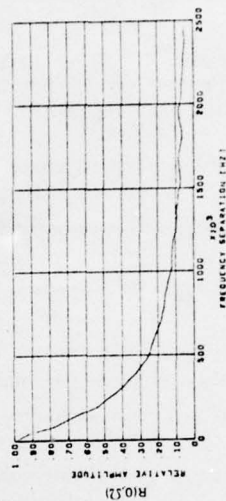
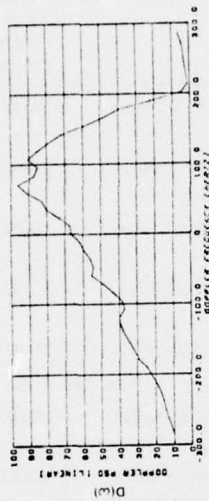
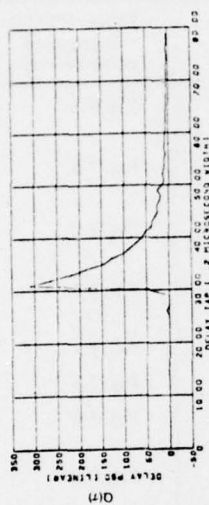
point return. In the receiver's delay-Doppler coordinate system these asymmetries manifest themselves as frequency perturbation and consequently have the potential to produce highly irregular Doppler spectra. Illustrating an example of this irregularity is the data presented in figure 7-17, which corresponds to a winter cross-plane flight with the probe crossing the Lake Winnipeg shoreline boundary. The negative Doppler returns represent scatter from the west side of the specular point and thereby correspond to lake region multipath, whereas the positive Doppler returns, which are highly attenuated, correspond to scatter from the shoreline terrain. Unlike the $S(\tau, \omega)$ and Doppler distributions, the $R(\xi, \Omega)$ function is quite symmetrical for this example. The symmetry of $R(\xi, \Omega)$ is relative to the time-separation variable, which is related to the Doppler frequency via the Fourier transform integral. Since $D(\omega)$ in figure 7-17 is quite symmetrical, the symmetry of $R(\xi, \Omega)$ is in accord with expectation.

7.2.4 Large Spreads (figs. 7-18 through 7-20)

Many CONUS terrain features produce scatter functions having a high degree of dispersion in both the delay and Doppler coordinate domain. The analyzed data generally indicates that this condition exists when the probe traverses harbor areas, large lakes, and snow-covered mountainous

DATE 2/18/75 HORIZONTAL POLARIZATION
TAP RESOLUTION 2 MICROSEC
TIME INTERVAL 11/12/30 482 TO 11/12/37 180
NOISE REMOVED

DELAY-DOPPLER SCATTER FUNCTION
DATE 2/18/75 HORIZONTAL POLARIZATION
TAP RESOLUTION 2 MICROSEC
TIME INTERVAL 11/12/30 482 TO 11/12/37 180
NOISE REMOVED



AXIS
X DELAY TAP 1 2 MICROSEC WIDTH
Y DOPPLER FREQUENCY (HERTZ)
Z DELAY-DOPPLER PSD (LINEAR)

MINIMUM MAXIMUM INCREMENT
0 80.0 10.0
-300 300 100
-30 4.00 50

Figure 7-18. CONUS Scatter Channel Parameters, $S(r, \omega)$

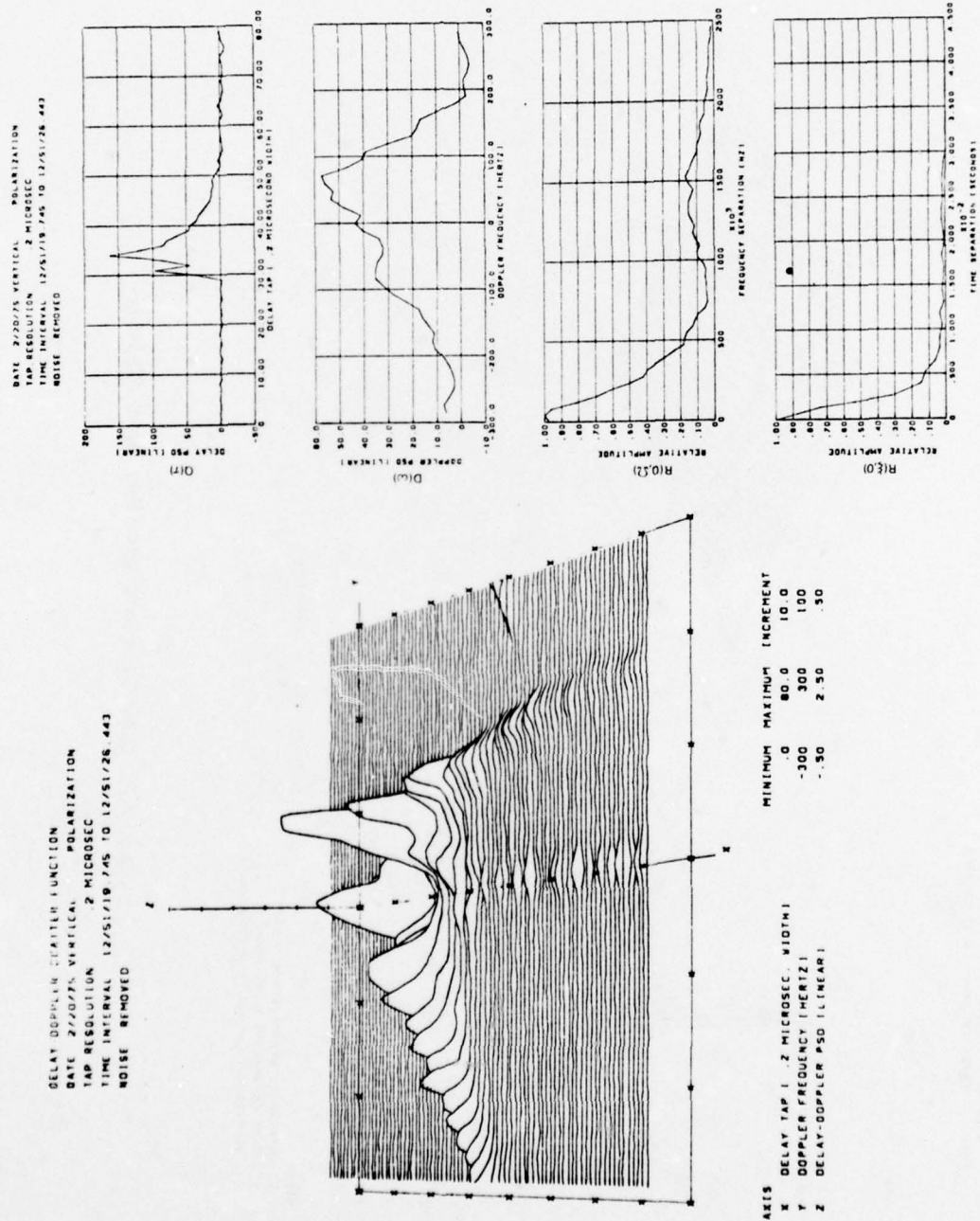
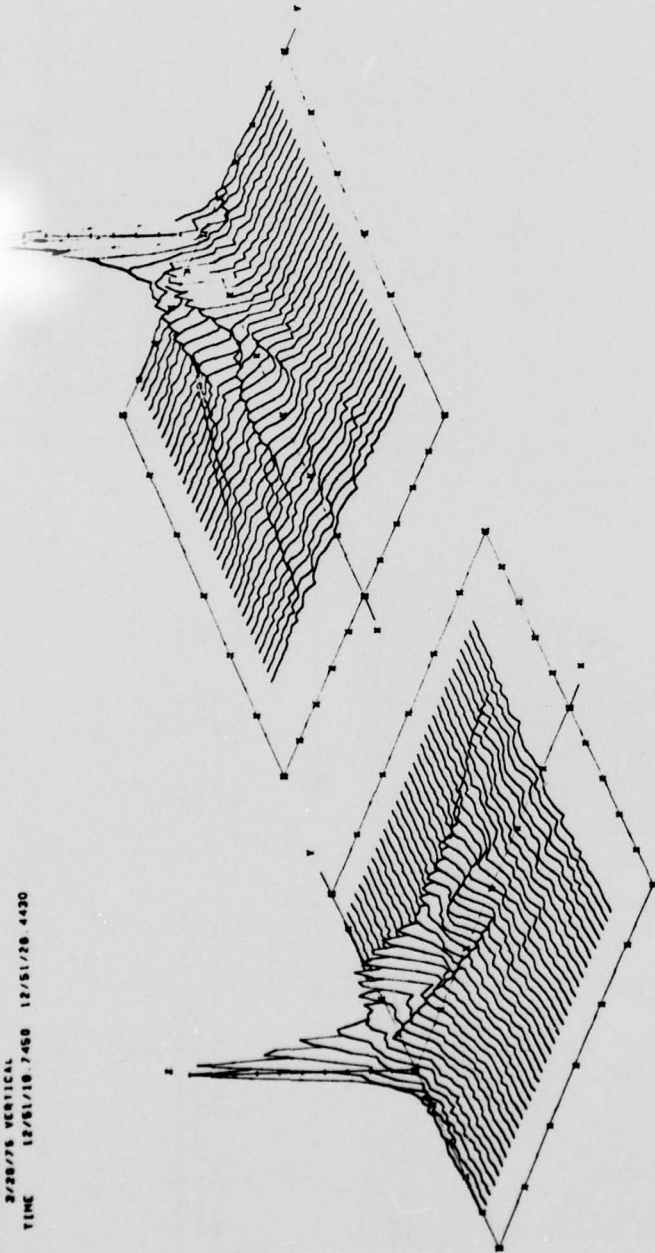


Figure 7-19. CONUS Scatter Channel Parameters, $S(\tau, \omega)$ 74

TIME FREQUENCY AUTOCORRELATION FUNCTION
 2/28/75 VERTICAL
 TIME 12/51/10 7450 12/51/29 4430



AXIS	MINIMUM	MAXIMUM	INCREMENT
X FREQUENCY SEPARATION (KHZ)	0	3000	500
Y TIME SEPARATION (MILLISEC)	-50.0	50.0	10.0
Z TIME-FREQ. AUTOCOR. FUNCTION (PWR)	.00	1.00	.10

Figure 7-20. CONUS Scatter Channel Parameters, $R(\xi, \Omega)$ 74

terrain. To illustrate conditions resulting in large spreads, two examples are presented: one taken from the Lake Michigan probe and the other representing scatter returns from snow-covered mountainous terrain.

The Lake Michigan scatter characteristics are given in figure 7-18 and represent data gathered at a grazing angle of approximately 38° with an in-plane flight direction vector. These results are similar to the overocean channel measurements for high-angle conditions as presented in section 5 and correspond to one of the most broadly spread multipath returns that have been observed for both oceanic and CONUS data sets.

Informal discussions with the Great Lakes Environmental Research Laboratory have confirmed that the central portion of Lake Michigan was *not* frozen during the time period over which the multipath probe was conducted. Thus it is of interest to compare the results of figure 7-18 with those corresponding to multipath return from a large frozen lake. Examples of frozen lake signatures are used in subsequent paragraphs to illustrate the Brewster angle effects on high-angle CONUS scatter. Drawing from this source one may refer to figure 7-23, which represents multipath characteristics from the February 19, 1975, in-plane flight direction probe of Lake Winnipeg, to illustrate a $S(\tau, \omega)$ function considerably less spread than the Lake Michigan data. The results for the Lake Winnipeg probe are probably representative of frozen lake multipath signatures; one would expect the nonfrozen lake conditions to be strongly dependent upon wind and fetch conditions and, hence, more variable. For cases of low or negligible wind velocities and for certain shoreline regions, spectra similar to those of the ice-covered lake could be expected.

$S(\tau, \omega)$ and $R(\xi, \Omega)$ distributions for the snow-covered mountain scatter are presented in figures 7-19 and 7-20, respectively. The flight direction was in-plane and the grazing angle was roughly 36° . With the exception of the perturbation near the origin of the distribution, which produces a double peak in the delay spectra, the data for this set is to a first order fairly equivalent to the Lake Michigan scatter function. In fact, the Doppler distributions are quite similar in shape, with the 3-dB spreads being within approximately 10% of each other. In comparison with the results for the low-spread case, we observe that $R(\xi, \Omega)$ decays very rapidly and possesses a significant amount of secondary structure in its distribution. As discussed in section 5.2.1, a large portion of this structure can be attributed to the combination of large surface slopes coupled with the in-plane geometry flight conditions.

7.2.5 Multimode Scatter (figs. 7-21 and 7-22)

A large percentage of the CONUS scatter returns exhibit some multimodal characteristics in their signatures. These properties are particularly dramatic when a locally flat surface with high conductivity is (1) located amongst terrain with a heavy vegetation cover or (2) is surrounded by a mountainous region.

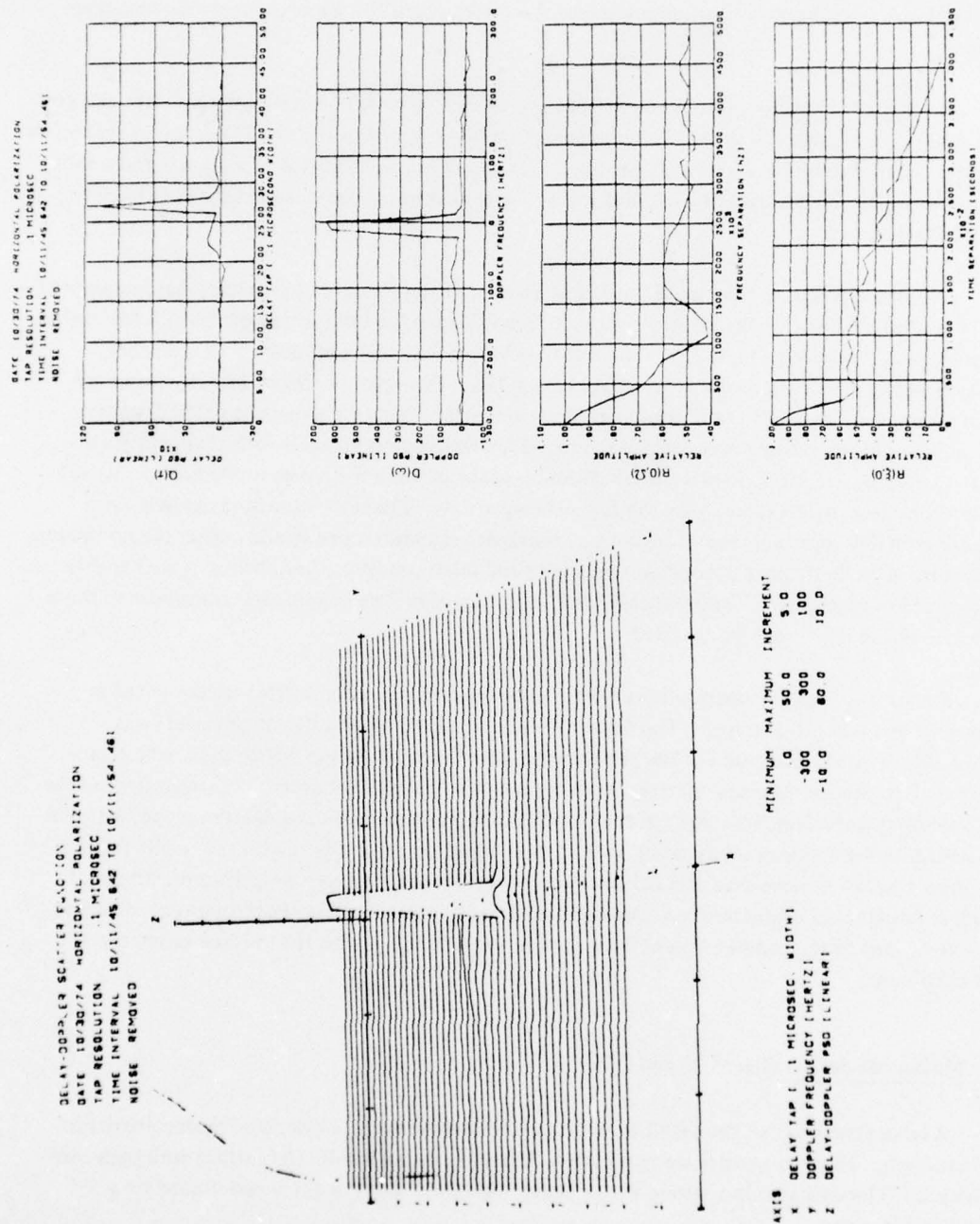


Figure 7-21. CONUS Scatter Channel Parameters, $S(\tau, \omega)$

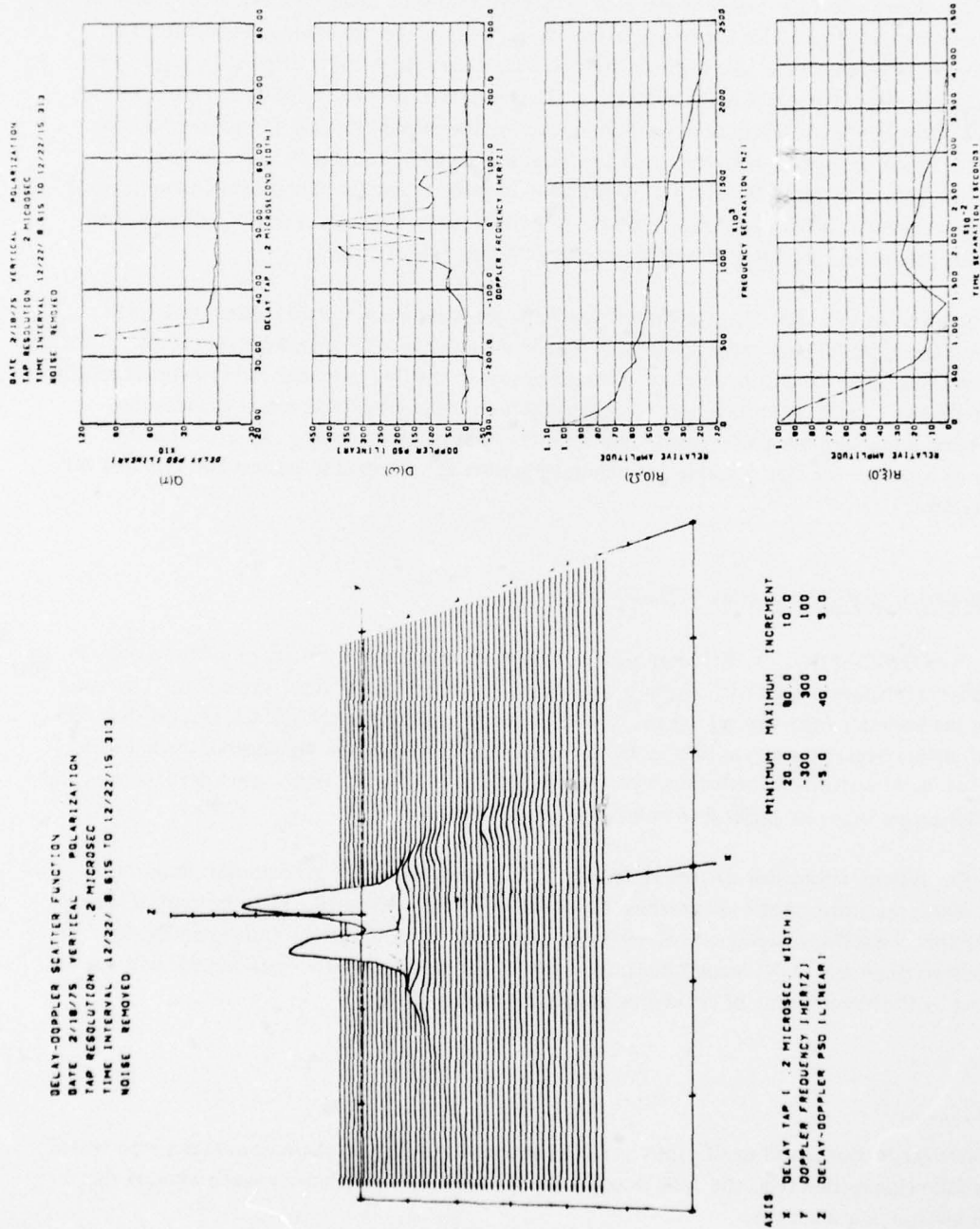


Figure 7-22. CONUS Scatter Channel Parameters, $S(\tau, \omega)/61$

Two examples of such returns are shown in figures 7-21 and 7-22. $S(\tau, \omega)_{43}$ presented in figure 7-21 corresponds to a specular-point trajectory that traverses a relatively small lake located in rather mountainous terrain with heavy vegetation cover. We note the high-density tap return corresponding to return from the lake and are barely able to discern the broadly dispersed background scatter returned from the surrounding mountains. The mountain return is much more visible on the delay- and Doppler-spectra distributions, where it takes on the low-level highly spread spectra characteristics. It is of interest to note that the lake return is delayed by roughly $0.5 \mu\text{sec}$ from the earliest mountain multipath. With respect to the autocorrelation function, the lake and mountainous returns have just the opposite influence, with the lake multipath resulting in a slowly decaying component and the mountain scatter providing a component that falls off rapidly.

Scatter function $S(\tau, \omega)_{61}$ given in figure 7-22 represents snow-covered terrain multipath where two low-spread scatter processes are superimposed upon a broadly spread diffuse return. Since the aircraft was flying toward the satellite, one may postulate that the more delayed low-spread return corresponds to a locally flat surface area tilted slightly toward the satellite direction whereas the least delayed unitap process arrives from a relatively flat nontilted surface area. As a result of the multimode nature of the scatter surface, the Doppler spectra are observed to possess two very distinct spectral peaks.²

7.2.6 Brewster Angle Scatter (figs. 7-23 and 7-24)

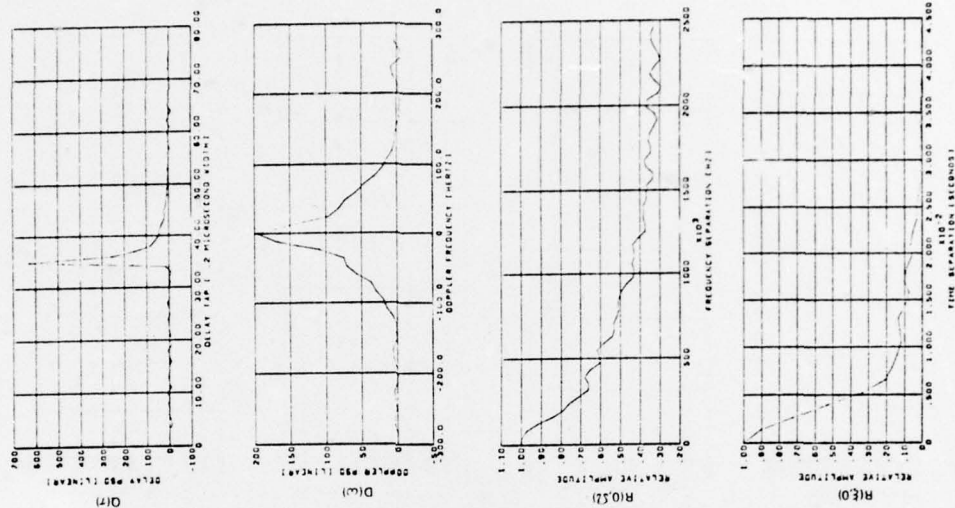
For CONUS scatter, the Brewster angle (i.e., that angle associated with the minimum vertical polarization reflection coefficient) occurs at a much higher value than for the oceanic case. The exact value of the Brewster angle depends on the relative dielectric constant of the surface, and (as shown in fig 7-26) it may occur at angles as high as 43° for some CONUS conditions. In general, the lower the content of liquid water in the reflecting medium, the higher the Brewster angle. Thus dry land, ice, and snow have higher Brewster angles than moist soil, marsh, and lakes.

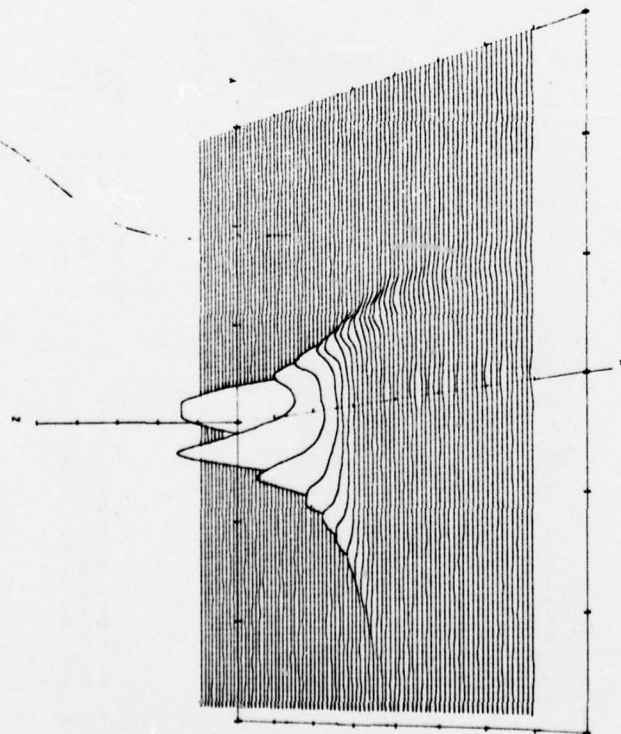
For systems employing circular polarization, the Brewster angle is of particular importance since it marks the grazing angle above which the scattered energy undergoes a sense reversal; at angles less than this, the reflected and incident waves have the same rotational sense. Consequently, for many low-grazing-angle CONUS conditions, the antenna system's multipath rejection ratio will not be enhanced by the phenomenon of circular polarization sense reversal.

²Such effects, of course, will significantly perturb the spread parameter calculations that are presented in the following section (e.g., the 3-dB Doppler spread for this case is relatively small whereas the 10-dB measure is quite high).

AXIS	MINIMUM	MAXIMUM	INCREMENT
X	DELAY TAP 1	2 MICROSEC WIDTH	0
			80.0
			10.0
Y	DOPPLER FREQUENCY [HERTZ]		300
			100
Z	DOPPLER PSD [LINEAR]		25.0
			5.0

DATE 2/18/76 HORIZONTAL POLARIZATION
TAP RESOLUTION 2 MICRONS
TIME INTERVAL 0.43/18.43 TO 0.43/26.341
NOISE 800MB 1810N

Figure 7-23. CONUS Scatter Channel Parameters, $S(\tau, \omega)$ 44



AXIS		MINIMUM	MAXIMUM	INCREMENT
X	DELTA TAP 1 Z MICROSEC WIDTH	0	80 0	10 0
Y	DOPPLER FREQUENCY [HERTZ]	-300	300	100
Z	DELAY-DOPPLER PSD [LINEAR]	-5 0	20 0	5 0

Time Separation (s)	Relative Amplitude $R(t)$
0	1.00
100	0.95
200	0.90
300	0.85
400	0.80
500	0.75
600	0.70
700	0.65
800	0.60
900	0.55
1000	0.50
1050	0.60
1100	0.85
1200	0.85
1300	0.85
1400	0.85
1500	0.85
1600	0.85
1700	0.85
1800	0.85
1900	0.85
2000	0.85

Figure 7-24. CONUS Scatter Channel Parameters, $S(\tau, \omega)$ 45

When geometrical conditions exist such that the specular-point grazing angle coincides with the surface's Brewster angle, the scatter function signatures for the vertical and horizontal polarization probes differ appreciably. We illustrate this by the data presented in figures 7-23 and 7-24, which correspond to the returns gathered over the simultaneous horizontal and vertical polarization probes, respectively. The flight took place over Lake Winnipeg (frozen) with in-plane geometry conditions and a specular-point grazing angle of 26.9° , which is roughly equivalent to the Brewster angle for ice. On comparing the two $S(\tau, \omega)$ functions, one readily observes the relative predominance of the specular-point tap for the horizontal polarization case; for the vertical polarization distribution the specular-point tap is much less significant and is, in fact, seen to contain less energy than the tap adjacent to it. Discussion pertaining to this polarization effect, referred to as "Brewster angle fill-in," is given in section 5.1. Similar to the oceanic case, this phenomenon results in the vertical polarization probe having significantly larger delay- and Doppler-spectra spreads than its horizontal polarization counterpart. Conversely, the opposite is seen for the time and frequency autocorrelation function spreads included in figures 7-23 and 7-24.

7.3 RMS SCATTER COEFFICIENTS

The multipath signal's rms scatter coefficient (Γ) is defined as the ratio of total received scattered energy to the energy incident upon the surface. This parameter provides a quantitative measure of the total scatter intensity and is obtained for both the horizontal and vertical polarization probes through the following relationship:

$$\Gamma = \frac{\langle |I|^2 \rangle}{\langle |D|^2 \rangle} + G_D/G_I, \text{ dB} \quad (7-1)$$

where:

- $\langle |D|^2 \rangle$ = mean square direct-path signal; derived from the quad-helix antenna's direct line-of-sight component
- $\langle |I|^2 \rangle$ = mean square multipath power obtained by integrating $S(\tau, \omega)$ over both its delay and Doppler variables
- G_D/G_I = adjustment factor to account for parameters such as the direct and indirect signal transmission ERP's, etc. (see section 5.2.6 for details of this factor).

Figures 7-25 and 7-26 present the experimentally derived values of Γ for horizontal and vertical polarization, respectively. These data are given as a function of grazing angle and are accompanied by theoretical Fresnel "smooth earth" reflection coefficient curves and a series of mid-angle results corresponding to the ATS-5 L-band experiment (ref 7-1). ATS-5 results are included in this presentation since they include a range of grazing angles (15° to 20°) for which data could not be acquired effectively during this program because of the ATS-6 satellite location. As indicated in the

figures, all data points have been tagged; the ATS-6 experimental data points have a subscript number cross-referenced to the locations indicated on the specular-point overlays of figures 7-1 through 7-5.

The ATS-5 data ensemble has been segregated into winter and summer test conditions. Summer data was obtained from the southern portion of Alaska and from the Yukon and Northwest Territories of Canada. These data collection stations covered terrain profiles ranging from flat marshland to very precipitous mountains. Typically, the lower altitude marshland regions correspond to modest to heavy vegetation cover and the mountainous areas provide a barren rock or glaciated surface. The winter ATS-5 results were obtained from high-latitude regions in northern and northeastern Canada. Terrain profiles varying from flat to mountainous were subtended and we may consider the areas to be barren or snow-covered, with little or no vegetation.

It is well known that the water content of a scatter surface is perhaps the most significant single parameter influencing the magnitude of the Fresnel reflection coefficient. We also expect the CONUS flight vector to traverse surface areas that vary markedly in their water content properties. Thus the theoretical reflection coefficient relationships have been plotted for a variety of electrical characteristics; see table 7-3.

TABLE 7-3. REFERENCE PERMITTIVITY AND CONDUCTIVITY VALUES ASSUMED FOR VARIOUS TERRAINS

Terrain	Relative permittivity	Conductivity, mho/m
Sea water	81	4.6
Fresh water	81	5×10^{-3}
Marsh	30	1.1×10^{-1}
Ice	3.2	2×10^{-3}
Moderately dry soil	2.5	1×10^{-4}
Wet soil	20	1×10^{-2}
Wet snow	1.6	5×10^{-3}
Dry snow	1.15	1×10^{-4}

In general, the data points of figures 7-25 and 7-26 are observed to be fairly well bracketed by the Γ_H and Γ_V relationships corresponding to the above parameters. Horizontal Γ values range from a low of -18 dB to a high of +2 dB whereas the vertical coefficients range from -24 to -3 dB. On a total point basis, it appears that the vertical coefficients are more biased to the high side of the theoretical predictions than the horizontal coefficients. This is especially true in the vicinity of the Brewster angle and is most likely attributed to the concept of "Brewster angle fill-in" (see sec. 5.2.6) as well as the influence of depolarization, which is a natural phenomenon affecting multipath components returned from locations that are not on the great circle path joining the subaircraft and subsatellite points.

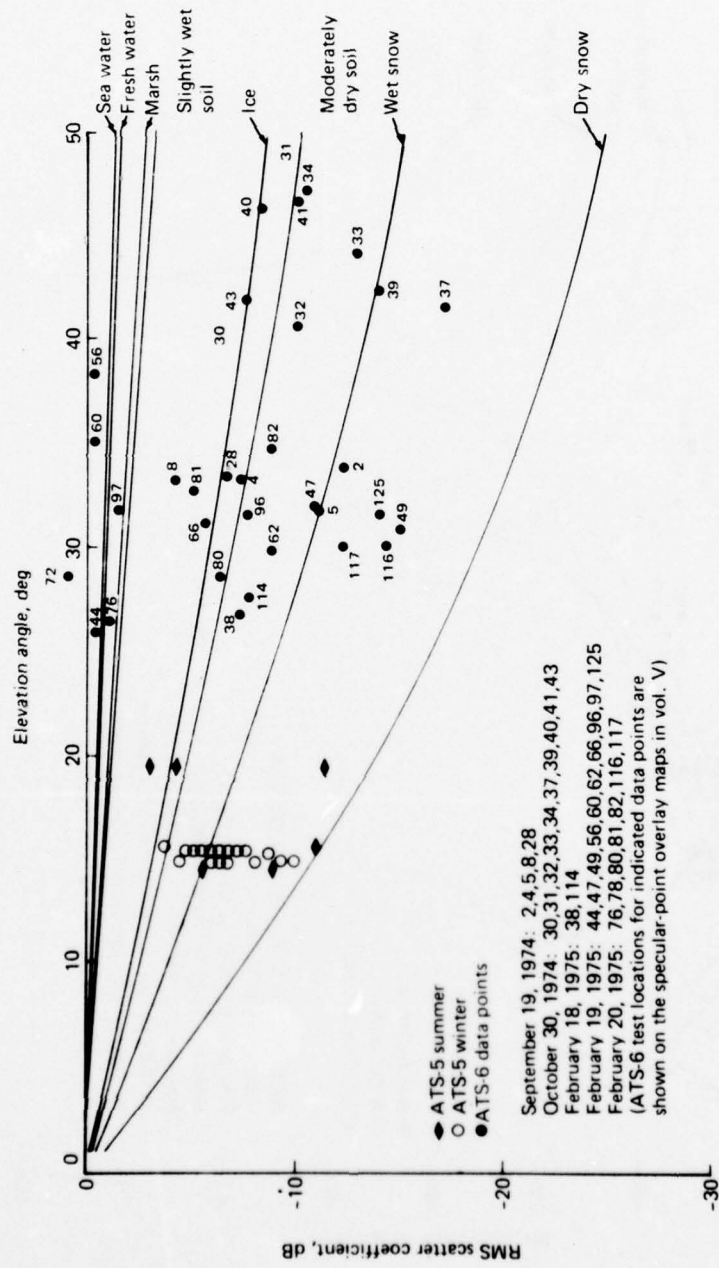


Figure 7-25. CONUS RMS Scatter Coefficients — Horizontal Polarization

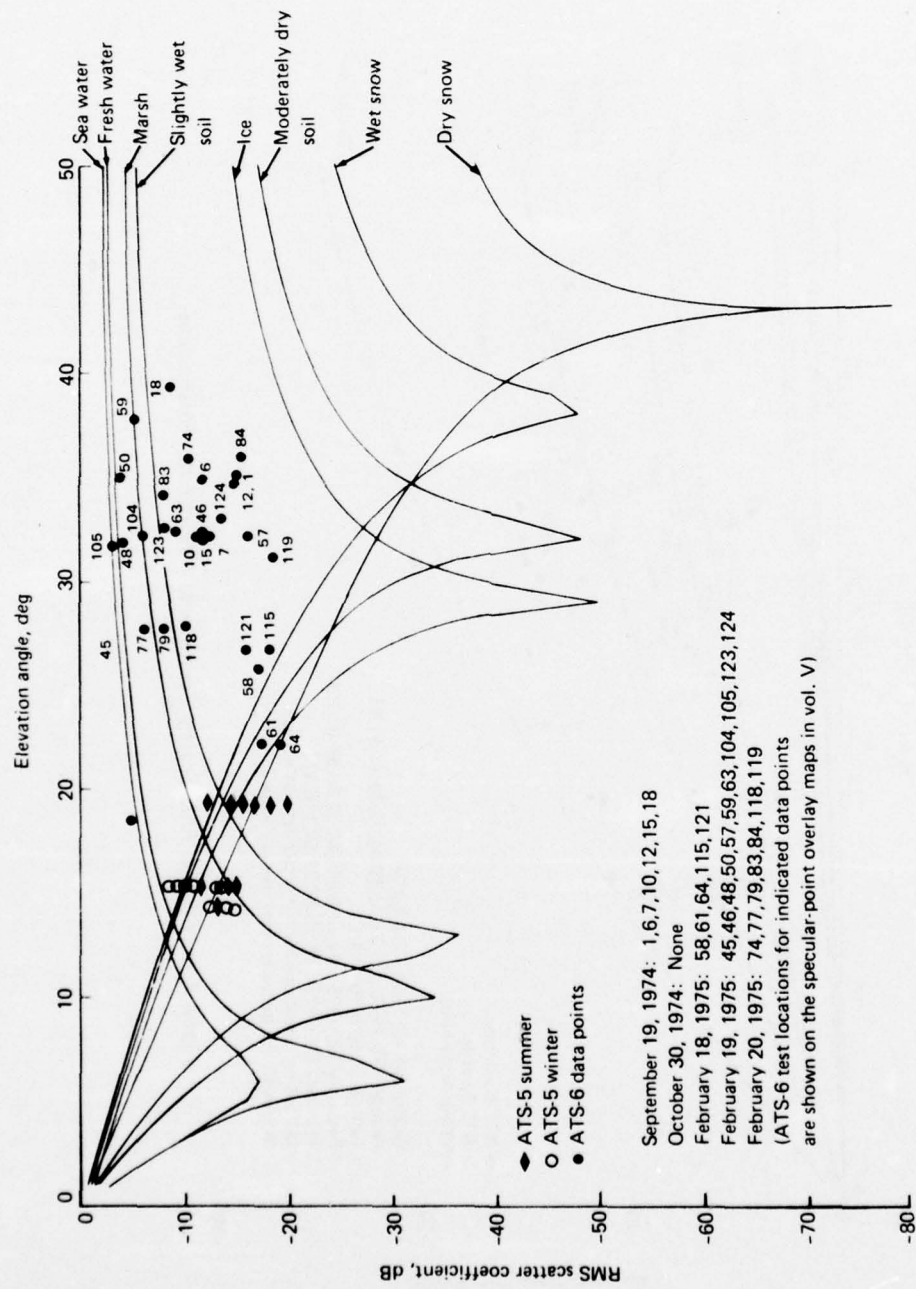


Figure 7-26. CONUS RMS Scatter Coefficients — Vertical Polarization

We have included only a small number of Γ values corresponding to scatter from regions completely covered by vegetation since these returns are attenuated to a level that usually transcends the precision of the system capabilities and are therefore of lesser interest for the design of an operational CONUS system. The Γ - value data points with subscript numbers 2 and 1 (for the horizontal and vertical reflection coefficient data, respectively) are two examples illustrating the influence of heavy vegetation cover on the intensity of the returned multipath signal. These scatter coefficients were measured for the September 1974 flight test probe over the east coast of the United States (see fig 7-6), and were observed to be roughly 12 dB below the values one might expect for typical underlying soil conditions (slightly moist soil). On many other occasions for the September 19 and October 30 flights, the delay-spectra time history information indicates Γ values substantially below those associated with the above two examples. In general, the data included in this section for the non-snow-covered terrain relates to time segments during which the $Q(t, \tau)$ plots indicate the presence of a significant amount of returned energy. With the use of detailed map overlays, these conditions may almost always be correlated with times when the specular point traverses nonforested regions such as small bodies of water, highways, manmade structures, or rock outcroppings.

7.4 DELAY SPREADS

Using the delay spread definitions of figure 5-18, the 3- and 10-dB CONUS delay spread values have been determined for a variety of terrain profiles and are presented in figures 7-27 and 7-28. The data, which have been segregated into winter and fall conditions, are given for both horizontal and vertical probe polarizations and provide a measure of the time-delay dispersion characteristics of the multipath process. As a general observation, we note that the 3-dB spread values range from a low of approximately 0.1 μ sec to a high of 1.2 μ sec whereas the 10-dB measures range between 0.1 and 3.0 μ sec. In general, all data sets exhibit very little dependence upon grazing angle, which is in accord with model predictions for a Gaussian surface (see sec 6.4). The data ensembles exhibit a rather large variance, most likely due to the gross inhomogeneities of the CONUS surface, which tends to mask any small grazing angle dependence that might be present.

In comparing the fall and winter delay spreads, we detect a slight tendency for the winter results to exceed those of the fall series. This could be directly related to the terrain over which the respective flight tests were conducted but is thought to more likely reflect the manner in which the fall series data analysis intervals were chosen. As previously stated, most of the fall flight tests were flown over terrain with heavy vegetation cover, which highly attenuated the multipath signal. Very few of these weak returns were analyzed; preference was given to intervals during which the specular point traversed a vegetation-free region. Typically, these regions are relatively small and flat (e.g., small lakes, roads, building tops, etc.) and thereby produce multipath returns that are subject to fairly small dispersions in both the delay and Doppler signal coordinates. On the other hand the winter flight tests pertain to scatter off snow-covered terrain or large lakes (Lake Superior, Lake Michigan) and thus have potential for relatively extensive delay and Doppler spreads.

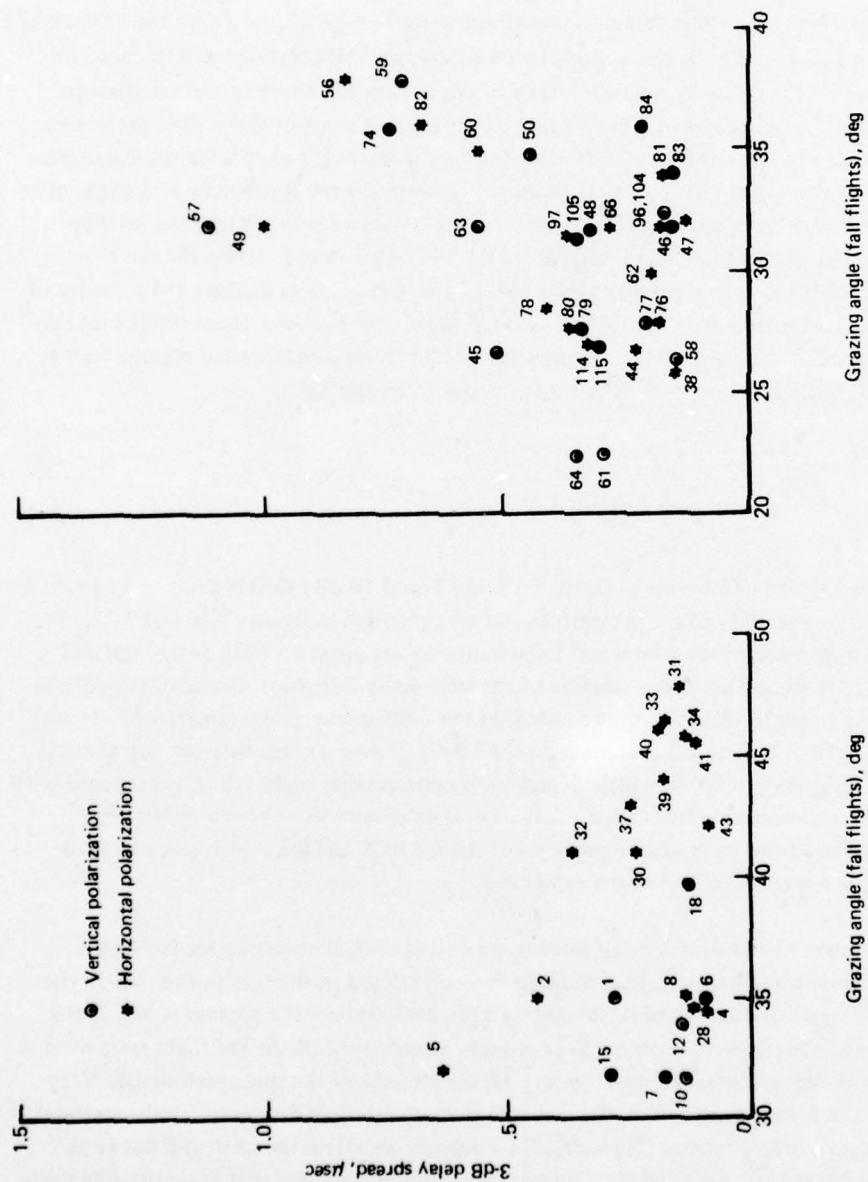


Figure 7-27. CONUS Scatter Delay Spread, 3-dB Value

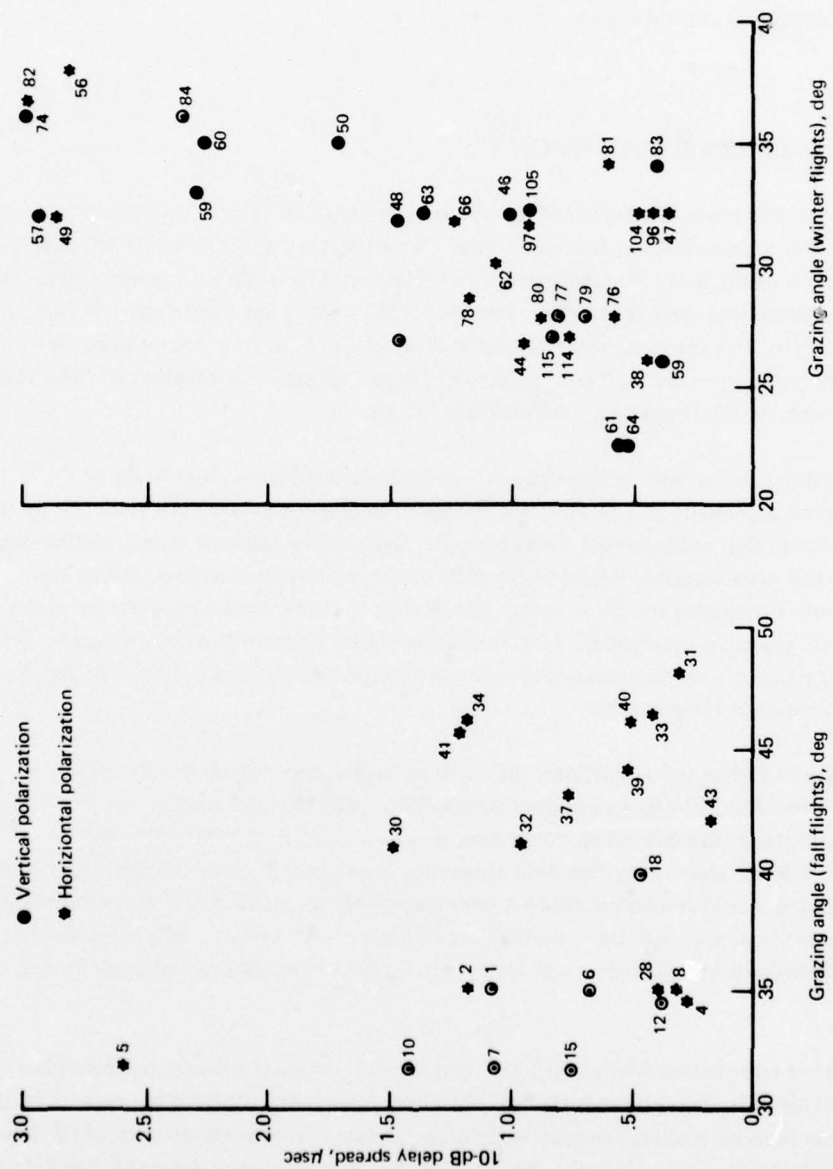


Figure 7-28. CONUS Scatter Delay Spread, 10-dB Value

Finally, we note that the winter spread values are typically lower than the oceanic spread results. This is to be expected since the winter tests, for the most part, were flown over the relatively flat or gently rolling plains of central Canada.

7.5 FREQUENCY COHERENCE BANDWIDTHS

The frequency coherence bandwidth of the overland reflected signal is in essence a measure of the channel's frequency autocorrelation function spread. We therefore expect it to be somewhat proportional to the inverse of the delay spread measures and interpret it to represent the upper frequency limit to which two transmitted carriers may be separated yet still meet a specified degree of correlation (e.g., 0.5) at the receiver. In a manner similar to that used for the oceanic data presentation, we restrict our attention entirely to the multipath signal and do not consider the influence of the direct line-of-sight component on the frequency coherence bandwidth.

Experimental results for both horizontal and vertical polarization are given in figure 7-29. We have segregated the measurements into fall and winter flight test categories and note immediately the high degree of dispersion that exists in each data ensemble. This follows directly from a similar delay spread observation and most certainly relates to the wide variety of terrain characteristics in the CONUS environment. Comparing the delay spread results with the coherence bandwidth measurements confirms the general "inverse proportional" relationship that exists between the two measures. Since the overland scatter process is on occasion multimodal, the relationship should not be expected for each and every data point of the ensemble.

Considering all CONUS test conditions, the range of 3-dB coherence bandwidth measures varies from a low of roughly 150 kHz to a high of several MHz (note that the resolution capabilities of the prober chip width duration establish an upper limit to which coherence bandwidth may be measured). For the fall test series, a median 3-dB coherence bandwidth measure of roughly 750 kHz is observed, whereas the winter results produce a somewhat smaller median value of approximately 600 kHz. As discussed in section 7.4, these findings are thought to be indicative of the terrain over which the winter flights were conducted as well as the criteria used to select time intervals for the fall data analysis.

It is of interest to note that when compared with the fall results, the winter test series has a much larger percentage of its data points with 3-dB coherence bandwidth values in excess of 2 MHz. However, both series produce roughly the same percentage of data points in the vicinity of the lower limit to the delay spread measures. This most likely results because the winter data with low delay spreads probably corresponds to scatter from a fairly smooth surface that is somewhat extensive and homogeneous. These conditions are known to produce delay spectra that decay rapidly and have essentially no energy in their distribution tails; these attributes in turn imply a frequency autocorrelation function that decays slowly and possesses a very large spread measure. On the other hand,

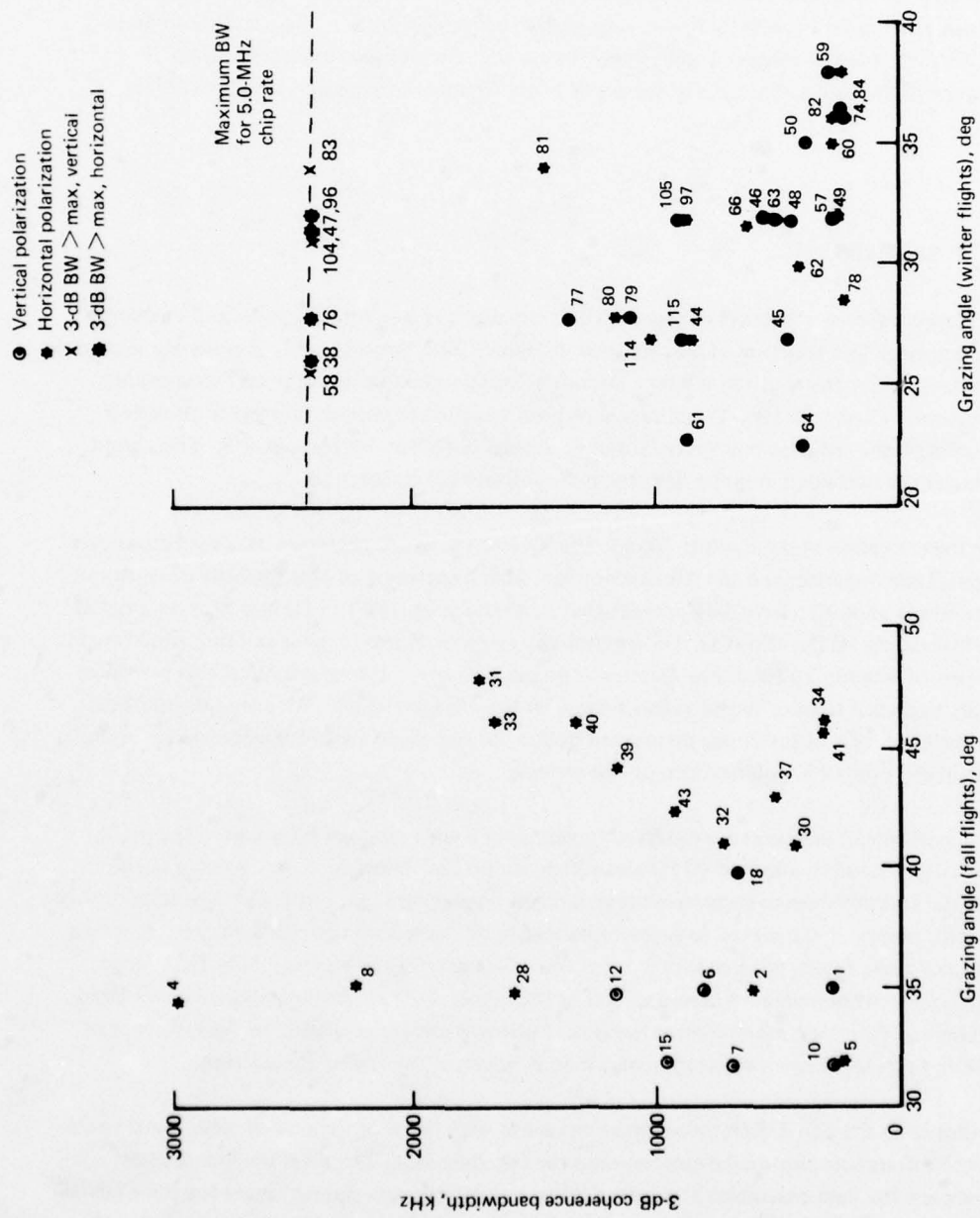


Figure 7-29. CONUS Scatter Coherence Bandwidth

the fall data with low delay spreads were taken at time intervals during which the specular point traversed a small region of relatively high conductivity (e.g., rivers, roads, etc.) typically surrounded by foliage-covered terrain. This condition produces delay spectra with a high-energy unitap component superimposed upon a relatively low-energy highly spread distribution. The latter component is a result of scatter from the foliage or underlying terrain that encompasses the area of high reflectivity and will produce an increase in the decay of the channel's frequency autocorrelation function.

7.6 DOPPLER SPREADS

The Doppler spread attributes of the CONUS vertically and horizontally polarized multipath probe signals are given as a function of grazing angle in figures 7-30 through 7-33. Results are segregated according to flight test series (fall and winter), aircraft velocity direction (in-plane and cross-plane), and spread measures (3 and 10 dB). Delimiters have been attached to each data point to provide a cross-reference with the specular-point trajectories presented in figures 7-1 through 7-5. The spread measures refer to the two-sided Doppler dispersion as illustrated in figure 5-18.

With the exception of data points 50, 56, 59, 60, and 74, which represent data collection over Lake Michigan, Lake Superior, and the Adirondack Mountains northeast of Montreal, the majority of the Doppler spreads appear to have 3-dB spreads that lie between 20 and 125 Hz and take on a typical value of approximately 60 Hz. The CONUS spectral analysis procedures (data-smoothing windows, etc.) set a lower limit of roughly 20 Hz on the frequency spread measures. Hence several of the low-value data points are expected to have spread values somewhat less than indicated. We note that the 3-dB values, with the exception of the above mentioned points, do not exhibit a strong dependence upon grazing angle, flight direction, polarization, or test series.

The 10-dB spread measures are observed to vary over a wide range of values, with the majority of the points falling between a low of 40 Hz and a high of 500 Hz. We are able to discern a slight tendency for the spread values to increase with an increase in grazing angle. Although this relationship is in accord with theory, it is believed to be more indicative of the terrain type differences over which the high- and low-angle flights were conducted (i.e., the low-angle flights were typically flown over gently rolling, snow-covered plains whereas several of the higher angle conditions occurred over large bodies of water and east coast mountainous terrain). Further discussions relating to the influence of grazing angle and rms slope upon the Doppler spreads are given at the end of this section.

In comparing the CONUS Doppler spread measures with those of the oceanic test, we are able to discern both differences and similarities between the two data sets. The most obvious area of departure between the data ensembles is the propensity toward very low spread values for the CONUS results. This is especially true for the 3-dB measure, where most of the CONUS results fall below the

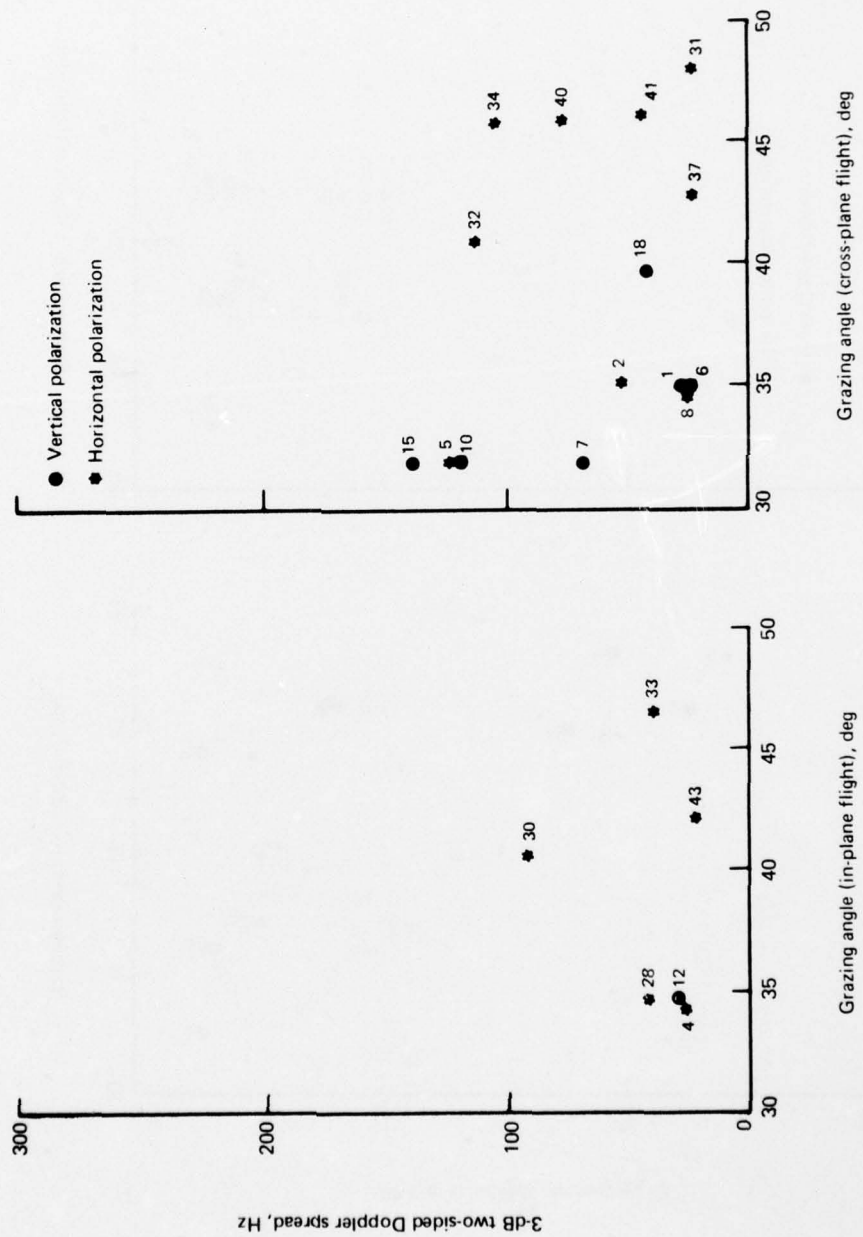


Figure 7-30. Three-dB CONUS Scatter Doppler Spread, Fall Flights

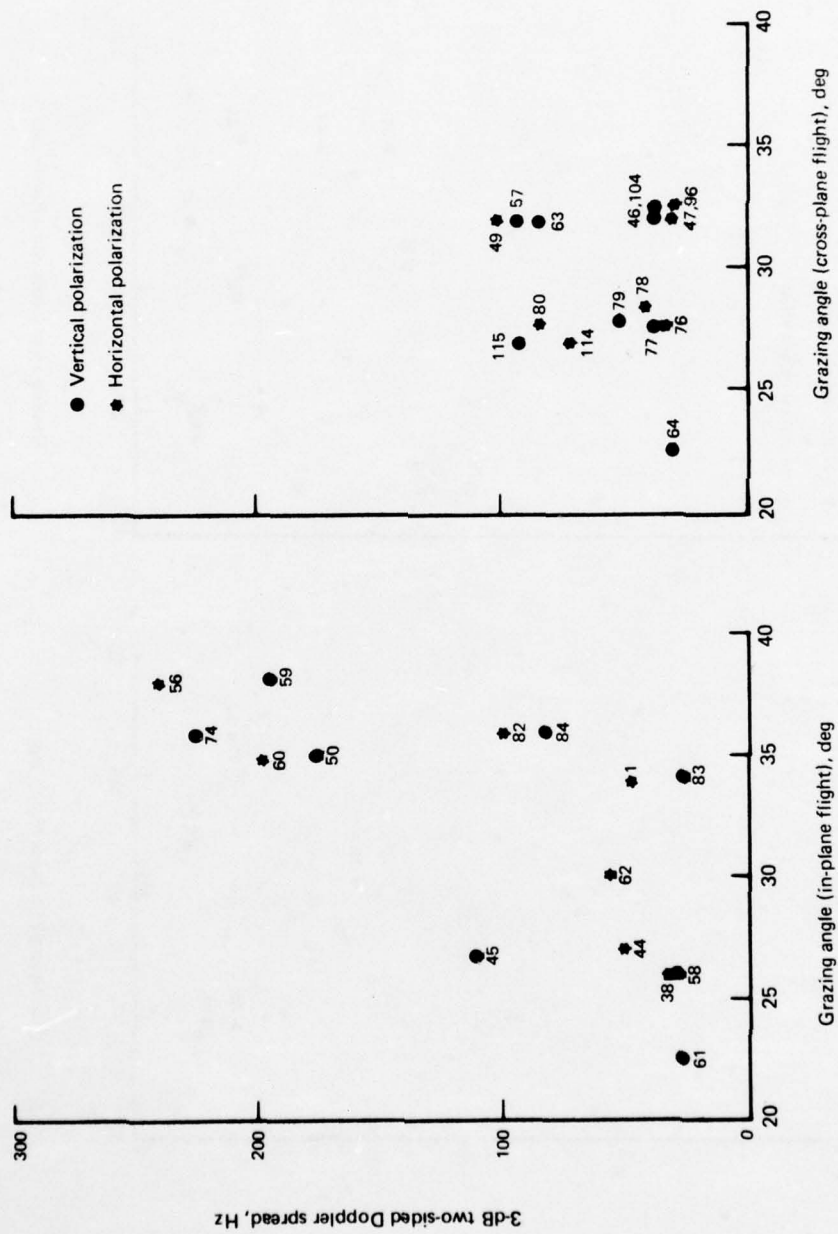


Figure 7-31. Three-dB CONUS Scatter Doppler Spread, Winter Flights

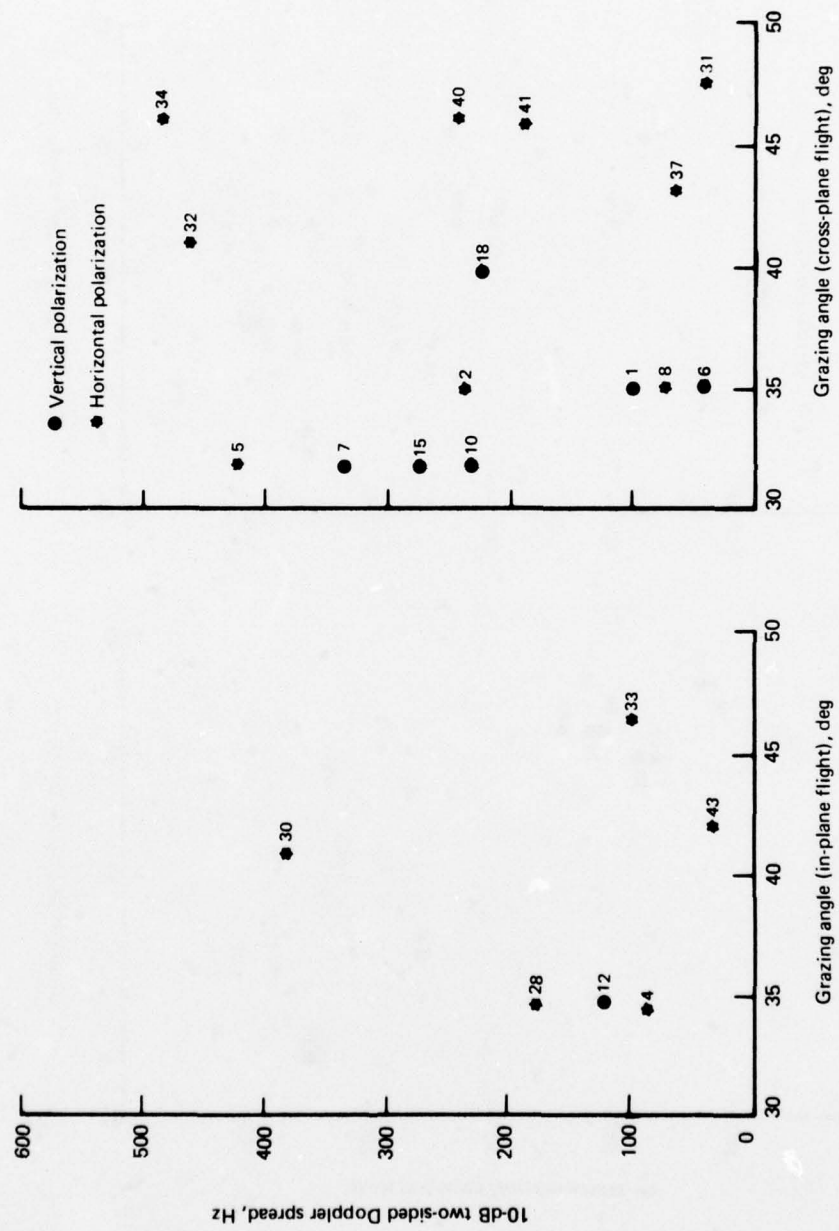


Figure 7-32. Ten-dB CONUS Scatter Doppler Spread, Fall Flights

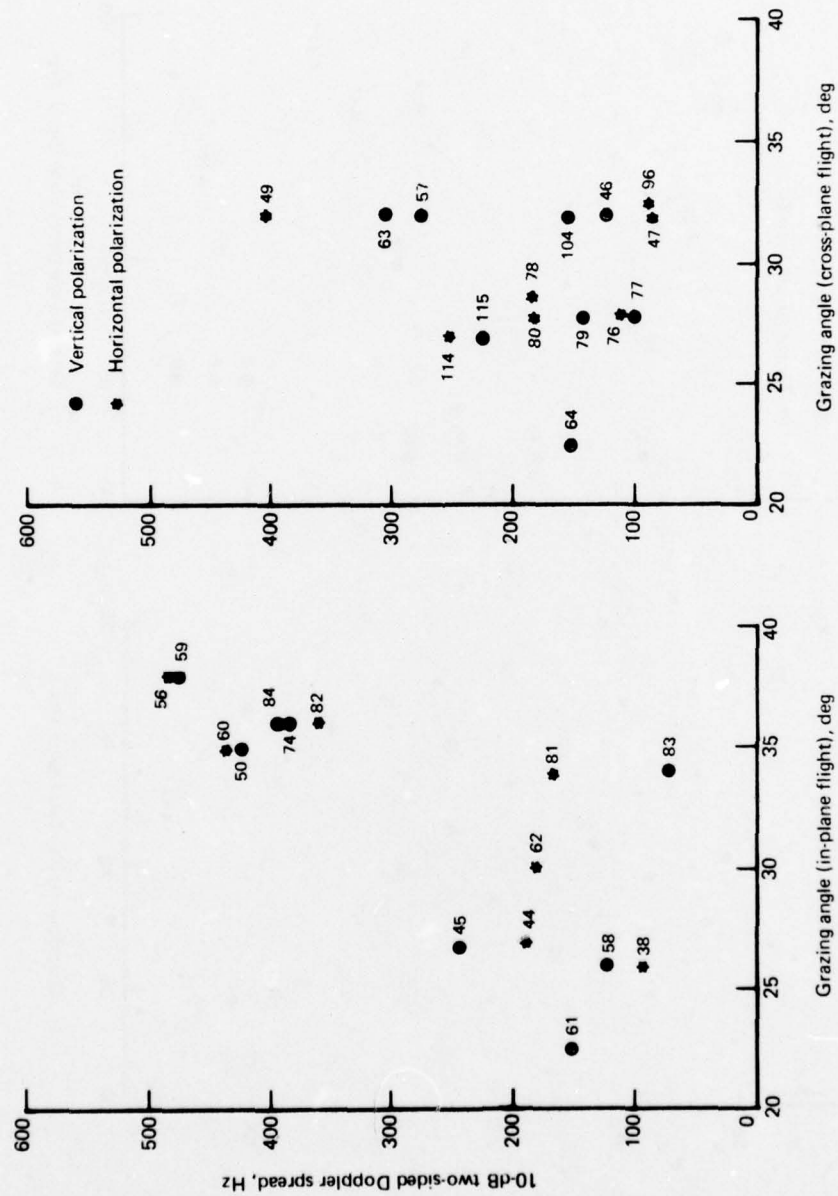


Figure 7-33. Ten-dB CONUS Scatter Doppler Spread, Winter Flights

100-Hz values; generally the opposite is observed for the high-angle (e.g., $\geq 20^\circ$) oceanic conditions. Because the aircraft velocity magnitudes for the two tests were roughly equivalent, one concludes that the oceanic test conditions generally encountered surfaces whose slope characteristics were more precipitous than those for the CONUS probes. This comparison is believed to be valid for the winter flights which, as previously stated, were conducted mainly over gently rolling terrain. On the other hand, the criteria used for selecting the data intervals to be analyzed for the fall CONUS tests most likely caused an overemphasis of low-spread signal analyses.

As compared with the 3-dB spread results, we note that the 10-dB CONUS spreads appear to be in closer accord with the high-angle oceanic data. This is especially true for the fall flights and may be due in part to the influence of vegetation scatter on the tails of the Doppler distribution (see section 7.5 for a similar discussion) or to the fact that the overland slope distribution is more closely fit to an exponential relationship as opposed to the well-verified Gaussian slope pdf for oceanic surfaces. Spreads associated with CONUS specular-point trajectories subtending large lakes and winter mountainous regions are well correlated with the observed high-angle oceanic results. In particular, the previously delineated points corresponding to flights over Lake Superior (50 and 60), Lake Michigan (56 and 59), and the Adieudacy mountains (74) provide typical 3- and 10-dB spread values of 200 and 450 Hz, respectively. These values may be compared with typical high-angle ($\approx 31^\circ$) oceanic 3- and 10-dB spreads of 170 and 300 Hz. The small difference between the grazing angles associated with the test conditions should not induce a significant perturbation to the above comparison (roughly 15% bias in favor of the CONUS results).

To relate the spread measures to theoretical expectation, one may use the steepest descent predictions given in section 5.3.3; i.e.,

$$B \tan \beta_0 \left[V_\perp^2 + V_\parallel^2 \right]^{1/2} \sin \gamma$$

where:

- B = Doppler spread measure
- $\tan \beta_0$ = rms surface slope
- V_\perp = cross-plane velocity component
- V_\parallel = in-plane velocity component
- γ = grazing angle at specular point.

This relationship is valid if: (1) the elevation angle is greater than the surface rms slope and (2) the surface is very rough (electromagnetically) and has a Gaussian slope distribution that is isotropic over the total effective scatter region. For CONUS applications, the latter restrictions on the surface's slope distribution are not in general expected to be met; thus, the above steepest descent Doppler spread relationship must be considered to be a crude estimate. However, it seems reasonable to expect that, for the range of grazing angles probed, the $\sin \gamma$ and velocity direction dependencies of B are relatively insignificant as compared to the variation in the surface rms slope parameter. As a first-order

approach one might also use the above relationship for B to extend the data observation base to alternate grazing angle and velocity magnitude conditions.

7.7 DECORRELATION TIMES

In this section the CONUS 3-dB decorrelation times are given as a function of grazing angle for both the horizontal and vertical polarization probes. The data sets, segregated according to test series (fall and winter) and aircraft heading (in-plane and cross-plane), are presented in figures 7-34 and 7-35. The decorrelation time parameter represents the upper time limit separation to which two identical frequency L-band carriers may be spaced yet still meet a specified degree of coherency (0.5) at the receiver. The decorrelation time is obtained from the channel's time autocorrelation function and, to good approximation, is inversely proportional to the Doppler spread measure.

As shown in figures 7-34 and 7-35, decorrelation times of the CONUS multipath signal are spread over a wide range of values. The trend of the data does not indicate a pronounced *grazing* angle, polarization, flight direction, or flight series dependence. For all but one data point, the decorrelation measures lie between values of 1 and 10 msec, and we may ascribe an average value of roughly 4 msec to the total ensemble. Comparing the data values of this section to the Doppler spreads of the previous section provides a general confirmation of the predicted inverse dependence relationship between the two channel measures. As a first-order approximation, the inverse of the Doppler spread relationship found in section 7.6 may be used to extend the decorrelation time measures to alternate velocity and grazing angle conditions. We note that the Lake Michigan, Lake Superior, and Adieundacy mountainous terrain conditions (i.e., points 50, 60, 56, 59, and 74 for the winter series) produce decorrelation time values on the order of 2 msec, which in turn is representative of the high-angle oceanic data set measures.

7.8 AIRPORT MULTIPATH ENVIRONMENTS

Multipath airport environment data were gathered on the approach, landing, and taxi phases at three airports: O'Hare International (Chicago), JFK International (New York), and NAFEC, located northwest of Atlantic City, New Jersey. All probes were conducted with a 10-MHz chip rate and used a single low-gain crossed-slot antenna located close to the top centerline of the airplane. This antenna possessed nominal LHC polarization characteristics and thus provided an enhanced *multipath return* at the expense of a direct signal polarization mismatch relative to the RHC polarized ATS-6 uplink. For all three airports the elevation angle to ATS-6 was approximately 39° .

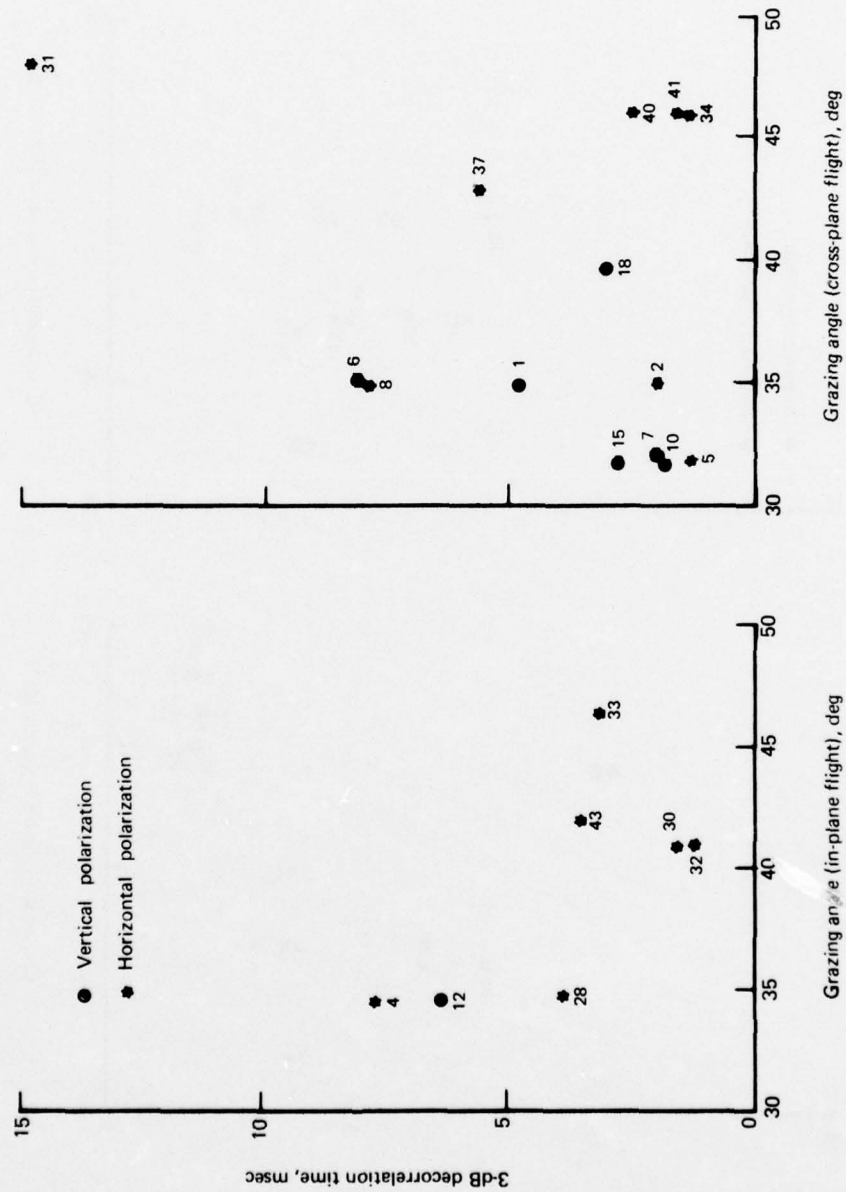


Figure 7-34. CONUS Scatter Decorrelation Time, Fall Flights

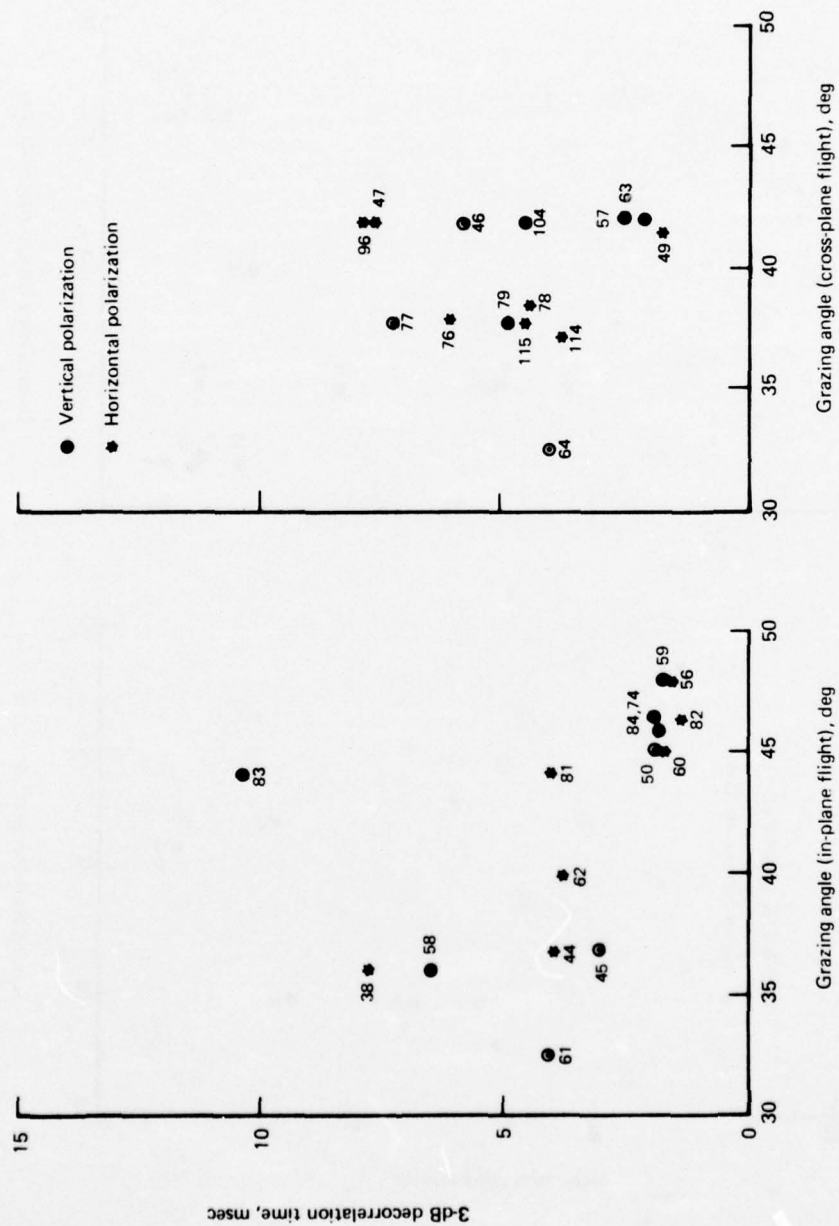


Figure 7-35. CONUS Scatter Decorrelation Time, Winter Flights

7.8.1 Runway Taxi Conditions

With the airplane on the ground and conducting typical taxi maneuvers, the returned signal structure possessed the following attributes.

- a. Significant amplitude fluctuations were observed on the received direct tap³ signal of the crossed-slot operational antenna. This may be attributed to a number of factors, such as building shielding of the direct line-of-sight signal, antenna pattern variation as a function of aircraft orientation, and interference (both constructive and destructive) due to multipath arrivals falling within the direct tap bank.
- b. Very little multipath energy was returned with delays greater than 0.2 μ sec relative to the direct signal arrival. The level of multipath energy with delays greater than 0.2 μ sec was at least 20 dB below the direct-path signal.

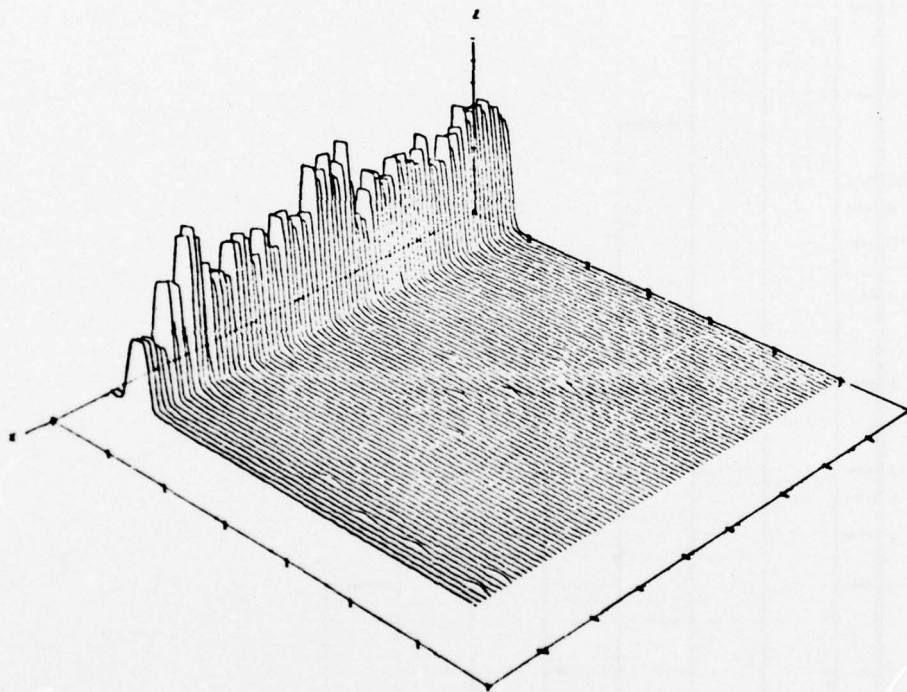
These observations are illustrated with the sample results taken from the February 19, 1976, O'Hare airport test sequence. Presented in figure 7-36 is a time log of the airplane location superimposed on a runway building structure descriptor of O'Hare; also included is an arrow indicating the direction toward ATS-6. The delay-spectra time history presented in figure 7-37 demonstrates the variations in the direct tap signal amplitude when using the crossed-slot antenna during the time interval 1204 to 1207:30. The direct signal is located midway between taps 22 and 23 of the bank and corresponds to the plateau-like signal in the display. Through analysis of the corresponding numerical output, the direct signal is observed to have peak-to-trough variations in excess of 5.2 dB. More detailed plots illustrating the delay spectra of the total (direct plus multipath) signal from the crossed-slot antenna are given in figures 7-38 and 7-39. These data correspond to 2-sec sample spaces centered about experiment times 1205:17 and 1206:24, respectively, and are representative of the typical delay-spectra signatures obtained for the taxi scenarios. They have been subjected to a first-order noise-removal process wherein noise is determined from delay spectra of a multipath-free region of the tap bank and then subtracted from all taps. Results generally indicate that the bulk of the delay returns arrive no later than 0.1 or 0.2 μ sec after the direct signal.

7.8.2 Approach and Landing Maneuvers

Due to fairly rapid airplane altitude and attitude changes, the multipath characteristics in the landing and approach phases of an airport environment are somewhat different from those associated

³With the aircraft on the ground, the 10-MHz chip rate (the highest available with the SACP equipment) resolution is insufficient to completely discriminate against terrain and building scatter returns falling into the direct-path taps.

DELAY SPECTRA TIME HISTORY
 DATE 2/19/75 O'HARE
 TAP RESOLUTION .2 MICROSEC
 TIME INTERVAL 12/ 4/50.082 TO 12/ 7/30.357



AXIS		MINIMUM	MAXIMUM	INCREMENT
X	EXPERIMENT TIME RELATIVE TO T-START (SEC)	.00	180.00	20.00
Y	DELAY TAP (.2 MICROSEC. WIDTH)	20.00	55.00	5.00
Z	DELAY PSD (LINEAR)	.00	4000.00	500.00

Figure 7-37. O'Hare Delay-Spectra Time History

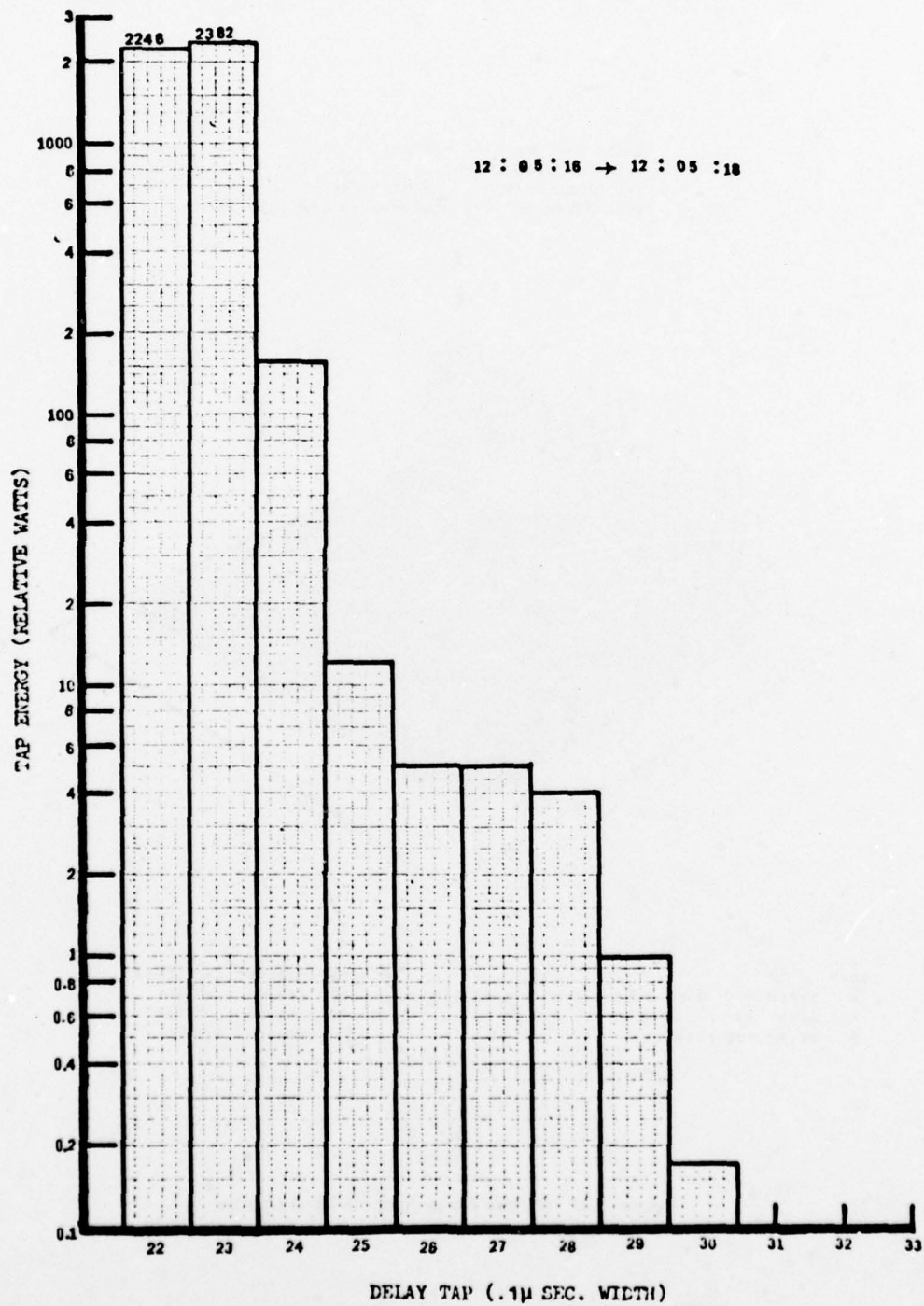


Figure 7-38. O'Hare Delay Spectra (1205:17 GMT)

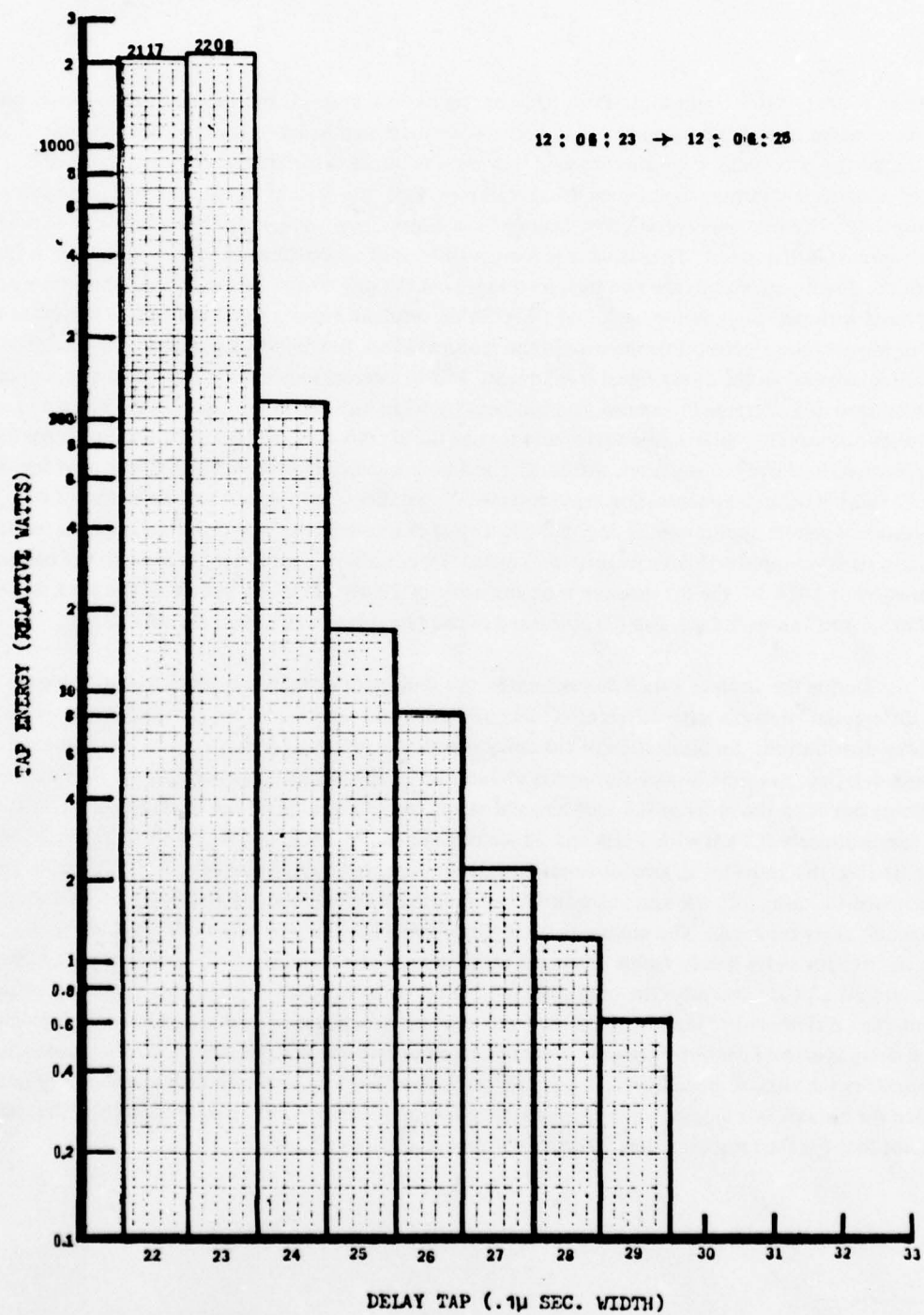


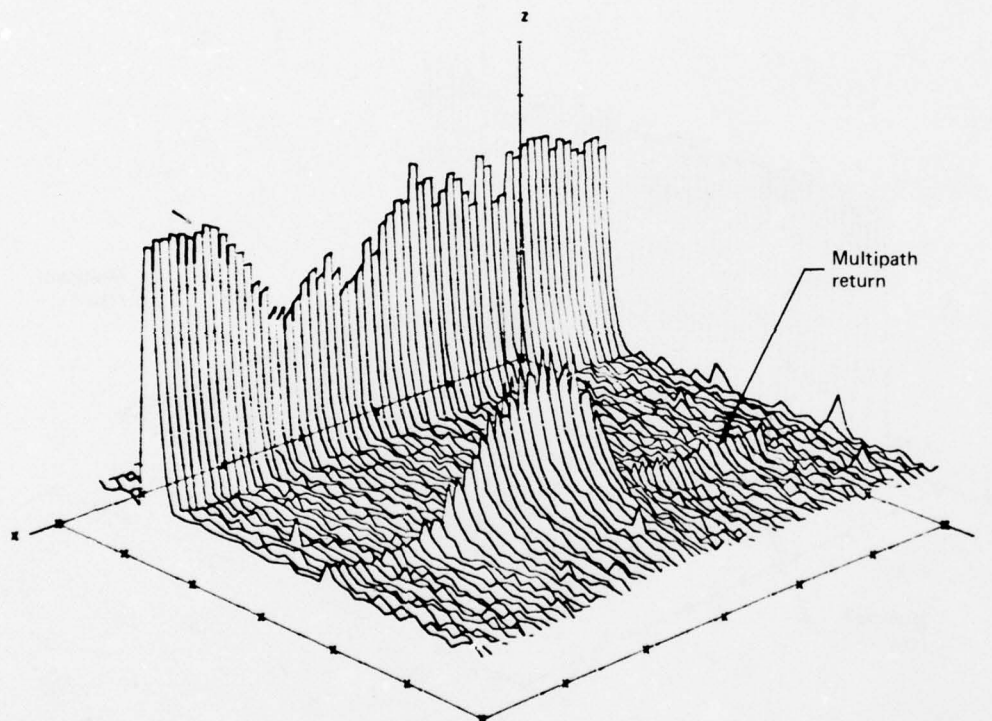
Figure 7-39. O'Hare Delay Spectra (1206:24 GMT)

with en route CONUS conditions. Prior to or during its final descent, the airplane may perform one or more rather steep banking maneuvers. Perhaps the most significant impact of these attitude changes relates to the potentially large antenna gain that may be directed toward the effective multipath "glistening region" during banking maneuvers. An example illustrating such an occurrence is given in figure 7-40, where a delay-spectra time history for a 2-min flight segment in the vicinity of the NAFEC FAA airport is illustrated. The airplane was at an altitude of approximately 580 m, which allowed both the direct-path signal (the two high-level taps near the origin) and the multipath return to be captured within a common tap bank. At 1424:30 the airplane began a banking maneuver (toward the satellite); we note a perceptible increase in the multipath return, which is accompanied by a corresponding decrease in the direct signal component. It is of interest to note that the direct signal decreases not because of a decrease in antenna gain but because of an increase in the polarization mismatch between the satellite polarization vector and that of the aircraft antenna (becomes maximum for look angles directly above the airplane). Although the antenna and the mode in which it was used for this probe (with its circular polarization sense reversed on the direct path) is not representative of an operational system application, it does provide a vivid example of the banking effects upon a receiving system signal-to-multipath interference (S/I) ratio. Specifically we note that (1) prior to the banking maneuver at 1424:14, the S/I measure is on the order of 22 dB, (2) in the middle of the bank at 1424:42, S/I drops to a low of 1.2 dB, and (3) at the end of the test segment S/I again exceeds 20 dB.

During the airplane's final descent mode, the multipath signal is subjected to rapid changes in its differential⁴ delay, a large differential⁴ Doppler shift, and significant changes in its delay-spectra energy distribution. An illustration of the delay coordinate effects is given in figure 7-41, where a 2-min delay-spectra time history segment is shown for the JFK airport approach phase. The airplane's descent rate is on the order of 0.3 km/min, and at the end of the interval the airplane is at an altitude of approximately 0.7 km with 2 min and 20 sec remaining until touchdown. Runway 31R was used for the landing; this provides an aircraft-to-satellite azimuth angle of approximately 90°. As for the banking maneuver case, both the antenna's direct and multipath signal components are captured within a common delay tap bank. The multipath is on the order of 20 to 30 dB below the level of the direct signal strength and is barely visible above the noise floor of the receiver. We do note, however, that as the aircraft altitude decreases the multipath process moves in toward the direct signal portion of the bank (i.e., differential time delay decreases) and undergoes a change in its delay spectrum properties. The delay spectrum characteristics are generally noted to become less spread (or, in other words, more peaked) as the aircraft altitude decreases. This is in accord with expectation and, as previously noted when the aircraft was located on the ground, the multipath components are dispersed to such a small extent that for the most part they all arrive within 0.1 μ sec of each other.

⁴With respect to the direct signal's time of arrival and Doppler frequency shift.

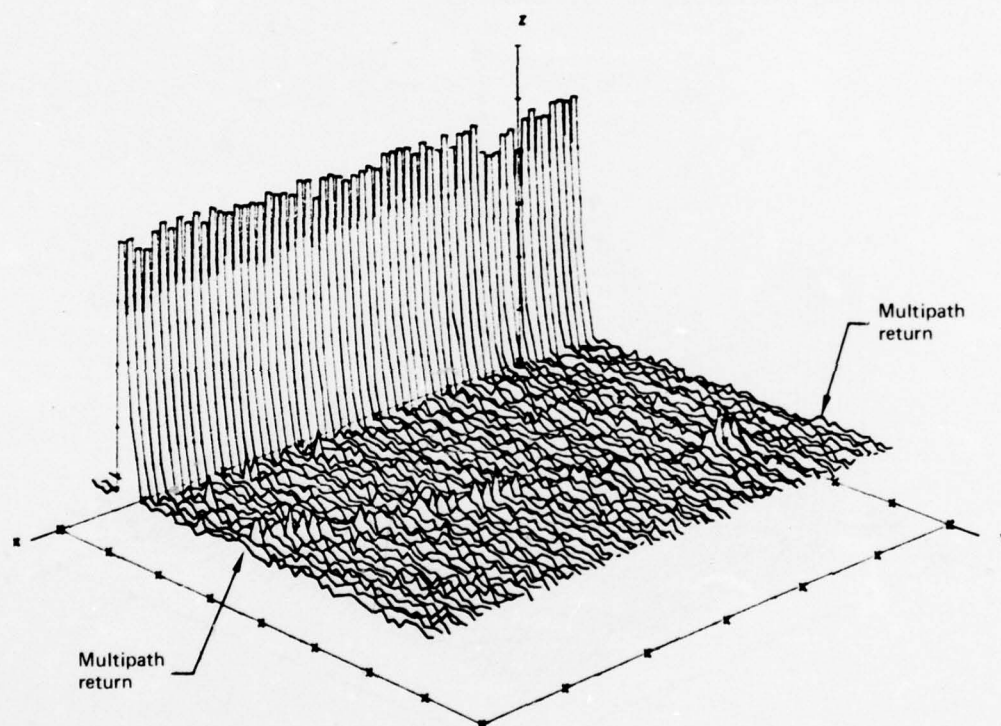
DELAY SPECTRA TIME HISTORY
 DATE 2/20/75 RHC-KSLT POLARIZATION
 TAP RESOLUTION .1 MICROSEC
 TIME INTERVAL 14/23/30.000 TO 14/25/30.201



AXIS	MINIMUM	MAXIMUM	INCREMENT
X EXPERIMENT TIME RELATIVE TO T-START(SEC)	0	120	20
Y DELAY TAP (.1 MICROSEC. WIDTH)	20.0	80.0	10.0
Z DELAY PSD (DECIBEL)	15.0	45.0	5.0

Figure 7-40. Airport Environment Multipath Probe — Banking Maneuver

DELAY SPECTRA TIME HISTORY
 DATE 2/20/75 RHC-KSLT POLARIZATION
 TAP RESOLUTION .1 MICROSEC
 TIME INTERVAL 13/36/ .030 TO 13/38/ 1.033



AXIS		MINIMUM	MAXIMUM	INCREMENT
X	EXPERIMENT TIME RELATIVE TO T-START(SEC)	0	120	20
Y	DELAY TAP (.1 MICROSEC. WIDTH)	.0	80.0	10.0
Z	DELAY PSD (DECIBEL)	15.0	45.0	5.0

Figure 7-41. Airport Environment Multipath Probe — Landing Descent Phase

Fourier analysis of a time interval taken at the end of the segment used for figure 7-41 reveals that the specular-point return is shifted upward in frequency from the direct path return by 34 Hz. This position-differential Doppler is induced upon the signal since the aircraft's separation from the specular point is decreasing whereas its distance to the satellite is increasing.

7.9 CONUS MULTIPATH TEST CONCLUSIONS

A summary of results and conclusions for the CONUS multipath channel characterization test is given in section 2.2.

REFERENCES

- 1-1 "Integrated Test Plan for ATS-F L-Band Experiment," NASA/GSFC report TP-750-73-1, September 1973.
- 3-1 P. A. Bello et al., "Impact of Satellite Aeronautical Channel on Modem Specifications," report FAA-RD-74-54, March 1974.
- 3-2 "ATS-5 Multipath/Ranging Digital Data L-Band Experimental Program, Phase III - Terminal Design and Subsystem Performance Characteristics," report FAA-RD-73-57-III, Boeing Commercial Airplane Company, April 1973.
- 3-3 T. Olsson and B. P. Stapleton, "L-Band Orthogonal-Mode Crossed-Slot Antenna and VHF Crossed Loop Antenna," final report DOT-TSC-130, August 1972.
- 5-1 P.A. Bello, "Aeronautical Channel Characterization," IEEE Trans. on Comm., vol. COM-21, no. 5, p. 548-563, May 1973.
- 5-2 A.D. Mallinckrodt, "Ground Multipath in Satellite-Aircraft Propagation," paper presented at the Symposium on Application of Atmospheric Studies to Satellite Transmissions, Boston MA, September 1969.
- 5-3 A. Schneider, "Multipath Channel Characterization for AEROSAT," paper presented at IEEE International Conference on Communications, Seattle WA, June 1973.
- 5-4 J. K. DeRosa, "The Characterization of Multipath and Doppler Rading in Earth Scatter Communication, Navigation and Radar Links," Ph.D. dissertation, Northeastern University, Boston MA, June 1972.
- 5-5 P. A. Bello et al., "Impact of Satellite Aeronautical Channel on Modem Specifications, Phase II," final report to DOT/TSC, CNR, Inc., January 1975.
- 5-6 "ATS-5 Multipath/Ranging/Digital Data L-Band Experimental Program, Phase V - Multipath/Ranging Analysis and Results," report FAA-RD-73-57-V, Boeing Commerical Airplane Company, April 1973.
- 5-7 H. Staras, "Rough Surface Scattering on a Communication Link," Radio Science, vol. 3 (new series), no. 6, June 1968, p. 623-631
- 5-8 P. Beckman and A. Spizzichino, THE SCATTERING OF ELECTROMAGNETIC WAVES FROM ROUGH SURFACES, Macmillan Co., New York, 1963, p. 320.
- 5-9 A. J. Mallinckrodt, "Propagation Errors," notes for UCLA short course entitled Satellite-Based Navigation Traffic Control and Communications to Mobile Terminals, October 1969.
- 5-10 G. M. Jenkins and D. G. Watts, SPECTRAL ANALYSIS AND ITS APPLICATIONS, Holden-Day, San Francisco, 1969, p. 338.
- 5-11 J. N. Pierce and S. Stein, "Multiple Diversity With Non-Independent Fading," Proc. IRE, vol 48, app V, January 1960, p. 89-104. .
- 5-12 C. Cox and W. Munk, SLOPES OF THE SEA SURFACE DEDUCED FROM PHOTOGRAPHS OF SUN GLITTER, University of California Press, Berkely and Los Angeles, 1956, p. 431.

REFERENCES (Concluded)

- 5-13 DeRosa, "Multipath Antenna Specification for a Synchronous Satellite - Aircraft Link," 1974 International IEEE/AP-5 Symposium, Atlanta GA, paper 74-CH0853-3AP, June 1974, p. 232-235.
- 6-1 D. E. Barrick and W. H. Peake, "A Review of Scattering From Surfaces With Different Roughness Scales," *Radio Science*, vol 3 (new series), no. 8, August 1968.
- 6-2 L. M. Brekhovskikh, "The Diffraction of Waves by a Rough Surface" (in Russian), *Zh. Eksp. Teor. Fiz.*, vol 23, 1952, p. 275-289.
- 6-3 G. T. Ruck et al., *RADAR CROSS-SECTION HANDBOOK*, Plenum Press, New York, 1970.
- 6-4 J. K. DeRosa, "On the Determination of the Delay-Doppler Scattering Function for a Ground-to-Aircraft Link," *IEEE Canadian Symposium on Communications*, paper 70C 67-REG-7, November 1970, p. 51-52.
- 6-5 W. H. Peake, "Satellite-to-Aircraft Multipath Signals Over the Ocean," final report 3266-2, Ohio State University Electro-Science Laboratory, May 1974.
- 6-6 T. Hagfors, "Relationship of Geometrical Optics and Autocorrelation Approaches to the Analysis of Lunar and Planetary Radar," *Geophys. Res.*, vol. 71, no. 2, January 15, 1966.
- 6-7 B. Kinsman, *WIND WAVES*, Prentice-Hall, Inc., Englewood Cliffs NJ, 1965, p. 23.
- 6-8 R. O. Pilon, "Determination of Ocean Surface Descriptors Using Sea Photo Analysis Techniques," final report FAA-RD-72-110, U.S. Naval Research Laboratory, October 1972.
- 6-9 L. Moskowitz, "Estimates of the Power Spectrums for Fully Developed Seas for Wind Speeds of 20 to 40 Knots," *J. Geophys. Res.*, vol. 69, no. 23, 1964, p. 5161.
- 7-1 "ATS-5 Multipath/Ranging/Digital Data L-Band Experimental Program, Phase IVD, Volume II - Overland Multipath, Pacific Multipath, Scintillation Tests," report FAA-RD-73-57-IVD, Boeing Commerical Airplane Company, April 1973.
- A-1 D. C. Cox, "Delay Doppler Characteristics of Multipath Propagation of 910 MHz in a Suburban Mobile Radio Environment," *IEEE Trans. on Antennas and Propagation*, September 1972, p. 625-635.

APPENDIX A **EFFECTS OF RESOLUTION LIMITATIONS BECAUSE OF FINITE FILTER** **BANDWIDTHS AND PROBER CHIP RATES**

The signal structure used to characterize the surface scatter phenomena is influenced not only by the multipath phenomena but also by the equipment filters (transmitter, satellite transceiver and receiver), prober chip rate, and the refractive index perturbation of the earth. Under the linear system representation of the total channel, the work of Cox (ref A-1) may be used to express the effects of the prober signal and all system filters upon the received signal measurement:

$$\left| \int_{-\infty}^{\infty} Q_T(\tau) e^{j\Omega\tau} d\tau \right| = \frac{1}{4\pi} |R_p(0, \Omega)| \cdot |R_{T-R}(\Omega)|$$

where:

- $Q_T(\tau)$ = delay spectrum including all effects
- $R_p(0, \Omega)$ = frequency autocorrelation function associated with the propagation medium alone
- $R_{T-R}(\Omega)$ = the correlation function of the probe signal's power spectrum including all system filters.

Thus the equipment bandwidth effects upon the propagation medium measurements appear as a multiplicative factor in the frequency autocorrelation function. Correspondingly, the desired delay spectrum is contained within the output of the prober as the convolution of itself with the spectral density of $R_{T-R}(\Omega)$.

One may therefore remove the effects of the finite equipment bandwidth by dividing the inverse transform of $Q_T(\tau)$ by $|R_{T-R}(\Omega)|$. This provides us with the channel's $|R(0, \Omega)|$ function, which in turn may be Fourier transformed to produce a delay spectra embodying only the effects of the propagation medium.

An estimate of $R_{T-R}(\Omega)$ was obtained through inverse Fourier transform analysis of the delay-spectra signal captured in the receiver's direct tap bank.¹ This signal traverses the direct line-of-sight path from the aircraft to the satellite where it is relayed to the ground station receiver. It does not include multipath influences; however, it does contain the effects of upper-troposphere and ionosphere propagation perturbations, which should be entirely negligible.

¹ Since the correlator taps are spaced one chip width apart, this estimate is considered to be relatively imprecise, especially in the tails of the function's distribution.

A plot of the experimentally derived $R_{T-R}(\Omega)$ function (5-MHz probe rate) is given in figure A-1. It is noted that to close approximation this result for the frequency range illustrated is nearly identical to that which would result from the probe code effects alone. Consistent with expectation, we observe that $R_{T-R}(\Omega)$ does not fall appreciably below unity for frequencies less than roughly 750 kHz. Typically² at this value the total $|R(0,\Omega)|$ function is well below its maximum value and is asymptotically approaching a relatively low level. Thus to good approximation the finite bandwidth limitations of the probing system should have negligible effects upon the bulk of the $|R(0,\Omega)|$ distribution (i.e., 3 dB and 1/e spread measures). On the other hand, for frequency separations greater than roughly 1 MHz, we expect the multipath channel $|R(0,\Omega)|$ distribution to be low by at least 10%. This is thought to be substantiated by the model predictions yielding $|R(0,\Omega)|$ functions that exhibit a propensity to be heavier tailed than their oceanic experimental counterparts.

Since $Q(\tau)$ and $R(0,\Omega)$ are Fourier transform pairs, the above discussion is easily adapted to deduce the finite system bandwidth effects upon the delay-spectra measurements. Specifically, one expects the multipath spectra to be less spread in delay than the total measurements imply. In that $R(0,\Omega)$ is relatively unmodified over the bulk of its distribution, one does not expect $Q(\tau)$ to be greatly perturbed by the system parameter bandwidth effects.

²For the oceanic results.

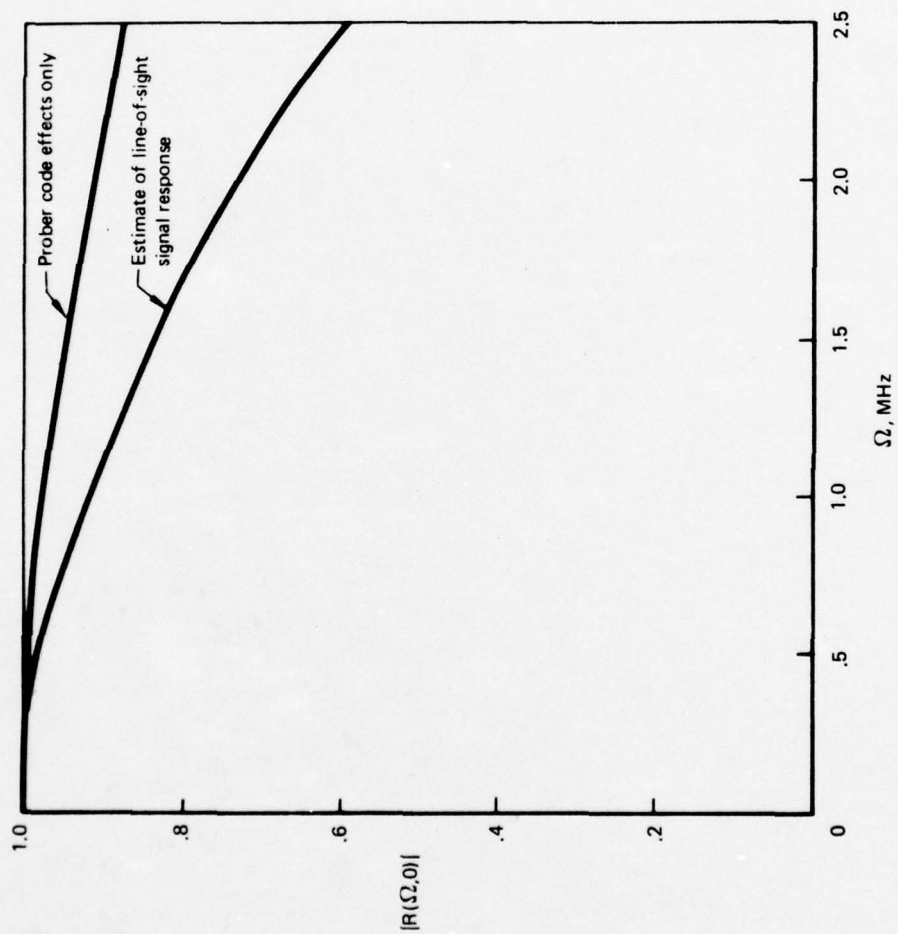


Figure A-1. Line-of-Sight Prober Frequency Autocorrelation Magnitude

APPENDIX B

EFFECT OF GAIN DIFFERENTIAL BETWEEN QUADRATURE CHANNELS OF MULTIPATH SACP RECEIVER

Analysis of the amplitude statistics associated with multipath-free regions of the SACP receiver indicates that the gains of the I and Q receiver signal paths are somewhat unbalanced (see sec 5.4.1). Although the gain differential appears to vary from test to test, it is typically on the order of 1 to 2 dB. The effect of this on $S(\tau, \omega)$ is illustrated by the following discussion.

Assume that the baseband input signal to the receiver is given by:

$$i(t) = e^{j\omega t} ,$$

which represents a one-sided spectral distribution with total energy located at frequency $-\omega$. After processing by the receiver, the output signal (neglecting filter attenuation, etc.) becomes:

$$O(t) \begin{cases} = A I(t) + B Q(t) \\ = A \cos \omega t - jB \sin \omega t \\ = A L(t) + (A-B) \sin \omega t \end{cases}$$

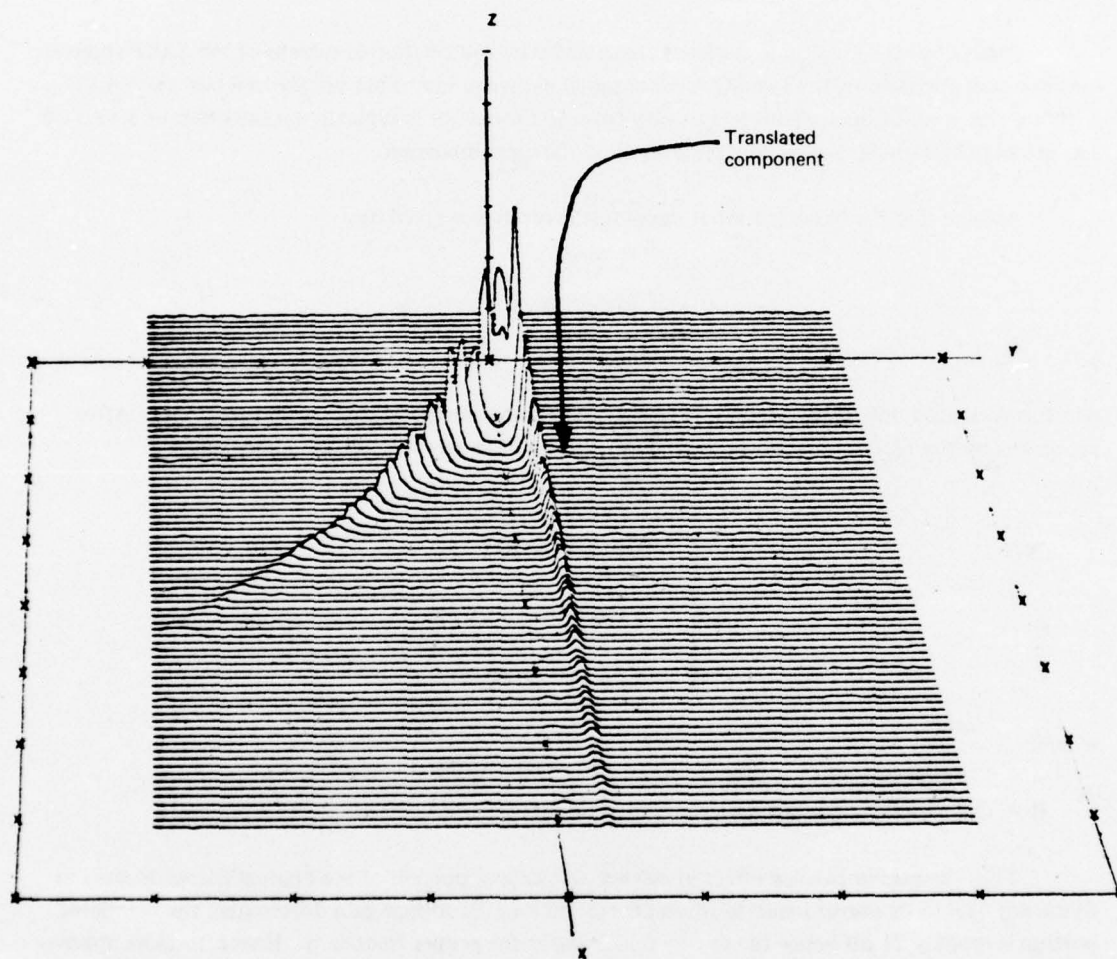
where:

A = I component channel gain

B = Q component channel gain.

Thus the gain imbalance effect in essence translates a portion of the original energy located at frequency $-\omega$ to its mirror image location at $+\omega$. For a 20% voltage gain differential, the translated portion is roughly 21 dB below the energy remaining at the proper frequency. Hence, to close approximation the I/Q channel gain imbalance should have only a small impact on $S(\tau, \omega)$ parameter estimation. A visual indication of this effect is given in figure B-1, where we have delineated the (barely visible) component translated from the negative-frequency hump of the $S(\tau, \omega)$ distribution.

DELAY-DOPPLER SCATTER FUNCTION
 DATE 3/31/75 LHC POLARIZATION
 TAP RESOLUTION .2 MICROSEC
 TIME INTERVAL 9/ 8/54.821 TO 9/ 8/59.849
 NOISE REMOVED



AXIS	MINIMUM	MAXIMUM	INCREMENT
X DELAY TAP [.2 MICROSEC. WIDTH]	.0	80.0	10.0
Y DOPPLER FREQUENCY [HERTZ]	-400	400	100
Z DELAY-DOPPLER PSD [LINEAR]	-5.0	25.0	5.0

Figure B-1. Gain Differential Effects Upon $S(\tau, \omega)$

APPENDIX C
EQUIPMENT EFFECTS ON DELAY-DOPPLER SPECTRUM ESTIMATES

C.1. System Description

In the multipath prober, the signal consists of a $\pm 180^\circ$ phase-modulated sequence with the phases chosen to agree with the sequence of binary states of a maximal length shift register output. Passage of this signal through the aircraft RF and IF amplifiers, the satellite repeater, the propagation media, and the ground station receiver RF and IF amplifiers, results in a sequence of linear distortions which may be regarded as being caused by two composite channels: an equipment channel and a propagation channel. The purpose of this Appendix is to discuss the effects of the composite equipment transfer function on measurement of propagation channel characteristics, and to predict the magnitude of equipment-induced distortion.

Figure C-1 defines the basic signal processing operations of the probing system. A periodic probing signal with complex envelope $z(t)$ is filtered at the transmitter by IF and RF filters prior to transmission. All the filtering operations in the transmitter are lumped together as one filter, called the transmitter filter, which has impulse response $h_T(t)$. The propagation medium is represented by the complex time-variant impulse response $h(t, \tau)$ and the additive noise by the complex process $n(t)$. All the linear operations in the satellite and ground station receivers prior to the correlation operations are lumped together into one receiver filter with impulse response $h_R(t)$. The output of the filter is subjected to correlation processing as illustrated in the figure. Complex notation is used to describe the correlation operation as a multiplication of the receiver filter output by the complex conjugate of a shifted probing signal, followed by a complex lowpass filtering operation.

The impulse response of the propagation channel consists of two distinct parts: a direct path and a continuum of delayed multipath components grouped together and well separated from the direct path. The PN-PSK signal received on the direct channel is tracked in delay and Doppler and is used to provide a delay and Doppler reference in measuring the impulse response of the multipath channel.

The multipath measurement consists of the extraction of the in-phase and quadrature samples of the impulse response. Due to the time-variant nature of the channel, these samples are lowpass with bandwidth equal to the Doppler spread of the channel (referenced to the direct path Doppler shift). This set of lowpass functions is sampled and multiplexed to prepare it for analog tape recording.

C.2. Formulation of Prober Output

The complex representation of the receiver filter output in the absence of noise is given by the sequence of convolutions,

$$w(t) = z(t) \otimes h_T(\tau) \otimes h(t, \tau) \otimes h_R(\tau), \quad (C-1)$$

where \otimes denotes convolution and z is the transmitted signal. We assume that the time constants of $h_T(\tau)$ and $h_R(\tau)$ are very much smaller than the fading time constant. In this case one may lump the transmitter and receiver filters together, i.e.,

$$w(t) = z(\tau) \otimes e(\tau) \otimes h(t, \tau), \quad (C-2)$$

where $e(\tau)$ is the impulse response of a hypothetical filter, called the "equipment" filter,

$$e(\tau) = h_T(\tau) \otimes h_R(\tau), \quad (C-3)$$

which represents the combined filtering operations of the transmitter and receiver.

The combination of the equipment filters and the probing signal may be regarded as an equivalent probing signal

$$y(t) = e(t) \otimes z(t) , \quad (C-4)$$

so that (in the absence of additive noise) the received signal

$$w(t) = \int y(t - \tau) h(t, \tau) d\tau , \quad (C-5)$$

and the complex lowpass filter input is given by the equivalent form

$$\mu(t) = z^*(t - \eta) w(t) . \quad (C-6)$$

The probing signal is assumed to be periodic with period T.

For 10- and 5-MHz chip rates, the prober performs the lowpass filtering operation shown in Figure C-1 as an integrate-and-dump over T seconds and $\frac{T}{2}$ seconds, respectively. Using the second of these choices as an example, it therefore follows that

$$\begin{aligned} \hat{h}(t, \eta) &= \int_0^{\frac{T}{2}} \mu(t') dt' \\ &= \int_0^{\frac{T}{2}} \int_{-\infty}^{\infty} z^*(t' - \eta) y(t' - \tau) h(t, \tau) d\tau dt' . \end{aligned} \quad (C-7)$$

Writing

$$R(\tau) = \int_0^{\frac{T}{2}} z^*(t) y(t + \tau) dt , \quad (C-8)$$

we have

$$\hat{h}(t, \eta) = \int_{-\infty}^{\infty} R(\eta - \tau) h(t, \tau) d\tau ; \quad (C-9)$$

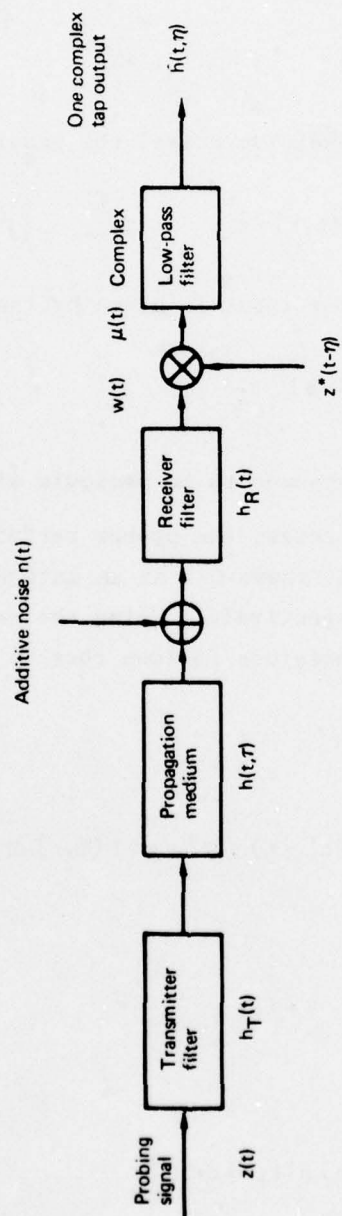


Figure C-1. Definition of Basic Signal-Processing Operation in Prober System

i.e., the measured impulse response is related to the true impulse response via a convolution with the cross-correlation function $R(\tau)$. This function is discussed at greater length in the next section.

In passing, it should be observed that when the impulse response $h(t, \tau)$ is a time-invariant impulse,

$$h(t, \tau) = \delta(\tau) \quad (C-10)$$

the measured quantity $\hat{h}(t, \eta)$ is then

$$\begin{aligned} \hat{h}(t, \eta) &= \int_{-\infty}^{\infty} R(\eta - \tau) \delta(\tau) d\tau \\ &= R(\eta) \end{aligned} \quad (C-11)$$

This should be the situation on two distinct occasions:

- (1) Direct path signals are correlated by delayed reference signals, with the result available in the direct path taps.
- (2) Multipath uplook calibration signals. When the multipath antenna was directed upward to provide H-V calibration, the quantity $R(\eta)$ should have been present in the indirect taps.

In each case it is apparent that a sampled form of $R(\eta)$ is obtained.

C.3. The Signal Correlation Function

Before the function $R(\tau)$ can be specified in detail, it is necessary to describe the physical operations performed by the probing equipment. Our main interest centers on the demodulator which contains the most restrictive filters and performs the correlation function.

Figure C-2 illustrates the operations of interest in block diagram form. The IF section contains a four-pole Butterworth-Thompson filter centered on 70 MHz with 8-MHz 3-dB bandwidth. This is followed by in-phase and quadrature demodulation and lowpass filtering for each resultant signal. The lowpass signals are sampled at a 10-MHz rate regardless of the chip rate selected, and the 4-bit samples are then multiplied by ± 1 as determined by an appropriately delayed PN sequence. The result is integrated for a complete sequence period T , or a sub-multiple of the period. The sampled version of $z(t)$ used in the correlation can be expressed as

$$\tilde{z}(t) = \sum_{n=-\infty}^{\infty} z^* \left(\frac{T_0}{4} + n \frac{T_0}{2} \right) \delta \left(t - \frac{T_0}{4} - n \frac{T_0}{2} \right), \quad (C-12)$$

for the 5-MHz chip rate (10-MHz sampling), and

$$\tilde{z}(t) = \sum_{n=-\infty}^{\infty} z^* \left(\frac{T_0}{2} + n T_0 \right) \delta \left(t - \frac{T_0}{2} - n T_0 \right), \quad (C-13)$$

for the 10-MHz chip rate. In each instance, T_0 represents the selected chip duration. Returning to the expression for $R(\tau)$, it is therefore apparent that

$$R_5(\tau) = \int_0^{\frac{T}{2}} \tilde{z}(t') y(t' + \tau) dt'. \quad (C-14)$$

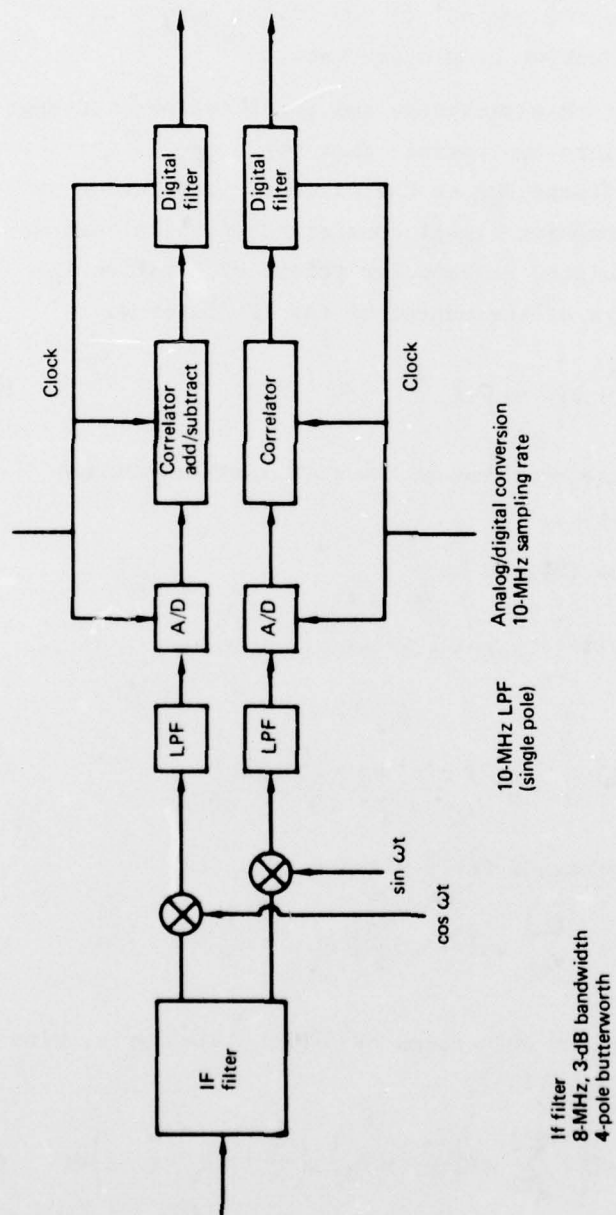


Figure C-2. Correlation Processing of Multipath Returns

The accumulated result is filtered by a four-pole lowpass digital filter with selectable bandwidth, and output samples are provided at a rate equal to twice the nominal (1 dB) filter bandwidth by downsampling the 10-MHz output sample sequence.

For the purposes of this analysis, the total equipment distortion will be separated into two parts: that which can be attributed to the IF filter, and effects due to the discrete correlation processing. The original probing signal consisting of a periodic sequence of N biphas-modulated rectangular pulses of duration T_0 seconds therefore appears at the output of the IF filter as

$$y(t) = \int_{-\infty}^{\infty} e(\xi) z(t - \xi) d\xi, \quad (C-15)$$

where $e(\xi)$ is the impulse response of the Butterworth-Thompson filter (complex envelope).

Using Eqs. (15) and (8), we have

$$\begin{aligned} R(\tau) &= \int_0^{\frac{T}{2}} \tilde{z}(t') \int_{-\infty}^{\infty} e(\xi) z(t' + \tau - \xi) d\xi dt' \\ &= \int_{-\infty}^{\infty} e(\xi) \int_0^{\frac{T}{2}} \tilde{z}(t') z(t' + \tau - \xi) d\xi dt'. \end{aligned} \quad (C-16)$$

Therefore, with the expression for \tilde{z} given by Eq. (12),

$$R_5(\tau) = \int_{-\infty}^{\infty} e(\xi) \sum_{n=0}^{N-1} z^*\left(\frac{T_0}{4} + n\frac{T_0}{2}\right) z\left(\frac{T_0}{4} + n\frac{T_0}{2} + \tau - \xi\right) d\xi. \quad (C-17)$$

This expression applies for chip rates of 5 MHz. Similarly, with a 10-MHz chip rate [from Eq. (13)],

$$R_{10}(\tau) = \int_{-\infty}^{\infty} e(\xi) \sum_{n=0}^{N-1} z^*\left(\frac{T_0}{2} + nT_0\right) z\left(\frac{T_0}{2} + nT_0 + \tau - \xi\right) d\xi. \quad (C-18)$$

The inner summation is recognizable as being a form of autocorrelation function for the PN sequence $z(t)$ evaluated at $(\tau - \xi)$. When $(\tau - \xi)$ is greater than T_0 seconds, the autocorrelation function has a very low value, while for values less than T_0 , the result is closely approximated by the autocorrelation properties of a single rectangular pulse of duration T_0 seconds. Note that the 5-MHz chip rates involve integration over a half period $\frac{T}{2}$ rather than the full PN sequence period T , so that precise results cannot be obtained. With the above approximations,

$$R_5(\tau) = \int_{-\infty}^{\infty} e(\xi) \psi_5(\tau - \xi) d\xi \quad (C-19)$$

$$R_{10}(\tau) = \int_{-\infty}^{\infty} e(\xi) \psi_{10}(\tau - \xi) d\xi \quad (C-20)$$

where ψ_5 and ψ_{10} are shown in Figure C-3; i.e.,

$$\psi_5(\tau) = \begin{cases} N & -\frac{3T_0}{4} < \tau < -\frac{T_0}{4}, \frac{T_0}{4} < \tau < \frac{3T_0}{4} \\ 2N & |\tau| < \frac{T_0}{4} \\ 0 & \text{otherwise} \end{cases} \quad (C-21)$$

$$\psi_{10}(\tau) = \begin{cases} N & |\tau| < \frac{T_0}{2} \\ 0 & \text{otherwise.} \end{cases} \quad (C-22)$$

Note that the IF filter has a fixed structure, so that with lower chip rates, the 8-MHz 3-dB bandwidth far exceeds the bandwidth required to pass the signal without distortion. For the 5-MHz chip rate, ψ_5 should therefore be a good approximation to R_5 .

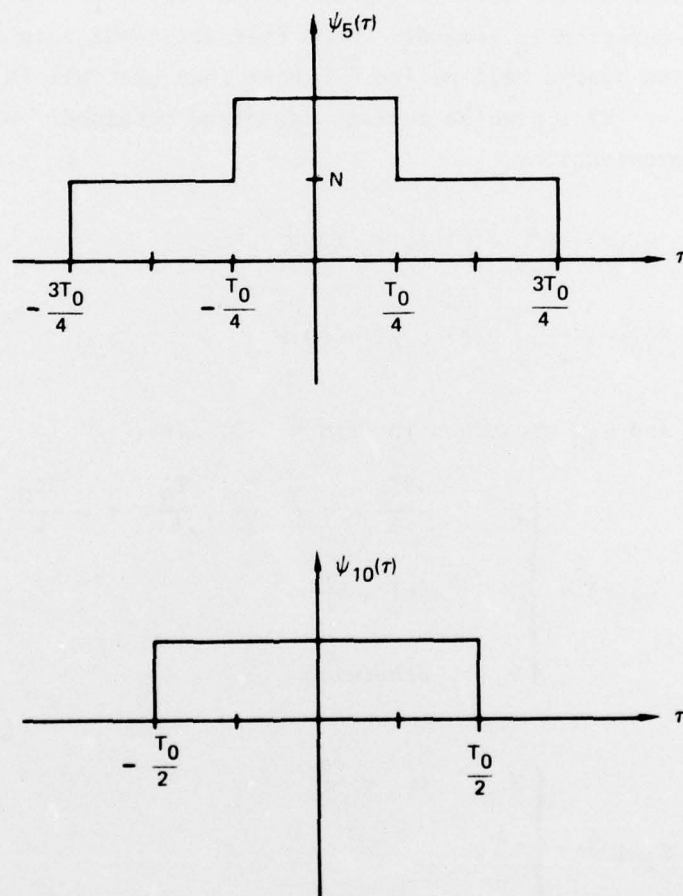


Figure C-3. Signal-Processing Correlation Functions

C.4. Delay Power Spectrum Properties

The results obtained in the previous section will now be employed to compute intertap correlation effects.

The estimated impulse response in the absence of noise is

$$\hat{h}(t, \eta) = \int_{-\infty}^{\infty} R(\eta - \tau) h(t, \tau) d\tau, \quad (C-23)$$

and is available for discrete values of η .

If we assume that the true channel is wide sense stationary uncorrelated scattering with zero mean, the intertap correlation can be established from

$$\begin{aligned} E[\hat{h}(t, \eta_1) \hat{h}^*(t, \eta_2)] &= \iint R(\eta_1 - \tau_1) R^*(\eta_2 - \tau_2) E[h(t, \tau_1) h^*(t, \tau_2)] d\tau_1 d\tau_2 \\ &= \int R(\eta_1 - \tau) R^*(\eta_2 - \tau) Q(\tau) d\tau, \end{aligned} \quad (C-24)$$

with the assumption that

$$E[h(t, \tau_1) h^*(t, \tau_2)] = Q(\tau_1) \delta(\tau_1 - \tau_2). \quad (C-25)$$

$Q(\tau)$ is the delay power spectrum for the channel.

In the channel probing equipment, the correlation operations can be selected to occur at full or half chip increments of time; i.e., T_0 or $T_0/2$. For the ocean tests of interest, the tap spacing was set equal to the chip duration T_0 .

The correlation between taps n and m can, therefore, be expressed as:

$$\begin{aligned}
 R_{nm} &= E[h(t, nT_0) h^*(t, mT_0)] \\
 &= \int_{-\infty}^{\infty} Q(\tau) R(nT_0 - \tau) R^*(mT_0 - \tau) d\tau.
 \end{aligned}
 \tag{C-26}$$

At this point it is instructive to compute the correlation for a function $Q(\tau)$ that is somewhat smoother than the function R . Since $R(\tau)$ falls off rapidly for τ exceeding $\pm 0.75T_0$, the delay power spectrum $Q(\tau)$ only needs to be flat over three taps for the ensuing simplification to be valid, i.e.,

$$R_{nm} \approx Q(\tau_0) \int_{-\infty}^{\infty} R(\tau - nT_0) R^*(\tau - mT_0) d\tau, \tag{C-27}$$

with τ_0 representing a nominal value of τ between nT_0 and mT_0 . For example, without the IF filter present, i.e.,

$$e(\tau) = \delta(\tau), \tag{C-28}$$

we have $R(\tau) = e(\tau)$. Computation of R_{nm} above, with e_5 , yields

$$\begin{aligned}
 \frac{R_{nm}}{R_{nn}} &= \frac{N^2 \frac{T_0}{2}}{4N^2 \frac{T_0}{2} + N^2 T_0} \\
 &= \frac{1}{6} \quad \text{for } |n - m| = 1,
 \end{aligned}
 \tag{C-29}$$

with $R_{nm} = 0$ for larger $|n - m|$.

C.5. Doppler Spectrum Properties

We now examine the influence of the correlator output lowpass filters on the measured spectra. The digital filters have adjustable bandwidth for each choice of chip rate. Here we examine only the configurations utilized in the oceanic and CONUS tests. In particular, we analyze the spectral properties of digital filters for 305-Hz bandwidth in the normal and multiplexed modes (610 samples/second). The chip rates of interest are 5 MHz and 10 MHz.

Table C-1 indicates the filter input sample format and other filter parameters, while Table C-2 lists the filter coefficients for filters B and C. Each filter consists of a two-stage four-pole Butterworth resulting in a 1-dB bandwidth of 305 Hz when used with an input sample rate of 5 kHz and 10 kHz, respectively. Note that the 5-MHz chip rate multiplexed mode results in alternate samples that are set to zero. It can be shown that the net effect is that of an input sequence of samples spaced by 204.6 μ s rather than 409.2 μ s, i.e., by representing the zero stuffed sequence as the sum of two sequences at the high rate, one of which has alternating positive and negative samples. An output signal reduction of 6 dB will occur but this is of little consequence in the data reduction.

TABLE C-1. SACP LOW-PASS FILTERING

Chip rate, MHz	Mode	sample spacing, μ sec	Filter clock rate, kHz	Filter bandwidth, Hz	Countdown ratio	Filter type
10	Normal	102.3	10	305	16	C
10	Mux	204.6 ^a	5	305	8	B
5	Normal	102.3	10	305	16	C
5	Mux	204.6 ^a	5	305	8	B

^aThe multiplexer mode was used in the oceanic multipath tests for both linear and circular polarization experiments.

TABLE C-2. DIGITAL FILTER COEFFICIENTS

Filter	1st stage		2nd stage		Countdown ratio
	K_1	K_2	K_1	K_2	
C	115 64	- 108 128	103 64	- 84 128	16
B	98 64	- 91 128	82 64	- 54 128	8

The digital filters are implemented in two stages, each according to the algorithm

$$x_n = K_1 x_{n-1} + K_2 x_{n-2} + u_n \quad (C-30)$$

$$y_n = \frac{1}{4} x_n + \frac{1}{2} x_{n-1} + \frac{1}{4} x_{n-2}, \quad (C-31)$$

where $\{x_{n-k}\}$ is the sequence $\{x_n\}$ delayed k clock periods, y_n is the output sample, and K_1 and K_2 are filter coefficients.

The discrete transfer function can therefore be written as

$$\begin{aligned} F(z) &= \frac{y(z)}{u(z)} \\ &= \frac{1}{4} \left(\frac{1 - 2z^{-1} + z^{-2}}{1 - K_1 z^{-1} - K_2 z^{-2}} \right). \end{aligned} \quad (C-32)$$

The response to a sampled sinusoid can be expressed as

$$\begin{aligned} H_1(f) &= F(z) \Big|_{z=e^{j2\pi f\Delta}} \\ &= \frac{1}{4} \left(\frac{1 + 2e^{-j2\pi f\Delta} + e^{-j4\pi f\Delta}}{1 - K_1 e^{-j2\pi f\Delta} - K_2 e^{-j4\pi f\Delta}} \right). \end{aligned} \quad (C-33)$$

It can then be shown that

$$|H_1(f)|^2 = \frac{\cos^4 \pi f \Delta}{\left(1 + K_1^2 + K_2^2\right) + 2K_1(K_2 - 1) \cos 2\pi f \Delta - 2K_2 \cos 4\pi f \Delta} \quad (C-34)$$

where Δ is the clock period for the filter (102.3 or 204.6 μ s). The complete filter is made up of two stages with different values for K_1 and K_2 . Thus, the composite filter can be represented by

$$H(f) = H_1(f) H_2(f). \quad (C-35)$$

The filtering algorithm produces samples of the process of interest, each sample spaced by Δ seconds. To reduce the burden in data recording, these sequences are downsampled by a factor of 16 or 8, depending on the mode of operation. If the analog waveform $s(t)$ represented by the original filter samples has a spectrum $S(f)$, then the downsampled sequence will have a spectrum

$$\tilde{S}(f) = \sum_{n=-\infty}^{\infty} S(f + nW) \quad (C-36)$$

with

$$\begin{aligned} W &= \text{output sample rate} \\ &= 610 \text{ Hz.} \end{aligned}$$

Of course, $S(f)$ consists of signal and noise after passage through the lowpass digital filter. Let $N(f)$ be the spectrum of the noise, $G(f)$ be the spectrum of the desired signal, and $H(f)$ be the filter transfer function. Then we have

$$S(f) = H(f)[G(f) + N(f)] \quad (C-37)$$

and

$$\tilde{S}(f) = \sum_{n=-\infty}^{\infty} H(f + nW)[G(f + nW) + N(f + nW)] \quad (C-38)$$

The spectral analysis of the tap samples yields an estimate of $\tilde{S}(f)$ over the range $-\frac{W}{2} < f < \frac{W}{2}$ and includes contributions due to aliasing from the tails of $S(f+nW)$ for each n . For the moment, we ignore the effects of windows used in the spectrum estimation algorithms and investigate the properties of the power spectrum determined directly from $\tilde{S}(f)$ of Eq. (38). The most straightforward procedure of estimating power spectra involves squaring and averaging. Thus, the expected value of the estimate $\hat{P}(f)$ will be:

$$\begin{aligned} E\{\hat{P}(f)\} &= E\{|\tilde{S}(f)|^2\} \\ &= E\left\{\left|\sum_{n=-\infty}^{\infty} H(f+nW)[G(f+nW)+N(f+nW)]\right|^2\right\} \\ &= E\left\{\left|\sum_n H(f+nW)G(f+nW)\right|^2 + \left|\sum_n H(f+nW)N(f+nW)\right|^2\right\}. \end{aligned} \quad (C-39)$$

The last relationship follows from the assumption of statistical independence of noise and scattered return. Expansion of each term in Eq. (39) yields products of the form:

$$H(f+nW)G(f+nW)H^*(f+mW)G^*(f+mW), \quad (C-40)$$

It is readily shown that the expected value of $G(f_1)G^*(f_2)$ is zero for $f_1 \neq f_2$, when the observation time interval is long compared with the correlation time of the equivalent tap process $g(t)$. Thus, Eq. (39) reduces to

$$E\{\hat{P}(f)\} = \sum_{n=-\infty}^{\infty} |H(f+nW)|^2 E\{|G(f+nW)|^2\} + \sum_{n=-\infty}^{\infty} |H(f+nW)|^2 E\{|N(f+nW)|^2\}. \quad (C-41)$$

If we denote the true spectrum by $P(f)$, i.e., the power spectrum for the tap process, and the noise power spectrum by N_0 , it is seen that

$$E\{\hat{P}(f)\} = \sum_{n=-\infty}^{\infty} |H(f+nW)|^2 P(f+nW) + N_0 \sum_{n=-\infty}^{\infty} |H(f+nW)|^2. \quad (C-42)$$

In the situations of interest, it should be noted that the filter characteristic $|H(f)|^2$ is only down 1 dB at the folding frequency of $\frac{W}{2}$. Figure C-4 illustrates the characteristic $|H(f)|^2$ for the 5-MHz multiplexed mode (filter B) plotted in dB below maximum gain. The resulting average noise background will have a shape indicated in Figure C-5, which represents the composite filter characteristic $\sum_{n=-\infty}^{\infty} |H(f+nW)|^2$. Its influence in shaping the noise floor can be accounted for in the data reduction programs. Shaping of the true spectrum $P(f)$ is not significant since $P(f)$ is likely to be contained within the 1-dB frequencies of $|H(f)|^2$, thus avoiding aliasing difficulties.

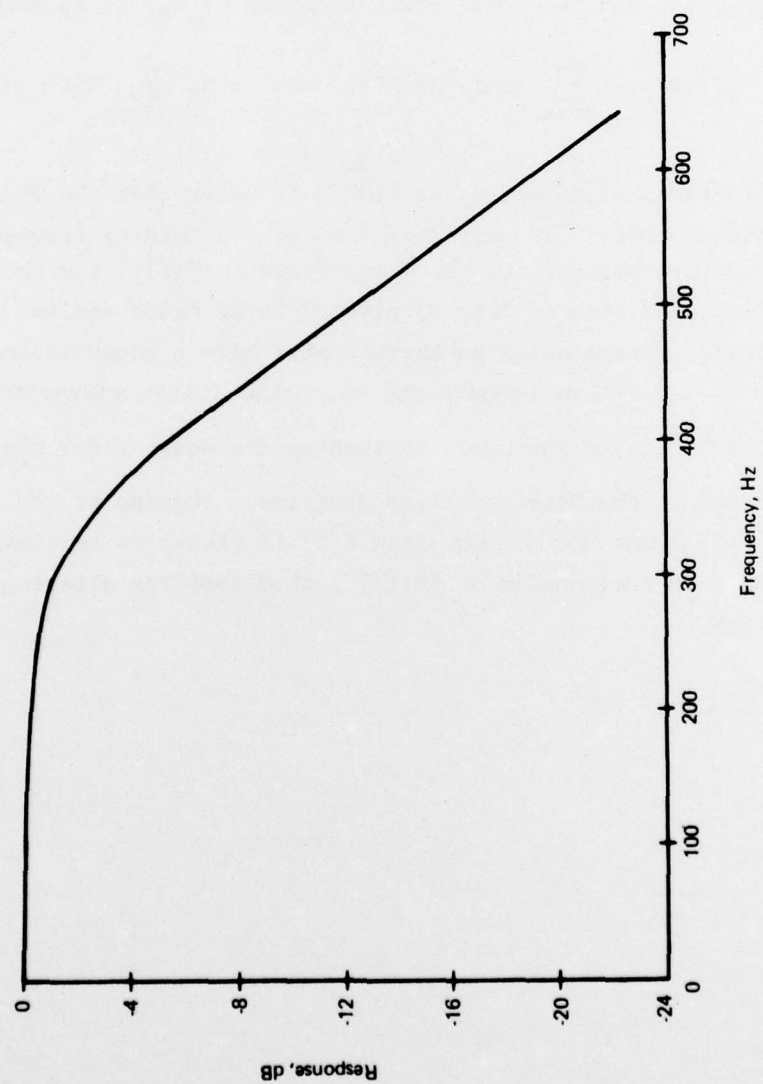


Figure C-4. Digital Filter B Frequency Response (5-MHz Clock Rate)

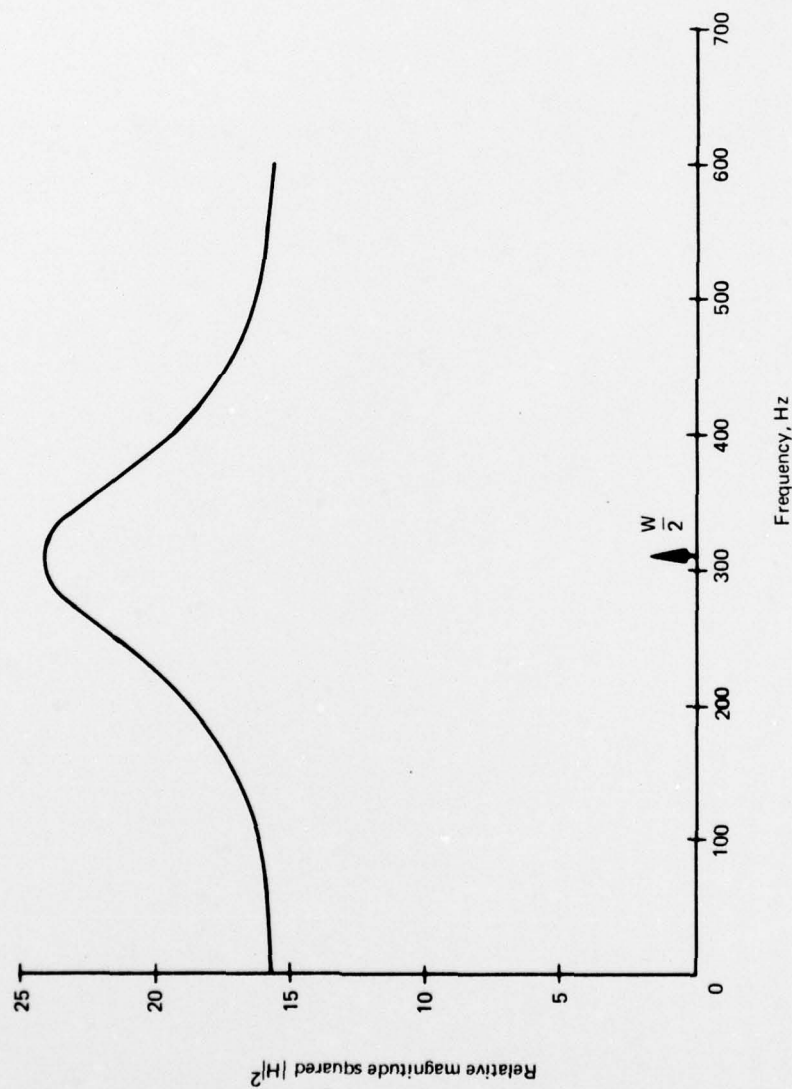


Figure C-5. Digital Filter Response With Aliasing